A Variational Framework for Gradient-Extended Dissipative Continua. Application to Damage Mechanics, Fracture, and Plasticity

Fabian Richard Welschinger

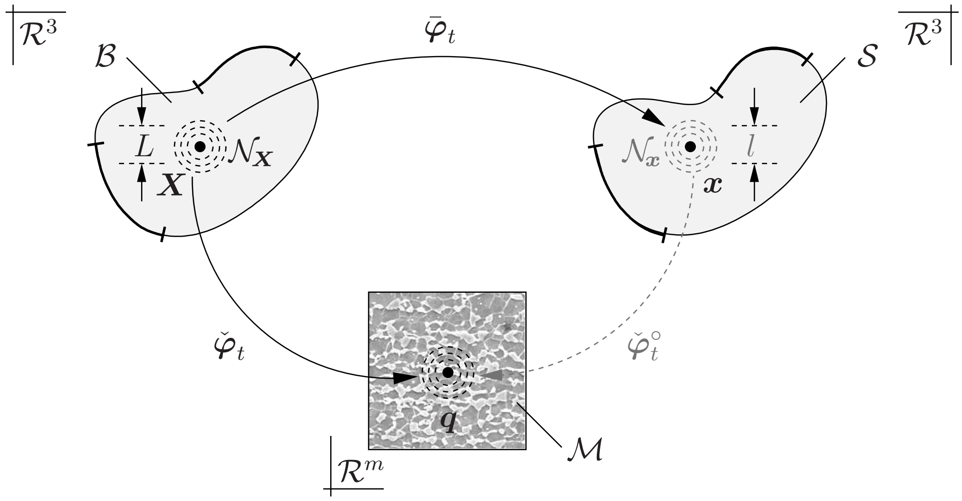
$\mathcal{R}^3$
$\bar{\boldsymbol{\varphi}}_t$
$\mathcal{R}^3$
$\mathcal{B}$
$\mathcal{S}$
L
$\mathcal{N}_{\boldsymbol{X}}$
$\boldsymbol{X}$
$\mathcal{N}_{\boldsymbol{x}}$
l
$\boldsymbol{x}$
$\breve{\boldsymbol{\varphi}}_t$
$\breve{\boldsymbol{\varphi}}_t^\circ$
$\boldsymbol{q}$
$\mathcal{M}$
$\mathcal{R}^m$

$$\{\bar{\boldsymbol{\varphi}}, \breve{\boldsymbol{\varphi}}\} = \arg\left\{ \inf_{\bar{\boldsymbol{\varphi}}} \inf_{\breve{\boldsymbol{\varphi}}} \left[\int_{\mathcal{B}} \pi^\tau(\nabla_{\boldsymbol{X}}\bar{\boldsymbol{\varphi}}, \breve{\boldsymbol{\varphi}}, \nabla_{\boldsymbol{X}}\breve{\boldsymbol{\varphi}})\, dV - W^\tau(\bar{\boldsymbol{\varphi}}, \breve{\boldsymbol{\varphi}}) \right] \right\}$$

Bericht Nr.: I-24 (2011)
Institut für Mechanik (Bauwesen), Lehrstuhl I
Professor Dr.-Ing. C. Miehe
Stuttgart 2011

A Variational Framework for Gradient-Extended Dissipative Continua. Application to Damage Mechanics, Fracture, and Plasticity

Von der Fakultät Bau- und Umweltingenieurwissenschaften
der Universität Stuttgart zur Erlangung der Würde
eines Doktor-Ingenieurs (Dr.-Ing.)
genehmigte Abhandlung

vorgelegt von

Fabian Richard Welschinger

aus Radolfzell am Bodensee

Hauptberichter: Prof. Dr.-Ing. Christian Miehe
Mitberichter : Prof. Dr. Samuel Forest

Tag der mündlichen Prüfung: 29. November 2010

Institut für Mechanik (Bauwesen) der Universität Stuttgart
2011

Herausgeber:
Prof. Dr.-Ing. habil. C. Miehe

Organisation und Verwaltung:

Institut für Mechanik (Bauwesen)
Lehrstuhl I
Universität Stuttgart
Pfaffenwaldring 7
70550 Stuttgart
Tel.: ++49–(0)711/685–66378
Fax : ++49–(0)711/685–66347

© Fabian Richard Welschinger
Institut für Mechanik (Bauwesen)
Lehrstuhl I
Universität Stuttgart
Pfaffenwaldring 7
70550 Stuttgart
Tel.: ++49–(0)711/685–69260
Fax : ++49–(0)711/685–66347

Alle Rechte, insbesondere das der Übersetzung in fremde Sprachen, vorbehalten. Ohne Genehmigung des Autors ist es nicht gestattet, dieses Heft ganz oder teilweise auf fotomechanischem Wege (Fotokopie, Mikrokopie) zu vervielfältigen.

ISBN 3-937859-12-8 (D 93 Stuttgart)

Zusammenfassung

Die vorliegende Arbeit befasst sich mit der Entwicklung eines konstitutiven Rahmens für gradientenbasierte standard dissipative Materialmodelle, die einem Variationsprinzip zu Grunde liegen. Ein Fokus liegt dabei auf der Formulierung theoretischer und computerorientierter Methoden zur Beschreibung von Größeneffekten in inelastischen Festkörpern. Im Mittelpunkt steht eine vereinheitlichende Theorie und die numerische Behandlung der inkrementellen Variationsformulierung, die im Verlauf der Arbeit auf eine breite Klasse von gradientenbasierten Materialmodellen mit intrinsischen Längenskalen angewandt wird. Mit diesen gekoppelten, symmetrischen Mehrfeldproblemen werden zunächst ein gradientenerweitertes Schädigungsmodell formuliert, das Nachteile lokaler Schädigungsmodelle in Hinblick auf Netzabhängigkeiten bei Finite Elemente Analysen überwindet. Eine zweite Anwendung des Variationsprinzips befasst sich mit der Phasenfeldmodellierung von Bruchvorgängen, die in der Lage ist krummlinige Risse, Rissverzweigungen und Rissbildung in Körpern frei von Imperfektionen abzubilden. Diese Formulierung vermeidet die Modellierung von scharfen Diskontinuitäten, wie sie in klassischen Ansätzen zur Bruchmechanik verwendet wird. Formal weist dieses Bruchmodell wesentliche Ähnlichkeiten zu dem zuvor diskutierten Schädigungsmodell auf. Eine Herausforderung bei der Phasenfeldmodellierung von Bruchvorgängen entsteht in Hinblick auf die approximative Beschreibung der Risstopologie. Genaue numerische Ergebnisse erfordern die Verwendung von hoch verdichteten Finite Elemente Netzen in der kritischen Risszone. Eine Verbesserung der numerischen Effizienz wird durch ein h-adaptives Verfahren erreicht, das ausschließlich durch diskrete materielle Kräfte gesteuert wird. Eine letzte Anwendung des entwickelten Prinzips beschäftigt sich mit phänomenologischer Plastizität mit gradientenerweiterter Verfestigung bei kleinen und großen Verformungen, die eine Regularisierung von Scherbändern und die Vorhersage des Hall-Petch Effekts ermöglicht.

Abstract

The thesis addresses the development of a variational-based framework for gradient-type standard dissipative solids. A focus lies on the design of theoretical and computational approaches towards the description of length-scale effects in inelastically deforming solids. A strong emphasis is put on a unifying theoretical and numerical treatment of the incremental variational formulation that is applied to a broad class of gradient-type solids with intrinsic length scales. The coupled, symmetric multi-field formulation is first used to model gradient-type damage mechanics that overcomes drawbacks of local constitutive damage models regarding mesh sensitivity. A second application of the variational-based framework for gradient-type solids is concerned with the phase field modeling of fracture, allowing for the prediction of curvilinear crack patterns, crack kinking, and crack initiation in solids free of imperfections. This formulation avoids the modeling of sharp discontinuities usually done in classical approaches towards fracture and turns out to be conceptually in line with the previously discussed model of gradient-type damage mechanics. A challenge of the phase field modeling of fracture arises with regard to the approximate description of the crack topology. Accurate results demand the employment of highly densified finite element meshes in the crack evolution zone. An improvement of the numerical efficiency is obtained by an h-adaptive solution procedure that is exclusively governed by discrete configurational forces. A last application of the proposed framework covers models of phenomenological plasticity with gradient-type hardening at small and large deformations. These models allow for the regularization of shear bands and the description of the so-called Hall-Petch effect.

Acknowledgments

The work presented in this thesis was carried out between 2005 and 2010, during which time I worked as a research associate at the Institute of Applied Mechanics (Civil Engineering) at the University of Stuttgart. Here I extend a few words of acknowledgment to the many people who have contributed in countless ways to the success of this work.

First of all, I would like to express my deep gratitude to Professor Christian Miehe for giving me the opportunity to work as an assistant lecturer in his research group and for the numerous fruitful discussions that contributed decisively to the achievement of this work. Another big thanks goes to Professor Samuel Forest for his interest in this project and his willingness to participate as the co-examiner for my doctoral thesis.

Next, I would like to thank all my colleagues from both chairs of the institute for the warm and friendly working atmosphere. Special thanks go to my officemates Dr. Dominik Zimmermann and Martina Hofacker for their friendship and support, not only in scientific, but also in personal matters. To my colleagues Ilona Frankenreiter and Felix Hildebrand I would like to convey my gratitude for their enthusiastic cooperation during the last few years and for their friendship.

I am deeply indebted to the former students Dominic Zäh, Malak Baydoun, and Axel Widmer who contributed significantly to my dissertation with their own diploma/master theses. The supervision of their theses was a true pleasure.

Furthermore, I would like to thank my girlfriend Tina Löffler for the motivation she provided and especially her patience during all these years.

Finally, I am very grateful to my parents Brigitte and Alois, my late grandmother Sophie, and my two brothers Patrick and Markus and their families. Regardless of the plans I have had over the past several years, I could have always been able to count on their unconditional love and support. Their encouragement has certainly given me the confidence to tackle such a project, and will always be remembered.

Stuttgart, January 2011 Fabian Welschinger

Contents

1. Introduction **1**

1.1. Motivation and State of the Art 1

1.2. Objectives and Overview 3

2. Fundamentals of Local Continuum Mechanics **7**

2.1. Kinematics of Finite Deformations 7

2.1.1. Basic Elements of Euclidian Base Systems 7

2.1.2. Geometric Setting and Motion of a Material Body 9

2.1.3. Material and Spatial Velocities and Accelerations 10

2.1.4. The Deformation Gradient and Deduced Mappings 11

2.1.5. Fundamental Strain Measures 15

2.2. Concept of Stresses and Heat Flux 16

2.2.1. Representations of the Stress Tensor 17

2.2.2. Heat Flux 18

2.3. Dual Stresses and Strains 19

2.4. Physical Balance Principles 19

2.4.1. Conservation of Mass 20

2.4.2. Balance of Linear Momentum 20

2.4.3. Balance of Angular Momentum 21

2.4.4. First Law of Thermodynamics. Balance of Energy 21

2.4.5. Second Law of Thermodynamics. Entropy Inequality Principle 22

3. Continuum Mechanics of Gradient-Type Dissipative Continua **25**

3.1. Generalized Kinematics of Solids with Microstructure 26

3.1.1. Notation 26

3.1.2. Extended Geometric Setting and Motion 26

3.1.3. Macro- and Microscopic Deformation Gradients 27

3.2. Concept of Generalized Stresses 29

3.3. Macro- and Microscopic Dual Stresses and Strains 31

3.4. External Loading of Continua with Microstructure 31

3.5. Constitutive Response of Order-Parameter Materials 32

3.5.1. Energy Storage and Dissipation 32

3.5.2. Material Frame Invariance. Effective State Variables 33
3.5.3. Rate of Energy Storage and Dissipation Functionals 34
3.5.4. Irreversibility Constraint and Convex Dissipation Function 35
3.5.5. Non-Smooth Dissipation Functions and Notion of Sub-Gradients . . 35
3.6. Exploitation of the Principle of Virtual Power 36
3.6.1. Coupled Two-Field Balances of Gradient-Type Solids 36
3.6.2. Coupled Three-Field Balance Equations of Gradient-Type Solids . . 37
3.6.3. Threshold-Function-Based Rate-Independent Coupled Balances . . . 39
3.6.4. Threshold-Function-Based Rate-Dependent Coupled Balances 40
3.7. Time-Discrete Incremental Variational Principles 41
3.7.1. Time-Discrete Field Variables in Incremental Setting 41
3.7.2. Incremental Energy, Dissipation, and Load Functionals 42
3.7.3. The Canonical Incremental Minimization Principle 44
3.7.4. The Extended Incremental Variational Principle 45
3.7.5. Rate-Independent Principle with Threshold Function 46
3.7.6. Rate-Dependent Principle with Threshold Function 48
3.7.7. Rate-Dependent Principle with Local History 49
3.8. Finite Element Discretization of Incremental Variational Principles 52
3.8.1. Canonical Incremental Minimization Principle 53
3.8.2. Extended Incremental Variational Principle 54
3.8.3. Extended Incremental Variational Principle with Local History . . . 55
3.9. Restriction to Geometric Linear Theory 57
3.9.1. Generalized Kinematics at Small Strains 57
3.9.2. Constitutive Response of Generalized Continua 58
3.9.3. Time-Discrete Incremental Variational Formulation 59
3.9.4. FE-Discretization of Incremental Variational Formulation 63

4. Variational-Based Formulation of Gradient-Type Damage 67
4.1. Material Instabilities and Mesh Sensitivity 67
4.1.1. Stability and Ellipticity 69
4.1.2. Localization and Mesh Sensitivity in One Dimension 71
4.2. Fundamentals of Continuum Damage Mechanics 74
4.3. Isotropic Strain-Gradient Damage Mechanics at Small Strains 76

4.3.1. Basic Kinematics and State Variables 76
4.3.2. Isotropic Degradation of Stored Bulk Energy 77
4.3.3. Dissipation Functions for Damage Evolution 78
4.3.4. Governing Balance Equations of Coupled Problem 80
4.3.5. Incremental Variational Principles for Gradient-Type Damage 81
4.3.6. FE-Discretization of Incremental Variational Principle 84
4.3.7. Numerical Examples. Regularization of Shear Bands 86

5. Variational-Based Phase Field Modeling of Fracture 91
5.1. A Review on Griffith's Energetic Approach to Fracture 92
5.2. Phase Field Approximation of Crack Topology 94
5.2.1. Motivation. One-Dimensional Cracked Bar 94
5.2.2. Variational Problem of Regularized Crack Topology 96
5.2.3. FE-Discretization of Variational Problem 96
5.2.4. Numerical Example. Approximation of Crack Topology 97
5.3. A Framework for Diffusive Fracture at Small Strains 98
5.3.1. Basic Kinematics and State Variables 98
5.3.2. Dissipation Functions for Crack Evolution 99
5.3.3. Degradation of Energy in Fracturing Solids 102
5.3.4. Governing Balance Equations of Coupled Problem 104
5.3.5. Incremental Variational Principles for Phase Field Fracture 106
5.3.6. FE-Discretization of Incremental Variational Principle 109
5.3.7. Numerical Examples. Crack Propagation in Solids 112

6. Material-Force-Based *h*-Adaptive Phase-Field-Type Fracture 121
6.1. Configurational Setting of Phase Field Fracture 121
6.1.1. Basic Kinematics with Structural Changes 122
6.1.2. Time Derivatives of Kinematic Objects 122
6.1.3. Dissipation Function for Crack Evolution 123
6.1.4. Anisotropic Degradation of Stored Bulk Energy 125
6.1.5. Governing Balance Equations in Physical and Material Space 125
6.2. Algorithmic Incremental Variational Principle 127
6.2.1. Time-Discrete Field Variables in an Incremental Sense 127
6.2.2. Incremental Energy, Dissipation, and Work Functionals 128

6.2.3. Incremental Variational Principle in Physical and Material Space . . 129
6.3. Finite Element Formulation of Incremental Variational Principle 131
6.3.1. Discrete Variational Principle in Physical and Material Space 131
6.3.2. Staggered Computation of Discrete Configurational Nodal Forces . . 132
6.3.3. Numerical Example. Evolving Discrete Material Forces 134
6.4. Material-Force-Based h-Adaptive Algorithm for Phase Field Fracture 135
6.4.1. Configurational-Force-Based Indicators for Mesh-Refinement 135
6.4.2. Staggered Solution Algorithm for Physical and Material Balances . . 137
6.4.3. Mesh Generation and Mapping of State Variables 138
6.4.4. Numerical Examples. h-Adaptive Phase Field Fracture 140

7. Variational-Based Gradient-Type von Mises Plasticity 147
7.1. Gradient-Type von Mises Plasticity at Small Strains 147
7.1.1. Basic Kinematics and State Variables 147
7.1.2. Energy Storage Mechanism 148
7.1.3. Threshold-Type Dissipation Functions 149
7.1.4. Governing Balance Equations of Coupled Problem 150
7.1.5. Incremental Variational Principle for Gradient-Type Plasticity 151
7.1.6. Fast Update Algorithm for Local Plastic Strains 153
7.1.7. FE-Discretization of Incremental Variational Principle 154
7.1.8. Numerical Examples. Regularization of Shear Bands 156
7.2. Additive Finite Plasticity in the Logarithmic Strain Space 159
7.2.1. Strain Measures based on Current Metric and Plastic Metric 159
7.2.2. Geometric Pre-Processing of the Logarithmic Strain Space 161
7.2.3. Constitutive Model in the Logarithmic Strain Space 162
7.2.4. Geometric Post-Processing of Lagrangian Objects 162
7.3. Gradient-Type von Mises Plasticity at Large Deformations 163
7.3.1. Basic Kinematics and State Variables 163
7.3.2. Incremental Variational Principle 163
7.3.3. Finite Element Discretization of Incremental Variational Principle . 164
7.3.4. Numerical Examples. Regularization of Shear Bands 166
7.3.5. Numerical Examples. Hall-Petch Effect 170

8. Conclusion 175

A. Gradient-Type Continua in Macroscopic Lagrangian Setting 177
  A.1. Time-Discrete Rate-Dependent Variational Principle 177
  A.2. Finite Element Discretization of Variational Principle 179

B. Enhanced Multi-Field Finite Element Formulations 181
  B.1. Enhanced Strain Formulation for Geometrically Linear Problems 181
    B.1.1. Time-Discrete Incremental Variational Formulation 181
    B.1.2. Algorithmic Finite Element Discretization of the Weak Form 182
  B.2. Enhanced Strain Formulation for Geometrically Nonlinear Problems 184
    B.2.1. Time-Discrete Incremental Variational Principle 185
    B.2.2. Finite-Element Discretization of Weak Form 186

References 189

1. Introduction

The overall goal of this work is to develop an incremental variational formulation for gradient-type standard dissipative solids. The focus thereby lies on the design of theoretical and computational approaches for the description of *size effects* and *length-scale effects* in inelastically deforming solids. A strong emphasis is put on a unifying theoretical and numerical treatment of the incremental variational formulation that can be applied to a broad class of gradient-type solids with intrinsic length scales. In order to demonstrate the performance of the incremental variational framework for gradient-type solids, applications in the fields of *(i) damage mechanics*, *(ii) phase field modeling of fracture*, and *(iii) gradient-type phenomenological plasticity* are investigated.

1.1. Motivation and State of the Art

In classical theories of local continuum mechanics, only the placement within the Euclidian space is assigned to each material patch. Changes in relative placements are evaluated to measure the local deformation of a material element. Following this methodology, the features of the material substructure are overlooked. In order to take into account the material's microstructure, besides the placement of a material point within the Euclidian space, *additional global fields* can be introduced that describe the substructural configuration of the material patch. Additional scalar-valued fields describe e.g. the volume fraction in porous media, vectorial fields are used to describe oriented media like rods and shells, and additional second order tensorial fields characterize e.g. Nye's tensor in dislocated continua. Hereby, the material's microstructure is associated with an *intrinsic length scale* yielding so-called *size effects* in the constitutive response. The additional fields are considered as *observable quantities* that together with the placement in the Euclidian space characterize the physical configuration of the solid. Associated with the additional fields, substructural interactions are introduced that depend on the nature of the material's microstructure. These interactions develop explicit power in the rate of the additional microscopic fields and perhaps of their gradient. As a consequence, additional balance equations have to be considered that describe the evolution of these additional microscopic fields and thus the state of the material's substructure. Another more classical possibility to take into account the material's microstructure is based on the introduction of *local internal variables* that are considered as *non-observable variables.* Thus, no additional mechanical power associated with the internal variables develops and no additional balance equations are evaluated. The driving forces, i.e. the derivatives of the free energy with respect to the internal variables and possibly with respect to their gradients, characterize no real substructural interactions. They are relations that only have to satisfy the second law of thermodynamics.

Following Eringen [37, 38], the departure from classical local theories begins with so-called *polar theories.* In these theories the material patches are considered as geometric objects that possess properties similar to *rigid* sub-bodies leading to so-called *micropolar media*, and *deformable* sub-bodies yielding the theory of *micromorphic media.* In this scenario, the additional fields are introduced as independent degrees of freedom characterized by a set of three vectors that are attached to the material patches. In micropolar theories, these vectors are considered as rigid directors, whereas in micromorphic theories they are considered deformable. Higher-order polar theories can be constructed by the introduction of tensors of arbitrary order that are attached to the material points.

Non-standard continuum theories for continua containing independent microstructural degrees of freedom can be traced back to the pioneering work by COSSERAT & COSSERAT [30] who considered the material sub-structure as a rigid body that can rotate independently of neighboring patches. This microscopic rigid body motion is characterized by a peculiar triad of rigid vectors. Couple stresses dual to the rotational degrees of freedom are introduced and taken into account by additional balance equations. The work by ERICKSEN & TRUESDELL [36] is concerned with a generalization of the Cosserat medium in view of the description of rods and shells. Here, each point is endowed by triads of mutually perpendicular vectors that, in contrast to the Cosserat medium, are considered as stretchable vectors. An extension of this idea towards the mechanics of elastic solids with microstructure can be found in the work by TOUPIN [171], see also MINDLIN [134]. In the work by MINDLIN [133], the very general concept of an elastic continuum each point of which is in itself a deformable medium has been introduced. If each micro-continuum is constrained to deform homogeneously, such a model reverts to the oriented medium with deformable directors suggested by ERICKSEN & TRUESDELL [36]. A comprehensive treatment and a classification of various theories for generalized continua can be found in the recent publications by FOREST & SIEVERT [47, 48] and FOREST [45].

However, all these types of multi-field theories for the description of generalized solids can be considered as specific classes of *continua with affine microstructure* as intensively discussed by CAPRIZ, PODIO-GUIDUGLI & WILLIAMS [24], CAPRIZ & PODIO-GUIDUGLI [23], CAPRIZ & VIRGA [25], and CAPRIZ [20, 21, 22] giving a sound mathematical basis for the definition of an order-parameter-based framework for continua with substructure. Continua with microstructure are regarded as refined mathematical models for a broad class of material bodies endowed with some sort of arbitrary microscopic order. In this scenario the material substructure influences the gross mechanical behavior of the solid, where additional fields are introduced capturing the microstructural state of the material. These fields are often denoted as *order parameters*, *phase fields*, *microstructural fields*, *micro displacements*, or *micro deformations*. Follow-up comprehensive treatments in this spirit with application to microcracked continua can be found in MARIANO & AUGUSTI [107], a more general description with extension to configurational mechanics in MARIANO [105, 106]. The book by FRÉMOND [51] offers a very general approach to gradient-type dissipative materials with an intense focus on the full thermodynamic setting. In all of these treatments, the critical point is to account for the *working of independent kinematic processes associated with the microstructure* of the material described by the micro structural fields. Hence substructural interactions are accompanied by explicit power expressions in the rate of the micro structural variables, yielding additional balance equations associated with the microstructure. As a consequence, the standard macro-balances of mass and momentum are coupled with an additional micro-balance equation, which governs a micro-force system associated with the order parameters. This perspective on generalized continua with microstructure builds the point of departure for the further development.

Representative examples of the above mentioned theoretical framework for continua with affine microstructure cover the works by FRIED & GURTIN [53] on phase transformations, FRÉMOND & NEDJAR [52] on gradient-type damage mechanics, and BOURDIN, FRANCFORT & MARIGO [17] on regularized brittle fracture. They all consider scalar-valued fields as microscopic order parameter field variables. Recent non-standard gradient-type formulations for theories of plasticity are also covered by the general framework for continua with microstructure. In this context, size effects associated with dislocation density induced lattice curvature are incorporated by this approach, see NYE [144], KRÖNER [94], ASHBY [5], FLECK, MULLER, ASHBY & HUTCHINSON [43], FLECK & HUTCHINSON [42], NIX & GAO [143], and ARZT [4]. Strain-gradient theories for single crystal plasticity that are based on additional micro-force balances are proposed by GURTIN [65, 66, 68], SVENDSEN [168], EVERS, BREKELMANS & GEERS [41], and in the recent work by FOREST [44]. Phenomenological theories for gradient-type plasticity with additional microstructural field variables are discussed in GURTIN [67], GUDMUNDSON [60], and ANAND, GURTIN, LELE & GETHING [3]. These contributions consider the working of the additional microstructural fields and derive additional microscopic balance equations that drive the evolution of the microstructural state of the material. However, a unifying theoretical and numerical treatment of an incremental variational formulation that governs this sort of gradient-type material response is still missing in literature.

Variational formulations for inelastic solid materials can be found in the works by ORTIZ & REPETTO [145], MIEHE [118], and CARSTENSEN, HACKL & MIELKE [26]. In the works by MIEHE, SCHOTTE & LAMBRECHT [127] and MIEHE, LAMBRECHT & GÜRSES [126] a general variational framework for local standard dissipative materials is outlined and applied to a variational based definition of homogenization and relaxation in dissipative solids. These minimization principles are considered as the key to the incremental response of inelastic solids. They exhibit basic features of standard dissipative materials such as formulated by BIOT [13], ZIEGLER & WEHRLI [182], GERMAIN [55], and HALPHEN & NGUYEN [76], which are exclusively based on two scalar valued functions, namely the energy storage function and the dissipation function. However, all these treatments can be related to local theories of inelasticity, where the evolution of the internal variables is governed by local evolution equations. First steps towards a generalization of the variational formulations towards strain-gradient theories are outlined in the works by MIELKE & MÜLLER [131], FRANCFORT & MIELKE [49], and MIELKE & ROUBÍČEK [132] for rate-independent plasticity and damage mechanics, respectively.

1.2. Objectives and Overview

The first part of the thesis is devoted to the outline of a general theoretical framework for gradient-type standard dissipative solids that is based on incremental variational formulations. An emphasis is thereby put on the unifying numerical implementation of the resulting *symmetric systems*. In the second part of the thesis, this general framework is applied to the description of specific classes of gradient-type standard dissipative solids.

The foundation for a *variational-based framework for gradient-type standard dissipative solids* is laid in **Chapter 3** and is conceptually in line with the recent work by MIEHE [120]. Hereby, a focus is put on the geometric setting and the mapping properties of the additional microscopic deformation- and strain-measures. A compact notation is introduced that points out the strict duality between macro- and microscopic motions, where the latter ones are identified as the above mentioned order-parameters. The rates of the macro- and microscopic fields characterize external power expressions that are balanced with internal power mechanisms. Focusing on gradient-type standard dissipative solids, the internal constitutive response is characterized by two constitutive functions, namely the energy storage and dissipation functions. The governing equations of the multi-field problem are obtained by a global form of the Clausius-Planck inequality, or alternatively as the

Euler equations of a continuous variational formulation expressed in the rate-arguments. However, the focus is directly put on a time-discrete incremental variational principle that yields an algorithmic version of the coupled macro- and microscopic balance equations. Depending on the nature of the dissipation function, these balance equations can take different representations that in the subsequent treatment are discussed in detail. This chapter closes with a *unifying finite element treatment* of the fully coupled multi-field problem for all possible representations of the dissipation function. Thereby, details of the matrix notation needed for the numerical treatment of the resulting *symmetric systems* are pointed out.

The objective of **Chapter 4** is the application of the previously developed framework for gradient-type standard dissipative solids to a model problem of *gradient-type damage mechanics*. The fundamental works by KACHANOV [90], LEMAITRE & CHABOCHE [99], LEMAITRE [98], and LEMAITRE & DESMORAT [100] provide a comprehensive introduction to continuum damage mechanics. Like other strain softening materials, damage mechanics shows the phenomenon of localization. An overview of this subject is given by FOREST & LORENTZ [46] and DE BORST[33], where the effect of material instability and the effect of mesh sensitivity are explained. Damage models that overcome the severe drawback of mesh-dependent results are based on a damage-gradient extension of the constitutive functions, see e.g. PEERLING, GEERS, DE BORST & BREKELMANS [147]. The model introduced in the underlying chapter exhibits similarities to the model of gradient-type damage discussed by FRÉMOND & NEDJAR [52]. In this work, the rate of damage and its gradient enter the power of internal forces as additional contributions. As a consequence, an additional balance equation is obtained that characterizes the evolution of the global damage field. This motivates the fitting of such types of damage formulations into the variational-based framework for gradient-type standard dissipative solids. The chapter is organized as follows. Initially, the effects of material instabilities and mesh sensitivity in strain softening solids are briefly summarized and the fundamentals of continuum damage mechanics are given. The basic kinematic relations are set up, an isotropic degradation of the stored bulk energy is suggested, and a rate-independent formulation of the dissipation function is introduced. Alternative smooth representations of the rate-independent/non-smooth dissipation function are discussed yielding a *penalty-type model I* and a *viscous over-force model II*. For these constitutive functions, the application of the incremental variational framework delivers the algorithmic representation of the governing balance equations and provides the basis for a unified numerical implementation. An investigation of the constitutive characteristics of both models shows that model II is more convenient regarding a numerical treatment. Thus, several mesh-objective numerical tests are performed for model II that demonstrate the performance of the gradient-type damage formulation regarding the regularization of shear bands.

In **Chapter 5**, a *thermodynamically consistent model of phase field fracture* is constructed that overcomes difficulties that arise in classical approaches to brittle fracture. This model is in line with the recent publication by MIEHE, WELSCHINGER & HOFACKER [130]. Of particular interest is a descriptive and comprehensive representation of the basic ingredients and the embedding of the proposed model into the very general theory of gradient-type standard dissipative solids. Theoretical foundations of classical brittle fracture can be found in the works by GRIFFITH [58], IRWIN [86], and BARENBLATT [6]. According to Griffith and Irwin, a crack propagates if the energy release rate reaches a critical value. Griffith's theory can predict when a crack propagates but cannot determine curvilinear crack patters, crack kinking, crack branching angles, or crack initiation in solids free of defects. These drawbacks can be overcome by variational-based energy minimization methods as suggested by FRANCFORT & MARIGO [50], BOURDIN, FRANCFORT & MARIGO [16], and DAL MASO & TOADER [31]. The regularized setting of their proposed theory is discussed in BOURDIN, FRANCFORT & MARIGO [16, 17] and is obtained by the method of Γ-convergence inspired by the work on image segmentation by MUMFORD & SHAH [137]. For details on Γ-convergent approximation of free discontinuity problems see AMBROSIO & TORTORELLI [2] and BRAIDES [18, 19]. In this spirit, a sharp crack surface topology in the solid is approximated by a diffusive crack zone characterized by an auxiliary variable. This variable is considered as a damage-like order-parameter field that interpolates between the unbroken and the broken state of the material. Conceptually similar approaches can be found in EASTGATE, SETHNA, RAUSCHER, CRETEGNY, CHEN & MYERS [35], KARMA, KESSLER & LEVINE [91], and HAKIM & KARMA [74] that can be considered as time-dependent viscous regularizations of the above mentioned theories of energy minimization based on a Ginzburg-Landau type evolution equation. These phase field approaches towards the modeling of brittle fracture avoid the modeling of sharp discontinuities but still have several drawbacks regarding the postulate of irreversibility and their restriction to boundary value problems where tensile stresses are present in the full solid domain. Starting with the approximate description of the crack topology by a crack surface functional, a rate-independent, gradient-type dissipation function is constructed that allows the crack topology to grow or to stay constant in time only. In analogy to the previous model problem of gradient-type damage, smooth representations of this dissipation function are introduced yielding *model I in a penalty-type two-field setting* and *model II in a viscous over-force formulation.* The isotropic formulation of the above mentioned theories of regularized fracture exhibit the problem of crack propagation in compression and tension. To improve this characteristic, an *anisotropic degradation of the stored energy* is introduced, which allows for the analysis of physically motivated, more complex boundary value problems. With these two constitutive functions at hand, the discrete incremental variational principle for gradient-type standard dissipative solids can be applied, which allows for the discussion of several numerical benchmark tests at the end of this chapter.

It is the purpose of **Chapter 6** to *improve the numerical efficiency* of the previously introduced phase field model of fracture. One challenge of phase field modeling of fracture arises when approximating the smooth crack topology. On the one hand the length scale parameter related to the crack surface functional has to be chosen as small as possible, which is on the other hand limited by the local element size. As a consequence, accurate results for a small length scale parameter are only obtained with a huge number of elements, especially in cases where the crack pattern is not known a priori and a uniform dense mesh has to be employed. A tremendous improvement of the numerical efficiency can be obtained by the *construction of an h-adaptive finite element solution scheme* that locally adapts the mesh during crack propagation. Basic ingredients of an h-adaptive solution scheme are the global and local mesh refinement indicators. In the underlying work such indicators are introduced that solely depend on discrete configurational forces. The concept of configurational mechanics describes the effect of forces acting on singularities, inhomogeneities, and defects. The probably most prominent application of configuration mechanics can be found in the description of material configurational forces acting on crack tip singularities in the sense of ESHELBY [39, 40] and RICE [152], see also MAUGIN [111], GURTIN [63, 64], Kienzler & Herrmann [92], Gurtin & Podio-Guidugli [72, 73], and Steinmann & Maugin [167] for a broader context. An exploitation of discrete configurational forces with regard to the construction of an h-adaptive method has been successfully developed by Zimmermann [184]. In order to construct a configurational force based h-adaptive algorithm, the configurational setting of phase field fracture is investigated and the governing dual balance equations in physical and material space derived. The focus hereby lies on *model II* introduced in the previous chapter. An algorithmic version of these coupled equations can alternatively be obtained by the design of an adequate incremental variational principle. Discrete configurational forces are obtained by the application of a *staggered numerical solution scheme*, where the balance in physical space is solved and the balance in material space simply evaluated. These discrete configurational forces are the point of departure for the design of an h-adaptive solution method.

Chapter 7 is concerned with the development of *gradient-type models of phenomenological plasticity* at small and large deformations. Similar phenomenological theories for gradient-type plasticity with additional microstructural field variables are discussed in the works by Gurtin [67], Gudmundson [60], and Anand, Gurtin, Lele & Gething [3]. In these contributions the working of the additional microstructural fields are taken into account and additional microscopic balance equations are derived that prescribe the evolution of the order-parameter fields. In a first part of this chapter, the constitutive equations for gradient-type J_2-plasticity are specified for the case of small deformations. The application of the incremental variational framework for gradient-type solids then provides the governing balance equations and delivers a unified finite element treatment of the coupled system. Two elementary numerical examples describing shear band formations confirm the mesh-objectivity of the proposed model. In view of an extension of the material model towards geometrically large deformations, a short summary of the additive approach to finite plasticity in the logarithmic strain space is given. This approach mainly bases on the developments by Miehe [116, 117] and Miehe, Apel & Lambrecht [121]. The latter work provides a modular structure that consists in its core of the initially introduced small strain material model for gradient-type plasticity. The logarithmic constitutive core is framed by purely geometric pre- and post-processing steps. This kinematic picture is embedded into the variational structure of gradient-type dissipative solids which on the one hand allows for an extremely compact notation and on the other hand for an effective numerical treatment of the resulting *symmetric system*. At the end of this chapter several numerical examples demonstrate the performance of the model with regard to the regularization of shear bands and the prediction of the so-called Hall-Petch effect.

2. Fundamentals of Local Continuum Mechanics

The purpose of this chapter is to give a short introduction to the concept of a continuous medium as a *macroscopic physical model* that is used to describe certain phenomena in deforming mechanical systems and builds the basis for a further development of the underlying work. Shortly, the basic notation of continuum mechanics, the kinematics, and the geometric setting are reiterated. The concepts of stresses and heat flux are discussed, allowing for the introduction of the essential governing balance laws. This chapter has an introductory character and is by no means complete. For further reading in this broad field of knowledge, the reader is referred to the textbooks on continuum mechanics by Başar & Weichert [7], Chadwick [27], Haupt [77], Holzapfel [83], Malvern [104], Marsden & Hughes [108], Salençon [155], Šilhavý [159], and Truesdell & Noll [172] and the textbooks on tensor algebra and analysis by Iben [84] and Itskov [87], only to mention a few among others.

2.1. Kinematics of Finite Deformations

This section aims at a straightforward understanding of the kinematics of continuous bodies undergoing large deformations that bases on modern terminologies of differential geometry and is closely related to the lecture notes by Miehe [119].

2.1.1. Basic Elements of Euclidian Base Systems. Regarding a unique identification of tensorial objects in the three-dimensional space, a reference frame has to be set up. A widely used coordinate system is the Cartesian coordinate system. In most cases it is sufficient for the description of continuum mechanical processes. Aiming at a precise geometric interpretation of the motion of material bodies, it is very illustrative to introduce arbitrary, convected coordinate systems that are discussed briefly in the sequel.

2.1.1.1. Orthonormal Base Systems. First, the focus is put on some basic elements of Cartesian coordinate systems. The standard Cartesian base vectors $\{\boldsymbol{e}_i\}_{i=1,2,3}$ of the three-dimensional space $\mathcal{R}^3$ satisfy the *orthonormality condition* and possess a *positive orientation* characterized by the inner product and the cross product

$$\boldsymbol{e}_i \cdot \boldsymbol{e}_j = \delta_{ij} \quad \text{and} \quad \boldsymbol{e}_i \times \boldsymbol{e}_j = \epsilon_{ijk}\, \boldsymbol{e}_k\,, \tag{2.1}$$

where δ_{ij} denotes the Kronecker delta and ϵ_{ijk} the permutation symbol with

$$\delta_{ij} := \begin{cases} 1 & \text{for } i = j \\ 0 & \text{otherwise} \end{cases} \quad \text{and} \quad \epsilon_{ijk} := \begin{cases} +1 & \text{for } (i,j,k) \text{ even} \\ -1 & \text{for } (i,j,k) \text{ odd} \\ \;\;0 & \text{otherwise}\,. \end{cases} \tag{2.2}$$

According to Einstein's convention two identical indices imply a summation.

2.1.1.2. Arbitrary Base Systems. Metric Tensors. In what follows, the above outlined Cartesian frame is extended to arbitrary base systems of the three-dimensional space $\mathcal{R}^3$. The assumption of orthonormal bases $(2.1)_1$ is dropped and *dual co- and contravariant base systems* $\{\boldsymbol{g}_i\}_{i=1,2,3}$ and $\{\boldsymbol{g}^i\}_{i=1,2,3}$ are introduced. The relation between their linearly independent base vectors of arbitrary length and orientation to a Cartesian reference *self dual base* $\{\boldsymbol{e}_i\}_{i=1,2,3}$ and $\{\boldsymbol{e}^i\}_{i=1,2,3}$ reads

$$\boldsymbol{g}_i := \boldsymbol{j} \cdot \boldsymbol{e}_i \quad \text{and} \quad \boldsymbol{g}^i := \boldsymbol{j}^{-T} \cdot \boldsymbol{e}^i\,. \tag{2.3}$$

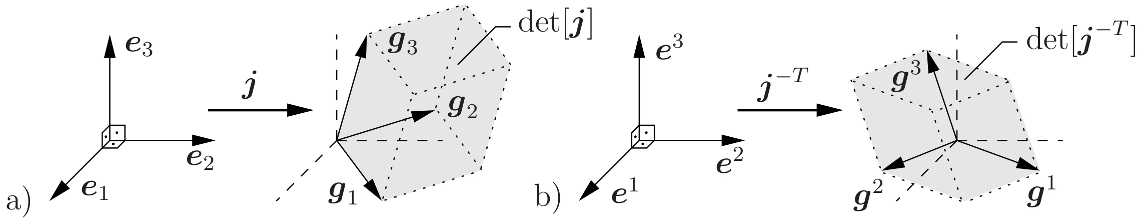

Figure 2.1: Definition of co- and contra-variant base vectors $\boldsymbol{g}_i = \boldsymbol{j} \cdot \boldsymbol{e}_i$ and $\boldsymbol{g}^i = \boldsymbol{j}^{-T} \cdot \boldsymbol{e}^i$ in a Cartesian self dual reference frame $\boldsymbol{e}_i = \boldsymbol{e}^i$.

The second-order tensor $\boldsymbol{j}$ is understood as a deformation that maps the Cartesian base vectors $\{\boldsymbol{e}_i\}_{i=1,2,3}$ onto the co-variant base vectors $\{\boldsymbol{g}_i\}_{i=1,2,3}$, see Figure 2.1a). As illustrated in Figure 2.1b), the adjoint tensor $\boldsymbol{j}^{-T}$ maps the Cartesian base vectors $\{\boldsymbol{e}^i\}_{i=1,2,3}$ onto the contra-variant base vectors $\{\boldsymbol{g}^i\}_{i=1,2,3}$. The mapping $\boldsymbol{j}$ and the adjoint mapping $\boldsymbol{j}^{-T}$ are constrained by the condition

$$\sqrt{g} := \det[\boldsymbol{j}] = \boldsymbol{g}_1 \cdot (\boldsymbol{g}_2 \times \boldsymbol{g}_3) > 0 \quad \text{and} \quad \frac{1}{\sqrt{g}} = \det[\boldsymbol{j}^{-T}] = \boldsymbol{g}^1 \cdot (\boldsymbol{g}^2 \times \boldsymbol{g}^3) > 0 \tag{2.4}$$

ensuring that the co- and contra-variant base vectors $\{\boldsymbol{g}_i\}_{i=1,2,3}$ and $\{\boldsymbol{g}^i\}_{i=1,2,3}$ are linearly independent and span parallelepipeds of volume $\sqrt{g}$ and $1/\sqrt{g}$, respectively. Based on definition (2.3), the dual bases satisfy the *generalized orthogonality condition*

$$\boldsymbol{g}^i \cdot \boldsymbol{g}_j = \boldsymbol{e}^i \cdot (\boldsymbol{j}^{-1}\,\boldsymbol{j}) \cdot \boldsymbol{e}_j = \boldsymbol{e}^i \cdot \boldsymbol{e}_j \quad \text{and} \quad \boldsymbol{g}_i \cdot \boldsymbol{g}^j = \boldsymbol{e}_i \cdot (\boldsymbol{j}^T\,\boldsymbol{j}^{-T}) \cdot \boldsymbol{e}^j = \boldsymbol{e}_i \cdot \boldsymbol{e}^j \tag{2.5}$$

allowing for the deduction of the fundamental reciprocal conditions

$$\boldsymbol{g}^i \cdot \boldsymbol{g}_j = \delta^i_{\;j} \quad \text{and} \quad \boldsymbol{g}_i \cdot \boldsymbol{g}^j = \delta_i^{\;j} \quad \text{with} \quad \delta^i_{\;j} = \delta_i^{\;j} = \delta^{ij} = \delta_{ij} \tag{2.6}$$

between the co- and contra-variant base vectors expressed in terms of the Kronecker delta as introduced in $(2.2)_1$. Here, the summation convention is applied as follows. When an index is diagonally repeated, a sum of all terms associated with the index values $i = 1, 2, 3$ is understood. From (2.3) it further follows that the columns of $\boldsymbol{j}$ and $\boldsymbol{j}^{-T}$ correspond to the co- and contra-variant base vectors

$$\boldsymbol{j} = \boldsymbol{g}_i \otimes \boldsymbol{e}^i = [\boldsymbol{g}_1, \boldsymbol{g}_2, \boldsymbol{g}_3] \quad \text{and} \quad \boldsymbol{j}^{-T} = \boldsymbol{g}^i \otimes \boldsymbol{e}_i = [\boldsymbol{g}^1, \boldsymbol{g}^2, \boldsymbol{g}^3]\,. \tag{2.7}$$

Assume the co-variant or the contra-variant base vectors to be known. By inversion of (2.7), their individual reciprocal counterparts are obtained via

$$\boldsymbol{g}^i \otimes \boldsymbol{e}_i = [\boldsymbol{g}_i \otimes \boldsymbol{e}^i]^{-T} \quad \text{and} \quad \boldsymbol{g}_i \otimes \boldsymbol{e}^i = [\boldsymbol{g}^i \otimes \boldsymbol{e}_i]^{-T}\,. \tag{2.8}$$

For a cyclic permutation of the indices (i, j, k), in combination with the generalized orthogonality condition (2.5), one can write

$$\boldsymbol{g}^i \cdot \boldsymbol{g}_l = c^i\,(\boldsymbol{g}_j \times \boldsymbol{g}_k) \cdot \boldsymbol{g}_l = \delta^i_{\;l} \quad \text{and} \quad \boldsymbol{g}_i \cdot \boldsymbol{g}^l = c_i\,(\boldsymbol{g}^j \times \boldsymbol{g}^k) \cdot \boldsymbol{g}^l = \delta_i^{\;l}\,. \tag{2.9}$$

Nonzero values are obtained for $i = l$ yielding the unknown coefficients $c^1 = c^2 = c^3 = 1/\sqrt{g}$ and $c_1 = c_2 = c_3 = \sqrt{g}$ and finally the crucial relationship

$$\boldsymbol{g}^i = \frac{1}{\sqrt{g}}\,\boldsymbol{g}_j \times \boldsymbol{g}_k \quad \text{and} \quad \boldsymbol{g}_i = \sqrt{g}\,\boldsymbol{g}^j \times \boldsymbol{g}^k \tag{2.10}$$

for even permutations of the indices (i, j, k). This gives a clear geometric interpretation for the construction of dual base vectors. From (2.10), the *cross products*

$$\boldsymbol{g}_i \times \boldsymbol{g}_j = \mathrm{e}_{ijk}\, \boldsymbol{g}^k \quad \text{and} \quad \boldsymbol{g}^i \times \boldsymbol{g}^j = \mathrm{e}^{ijk}\, \boldsymbol{g}_k \tag{2.11}$$

for co- and contra-variant base vectors are obtained, where the permutation symbols

$$\mathrm{e}_{ijk} := \sqrt{g}\, \epsilon_{ijk} \quad \text{and} \quad \mathrm{e}^{ijk} := \frac{1}{\sqrt{g}}\, \epsilon^{ijk} \quad \text{with} \quad \epsilon_{ijk} = \epsilon^{ijk} \tag{2.12}$$

are introduced, see also equation $(2.2)_2$. The inner product of the co- and contra-variant base vectors define the co- and contra-variant *metric coefficients*

$$g_{ij} := \boldsymbol{g}_i \cdot \boldsymbol{g}_j = \boldsymbol{e}_i \cdot (\boldsymbol{j}^T \boldsymbol{j}) \cdot \boldsymbol{e}_j \quad \text{and} \quad g^{ij} := \boldsymbol{g}^i \cdot \boldsymbol{g}^j = \boldsymbol{e}^i \cdot (\boldsymbol{j}^{-1} \boldsymbol{j}^{-T}) \cdot \boldsymbol{e}^j \,, \tag{2.13}$$

where the co- and contra-variant base vectors (2.3) have been employed. The Cartesian coordinates of the co- and contra-variant metric tensors

$$\boldsymbol{g} := \boldsymbol{j}^T \boldsymbol{j} = g_{ij}\, \boldsymbol{e}^i \otimes \boldsymbol{e}^j \quad \text{and} \quad \boldsymbol{g}^{-1} := \boldsymbol{j}^{-1} \boldsymbol{j}^{-T} = g^{ij}\, \boldsymbol{e}_i \otimes \boldsymbol{e}_j \tag{2.14}$$

are the dual metric coefficients in the Cartesian base system. Note that both are inverse to each other, i.e. $(\boldsymbol{j}^T \boldsymbol{j})^{-1} = \boldsymbol{j}^{-1} \boldsymbol{j}^{-T}$. The metric coefficients possess the important property of *index lowering* and *index raising*

$$\boldsymbol{g}_i = g_{ij}\, \boldsymbol{g}^j \quad \text{and} \quad \boldsymbol{g}^i = g^{ij}\, \boldsymbol{g}_j \,. \tag{2.15}$$

For known metric coefficients (2.13), the according dual base vectors

$$\boldsymbol{g}_i = (\boldsymbol{g}_i \cdot \boldsymbol{g}_j) \boldsymbol{g}^j = (\boldsymbol{g}^j \otimes \boldsymbol{g}_j) \cdot \boldsymbol{g}_i = \boldsymbol{1} \cdot \boldsymbol{g}_i \quad \text{and} \quad \boldsymbol{g}^i = (\boldsymbol{g}^i \cdot \boldsymbol{g}^j) \boldsymbol{g}_j = (\boldsymbol{g}_j \otimes \boldsymbol{g}^j) \cdot \boldsymbol{g}^i = \boldsymbol{1} \cdot \boldsymbol{g}^i \tag{2.16}$$

are obtained and the second-order identity tensor

$$\boldsymbol{g}^i \otimes \boldsymbol{g}_i = \boldsymbol{j}^{-T} (\boldsymbol{e}^i \otimes \boldsymbol{e}_i)\, \boldsymbol{j}^T = \boldsymbol{1} \quad \text{and} \quad \boldsymbol{g}_i \otimes \boldsymbol{g}^i = \boldsymbol{j}\, (\boldsymbol{e}_i \otimes \boldsymbol{e}^i)\, \boldsymbol{j}^{-1} = \boldsymbol{1} \tag{2.17}$$

can be identified, see also definition (2.3).

2.1.2. Geometric Setting and Motion of a Material Body. A *material body* is a physical object equipped with certain properties like texture, microstructure, etc. characterizing its behavior under loading. One key property of the body is that it occupies a certain domain in the Euclidian three-dimensional space $\mathcal{R}^3$. Mathematically speaking, a material body B consists of infinitely many *material points* $P \in B$ associated with geometric coordinates in the Euclidian space $\mathcal{R}^3$. The *motion of the body* B in $\mathcal{R}^3$ is determined by a one parameter family of placements

$$\boldsymbol{\chi}_t(P) : \begin{cases} B \to \mathcal{S} \subset \mathcal{R}^3 \\ P \mapsto \boldsymbol{x} = \boldsymbol{\chi}_t(P) \,. \end{cases} \tag{2.18}$$

At frozen time t, the map $\boldsymbol{\chi}_t(P)$ for $P \in B$ uniquely maps a material point P onto a coordinate triple $\boldsymbol{x} \in \mathcal{R}^3$. Regarding a description of the motion of a deformable solid, it is common sense to introduce at the initial time $t = t_0$ an arbitrarily chosen *reference configuration*, which in general possesses an undistorted, stress-free state

$$\boldsymbol{\chi}_{t_0}(P) : \begin{cases} B \to \mathcal{B} \subset \mathcal{R}^3 \\ P \mapsto \boldsymbol{X} = \boldsymbol{\chi}_{t_0}(P) \,. \end{cases} \tag{2.19}$$

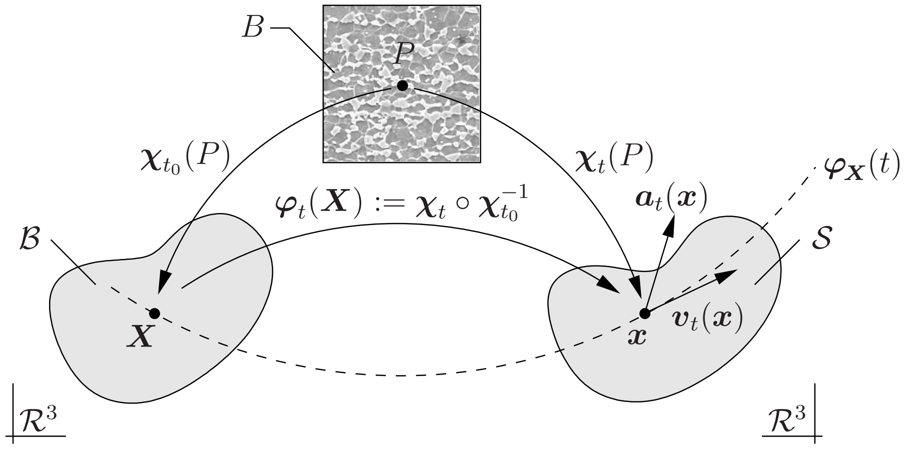
B
P
$\chi_{t_0}(P)$
$\chi_t(P)$
$\varphi_{\boldsymbol{X}}(t)$
$\boldsymbol{a}_t(\boldsymbol{x})$
$\varphi_t(\boldsymbol{X}) := \chi_t \circ \chi_{t_0}^{-1}$
$\mathcal{B}$
$\mathcal{S}$
$\boldsymbol{X}$
$\boldsymbol{x}$
$\boldsymbol{v}_t(\boldsymbol{x})$
$\mathcal{R}^3$
$\mathcal{R}^3$

Figure 2.2: The motion of a material body B in the Euklidian space $\mathcal{R}^3$ is governed by a one parameter family of placements χ_t. In a reference description of the *motion* $\varphi(\boldsymbol{X}, t)$, the *configuration* $\varphi_t(\boldsymbol{X})$ of the solid and the *path* $\varphi_{\boldsymbol{X}}(t)$ of a particle P are identified.

In what follows, the notation $\mathcal{B} := \chi_{t_0}(B)$ is introduced for the *reference*, *material* or *Lagrangian configuration* and $\mathcal{S} := \chi_t(B)$ is chosen for the *current*, *spatial* or *Eulerian configuration*. The corresponding reference and current positions of the material point P in the Euclidian space are denoted by $\boldsymbol{X} := \chi_{t_0}(P) \in \mathcal{B}$ and $\boldsymbol{x} := \chi_t(P) \in \mathcal{S}$, respectively. A relative description of the solid's motion is obtained by a composition of the mappings (2.18) and (2.19) defining the nonlinear *deformation map*

$$\varphi(\boldsymbol{X}, t) : \begin{cases} \mathcal{B} \times \mathcal{T} \to \mathcal{S} \\ (\boldsymbol{X}, t) \mapsto \boldsymbol{x} = \varphi(\boldsymbol{X}, t) := \chi_t \circ \chi_{t_0}^{-1}(\boldsymbol{X}) \, . \end{cases} \tag{2.20}$$

At current time $t \in \mathcal{R}_+$ a reference position $\boldsymbol{X} \in \mathcal{B}$ of the Lagrangian configuration is mapped onto its deformed spatial position $\boldsymbol{x} = \varphi_t(\boldsymbol{X}) \in \mathcal{S}$ in the Eulerian setting.

2.1.3. Material and Spatial Velocities and Accelerations. Based on the relative description of the motion (2.20), the following notation is introduced

$$\boldsymbol{x} = \varphi(\boldsymbol{X}, t) = \varphi_t(\boldsymbol{X}) = \varphi_{\boldsymbol{X}}(t) \, , \tag{2.21}$$

where $\varphi(\boldsymbol{X}, t)$ is the entire *motion* and $\varphi_t(\boldsymbol{X})$ the *configuration* of the solid at time t. The *path* of a particle P labeled by its Lagrangian position $\boldsymbol{X}$ is denoted by $\varphi_{\boldsymbol{X}}(t)$, see Figure 2.2. The *material velocity* and *material acceleration*

$$\boldsymbol{V}(\boldsymbol{X}, t) = \frac{d}{dt}\varphi_{\boldsymbol{X}}(t) = \frac{\partial}{\partial t}\varphi(\boldsymbol{X}, t) \quad \text{and} \quad \boldsymbol{A}(\boldsymbol{X}, t) = \frac{d^2}{dt^2}\varphi_{\boldsymbol{X}}(t) = \frac{\partial^2}{\partial t^2}\varphi(\boldsymbol{X}, t) \tag{2.22}$$

are spatial vector fields parametrized by the Lagrangian coordinates $\boldsymbol{X} \in \mathcal{B}$. The *spatial velocity* and *spatial acceleration* are spatial vector fields that are parametrized by the current position $\boldsymbol{x} \in \mathcal{S}$ obtained by a composition with the inverse motion

$$\boldsymbol{v}(\boldsymbol{x}, t) = \boldsymbol{V}(\boldsymbol{X}, t) \circ \varphi_t^{-1}(\boldsymbol{x}) \quad \text{and} \quad \boldsymbol{a}(\boldsymbol{x}, t) = \boldsymbol{A}(\boldsymbol{X}, t) \circ \varphi_t^{-1}(\boldsymbol{x}) \, . \tag{2.23}$$

Note that the material and spatial objects (2.22) and (2.23) are the same Eulerian objects, they only differ in their parametrization. Without knowing the motion $\varphi(\boldsymbol{X}, t)$, which is

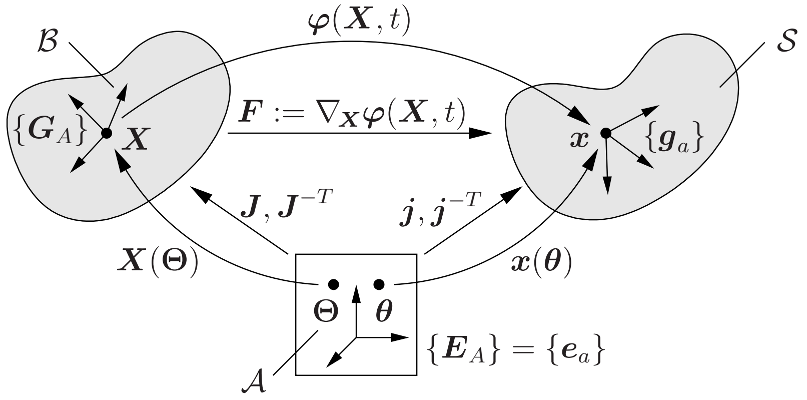
$\varphi(\boldsymbol{X},t)$
$\mathcal{B}$
$\mathcal{S}$
$\{\boldsymbol{G}_A\}$
$\boldsymbol{X}$
$\boldsymbol{F} := \nabla_{\boldsymbol{X}}\varphi(\boldsymbol{X},t)$
$\boldsymbol{x}$
$\{\boldsymbol{g}_a\}$
$\boldsymbol{J}, \boldsymbol{J}^{-T}$
$\boldsymbol{j}, \boldsymbol{j}^{-T}$
$\boldsymbol{X}(\boldsymbol{\Theta})$
$\boldsymbol{x}(\boldsymbol{\theta})$
$\boldsymbol{\Theta}$
$\boldsymbol{\theta}$
$\{\boldsymbol{E}_A\} = \{\boldsymbol{e}_a\}$
$\mathcal{A}$

Figure 2.3: Coordinate frame for the description of kinematic objects. *Curvilinear description* for $\boldsymbol{\Theta} \neq \boldsymbol{\theta}$ where the Lagrangian and Eulerian base vectors $\{\boldsymbol{G}_A\}$ and $\{\boldsymbol{g}_a\}$ are independent and *convective curvilinear description* for for $\boldsymbol{\Theta} = \boldsymbol{\theta}$ where the Eulerian base vectors $\{\boldsymbol{g}_a\}$ are the deformed images of $\{\boldsymbol{G}_A\}$.

the case e.g. in fluid mechanics, the material acceleration can alternatively be obtained by the *material time derivative* of the spatial velocity

$$\boldsymbol{a}(\boldsymbol{x},t) = \frac{d}{dt}\boldsymbol{v}(\boldsymbol{x},t) = \frac{\partial}{\partial t}\boldsymbol{v}(\boldsymbol{x},t) + \boldsymbol{l}\cdot\boldsymbol{v}(\boldsymbol{x},t) \quad \text{with} \quad \boldsymbol{l} := \nabla_{\boldsymbol{x}}\boldsymbol{v}(\boldsymbol{x},t) \tag{2.24}$$

exhibiting the classical split into a *local* and *convective part*. In addition, the *spatial velocity gradient* $\boldsymbol{l} := \nabla_{\boldsymbol{x}}\boldsymbol{v}$ can be identified that later plays an important role when introducing the work conjugate internal power expressions.

2.1.4. The Deformation Gradient and Deduced Mappings. The probably most fundamental object in the description of finite strain kinematics is the *deformation gradient*. It is defined by the *Fréchet derivative* of the nonlinear deformation map (2.20) with respect to the material coordinates

$$\boldsymbol{F} := \nabla_{\boldsymbol{X}}\varphi(\boldsymbol{X},t)\,. \tag{2.25}$$

So far no reference coordinate frame has been introduced to describe the nonlinear deformation map (2.20) and the associated deformation gradient (2.25). In what follows, the focus is put on a description of the geometric setup within the frame of *convective curvilinear coordinate systems*. It can be looked at as an extension of the concept of arbitrary base systems as introduced in Section 2.1.1.2. In convective curvilinear coordinate systems, the Lagrangian coordinate lines are oriented along material lines that are deformed together with the entire body. The spatial deformed images of these lines are identified with the Eulerian coordinate lines. This point of view is illustrated in Figure 2.3 for the case of equal Lagrangian and Eulerian curvilinear coordinates $\boldsymbol{\Theta} = \boldsymbol{\theta}$. Based on this idea, a *local parametrization* of a Lagrangian and Eulerian patch is introduced

$$\boldsymbol{X}(\boldsymbol{\theta}) : \begin{cases} \mathcal{A} \to \mathcal{B} \\ \boldsymbol{\theta} \mapsto \boldsymbol{X}(\boldsymbol{\theta}) \end{cases} \quad \text{and} \quad \boldsymbol{x}(\boldsymbol{\theta}) : \begin{cases} \mathcal{A} \to \mathcal{S} \\ \boldsymbol{\theta} \mapsto \boldsymbol{x}(\boldsymbol{\theta})\,, \end{cases} \tag{2.26}$$

in terms of the curvilinear coordinates $\boldsymbol{\theta} \in \mathcal{A}$ belonging to the parameter space $\mathcal{A}$. The associated linear mappings

$$\boldsymbol{J} = \nabla_{\boldsymbol{\theta}}\boldsymbol{X} = [\boldsymbol{G}_1, \boldsymbol{G}_2, \boldsymbol{G}_3] \quad \text{and} \quad \boldsymbol{J}^{-T} = [\boldsymbol{G}^1, \boldsymbol{G}^2, \boldsymbol{G}^3] \tag{2.27}$$

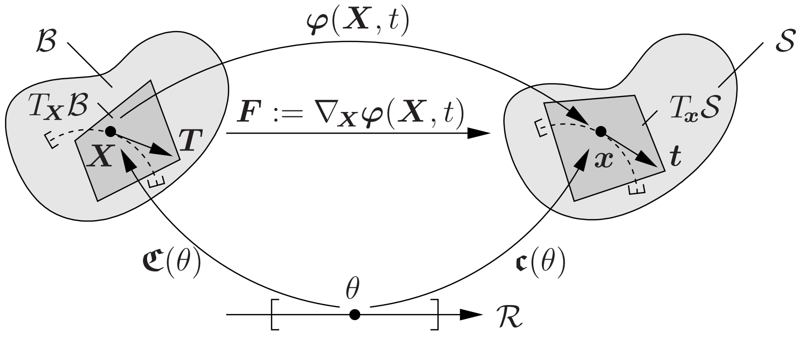
$\mathcal{B}$
$\varphi(\boldsymbol{X},t)$
$\mathcal{S}$
$T_{\boldsymbol{X}}\mathcal{B}$
$\boldsymbol{F} := \nabla_{\boldsymbol{X}}\varphi(\boldsymbol{X},t)$
$T_{\boldsymbol{x}}\mathcal{S}$
$\boldsymbol{X}$
$\boldsymbol{T}$
$\boldsymbol{x}$
$\boldsymbol{t}$
$\mathfrak{C}(\theta)$
$\mathfrak{c}(\theta)$
θ
$\mathcal{R}$

Figure 2.4: The deformation gradient $\boldsymbol{F}_t$ linearly maps tangents $\boldsymbol{T} \in T_{\boldsymbol{X}}\mathcal{B}$ to material curves $\mathfrak{C}(\theta)$ at $\boldsymbol{X}$ onto tangents $\boldsymbol{t} \in T_{\boldsymbol{x}}\mathcal{S}$ to deformed material curves $\mathfrak{c}(\theta) := \varphi_t(\mathfrak{C}(\theta))$ at $\boldsymbol{x}$.

locally characterize the Lagrangian dual co- and contra-variant base vectors attached to the Lagrangian position $\boldsymbol{X} \in \mathcal{B}$. The linear mappings

$$\boldsymbol{j} = \nabla_{\boldsymbol{\theta}}\boldsymbol{x} = [\boldsymbol{g}_1, \boldsymbol{g}_2, \boldsymbol{g}_3] \quad \text{and} \quad \boldsymbol{j}^{-T} = [\boldsymbol{g}^1, \boldsymbol{g}^2, \boldsymbol{g}^3] \tag{2.28}$$

locally determine the *time* and *deformation dependent* Eulerian dual co- and contra-variant base vectors attached to the Eulerian position $\boldsymbol{x} \in \mathcal{S}$. Obviously, the natural Eulerian base vectors are not independent of the Lagrangian base vectors, they are their deformed images. For a geometric interpretation of the linear mappings (2.27) and (2.28) see Figure 2.1. Focus now on one single material curve in the Lagrangian configuration $\mathfrak{C}(\theta)$ and its deformed Eulerian counterpart $\mathfrak{c}(\theta,t) = \varphi(\mathfrak{C}(\theta),t)$, parametrized by the scalar curvilinear coordinate θ, see Figure 2.4 for an illustration. The tangent to this curve with base point $\boldsymbol{X}(\theta) \in \mathfrak{C}(\theta)$ deforms via

$$\boldsymbol{t} = \frac{d}{d\theta}\mathfrak{c}(\theta,t) = \nabla_{\boldsymbol{X}}\varphi(\mathfrak{C}(\theta),t)\frac{d}{d\theta}\mathfrak{C}(\theta) = \boldsymbol{F}\boldsymbol{T} \tag{2.29}$$

and delivers a precise geometric interpretation of the deformation gradient. All tangent vectors to undeformed Lagrangian material curves $\boldsymbol{T}$ with base point $\boldsymbol{X}$ live in the tangent space $T_{\boldsymbol{X}}\mathcal{B}$ spanned by the Lagrangian co-variant base vectors $\{\boldsymbol{G}_A\}_{A=1,2,3}$. Tangents to the deformed Eulerian curves $\boldsymbol{t}$ with base point $\boldsymbol{x} = \varphi(\boldsymbol{X},t)$ live in the tangent space $T_{\boldsymbol{x}}\mathcal{S}$ spanned by the Eulerian co-variant base vectors $\{\boldsymbol{g}_a\}_{a=1,2,3}$. Thus, the deformation gradient can be identified as the *tangent map*

$$\boldsymbol{F} : \left\{ \begin{array}{lll} T_{\boldsymbol{X}}\mathcal{B} & \rightarrow & T_{\boldsymbol{x}}\mathcal{S} \\ \boldsymbol{T} & \mapsto & \boldsymbol{t} = \boldsymbol{F}\boldsymbol{T} \end{array} \right. \tag{2.30}$$

between the tangent spaces $T_{\boldsymbol{X}}\mathcal{B}$ and $T_{\boldsymbol{x}}\mathcal{S}$ of the manifolds $\mathcal{B}$ and $\mathcal{S}$, respectively. In convective curvilinear coordinates, the constant linear maps (2.27) and the deformation dependent linear maps (2.28) characterize the deformation gradient

$$\boldsymbol{F} := \boldsymbol{j}\boldsymbol{J}^{-1}\,. \tag{2.31}$$

Exploitation of (2.7) for arbitrary Lagrangian and Eulerian co- and contra-variant base vectors yields the deformation gradient in convective curvilinear coordinates

$$\boldsymbol{F} = (\boldsymbol{g}_a \otimes \boldsymbol{e}^a)\,(\boldsymbol{E}_A \otimes \boldsymbol{G}^A) = {\delta^a}_A\, \boldsymbol{g}_a \otimes \boldsymbol{G}^A\,. \tag{2.32}$$

Note that in this representation the coordinates of the mixed-variant tensor $\boldsymbol{F}$ simply correspond to the Kronecker delta. All the information about the deformation is stored in the convected, deformation dependent current base vectors.

When *curvilinear coordinates* are employed, the Lagrangian and Eulerian configurations are parametrized independently with $\boldsymbol{\Theta} \neq \boldsymbol{\theta}$. Thus, the re-parametrization is introduced

$$\boldsymbol{X}(\boldsymbol{\Theta}) : \begin{cases} \mathcal{A} \to \mathcal{B} \\ \boldsymbol{\Theta} \mapsto \boldsymbol{X}(\boldsymbol{\Theta}) \end{cases} \quad \text{and} \quad \boldsymbol{x}(\boldsymbol{\theta}) : \begin{cases} \mathcal{A} \to \mathcal{S} \\ \boldsymbol{\theta} \mapsto \boldsymbol{x}(\boldsymbol{\theta}) \, , \end{cases} \tag{2.33}$$

in terms of the curvilinear Lagrangian $\boldsymbol{\Theta} \in \mathcal{A}$ and Eulerian $\boldsymbol{\theta} \in \mathcal{A}$ coordinates, both belonging to the parameter space $\mathcal{A}$. The associated linear mappings

$$\boldsymbol{J} = \nabla_{\boldsymbol{\Theta}} \boldsymbol{X} = [\boldsymbol{G}_1, \boldsymbol{G}_2, \boldsymbol{G}_3] \quad \text{and} \quad \boldsymbol{J}^{-T} = [\boldsymbol{G}^1, \boldsymbol{G}^2, \boldsymbol{G}^3] \tag{2.34}$$

characterize the Lagrangian dual co- and contra-variant base vectors locally at the Lagrangian position $\boldsymbol{X} \in \mathcal{B}$. The linear mappings

$$\boldsymbol{j} = \nabla_{\boldsymbol{\theta}} \boldsymbol{x} = [\boldsymbol{g}_1, \boldsymbol{g}_2, \boldsymbol{g}_3] \quad \text{and} \quad \boldsymbol{j}^{-T} = [\boldsymbol{g}^1, \boldsymbol{g}^2, \boldsymbol{g}^3] \tag{2.35}$$

determine the *constant* Eulerian dual co- and contra-variant base vectors locally at $\boldsymbol{x} \in \mathcal{S}$. As a consequence, the base vectors in the Eulerian configuration can not be considered as deformed images of the Lagrangian base vectors. Therefore, the linear mappings (2.35) are independent of (2.34), they only provide the metric tensors that are necessary for the evaluation of tensor operations in curvilinear coordinate systems. Following (2.14), they are evaluated in the Lagrangian setting via

$$\boldsymbol{G} = \boldsymbol{J}^T \boldsymbol{J} = G_{AB} \, \boldsymbol{G}^A \otimes \boldsymbol{G}^B \quad \text{and} \quad \boldsymbol{G}^{-1} = \boldsymbol{J}^{-1} \boldsymbol{J}^{-T} = G^{AB} \, \boldsymbol{G}_A \otimes \boldsymbol{G}_B \tag{2.36}$$

and accordingly in the Eulerian configuration via

$$\boldsymbol{g} = \boldsymbol{j}^T \boldsymbol{j} = g_{ab} \, \boldsymbol{g}^a \otimes \boldsymbol{g}^b \quad \text{and} \quad \boldsymbol{g}^{-1} = \boldsymbol{j}^{-1} \boldsymbol{j}^{-T} = g^{ab} \, \boldsymbol{g}_a \otimes \boldsymbol{g}_b \, . \tag{2.37}$$

Note that in (2.36) and (2.37) the metric coefficients are given with respect to their curvilinear basis. In this setting the mixed variant deformation gradient

$$\boldsymbol{F} = F^a_{\ A} \, \boldsymbol{g}_a \otimes \boldsymbol{G}^A \tag{2.38}$$

is based on its mixed curvilinear coordinates $F^a_{\ A} = \partial x^a / \partial X^A$ in arbitrary Lagrangian and Eulerian base systems that are independent of each other.

When choosing a *Cartesian reference system*, the above explanations simplify significantly. The Cartesian reference system is obtained by evaluation of the parametrization (2.33) for the case $\boldsymbol{\Theta} = \boldsymbol{X}$ and $\boldsymbol{\theta} = \boldsymbol{x}$. In this case, the linear mappings (2.34) and (2.35) reduce to the identity map leading to the simple representation of the metric tensors

$$\boldsymbol{G} = \boldsymbol{J}^T \boldsymbol{J} = \delta_{AB} \, \boldsymbol{E}^A \otimes \boldsymbol{E}^B \quad \text{and} \quad \boldsymbol{G}^{-1} = \boldsymbol{J}^{-1} \boldsymbol{J}^{-T} = \delta^{AB} \, \boldsymbol{E}_A \otimes \boldsymbol{E}_B \tag{2.39}$$

in the Lagrangian setting and in analogy for the Eulerian configuration

$$\boldsymbol{g} = \boldsymbol{j}^T \boldsymbol{j} = \delta_{ab} \, \boldsymbol{e}^a \otimes \boldsymbol{e}^b \quad \text{and} \quad \boldsymbol{g}^{-1} = \boldsymbol{j}^{-1} \boldsymbol{j}^{-T} = \delta^{ab} \, \boldsymbol{e}_a \otimes \boldsymbol{e}_b \, . \tag{2.40}$$

With these definitions at hand, the deformation gradient

$$\boldsymbol{F} = F^a_{\ A}\,\boldsymbol{e}_a \otimes \boldsymbol{E}^A \tag{2.41}$$

is expressed in terms of its Cartesian components $F^a_{\ A} = \partial x^a / \partial X^A$. In what follows Cartesian coordinates are employed with keeping in mind the above geometric interpretations.

In a proceeding step, *material surfaces* are considered that are embedded into the solid. Following the concept of tangents to material curves, see Figure 2.4, a combination of two Lagrangian tangents $\boldsymbol{T}_1$ and $\boldsymbol{T}_2$ is considered. Their cross product defines the *area vector* $\boldsymbol{A} = \boldsymbol{T}_1 \times \boldsymbol{T}_2 = \boldsymbol{N} A$, expressed in terms of the normal vector $\boldsymbol{N}$. Due to the placement of the normal's index, see the cross product's fundamental definition (2.11), the normal can be identified as an object of the Lagrangian co-tangent space $T^*_{\boldsymbol{X}}\mathcal{B}$. The mapping of the normal $\boldsymbol{N}$ onto the Eulerian co-tangent space $T^*_{\boldsymbol{x}}\mathcal{S}$ is given by the *normal map*

$$\boldsymbol{F}^{-T} : \begin{cases} T^*_{\boldsymbol{X}}\mathcal{B} \to T^*_{\boldsymbol{x}}\mathcal{S} \\ \boldsymbol{N} \quad\ \mapsto \boldsymbol{n} = \boldsymbol{F}^{-T}\,\boldsymbol{N}\,. \end{cases} \tag{2.42}$$

Here, the co-tangent space $T^*_{\boldsymbol{X}}\mathcal{B}$ is spanned by the contra-variant base vectors $\{\boldsymbol{G}^A\}_{A=1,2,3}$ and the Eulerian co-tangent space $T^*_{\boldsymbol{x}}\mathcal{S}$ by the contra-variant base vectors $\{\boldsymbol{g}^a\}_{a=1,2,3}$. The area element A is mapped via the *Jacobian determinant* $J := \det[\boldsymbol{F}]$ by the *area map*

$$J : \begin{cases} \mathcal{R}_+ \to \mathcal{R}_+ \\ A \quad \mapsto a = J\,A\,. \end{cases} \tag{2.43}$$

Combination of the normal map (2.42) and the area map (2.43) yields *Nanson's formula*

$$\boldsymbol{n}\,a = J\boldsymbol{F}^{-T}\boldsymbol{N}\,A = \operatorname{cof}[\boldsymbol{F}]\,\boldsymbol{N}\,A \quad \text{with} \quad J\,\boldsymbol{F}^{-T} = \operatorname{cof}[\boldsymbol{F}]\,. \tag{2.44}$$

The volume of a parallelepiped spanned by three linearly independent Lagrangian tangents $\boldsymbol{T}_1$, $\boldsymbol{T}_2$, and $\boldsymbol{T}_3$ is given by the product $V = (\boldsymbol{T}_1 \times \boldsymbol{T}_2) \cdot \boldsymbol{T}_3$. The volume of the deformed parallelepiped is determined by the *volume map*

$$J : \begin{cases} \mathcal{R}_+ \to \mathcal{R}_+ \\ V \quad \mapsto v = J\,V \end{cases} \tag{2.45}$$

which, in analogy to (2.43), is characterized by the Jacobian determinant. So far, the mappings (2.30) and (2.42) have been identified as mappings between the Lagrangian and Eulerian tangent and co-tangent spaces, respectively. For instance when measuring the length of a Lagrangian vector, the reference metric has to be known. To this end, consider the Lagrangian tangent $\boldsymbol{T} \in T_{\boldsymbol{X}}\mathcal{B}$ that possesses the length

$$|\boldsymbol{T}|_{\boldsymbol{G}} = \sqrt{\boldsymbol{T}\,(\boldsymbol{G}\,\boldsymbol{T})} = \sqrt{T^A G_{AB} T^B} = \sqrt{T^A N_A} = \sqrt{\boldsymbol{T}\,\boldsymbol{N}}\,, \tag{2.46}$$

where the normal $\boldsymbol{N} = \boldsymbol{G}\boldsymbol{T} \in T^*_{\boldsymbol{X}}\mathcal{B}$ is considered as an element of the co-tangent space of the Lagrangian configuration. Vice versa, when measuring the length of an Eulerian tangent $\boldsymbol{t} \in T_{\boldsymbol{x}}\mathcal{S}$, the current metric has to be known

$$|\boldsymbol{t}|_{\boldsymbol{g}} = \sqrt{\boldsymbol{t}\,(\boldsymbol{g}\,\boldsymbol{t})} = \sqrt{t^a g_{ab} t^b} = \sqrt{t^a n_a} = \sqrt{\boldsymbol{t}\,\boldsymbol{n}}\,. \tag{2.47}$$

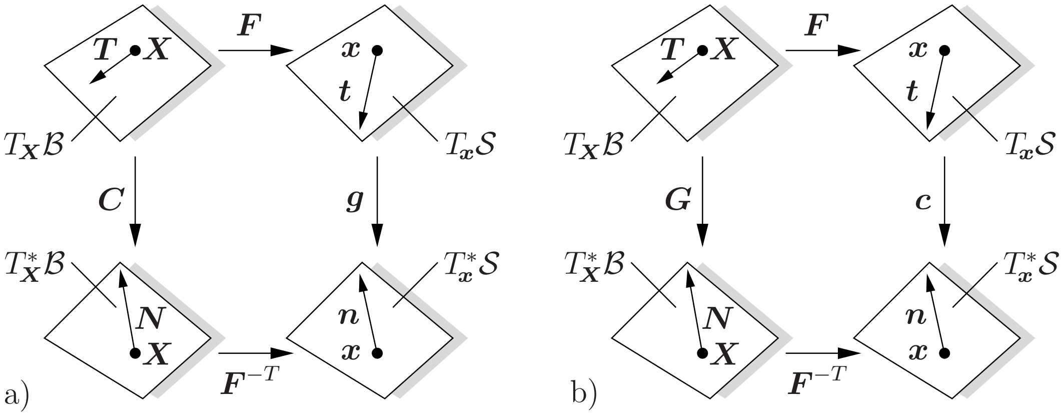

Figure 2.5: Mapping properties of fundamental metric tensors. a) Right Cauchy Green tensor $\boldsymbol{C}$ as *pull back* $\boldsymbol{\varphi}^*(\boldsymbol{g}) = \boldsymbol{F}^T\boldsymbol{g}\boldsymbol{F}$ of spatial metric $\boldsymbol{g}$ and b) left Cauchy Green tensor $\boldsymbol{c}$ as *push forward* $\boldsymbol{\varphi}_*(\boldsymbol{G}) = \boldsymbol{F}^{-T}\boldsymbol{G}\boldsymbol{F}^{-1}$ of reference metric $\boldsymbol{G}$.

The normal $\boldsymbol{n} = \boldsymbol{g}\boldsymbol{t} \in T^*_{\boldsymbol{x}}\mathcal{S}$ is considered as an element of the co-tangent space of the Eulerian configuration. As a consequence, the following mapping properties are assigned to the Lagrangian and Eulerian metric tensors

$$\boldsymbol{G} := \begin{cases} T_{\boldsymbol{X}}\mathcal{B} \to T^*_{\boldsymbol{X}}\mathcal{B} \\ \boldsymbol{T} \quad \mapsto \boldsymbol{N} = \boldsymbol{G}\boldsymbol{T} \end{cases} \quad \text{and} \quad \boldsymbol{g} := \begin{cases} T_{\boldsymbol{x}}\mathcal{S} \to T^*_{\boldsymbol{x}}\mathcal{S} \\ \boldsymbol{t} \quad \mapsto \boldsymbol{n} = \boldsymbol{g}\boldsymbol{t}\,. \end{cases} \tag{2.48}$$

Note in this context the index raising and index lowering properties of the symmetric, positive definite metric tensors (2.15). In many textbooks N_A and T^A are the Lagrangian and n_a and t^a the Eulerian co- and contra-variant coordinates of the same vectors. In what follows the normals and tangents are considered as different geometric objects associated with the co-tangent and tangent spaces.

2.1.5. Fundamental Strain Measures. In a *Lagrangian strategy*, the deformation of a Lagrangian unit vector $\boldsymbol{T}$ with $|\boldsymbol{T}|_{\boldsymbol{G}} = 1$ is investigated. The deformed Eulerian stretch vector can be expressed by $\boldsymbol{\lambda} = \boldsymbol{F}\boldsymbol{T}$ and its scalar valued stretch reads

$$\lambda := |\boldsymbol{\lambda}|_{\boldsymbol{g}} = \sqrt{\boldsymbol{\lambda}\,\boldsymbol{g}\,\boldsymbol{\lambda}} = \sqrt{\boldsymbol{T}\,(\boldsymbol{F}^T\boldsymbol{g}\boldsymbol{F})\,\boldsymbol{T}} = \sqrt{\boldsymbol{T}\,\boldsymbol{C}\,\boldsymbol{T}} = |\boldsymbol{T}|_{\boldsymbol{C}}\,. \tag{2.49}$$

Here, the *right Cauchy Green tensor* $\boldsymbol{C}$ is introduced that links the tangent and the co-tangent spaces in the sense of an *Eulerian metric* $\boldsymbol{g}$ *in the Lagrangian configuration.* It is obtained by the so-called *pull back* operation of the Eulerian metric

$$\boldsymbol{C} := \boldsymbol{\varphi}^*(\boldsymbol{g}) = \boldsymbol{F}^T\boldsymbol{g}\boldsymbol{F} \quad \text{or} \quad C_{AB} = F^a_{\ A}\, g_{ab}\, F^b_{\ B}\,. \tag{2.50}$$

For an illustration of the mapping properties see Figure 2.5a). In an *Eulerian strategy*, a spatial unit vector $\boldsymbol{t}$ with $|\boldsymbol{t}|_{\boldsymbol{g}} = 1$ is considered. Looking back at the reference configuration, this unit vector has been obtained by an undeformed Lagrangian stretch vector characterized by $\boldsymbol{\Lambda} = \boldsymbol{F}^{-1}\boldsymbol{t}$ with the length $|\boldsymbol{\Lambda}|_{\boldsymbol{G}} = 1/\lambda$. These considerations yield

$$\frac{1}{\lambda} := |\boldsymbol{\Lambda}|_{\boldsymbol{G}} = \sqrt{\boldsymbol{\Lambda}\boldsymbol{G}\boldsymbol{\Lambda}} = \sqrt{\boldsymbol{t}\,(\boldsymbol{F}^{-T}\boldsymbol{G}\boldsymbol{F}^{-1})\,\boldsymbol{t}} = \sqrt{\boldsymbol{t}\,\boldsymbol{c}\,\boldsymbol{t}} = |\boldsymbol{t}|_{\boldsymbol{c}}\,, \tag{2.51}$$

where the Eulerian tensor field $\boldsymbol{c}$ is identified as the *left Cauchy Green tensor* corresponding to the *Lagrangian metric* $\boldsymbol{G}$ *in the Eulerian configuration.* It is obtained by the *push* *forward* operation of the Lagrangian metric

$$\boldsymbol{c} := \boldsymbol{\varphi}_*(\boldsymbol{G}) = \boldsymbol{F}^{-T}\boldsymbol{G}\boldsymbol{F}^{-1} \quad \text{or} \quad c_{ab} = (F^{-1})^A{}_a \, G_{AB} \, (F^{-1})^B{}_b \; . \tag{2.52}$$

A geometric interpretation is given in Figure 2.5b). In a proceeding step, the strain tensors are defined based on the comparison of metric tensors in either the Lagrangian or Eulerian configuration. In a *Lagrangian strategy*, the Lagrangian line element $\boldsymbol{T}$ with unit length $|\boldsymbol{T}|_{\boldsymbol{G}} = 1$ is compared to its deformed counterpart $\boldsymbol{\lambda}$ stretched by the value $|\boldsymbol{\lambda}|_{\boldsymbol{C}} = \lambda$. Following this idea, the Green strain takes the form

$$\epsilon_{Green} := \tfrac{1}{2}\,(\lambda^2 - 1) = \tfrac{1}{2}\,(|\boldsymbol{T}|^2_{\boldsymbol{C}} - |\boldsymbol{T}|^2_{\boldsymbol{G}}) = \boldsymbol{T}\,\tfrac{1}{2}\,(\boldsymbol{C} - \boldsymbol{G})\boldsymbol{T} = \boldsymbol{T}\boldsymbol{E}\boldsymbol{T}\,, \tag{2.53}$$

where the so-called *Green strain tensor*

$$\boldsymbol{E} := \tfrac{1}{2}\,(\boldsymbol{C} - \boldsymbol{G}) = \tfrac{1}{2}\,(\boldsymbol{F}^T\boldsymbol{g}\boldsymbol{F} - \boldsymbol{G}) = \tfrac{1}{2}\,(\boldsymbol{\varphi}^*(\boldsymbol{g}) - \boldsymbol{G}) \quad \text{or} \quad E_{AB} = \tfrac{1}{2}\,(C_{AB} - G_{AB}) \tag{2.54}$$

can be identified. It defines the Lagrangian strain by comparing the current and the reference metric in the Lagrangian setting. In an *Eulerian strategy*, the deformed Eulerian line element $\boldsymbol{t}$ with unit length $|\boldsymbol{t}|_{\boldsymbol{g}} = 1$ is compared to its Lagrangian origin line element with the initial length $|\boldsymbol{t}|_{\boldsymbol{c}} = 1/\lambda$. The Almansi strain then reads

$$\epsilon_{Almansi} := \tfrac{1}{2}\,(1 - 1/\lambda^2) = \tfrac{1}{2}\,(|\boldsymbol{t}|^2_{\boldsymbol{g}} - |\boldsymbol{t}|^2_{\boldsymbol{c}}) = \boldsymbol{t}\,\tfrac{1}{2}\,(\boldsymbol{g} - \boldsymbol{c})\boldsymbol{t} = \boldsymbol{t}\boldsymbol{e}\boldsymbol{t}\,, \tag{2.55}$$

where the *Almansi strain tensor*

$$\boldsymbol{e} := \tfrac{1}{2}\,(\boldsymbol{g} - \boldsymbol{c}) = \tfrac{1}{2}\,(\boldsymbol{g} - \boldsymbol{F}^{-T}\boldsymbol{G}\boldsymbol{F}^{-1}) = \tfrac{1}{2}\,(\boldsymbol{g} - \boldsymbol{\varphi}_*(\boldsymbol{G})) \quad \text{or} \quad e_{ab} = \tfrac{1}{2}\,(g_{ab} - c_{ab}) \tag{2.56}$$

can be identified. It defines the Eulerian strain by comparing the current metric and the reference metric in the Eulerian setting. Further strain measures are summarized by the family of *Seth-Hill strain tensors*. In a Lagrangian setting these tensors are given by

$$\boldsymbol{E}_m(\boldsymbol{C}) = \begin{cases} \frac{1}{m}(\boldsymbol{C}^{m/2} - \boldsymbol{G}) & \text{for} \quad m \neq 0 \\ \frac{1}{2}\,\ln[\boldsymbol{C}] & \text{for} \quad m = 0\,, \end{cases} \tag{2.57}$$

whereas in the Eulerian setting they are determined by

$$\boldsymbol{e}_m(\boldsymbol{c}) = \begin{cases} \frac{1}{m}(\boldsymbol{g} - \boldsymbol{c}^{m/2}) & \text{for} \quad m \neq 0 \\ \frac{1}{2}\,\ln[\boldsymbol{c}] & \text{for} \quad m = 0\,. \end{cases} \tag{2.58}$$

For $m = 2$ in (2.57), the Green strain tensor (2.54) and for $m = 2$ in (2.58), the Almansi strain tensor (2.56) is received.

2.2. Concept of Stresses and Heat Flux

This section is concerned with the introduction of stresses and the heat flux of a thermomechanically loaded continuum. To this end, consider a solid $\mathcal{S}$ in its deformed configuration and a cut section in the deformed configuration $\mathcal{P}_{\mathcal{S}} \subset \mathcal{S}$, see Figure 2.6. Following *Euler's cut principle*, the force action of the cut-off part on the remaining cut section in the Eulerian configuration is replaced by the surface traction $\boldsymbol{t}$ and the heat flux q. An alternative representation of Euler's cut principle in the Lagrangian setting is discussed accordingly. In the previous sections, the notation $\boldsymbol{T} \in T_{\boldsymbol{X}}\mathcal{B}$ and $\boldsymbol{t} \in T_{\boldsymbol{x}}\mathcal{S}$ has been employed to indicate Lagrangian and Eulerian tangents to material curves as purely geometric objects. To avoid confusions, note that the notation changes and the aforementioned variables get a completely different meaning and denote the traction vectors as physical objects.

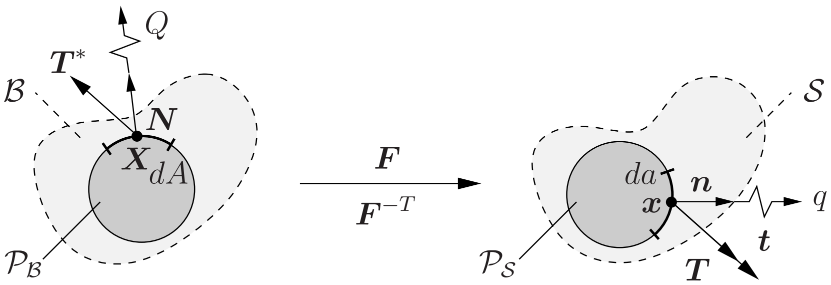

Figure 2.6: Euler's cut principle. Lagrangian $\boldsymbol{T}^*(\boldsymbol{X},t;\boldsymbol{N}) \in T_{\boldsymbol{X}}\mathcal{B}$ and Eulerian $\boldsymbol{t}(\boldsymbol{x},t;\boldsymbol{n}) \in T_{\boldsymbol{x}}\mathcal{S}$ and $\boldsymbol{T}(\boldsymbol{X},t;\boldsymbol{N}) \in T_{\boldsymbol{x}}\mathcal{S}$ traction vectors representing the mechanical action and Lagrangian $Q(\boldsymbol{X},t;\boldsymbol{N})$ and Eulerian $q(\boldsymbol{x},t;\boldsymbol{n})$ heat fluxes representing the heat conduction of the rest of the body at the vicinity on the surface of the cut out parts $\partial\mathcal{P}_{\mathcal{B}}$ and $\partial\mathcal{P}_{\mathcal{S}}$.

2.2.1. Representations of the Stress Tensor. Regarding purely mechanical problems, consider a cut section $\mathcal{P}_{\mathcal{B}} \subset \mathcal{B}$ of the solid in the Lagrangian configuration and its Eulerian counterpart $\mathcal{P}_{\mathcal{S}} \subset \mathcal{S}$ circumscribed by the inner boundaries $\partial\mathcal{P}_{\mathcal{B}}$ and $\partial\mathcal{P}_{\mathcal{S}}$. As illustrated in Figure 2.6, the stress vector $\boldsymbol{t}$ acts on the surface element $da \subset \partial\mathcal{P}_{\mathcal{S}}$ of the cut section in the deformed configuration. This stress vector replaces the mechanical action of the cut-off part on the cut section. The *Cauchy theorem* postulates a linear relationship between the spatial traction vector $\boldsymbol{t} \in T_{\boldsymbol{x}}\mathcal{S}$ and the Eulerian normal $\boldsymbol{n} \in T^*_{\boldsymbol{x}}\mathcal{S}$

$$\boldsymbol{t}(\boldsymbol{x},t;\boldsymbol{n}) := \boldsymbol{\sigma}(\boldsymbol{x},t)\,\boldsymbol{n} \quad \text{or} \quad t^a = \sigma^{ab}\,n_b\,, \tag{2.59}$$

in terms of the *Cauchy stress tensor* $\boldsymbol{\sigma}$ that is interpreted as a contra-variant mapping that transforms Eulerian normals $\boldsymbol{n} \in T^*_{\boldsymbol{x}}\mathcal{S}$ onto Eulerian traction vectors $\boldsymbol{t} \in T_{\boldsymbol{x}}\mathcal{S}$

$$\boldsymbol{\sigma} : \begin{cases} T_{\boldsymbol{x}}\mathcal{S} \to T^*_{\boldsymbol{x}}\mathcal{S} \\ \boldsymbol{n} \quad\ \mapsto \boldsymbol{t} = \boldsymbol{\sigma}\,\boldsymbol{n}\,. \end{cases} \tag{2.60}$$

In this expression, the current force state in the Eulerian configuration is related to the deformed area element da. Thus, the Cauchy stress tensor is often denoted as true stress tensor. The so-called *Kirchhoff stress tensor*

$$\boldsymbol{\tau} := J\boldsymbol{\sigma} \tag{2.61}$$

is used when the spatial stress power is set up with respect to the reference volume. Consider a Lagrangian normal $\boldsymbol{N}$ to the surface element $dA \subset \partial\mathcal{P}_{\mathcal{B}}$ that is mapped onto the current configuration. The material version of Cauchy's theorem states a linear relation between the material traction vector $\boldsymbol{T} \in T_{\boldsymbol{x}}\mathcal{S}$ and the Lagrangian normal $\boldsymbol{N} \in T^*_{\boldsymbol{X}}\mathcal{B}$

$$\boldsymbol{T}(\boldsymbol{X},t;\boldsymbol{N}) := \boldsymbol{P}(\boldsymbol{X},t)\,\boldsymbol{N} \quad \text{or} \quad T^a = P^{aB}\,N_B\,, \tag{2.62}$$

in terms of the *first Piola-Kirchhoff stress tensor* $\boldsymbol{P}$. Material traction vectors and the true traction vectors are linked via $\boldsymbol{t}\,da = \boldsymbol{T}\,dA$ allowing for the reformulation $\boldsymbol{\sigma n}\,da = \boldsymbol{PN}\,dA$ which yields together with Nanson's formula (2.44) the relation

$$\boldsymbol{P} = \boldsymbol{\tau}\boldsymbol{F}^{-T} = J\boldsymbol{\sigma}\,\boldsymbol{F}^{-T}\,. \tag{2.63}$$

The first Piola-Kirchhoff stress tensor possesses the geometric mapping property

$$\boldsymbol{P} : \begin{cases} T^*_{\boldsymbol{X}}\mathcal{B} \to T_{\boldsymbol{x}}\mathcal{S} \\ \boldsymbol{N} \quad\ \mapsto \boldsymbol{T} = \boldsymbol{PN}\,. \end{cases} \tag{2.64}$$

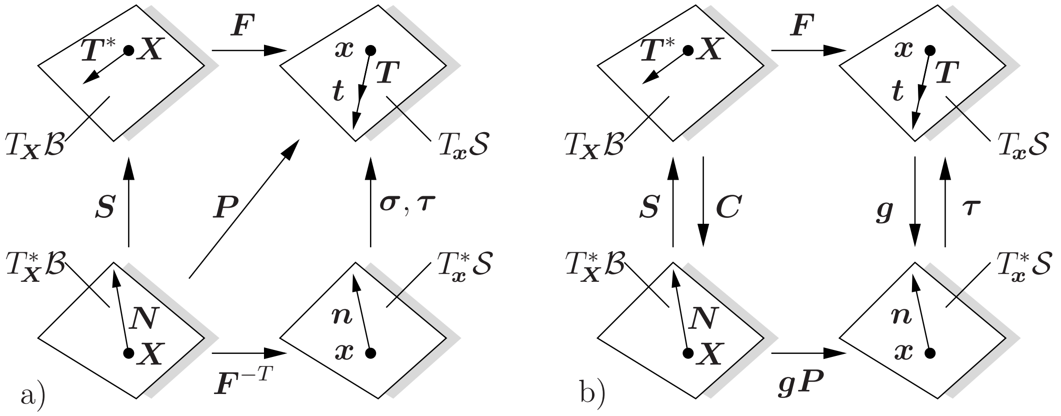
$\boldsymbol{F}$
$\boldsymbol{T}^*$
$\boldsymbol{X}$
$\boldsymbol{x}$
$\boldsymbol{t}$
$\boldsymbol{T}$
$T_{\boldsymbol{X}}\mathcal{B}$
$T_{\boldsymbol{x}}\mathcal{S}$
$\boldsymbol{S}$
$\boldsymbol{P}$
$\boldsymbol{\sigma}, \boldsymbol{\tau}$
$T^*_{\boldsymbol{X}}\mathcal{B}$
$T^*_{\boldsymbol{x}}\mathcal{S}$
$\boldsymbol{N}$
$\boldsymbol{X}$
$\boldsymbol{n}$
$\boldsymbol{x}$
$\boldsymbol{F}^{-T}$
a)
$\boldsymbol{F}$
$\boldsymbol{T}^*$
$\boldsymbol{X}$
$\boldsymbol{x}$
$\boldsymbol{t}$
$\boldsymbol{T}$
$T_{\boldsymbol{X}}\mathcal{B}$
$T_{\boldsymbol{x}}\mathcal{S}$
$\boldsymbol{S}$
$\boldsymbol{C}$
$\boldsymbol{g}$
$\boldsymbol{\tau}$
$T^*_{\boldsymbol{X}}\mathcal{B}$
$T^*_{\boldsymbol{x}}\mathcal{S}$
$\boldsymbol{N}$
$\boldsymbol{X}$
$\boldsymbol{n}$
$\boldsymbol{x}$
$\boldsymbol{gP}$
b)

Figure 2.7: Mapping properties of stress tensors and stress power. a) The representations of the stress tensor $\boldsymbol{\sigma}$, $\boldsymbol{\tau}$, $\boldsymbol{P}$ and $\boldsymbol{S}$ are related through the tangent and normal mapping $\boldsymbol{F}$ and $\boldsymbol{F}^{-T}$, respectively. b) Stress power of dual objects $\mathcal{P} = (\boldsymbol{gP}) : \dot{\boldsymbol{F}} = \boldsymbol{S} : \frac{1}{2}\dot{\boldsymbol{C}} = \boldsymbol{\tau} : \frac{1}{2}\mathcal{L}_{\boldsymbol{v}}\boldsymbol{g}$.

Lagrangian traction vectors $\boldsymbol{T}^* \in T_{\boldsymbol{X}}\mathcal{B}$ are obtained by a pull-back operation of the spatial traction vectors $\boldsymbol{T} \in T_{\boldsymbol{x}}\mathcal{S}$ via

$$\boldsymbol{T}^* = \boldsymbol{\varphi}^*(\boldsymbol{T}) = \boldsymbol{F}^{-1}\boldsymbol{T} \quad \text{or} \quad T^{*A} = (F^{-1})^A{}_a T^a \,. \tag{2.65}$$

A relation between the Lagrangian traction vector $\boldsymbol{T}^*$ and the Lagrangian normal $\boldsymbol{N}$ to the Lagrangian surface element $dA \subset \partial\mathcal{P}_{\mathcal{B}}$ is given by

$$\boldsymbol{T}^*(\boldsymbol{X}, t; \boldsymbol{N}) = \boldsymbol{S}(\boldsymbol{X}, t)\, \boldsymbol{N} \quad \text{or} \quad T^{*A} = S^{AB}\, N_B \,, \tag{2.66}$$

in terms of the *second Piola-Kirchhoff stress tensor* $\boldsymbol{S}$ with the mapping properties

$$\boldsymbol{S} : \begin{cases} T^*_{\boldsymbol{X}}\mathcal{B} \to T_{\boldsymbol{X}}\mathcal{B} \\ \boldsymbol{N} \quad\; \mapsto \boldsymbol{T}^* = \boldsymbol{SN} \,. \end{cases} \tag{2.67}$$

A combination of (2.60)-(2.62) allows to reformulate the second Piola-Kirchhoff stresses

$$\boldsymbol{S} = \boldsymbol{F}^{-1}\boldsymbol{P} = \boldsymbol{F}^{-1}\boldsymbol{\tau}\boldsymbol{F}^{-T} \quad \text{or} \quad S^{AB} = (F^{-1})^A{}_a P^{aB} = (F^{-1})^A{}_a \tau^{ab} (F^{-1})^B{}_b \tag{2.68}$$

expressed in terms of the first Piola-Kirchhoff stress tensor $\boldsymbol{P}$ or in terms of the Kirchhoff stress tensor $\boldsymbol{\tau}$. Similarly, for the Kirchhoff stresses the representations hold

$$\boldsymbol{\tau} = J\boldsymbol{\sigma} = \boldsymbol{PF}^T = \boldsymbol{FSF}^T \quad \text{or} \quad \tau^{ab} = J\sigma^{ab} = P^{aB} F^b{}_B = F^a{}_A S^{AB} F_B{}^b \,. \tag{2.69}$$

A compact illustration of the geometric mapping properties of the introduced stress measures is given in Figure 2.7a).

2.2.2. Heat Flux. The counterpart of Cauchy's stress theorem (2.59) in continuum mechanics corresponds to the *Stokes' heat flux theorem* in thermodynamics. It postulates the heat flux as the linear relationship

$$q(\boldsymbol{x}, t; \boldsymbol{n}) := -\boldsymbol{q}(\boldsymbol{x}, t)\boldsymbol{n} \tag{2.70}$$

between the *Cauchy heat flux vector* $\boldsymbol{q}$ and the outward unit normal $\boldsymbol{n}$ to an infinitesimal spatial surface element $da \subset \partial\mathcal{P}_{\mathcal{S}}$ at position $\boldsymbol{x}$. The *Piola-Kirchhoff heat flux theorem*

$$Q(\boldsymbol{X}, t; \boldsymbol{N}) := -\boldsymbol{Q}(\boldsymbol{X}, t)\boldsymbol{N} \tag{2.71}$$

relates the *nominal heat flux vector* $\boldsymbol{Q}$ with the normal $\boldsymbol{N}$ to a Lagrangian surface element $dA \subset \partial\mathcal{P}_{\mathcal{B}}$ at position $\boldsymbol{X}$. The equivalence of (2.70) and (2.71) states $Q\, dA = q\, da$ allowing for the reformulation $\boldsymbol{QN}\, dA = \boldsymbol{qn}\, da$ which yields together with Nanson's formula (2.44) the relation between the Cauchy heat flux and the nominal heat flux

$$\boldsymbol{Q} = J\boldsymbol{F}^{-1}\boldsymbol{q}\,. \tag{2.72}$$

The minus signs in (2.70) and (2.71) indicate that heat enters the body which corresponds to an inward normal flux in opposite direction of the normal vectors.

2.3. Dual Stresses and Strains

In order to obtain a precise interpretation of the stress tensors and their dual strain tensors, consider the *stress power* associated with a unit volume in the undeformed configuration

$$\mathcal{P} = (\boldsymbol{gP}) : \dot{\boldsymbol{F}} \quad \text{or} \quad \mathcal{P} = (g_{ab}P^{bA})\, \dot{F}^{a}{}_{A}\,. \tag{2.73}$$

The first Piola-Kirchhoff stress tensor $\boldsymbol{gP}$ and the deformation gradient $\boldsymbol{F}$ are *dual two point tensors*. Consider the second Piola-Kirchhoff tensor $\boldsymbol{S}$ in terms of $\boldsymbol{gP} = \boldsymbol{gFS}$, which gives together with definition (2.73) the alternative representation of the stress power

$$\mathcal{P} = (\boldsymbol{gFS}) : \dot{\boldsymbol{F}} = \boldsymbol{S} : \tfrac{1}{2}\dot{\boldsymbol{C}} = \boldsymbol{S} : \dot{\boldsymbol{E}} \quad \text{or} \quad \mathcal{P} = S^{AB}\, \dot{E}_{AB}\,, \tag{2.74}$$

where the second Piola-Kirchhoff tensor $\boldsymbol{S}$ and the right Cauchy Green tensor $\boldsymbol{C}$ are identified as dual objects. The rate of $\boldsymbol{C}$ can alternatively be formulated in terms of the *strain rate tensor* $\dot{\boldsymbol{E}}$. The push-forward of (2.74) gives the Eulerian representation

$$\mathcal{P} = \boldsymbol{\tau} : \tfrac{1}{2}\mathcal{L}_{\boldsymbol{v}}\boldsymbol{g} = \boldsymbol{\tau} : \boldsymbol{d} \quad \text{or} \quad \mathcal{P} = \tau^{ab}\, d_{ab} \tag{2.75}$$

identifying the Kirchhoff stress tensor $\boldsymbol{\tau}$ as dual quantity to the Eulerian metric $\boldsymbol{g}$. In this expression the so-called *Lie-derivative*

$$\mathcal{L}_{\boldsymbol{v}}(\cdot) := \boldsymbol{\varphi}_{*}\left[\frac{d}{dt}\boldsymbol{\varphi}^{*}(\cdot)\right] \tag{2.76}$$

is introduced which has to be understood as a combination of three steps. In a first step, the Eulerian object is brought to the time invariant Lagrangian setting via a pull back operation (2.50). Then, the material time derivative is computed and in a last step, the resulting quantity is pushed forward (2.52) to the Eulerian configuration. Application of the Lie-derivative (2.76) to the current metric $\boldsymbol{g}$ delivers the *rate of deformation tensor* $\boldsymbol{d}$

$$\mathcal{L}_{\boldsymbol{v}}\boldsymbol{g} = \boldsymbol{l}^{T}\boldsymbol{g} + \boldsymbol{gl} = 2\,\mathrm{sym}[\boldsymbol{gl}] = 2\boldsymbol{d} \quad \text{with} \quad \boldsymbol{l} := \nabla_{\boldsymbol{x}}\boldsymbol{v} = \dot{\boldsymbol{F}}\boldsymbol{F}^{-1}\,, \tag{2.77}$$

in terms of the *spatial velocity gradient* $\boldsymbol{l} := \nabla_{\boldsymbol{x}}\boldsymbol{v} = \dot{\boldsymbol{F}}\boldsymbol{F}^{-1}$, see also (2.24). Figure 2.7b) gives a clear illustration of the conjugate dual stresses and strains.

2.4. Physical Balance Principles

The aim of this section is to provide the classical balance principles of continuum thermomechanics. The fundamental balance principles, i.e. the conservation of mass, the balances of momentum, and the first and second law of thermodynamics must be satisfied for every particular material at all times. Starting with their integral representations with respect to a cut section $\mathcal{P}_{\mathcal{S}} \subset \mathcal{S}$ subjected to mechanical and thermal surface and volume loading, the fundamental balance principles are transformed to local or strong statements that are valid at arbitrary spatial positions $\boldsymbol{x} \in \mathcal{S}$. Regarding the undeformed counterpart $\mathcal{P}_{\mathcal{B}}$ of the Eulerian subregion $\mathcal{P}_{\mathcal{S}}$ in the Lagrangian configuration, the local statements can alternatively be expressed with respect to arbitrary reference positions $\boldsymbol{X} \in \mathcal{B}$.

2.4.1. Conservation of Mass. The balance of mass demands the mass of the subregion $\mathcal{P}_{\mathcal{S}} \subset \mathcal{S}$, see Figure 2.6, being constant in time. No transport of mass into $\mathcal{P}_{\mathcal{S}}$ and no production of mass inside $\mathcal{P}_{\mathcal{S}}$ is investigated

$$\frac{d}{dt} m = 0\,. \tag{2.78}$$

Here, the total mass m of the cut section $\mathcal{P}_{\mathcal{S}} \subset \mathcal{S}$ has been introduced

$$m = \int_{\mathcal{P}_{\mathcal{S}}} dm = \int_{\mathcal{P}_{\mathcal{S}}} \rho \, dv = \int_{\mathcal{P}_{\mathcal{B}}} \rho_0 \, dV\,, \tag{2.79}$$

in terms of the current density function ρ and the reference density function $\rho_0 = J\rho$. The *material time derivative* of the reference density $\rho_0(\boldsymbol{X}, t)$ at fixed Lagrangian position $\boldsymbol{X} = const$ commutes with its partial time derivative, i.e. $\dot{\rho}_0 = \partial_t \rho_0$. In contrast, the material time derivative of the current density function $\rho(\boldsymbol{x}, t)$ consists of a local and convective part, i.e. $\dot{\rho} = \partial_t \rho + \nabla_{\boldsymbol{x}} \rho \cdot \boldsymbol{v}$. Together with $\dot{J} = J \operatorname{div}[\boldsymbol{v}]$, a simple reformulation of (2.79) with application of the localization theorem yields the local or strong forms

$$\dot{\rho} + \rho \operatorname{div}[\boldsymbol{v}] = 0 \quad \text{and} \quad J\rho - \rho_0 = 0 \tag{2.80}$$

in the Eulerian and Lagrangian representation valid at arbitrary current $\boldsymbol{x} \in \mathcal{S}$ and reference positions $\boldsymbol{X} \in \mathcal{B}$, respectively. Note that the Eulerian strong form $(2.80)_1$ is an outcome of the important integral equation for spatial scalar fields $f(\boldsymbol{x}, t)$

$$\frac{d}{dt} \int_{\mathcal{P}_{\mathcal{S}}} f(\boldsymbol{x}, t) \, dv = \int_{\mathcal{P}_{\mathcal{S}}} \{\, \dot{f} + f \operatorname{div}[\boldsymbol{v}] \,\} \, dv\,, \tag{2.81}$$

also known as *Reynold's transport theorem.* For incompressible materials with $\rho = const$, the Eulerian strong form $(2.80)_1$ delivers the continuity equation of fluid mechanics.

2.4.2. Balance of Linear Momentum. The balance of linear momentum postulates the temporal change of the linear momentum $\boldsymbol{I}$ of an arbitrary subregion $\mathcal{P}_{\mathcal{S}} \subset \mathcal{S}$ being equal to the resulting force $\boldsymbol{F}_{ext}$ acting on that region

$$\frac{d}{dt} \boldsymbol{I} = \boldsymbol{F}_{ext}\,. \tag{2.82}$$

Here, the *linear momentum* has been introduced

$$\boldsymbol{I} = \int_{\mathcal{P}_{\mathcal{S}}} \dot{\boldsymbol{x}} \, dm = \int_{\mathcal{P}_{\mathcal{S}}} \rho \boldsymbol{v} \, dv = \int_{\mathcal{P}_{\mathcal{B}}} \rho_0 \boldsymbol{V} \, dV\,, \tag{2.83}$$

in terms of the material and spatial velocities $(2.22)_1$ and $(2.23)_1$. The external forces acting in or on this subregion are defined by

$$\boldsymbol{F}_{ext} = \int_{\mathcal{P}_{\mathcal{S}}} \boldsymbol{\gamma} \, dv + \int_{\partial \mathcal{P}_{\mathcal{S}}} \boldsymbol{t} \, da = \int_{\mathcal{P}_{\mathcal{B}}} \boldsymbol{\gamma}_0 \, dV + \int_{\partial \mathcal{P}_{\mathcal{B}}} \boldsymbol{T} \, dA \tag{2.84}$$

consisting of the spatial volume force $\boldsymbol{\gamma} = \rho \boldsymbol{b}$ and the surface traction $\boldsymbol{t}$ in the Eulerian setting and $\boldsymbol{\gamma}_0 = \rho_0 \boldsymbol{b}$ and $\boldsymbol{T}$ in the Lagrangian setting. The vector $\boldsymbol{b}$ denotes a prescribed acceleration field. Application of Gauss' theorem transforms the surface integrals into volume integrals and application of the localization theorem yields together with the accelerations $(2.22)_2$ and $(2.23)_2$ the Eulerian and Lagrangian strong forms

$$\rho \boldsymbol{a} = \operatorname{div}[\boldsymbol{\sigma}] + \boldsymbol{\gamma} \quad \text{and} \quad \rho_0 \boldsymbol{A} = \operatorname{DIV}[\boldsymbol{P}] + \boldsymbol{\gamma}_0\,, \tag{2.85}$$

where the identity $\operatorname{DIV}[\boldsymbol{P}] = J \operatorname{div}[\boldsymbol{\sigma}]$ has been exploited. The strong expressions (2.85) are locally valid at Eulerian and Lagrangian positions $\boldsymbol{x} \in \mathcal{S}$ and $\boldsymbol{X} \in \mathcal{B}$, respectively.

2.4.3. Balance of Angular Momentum. The balance of angular momentum states that the temporal change of the angular momentum $\boldsymbol{D}^o$ with respect to the origin "o" of a fixed coordinate system is equal to the resultant torque $\boldsymbol{M}^o_{ext}$ acting on that region with respect to the same reference point

$$\frac{d}{dt}\boldsymbol{D}^o = \boldsymbol{M}^o_{ext}\,. \tag{2.86}$$

The *angular momentum* $\boldsymbol{D}^o$ in the subregion $\mathcal{P}_\mathcal{S} \subset \mathcal{S}$ with respect to "o" is defined by

$$\boldsymbol{D}^o = \int_{\mathcal{P}_\mathcal{S}} \boldsymbol{x} \times \dot{\boldsymbol{x}}\, dm = \int_{\mathcal{P}_\mathcal{S}} \boldsymbol{x} \times \rho \boldsymbol{v}\, dv = \int_{\mathcal{P}_\mathcal{B}} \boldsymbol{x} \times \rho_0 \boldsymbol{V}\, dV\,. \tag{2.87}$$

The sum of the applied moments resulting from the body forces $\boldsymbol{\gamma}$ and $\boldsymbol{\gamma}_0$ and the surface tractions $\boldsymbol{t}$ and $\boldsymbol{T}$ acting in or on the subdomains $\mathcal{P}_\mathcal{S} \subset \mathcal{S}$ and $\mathcal{P}_\mathcal{B} \subset \mathcal{B}$ yields the torque

$$\boldsymbol{M}^o_{ext} = \int_{\mathcal{P}_\mathcal{S}} \boldsymbol{x} \times \boldsymbol{\gamma}\, dv + \int_{\partial\mathcal{P}_\mathcal{S}} \boldsymbol{x} \times \boldsymbol{t}\, da = \int_{\mathcal{P}_\mathcal{B}} \boldsymbol{x} \times \boldsymbol{\gamma}_0\, dV + \int_{\partial\mathcal{P}_\mathcal{B}} \boldsymbol{x} \times \boldsymbol{T}\, dA\,. \tag{2.88}$$

Some transformations and identification of the balance of linear momentum (2.85) and the axial vector of Cauchy's stress tensor allow for the representations of the local forms

$$\boldsymbol{\sigma} = \boldsymbol{\sigma}^T \quad \text{or} \quad \boldsymbol{\tau} = \boldsymbol{\tau}^T \quad \text{and} \quad \boldsymbol{S} = \boldsymbol{S}^T \tag{2.89}$$

identifying the Cauchy stress tensor $\boldsymbol{\sigma}$ and thus the Kirchhoff stress tensor $\boldsymbol{\tau}$ and the second Piola-Kirchhoff stress tensor $\boldsymbol{S}$ as *symmetric quantities.* In contrast, the first Piola-Kirchhoff stress tensor $\boldsymbol{P}$ is not symmetric, but possesses the property

$$\boldsymbol{P}\boldsymbol{F}^T = \boldsymbol{F}\boldsymbol{P}^T \tag{2.90}$$

obtained by application of the Piola-transformation (2.69) on $(2.89)_1$.

2.4.4. First Law of Thermodynamics. Balance of Energy. The first law of thermodynamics postulates that the temporal change of the total energy $\mathcal{E}_{tot}$ in the subregion $\mathcal{P}_\mathcal{S} \subset \mathcal{S}$ is equal to the sum of external mechanical $\mathcal{P}_{ext}$ and thermal power $\mathcal{Q}_{ext}$

$$\frac{d}{dt}\mathcal{E}_{tot} = \mathcal{P}_{ext} + \mathcal{Q}_{ext}\,. \tag{2.91}$$

In this equation, the total energy of the subbody $\mathcal{P}_\mathcal{S}$ is given by the expression

$$\mathcal{E}_{tot} := \int_{\mathcal{P}_\mathcal{S}} \rho e\, dv = \int_{\mathcal{P}_\mathcal{B}} \rho_0 e\, dV\,, \tag{2.92}$$

where e denotes the *specific energy per unit mass.* Focusing on thermomechanical processes, the external, mechanically caused power reads

$$\mathcal{P}_{ext} := \int_{\mathcal{P}_\mathcal{S}} \boldsymbol{\gamma} \cdot \boldsymbol{g}\boldsymbol{v}\, dv + \int_{\partial\mathcal{P}_\mathcal{S}} \boldsymbol{t} \cdot \boldsymbol{g}\boldsymbol{v}\, da = \int_{\mathcal{P}_\mathcal{B}} \boldsymbol{\gamma}_0 \cdot \boldsymbol{g}\boldsymbol{V}\, dV + \int_{\partial\mathcal{P}_\mathcal{B}} \boldsymbol{T} \cdot \boldsymbol{g}\boldsymbol{V}\, dA\,, \tag{2.93}$$

in terms of the volume forces $\boldsymbol{\gamma}$ and $\boldsymbol{\gamma}_0$ and the surface tractions $\boldsymbol{t}$ and $\boldsymbol{T}$, respectively. The thermally caused external power can be summarized by

$$\mathcal{Q}_{ext} := \int_{\mathcal{P}_\mathcal{S}} \rho r\, dv + \int_{\partial\mathcal{P}_\mathcal{S}} q\, da = \int_{\mathcal{P}_\mathcal{B}} \rho_0 R\, dV + \int_{\partial\mathcal{P}_\mathcal{B}} Q\, dA\,, \tag{2.94}$$

in terms of the *heat source per unit volume* r and its re-parametrization $R(\boldsymbol{X},t) = r(\boldsymbol{x},t) \circ \boldsymbol{\varphi}_t(\boldsymbol{X})$ and the Eulerian or Lagrangian heat fluxes q and Q as introduced in (2.70) and (2.71). The Eulerian and Lagrangian local counterparts to (2.91) read

$$\rho \dot{e} = \operatorname{div}[\boldsymbol{g}\boldsymbol{v} \cdot \boldsymbol{\sigma} - \boldsymbol{q}] + \boldsymbol{\gamma} \cdot \boldsymbol{g}\boldsymbol{v} + \rho r \quad \text{and} \quad \rho_0 \dot{e} = \operatorname{DIV}[\boldsymbol{g}\boldsymbol{V} \cdot \boldsymbol{P} - \boldsymbol{Q}] + \boldsymbol{\gamma}_0 \cdot \boldsymbol{g}\boldsymbol{V} + \rho_0 R \,, \tag{2.95}$$

to be satisfied at the current and reference positions $\boldsymbol{x} \in \mathcal{S}$ and $\boldsymbol{X} \in \mathcal{B}$. The total energy $\mathcal{E}_{tot} = \mathcal{K} + \mathcal{U}$ can further be decomposed into a kinetic contribution

$$\mathcal{K} := \int_{\mathcal{P}_\mathcal{S}} \tfrac{1}{2}\,\dot{\boldsymbol{x}} \cdot \boldsymbol{g}\dot{\boldsymbol{x}}\; dm = \int_{\mathcal{P}_\mathcal{S}} \tfrac{1}{2}\,\rho \boldsymbol{v} \cdot \boldsymbol{g}\boldsymbol{v}\; dv = \int_{\mathcal{P}_\mathcal{B}} \tfrac{1}{2}\,\rho_0 \boldsymbol{V} \cdot \boldsymbol{g}\boldsymbol{V}\; dV \tag{2.96}$$

and a contribution related to internal energy storage mechanisms

$$\mathcal{U} := \int_{\mathcal{P}_\mathcal{S}} \rho u \, dv = \int_{\mathcal{P}_\mathcal{B}} \rho_0 u \, dV \tag{2.97}$$

based on the *specific internal energy density per unit volume* u. Insertion of the definitions (2.96) and (2.97) into (2.91) yields on the one hand the *balance of kinetic energy*

$$\frac{d}{dt}\mathcal{K} = \mathcal{P}_{ext} - \mathcal{S} \,, \tag{2.98}$$

in terms of the so-called *stress power*

$$\mathcal{S} = \int_{\mathcal{P}_\mathcal{S}} \boldsymbol{\sigma} : \boldsymbol{d} \, dv = \int_{\mathcal{P}_\mathcal{B}} (\boldsymbol{g}\boldsymbol{P}) : \dot{\boldsymbol{F}} \, dV \,. \tag{2.99}$$

See Section 2.3 for work conjugate stresses and strains. The local form of the balance of kinetic energy (2.98) is equivalent to the equilibrium condition obtained from the balance of linear momentum. On the other hand the balance of kinetic energy comes along with the *balance of internal energy* also denoted as *first law of thermodynamics*

$$\frac{d}{dt}\mathcal{U} = \mathcal{S} + \mathcal{Q}_{ext} \tag{2.100}$$

expressed in terms of the stress power as defined in (2.99). The according local forms

$$\rho \dot{u} = \boldsymbol{\sigma} : \boldsymbol{d} - \operatorname{div}[\boldsymbol{q}] + \rho r \quad \text{and} \quad \rho_0 \dot{u} = (\boldsymbol{g}\boldsymbol{P}) : \dot{\boldsymbol{F}} - \operatorname{DIV}[\boldsymbol{Q}] + \rho_0 R \tag{2.101}$$

are valid at arbitrary Eulerian and Lagrangian material points $\boldsymbol{x} \in \mathcal{S}$ and $\boldsymbol{X} \in \mathcal{B}$.

2.4.5. Second Law of Thermodynamics. Entropy Inequality Principle. Entropy in thermodynamics is considered as a measure of how organized or disorganized a system is. It is probably the most important state variable of thermodynamics and governs the evolution of internal dissipative processes. The entropy inequality condition states a *positive entropy production*

$$\mathcal{G} = \frac{d}{dt}\mathcal{H} - \mathcal{Q} \geq 0 \,. \tag{2.102}$$

Within the subregion $\mathcal{P}_\mathcal{S} \subset \mathcal{S}$, the *rate of entropy production* $\mathcal{G}$ and the *entropy* $\mathcal{H}$

$$\mathcal{G} := \int_{\mathcal{P}_\mathcal{S}} \rho\gamma \, dv = \int_{\mathcal{P}_\mathcal{B}} \rho_0\gamma \, dV \quad \text{and} \quad \mathcal{H} := \int_{\mathcal{P}_\mathcal{S}} \rho\eta \, dv = \int_{\mathcal{P}_\mathcal{B}} \rho_0\eta \, dV \tag{2.103}$$

base on the *local entropy production per unit mass* γ and the *local entropy per unit mass* η. The *rate of entropy input* $\mathcal{Q}$ is characterized by

$$\mathcal{Q} := \int_{\mathcal{P}_\mathcal{S}} \rho \frac{r}{\theta}\, dv + \int_{\partial\mathcal{P}_\mathcal{S}} \frac{q}{\theta}\, da = \int_{\mathcal{P}_\mathcal{B}} \rho_0 \frac{R}{\theta}\, dV + \int_{\partial\mathcal{P}_\mathcal{B}} \frac{Q}{\theta}\, dA\,, \tag{2.104}$$

in terms of the heat fluxes q and Q, the heat sources r and R and the *absolute temperature* $\theta > 0$. A thermodynamic process without any entropy production $\mathcal{G} = 0$ is called a *reversible process*. Solving (2.102) for the local forms, the so-called *Clausius-Duhem inequality* is obtained as a result of positive local entropy production

$$\begin{aligned} \rho\gamma &= \rho\dot{\eta} - \rho\frac{r}{\theta} + \frac{1}{\theta}\operatorname{div}[\boldsymbol{q}] - \frac{1}{\theta^2}\boldsymbol{q}\cdot\nabla_{\boldsymbol{x}}\theta \geq 0 \\ \rho_0\gamma &= \rho\dot{\eta} - \rho_0\frac{R}{\theta} + \frac{1}{\theta}\operatorname{DIV}[\boldsymbol{Q}] - \frac{1}{\theta^2}\boldsymbol{Q}\cdot\nabla_{\boldsymbol{X}}\theta \geq 0 \end{aligned} \tag{2.105}$$

valid at arbitrary Eulerian and Lagrangian positions $\boldsymbol{x} \in \mathcal{S}$ and $\boldsymbol{X} \in \mathcal{B}$. The introduction of the *Helmholtz free energy per unit mass* $\Psi = u - \theta\eta$ via a Legendre transformation allows together with (2.101) for a reformulation of (2.105) in the sense

$$\begin{aligned} \rho\gamma\theta &= \boldsymbol{\sigma} : \boldsymbol{d} - \rho\dot{\Psi} - \rho\dot{\theta}\eta - \frac{1}{\theta}\boldsymbol{q}\cdot\nabla_{\boldsymbol{x}}\theta \geq 0 \\ \rho_0\gamma\theta &= (\boldsymbol{g}\boldsymbol{P}) : \dot{\boldsymbol{F}} - \rho_0\dot{\Psi} - \rho_0\dot{\theta}\eta - \frac{1}{\theta}\boldsymbol{Q}\cdot\nabla_{\boldsymbol{X}}\theta \geq 0\,. \end{aligned} \tag{2.106}$$

A stronger representation is obtained by the introduction of the *mechanical dissipation per unit volume* $\mathcal{D} := \gamma\theta \geq 0$ and its additive split $\mathcal{D} = \mathcal{D}_{con} + \mathcal{D}_{loc}$ into a local part

$$\rho\mathcal{D}_{loc} = \boldsymbol{\sigma} : \boldsymbol{d} - \rho\dot{\Psi} - \rho\dot{\theta}\eta \geq 0 \quad \text{and} \quad \rho_0\mathcal{D}_{loc} = (\boldsymbol{g}\boldsymbol{P}) : \dot{\boldsymbol{F}} - \rho_0\dot{\Psi} - \rho_0\dot{\theta}\eta \geq 0\,, \tag{2.107}$$

also known as *Clausius-Planck inequality* and a convective part

$$\rho\mathcal{D}_{con} = -\frac{1}{\theta}\boldsymbol{q}\cdot\nabla_{\boldsymbol{x}}\theta \geq 0 \quad \text{and} \quad \rho_0\mathcal{D}_{con} = -\frac{1}{\theta}\boldsymbol{Q}\cdot\nabla_{\boldsymbol{X}}\theta \geq 0\,, \tag{2.108}$$

widely denoted as *Fourier inequality*. Note that in (2.107) and (2.108) the inequality constraint has to be satisfied independently and thus forms a more strict condition.

3. Continuum Mechanics of Gradient-Type Dissipative Continua

The central goal of this chapter is the outline of a general theory for gradient-type standard dissipative solids that is based on variational formulations. A compact notation is introduced that points out in a rigorous way the duality between macro- and microstructural observations. The central idea is founded on a multi-scale viewpoint, where macro- and microscopic motions are introduced. The latter one represent the so-called order parameter fields or generalized internal variables. The rates of these fields are associated with dual macro- and microstructural power expressions. The constitutive response is defined as a gradient-type standard dissipative material based on an energy storage and a dissipation function. Focusing on materials of grade one, these constitutive functions are assumed to depend on the macro- and microscopic motion and their first gradients. Reduced constitutive functions are obtained from the principle of material frame invariance. Evaluation of a global form of the Clausius-Planck inequality in the sense of Coleman's method yields the set of coupled balance equations. This approach is conceptually in line with Coleman & Gurtin [29]. For quasi-static processes, this statement postulates an equivalence of internal and external power accompanied by the irreversibility constraint of the second axiom of thermodynamics. As a consequence, the derivation of the macro- and micro-structural balances is conceptually similar to the virtual power based treatment of gradient-type plasticity as discussed by Gurtin, Anand & Lele [71], Gurtin [69] and Gurtin & Anand [70]. For prescribed Dirichlet-type boundary conditions for the macro- and microscopic partition, the argument of virtual power yields the fully coupled macro- and microstructural balance equations in combination with the according Neumann-type boundary conditions. These coupled field equations cover a broad class of gradient-type standard dissipative materials that extend in a natural way the classical local treatments of Biot [13], Ziegler & Wehrli [182], and Halphen & Nguyen [76] to gradient-dependencies of the order parameter fields. The coupled field equations are hereby solely governed by the two constitutive functions for the free energy and the dissipation. The focus is put on rate-dependent dissipative processes characterized by smooth dissipation functions and their transition towards rate-independent processed governed by non-smooth dissipation functions. Such a framework of gradient-type standard dissipative solids is consistent with a global rate-type variational formulation. However, instead of constructing a continuous version of the global variational formulation that delivers the coupled field equations as the Euler equations of the continuous variational statement, a time-discrete variational statement is set up. Within a sequence of discrete time steps, the optimization of an incremental potential yields the algorithmic representation of the Euler equations evaluated at current time. Having the time-discrete incremental variational principle at hand, an appropriate finite element discretization scheme is introduced to tackle the resulting multi-field problem consisting of macro- and microstructural fields. Hereby, details of the matrix representation needed for the numerical solution are pointed out. One clear advantage of the proposed framework is the *symmetry of the monolithic tangent matrix* of the fully coupled problem.

The chapter is organized as follows. In a first step, the geometric setting and the generalized kinematics of solids with microstructure are introduced. The focus hereby lies on a precise differential geometric interpretation of the arising microscopic quantities. Then, the concept of generalized stresses is introduced, where in addition to the well known macroscopic stresses additional microstructural stresses show up. The dual stresses and strains are identified, the external loading of a continuum with microstructure is defined, and the constitutive response of gradient-type standard dissipative solids is specified. The exploitation of the principle of virtual power then provides the governing coupled field equations whose algorithmic representation alternatively can be obtained by a time-discrete incremental variational principle. Furthermore, a multi-field finite element solution scheme is introduced to solve the incremental variational principle. The section closes with a reduction of the proposed framework to the case of geometrically small deformations.

3.1. Generalized Kinematics of Solids with Microstructure

The scope of this section lies on the discussion of the geometric setting of a solid with microstructure undergoing large deformations. Besides the standard macroscopic deformation field additional microscopic fields are introduced, describing the current microstructural state of the material.

3.1.1. Notation. Let $\mathcal{B} \subset \mathcal{R}^3$ be the time-invariant reference configuration of a material body and $\partial\mathcal{B} \subset \mathcal{R}^2$ its surface. In the following treatment, the deformation of the material body under mechanical loading is investigated. In order to predict the macroscopic deformation, besides the macroscopic deformation field an additional global field is introduced that describes the microscopic state of the material. Thus, the focus lies on a *multi-field viewpoint* that characterizes the inelastic response of the material, where dissipative effects are related to *microstructural variable fields.* Aiming at a compact notation, the macro- and microstructural fields parametrized in the Lagrangian or Eulerian setting

$$\bar{(\cdot)}(\boldsymbol{X},t) \quad \text{and} \quad \check{(\cdot)}(\boldsymbol{X},t) \quad \text{or} \quad \bar{(\cdot)}(\boldsymbol{x},t) \quad \text{and} \quad \check{(\cdot)}(\boldsymbol{x},t) \tag{3.1}$$

are indicated with a bar and a check-accent, respectively. The gradient of the field $(\cdot)$ in the Lagrangian and Eulerian setting is given by $\nabla_{\boldsymbol{X}}(\cdot) = \partial_{\boldsymbol{X}}(\cdot)$ and $\nabla_{\boldsymbol{x}}(\cdot) = \partial_{\boldsymbol{x}}(\cdot)$.

3.1.2. Extended Geometric Setting and Motion. Within the context of generalized continua subjected to large deformations, the macroscopic motion of the material body is given by the nonlinear *macroscopic deformation map*

$$\bar{\boldsymbol{\varphi}}(\boldsymbol{X},t) : \begin{cases} \mathcal{B} \times \mathcal{T} \rightarrow \mathcal{S} \\ (\boldsymbol{X},t) \mapsto \boldsymbol{x} = \bar{\boldsymbol{\varphi}}(\boldsymbol{X},t)\,. \end{cases} \tag{3.2}$$

At time $t \in \mathcal{R}_+$ the macroscopic deformation map $\bar{\boldsymbol{\varphi}}_t$ maps the Lagrangian position $\boldsymbol{X} \in \mathcal{B}$ of the reference configuration $\mathcal{B} \subset \mathcal{R}^3$ onto the Eulerian position $\boldsymbol{x} \in \mathcal{S}$ of the current configuration $\mathcal{S} \subset \mathcal{R}^3$. The exterior surface of the body is decomposed into a part $\partial\mathcal{B}_{\bar{\boldsymbol{\varphi}}}$, where the macroscopic deformation is prescribed by Dirichlet boundary conditions

$$\bar{\boldsymbol{\varphi}}(\boldsymbol{X},t) = \bar{\boldsymbol{\varphi}}_D(\boldsymbol{X},t) \;\text{ on } \partial\mathcal{B}_{\bar{\boldsymbol{\varphi}}}\,, \tag{3.3}$$

and a part $\partial\mathcal{B}_{\bar{\boldsymbol{t}}}$, where the macro-tractions $\bar{\boldsymbol{T}}_N(\boldsymbol{X},t)$ are prescribed by Neumann boundary conditions. Clearly, the common boundary set $\partial\mathcal{B}_{\bar{\boldsymbol{\varphi}}} \cap \partial\mathcal{B}_{\bar{\boldsymbol{t}}} = \emptyset$ is equal to the empty set. In the context of generalized continua, the material point P is equipped with additional microstructural information $\boldsymbol{q} \in \mathcal{M}$ living in an abstract microscopic manifold $\mathcal{M} \subset \mathcal{R}^m$. The order m of the microstructure depends on the nature of the particular model under focus. In analogy to the standard concept of internal variables, these fields are related to

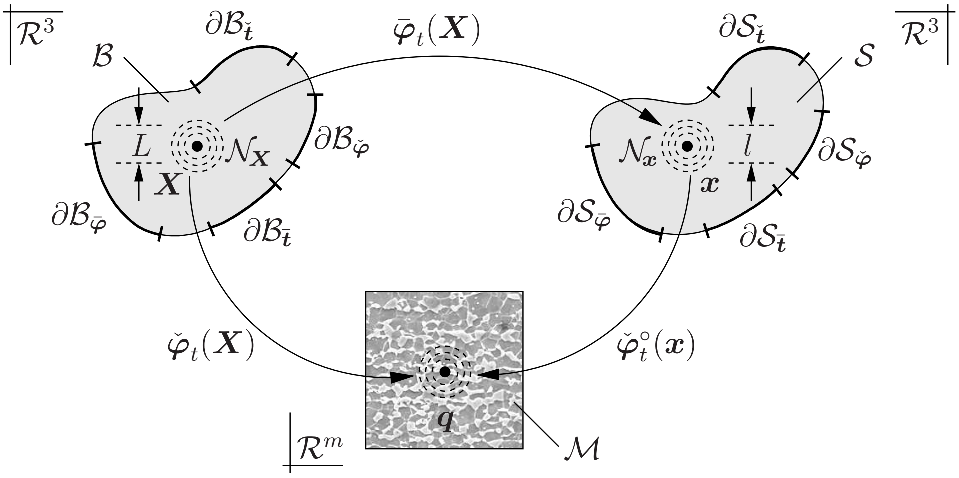
$\mathcal{R}^3$
$\partial\mathcal{B}_{\check{t}}$
$\bar{\boldsymbol{\varphi}}_t(\boldsymbol{X})$
$\partial\mathcal{S}_{\check{t}}$
$\mathcal{S}$
$\mathcal{R}^3$
$\mathcal{B}$
L
$\mathcal{N}_{\boldsymbol{X}}$
$\partial\mathcal{B}_{\check{\varphi}}$
$\boldsymbol{X}$
$\mathcal{N}_{\boldsymbol{x}}$
l
$\partial\mathcal{S}_{\check{\varphi}}$
$\boldsymbol{x}$
$\partial\mathcal{B}_{\bar{\varphi}}$
$\partial\mathcal{B}_{\bar{t}}$
$\partial\mathcal{S}_{\bar{\varphi}}$
$\partial\mathcal{S}_{\bar{t}}$
$\check{\boldsymbol{\varphi}}_t(\boldsymbol{X})$
$\check{\boldsymbol{\varphi}}^\circ_t(\boldsymbol{x})$
$\boldsymbol{q}$
$\mathcal{R}^m$
$\mathcal{M}$

Figure 3.1: Fundamental mappings. Time-invariant reference configuration $\mathcal{B}$ with coordinates $\boldsymbol{X}$, time dependent current configuration $\mathcal{S}$ with coordinates $\boldsymbol{x}$, and configuration of the microstructure $\mathcal{M}$ with microscopic state $\boldsymbol{q}$. Microstructural information in a Lagrangian $\mathcal{N}_{\boldsymbol{X}}$ or Eulerian neighborhood $\mathcal{N}_{\boldsymbol{x}}$ are considered by the length scales L or l, respectively.

dissipative processes, but in contrast are driven by additional balance equations and thus exhibit a field character. The Lagrangian and Eulerian representations of the *microscopic deformation map* read

$$\check{\boldsymbol{\varphi}}(\boldsymbol{X},t) : \begin{cases} \mathcal{B}\times\mathcal{T} \rightarrow \mathcal{M} \\ (\boldsymbol{X},t) \ \mapsto \boldsymbol{q} = \check{\boldsymbol{\varphi}}(\boldsymbol{X},t) \end{cases} \quad \text{and} \quad \check{\boldsymbol{\varphi}}^\circ(\boldsymbol{x},t) : \begin{cases} \mathcal{S}\times\mathcal{T} \rightarrow \mathcal{M} \\ (\boldsymbol{x},t) \ \ \mapsto \boldsymbol{q} = \check{\boldsymbol{\varphi}}^\circ(\boldsymbol{x},t) \end{cases} \tag{3.4}$$

mapping the Lagrangian or Eulerian coordinates to the abstract order parameter space $\mathcal{M}$. The mappings $\check{\boldsymbol{\varphi}}_t$ and $\check{\boldsymbol{\varphi}}^\circ_t$ cover m scalar variables at each material point P at time $t \in \mathcal{R}_+$. Due to the global character of these fields, boundary conditions have to be introduced. In full analogy to the macroscopic deformation field, the exterior surface of the body is decomposed into a part $\partial\mathcal{B}_{\check{\varphi}}$, where the micro-deformation is prescribed by Dirichlet-type boundary conditions

$$\check{\boldsymbol{\varphi}}(\boldsymbol{X},t) = \check{\boldsymbol{\varphi}}_D(\boldsymbol{X},t) \ \text{ on } \partial\mathcal{B}_{\check{\varphi}}\,, \tag{3.5}$$

and a part $\partial\mathcal{B}_{\check{t}}$, where the micro-traction $\check{\boldsymbol{T}}_N(\boldsymbol{X},t)$ is prescribed by Neumann-type boundary conditions. Again, the common microscopic boundary corresponds to the empty set, i.e. $\partial\mathcal{B}_{\check{\varphi}}\cap\partial\mathcal{B}_{\check{t}} = \emptyset$. The mapping properties of the fundamental macro- and microscopic primary kinematic quantities (3.2) and (3.4) are illustrated in Figure 3.1, where the deformed spatial surfaces $\partial\mathcal{S}_{\bar{\varphi}} = \bar{\boldsymbol{\varphi}}_t(\partial\mathcal{B}_{\bar{\varphi}})$, $\partial\mathcal{S}_{\bar{t}} = \bar{\boldsymbol{\varphi}}_t(\partial\mathcal{B}_{\bar{t}})$, $\partial\mathcal{S}_{\check{\varphi}} = \bar{\boldsymbol{\varphi}}_t(\partial\mathcal{B}_{\check{\varphi}})$, and $\partial\mathcal{S}_{\check{t}} = \bar{\boldsymbol{\varphi}}_t(\partial\mathcal{B}_{\check{t}})$ have been introduced.

3.1.3. Macro- and Microscopic Deformation Gradients. The macroscopic deformation gradient has been introduced in Section 2.1.4 as the fundamental quantity in the kinematics of finite deformations. Recalling definition (2.25), the macroscopic deformation gradient is given by the Fréchet derivative of the deformation map (3.2) with respect to the Lagrangian coordinate $\boldsymbol{X}$ and reads

$$\bar{\boldsymbol{F}} = \nabla_{\boldsymbol{X}}\bar{\boldsymbol{\varphi}}(\boldsymbol{X},t)\,. \tag{3.6}$$

The macroscopic deformation gradient is considered as a linear mapping of line elements mapping tangent vectors $\bar{\boldsymbol{T}} \in \mathcal{B}$ to material curves onto tangent vectors $\bar{\boldsymbol{t}} \in \mathcal{S}$ to deformed

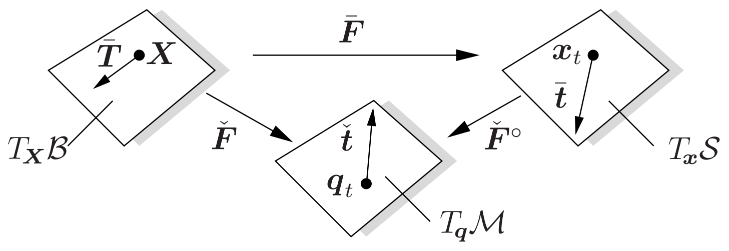

Figure 3.2: Mapping properties of macro- and microscopic deformation gradients. The microscopic deformation gradients $\check{\boldsymbol{F}}$ and $\check{\boldsymbol{F}}^\circ$ map Lagrangian and Eulerian tangents $\bar{\boldsymbol{T}} \in T_{\boldsymbol{X}}\mathcal{B}$ and $\bar{\boldsymbol{t}} \in T_{\boldsymbol{x}}\mathcal{S}$ onto elements of the abstract order parameter space $\check{\boldsymbol{t}} \in T_{\boldsymbol{q}}\mathcal{M}$ that describe the spatial change of the order parameter field.

spatial curves. As intensively discussed in Section 2.1.4 the co-variant bases $\{\bar{\boldsymbol{G}}_i\}_{i=1,2,3}$ and $\{\bar{\boldsymbol{g}}_i\}_{i=1,2,3}$ span the tangent spaces $T_{\boldsymbol{X}}\mathcal{B}$ and $T_{\boldsymbol{x}}\mathcal{S}$ in the Lagrangian and Eulerian setting, respectively. These fully three-dimensional patches live locally at every Lagrangian or Eulerian material point and contain all possible tangent vectors to arbitrary material or spatial curves

$$\bar{\boldsymbol{F}} : \begin{cases} T_{\boldsymbol{X}}\mathcal{B} \to T_{\boldsymbol{x}}\mathcal{S} \\ \bar{\boldsymbol{T}} \quad\;\; \mapsto \bar{\boldsymbol{t}} = \bar{\boldsymbol{F}}\,\bar{\boldsymbol{T}}\,. \end{cases} \tag{3.7}$$

The microscopic deformation gradient is introduced in full analogy to the definition of the macroscopic deformation gradient (3.6). Due to the two possible parametrizations of the microscopic deformation maps (3.4), the micro-deformation gradients can be given by

$$\check{\boldsymbol{F}} = \nabla_{\boldsymbol{X}}\check{\boldsymbol{\varphi}}(\boldsymbol{X}, t) \quad \text{and} \quad \check{\boldsymbol{F}}^\circ = \nabla_{\boldsymbol{x}}\check{\boldsymbol{\varphi}}^\circ(\boldsymbol{x}, t)\,. \tag{3.8}$$

In what follows, the microscopic deformation gradients are considered as mappings of macroscopic Lagrangian and Eulerian line elements. The Lagrangian micro-deformation gradient $\check{\boldsymbol{F}}$ maps tangent vectors $\bar{\boldsymbol{T}} \in \mathcal{B}$ to material curves onto elements of the abstract tangent space $\check{\boldsymbol{t}} \in \mathcal{M}$. The Eulerian micro-deformation gradient $\check{\boldsymbol{F}}^\circ$ maps tangent vectors $\bar{\boldsymbol{t}} \in \mathcal{S}$ to spatial curves onto elements of the abstract tangent space $\check{\boldsymbol{t}} \in \mathcal{M}$. In full analogy to the macroscopic setting, co-variant base vectors $\{\check{\boldsymbol{g}}_i\}_{i=1,\dots,m}$ are introduced to span the tangent space $T_{\boldsymbol{q}}\mathcal{M}$. This allows for the identification of the mapping properties that are assigned to the microscopic deformation gradient

$$\check{\boldsymbol{F}} : \begin{cases} T_{\boldsymbol{X}}\mathcal{B} \to T_{\boldsymbol{q}}\mathcal{M} \\ \bar{\boldsymbol{T}} \quad\;\; \mapsto \check{\boldsymbol{t}} = \check{\boldsymbol{F}}\,\bar{\boldsymbol{T}} \end{cases} \quad \text{and} \quad \check{\boldsymbol{F}}^\circ : \begin{cases} T_{\boldsymbol{x}}\mathcal{S} \to T_{\boldsymbol{q}}\mathcal{M} \\ \bar{\boldsymbol{t}} \quad\;\; \mapsto \check{\boldsymbol{t}} = \check{\boldsymbol{F}}^\circ\,\bar{\boldsymbol{t}}\,. \end{cases} \tag{3.9}$$

Regarding nonlocal effects, the elements of the abstract tangent space $\check{\boldsymbol{t}} \in T_{\boldsymbol{q}}\mathcal{M}$ describe the spatial change of the microscopic deformation within a Lagrangian $\mathcal{N}_{\boldsymbol{X}}$ or Eulerian neighborhood $\mathcal{N}_{\boldsymbol{x}}$ in the direction of the Lagrangian or Eulerian tangent $\bar{\boldsymbol{T}}$ and $\bar{\boldsymbol{t}}$, respectively. As discussed by Steinmann [166] and Geers, Ubachs & Engelen [54], the Lagrangian neighborhood $\mathcal{N}_{\boldsymbol{X}}$ and the Eulerian neighborhoods $\mathcal{N}_{\boldsymbol{x}}$ are associated with a material and spatial length scale parameter L and l, respectively. Note that L describes a constant undeformed region in the reference configuration with a constant set of material points P, whereas l refers to a deformed domain in the current configuration where material points P, depending on the deformation, can enter or leave the domain of influence. The relationship between the microscopic deformation gradients is obtained by $\check{\boldsymbol{F}} = \check{\boldsymbol{F}}^\circ\bar{\boldsymbol{F}}$, a summary of these basic kinematic relations is given in Figure 3.2. In the

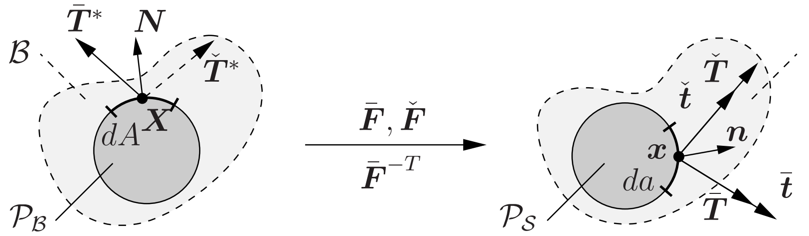

Figure 3.3: Generalized Euler's cut principle. Lagrangian macroscopic $\bar{\boldsymbol{T}}^*(\boldsymbol{X}, t; \boldsymbol{N}) \in T_{\boldsymbol{X}}\mathcal{B}$ and microscopic $\check{\boldsymbol{T}}^*(\boldsymbol{X}, t; \boldsymbol{N}) \in T_{\boldsymbol{q}}\mathcal{M}$ as well as Eulerian macroscopic $\bar{\boldsymbol{t}}(\boldsymbol{x}, t; \boldsymbol{n}) \in T_{\boldsymbol{x}}\mathcal{S}$ and microscopic $\check{\boldsymbol{t}}(\boldsymbol{x}, t; \boldsymbol{n}) \in T_{\boldsymbol{q}}\mathcal{M}$ traction vectors representing the force action of the rest of the body at the vicinity on the surface of the cut out parts $\partial\mathcal{P}_{\mathcal{B}}$ and $\partial\mathcal{P}_{\mathcal{S}}$.

following treatment, the focus lies on a purely Lagrangian nonlocality expressed in terms of the microscopic deformation gradient $\check{\boldsymbol{F}}$. The micro-deformation gradient $\check{\boldsymbol{F}}^\circ$ has been introduced for the sake of completeness.

3.2. Concept of Generalized Stresses

Consider a cut section $\mathcal{P}_{\mathcal{B}} \subset \mathcal{B}$ of the material body in the reference configuration and its spatial counterpart $\mathcal{P}_{\mathcal{S}} \subset \mathcal{S}$ enclosed by the respective boundaries $\partial\mathcal{P}_{\mathcal{B}}$ and $\partial\mathcal{P}_{\mathcal{S}}$. As depicted in Figure 3.3, the *macroscopic stress vector* $\bar{\boldsymbol{t}}$ and the *microscopic stress vector* $\check{\boldsymbol{t}}$ are introduced in the deformed configuration. They act on the surface element $da \subset \partial\mathcal{P}_{\mathcal{S}}$ and represent the force action of the rest of the body. A *generalized Cauchy stress theorem* is introduced that postulates a linear dependency between the macroscopic traction vector $\bar{\boldsymbol{t}} \in T_{\boldsymbol{x}}\mathcal{S}$, the microscopic traction vector $\check{\boldsymbol{t}} \in T_{\boldsymbol{q}}\mathcal{M}$, and the spatial normal $\boldsymbol{n} \in T^*_{\boldsymbol{x}}\mathcal{S}$, i.e.

$$\bar{\boldsymbol{t}}(\boldsymbol{x}, t; \boldsymbol{n}) := \bar{\boldsymbol{\sigma}}(\boldsymbol{x}, t)\, \boldsymbol{n} \quad \text{and} \quad \check{\boldsymbol{t}}(\boldsymbol{x}, t; \boldsymbol{n}) := \check{\boldsymbol{\sigma}}(\boldsymbol{x}, t)\, \boldsymbol{n}\,, \tag{3.10}$$

in terms of the *macroscopic and microscopic Cauchy stress tensor* $\bar{\boldsymbol{\sigma}}$ and $\check{\boldsymbol{\sigma}}$, respectively. In index notation (3.10) reads $\bar{t}^a = \bar{\sigma}^{ab} n_b$ and $\check{t}^\alpha = \check{\sigma}^{\alpha b} n_b$, where Greek letters are introduced for the components of the microscopic order parameter space $\mathcal{M}$. Within the geometric setup for continua with microstructure, the macroscopic Cauchy stress tensor can be interpreted as a contra-variant mapping transforming normals $\boldsymbol{n} \in T^*_{\boldsymbol{x}}\mathcal{S}$ onto spatial macroscopic traction vectors $\bar{\boldsymbol{t}} \in T_{\boldsymbol{x}}\mathcal{S}$ and the microscopic Cauchy stress tensor as a mapping transforming normals $\boldsymbol{n} \in T^*_{\boldsymbol{x}}\mathcal{S}$ onto microscopic traction vectors $\check{\boldsymbol{t}} \in T_{\boldsymbol{q}}\mathcal{M}$

$$\bar{\boldsymbol{\sigma}} : \begin{cases} T^*_{\boldsymbol{x}}\mathcal{S} \to T_{\boldsymbol{x}}\mathcal{S} \\ \boldsymbol{n} \quad \mapsto \bar{\boldsymbol{t}} = \bar{\boldsymbol{\sigma}}\, \boldsymbol{n} \end{cases} \quad \text{and} \quad \check{\boldsymbol{\sigma}} : \begin{cases} T^*_{\boldsymbol{x}}\mathcal{S} \to T_{\boldsymbol{q}}\mathcal{M} \\ \boldsymbol{n} \quad \mapsto \check{\boldsymbol{t}} = \check{\boldsymbol{\sigma}}\, \boldsymbol{n}\,. \end{cases} \tag{3.11}$$

The Cauchy stresses are also denoted as true stresses, because they describe the present force state in the current configuration acting on the deformed area element da. The *generalized macroscopic and microscopic Kirchhoff stress tensors* are defined by

$$\bar{\boldsymbol{\tau}} := J\bar{\boldsymbol{\sigma}} \quad \text{and} \quad \check{\boldsymbol{\tau}} := J\check{\boldsymbol{\sigma}} \tag{3.12}$$

and are used for the construction of spatial stress power terms with respect to the undeformed reference volume. An alternative stress measure can be set up when regarding modified stress vectors $\bar{\boldsymbol{T}} \in T_{\boldsymbol{x}}\mathcal{S}$ and $\check{\boldsymbol{T}} \in T_{\boldsymbol{q}}\mathcal{M}$ that are obtained by scaling the spatial

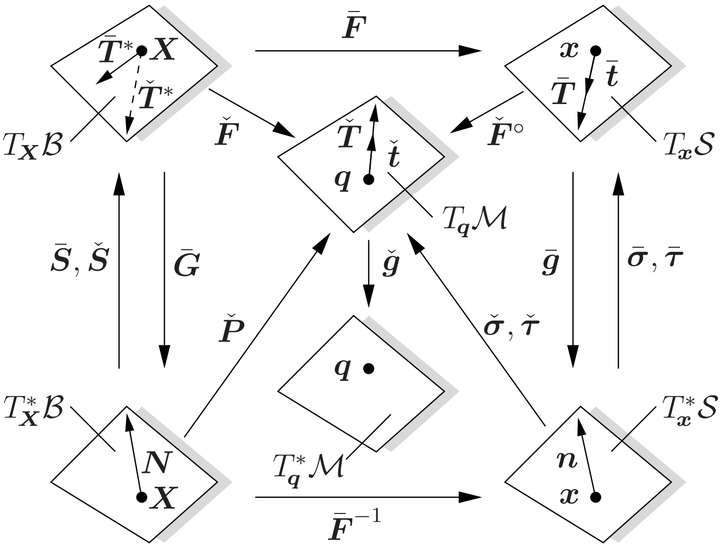
$\bar{\boldsymbol{F}}$
$\bar{\boldsymbol{T}}^*$
$\boldsymbol{X}$
$\check{\boldsymbol{T}}^*$
$T_{\boldsymbol{X}}\mathcal{B}$
$\check{\boldsymbol{F}}$
$\check{\boldsymbol{T}}$
$\check{\boldsymbol{t}}$
$\boldsymbol{q}$
$T_{\boldsymbol{q}}\mathcal{M}$
$\check{\boldsymbol{F}}^\circ$
$\boldsymbol{x}$
$\bar{\boldsymbol{t}}$
$\bar{\boldsymbol{T}}$
$T_{\boldsymbol{x}}\mathcal{S}$
$\bar{\boldsymbol{S}}, \check{\boldsymbol{S}}$
$\bar{\boldsymbol{G}}$
$\check{\boldsymbol{g}}$
$\bar{\boldsymbol{g}}$
$\bar{\boldsymbol{\sigma}}, \bar{\boldsymbol{\tau}}$
$\check{\boldsymbol{P}}$
$\check{\boldsymbol{\sigma}}, \check{\boldsymbol{\tau}}$
$T^*_{\boldsymbol{X}}\mathcal{B}$
$\boldsymbol{N}$
$\boldsymbol{X}$
$\boldsymbol{q}$
$T^*_{\boldsymbol{q}}\mathcal{M}$
$T^*_{\boldsymbol{x}}\mathcal{S}$
$\boldsymbol{n}$
$\boldsymbol{x}$
$\bar{\boldsymbol{F}}^{-1}$

Figure 3.4: Mapping properties of generalized stress tensors. The macroscopic stress tensors $\bar{\boldsymbol{\sigma}}$, $\bar{\boldsymbol{\tau}}$, $\bar{\boldsymbol{P}}$, and $\bar{\boldsymbol{S}}$ and microscopic stress tensors $\check{\boldsymbol{\sigma}}$, $\check{\boldsymbol{\tau}}$, $\check{\boldsymbol{P}}$, and $\check{\boldsymbol{S}}$ are related through the macro- and microscopic deformation gradients $\bar{\boldsymbol{F}}$, $\check{\boldsymbol{F}}$, and $\check{\boldsymbol{F}}^\circ$.

force terms $\bar{\boldsymbol{t}}\,da$ and $\check{\boldsymbol{t}}\,da$ with the reference area element dA. Based on this idea, the exploitation of a reference Cauchy-type theorem

$$\bar{\boldsymbol{T}}(\boldsymbol{X},t;\boldsymbol{N}) := \bar{\boldsymbol{P}}(\boldsymbol{X},t)\,\boldsymbol{N} \quad \text{and} \quad \check{\boldsymbol{T}}(\boldsymbol{X},t;\boldsymbol{N}) := \check{\boldsymbol{P}}(\boldsymbol{X},t)\,\boldsymbol{N} \tag{3.13}$$

yields the macro- and microscopic *generalized first Piola-Kirchhoff stress tensors* $\bar{\boldsymbol{P}}$ and $\check{\boldsymbol{P}}$. The following mapping properties can be assigned

$$\bar{\boldsymbol{P}} : \begin{cases} T^*_{\boldsymbol{X}}\mathcal{B} \to T_{\boldsymbol{x}}\mathcal{S} \\ \boldsymbol{N} \quad \mapsto \bar{\boldsymbol{T}} = \bar{\boldsymbol{P}}\,\boldsymbol{N} \end{cases} \quad \text{and} \quad \check{\boldsymbol{P}} : \begin{cases} T^*_{\boldsymbol{X}}\mathcal{B} \to T_{\boldsymbol{q}}\mathcal{M} \\ \boldsymbol{N} \quad \mapsto \check{\boldsymbol{T}} = \check{\boldsymbol{P}}\,\boldsymbol{N}\,. \end{cases} \tag{3.14}$$

The macroscopic Lagrangian stress vector $\bar{\boldsymbol{T}}^* \in T_{\boldsymbol{X}}\mathcal{B}$ is defined by the macroscopic pull-back operation of the spatial stress vector $\bar{\boldsymbol{T}} \in T_{\boldsymbol{x}}\mathcal{S}$

$$\bar{\boldsymbol{T}}^* = \bar{\boldsymbol{F}}^{-1}\,\bar{\boldsymbol{T}} \quad \text{or} \quad \bar{T}^{*A} = (\bar{F}^{-1})^A{}_a\,\bar{T}^a\,. \tag{3.15}$$

A strict dual treatment of the microscopic spatial stress vector $\check{\boldsymbol{T}} \in T_{\boldsymbol{q}}\mathcal{M}$ with a microscopic pull-back operation yields the microscopic Lagrangian stress vector $\check{\boldsymbol{T}}^* \in T_{\boldsymbol{X}}\mathcal{B}$

$$\check{\boldsymbol{T}}^* = \check{\boldsymbol{F}}^{-1}\,\check{\boldsymbol{T}} \quad \text{or} \quad \check{T}^{*A} = (\check{F}^{-1})^A{}_\alpha\,\check{T}^\alpha\,. \tag{3.16}$$

Note that regarding an arbitrary order of the microstructure m, the inverse microscopic deformation gradient $\check{\boldsymbol{F}}^{-1}$ does not necessarily exist. Nevertheless, the material Cauchy-type theorem states the linear relationship

$$\bar{\boldsymbol{T}}^*(\boldsymbol{X},t;\boldsymbol{N}) := \bar{\boldsymbol{S}}(\boldsymbol{X},t)\,\boldsymbol{N} \quad \text{and} \quad \check{\boldsymbol{T}}^*(\boldsymbol{X},t;\boldsymbol{N}) := \check{\boldsymbol{S}}(\boldsymbol{X},t)\,\boldsymbol{N}\,, \tag{3.17}$$

in terms of the *generalized second Piola-Kirchhoff stress tensors* $\bar{\boldsymbol{S}}$ and $\check{\boldsymbol{S}}$. The following formal mapping properties can be deduced

$$\bar{\boldsymbol{S}} : \begin{cases} T^*_{\boldsymbol{X}}\mathcal{B} \to T_{\boldsymbol{X}}\mathcal{B} \\ \boldsymbol{N} \quad \mapsto \bar{\boldsymbol{T}}^* = \bar{\boldsymbol{S}}\,\boldsymbol{N} \end{cases} \quad \text{and} \quad \check{\boldsymbol{S}} : \begin{cases} T^*_{\boldsymbol{X}}\mathcal{B} \to T_{\boldsymbol{X}}\mathcal{B} \\ \boldsymbol{N} \quad \mapsto \check{\boldsymbol{T}}^* = \check{\boldsymbol{S}}\,\boldsymbol{N}\,. \end{cases} \tag{3.18}$$

A combination of equations (3.14)-(3.18) allows for the reformulation of the macroscopic second Piola-Kirchhoff stress tensor

$$\bar{\boldsymbol{S}} = \bar{\boldsymbol{F}}^{-1}\,\bar{\boldsymbol{P}} = \bar{\boldsymbol{F}}^{-1}\,\bar{\boldsymbol{\tau}}\,\bar{\boldsymbol{F}}^{-T} \quad \text{or} \quad \bar{S}^{AB} = (\bar{F}^{-1})^{A}{}_{a}\,\bar{P}^{aB} = (\bar{F}^{-1})^{A}{}_{a}\,\bar{\tau}^{ab}(\bar{F}^{-1})^{B}{}_{b} \tag{3.19}$$

and for the microscopic second Piola-Kirchhoff stress tensor

$$\check{\boldsymbol{S}} = \check{\boldsymbol{F}}^{-1}\,\check{\boldsymbol{P}} = \check{\boldsymbol{F}}^{-1}\,\check{\boldsymbol{\tau}}\,\bar{\boldsymbol{F}}^{-T} \quad \text{or} \quad \check{S}^{AB} = (\check{F}^{-1})^{A}{}_{\alpha}\,\check{P}^{\alpha B} = (\check{F}^{-1})^{A}{}_{\alpha}\,\check{\tau}^{\alpha b}(\bar{F}^{-1})^{B}{}_{b}\ , \tag{3.20}$$

both expressed in terms of the macro- and microscopic first Piola-Kirchhoff stress tensors $\bar{\boldsymbol{P}}$ and $\check{\boldsymbol{P}}$ or in terms of the Kirchhoff stress tensors $\bar{\boldsymbol{\tau}}$ and $\check{\boldsymbol{\tau}}$, respectively. The same relation holds for the macroscopic Kirchhoff stress tensor

$$\bar{\boldsymbol{\tau}} = J\bar{\boldsymbol{\sigma}} = \bar{\boldsymbol{P}}\,\bar{\boldsymbol{F}}^{T} = \bar{\boldsymbol{F}}\,\bar{\boldsymbol{S}}\,\bar{\boldsymbol{F}}^{T} \quad \text{or} \quad \bar{\tau}^{ab} = J\bar{\sigma}^{ab} = \bar{P}^{aB}\bar{F}^{b}{}_{B} = \bar{F}^{a}{}_{A}\bar{S}^{AB}\bar{F}_{B}{}^{b} \tag{3.21}$$

and for the microscopic Kirchhoff stress tensor

$$\check{\boldsymbol{\tau}} = J\check{\boldsymbol{\sigma}} = \check{\boldsymbol{P}}\,\bar{\boldsymbol{F}}^{T} = \check{\boldsymbol{F}}\,\check{\boldsymbol{S}}\,\bar{\boldsymbol{F}}^{T} \quad \text{or} \quad \check{\tau}^{\alpha b} = J\bar{\sigma}^{\alpha b} = \check{P}^{\alpha B}\bar{F}^{b}{}_{B} = \check{F}^{\alpha}{}_{A}\check{S}^{AB}\bar{F}_{B}{}^{b}\ . \tag{3.22}$$

A compact illustration of the geometric mapping properties of the proposed generalized stress measures is given in Figure 3.4, see also ZÄH [181] for more detailed information.

3.3. Macro- and Microscopic Dual Stresses and Strains

The book by FRÉMOND [51] offers a very general approach to gradient-type dissipative materials with an intense focus on the full thermodynamic setting. In all of these treatments, the critical point is to account for the *working of independent kinematic processes associated with the microstructure* of the material characterized by the micro structural fields. Substructural interactions are accompanied by explicit power expressions in the rate of the microstructural variables yielding additional balance equations associated with the microstructure. As a consequence, the standard macro-balances of mass and momentum are coupled with additional micro-balance equations that govern the micro force systems associated with the order parameters. Thus, the dual stresses and strains defined for a standard continuum (2.73) have to be extended to take into account the working of the microstructural fields. The generalized stress power in a microscopic Lagrangian setting

$$\mathcal{P} = (\bar{\boldsymbol{g}}\bar{\boldsymbol{P}}) : \dot{\bar{\boldsymbol{F}}} + \check{\boldsymbol{p}}\cdot\dot{\check{\boldsymbol{\varphi}}} + (\check{\boldsymbol{g}}\check{\boldsymbol{P}}) : \dot{\check{\boldsymbol{F}}} \quad \text{or} \quad \mathcal{P} = (\bar{g}_{ab}\bar{P}^{bA})\,\dot{\bar{F}}^{a}{}_{A} + \check{p}_{\alpha}\dot{\check{\varphi}}^{\alpha} + (\check{g}_{\alpha\beta}\check{P}^{\beta A})\dot{\check{F}}^{\alpha}{}_{A} \tag{3.23}$$

contains the macroscopic first Piola-Kirchhoff stress tensor $\bar{\boldsymbol{g}}\bar{\boldsymbol{P}}$ and the macroscopic deformation gradient $\bar{\boldsymbol{F}}$, the microscopic force $\check{\boldsymbol{p}}$ and the microscopic deformation $\check{\boldsymbol{\varphi}}$, and the microscopic stress tensor $\check{\boldsymbol{g}}\check{\boldsymbol{P}}$ and the macroscopic deformation gradient $\check{\boldsymbol{F}}$ as *dual objects*. In a microscopic Eulerian setting, the generalized stress power

$$\mathcal{P} = (\bar{\boldsymbol{g}}\bar{\boldsymbol{P}}) : \dot{\bar{\boldsymbol{F}}} + \check{\boldsymbol{p}}\cdot\dot{\check{\boldsymbol{\varphi}}} + (\check{\boldsymbol{g}}\check{\boldsymbol{\sigma}}) : \dot{\check{\boldsymbol{F}}}{}^{\circ} \quad \text{or} \quad \mathcal{P} = (\bar{g}_{ab}\bar{P}^{bA})\,\dot{\bar{F}}^{a}{}_{A} + \check{p}_{\alpha}\dot{\check{\varphi}}^{\alpha} + (\check{g}_{\alpha\beta}\check{\sigma}^{\beta a})\dot{\check{F}}^{\circ\alpha}{}_{a} \tag{3.24}$$

contains the microscopic stress $\check{\boldsymbol{g}}\check{\boldsymbol{\sigma}}$ and the micro-deformation gradient $\check{\boldsymbol{F}}^{\circ}$ as *dual objects*.

3.4. External Loading of Continua with Microstructure

The continuum with microstructure is assumed to be loaded by macroscopic and microscopic external field actions. As visualized in Figure 3.5, the continuum is loaded by a

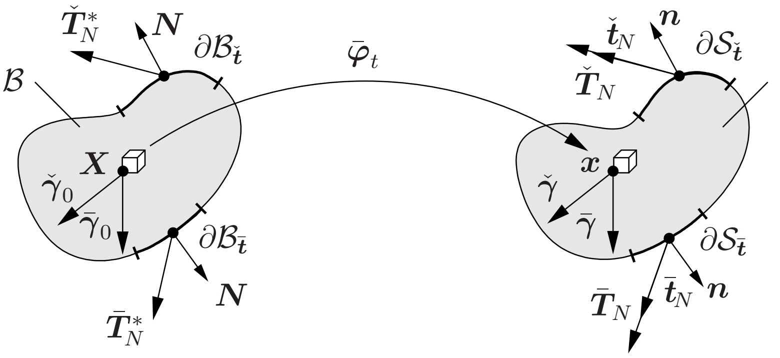
$\check{\boldsymbol{T}}^*_N$
$\boldsymbol{N}$
$\partial\mathcal{B}_{\check{t}}$
$\bar{\boldsymbol{\varphi}}_t$
$\check{\boldsymbol{t}}_N$
$\boldsymbol{n}$
$\partial\mathcal{S}_{\check{t}}$
$\mathcal{B}$
$\check{\boldsymbol{T}}_N$
$\mathcal{S}$
$\boldsymbol{X}$
$\boldsymbol{x}$
$\check{\gamma}_0$
$\bar{\gamma}_0$
$\check{\gamma}$
$\bar{\gamma}$
$\partial\mathcal{B}_{\bar{t}}$
$\partial\mathcal{S}_{\bar{t}}$
$\boldsymbol{N}$
$\bar{\boldsymbol{T}}_N$
$\bar{\boldsymbol{t}}_N$
$\boldsymbol{n}$
$\bar{\boldsymbol{T}}^*_N$

Figure 3.5: External loading of continua with microstructure. Prescribed Eulerian macro- and microscopic volume forces $\bar{\gamma}$ and $\check{\gamma}$ and Neumann-type surface tractions $\bar{\boldsymbol{T}}_N$ and $\check{\boldsymbol{T}}_N$.

macroscopic body force field $\bar{\gamma}_0$ per unit volume of the domain $\mathcal{B}$. Furthermore, on the surface $\partial\mathcal{B}_{\bar{t}}$, a traction field $\bar{\boldsymbol{T}}_N$ is defined representing the macroscopic Neumann boundary condition. The power of external macroscopic loading reads

$$\bar{\mathcal{P}}_{ext}(\dot{\bar{\boldsymbol{\varphi}}}) := \int_{\mathcal{B}} \bar{\gamma}_0(\boldsymbol{X}, t) \cdot \dot{\bar{\boldsymbol{\varphi}}} \, dV + \int_{\partial\mathcal{B}_{\bar{t}}} \bar{\boldsymbol{g}} \bar{\boldsymbol{T}}_N(\boldsymbol{X}, t) \cdot \dot{\bar{\boldsymbol{\varphi}}} \, dA \, . \tag{3.25}$$

In analogy to the macroscopic loading, possible external actions related to microscopic fields associated with the abstract micro-motion are considered. To this end, an abstract microscopic source $\check{\gamma}_0$ per unit volume of the continuum $\mathcal{B}$ and a prescribed micro-traction field $\check{\boldsymbol{T}}_N$ on the surface $\partial\mathcal{B}_{\check{t}}$ representing the Neumann-type boundary condition are introduced. Thus, the microscopic power contribution of external loading reads

$$\check{\mathcal{P}}_{ext}(\dot{\check{\boldsymbol{\varphi}}}) := \int_{\mathcal{B}} \check{\gamma}_0(\boldsymbol{X}, t) \cdot \dot{\check{\boldsymbol{\varphi}}} \, dV + \int_{\partial\mathcal{B}_{\check{t}}} \check{\boldsymbol{g}} \check{\boldsymbol{T}}_N(\boldsymbol{X}, t) \cdot \dot{\check{\boldsymbol{\varphi}}} \, dA \, . \tag{3.26}$$

Having both contributions at hand, the total external power due to prescribed external loading fields can additively be expressed by

$$\mathcal{P}_{ext} = \bar{\mathcal{P}}_{ext} + \check{\mathcal{P}}_{ext} \tag{3.27}$$

and characterizes the external multi-field loading of the continuum with microstructure.

3.5. Constitutive Response of Order-Parameter Materials

The focus of this subsection lies on the introduction of the constitutive equations and the according reduced forms. Ideas of local standard dissipative materials, see e.g. Biot [13, 14], Nguyen [141], Halphen & Nguyen [76], Nguyen & Andrieux [142], and Ziegler & Wehrli [182] are generalized and adopted for the underlying multi-field framework. So-called reduced forms are derived that a priori fulfill the second law of thermodynamics and the power of internal mechanisms is set up. Hereby, the subsequent formulation extends ideas outlined in Miehe [120] to the large strain format.

3.5.1. Energy Storage and Dissipation. Within the context of standard dissipative materials, the constitutive response is exclusively determined by two scalar-valued functionals, namely the *energy storage* and the *dissipation functionals*

$$E(\bar{\boldsymbol{\varphi}}, \check{\boldsymbol{\varphi}}) := \int_{\mathcal{B}} \psi \, dV \quad \text{and} \quad D(\dot{\bar{\boldsymbol{\varphi}}}, \dot{\check{\boldsymbol{\varphi}}}; \bar{\boldsymbol{\varphi}}, \check{\boldsymbol{\varphi}}) := \int_{\mathcal{B}} \phi \, dV \, . \tag{3.28}$$

The functional E represents the free energy stored inside the body $\mathcal{B}$ due to its macro- and microscopic deformation. The functional D describes internal dissipative mechanisms. The local quantities ψ and ϕ are called the *energy storage function* and *dissipation function*, respectively. Locally at a material point, they describe the density of the stored energy and the dissipation. Focusing on *materials of grade one*, the free energy and the dissipation function depend on the macro- and micro-motion, their first gradients, and their rates. The set of independent constitutive state variables is given by

$$\mathfrak{c}_0 := \{\, \bar{\boldsymbol{\varphi}}, \bar{\boldsymbol{F}}, \check{\boldsymbol{\varphi}}, \check{\boldsymbol{F}} \,\} \quad \text{or} \quad \mathfrak{c}_0^\circ := \{\, \bar{\boldsymbol{\varphi}}, \bar{\boldsymbol{F}}, \check{\boldsymbol{\varphi}}^\circ, \check{\boldsymbol{F}}^\circ \,\}\,, \tag{3.29}$$

where a material or spatial parametrization of the micro-deformation can be chosen, see definition (3.4). With this definition, a material or spatial constitutive description

$$\psi = \psi(\mathfrak{c}_0) \quad \text{and} \quad \phi = \phi(\dot{\mathfrak{c}}_0; \mathfrak{c}_0) \quad \text{or} \quad \psi = \psi(\mathfrak{c}_0^\circ) \quad \text{and} \quad \phi = \phi(\dot{\mathfrak{c}}_0^\circ; \mathfrak{c}_0^\circ) \tag{3.30}$$

can be introduced. An intense discussion of material and spatial nonlocality can be found in the contributions by Geers, Ubachs & Engelen [54] and Steinmann [166].

3.5.2. Material Frame Invariance. Effective State Variables. The basic *principle of material frame invariance* or *principle of material objectivity* can be traced back to Truesdell & Noll [172] and demands the constitutive functions being invariant with respect to macroscopic rigid body motions superimposed onto the current configuration. To this end, consider a time-dependent macroscopic rigid body motion

$$\boldsymbol{x}^+ : \begin{cases} \mathcal{S} \rightarrow \mathcal{S}^+ \\ \boldsymbol{x} \mapsto \boldsymbol{x}^+ = \bar{\boldsymbol{Q}}\, \boldsymbol{x} + \bar{\boldsymbol{c}} \end{cases} \tag{3.31}$$

characterized by the time-dependent orthogonal rotation matrix $\bar{\boldsymbol{Q}}(t)$ with the properties

$$\bar{\boldsymbol{Q}} \in \mathcal{SO}(3) := \{ \bar{\boldsymbol{Q}} \mid \bar{\boldsymbol{Q}}\, \bar{\boldsymbol{Q}}^T = \boldsymbol{1} \text{ and } \det[\bar{\boldsymbol{Q}}] = 1 \}\,, \tag{3.32}$$

where $\mathcal{SO}(3)$ represents the special orthogonal linear group in the Euclidian space $\mathcal{R}^3$ and the vector $\bar{\boldsymbol{c}}(t)$ characterizes a time-dependent translation. In order to guarantee material frame invariance, the free energy function needs to satisfy the condition

$$\psi(\mathfrak{c}_0) = \psi(\mathfrak{c}_0^+) \quad \text{or} \quad \psi(\mathfrak{c}_0^\circ) = \psi(\mathfrak{c}_0^{\circ +})\,, \tag{3.33}$$

whereas the dissipation function needs to satisfy

$$\phi(\dot{\mathfrak{c}}_0; \mathfrak{c}_0) = \phi(\dot{\mathfrak{c}}_0^+; \mathfrak{c}_0^+) \quad \text{or} \quad \phi(\dot{\mathfrak{c}}_0^\circ; \mathfrak{c}_0^\circ) = \phi(\dot{\mathfrak{c}}_0^{\circ +}; \mathfrak{c}_0^{\circ +})\,, \tag{3.34}$$

for arbitrary rotation matrices $\bar{\boldsymbol{Q}} \in \mathcal{SO}(3)$. This rotation matrix is used to define the modified states $\mathfrak{c}_0^+ = \{\, \bar{\boldsymbol{\varphi}}^+, \bar{\boldsymbol{F}}^+, \check{\boldsymbol{\varphi}}, \check{\boldsymbol{F}} \,\}$ and $\mathfrak{c}_0^{\circ +} = \{\, \bar{\boldsymbol{\varphi}}^+, \bar{\boldsymbol{F}}^+, \check{\boldsymbol{\varphi}}^\circ, \check{\boldsymbol{F}}^\circ \,\}$. As a consequence, the free energy ψ and the dissipation function ϕ cannot depend on the macroscopic deformation field $\bar{\boldsymbol{\varphi}}$ and its rate $\dot{\bar{\boldsymbol{\varphi}}}$, respectively. In a first step, this constraint motivates the introduction of a reduced set of state variables

$$\mathfrak{c} := \{\, \bar{\boldsymbol{F}}, \check{\boldsymbol{\varphi}}, \check{\boldsymbol{F}} \,\} \quad \text{or} \quad \mathfrak{c}^\circ := \{\, \bar{\boldsymbol{F}}, \check{\boldsymbol{\varphi}}^\circ, \check{\boldsymbol{F}}^\circ \,\}\,. \tag{3.35}$$

A further outcome of (3.33) and (3.34) is another reduced set of state variables that a priori fulfills the objectivity constraint and is obtained by replacing the dependency on the macroscopic deformation gradient $\bar{\boldsymbol{F}}$ in the constitutive state (3.35) by the macroscopic right Cauchy-Green tensor. The reason can be found in the invariance property of the right Cauchy-Green tensor

$$\bar{\boldsymbol{C}}^{+} = \bar{\boldsymbol{F}}^{+T}\bar{\boldsymbol{g}}\bar{\boldsymbol{F}}^{+} = (\bar{\boldsymbol{F}}^{T}\bar{\boldsymbol{Q}}^{T})\,\bar{\boldsymbol{g}}\,(\bar{\boldsymbol{Q}}\bar{\boldsymbol{F}}) = \bar{\boldsymbol{F}}^{T}\bar{\boldsymbol{g}}\bar{\boldsymbol{F}} = \bar{\boldsymbol{C}} \tag{3.36}$$

with respect to superimposed rotations $\bar{\boldsymbol{Q}}$. Thus, an a priori objective constitutive state

$$\mathfrak{c}_{L} := \{\, \bar{\boldsymbol{C}}, \check{\boldsymbol{\varphi}}, \check{\boldsymbol{F}} \,\} \quad \text{or} \quad \mathfrak{c}^{\circ}_{L} := \{\, \bar{\boldsymbol{C}}, \check{\boldsymbol{\varphi}}^{\circ}, \check{\boldsymbol{F}}^{\circ} \,\} \tag{3.37}$$

can be introduced. For the sake of simplicity, in the remaining part of this section the constitutive state (3.35) is employed. This yields the constitutive descriptions

$$\boxed{\psi = \psi(\mathfrak{c}) \quad \text{and} \quad \phi = \phi(\dot{\mathfrak{c}}; \mathfrak{c}) \quad \text{or} \quad \psi = \psi(\mathfrak{c}^{\circ}) \quad \text{and} \quad \phi = \phi(\dot{\mathfrak{c}}^{\circ}; \mathfrak{c}^{\circ})\,.} \tag{3.38}$$

Note that the microscopic material description $(3.4)_1$ is used throughout the remaining part of this work. The microscopic spatial counterpart can easily be obtained by an analogous approach.

3.5.3. Rate of Energy Storage and Dissipation Functionals. The above constitutive functions determine the power expressions of energetic and dissipative mechanisms caused by a deformation of the solid. The *power of energy storage mechanisms* is defined as the total time derivative of the energy storage functional $(3.28)_1$, i.e.

$$\begin{aligned}
\mathcal{E}(\dot{\bar{\boldsymbol{\varphi}}}, \dot{\check{\boldsymbol{\varphi}}}; \bar{\boldsymbol{\varphi}}, \check{\boldsymbol{\varphi}}) := \frac{d}{dt}E &= \int_{\mathcal{B}} \partial_{\mathfrak{c}}\psi \cdot \dot{\mathfrak{c}}\, dV \\
&= \int_{\mathcal{B}} \{\, \delta_{\bar{\boldsymbol{\varphi}}}\psi \cdot \dot{\bar{\boldsymbol{\varphi}}} + \delta_{\check{\boldsymbol{\varphi}}}\psi \cdot \dot{\check{\boldsymbol{\varphi}}} \,\}\, dV \\
&+ \int_{\partial\mathcal{B}_{\bar{\boldsymbol{t}}}} \{\, (\partial_{\bar{\boldsymbol{F}}}\psi \cdot \boldsymbol{N}) \cdot \dot{\bar{\boldsymbol{\varphi}}} \,\}\, dA + \int_{\partial\mathcal{B}_{\check{\boldsymbol{t}}}} \{\, (\partial_{\check{\boldsymbol{F}}}\psi \cdot \boldsymbol{N}) \cdot \dot{\check{\boldsymbol{\varphi}}} \,\}\, dA
\end{aligned} \tag{3.39}$$

In this expression, the variational or functional derivatives of the free energy function ψ with respect to the macro- and micro-motion fields are introduced

$$\delta_{\bar{\boldsymbol{\varphi}}}\psi := -\operatorname{DIV}[\partial_{\bar{\boldsymbol{F}}}\psi] \quad \text{and} \quad \delta_{\check{\boldsymbol{\varphi}}}\psi := \partial_{\check{\boldsymbol{\varphi}}}\psi - \operatorname{DIV}[\partial_{\check{\boldsymbol{F}}}\psi]\,. \tag{3.40}$$

In contrast, the *dissipation functional* is not the time derivative of the dissipation functional $(3.28)_2$, but is defined by the expression

$$\begin{aligned}
\mathcal{D}(\dot{\bar{\boldsymbol{\varphi}}}, \dot{\check{\boldsymbol{\varphi}}}; \bar{\boldsymbol{\varphi}}, \check{\boldsymbol{\varphi}}) \; &:= \int_{\mathcal{B}} \partial_{\dot{\mathfrak{c}}}\phi \cdot \dot{\mathfrak{c}}\, dV \\
&= \int_{\mathcal{B}} \{\, \delta_{\dot{\bar{\boldsymbol{\varphi}}}}\phi \cdot \dot{\bar{\boldsymbol{\varphi}}} + \delta_{\dot{\check{\boldsymbol{\varphi}}}}\phi \cdot \dot{\check{\boldsymbol{\varphi}}} \,\}\, dV \\
&+ \int_{\partial\mathcal{B}_{\bar{\boldsymbol{t}}}} \{\, (\partial_{\dot{\bar{\boldsymbol{F}}}}\phi \cdot \boldsymbol{N}) \cdot \dot{\bar{\boldsymbol{\varphi}}} \,\}\, dA + \int_{\partial\mathcal{B}_{\check{\boldsymbol{t}}}} \{\, (\partial_{\dot{\check{\boldsymbol{F}}}}\phi \cdot \boldsymbol{N}) \cdot \dot{\check{\boldsymbol{\varphi}}} \,\}\, dA
\end{aligned} \tag{3.41}$$

Analogous to (3.40), the functional derivatives of the dissipation function ϕ with respect to the rates of the macro- and micro-motion fields are specified to

$$\delta_{\dot{\bar{\boldsymbol{\varphi}}}}\phi := -\operatorname{DIV}[\partial_{\dot{\bar{\boldsymbol{F}}}}\phi] \quad \text{and} \quad \delta_{\dot{\check{\boldsymbol{\varphi}}}}\phi := \partial_{\dot{\check{\boldsymbol{\varphi}}}}\phi - \operatorname{DIV}[\partial_{\dot{\check{\boldsymbol{F}}}}\phi]\,. \tag{3.42}$$

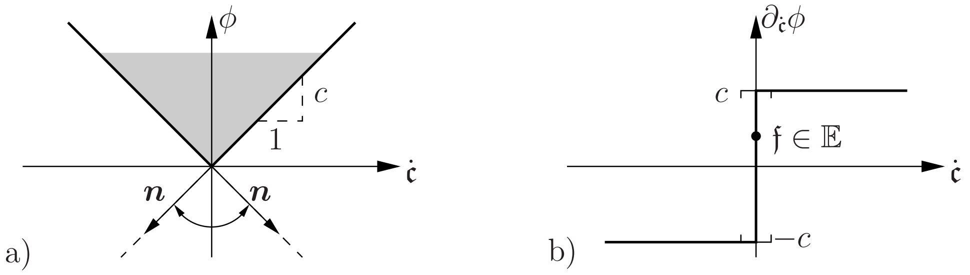

Figure 3.6: One-dimensional positively homogeneous function of degree one. a) Dissipation function $\phi(\dot{\mathfrak{c}}) = c\,|\dot{\mathfrak{c}}|$ with normal cone at $\dot{\mathfrak{c}} = 0$ and b) subgradient $\partial_{\dot{\mathfrak{c}}}\phi(\dot{\mathfrak{c}})$ with elastic domain $\mathbb{E}$ bounding the thermodynamic force $\mathfrak{f}$.

Thus, the total power of internal mechanisms in generalized standard dissipative materials additively decomposes into the energy storage and dissipative contributions

$$\mathcal{P}_{int} = \mathcal{E} + \mathcal{D} \tag{3.43}$$

and is exclusively governed by the constitutive functions ψ and ϕ. Clearly, both contributions contain coupling effects from the macro- and microscopic actions.

3.5.4. Irreversibility Constraint and Convex Dissipation Function. The central idea of the second axiom of thermodynamics demands that the dissipative power remains positive for all admissible thermodynamic processes

$$\mathcal{D} \geq 0\,. \tag{3.44}$$

This constraint is satisfied if the integrand in (3.41) is positive for arbitrary arguments. The above inequality serves as a fundamental physically-based constraint on the constitutive dissipation function ϕ, which is a priori satisfied if the following conditions hold. The dissipation function ϕ needs to satisfy the *normalization condition* and has to be *positive* for arbitrary deformation arguments

$$\phi(\boldsymbol{0};\mathfrak{c}) = 0 \quad \text{and} \quad \phi(\dot{\mathfrak{c}};\mathfrak{c}) \geq 0\,. \tag{3.45}$$

The dissipation function ϕ has to be *convex* with respect to the rate arguments

$$\alpha\,\phi(\dot{\mathfrak{c}}_1;\mathfrak{c}) + (1-\alpha)\phi(\dot{\mathfrak{c}}_2;\mathfrak{c}) > \phi(\alpha\,\dot{\mathfrak{c}}_1 + (1-\alpha)\dot{\mathfrak{c}}_2;\mathfrak{c}) \tag{3.46}$$

for $\alpha \in [0,1]$. When these conditions are satisfied, the integrand in (3.41) remains positive.

3.5.5. Non-Smooth Dissipation Functions and Notion of Sub-Gradients. Plasticity and dry friction are rate-independent irreversible processes governed by non-smooth dissipation functions ϕ. Rate-independent processes are characterized by dissipation functions that are *positively homogeneous of degree one* with respect to the fluxes

$$\phi(\alpha\,\dot{\mathfrak{c}};\mathfrak{c}) = \alpha\,\phi(\dot{\mathfrak{c}};\mathfrak{c})\,. \tag{3.47}$$

Such a function has a cone-like graph and is not differentiable evaluated at zero arguments $(\boldsymbol{0};\mathfrak{c})$, see Figure 3.6 for a one-dimensional representation. As a consequence, the differential operator for smooth functions needs to be generalized and the notion of *sub* *differentials* is introduced. Thus, $\partial_{\dot{\mathfrak{c}}}(\cdot)$ denotes the sub-differential of a non-smooth, convex dissipation function, see Moreau [135], Maugin [110], and references therein. The set

$$\mathbb{E} := \partial_{\dot{\mathfrak{c}}}\phi|_{(\boldsymbol{0};\mathfrak{c})} = \{\, \mathfrak{f} \,|\, \mathfrak{f} \cdot \dot{\mathfrak{c}} \le \phi(\dot{\mathfrak{c}};\mathfrak{c}) \,\} \tag{3.48}$$

is a convex domain for the admissible thermodynamic forces $\mathfrak{f}$ for all rates $\dot{\mathfrak{c}}$, often denoted as elastic domain. Elements $\mathfrak{f} \in \mathbb{E}$ are sub-gradients of the non-smooth function $\phi(\boldsymbol{0};\mathfrak{c})$ evaluated at zero rate-arguments. Using terminologies of convex non-smooth analysis, the dissipation function ϕ is the support function of the convex set $\mathbb{E}$. When taking the derivative of (3.47) with respect to α, the following relationship is obtained

$$\partial_{\dot{\mathfrak{c}}}\phi \cdot \dot{\mathfrak{c}} = \phi(\dot{\mathfrak{c}};\mathfrak{c})\,. \tag{3.49}$$

Integration over the domain under focus and comparison with $(3.28)_2$ finally gives

$$\mathcal{D}(\dot{\bar{\boldsymbol{\varphi}}},\dot{\check{\boldsymbol{\varphi}}};\bar{\boldsymbol{\varphi}},\check{\boldsymbol{\varphi}}) = \int_{\mathcal{B}} \partial_{\dot{\mathfrak{c}}}\phi(\dot{\mathfrak{c}};\mathfrak{c}) \cdot \dot{\mathfrak{c}}\, dV \equiv \int_{\mathcal{B}} \phi(\dot{\mathfrak{c}};\mathfrak{c})\, dV = D(\dot{\bar{\boldsymbol{\varphi}}},\dot{\check{\boldsymbol{\varphi}}};\bar{\boldsymbol{\varphi}},\check{\boldsymbol{\varphi}})\,, \tag{3.50}$$

leading to the conclusion that for rate-independent processes the dissipation $(3.28)_2$ coincides with the dissipation functional (3.41).

3.6. Exploitation of the Principle of Virtual Power

This subsection is concerned with the derivation of the governing coupled field equations for gradient-type standard dissipative solids. Starting from the global equilibration of internal and external virtual power, the balance equations for quasi-static processes are obtained. The focus hereby lies on the different possibilities to express the dissipation function. First, a canonical dissipation function, then a conjugate rate-independent and rate-dependent representation of the dissipation function are investigated.

3.6.1. Coupled Two-Field Balances of Gradient-Type Solids. In order to determine the coupled macro- and micro-balance equations, the standard argument of virtual power is exploited. At time t with a given state of the system $\{\bar{\boldsymbol{\varphi}},\check{\boldsymbol{\varphi}}\}$, the argument

$$0 \in \mathcal{E}(\dot{\bar{\boldsymbol{\varphi}}},\dot{\check{\boldsymbol{\varphi}}};\bar{\boldsymbol{\varphi}},\check{\boldsymbol{\varphi}}) + \mathcal{D}(\dot{\bar{\boldsymbol{\varphi}}},\dot{\check{\boldsymbol{\varphi}}};\bar{\boldsymbol{\varphi}},\check{\boldsymbol{\varphi}}) - \mathcal{P}_{ext}(\dot{\bar{\boldsymbol{\varphi}}},\dot{\check{\boldsymbol{\varphi}}}) \tag{3.51}$$

has to be satisfied for all admissible rates $\dot{\bar{\boldsymbol{\varphi}}}$ and $\dot{\check{\boldsymbol{\varphi}}}$ of the macro- and micro-motion satisfying the homogeneous form of the Dirichlet-type boundary condition

$$\dot{\bar{\boldsymbol{\varphi}}} \in \mathcal{W}^0_{\bar{\boldsymbol{\varphi}}} := \{\, \dot{\bar{\boldsymbol{\varphi}}} \,|\, \dot{\bar{\boldsymbol{\varphi}}} = \boldsymbol{0} \;\text{ on }\; \partial\mathcal{B}_{\bar{\boldsymbol{\varphi}}}\} \quad \text{and} \quad \dot{\check{\boldsymbol{\varphi}}} \in \mathcal{W}^0_{\check{\boldsymbol{\varphi}}} := \{\, \dot{\check{\boldsymbol{\varphi}}} \,|\, \dot{\check{\boldsymbol{\varphi}}} = \boldsymbol{0} \;\text{ on }\; \partial\mathcal{B}_{\check{\boldsymbol{\varphi}}}\}\,. \tag{3.52}$$

When restricting to quasi-static processes, the principle of virtual power (3.51) *equilibrates the internal* and *external virtual power* $\mathcal{P}_{int}$ and $\mathcal{P}_{ext}$. Insertion of the rate of energy storage functional (3.39), the dissipation functional (3.41), and the external power functional (3.27) and application of Gauss' theorem gives

$$\begin{aligned} 0 \;\in\; & \int_{\mathcal{B}} \{[\delta_{\bar{\boldsymbol{\varphi}}}\psi + \delta_{\dot{\bar{\boldsymbol{\varphi}}}}\phi - \bar{\gamma}_0] \cdot \dot{\bar{\boldsymbol{\varphi}}}\}\, dV + \int_{\partial\mathcal{B}_{\bar{t}}} \{[(\partial_{\bar{\boldsymbol{F}}}\psi + \partial_{\dot{\bar{\boldsymbol{F}}}}\phi) \cdot \boldsymbol{N} - \bar{\boldsymbol{g}}\bar{\boldsymbol{T}}_N] \cdot \dot{\bar{\boldsymbol{\varphi}}}\}\, dA \\ & + \int_{\mathcal{B}} \{[\delta_{\check{\boldsymbol{\varphi}}}\psi + \delta_{\dot{\check{\boldsymbol{\varphi}}}}\phi - \check{\gamma}_0] \cdot \dot{\check{\boldsymbol{\varphi}}}\}\, dV + \int_{\partial\mathcal{B}_{\check{t}}} \{[(\partial_{\check{\boldsymbol{F}}}\psi + \partial_{\dot{\check{\boldsymbol{F}}}}\phi) \cdot \boldsymbol{N} - \check{\boldsymbol{g}}\check{\boldsymbol{T}}_N] \cdot \dot{\check{\boldsymbol{\varphi}}}\}\, dA \end{aligned} \tag{3.53}$$

Table 3.1: Coupled two-field balances of gradient-type solids.

Macroscopic equilibrium condition

$$\boldsymbol{0} \in \mathrm{DIV}[\,\partial_{\bar{\boldsymbol{F}}}\psi + \partial_{\dot{\bar{\boldsymbol{F}}}}\phi\,] + \bar{\gamma}_0 \quad \text{in} \;\; \mathcal{B}$$

$$\bar{\boldsymbol{g}}\bar{\boldsymbol{T}}_N = (\partial_{\bar{\boldsymbol{F}}}\psi + \partial_{\dot{\bar{\boldsymbol{F}}}}\phi) \cdot \boldsymbol{N} \quad \text{on} \;\; \partial\mathcal{B}_{\bar{\boldsymbol{t}}}$$

Microscopic evolution equation

$$\boldsymbol{0} \in \mathrm{DIV}[\,\partial_{\check{\boldsymbol{F}}}\psi + \partial_{\dot{\check{\boldsymbol{F}}}}\phi\,] - [\,\partial_{\check{\boldsymbol{\varphi}}}\psi + \partial_{\dot{\check{\boldsymbol{\varphi}}}}\phi\,] + \check{\gamma}_0 \quad \text{in} \;\; \mathcal{B}$$

$$\check{\boldsymbol{g}}\check{\boldsymbol{T}}_N = (\partial_{\check{\boldsymbol{F}}}\psi + \partial_{\dot{\check{\boldsymbol{F}}}}\phi) \cdot \boldsymbol{N} \quad \text{on} \;\; \partial\mathcal{B}_{\check{\boldsymbol{t}}}$$

for all $\dot{\bar{\boldsymbol{\varphi}}} \in \mathcal{W}^0_{\bar{\boldsymbol{\varphi}}}$ and $\dot{\check{\boldsymbol{\varphi}}} \in \mathcal{W}^0_{\check{\boldsymbol{\varphi}}}$. As a result the coupled balance equations

$$\boldsymbol{0} \in \delta_{\bar{\boldsymbol{\varphi}}}\psi + \delta_{\dot{\bar{\boldsymbol{\varphi}}}}\phi - \bar{\gamma}_0 \quad \text{and} \quad \boldsymbol{0} \in \delta_{\check{\boldsymbol{\varphi}}}\psi + \delta_{\dot{\check{\boldsymbol{\varphi}}}}\phi - \check{\gamma}_0 \tag{3.54}$$

are obtained in the domain $\mathcal{B}$ coming along with the Neumann-type boundary condition for the macro- and microscopic traction on the traction boundaries

$$(\partial_{\bar{\boldsymbol{F}}}\psi + \partial_{\dot{\bar{\boldsymbol{F}}}}\phi) \cdot \boldsymbol{N} = \bar{\boldsymbol{g}}\bar{\boldsymbol{T}}_N \;\; \text{on } \partial\mathcal{B}_{\bar{\boldsymbol{t}}} \quad \text{and} \quad (\partial_{\check{\boldsymbol{F}}}\psi + \partial_{\dot{\check{\boldsymbol{F}}}}\phi) \cdot \boldsymbol{N} = \check{\boldsymbol{g}}\check{\boldsymbol{T}}_N \;\; \text{on } \partial\mathcal{B}_{\check{\boldsymbol{t}}}\,. \tag{3.55}$$

An explicit representation that follows by execution of the variational derivative is given in Table 3.1. It consists of the *macroscopic stress equilibrium* condition and a *microscopic balance-type evolution equation* valid in the domain $\mathcal{B}$. The last equation determines the evolution of the micro-deformation field $\check{\boldsymbol{\varphi}}$. This summarizes the basic ingredients of gradient-type standard dissipative solids in the multi-field context in terms of the *two fields* $\bar{\boldsymbol{\varphi}}$ and $\check{\boldsymbol{\varphi}}$ introduced in (3.2) and $(3.4)_1$.

3.6.2. Coupled Three-Field Balance Equations of Gradient-Type Solids. An alternative three-field representation of the coupled balance equations bases on the introduction of a variable *dual* to the rate of the constitutive state, see also Section 3.5.5. To this end, the following representation of the dissipation is introduced

$$\mathcal{D} := \int_{\mathcal{B}} \boldsymbol{\mathfrak{f}} \cdot \dot{\boldsymbol{\mathfrak{c}}}\, dV \geq 0 \tag{3.56}$$

containing the inner product of the thermodynamic dissipative force array and the rate of the constitutive state

$$\boldsymbol{\mathfrak{f}} := \{\, \bar{\boldsymbol{\mathcal{F}}}, \check{\boldsymbol{f}}, \check{\boldsymbol{\mathcal{F}}} \,\} \quad \text{and} \quad \dot{\boldsymbol{\mathfrak{c}}} = \{\, \dot{\bar{\boldsymbol{F}}}, \dot{\check{\boldsymbol{\varphi}}}, \dot{\check{\boldsymbol{F}}} \,\}\,. \tag{3.57}$$

The thermodynamic dissipative driving forces $\boldsymbol{\mathfrak{f}}$ and the rate $\dot{\boldsymbol{\mathfrak{c}}}$ are *dual variables*

$$\mathcal{D} = \int_{\mathcal{B}} \{\, \bar{\boldsymbol{\mathcal{F}}} : \dot{\bar{\boldsymbol{F}}} + \check{\boldsymbol{f}} \cdot \dot{\check{\boldsymbol{\varphi}}} + \check{\boldsymbol{\mathcal{F}}} : \dot{\check{\boldsymbol{F}}} \,\}\, dV \geq 0\,. \tag{3.58}$$

In this setting, the thermodynamic force $\bar{\boldsymbol{\mathcal{F}}}$ is dual to the macroscopic deformation gradient $\bar{\boldsymbol{F}}$, the force $\check{\boldsymbol{f}}$ dual to the microscopic deformation $\check{\boldsymbol{\varphi}}$, and the force $\check{\boldsymbol{\mathcal{F}}}$ dual to the microscopic deformation gradient $\check{\boldsymbol{F}}$. With this definition at hand, a conjugate representation of the dissipation function expressed in terms of the thermodynamic driving forces

Table 3.2: Coupled three-field balances of gradient-type solids.

Macroscopic equilibrium condition

$$\boldsymbol{0} = \mathrm{DIV}[\, \partial_{\bar{\boldsymbol{F}}}\psi + \bar{\boldsymbol{\mathcal{F}}}\,] + \bar{\gamma}_0 \quad \text{in} \;\; \mathcal{B}$$

$$\bar{\boldsymbol{g}}\bar{\boldsymbol{T}}_N = (\partial_{\bar{\boldsymbol{F}}}\psi + \bar{\boldsymbol{\mathcal{F}}}) \cdot \boldsymbol{N} \quad \text{on} \;\; \partial\mathcal{B}_{\bar{\boldsymbol{t}}}$$

Microscopic evolution equation

$$\boldsymbol{0} = \mathrm{DIV}[\, \partial_{\check{\boldsymbol{F}}}\psi + \check{\boldsymbol{\mathcal{F}}}\,] - [\, \partial_{\check{\boldsymbol{\varphi}}}\psi + \check{\boldsymbol{f}}\,] + \check{\gamma}_0 \quad \text{in} \;\; \mathcal{B}$$

$$\check{\boldsymbol{g}}\check{\boldsymbol{T}}_N = (\partial_{\check{\boldsymbol{F}}}\psi + \check{\boldsymbol{\mathcal{F}}}) \cdot \boldsymbol{N} \quad \text{on} \;\; \partial\mathcal{B}_{\check{\boldsymbol{t}}}$$

Inverse definition of dissipative driving forces

$$\dot{\bar{\boldsymbol{F}}} \in \partial_{\bar{\boldsymbol{\mathcal{F}}}}\phi^* \quad \text{and} \quad \dot{\check{\boldsymbol{\varphi}}} \in \partial_{\check{\boldsymbol{f}}}\phi^* \quad \text{and} \quad \dot{\check{\boldsymbol{F}}} \in \partial_{\check{\boldsymbol{\mathcal{F}}}}\phi^* \quad \text{in} \;\; \mathcal{B}$$

$\mathfrak{f}$ is obtained by a partial Legendre-Fenchel transformation in the rate slots. These types of transformations are discussed in Glocker [56], Maugin & Morro [112], Rockafellar [153, 154], and Heinrich & Demoment [78]. For the dissipation function discussed so far, one gets at a given constitutive state $\mathfrak{c}$ the conjugate dissipation function in combination with the corresponding Euler equation

$$\phi^*(\mathfrak{f}; \mathfrak{c}) = \sup_{\dot{\mathfrak{c}}}[\, \mathfrak{f} \cdot \dot{\mathfrak{c}} - \phi(\dot{\mathfrak{c}}; \mathfrak{c})\,] \quad \text{with} \quad \mathfrak{f} \in \partial_{\dot{\mathfrak{c}}}\phi(\dot{\mathfrak{c}}; \mathfrak{c})\,. \tag{3.59}$$

Dealing with convex functions, the dissipation function in its primal representation can be recovered by an inverse application of the Legendre transformation

$$\phi(\dot{\mathfrak{c}}; \mathfrak{c}) = \sup_{\mathfrak{f}}[\, \mathfrak{f} \cdot \dot{\mathfrak{c}} - \phi^*(\mathfrak{f}; \mathfrak{c})\,] \quad \text{with} \quad \dot{\mathfrak{c}} \in \partial_{\mathfrak{f}}\phi^*(\mathfrak{f}; \mathfrak{c})\,, \tag{3.60}$$

expressed in terms of the Euler equation that relates the evolution $\dot{\mathfrak{c}}$ of the constitutive state to the dissipative forces $\mathfrak{f}$. In what follows all *dissipative forces* are considered as a third variable field in the solid domain $\mathcal{B}$ in a *mixed setting*. Evaluation of the principle of virtual power (3.51) in combination with this choice of dissipation function, application of Gauss' theorem, and localization theorem gives the balances

$$\boldsymbol{0} = \mathrm{DIV}[\partial_{\bar{\boldsymbol{F}}}\psi + \bar{\boldsymbol{\mathcal{F}}}] + \bar{\gamma}_0 \quad \text{and} \quad \boldsymbol{0} = \mathrm{DIV}[\partial_{\check{\boldsymbol{F}}}\psi + \check{\boldsymbol{\mathcal{F}}}] - [\partial_{\check{\boldsymbol{\varphi}}}\psi + \check{\boldsymbol{f}}] + \check{\gamma}_0 \tag{3.61}$$

inside the domain $\mathcal{B}$ completed by the Neumann-type boundary conditions

$$(\partial_{\bar{\boldsymbol{F}}}\psi + \bar{\boldsymbol{\mathcal{F}}}) \cdot \boldsymbol{N} = \bar{\boldsymbol{g}}\bar{\boldsymbol{T}}_N \;\; \text{on } \partial\mathcal{B}_{\bar{\boldsymbol{t}}} \quad \text{and} \quad (\partial_{\check{\boldsymbol{F}}}\psi + \check{\boldsymbol{\mathcal{F}}}) \cdot \boldsymbol{N} = \check{\boldsymbol{g}}\check{\boldsymbol{T}}_N \;\; \text{on } \partial\mathcal{B}_{\check{\boldsymbol{t}}} \tag{3.62}$$

and the inverse definition of the dissipative driving forces via the *evolution equations*

$$\dot{\bar{\boldsymbol{F}}} \in \partial_{\bar{\boldsymbol{\mathcal{F}}}}\phi^* \quad \text{and} \quad \dot{\check{\boldsymbol{\varphi}}} \in \partial_{\bar{\boldsymbol{f}}}\phi^* \quad \text{and} \quad \dot{\check{\boldsymbol{F}}} \in \partial_{\check{\boldsymbol{\mathcal{F}}}}\phi^*\,. \tag{3.63}$$

A summary of the governing equations is given in Table 3.2, where the basic ingredients of gradient-type standard dissipative solid in a multi-field context are summarized in terms of the *three fields* $\bar{\boldsymbol{\varphi}}$, $\check{\boldsymbol{\varphi}}$, and $\mathfrak{f} := \{\, \bar{\boldsymbol{\mathcal{F}}}, \check{\boldsymbol{f}}, \check{\boldsymbol{\mathcal{F}}}\,\}$ introduced in (3.2), $(3.4)_1$, and (3.57).

Table 3.3: Rate-independent balances of gradient-type solids.

Macroscopic equilibrium condition

$$\boldsymbol{0} = \mathrm{DIV}[\,\partial_{\bar{\boldsymbol{F}}}\psi + \bar{\boldsymbol{\mathcal{F}}}\,] + \bar{\gamma}_0 \quad \text{in} \;\; \mathcal{B}$$

$$\bar{\boldsymbol{g}}\bar{\boldsymbol{T}}_N = (\partial_{\bar{\boldsymbol{F}}}\psi + \bar{\boldsymbol{\mathcal{F}}}) \cdot \boldsymbol{N} \quad \text{on} \;\; \partial\mathcal{B}_{\bar{\boldsymbol{t}}}$$

Microscopic evolution equation

$$\boldsymbol{0} = \mathrm{DIV}[\,\partial_{\check{\boldsymbol{F}}}\psi + \check{\boldsymbol{\mathcal{F}}}\,] - [\,\partial_{\check{\boldsymbol{\varphi}}}\psi + \check{\boldsymbol{f}}\,] + \check{\gamma}_0 \quad \text{in} \;\; \mathcal{B}$$

$$\check{\boldsymbol{g}}\check{\boldsymbol{T}}_N = (\partial_{\check{\boldsymbol{F}}}\psi + \check{\boldsymbol{\mathcal{F}}}) \cdot \boldsymbol{N} \quad \text{on} \;\; \partial\mathcal{B}_{\check{\boldsymbol{t}}}$$

Inverse definition of dissipative driving forces

$$\dot{\bar{\boldsymbol{F}}} = \lambda\,\partial_{\bar{\boldsymbol{\mathcal{F}}}}\varphi \quad \text{and} \quad \dot{\check{\boldsymbol{\varphi}}} = \lambda\,\partial_{\check{\boldsymbol{f}}}\varphi \quad \text{and} \quad \dot{\check{\boldsymbol{F}}} = \lambda\,\partial_{\check{\boldsymbol{\mathcal{F}}}}\varphi \quad \text{in} \;\; \mathcal{B}$$

Loading/unloading condition

$$\lambda \geq 0 \quad \text{and} \quad \varphi(\mathfrak{f};\mathfrak{c}) \leq 0 \quad \text{and} \quad \lambda\,\varphi(\mathfrak{f};\mathfrak{c}) = 0 \quad \text{in} \;\; \mathcal{B}$$

3.6.3. Threshold-Function-Based Rate-Independent Coupled Balances. In practical engineering applications, rate-independent dissipation functions are often modeled by the so-called *concept of maximum dissipation*. In this scenario, the dissipation is maximized for permissible thermodynamic forces $\mathfrak{f}$ inside the elastic domain $\mathbb{E}$

$$\phi(\dot{\mathfrak{c}};\mathfrak{c}) = \sup_{\mathfrak{f}\in\mathbb{E}}[\,\mathfrak{f}\cdot\dot{\mathfrak{c}}\,] \quad \text{with} \quad \mathbb{E} := \{\,\mathfrak{f} \,|\, \varphi(\mathfrak{f};\mathfrak{c}) \leq 0\,\} \tag{3.64}$$

characterized by the yield function $\varphi(\mathfrak{f};\mathfrak{c})$ that bounds the thermodynamic forces inside the elastic domain. Note that this particular form of the dissipation function expressed in terms of the yield function φ can also be obtained by choosing

$$\phi^*(\mathfrak{f};\mathfrak{c}) = \begin{cases} \;\;0 & \text{if } \varphi(\mathfrak{f};\mathfrak{c}) \leq 0 \\ +\infty & \text{otherwise} \end{cases} \tag{3.65}$$

as conjugate dissipation function ϕ^* in combination with equation (3.60). The principle of maximum dissipation (3.64) is usually solved by a Lagrange multiplier method

$$\phi(\dot{\mathfrak{c}};\mathfrak{c}) = \sup_{\mathfrak{f},\,\lambda\geq 0}[\,\mathfrak{f}\cdot\dot{\mathfrak{c}} - \lambda\,\varphi(\mathfrak{f};\mathfrak{c})\,] \tag{3.66}$$

whose evaluation yields the evolution equation for the constitutive state

$$\dot{\mathfrak{c}} = \lambda\,\partial_{\mathfrak{f}}\varphi(\mathfrak{f};\mathfrak{c})\,. \tag{3.67}$$

The evolution $\dot{\mathfrak{c}}$ is related to the dissipative driving forces $\mathfrak{f}$ in combination with the according loading/unloading conditions

$$\lambda \geq 0 \quad \text{and} \quad \varphi(\mathfrak{f};\mathfrak{c}) \leq 0 \quad \text{and} \quad \lambda\,\varphi(\mathfrak{f};\mathfrak{c}) = 0 \tag{3.68}$$

that are widely known as Karush-Kuhn-Tucker conditions. Evaluation of the principle of virtual power (3.51) and application of Gauss' theorem yields the three-field balance

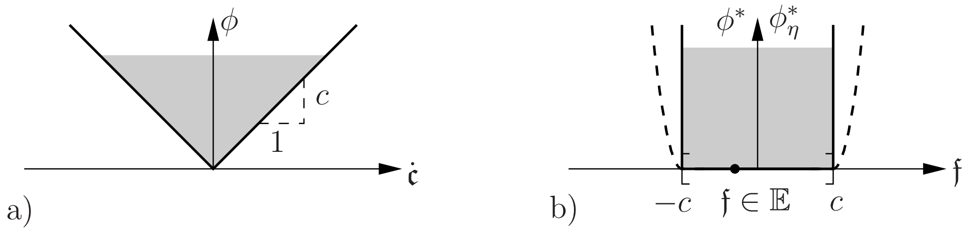

Figure 3.7: One-dimensional representations of the dissipation function. a) Primal $\phi(\dot{\mathfrak{c}}) = c\,|\dot{\mathfrak{c}}|$ and b) non-smooth dual representation $\phi^*(\mathfrak{f})$ with its regularized smooth counterpart $\phi^*_\eta(\mathfrak{f}) = \frac{1}{2\eta}\,\langle\varphi(\mathfrak{f})\rangle^2_+$ with $\varphi(\mathfrak{f}) = |\mathfrak{f}| - c$.

equations (3.61) and the Neumann-type boundary conditions (3.62). Only the *evolution equations* (3.63) have to be replaced by the specific rate-independent expressions

$$\dot{\bar{\boldsymbol{F}}} = \lambda\,\partial_{\bar{\boldsymbol{\mathcal{F}}}}\varphi \quad \text{and} \quad \dot{\check{\boldsymbol{\varphi}}} = \lambda\,\partial_{\check{\boldsymbol{f}}}\varphi \quad \text{and} \quad \dot{\check{\boldsymbol{F}}} = \lambda\,\partial_{\check{\boldsymbol{\mathcal{F}}}}\varphi\,, \tag{3.69}$$

accompanied by the loading conditions (3.68). A summary of the governing equations is given in Table 3.3. A detailed discussion of a purely rate-independent setting in a multi-field context which, regarding a numerical implementation, involves a global active set strategy can be found in LIEBE & STEINMANN [102], see also the proceeding contribution by WELSCHINGER & MIEHE [175].

3.6.4. Threshold-Function-Based Rate-Dependent Coupled Balances. A rate-dependent class of dissipation functions with elastic domain $\mathbb{E}$ defined by the yield function $\varphi(\boldsymbol{\mathfrak{f}};\boldsymbol{\mathfrak{c}})$ is obtained by a penalty-type solution of the principle of maximum dissipation (3.64). Following conceptually PERZYNA [148, 149], a viscous regularization

$$\phi(\dot{\boldsymbol{\mathfrak{c}}};\boldsymbol{\mathfrak{c}}) = \sup_{\boldsymbol{\mathfrak{f}}}[\,\boldsymbol{\mathfrak{f}}\cdot\dot{\boldsymbol{\mathfrak{c}}} - \frac{1}{2\eta}\,\langle\varphi(\boldsymbol{\mathfrak{f}};\boldsymbol{\mathfrak{c}})\rangle^2_+\,] \tag{3.70}$$

is set up, where the Foeppl-bracket $\langle(\cdot)\rangle_+ = \frac{1}{2}\,((\cdot) + |(\cdot)|)$ for the positive domain has been introduced. A one-dimensional illustration of the viscous regularization is given in

Table 3.4: Rate-dependent balances of gradient-type solids.

Macroscopic equilibrium condition

$$\boldsymbol{0} = \mathrm{DIV}[\,\partial_{\bar{\boldsymbol{F}}}\psi + \bar{\boldsymbol{\mathcal{F}}}\,] + \bar{\gamma}_0 \quad \text{in} \;\; \mathcal{B}$$

$$\bar{\boldsymbol{g}}\bar{\boldsymbol{T}}_N = (\partial_{\bar{\boldsymbol{F}}}\psi + \bar{\boldsymbol{\mathcal{F}}})\cdot\boldsymbol{N} \quad \text{on} \;\; \partial\mathcal{B}_{\bar{\boldsymbol{t}}}$$

Microscopic evolution equation

$$\boldsymbol{0} = \mathrm{DIV}[\,\partial_{\check{\boldsymbol{F}}}\psi + \check{\boldsymbol{\mathcal{F}}}\,] - [\,\partial_{\check{\boldsymbol{\varphi}}}\psi + \check{\boldsymbol{f}}\,] + \check{\gamma}_0 \quad \text{in} \;\; \mathcal{B}$$

$$\check{\boldsymbol{g}}\check{\boldsymbol{T}}_N = (\partial_{\check{\boldsymbol{F}}}\psi + \check{\boldsymbol{\mathcal{F}}})\cdot\boldsymbol{N} \quad \text{on} \;\; \partial\mathcal{B}_{\check{\boldsymbol{t}}}$$

Inverse smooth definition of dissipative driving forces with $\lambda := \frac{1}{\eta}\,\langle\varphi(\boldsymbol{\mathfrak{f}};\boldsymbol{\mathfrak{c}})\rangle_+$

$$\dot{\bar{\boldsymbol{F}}} = \lambda\,\partial_{\bar{\boldsymbol{\mathcal{F}}}}\varphi \quad \text{and} \quad \dot{\check{\boldsymbol{\varphi}}} = \lambda\,\partial_{\check{\boldsymbol{f}}}\varphi \quad \text{and} \quad \dot{\check{\boldsymbol{F}}} = \lambda\,\partial_{\check{\boldsymbol{\mathcal{F}}}}\varphi \quad \text{in} \;\; \mathcal{B}$$

Figure 3.7. The necessary condition of the maximum problem (3.70) provides the nonlinear smooth evolution equation for the constitutive state

$$\dot{\mathfrak{c}} = \frac{1}{\eta}\,\langle \varphi(\mathfrak{f};\mathfrak{c})\rangle_{+}\,\partial_{\mathfrak{f}}\varphi(\mathfrak{f};\mathfrak{c})\,. \tag{3.71}$$

Evaluation of the principle of virtual power (3.51) and application of Gauss' theorem finally yields the coupled three-field balance equations (3.61) and the Neumann-type boundary conditions (3.62). The *evolution equations* (3.69) of the rate-independent case are adopted

$$\dot{\bar{\boldsymbol{F}}} = \lambda\,\partial_{\bar{\boldsymbol{\mathcal{F}}}}\varphi \quad \text{and} \quad \dot{\check{\boldsymbol{\varphi}}} = \lambda\,\partial_{\check{\boldsymbol{\mathfrak{f}}}}\varphi \quad \text{and} \quad \dot{\check{\boldsymbol{F}}} = \lambda\,\partial_{\check{\boldsymbol{\mathcal{F}}}}\varphi\,, \tag{3.72}$$

where the Lagrange parameter is replaced by the constitutive definition

$$\lambda := \frac{1}{\eta}\,\langle \varphi(\mathfrak{f};\mathfrak{c})\rangle_{+} \geq 0 \tag{3.73}$$

characterizing rate-dependent loading. Obviously, for the limit case $\eta \rightarrow 0$ the rate-independent form (3.67) in combination with (3.68) is recovered. The strong forms of the coupled balance equations for the rate-dependent setting are summarized in Table 3.4.

3.7. Time-Discrete Incremental Variational Principles

Variationally consistent approaches for the treatment of elastoplastic systems can be traced back to the work by Martin [109]. General variational frameworks for standard dissipative materials are outlined in Miehe [118], Miehe, Schotte & Lambrecht [127], and Miehe, Lambrecht & Gürses [126], see also the references cited therein. The following incremental variational principle for gradient-type solids extends formulations discussed in Miehe [120] to the large strain setting.

3.7.1. Time-Discrete Field Variables in Incremental Setting. An algorithmic representation of the nonlinear algebraic equations for the macro- and microscopic response can alternatively be obtained by a variational principle. To this end, consider the time-discrete solution of the field variables at the discrete solution times $0, t_1, t_2, \ldots, t_n, t_{n+1}, \ldots, T$ of the process interval $[0, T]$. In order to maintain the solution within a typical time step, the focus is put on the discrete time increment $[t_n, t_{n+1}]$ with the typical time step

$$\tau_{n+1} := t_{n+1} - t_n > 0\,. \tag{3.74}$$

In what follows, all field variables at time t_n are assumed to be known. The global fields at time t_{n+1} are then derived based on a variational principle valid for the current time interval. Regarding a compact notation, the subscript $n+1$ is dropped, all variables without subscript are meant to be evaluated at time t_{n+1}. In particular one can write

$$\bar{\boldsymbol{\varphi}} := \bar{\boldsymbol{\varphi}}(\boldsymbol{X}, t_{n+1}) \quad \text{and} \quad \check{\boldsymbol{\varphi}} := \check{\boldsymbol{\varphi}}(\boldsymbol{X}, t_{n+1}) \tag{3.75}$$

for the actual macro- and microscopic deformation maps and

$$\bar{\boldsymbol{\varphi}}_n := \bar{\boldsymbol{\varphi}}(\boldsymbol{X}, t_n) \quad \text{and} \quad \check{\boldsymbol{\varphi}}_n := \check{\boldsymbol{\varphi}}(\boldsymbol{X}, t_n) \tag{3.76}$$

for the macro- and microscopic field variables evaluated at the previous solution time. As a consequence, the rates of these global fields are *constant quantities* within the time increment under focus. They are defined by

$$\dot{\bar{\boldsymbol{\varphi}}} := (\bar{\boldsymbol{\varphi}} - \bar{\boldsymbol{\varphi}}_n)/\tau \quad \text{and} \quad \dot{\check{\boldsymbol{\varphi}}} := (\check{\boldsymbol{\varphi}} - \check{\boldsymbol{\varphi}}_n)/\tau\,. \tag{3.77}$$

In full analogy, the rate of the constitutive state (3.35) is approximated by

$$\dot{\mathfrak{c}} := (\mathfrak{c} - \mathfrak{c}_n)/\tau \, . \tag{3.78}$$

In the extended setting, the dual dissipative driving forces need to be introduced

$$\bar{\boldsymbol{\mathcal{F}}} := \bar{\boldsymbol{\mathcal{F}}}(\boldsymbol{X}, t_{n+1}) \quad \text{and} \quad \check{\boldsymbol{f}} := \check{\boldsymbol{f}}(\boldsymbol{X}, t_{n+1}) \quad \text{and} \quad \check{\boldsymbol{\mathcal{F}}} := \check{\boldsymbol{\mathcal{F}}}(\boldsymbol{X}, t_{n+1}) \tag{3.79}$$

that, aiming at a compact notation, are summarized in the assembled array

$$\mathfrak{f} := \{ \bar{\boldsymbol{\mathcal{F}}}, \check{\boldsymbol{f}}, \check{\boldsymbol{\mathcal{F}}} \} \, . \tag{3.80}$$

This array represents the time-discrete dissipative forces evaluated at current time. Regarding a possibly non-smooth, rate-independent implementation, the global field

$$\lambda := \lambda(\boldsymbol{X}, t_{n+1}) \geq 0 \tag{3.81}$$

denotes in what follows the Lagrangian multiplier field at time t_{n+1}.

3.7.2. Incremental Energy, Dissipation, and Load Functionals. The incremental variational principle provides the macro- and microscopic deformation $\bar{\boldsymbol{\varphi}}$ and $\check{\boldsymbol{\varphi}}$ evaluated at current time t_{n+1}. The generation of such an incremental variational principle dramatically depends on the *incremental energy storage*, *dissipation*, and *load* expended to the system within the finite time step $[t_n, t_{n+1}]$ under focus.

3.7.2.1. Incremental Energy Functional. Associated with the discrete time interval (3.74), the incrementally stored energy inside a solid with microstructure is given by

$$E^\tau(\bar{\boldsymbol{\varphi}}, \check{\boldsymbol{\varphi}}) := \int_{t_n}^{t_{n+1}} \dot{E} \, dt = \int_{\mathcal{B}} \{ \psi(\mathfrak{c}) - \psi(\mathfrak{c}_n) \} \, dV \, , \tag{3.82}$$

expressed in terms of the energy functional as defined in $(3.28)_1$. Recalling the constitutive relationship $(3.38)_1$, the incremental energy is considered as a functional that depends on the macro- and microscopic field variables $\bar{\boldsymbol{\varphi}}$ and $\check{\boldsymbol{\varphi}}$ evaluated at current time t_{n+1} and governed by the free energy function ψ.

3.7.2.2. Incremental Dissipation Functional. In a next step, an expression for the incremental dissipation potential valid for the current time interval is set up

$$D^\tau(\bar{\boldsymbol{\varphi}}, \check{\boldsymbol{\varphi}}) := \int_{t_n}^{t_{n+1}} D \, dt \, . \tag{3.83}$$

As discussed in Section 3.6, there exist different possibilities to model the constitutive dissipation function. Making use of definition $(3.38)_2$ and the approximated constitutive rates (3.78), a canonical setting of the incremental dissipation functional is introduced

$$D^\tau(\bar{\boldsymbol{\varphi}}, \check{\boldsymbol{\varphi}}) := \int_{\mathcal{B}} \{ \tau \, \phi((\mathfrak{c} - \mathfrak{c}_n)/\tau; \mathfrak{c}_n) \} \, dV \tag{3.84}$$

depending on the primary field variables $\bar{\boldsymbol{\varphi}}$ and $\check{\boldsymbol{\varphi}}$ evaluated at current time t_{n+1}. By insertion of the Legendre transformation (3.60), an extended dissipation functional for the discrete time interval under focus can be obtained

$$D^{*\tau}(\bar{\boldsymbol{\varphi}}, \check{\boldsymbol{\varphi}}, \mathfrak{f}) := \int_{\mathcal{B}} \{ \mathfrak{f} \cdot (\mathfrak{c} - \mathfrak{c}_n) - \tau \, \phi^*(\mathfrak{f}; \mathfrak{c}_n) \} \, dV \, . \tag{3.85}$$

This extended dissipation functional is a function of an extended set of variables, including the thermodynamic dissipative driving forces $\mathfrak{f}$ as defined in (3.57). An exploitation of the rate-independent, yield function based dissipation function (3.66) allows for the third representation of the dissipation functional

$$D_\lambda^{*\tau}(\bar{\boldsymbol{\varphi}}, \check{\boldsymbol{\varphi}}, \mathfrak{f}, \lambda) := \int_{\mathcal{B}} \{\, \mathfrak{f} \cdot (\mathfrak{c} - \mathfrak{c}_n) - \tau\, \lambda\, \varphi(\mathfrak{f}; \mathfrak{c}_n) \,\}\, dV\,, \tag{3.86}$$

which shows an additional dependency on the Lagrange multiplier field λ, see also its definition (3.81). Starting with the smooth dissipation function (3.70), the last representation of the incremental dissipation functional is obtained

$$D_\eta^{*\tau}(\bar{\boldsymbol{\varphi}}, \check{\boldsymbol{\varphi}}, \mathfrak{f}) := \int_{\mathcal{B}} \{\, \mathfrak{f} \cdot (\mathfrak{c} - \mathfrak{c}_n) - \frac{\tau}{2\eta}\, \langle \varphi(\mathfrak{f}; \mathfrak{c}_n) \rangle_+^2 \,\}\, dV\,, \tag{3.87}$$

where $\eta > 0$ is the viscosity parameter. Obviously, for vanishing viscosity $\eta \to 0$ the incremental dissipation (3.86) is recovered. Thus, the penalty-type dissipation functional (3.87) is considered as the *viscous regularization* of the Lagrange-type dissipation functional (3.86).

3.7.2.3. Incremental Load Functional. The incrementally expended external work associated with the discrete time interval (3.74) is given by the expression

$$W^\tau(\bar{\boldsymbol{\varphi}}, \check{\boldsymbol{\varphi}}) := \int_{t_n}^{t_{n+1}} \mathcal{P}_{ext}\, dt \tag{3.88}$$

and takes into account external actions on the multi-field problem. Here, $\mathcal{P}_{ext}$ is the total power of external loading as defined in (3.25) and (3.26) describing macro- and microscopic contributions, respectively. Assuming constant rates within the time step under focus, see equation (3.77), the incremental work can be considered as a functional of the macro- and microscopic deformations $\bar{\boldsymbol{\varphi}}$ and $\check{\boldsymbol{\varphi}}$, respectively. Thus, at current time t_{n+1} the external work is defined by the *algorithmic expression*

$$\begin{aligned} W^\tau(\bar{\boldsymbol{\varphi}}, \check{\boldsymbol{\varphi}}) \;&:= \int_{\mathcal{B}} \bar{\gamma}_0 \cdot (\bar{\boldsymbol{\varphi}} - \bar{\boldsymbol{\varphi}}_n)\, dV + \int_{\partial\mathcal{B}_{\bar{\boldsymbol{t}}}} \bar{\boldsymbol{g}} \bar{\boldsymbol{T}}_N \cdot (\bar{\boldsymbol{\varphi}} - \bar{\boldsymbol{\varphi}}_n)\, dA \\ &\quad + \int_{\mathcal{B}} \check{\gamma}_0 \cdot (\check{\boldsymbol{\varphi}} - \check{\boldsymbol{\varphi}}_n)\, dV + \int_{\partial\mathcal{B}_{\check{\boldsymbol{t}}}} \check{\boldsymbol{g}} \check{\boldsymbol{T}}_N \cdot (\check{\boldsymbol{\varphi}} - \check{\boldsymbol{\varphi}}_n)\, dA \end{aligned} \tag{3.89}$$

in terms of the *prescribed* macro- and microscopic *body force* fields

$$\bar{\gamma}_0 := \bar{\gamma}_0(\boldsymbol{X}, t_{n+1}) \quad \text{and} \quad \check{\gamma}_0 := \check{\gamma}_0(\boldsymbol{X}, t_{n+1}) \tag{3.90}$$

and the *prescribed* macro- and microscopic *surface tractions*

$$\bar{\boldsymbol{T}}_N := \bar{\boldsymbol{T}}_N(\boldsymbol{X}, t_{n+1}) \quad \text{and} \quad \check{\boldsymbol{T}}_N := \check{\boldsymbol{T}}_N(\boldsymbol{X}, t_{n+1}) \tag{3.91}$$

evaluated at the current solution time t_{n+1}.

3.7.3. The Canonical Incremental Minimization Principle. The canonical incremental minimization principle for gradient-type dissipative solids is governed by the incremental potential

$$\underbrace{\Pi^\tau(\bar{\boldsymbol{\varphi}},\check{\boldsymbol{\varphi}})}_{potential} := \underbrace{E^\tau(\bar{\boldsymbol{\varphi}},\check{\boldsymbol{\varphi}})}_{energy} + \underbrace{D^\tau(\bar{\boldsymbol{\varphi}},\check{\boldsymbol{\varphi}})}_{dissipation} - \underbrace{W^\tau(\bar{\boldsymbol{\varphi}},\check{\boldsymbol{\varphi}})}_{work} . \tag{3.92}$$

It is based on the incremental energy storage (3.82), the dissipation functional in its canonical representation (3.84), and the external work functional as defined in (3.89). In order to obtain a compact notation of the canonical incremental minimization principle, the *generalized constitutive state vector* $\mathfrak{c}$ is introduced

$$\mathfrak{c}(\mathfrak{u}) := \{\, \bar{\boldsymbol{F}}, \check{\boldsymbol{\varphi}}, \check{\boldsymbol{F}} \,\} \quad \text{with} \quad \mathfrak{u} := \{\, \bar{\boldsymbol{\varphi}}, \check{\boldsymbol{\varphi}} \,\} \tag{3.93}$$

as a function of the *generalized deformation vector* $\mathfrak{u}$. The latter contains the macro- and microscopic deformation fields $\bar{\boldsymbol{\varphi}}$ and $\check{\boldsymbol{\varphi}}$. The constitutive state contains the macroscopic deformation gradient $\bar{\boldsymbol{F}}$, the micro-deformation map $\check{\boldsymbol{\varphi}}$, and the microscopic deformation gradient $\check{\boldsymbol{F}}$. The *generalized volume force vector* acting inside the solid is defined by

$$\mathfrak{g} := \{\, \bar{\gamma}_0, \check{\gamma}_0 \,\} \ \text{ in } \ \mathcal{B} \tag{3.94}$$

and contains macro- and microscopic body forces. The *generalized surface traction vector* summarizes the macro- and microscopic surface tractions $\bar{\boldsymbol{T}}_N$ and $\check{\boldsymbol{T}}_N$ in the way

$$\mathfrak{t}_N := \{\, \bar{\boldsymbol{g}}\bar{\boldsymbol{T}}_N, \check{\boldsymbol{g}}\check{\boldsymbol{T}}_N \,\} \ \text{ on } \ \partial\mathcal{B}_{\mathfrak{t}} := \{\, \partial\mathcal{B}_{\bar{\boldsymbol{t}}}, \partial\mathcal{B}_{\check{\boldsymbol{t}}} \,\} , \tag{3.95}$$

where the generalized traction surface $\partial\mathcal{B}_{\mathfrak{t}}$ has been introduced. It consists of the part of the surface $\partial\mathcal{B}_{\bar{\boldsymbol{t}}}$ where macroscopic tractions act and a possibly different part of the surface $\partial\mathcal{B}_{\check{\boldsymbol{t}}}$ where microscopic tractions perform work. With this compact notation at hand, the incremental potential (3.92) can be reformulated

$$\Pi^\tau(\mathfrak{u}) = \int_{\mathcal{B}} \{\, \pi^\tau(\mathfrak{c};\mathfrak{c}_n) - \mathfrak{g}\cdot(\mathfrak{u}-\mathfrak{u}_n) \,\}\, dV - \int_{\partial\mathcal{B}_{\mathfrak{t}}} \mathfrak{t}_N\cdot(\mathfrak{u}-\mathfrak{u}_n)\, dA \tag{3.96}$$

expressed in terms of the *incremental internal work density*

$$\pi^\tau(\mathfrak{c};\mathfrak{c}_n) = \psi(\mathfrak{c}) - \psi(\mathfrak{c}_n) + \tau\,\phi((\mathfrak{c}-\mathfrak{c}_n)/\tau;\mathfrak{c}_n) . \tag{3.97}$$

It is uniquely determined by the constitutive free energy function ψ and the constitutive dissipation function ϕ. Following this line, the finite step sized incremental *minimization principle* takes the form

$$\boxed{\{\, \bar{\boldsymbol{\varphi}}, \check{\boldsymbol{\varphi}} \,\} = \arg\{\, \inf_{\bar{\boldsymbol{\varphi}}} \inf_{\check{\boldsymbol{\varphi}}} \Pi^\tau(\bar{\boldsymbol{\varphi}},\check{\boldsymbol{\varphi}}) \,\}} \tag{3.98}$$

and delivers the current macro- and microscopic deformation $\bar{\boldsymbol{\varphi}}$ and $\check{\boldsymbol{\varphi}}$ as the minimum of the incremental functional (3.96). The according necessary condition reads

$$0 \in \delta\Pi^\tau = \delta_{\bar{\boldsymbol{\varphi}}}\Pi^\tau + \delta_{\check{\boldsymbol{\varphi}}}\Pi^\tau , \tag{3.99}$$

where the variations of the incremental potential with respect to the macro- and microscopic deformations are summarized by the explicit expressions

$$\begin{aligned}
\delta_{\bar{\boldsymbol{\varphi}}}\Pi^{\tau} := & \int_{\mathcal{B}} \{\, [\partial_{\bar{\boldsymbol{F}}}\psi + \partial_{\dot{\bar{\boldsymbol{F}}}}\phi] : \nabla_{\boldsymbol{X}}\delta\bar{\boldsymbol{\varphi}} - \bar{\gamma}_0 \cdot \delta\bar{\boldsymbol{\varphi}} \,\}\, dV \\
& - \int_{\partial\mathcal{B}_{\bar{\boldsymbol{t}}}} \bar{\boldsymbol{g}}\bar{\boldsymbol{T}}_N \cdot \delta\bar{\boldsymbol{\varphi}}\, dA \\
\delta_{\check{\boldsymbol{\varphi}}}\Pi^{\tau} := & \int_{\mathcal{B}} \{\, [\partial_{\check{\boldsymbol{F}}}\psi + \partial_{\dot{\check{\boldsymbol{F}}}}\phi] : \nabla_{\boldsymbol{X}}\delta\check{\boldsymbol{\varphi}} + [\partial_{\check{\boldsymbol{\varphi}}}\psi + \partial_{\dot{\check{\boldsymbol{\varphi}}}}\phi - \check{\gamma}_0] \cdot \delta\check{\boldsymbol{\varphi}} \,\}\, dV \\
& - \int_{\partial\mathcal{B}_{\check{\boldsymbol{t}}}} \check{\boldsymbol{g}}\check{\boldsymbol{T}}_N \cdot \delta\check{\boldsymbol{\varphi}}\, dA
\end{aligned} \tag{3.100}$$

based on the admissible variations $\delta\bar{\boldsymbol{\varphi}} \in \mathcal{W}^0_{\bar{\boldsymbol{\varphi}}}$ and $\delta\check{\boldsymbol{\varphi}} \in \mathcal{W}^0_{\check{\boldsymbol{\varphi}}}$. The Euler equations of the minimization principle (3.98) evaluated at current time t_{n+1} correspond to the coupled two-field balances as summarized in Table 3.1, where the rates $\dot{\bar{\boldsymbol{\varphi}}}$ and $\dot{\check{\boldsymbol{\varphi}}}$ are meant to be evaluated by the algorithmic expression (3.77). The strong form is obtained from (3.100) by application of Gauss' and localization theorem. Carefully observe that the above statement can be interpreted as a *virtual work balance* of internal and external actions at the discrete time t_{n+1}, where the internal work decomposes into an energetic and a dissipative part. A short discussion of the canonical two-field representation can be found in the proceeding contribution by WELSCHINGER, ZIMMERMANN & MIEHE [177].

3.7.4. The Extended Incremental Variational Principle. In this subsection, the focus is put on an extended incremental variational principle of gradient-type standard dissipative solids based on the extended dissipation functional (3.85). This extended variational principle is governed by the incremental potential

$$\underbrace{\Pi^{*\tau}(\bar{\boldsymbol{\varphi}}, \check{\boldsymbol{\varphi}}, \mathfrak{f})}_{potential} := \underbrace{E^{\tau}(\bar{\boldsymbol{\varphi}}, \check{\boldsymbol{\varphi}})}_{energy} + \underbrace{D^{*\tau}(\bar{\boldsymbol{\varphi}}, \check{\boldsymbol{\varphi}}, \mathfrak{f})}_{dissipation} - \underbrace{W^{\tau}(\bar{\boldsymbol{\varphi}}, \check{\boldsymbol{\varphi}})}_{work}\,, \tag{3.101}$$

where the constitutive state (3.93) has to be modified to take into account the thermodynamic driving forces. To this end, an *extended constitutive state vector* $\mathfrak{c}^*$ is introduced

$$\mathfrak{c}^*(\mathfrak{u}^*) := \{\, \bar{\boldsymbol{F}}, \check{\boldsymbol{\varphi}}, \check{\boldsymbol{F}}, \mathfrak{f} \,\} \quad \text{with} \quad \mathfrak{u}^* := \{\, \bar{\boldsymbol{\varphi}}, \check{\boldsymbol{\varphi}}, \mathfrak{f} \,\} \tag{3.102}$$

as a function of the *extended deformation vector* $\mathfrak{u}^*$. The extended constitutive state contains the macroscopic deformation gradient $\bar{\boldsymbol{F}}$, the microscopic deformation map $\check{\boldsymbol{\varphi}}$, the microscopic deformation gradient $\check{\boldsymbol{F}}$, and the dissipative thermodynamic driving forces $\mathfrak{f}$. Together with the generalized volume force vector (3.94) and the generalized surface traction vector (3.95), the incremental potential (3.101) is reformulated into

$$\Pi^{*\tau}(\mathfrak{u}^*) = \int_{\mathcal{B}} \{\, \pi^{*\tau}(\mathfrak{c}^*; \mathfrak{c}^*_n) - \mathfrak{g} \cdot (\mathfrak{u} - \mathfrak{u}_n) \,\}\, dV - \int_{\partial\mathcal{B}_{\mathfrak{t}}} \mathfrak{t}_N \cdot (\mathfrak{u} - \mathfrak{u}_n)\, dA \tag{3.103}$$

expressed in terms of the *extended incremental internal work density*

$$\pi^{*\tau}(\mathfrak{c}^*; \mathfrak{c}^*_n) = \psi(\mathfrak{c}) - \psi(\mathfrak{c}_n) + \mathfrak{f} \cdot (\mathfrak{c} - \mathfrak{c}_n) - \tau\, \phi^*(\mathfrak{f}; \mathfrak{c}_n)\,. \tag{3.104}$$

It contains the constitutive free energy function ψ and the conjugate constitutive dissipation function ϕ^*. In this scenario, the finite step sized incremental *stationary principle* takes the form

$$\boxed{\{\,\bar{\boldsymbol{\varphi}},\check{\boldsymbol{\varphi}},\boldsymbol{\mathfrak{f}}\,\} = \arg\{\,\inf_{\bar{\boldsymbol{\varphi}}}\inf_{\check{\boldsymbol{\varphi}}}\sup_{\boldsymbol{\mathfrak{f}}}\Pi^{*\tau}(\bar{\boldsymbol{\varphi}},\check{\boldsymbol{\varphi}},\boldsymbol{\mathfrak{f}})\,\}} \tag{3.105}$$

and characterizes the current macro- and microscopic deformation $\bar{\boldsymbol{\varphi}}$ and $\check{\boldsymbol{\varphi}}$ and the dissipative thermodynamic driving forces $\boldsymbol{\mathfrak{f}}$ as the saddle point of the incremental functional (3.103). The associated necessary condition takes the form

$$0 \in \delta\Pi^{*\tau} = \delta_{\bar{\boldsymbol{\varphi}}}\Pi^{*\tau} + \delta_{\check{\boldsymbol{\varphi}}}\Pi^{*\tau} + \delta_{\boldsymbol{\mathfrak{f}}}\Pi^{*\tau}\,, \tag{3.106}$$

where the variations with respect to the macro- and microscopic deformation and with respect to the thermodynamic forces are determined by the explicit expressions

$$\begin{aligned}
\delta_{\bar{\boldsymbol{\varphi}}}\Pi^{*\tau} :=& \int_{\mathcal{B}} \{\,[\partial_{\bar{\boldsymbol{F}}}\psi + \bar{\boldsymbol{\mathcal{F}}}] : \nabla_{\boldsymbol{X}}\delta\bar{\boldsymbol{\varphi}} - \bar{\boldsymbol{\gamma}}_0\cdot\delta\bar{\boldsymbol{\varphi}}\,\}\,dV \\
&- \int_{\partial\mathcal{B}_{\bar{\boldsymbol{t}}}} \bar{\boldsymbol{g}}\bar{\boldsymbol{T}}_N\cdot\delta\bar{\boldsymbol{\varphi}}\,dA \\
\delta_{\check{\boldsymbol{\varphi}}}\Pi^{*\tau} :=& \int_{\mathcal{B}} \{\,[\partial_{\check{\boldsymbol{F}}}\psi + \check{\boldsymbol{\mathcal{F}}}] : \nabla_{\boldsymbol{X}}\delta\check{\boldsymbol{\varphi}} + [\partial_{\check{\boldsymbol{\varphi}}}\psi + \check{\boldsymbol{f}} - \check{\boldsymbol{\gamma}}_0]\cdot\delta\check{\boldsymbol{\varphi}}\,\}\,dV \\
&- \int_{\partial\mathcal{B}_{\check{\boldsymbol{t}}}} \check{\boldsymbol{g}}\check{\boldsymbol{T}}_N\cdot\delta\check{\boldsymbol{\varphi}}\,dA \\
\delta_{\boldsymbol{\mathfrak{f}}}\Pi^{*\tau} :=& \int_{\mathcal{B}} \{\,[\boldsymbol{\mathfrak{c}} - \boldsymbol{\mathfrak{c}}_n - \tau\,\partial_{\boldsymbol{\mathfrak{f}}}\phi^*]\cdot\delta\boldsymbol{\mathfrak{f}}\,\}\,dV
\end{aligned} \tag{3.107}$$

in terms of the admissible variations $\delta\bar{\boldsymbol{\varphi}} \in \mathcal{W}^0_{\bar{\boldsymbol{\varphi}}}$, $\delta\check{\boldsymbol{\varphi}} \in \mathcal{W}^0_{\check{\boldsymbol{\varphi}}}$, and $\delta\boldsymbol{\mathfrak{f}}$ of the current macro- and microscopic deformation and the dissipative forces, respectively. Application of Gauss' and localization theorem yields the Euler equations of the stationary principle (3.105) evaluated at current time t_{n+1}. They correspond to the three-field balance equations as summarized in Table 3.2. Similar to the previously discussed setting (3.100), these equations can be interpreted as a *virtual work balance* which shows in addition weak statements for the definition of incremental update equations of the dissipative driving forces.

3.7.5. Rate-Independent Principle with Threshold Function. An alternative incremental variational principle for gradient-type standard dissipative solids containing a threshold-type yield function bases on the extended dissipation functional (3.86). The non-smooth evolution of the global fields is characterized by a constrained optimization principle involving a Lagrange multiplier method. The rate-independent variational principle with threshold function is governed by the incremental potential

$$\underbrace{\Pi^{*\tau}_{\lambda}(\bar{\boldsymbol{\varphi}},\check{\boldsymbol{\varphi}},\boldsymbol{\mathfrak{f}},\lambda)}_{\textit{potential}} := \underbrace{E^{\tau}(\bar{\boldsymbol{\varphi}},\check{\boldsymbol{\varphi}})}_{\textit{energy}} + \underbrace{D^{*\tau}_{\lambda}(\bar{\boldsymbol{\varphi}},\check{\boldsymbol{\varphi}},\boldsymbol{\mathfrak{f}},\lambda)}_{\textit{dissipation}} - \underbrace{W^{\tau}(\bar{\boldsymbol{\varphi}},\check{\boldsymbol{\varphi}})}_{\textit{work}} \tag{3.108}$$

expressed in terms of the yield function φ as introduced in Section 3.6.3. In view of a compact notation, the following *extended constitutive state vector* $\boldsymbol{\mathfrak{c}}^*_{\lambda}$ as a function of the *extended deformation vector* $\boldsymbol{\mathfrak{u}}^*_{\lambda}$ for the non-smooth problem is introduced

$$\boldsymbol{\mathfrak{c}}^*_{\lambda}(\boldsymbol{\mathfrak{u}}^*_{\lambda}) := \{\,\bar{\boldsymbol{F}},\check{\boldsymbol{\varphi}},\check{\boldsymbol{F}},\boldsymbol{\mathfrak{f}},\lambda\,\} \quad \text{with} \quad \boldsymbol{\mathfrak{u}}^*_{\lambda} := \{\,\bar{\boldsymbol{\varphi}},\check{\boldsymbol{\varphi}},\boldsymbol{\mathfrak{f}},\lambda\,\} \tag{3.109}$$

that characterizes a rate-independent constitutive response. This constitutive state contains the macroscopic deformation gradient $\bar{\boldsymbol{F}}$, the microscopic deformation map $\check{\boldsymbol{\varphi}}$, the microscopic deformation gradient $\check{\boldsymbol{F}}$, the thermodynamic driving forces $\mathfrak{f}$, and the Lagrangian multiplier field λ. Together with the generalized volume force vector (3.94) and the generalized surface traction (3.95), the incremental potential (3.108) is reformulated

$$\Pi^{*\tau}_{\lambda}(\mathfrak{u}^*_{\lambda}) = \int_{\mathcal{B}} \{\, \pi^{*\tau}_{\lambda}(\mathfrak{c}^*_{\lambda}; \mathfrak{c}^*_{\lambda n}) - \mathfrak{g} \cdot (\mathfrak{u} - \mathfrak{u}_n) \,\}\, dV - \int_{\partial\mathcal{B}_{\mathfrak{t}}} \mathfrak{t}_N \cdot (\mathfrak{u} - \mathfrak{u}_n)\, dA\,. \tag{3.110}$$

Here, the *extended incremental internal work density* for the internal energy storage and dissipation has been introduced. It takes the specific representation

$$\pi^{*\tau}_{\lambda}(\mathfrak{c}^*_{\lambda}; \mathfrak{c}^*_{\lambda n}) = \psi(\mathfrak{c}) - \psi(\mathfrak{c}_n) + \mathfrak{f} \cdot (\mathfrak{c} - \mathfrak{c}_n) - \tau\, \lambda\, \varphi(\mathfrak{f}; \mathfrak{c}_n) \tag{3.111}$$

and is uniquely determined by the constitutive free energy function ψ and the yield function φ, respectively. The finite step sized incremental *stationary principle* reads

$$\boxed{\{\, \bar{\boldsymbol{\varphi}}, \check{\boldsymbol{\varphi}}, \mathfrak{f}, \lambda \,\} = \arg\{ \inf_{\bar{\boldsymbol{\varphi}}} \inf_{\check{\boldsymbol{\varphi}}} \sup_{\mathfrak{f}} \sup_{\lambda \geq 0} \Pi^{*\tau}_{\lambda}(\bar{\boldsymbol{\varphi}}, \check{\boldsymbol{\varphi}}, \mathfrak{f}, \lambda) \,\}} \tag{3.112}$$

and identifies the current macro- and microscopic deformation $\bar{\boldsymbol{\varphi}}$ and $\check{\boldsymbol{\varphi}}$, the dissipative thermodynamic driving forces $\mathfrak{f}$, and the Lagrangian multiplier field $\lambda \geq 0$ as the saddle point of the incremental potential (3.110). The necessary condition reads

$$0 \in \delta\Pi^{*\tau}_{\lambda} = \delta_{\bar{\boldsymbol{\varphi}}}\Pi^{*\tau}_{\lambda} + \delta_{\check{\boldsymbol{\varphi}}}\Pi^{*\tau}_{\lambda} + \delta_{\mathfrak{f}}\Pi^{*\tau}_{\lambda} + \delta_{\lambda}\Pi^{*\tau}_{\lambda}\,, \tag{3.113}$$

where the single variations are summarized by the explicit expressions

$$\begin{aligned}
\delta_{\bar{\boldsymbol{\varphi}}}\Pi^{*\tau}_{\lambda} :=& \int_{\mathcal{B}} \{\, [\partial_{\bar{\boldsymbol{F}}}\psi + \bar{\boldsymbol{\mathcal{F}}}] : \nabla_{\boldsymbol{X}}\delta\bar{\boldsymbol{\varphi}} - \bar{\boldsymbol{\gamma}}_0 \cdot \delta\bar{\boldsymbol{\varphi}} \,\}\, dV \\
&- \int_{\partial\mathcal{B}_{\bar{\boldsymbol{t}}}} \bar{\boldsymbol{g}}\bar{\boldsymbol{T}}_N \cdot \delta\bar{\boldsymbol{\varphi}}\, dA \\
\delta_{\check{\boldsymbol{\varphi}}}\Pi^{*\tau}_{\lambda} :=& \int_{\mathcal{B}} \{\, [\partial_{\check{\boldsymbol{F}}}\psi + \check{\boldsymbol{\mathcal{F}}}] : \nabla_{\boldsymbol{X}}\delta\check{\boldsymbol{\varphi}} + [\partial_{\check{\boldsymbol{\varphi}}}\psi + \check{\boldsymbol{f}} - \check{\boldsymbol{\gamma}}_0] \cdot \delta\check{\boldsymbol{\varphi}} \,\}\, dV \\
&- \int_{\partial\mathcal{B}_{\check{\boldsymbol{t}}}} \check{\boldsymbol{g}}\check{\boldsymbol{T}}_N \cdot \delta\check{\boldsymbol{\varphi}}\, dA \\
\delta_{\mathfrak{f}}\Pi^{\tau *}_{\lambda} :=& \int_{\mathcal{B}} \{\, [\mathfrak{c} - \mathfrak{c}_n - \tau\, \lambda\, \partial_{\mathfrak{f}}\varphi] \cdot \delta\mathfrak{f} \,\}\, dV \\
\delta_{\lambda}\Pi^{\tau *}_{\lambda} :=& \int_{\mathcal{B}} \{\, [-\tau\, \varphi]\, \delta\lambda \,\}\, dV\,,
\end{aligned} \tag{3.114}$$

in terms of the admissible variations $\delta\bar{\boldsymbol{\varphi}} \in \mathcal{W}^0_{\bar{\boldsymbol{\varphi}}}$, $\delta\check{\boldsymbol{\varphi}} \in \mathcal{W}^0_{\check{\boldsymbol{\varphi}}}$, $\delta\mathfrak{f}$, and $\delta\lambda \geq 0$ of the current macro- and microscopic deformation, the dissipative forces, and the Lagrangian multiplier field, respectively. The Euler equations of the stationary principle (3.112) evaluated at current time t_{n+1} correspond to the three-field balance equations as summarized in Table 3.3. This statement *balances the virtual internal* and *external work* and involves weak incremental updates for the dissipative forces expressed in terms of a yield function. The evolution equations are complemented by the threshold-type loading conditions.

3.7.6. Rate-Dependent Principle with Threshold Function. The focus now lies on an incremental variational principle of gradient-type standard dissipative solids, which is based on the extended dissipation functional (3.87). It can be interpreted as a smooth viscous regularization of the representation (3.86) by means of an *over force penalty method.* The variational principle is governed by the incremental potential

$$\underbrace{\Pi_{\eta}^{*\mathcal{T}}(\bar{\boldsymbol{\varphi}}, \check{\boldsymbol{\varphi}}, \mathfrak{f})}_{potential} := \underbrace{E^{\mathcal{T}}(\bar{\boldsymbol{\varphi}}, \check{\boldsymbol{\varphi}})}_{energy} + \underbrace{D_{\eta}^{*\mathcal{T}}(\bar{\boldsymbol{\varphi}}, \check{\boldsymbol{\varphi}}, \mathfrak{f})}_{dissipation} - \underbrace{W^{\mathcal{T}}(\bar{\boldsymbol{\varphi}}, \check{\boldsymbol{\varphi}})}_{work} . \tag{3.115}$$

Based on the generalized deformation and constitutive state vectors (3.101), the extended generalized volume force vector (3.94), and the generalized surface traction vector (3.95), the incremental potential (3.115) is reformulated

$$\Pi_{\eta}^{*\mathcal{T}}(\mathfrak{u}^{*}) = \int_{\mathcal{B}} \{ \, \pi_{\eta}^{*\mathcal{T}}(\mathfrak{c}^{*}; \mathfrak{c}_{n}^{*}) - \mathfrak{g} \cdot (\mathfrak{u} - \mathfrak{u}_{n}) \, \} \, dV - \int_{\partial \mathcal{B}_{\mathfrak{t}}} \mathfrak{t}_{N} \cdot (\mathfrak{u} - \mathfrak{u}_{n}) \, dA \tag{3.116}$$

expressed in terms of the *extended incremental internal work density*

$$\pi_{\eta}^{*\mathcal{T}}(\mathfrak{c}^{*}; \mathfrak{c}_{n}^{*}) = \psi(\mathfrak{c}) - \psi(\mathfrak{c}_{n}) + \mathfrak{f} \cdot (\mathfrak{c} - \mathfrak{c}_{n}) - \frac{\mathcal{T}}{2\eta} \, \langle \varphi(\mathfrak{f}; \mathfrak{c}_{n}) \rangle_{+}^{2} \tag{3.117}$$

determined by the constitutive free energy function ψ and the yield function φ. In this sense, the finite step sized incremental *stationary principle* reads

$$\boxed{\{ \, \bar{\boldsymbol{\varphi}}, \check{\boldsymbol{\varphi}}, \mathfrak{f} \, \} = \arg\{ \, \inf_{\bar{\boldsymbol{\varphi}}} \inf_{\check{\boldsymbol{\varphi}}} \sup_{\mathfrak{f}} \Pi_{\eta}^{*\mathcal{T}}(\bar{\boldsymbol{\varphi}}, \check{\boldsymbol{\varphi}}, \mathfrak{f}) \, \}} \tag{3.118}$$

and uniquely determines the current macro- and microscopic deformation $\bar{\boldsymbol{\varphi}}$ and $\check{\boldsymbol{\varphi}}$ and the dissipative thermodynamic driving forces $\mathfrak{f}$ as the saddle point of the incremental potential (3.116). The variation of the functional (3.116) yields the *smooth condition*

$$0 = \delta \Pi_{\eta}^{*\mathcal{T}} = \delta_{\bar{\boldsymbol{\varphi}}} \Pi_{\eta}^{*\mathcal{T}} + \delta_{\check{\boldsymbol{\varphi}}} \Pi_{\eta}^{*\mathcal{T}} + \delta_{\mathfrak{f}} \Pi_{\eta}^{*\mathcal{T}} \, , \tag{3.119}$$

where the single variations are summarized by the explicit expressions

$$\begin{aligned}
\delta_{\bar{\boldsymbol{\varphi}}} \Pi_{\eta}^{*\mathcal{T}} := & \int_{\mathcal{B}} \{ \, [\partial_{\bar{\boldsymbol{F}}} \psi + \bar{\boldsymbol{\mathcal{F}}}] : \nabla_{\boldsymbol{X}} \delta \bar{\boldsymbol{\varphi}} - \bar{\boldsymbol{\gamma}}_{0} \cdot \delta \bar{\boldsymbol{\varphi}} \, \} \, dV \\
& - \int_{\partial \mathcal{B}_{\bar{\boldsymbol{t}}}} \bar{\boldsymbol{g}} \bar{\boldsymbol{T}}_{N} \cdot \delta \bar{\boldsymbol{\varphi}} \, dA \\
\delta_{\check{\boldsymbol{\varphi}}} \Pi_{\eta}^{*\mathcal{T}} := & \int_{\mathcal{B}} \{ \, [\partial_{\check{\boldsymbol{F}}} \psi + \check{\boldsymbol{\mathcal{F}}}] : \nabla_{\boldsymbol{X}} \delta \check{\boldsymbol{\varphi}} + [\partial_{\check{\boldsymbol{\varphi}}} \psi + \check{\boldsymbol{f}} - \check{\boldsymbol{\gamma}}_{0}] \cdot \delta \check{\boldsymbol{\varphi}} \, \} \, dV \\
& - \int_{\partial \mathcal{B}_{\check{\boldsymbol{t}}}} \check{\boldsymbol{g}} \check{\boldsymbol{T}}_{N} \cdot \delta \check{\boldsymbol{\varphi}} \, dA \\
\delta_{\mathfrak{f}} \Pi_{\eta}^{*\mathcal{T}} := & \int_{\mathcal{B}} \{ \, [\mathfrak{c} - \mathfrak{c}_{n} - \frac{\mathcal{T}}{\eta} \, \langle \varphi \rangle_{+} \partial_{\mathfrak{f}} \varphi] \cdot \delta \mathfrak{f} \, \} \, dV
\end{aligned} \tag{3.120}$$

in terms of the admissible variations $\delta \bar{\boldsymbol{\varphi}} \in \mathcal{W}_{\bar{\boldsymbol{\varphi}}}^{0}$, $\delta \check{\boldsymbol{\varphi}} \in \mathcal{W}_{\check{\boldsymbol{\varphi}}}^{0}$, and $\delta \mathfrak{f}$ of the current macro- and microscopic deformation and the dissipative forces, respectively. The Euler equations of the stationary principle (3.118) correspond to the smooth three-field balance equations as summarized in Table 3.4 evaluated at current time t_{n+1}. Such a formulation is particularly convenient due to the smooth nature of the viscous dissipation function.

3.7.7. Rate-Dependent Principle with Local History. In classical phenomenological theories of physically nonlinear continua, the energetic state of a solid is characterized by *local internal variables* $\boldsymbol{\mathcal{I}}$ whose evolution is described by an ordinary differential equation, see e.g. Coleman & Gurtin [29]. In general cases one wishes to keep these local variables in addition to the extended global constitutive state as introduced in $(3.35)_1$. Following this methodology, the constitutive descriptions $(3.38)_{1,2}$ are modified

$$\psi = \psi(\mathfrak{c}, \boldsymbol{\mathcal{I}}) \quad \text{and} \quad \phi = \phi(\dot{\mathfrak{c}}, \dot{\boldsymbol{\mathcal{I}}}; \mathfrak{c}, \boldsymbol{\mathcal{I}})\,. \tag{3.121}$$

In particular, the specific representation of the dissipation (3.56) has to be extended to take into account the effects of the local internal variables

$$\mathcal{D} := \int_{\mathcal{B}} \{\, \mathfrak{f} \cdot \dot{\mathfrak{c}} + \boldsymbol{\mathcal{F}} \cdot \dot{\boldsymbol{\mathcal{I}}} \,\}\, dV \geq 0\,. \tag{3.122}$$

Besides the already known dissipative force array $\mathfrak{f}$ introduced in $(3.57)_1$, the *local thermodynamic dissipative force* $\boldsymbol{\mathcal{F}}$ dual to the local internal variable $\boldsymbol{\mathcal{I}}$ has been introduced. With these definitions at hand, a conjugate representation of the dissipation function expressed in terms of the global and local thermodynamic driving forces $\mathfrak{f}$ and $\boldsymbol{\mathcal{F}}$ is obtained by a partial Legendre-Fenchel transformation in the rate slots. These types of transformations are discussed in Glocker [56], Maugin & Morro [112], Rockafellar [153, 154], and Heinrich & Demoment [78]. At a given constitutive state $\mathfrak{c}$ and $\boldsymbol{\mathcal{I}}$ one obtains the conjugate dissipation function

$$\phi^*(\mathfrak{f}, \boldsymbol{\mathcal{F}}; \mathfrak{c}, \boldsymbol{\mathcal{I}}) = \sup_{\dot{\mathfrak{c}}} \sup_{\dot{\boldsymbol{\mathcal{I}}}} [\, \mathfrak{f} \cdot \dot{\mathfrak{c}} + \boldsymbol{\mathcal{F}} \cdot \dot{\boldsymbol{\mathcal{I}}} - \phi(\dot{\mathfrak{c}}, \dot{\boldsymbol{\mathcal{I}}}; \mathfrak{c}, \boldsymbol{\mathcal{I}}) \,] \tag{3.123}$$

in combination with the according Euler equations defining the thermodynamic forces

$$\mathfrak{f} \in \partial_{\dot{\mathfrak{c}}} \phi(\dot{\mathfrak{c}}, \dot{\boldsymbol{\mathcal{I}}}; \mathfrak{c}, \boldsymbol{\mathcal{I}}) \quad \text{and} \quad \boldsymbol{\mathcal{F}} \in \partial_{\dot{\boldsymbol{\mathcal{I}}}} \phi(\dot{\mathfrak{c}}, \dot{\boldsymbol{\mathcal{I}}}; \mathfrak{c}, \boldsymbol{\mathcal{I}})\,. \tag{3.124}$$

Due to the convex characteristic of the dissipation function, its primal representation can be recovered by the inverse application of a Legendre transformation

$$\phi(\dot{\mathfrak{c}}, \dot{\boldsymbol{\mathcal{I}}}; \mathfrak{c}, \boldsymbol{\mathcal{I}}) = \sup_{\mathfrak{f}} \sup_{\boldsymbol{\mathcal{F}}} [\, \mathfrak{f} \cdot \dot{\mathfrak{c}} + \boldsymbol{\mathcal{F}} \cdot \dot{\boldsymbol{\mathcal{I}}} - \phi^*(\mathfrak{f}, \boldsymbol{\mathcal{F}}; \mathfrak{c}, \boldsymbol{\mathcal{I}}) \,] \tag{3.125}$$

coming along with the Euler equations of the global and local constitutive state variables

$$\dot{\mathfrak{c}} \in \partial_{\mathfrak{f}} \phi^*(\mathfrak{f}, \boldsymbol{\mathcal{F}}; \mathfrak{c}, \boldsymbol{\mathcal{I}}) \quad \text{and} \quad \dot{\boldsymbol{\mathcal{I}}} \in \partial_{\boldsymbol{\mathcal{F}}} \phi^*(\mathfrak{f}, \boldsymbol{\mathcal{F}}; \mathfrak{c}, \boldsymbol{\mathcal{I}})\,. \tag{3.126}$$

They relate the evolution $\dot{\mathfrak{c}}$ of the constitutive state to the dissipative forces $\mathfrak{f}$ and the evolution of the local internal variables $\dot{\boldsymbol{\mathcal{I}}}$ to the local dissipative force $\boldsymbol{\mathcal{F}}$. In what follows, the dissipative forces $\mathfrak{f}$ are considered as a third variable field on the solid domain in a *mixed setting*, whereas the local dissipative forces $\boldsymbol{\mathcal{F}}$ are treated as a local history field. In the subsequent treatment, the extended incremental variational principle discussed in Section 3.7.6 is modified to take into account dissipative effects sufficiently described by a local internal variable field $\boldsymbol{\mathcal{I}}$. The setup of an incremental variational principle bases on the construction of an incremental energy functional. To do so, ideas from equation (3.82) are augmented by an additional dependency on the local history

$$E^\tau(\bar{\boldsymbol{\varphi}}, \check{\boldsymbol{\varphi}}, \boldsymbol{\mathcal{I}}) := \int_{t_n}^{t_{n+1}} \dot{E}\, dt = \int_{\mathcal{B}} \{\, \psi(\mathfrak{c}, \boldsymbol{\mathcal{I}}) - \psi(\mathfrak{c}_n, \boldsymbol{\mathcal{I}}_n) \,\}\, dV\,. \tag{3.127}$$

Focusing on the rate-dependent threshold-type setting, the incremental dissipation is obtained in analogy to (3.87) and yields in combination with (3.125) the expression

$$D_\eta^{*\mathcal{T}}(\bar{\boldsymbol{\varphi}}, \check{\boldsymbol{\varphi}}, \boldsymbol{\mathfrak{f}}, \boldsymbol{\mathcal{I}}, \boldsymbol{\mathcal{F}}) := \int_{\mathcal{B}} \{\, \boldsymbol{\mathfrak{f}} \cdot (\boldsymbol{\mathfrak{c}} - \boldsymbol{\mathfrak{c}}_n) + \boldsymbol{\mathcal{F}} \cdot (\boldsymbol{\mathcal{I}} - \boldsymbol{\mathcal{I}}_n) - \frac{\mathcal{T}}{2\eta} \langle \varphi(\boldsymbol{\mathfrak{f}}, \boldsymbol{\mathcal{F}}; \boldsymbol{\mathfrak{c}}_n, \boldsymbol{\mathcal{I}}_n) \rangle_+^2 \,\} \, dV \, . \tag{3.128}$$

The extended variational formulation including the local history field variables is governed by the incremental potential

$$\underbrace{\Pi_\eta^{*\mathcal{T}}(\bar{\boldsymbol{\varphi}}, \check{\boldsymbol{\varphi}}, \boldsymbol{\mathfrak{f}}, \boldsymbol{\mathcal{I}}, \boldsymbol{\mathcal{F}})}_{potential} := \underbrace{E^{\mathcal{T}}(\bar{\boldsymbol{\varphi}}, \check{\boldsymbol{\varphi}}, \boldsymbol{\mathcal{I}})}_{energy} + \underbrace{D_\eta^{*\mathcal{T}}(\bar{\boldsymbol{\varphi}}, \check{\boldsymbol{\varphi}}, \boldsymbol{\mathfrak{f}}, \boldsymbol{\mathcal{I}}, \boldsymbol{\mathcal{F}})}_{dissipation} - \underbrace{W^{\mathcal{T}}(\bar{\boldsymbol{\varphi}}, \check{\boldsymbol{\varphi}})}_{work} \, , \tag{3.129}$$

where the incremental external load functional (3.89) remains unaffected and is used without any changes. In this setting, the *extended constitutive state vector* as a function of the *extended deformation vector* and the local solution pair

$$\boldsymbol{\mathfrak{c}}^*(\boldsymbol{\mathfrak{u}}^*) := \{\, \bar{\boldsymbol{F}}, \check{\boldsymbol{\varphi}}, \check{\boldsymbol{F}}, \boldsymbol{\mathfrak{f}} \,\} \quad \text{with} \quad \boldsymbol{\mathfrak{u}}^* := \{\, \bar{\boldsymbol{\varphi}}, \check{\boldsymbol{\varphi}}, \boldsymbol{\mathfrak{f}} \,\} \quad \text{and} \quad \boldsymbol{\mathfrak{p}} := \{\, \boldsymbol{\mathcal{I}}, \boldsymbol{\mathcal{F}} \,\} \tag{3.130}$$

are introduced. The constitutive state contains the macroscopic deformation gradient $\bar{\boldsymbol{F}}$, the microscopic deformation map $\check{\boldsymbol{\varphi}}$, the microscopic deformation gradient $\check{\boldsymbol{F}}$, and the thermodynamic driving force $\boldsymbol{\mathfrak{f}}$ summarized by the global constitutive state $\boldsymbol{\mathfrak{c}}^*$. The local solution pair $\boldsymbol{\mathfrak{p}}$ contains the local internal variable $\boldsymbol{\mathcal{I}}$ and its dual thermodynamic driving force $\boldsymbol{\mathcal{F}}$. Together with the generalized volume force vector (3.94) and the generalized surface traction vector (3.95), the incremental potential (3.129) can be reformulated according to

$$\Pi_\eta^{*\mathcal{T}}(\boldsymbol{\mathfrak{u}}^*, \boldsymbol{\mathfrak{p}}) = \int_{\mathcal{B}} \{\, \pi_\eta^{*\mathcal{T}}(\boldsymbol{\mathfrak{c}}^*, \boldsymbol{\mathfrak{p}}; \boldsymbol{\mathfrak{c}}_n^*, \boldsymbol{\mathfrak{p}}_n) - \boldsymbol{\mathfrak{g}} \cdot (\boldsymbol{\mathfrak{u}} - \boldsymbol{\mathfrak{u}}_n) \,\} \, dV - \int_{\partial \mathcal{B}_{\mathfrak{t}}} \boldsymbol{\mathfrak{t}}_N \cdot (\boldsymbol{\mathfrak{u}} - \boldsymbol{\mathfrak{u}}_n) \, dA \tag{3.131}$$

expressed in terms of the *extended incremental internal work density with local history*

$$\begin{aligned} \pi_\eta^{*\mathcal{T}}(\boldsymbol{\mathfrak{c}}^*, \boldsymbol{\mathfrak{p}}; \boldsymbol{\mathfrak{c}}_n^*, \boldsymbol{\mathfrak{p}}_n) = {} & \psi(\boldsymbol{\mathfrak{c}}, \boldsymbol{\mathcal{I}}) - \psi(\boldsymbol{\mathfrak{c}}_n, \boldsymbol{\mathcal{I}}_n) + \boldsymbol{\mathfrak{f}} \cdot (\boldsymbol{\mathfrak{c}} - \boldsymbol{\mathfrak{c}}_n) + \boldsymbol{\mathcal{F}} \cdot (\boldsymbol{\mathcal{I}} - \boldsymbol{\mathcal{I}}_n) \\ & - \frac{\mathcal{T}}{2\eta} \langle \varphi(\boldsymbol{\mathfrak{f}}, \boldsymbol{\mathcal{F}}; \boldsymbol{\mathfrak{c}}_n, \boldsymbol{\mathcal{I}}_n) \rangle_+^2 \, . \end{aligned} \tag{3.132}$$

It is determined by the constitutive free energy function ψ and the yield function φ. The finite step sized incremental *stationary principle* then reads

$$\boxed{\{\, \bar{\boldsymbol{\varphi}}, \check{\boldsymbol{\varphi}}, \boldsymbol{\mathfrak{f}}, \boldsymbol{\mathcal{I}}, \boldsymbol{\mathcal{F}} \,\} = \arg\{ \inf_{\bar{\boldsymbol{\varphi}}} \inf_{\check{\boldsymbol{\varphi}}} \sup_{\boldsymbol{\mathfrak{f}}} \inf_{\boldsymbol{\mathcal{I}}} \sup_{\boldsymbol{\mathcal{F}}} \Pi_\eta^{*\mathcal{T}}(\bar{\boldsymbol{\varphi}}, \check{\boldsymbol{\varphi}}, \boldsymbol{\mathfrak{f}}, \boldsymbol{\mathcal{I}}, \boldsymbol{\mathcal{F}}) \,\}} \tag{3.133}$$

and delivers the current macro- and microscopic deformations $\bar{\boldsymbol{\varphi}}$ and $\check{\boldsymbol{\varphi}}$ and the dissipative thermodynamic driving force $\boldsymbol{\mathfrak{f}}$ as global quantities and the local internal variable $\boldsymbol{\mathcal{I}}$ with its thermodynamic driving force $\boldsymbol{\mathcal{F}}$ as the saddle point of the incremental functional (3.131). The according necessary condition is given by the *smooth* expression

$$0 = \delta \Pi_\eta^{*\mathcal{T}} = \delta_{\bar{\boldsymbol{\varphi}}} \Pi_\eta^{*\mathcal{T}} + \delta_{\check{\boldsymbol{\varphi}}} \Pi_\eta^{*\mathcal{T}} + \delta_{\boldsymbol{\mathfrak{f}}} \Pi_\eta^{*\mathcal{T}} + \delta_{\boldsymbol{\mathcal{I}}} \Pi_\eta^{*\mathcal{T}} + \delta_{\boldsymbol{\mathcal{F}}} \Pi_\eta^{*\mathcal{T}} \, , \tag{3.134}$$

Table 3.5: Balances of gradient-type solids with local history.

Macroscopic equilibrium condition

$$\boldsymbol{0} = \mathrm{DIV}[\,\partial_{\bar{\boldsymbol{F}}}\psi + \bar{\boldsymbol{\mathcal{F}}}\,] + \bar{\boldsymbol{\gamma}}_0 \quad \text{in} \;\; \mathcal{B}$$

$$\bar{\boldsymbol{g}}\bar{\boldsymbol{T}}_N = (\partial_{\bar{\boldsymbol{F}}}\psi + \bar{\boldsymbol{\mathcal{F}}}) \cdot \boldsymbol{N} \quad \text{on} \;\; \partial\mathcal{B}_{\bar{\boldsymbol{t}}}$$

Microscopic evolution equation

$$\boldsymbol{0} = \mathrm{DIV}[\,\partial_{\check{\boldsymbol{F}}}\psi + \check{\boldsymbol{\mathcal{F}}}\,] - [\,\partial_{\check{\boldsymbol{\varphi}}}\psi + \check{\boldsymbol{f}}\,] + \check{\boldsymbol{\gamma}}_0 \quad \text{in} \;\; \mathcal{B}$$

$$\check{\boldsymbol{g}}\check{\boldsymbol{T}}_N = (\partial_{\check{\boldsymbol{F}}}\psi + \check{\boldsymbol{\mathcal{F}}}) \cdot \boldsymbol{N} \quad \text{on} \;\; \partial\mathcal{B}_{\check{\boldsymbol{t}}}$$

Inverse smooth definition of dissipative driving forces

$$\boldsymbol{\mathfrak{c}} = \boldsymbol{\mathfrak{c}}_n + \frac{\tau}{\eta}\,\langle\varphi\rangle_+ \partial_{\boldsymbol{\mathfrak{f}}}\varphi \quad \text{in} \;\; \mathcal{B}$$

Evolution subproblem of *internal variables*

$$\boldsymbol{0} = [\,\partial_{\boldsymbol{\mathcal{I}}}\psi + \boldsymbol{\mathcal{F}}\,] \quad \text{in} \;\; \mathcal{B}$$

Inverse smooth definition of local dissipative driving forces

$$\boldsymbol{\mathcal{I}} = \boldsymbol{\mathcal{I}}_n + \frac{\tau}{\eta}\,\langle\varphi\rangle_+ \partial_{\boldsymbol{\mathcal{F}}}\varphi \quad \text{in} \;\; \mathcal{B}$$

where the single variations are summarized by the explicit expressions

$$\begin{aligned}
\delta_{\bar{\boldsymbol{\varphi}}}\Pi^{*\tau}_{\eta} &:= \int_{\mathcal{B}} \{\,[\partial_{\bar{\boldsymbol{F}}}\psi + \bar{\boldsymbol{\mathcal{F}}}] : \nabla_{\boldsymbol{X}}\delta\bar{\boldsymbol{\varphi}} - \bar{\boldsymbol{\gamma}}_0 \cdot \delta\bar{\boldsymbol{\varphi}}\,\}\, dV \\
&\quad - \int_{\partial\mathcal{B}_{\bar{\boldsymbol{t}}}} \bar{\boldsymbol{g}}\bar{\boldsymbol{T}}_N \cdot \delta\bar{\boldsymbol{\varphi}}\, dA \\
\delta_{\check{\boldsymbol{\varphi}}}\Pi^{*\tau}_{\eta} &:= \int_{\mathcal{B}} \{\,[\partial_{\check{\boldsymbol{F}}}\psi + \check{\boldsymbol{\mathcal{F}}}] : \nabla_{\boldsymbol{X}}\delta\check{\boldsymbol{\varphi}} + [\partial_{\check{\boldsymbol{\varphi}}}\psi + \check{\boldsymbol{f}} - \check{\boldsymbol{\gamma}}_0] \cdot \delta\check{\boldsymbol{\varphi}}\,\}\, dV \\
&\quad - \int_{\partial\mathcal{B}_{\check{\boldsymbol{t}}}} \check{\boldsymbol{g}}\check{\boldsymbol{T}}_N \cdot \delta\check{\boldsymbol{\varphi}}\, dA \\
\delta_{\boldsymbol{\mathfrak{f}}}\Pi^{*\tau}_{\eta} &:= \int_{\mathcal{B}} \{\,[\boldsymbol{\mathfrak{c}} - \boldsymbol{\mathfrak{c}}_n - \frac{\tau}{\eta}\,\langle\varphi\rangle_+ \partial_{\boldsymbol{\mathfrak{f}}}\varphi] \cdot \delta\boldsymbol{\mathfrak{f}}\,\}\, dV \\
\delta_{\boldsymbol{\mathcal{I}}}\Pi^{*\tau}_{\eta} &:= \int_{\mathcal{B}} \{\,[\partial_{\boldsymbol{\mathcal{I}}}\psi + \boldsymbol{\mathcal{F}}] \cdot \delta\boldsymbol{\mathcal{I}}\,\}\, dV \\
\delta_{\boldsymbol{\mathcal{F}}}\Pi^{*\tau}_{\eta} &:= \int_{\mathcal{B}} \{\,[\boldsymbol{\mathcal{I}} - \boldsymbol{\mathcal{I}}_n - \frac{\tau}{\eta}\,\langle\varphi\rangle_+ \partial_{\boldsymbol{\mathcal{F}}}\varphi] \cdot \delta\boldsymbol{\mathcal{F}}\,\}\, dV\,,
\end{aligned} \tag{3.135}$$

in terms of the admissible variations $\delta\bar{\boldsymbol{\varphi}} \in \mathcal{W}^0_{\bar{\boldsymbol{\varphi}}}$, $\delta\check{\boldsymbol{\varphi}} \in \mathcal{W}^0_{\check{\boldsymbol{\varphi}}}$, $\delta\boldsymbol{\mathfrak{f}}$, $\delta\boldsymbol{\mathcal{I}}$, and $\delta\boldsymbol{\mathcal{F}}$ of the current macro- and microscopic deformation, the dissipative forces, the local internal variable, and its dual dissipative force. The algorithmic Euler equations of the stationary principle (3.133) correspond to the smooth three-field balance equations as summarized for the continuous setting in Table 3.4 augmented by the evolutionary subproblem for the local internal variables. The overall governing strong equations evaluated at current time t_{n+1} are summarized in Table 3.5.

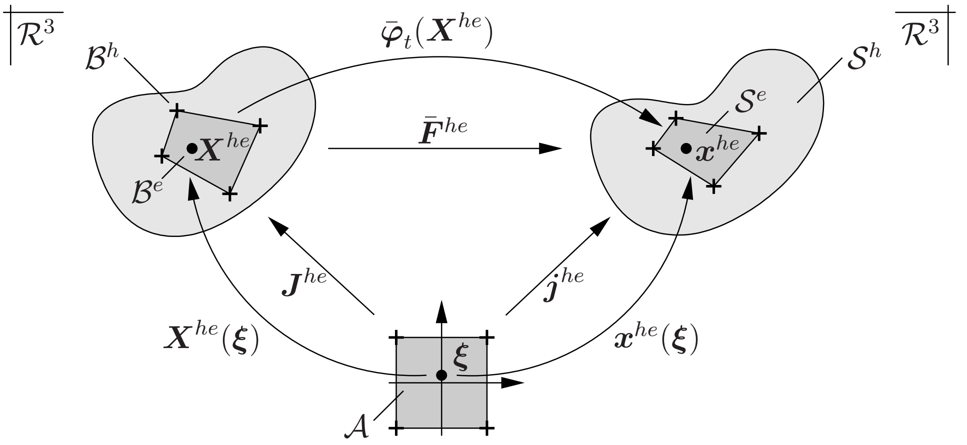

Figure 3.8: Isoparametric mapping of the geometry. The Lagrangian $\mathcal{B}^e \subset \mathcal{B}^h$ and Eulerian configuration $\mathcal{S}^e \subset \mathcal{S}^h$ are characterized by the isoparametric mappings $\boldsymbol{X}^{he}(\boldsymbol{\xi})$ and $\boldsymbol{x}^{he}(\boldsymbol{\xi})$.

3.8. Finite Element Discretization of Incremental Variational Principles

Regarding a large strain finite element implementation of the previously introduced variational principles, there exist two geometric configurations that have to be taken into account. Namely the Lagrangian configuration $\mathcal{B}$ and the Eulerian configuration $\mathcal{S}$. The first step towards a numerical treatment bases on a discretization of the continuous solution domains $\mathcal{B}$ and $\mathcal{S}$ into discrete domains $\mathcal{B}^h$ and $\mathcal{S}^h$. As illustrated in Figure 3.8, the discrete domains consist of the entity of all element sub domains $\mathcal{B}^e \subset \mathcal{B}^h$ and $\mathcal{S}^e \subset \mathcal{S}^h$

$$\mathcal{B}^h = \mathop{\mathsf{A}}_{e=1}^{n_{en}} \mathcal{B}^e \quad \text{and} \quad \mathcal{S}^h = \mathop{\mathsf{A}}_{e=1}^{n_{en}} \mathcal{S}^e \,. \tag{3.136}$$

In this expression, the symbol $\mathsf{A}_{e=1}^{n_{en}}$ has been introduced for the assembly operation of all elements $e = 1, \ldots, n_{en}$. Within the context of an isoparametric finite element formulation, the Lagrangian and the Eulerian configuration are approximated on *element level* by

$$\boldsymbol{X}^{he} = \sum_{i=1}^{n_{el}} N_i \, \boldsymbol{X}_i^e \quad \text{and} \quad \boldsymbol{x}^{he} = \sum_{i=1}^{n_{el}} N_i \, \boldsymbol{x}_i^e \tag{3.137}$$

based on the shape functions $N_i(\boldsymbol{\xi})$ as functions of the element's local isoparametric coordinates $\boldsymbol{\xi}$, the material and spatial nodal coordinates $\boldsymbol{X}_i^e$ and $\boldsymbol{x}_i^e$, and the number of nodes per element n_{el}. The discrete displacement field $\bar{\boldsymbol{u}}^{he}$ is introduced as difference between the positions $\boldsymbol{X}^{he}$ and $\boldsymbol{x}^{he}$ of a material point in its reference and current configuration

$$\bar{\boldsymbol{u}}^{he} = \boldsymbol{x}^{he} - \boldsymbol{X}^{he} = \sum_{i=1}^{n_{el}} N_i \, (\boldsymbol{x}_i^e - \boldsymbol{X}_i^e) =: \sum_{i=1}^{n_{el}} N_i \, \bar{\boldsymbol{d}}_i^e \,, \tag{3.138}$$

where the discrete nodal displacements $\bar{\boldsymbol{d}}_i^e := \boldsymbol{x}_i^e - \boldsymbol{X}_i^e$ associated with node i of the element e have been introduced. Note that (3.138) a priori fulfills the isoparametric concept. In analogy to the definition of the macroscopic deformation gradient $\bar{\boldsymbol{F}}^{he} = \nabla_{\boldsymbol{X}} \bar{\boldsymbol{u}}^{he} + \boldsymbol{1}^h$ as the material gradient of the nonlinear deformation map $\bar{\varphi}_t(\boldsymbol{X}^{he})$, the gradients of the isoparametric maps $\boldsymbol{X}^{he}$ and $\boldsymbol{x}^{he}$ are introduced

$$\boldsymbol{J}^{he} = \nabla_{\boldsymbol{\xi}} \boldsymbol{X}^{he} \quad \text{and} \quad \boldsymbol{j}^{he} = \nabla_{\boldsymbol{\xi}} \boldsymbol{x}^{he} \,. \tag{3.139}$$

Figure 3.8 shows the relation between the tangent maps

$$\boldsymbol{j}^{he} = \bar{\boldsymbol{F}}^{he}\,\boldsymbol{J}^{he} \quad \text{and} \quad \boldsymbol{J}^{he} = \bar{\boldsymbol{F}}^{he^{-1}}\boldsymbol{j}^{he} \quad \text{and} \quad \bar{\boldsymbol{F}}^{he} = \boldsymbol{j}^{he}\,\boldsymbol{J}^{he^{-1}}\,. \tag{3.140}$$

In what follows, the discrete representations of the previously discussed incremental variational principles are discussed.

3.8.1. Canonical Incremental Minimization Principle. Having the discrete geometry (3.137) and the discrete macroscopic deformation (3.138) at hand, it remains to specify the discrete counterpart to the generalized deformation

$$\mathfrak{u}^h = \mathop{\mathsf{A}}_{e=1}^{n_{en}} \left[\sum_{i=1}^{n_{el}} \begin{bmatrix} [\bar{\boldsymbol{N}}]_i^e & \boldsymbol{0} \\ \boldsymbol{0} & [\check{\boldsymbol{N}}]_i^e \end{bmatrix} \begin{bmatrix} \bar{\boldsymbol{d}} \\ \check{\boldsymbol{d}} \end{bmatrix}_i^e \right] = \mathop{\mathsf{A}}_{e=1}^{n_{en}} \begin{bmatrix} [\bar{\boldsymbol{N}}]^e & \boldsymbol{0} \\ \boldsymbol{0} & [\check{\boldsymbol{N}}]^e \end{bmatrix} \begin{bmatrix} \bar{\boldsymbol{d}} \\ \check{\boldsymbol{d}} \end{bmatrix}^e =: \mathfrak{N}(\boldsymbol{X})\,\mathfrak{d} \tag{3.141}$$

expressed in terms of the element's macro- and microscopic approximation matrices $[\bar{\boldsymbol{N}}]_i^e$ and $[\check{\boldsymbol{N}}]_i^e$ that, regarding a compact notation, can be summarized by the generalized global matrix $\mathfrak{N}$ containing the assembly and the element summation procedure. Clearly, the latter matrix is never build explicitly, it is introduced for the sake of a compact notation. At node i of the finite element discretization, the generalized nodal displacements are

$$\mathfrak{d}_i = [\,\bar{\boldsymbol{d}}, \check{\boldsymbol{d}}\,]_i^T\,. \tag{3.142}$$

The discretization of the generalized constitutive state vector takes the form

$$\mathfrak{c}^h(\mathfrak{d}) = \mathop{\mathsf{A}}_{e=1}^{n_{en}} \left[\sum_{i=1}^{n_{el}} \begin{bmatrix} [\bar{\boldsymbol{B}}]_i^e \bar{\boldsymbol{d}}_i^e \\ [\check{\boldsymbol{B}}]_i^e \check{\boldsymbol{d}}_i^e \end{bmatrix} + \begin{bmatrix} \boldsymbol{1}^h \\ \boldsymbol{0} \end{bmatrix} \right] = \mathop{\mathsf{A}}_{e=1}^{n_{en}} \begin{bmatrix} [\bar{\boldsymbol{B}}]^e \bar{\boldsymbol{d}}^e + \boldsymbol{1}^h \\ [\check{\boldsymbol{B}}]^e \check{\boldsymbol{d}}^e \end{bmatrix} = \mathop{\mathsf{A}}_{e=1}^{n_{en}} \begin{bmatrix} \bar{\boldsymbol{F}}^{he}(\bar{\boldsymbol{d}}^e) \\ [\check{\boldsymbol{B}}]^e\,\check{\boldsymbol{d}}^e \end{bmatrix}, \tag{3.143}$$

containing the element's approximation matrices for the macro- and microscopic gradient terms $[\bar{\boldsymbol{B}}]_i^e$ and $[\check{\boldsymbol{B}}]_i^e$, respectively. All element matrices discussed so far depend on the geometric and microstructural dimension, they are specified in the respective sections. The discretizations (3.141) and (3.143) govern the expressions of the incremental energy, dissipation, and work functionals. Thus, the incremental potential (3.96) is reformulated

$$\Pi^h(\mathfrak{d}) = \int_{\mathcal{B}^h} \{\, \pi^\tau(\mathfrak{c}^h(\mathfrak{d}); \mathfrak{c}^h(\mathfrak{d}_n)) - \mathfrak{g}\cdot\mathfrak{N}(\mathfrak{d}-\mathfrak{d}_n) \,\}\, dV - \int_{\partial\mathcal{B}^h_{\mathfrak{t}}} \mathfrak{t}_N \cdot \mathfrak{N}(\mathfrak{d}-\mathfrak{d}_n)\, dA\,, \tag{3.144}$$

leading to the discrete finite step sized incremental *minimization principle*

$$\boxed{\{\, \mathfrak{d} \,\} = \arg\{\, \inf_{\mathfrak{d}} \Pi^h(\mathfrak{d}) \,\}\,.} \tag{3.145}$$

It determines the generalized nodal displacements $\mathfrak{d}$ of the finite element mesh at current time t_{n+1}. Due to the linear dependency of the discrete macroscopic deformation gradient on the macroscopic displacement the variation of the discrete constitutive state vector (3.143) with respect to the nodal generalized displacements is introduced

$$\delta_{\mathfrak{d}}\mathfrak{c}^h = \mathop{\mathsf{A}}_{e=1}^{n_{en}} \begin{bmatrix} [\bar{\boldsymbol{B}}]^e & \boldsymbol{0} \\ \boldsymbol{0} & [\check{\boldsymbol{B}}]^e \end{bmatrix} \begin{bmatrix} \delta\bar{\boldsymbol{d}} \\ \delta\check{\boldsymbol{d}} \end{bmatrix}^e =: \mathfrak{B}(\boldsymbol{X})\,\delta\mathfrak{d}\,. \tag{3.146}$$

Thus, the necessary condition of the discrete variational problem (3.145) can be specified

$$\boldsymbol{0} \in \Pi^h_{,\mathfrak{d}} = \int_{\mathcal{B}^h} \{\, \mathfrak{B}^T[\boldsymbol{S}] - \mathfrak{N}^T \mathfrak{g} \,\}\, dV - \int_{\partial\mathcal{B}^h_{\mathfrak{t}}} \mathfrak{N}^T \mathfrak{t}_N \, dA \quad \text{with} \quad \boldsymbol{S} := \partial_{\mathfrak{c}^h} \pi^h \,, \tag{3.147}$$

where the *generalized stresses* $\boldsymbol{S}$ have been introduced. The necessary condition delivers a nonlinear algebraic system for the determination of the generalized nodal displacements. The coupled residual (3.147) is linearized

$$\operatorname{Lin} \Pi^h_{,\mathfrak{d}} = \Pi^h_{,\mathfrak{d}} + [\Pi^h_{,\mathfrak{d}\mathfrak{d}}] \cdot \Delta\mathfrak{d} = \boldsymbol{0} \,, \tag{3.148}$$

which builds the basis for a Newton iteration. Solving for the increments $\Delta\mathfrak{d}$, the update directive for the generalized displacements is summarized by the algorithm

$$\mathfrak{d} \Leftarrow \mathfrak{d} - [\Pi^h_{,\mathfrak{d}\mathfrak{d}}]^{-1} \cdot \Pi^h_{,\mathfrak{d}} \quad \text{until} \quad \|\Pi^h_{,\mathfrak{d}}\| \le \text{tol} \tag{3.149}$$

founded on the *symmetric* monolithic tangent matrix of the coupled problem

$$\Pi^h_{,\mathfrak{d}\mathfrak{d}} = \int_{\mathcal{B}^h} \{\, \mathfrak{B}^T [\mathbb{C}] \mathfrak{B} \,\}\, dV \quad \text{with} \quad \mathbb{C} := \partial^2_{\mathfrak{c}^h \mathfrak{c}^h} \pi^h \,. \tag{3.150}$$

Here, the *generalized moduli* $\mathbb{C}$ have been introduced as the second constitutive derivative of the incremental internal work density π^h with respect to the constitutive state $\mathfrak{c}^h$.

3.8.2. Extended Incremental Variational Principle. The focus of this section lies on the construction of a discrete extended incremental variational principle that employs the extended version of the incremental dissipation functional (3.85) or the threshold-type viscous incremental dissipation functional (3.87). Both dissipation functionals demand the extension of the discrete generalized constitutive state

$$\mathfrak{u}^{*h} = \mathop{\mathsf{A}}\limits_{e=1}^{n_{en}} \left[\sum_{i=1}^{n_{el}} \begin{bmatrix} [\mathfrak{N}]^e_i & \boldsymbol{0} \\ \boldsymbol{0} & [\boldsymbol{A}]^e_i \end{bmatrix} \begin{bmatrix} \mathfrak{d} \\ \boldsymbol{f} \end{bmatrix}_i \right]^e = \mathop{\mathsf{A}}\limits_{e=1}^{n_{en}} \begin{bmatrix} [\mathfrak{N}]^e & \boldsymbol{0} \\ \boldsymbol{0} & [\boldsymbol{A}]^e \end{bmatrix} \begin{bmatrix} \mathfrak{d} \\ \boldsymbol{f} \end{bmatrix}^e =: \mathfrak{N}^*(\boldsymbol{X})\, \mathfrak{d}^* \,, \tag{3.151}$$

where in addition to (3.141) also the thermodynamic driving forces are discretized via the approximation matrix $[\boldsymbol{A}]^e_i$. In this setting, the global matrix $\mathfrak{N}^*$ contains the assembly and the element summation procedure and is never build explicitly. It is introduced to allow for a compact notation. At node i of the discretization, the extended nodal displacement vector $\mathfrak{d}^*$ is defined by

$$\mathfrak{d}^*_i = [\, \mathfrak{d}, \boldsymbol{f} \,]^T_i = [\, \bar{\boldsymbol{d}}, \check{\boldsymbol{d}}, \boldsymbol{f} \,]^T_i \tag{3.152}$$

containing the nodal displacements $\bar{\boldsymbol{d}}_i$, the nodal micro-deformations $\check{\boldsymbol{d}}_i$, and the nodal thermodynamic forces $\boldsymbol{f}_i$. According to (3.143), the discrete extended constitutive state can be introduced

$$\mathfrak{c}^{*h}(\mathfrak{d}^*) = \mathop{\mathsf{A}}\limits_{e=1}^{n_{en}} \left[\sum_{i=1}^{n_{el}} \begin{bmatrix} [\bar{\boldsymbol{B}}]^e_i \bar{\boldsymbol{d}}^e_i \\ [\check{\boldsymbol{B}}]^e_i \check{\boldsymbol{d}}^e_i \\ [\boldsymbol{A}]^e_i \boldsymbol{f}^e_i \end{bmatrix} + \begin{bmatrix} \boldsymbol{1}^h \\ \boldsymbol{0} \\ \boldsymbol{0} \end{bmatrix} \right] = \mathop{\mathsf{A}}\limits_{e=1}^{n_{en}} \begin{bmatrix} [\bar{\boldsymbol{B}}]^e \bar{\boldsymbol{d}}^e + \boldsymbol{1}^h \\ [\check{\boldsymbol{B}}]^e \check{\boldsymbol{d}}^e \\ [\boldsymbol{A}]^e \boldsymbol{f}^e \end{bmatrix} = \mathop{\mathsf{A}}\limits_{e=1}^{n_{en}} \begin{bmatrix} \bar{\boldsymbol{F}}^{he}(\bar{\boldsymbol{d}}^e) \\ [\check{\boldsymbol{B}}]^e \, \check{\boldsymbol{d}}^e \\ [\boldsymbol{A}]^e \boldsymbol{f}^e \end{bmatrix} . \tag{3.153}$$

All element matrices depend on the geometric dimension and the nature of the materials microstructure, they are introduced in the respective sections. Based on the discretization (3.151) and (3.153), the extended potential (3.101) or (3.116) can be reformulated

$$\Pi^{*h}_\eta(\mathfrak{d}^*) = \int_{\mathcal{B}^h} \{\, \pi^{*h}_\eta(\mathfrak{c}^{*h}(\mathfrak{d}^*); \mathfrak{c}^{*h}(\mathfrak{d}^*_n)) - \mathfrak{g} \cdot \mathfrak{N}(\mathfrak{d} - \mathfrak{d}_n) \,\}\, dV - \int_{\partial\mathcal{B}^h_{\mathfrak{t}}} \mathfrak{t}_N \cdot \mathfrak{N}(\mathfrak{d} - \mathfrak{d}_n) \, dA \,, \tag{3.154}$$

which finally allows for the introduction of the discrete incremental *stationary principle*

$$\boxed{\{\,\boldsymbol{\mathfrak{d}}^*\,\} = \arg\{\,\underset{\boldsymbol{\mathfrak{d}}^*}{\operatorname{stat}}\,\Pi^{*h}_{\eta}(\boldsymbol{\mathfrak{d}}^*)\,\}\,.} \tag{3.155}$$

It identifies the generalized nodal displacements $\boldsymbol{\mathfrak{d}}$ and the nodal thermodynamic forces $\boldsymbol{f}$ of the discrete problem at time t_{n+1}. Based on the variation of the discrete constitutive state vector (3.153) with respect to the extended nodal generalized displacements

$$\delta_{\boldsymbol{\mathfrak{d}}^*}\boldsymbol{\mathfrak{c}}^{*h} = \mathop{\mathsf{A}}_{e=1}^{n_{en}} \begin{bmatrix} [\bar{\boldsymbol{B}}]^e & \boldsymbol{0} & \boldsymbol{0} \\ \boldsymbol{0} & [\breve{\boldsymbol{B}}]^e & \boldsymbol{0} \\ \boldsymbol{0} & \boldsymbol{0} & [\boldsymbol{A}]^e \end{bmatrix} \begin{bmatrix} \delta\bar{\boldsymbol{d}} \\ \delta\breve{\boldsymbol{d}} \\ \delta\boldsymbol{f} \end{bmatrix}^e =: \boldsymbol{\mathfrak{B}}^*(\boldsymbol{X})\,\delta\boldsymbol{\mathfrak{d}}^*\,, \tag{3.156}$$

the discrete necessary condition of the stationary principle (3.155) can be specified

$$\boldsymbol{0} \in \Pi^{*h}_{\eta,\boldsymbol{\mathfrak{d}}^*} = \int_{\mathcal{B}^h} \{\,\boldsymbol{\mathfrak{B}}^{*T}[\boldsymbol{S}^*] - \boldsymbol{\mathfrak{N}}^T\boldsymbol{\mathfrak{g}}\,\}\,dV - \int_{\partial\mathcal{B}^h_{\mathfrak{t}}} \boldsymbol{\mathfrak{N}}^T\boldsymbol{\mathfrak{t}}_N\,dA \quad \text{with} \quad \boldsymbol{S}^* := \partial_{\boldsymbol{\mathfrak{c}}^{*h}}\pi^{*h}_{\eta}\,, \tag{3.157}$$

expressed in terms of the *extended generalized stresses* $\boldsymbol{S}^*$. This system of nonlinear equations is solved iteratively in a Newton solution scheme based on the algorithm

$$\boldsymbol{\mathfrak{d}}^* \Leftarrow \boldsymbol{\mathfrak{d}}^* - [\Pi^{*h}_{\eta,\boldsymbol{\mathfrak{d}}^*\boldsymbol{\mathfrak{d}}^*}]^{-1}\cdot\Pi^{*h}_{\eta,\boldsymbol{\mathfrak{d}}^*} \quad \text{until} \quad \|\Pi^{*h}_{\eta,\boldsymbol{\mathfrak{d}}^*}\| \le \text{tol}\,. \tag{3.158}$$

This expression contains the *symmetric* monolithic tangent matrix

$$\Pi^{*h}_{\eta,\boldsymbol{\mathfrak{d}}^*\boldsymbol{\mathfrak{d}}^*} = \int_{\mathcal{B}^h} \{\,\boldsymbol{\mathfrak{B}}^{*T}[\mathbb{C}^*]\boldsymbol{\mathfrak{B}}^*\,\}\,dV \quad \text{with} \quad \mathbb{C}^* := \partial^2_{\boldsymbol{\mathfrak{c}}^{*h}\boldsymbol{\mathfrak{c}}^{*h}}\pi^{*h}_{\eta}\,, \tag{3.159}$$

where the *extended generalized moduli* $\mathbb{C}^*$ have been introduced as second constitutive derivative of the incremental internal work density π^{*h}_{η} with respect to the constitutive state $\boldsymbol{\mathfrak{c}}^{*h}$.

3.8.3. Extended Incremental Variational Principle with Local History. The focus is now put on a compact formulation of the discrete incremental variational principle which involves in addition to the global nodal unknowns the numerical treatment of the local history variables. According to (3.151) and (3.156), the discrete generalized displacements and the variation of the discrete constitutive state with respect to the nodal unknowns read

$$\boldsymbol{\mathfrak{u}}^{*h} = \boldsymbol{\mathfrak{N}}^*(\boldsymbol{X})\,\boldsymbol{\mathfrak{d}}^* \quad \text{and} \quad \delta_{\boldsymbol{\mathfrak{d}}^*}\boldsymbol{\mathfrak{c}}^{*h} = \boldsymbol{\mathfrak{B}}^*(\boldsymbol{X})\,\boldsymbol{\mathfrak{d}}^*\,. \tag{3.160}$$

The local solution pair is locally approximated on Gauss point level via

$$\boldsymbol{\mathfrak{p}}^h := \{\,\boldsymbol{\mathcal{I}}^h, \boldsymbol{\mathcal{F}}^h\,\}\,. \tag{3.161}$$

With these expressions, the incremental potential with local history (3.131) is discretized

$$\begin{aligned} \Pi^{*h}_{\eta}(\boldsymbol{\mathfrak{d}}^*, \boldsymbol{\mathfrak{p}}^h) = &\int_{\mathcal{B}^h} \{\,\pi^{*h}_{\eta}(\boldsymbol{\mathfrak{c}}^{*h}(\boldsymbol{\mathfrak{d}}^*), \boldsymbol{\mathfrak{p}}^h; \boldsymbol{\mathfrak{c}}^{*h}(\boldsymbol{\mathfrak{d}}^*_n), \boldsymbol{\mathfrak{p}}^h_n) - \boldsymbol{\mathfrak{g}}\cdot\boldsymbol{\mathfrak{N}}(\boldsymbol{\mathfrak{d}} - \boldsymbol{\mathfrak{d}}_n)\,\}\,dV \\ &- \int_{\partial\mathcal{B}^h_{\mathfrak{t}}} \boldsymbol{\mathfrak{t}}_N\cdot\boldsymbol{\mathfrak{N}}(\boldsymbol{\mathfrak{d}} - \boldsymbol{\mathfrak{d}}_n)\,dA\,. \end{aligned} \tag{3.162}$$

The discrete incremental stationary problem takes the form

$$\boxed{\{\,\boldsymbol{\mathfrak{d}}^*,\boldsymbol{\mathfrak{p}}^h\,\} = \arg\{\,\underset{\boldsymbol{\mathfrak{d}}^*,\boldsymbol{\mathfrak{p}}^h}{\operatorname{stat}}\,\Pi^{*h}_{\eta}(\boldsymbol{\mathfrak{d}}^*,\boldsymbol{\mathfrak{p}}^h)\,\}} \tag{3.163}$$

and identifies the extended generalized nodal displacements $\boldsymbol{\mathfrak{d}}^*$ and the discrete local solution pair $\boldsymbol{\mathfrak{p}}^h$ of the discrete problem at time t_{n+1}. The discrete necessary condition defines a *global FE-system* which is solved for the nodal unknowns $\boldsymbol{\mathfrak{d}}^*$

$$\boldsymbol{0}\in\Pi^{*h}_{\eta,\boldsymbol{\mathfrak{d}}^*} = \int_{\mathcal{B}^h}\{\,\boldsymbol{\mathfrak{B}}^{*T}[\boldsymbol{S}^*] - \boldsymbol{\mathfrak{N}}^T\boldsymbol{\mathfrak{g}}\,\}\,dV - \int_{\partial\mathcal{B}^h_{\mathfrak{t}}}\boldsymbol{\mathfrak{N}}^T\boldsymbol{\mathfrak{t}}_N\,dA \quad\text{with}\quad \boldsymbol{S}^* := \partial_{\boldsymbol{\mathfrak{c}}^{*h}}\pi^{*h}_{\eta} \tag{3.164}$$

expressed in terms of the *generalized stresses* $\boldsymbol{S}^*$ and a *local equation* for the computation of the local solution pair $\boldsymbol{\mathfrak{p}}^h$

$$\boldsymbol{0}\in\pi^{*h}_{\eta,\boldsymbol{\mathfrak{p}}^h} := \partial_{\boldsymbol{\mathfrak{p}}^h}\pi^{*h}_{\eta}\,. \tag{3.165}$$

The system of nonlinear equations (3.164) is solved iteratively in a Newton solution scheme which bases on the linearization

$$\operatorname{Lin}\Pi^{*h}_{\eta,\boldsymbol{\mathfrak{d}}^*} = \Pi^{*h}_{\eta,\boldsymbol{\mathfrak{d}}^*} + [\Pi^{*h}_{\eta,\boldsymbol{\mathfrak{d}}^*\boldsymbol{\mathfrak{d}}^*}]\cdot\Delta\boldsymbol{\mathfrak{d}}^* = \boldsymbol{0}\,. \tag{3.166}$$

The extended generalized displacements $\boldsymbol{\mathfrak{d}}^*$ are updated according to the algorithm

$$\boldsymbol{\mathfrak{d}}^* \Leftarrow \boldsymbol{\mathfrak{d}}^* - [\Pi^{*h}_{\eta,\boldsymbol{\mathfrak{d}}^*\boldsymbol{\mathfrak{d}}^*}]^{-1}\cdot\Pi^{*h}_{\eta,\boldsymbol{\mathfrak{d}}^*} \quad\text{until}\quad \|\Pi^{*h}_{\eta,\boldsymbol{\mathfrak{d}}^*}\| \le \text{tol} \tag{3.167}$$

expressed in terms of the *symmetric* monolithic tangent matrix

$$\Pi^{*h}_{\eta,\boldsymbol{\mathfrak{d}}^*\boldsymbol{\mathfrak{d}}^*} = \int_{\mathcal{B}^h}\{\,\boldsymbol{\mathfrak{B}}^{*T}[\mathbb{C}^*]\boldsymbol{\mathfrak{B}}^*\,\}\,dV \quad\text{with}\quad \mathbb{C}^* := \partial^2_{\boldsymbol{\mathfrak{c}}^{*h}\boldsymbol{\mathfrak{c}}^{*h}}\pi^{*h} + \partial^2_{\boldsymbol{\mathfrak{c}}^{*h}\boldsymbol{\mathfrak{p}}^h}\pi^{*h}\,\partial_{\boldsymbol{\mathfrak{c}}^{*h}}\boldsymbol{\mathfrak{p}}^h\,. \tag{3.168}$$

In contrast to (3.159), this tangent matrix contains the *generalized moduli* $\mathbb{C}^*$ that show additional softening contributions arising from the local update procedure. The discrete necessary condition (3.165) describes the *evolution subproblem* of the local internal variables $\boldsymbol{\mathfrak{p}}^h := \{\,\boldsymbol{\mathcal{I}}^h,\boldsymbol{\mathcal{F}}^h\,\}$. For rather more complex material models, this subproblem is a nonlinear equation that is solved in a *local Newton iteration* carried out on Gauss point level. To this end, consider the local linearization

$$\operatorname{Lin}\,\pi^{*h}_{\eta,\boldsymbol{\mathfrak{p}}^h} = \pi^{*h}_{\eta,\boldsymbol{\mathfrak{p}}^h} + [\pi^{*h}_{\eta,\boldsymbol{\mathfrak{p}}^h\boldsymbol{\mathfrak{p}}^h}]\cdot\Delta\boldsymbol{\mathfrak{p}}^h = \boldsymbol{0} \tag{3.169}$$

that builds the basis for the update procedure of the local solution pair

$$\boldsymbol{\mathfrak{p}}^h \Leftarrow \boldsymbol{\mathfrak{p}}^h - [\pi^{*h}_{\eta,\boldsymbol{\mathfrak{p}}^h\boldsymbol{\mathfrak{p}}^h}]^{-1}\cdot\pi^{*h}_{\eta,\boldsymbol{\mathfrak{p}}^h} \quad\text{until}\quad \|\pi^{*h}_{\eta,\boldsymbol{\mathfrak{p}}^h}\| \le \text{tol}\,. \tag{3.170}$$

This local update algorithm bases on the local, monolithic, and symmetric tangent matrix $\pi^{*h}_{\eta,\boldsymbol{\mathfrak{p}}^h\boldsymbol{\mathfrak{p}}^h}$. Note that within one iteration step of the global solution procedure (3.167) the global unknowns $\boldsymbol{\mathfrak{d}}^*$ are frozen. Thus, the sensitivity $\partial_{\boldsymbol{\mathfrak{c}}^{*h}}\boldsymbol{\mathfrak{p}}^h$ in the global tangent matrix (3.168) at one global iteration step has to be determined iteratively on local level via enforcing the condition

$$\partial_{\boldsymbol{\mathfrak{c}}^{*h}}\pi^{*h}_{\eta,\boldsymbol{\mathfrak{p}}^h} + [\pi^{*h}_{\eta,\boldsymbol{\mathfrak{p}}^h\boldsymbol{\mathfrak{p}}^h}]\cdot\partial_{\boldsymbol{\mathfrak{c}}^{*h}}\boldsymbol{\mathfrak{p}}^h = \boldsymbol{0}\,. \tag{3.171}$$

This finally gives the iterative update rule for the *algorithmic sensitivity*

$$\partial_{\boldsymbol{\mathfrak{c}}^{*h}}\boldsymbol{\mathfrak{p}}^h \Leftarrow \partial_{\boldsymbol{\mathfrak{c}}^{*h}}\boldsymbol{\mathfrak{p}}^h - [\pi^{*h}_{\eta,\boldsymbol{\mathfrak{p}}^h\boldsymbol{\mathfrak{p}}^h}]^{-1}\cdot\partial_{\boldsymbol{\mathfrak{c}}^{*h}}\pi^{*h}_{\eta,\boldsymbol{\mathfrak{p}}^h} \tag{3.172}$$

and is build simultaneously with the local update directive (3.170). It does not disturb the symmetry property of the global tangent matrix $(3.168)_2$.

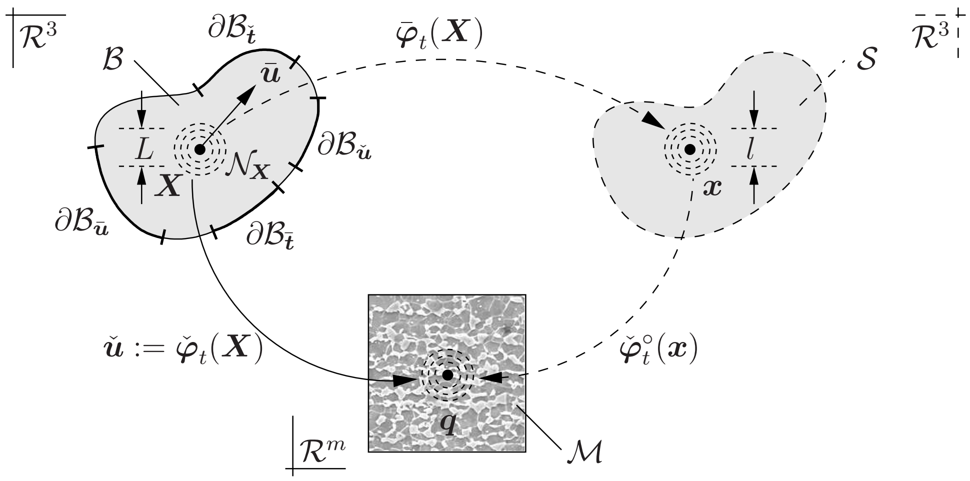
$\mathcal{R}^3$
$\partial\mathcal{B}_{\bar{\boldsymbol{t}}}$
$\bar{\boldsymbol{\varphi}}_t(\boldsymbol{X})$
$\mathcal{R}^3$
$\mathcal{B}$
$\bar{\boldsymbol{u}}$
$\mathcal{S}$
L
$\mathcal{N}_{\boldsymbol{X}}$
$\partial\mathcal{B}_{\bar{\boldsymbol{u}}}$
l
$\boldsymbol{X}$
$\boldsymbol{x}$
$\partial\mathcal{B}_{\bar{\boldsymbol{u}}}$
$\partial\mathcal{B}_{\bar{\boldsymbol{t}}}$
$\check{\boldsymbol{u}} := \check{\boldsymbol{\varphi}}_t(\boldsymbol{X})$
$\check{\boldsymbol{\varphi}}_t^{\circ}(\boldsymbol{x})$
$\boldsymbol{q}$
$\mathcal{R}^m$
$\mathcal{M}$

Figure 3.9: Linearization of macroscopic deformation map. For small macroscopic deformations the linearization of $\bar{\boldsymbol{\varphi}}_t(\boldsymbol{X})$ yields the macroscopic displacement field $\bar{\boldsymbol{u}}$ and the Eulerian configuration $\mathcal{S}$ coincides with the Lagrangian configuration $\mathcal{B}$, i.e. $\boldsymbol{x} = \boldsymbol{X}$.

3.9. Restriction to Geometric Linear Theory

This section aims at a reduction of the previously discussed framework for generalized continua undergoing large deformations to the small strain setting. First, the kinematics of *macroscopically small* deformations are discussed. Then, the objective constitutive state variables are introduced and the incremental variational principle is directly applied to the canonical two-field and the viscous, extended three-field setting. At the end of this section, an appropriate FE solution strategy is provided for both models.

3.9.1. Generalized Kinematics at Small Strains. In the context of small deformations, the *macroscopic deformation* is assumed to be small and can be obtained by a linearization of the macroscopic nonlinear deformation map $\bar{\boldsymbol{\varphi}}_t(\boldsymbol{X})$ evaluated in the reference configuration $\boldsymbol{x} = \boldsymbol{X}$. For a mathematical foundation of the linearization of the large deformation kinematics, see Marsden & Hughes [108]. As depicted in Figure 3.9, the Eulerian configuration $\mathcal{S}$ coincides with the Lagrangian configuration $\mathcal{B}$, where the Lagrangian and Eulerian gradients $\nabla_{\boldsymbol{X}}(\cdot)$ and $\nabla_{\boldsymbol{x}}(\cdot)$ of an arbitrary field $(\cdot)$ are equal. Thus, the gradient operator $\nabla(\cdot)$ is introduced to denote the spatial gradient of the vector field $(\cdot)$. As a consequence, the *macroscopic deformation field* reads

$$\bar{\boldsymbol{u}}(\boldsymbol{x},t) : \begin{cases} \mathcal{B} \times \mathcal{T} \to \mathcal{R}^3 \\ (\boldsymbol{x},t) \;\; \mapsto \bar{\boldsymbol{u}}(\boldsymbol{x},t)\,, \end{cases} \tag{3.173}$$

where $\bar{\boldsymbol{u}}(\boldsymbol{x},t)$ is the displacement of the material point P at position $\boldsymbol{x} \in \mathcal{B}$ at time $t \in \mathcal{T}$. The exterior of the solid is decomposed into a domain $\partial\mathcal{B}_{\bar{\boldsymbol{u}}}$ where the displacement is prescribed in the sense of a Dirichlet boundary condition

$$\bar{\boldsymbol{u}}(\boldsymbol{x},t) = \bar{\boldsymbol{u}}_D(\boldsymbol{x},t) \quad \text{on } \partial\mathcal{B}_{\bar{\boldsymbol{u}}} \tag{3.174}$$

and a part $\partial\mathcal{B}_{\bar{\boldsymbol{t}}}$ where the macroscopic traction $\bar{\boldsymbol{t}}_N(\boldsymbol{x},t)$ is prescribed by a Neumann boundary condition. Clearly, the common set of the displacement and traction boundaries correspond to the empty set, i.e. $\partial\mathcal{B}_{\bar{\boldsymbol{u}}} \cap \partial\mathcal{B}_{\bar{\boldsymbol{t}}} = \emptyset$. In the interior domain $\mathcal{B}$, the strains are assumed to be small. Thus, the norm of the macroscopic displacement gradient

$$\|\boldsymbol{h}\| < \epsilon \quad \text{with} \quad \boldsymbol{h} := \nabla\bar{\boldsymbol{u}}(\boldsymbol{x},t) \tag{3.175}$$

is bounded by a small number ϵ. In contrast, the microscopic deformation gradient is not bounded by a small number. Due to the coincidence of the Lagrangian and Eulerian coordinates $\boldsymbol{X} = \boldsymbol{x}$, the *microscopic deformation field* can be re-defined

$$\check{\boldsymbol{u}}(\boldsymbol{x}, t) : \begin{cases} \mathcal{B} \times \mathcal{T} \rightarrow \mathcal{R}^m \\ (\boldsymbol{x}, t) \;\; \mapsto \check{\boldsymbol{u}}(\boldsymbol{x}, t) = \check{\boldsymbol{\varphi}}(\boldsymbol{X}, t) \end{cases} \quad \text{with} \quad \boldsymbol{X} = \boldsymbol{x} \,. \tag{3.176}$$

Note that in the context of macroscopically small deformations, the Eulerian and Lagrangian microscopic deformation maps (3.4) coincide, i.e. $\check{\boldsymbol{\varphi}}_t(\boldsymbol{X}) = \check{\boldsymbol{\varphi}}_t^\circ(\boldsymbol{x})$. Regarding the microstructural field, the surface of the solid is decomposed into a domain $\partial\mathcal{B}_{\check{\boldsymbol{u}}}$, where the micro-motion is prescribed by the Dirichlet-type boundary condition

$$\check{\boldsymbol{u}}(\boldsymbol{x}, t) = \check{\boldsymbol{u}}_D(\boldsymbol{x}, t) \;\; \text{on } \partial\mathcal{B}_{\check{\boldsymbol{u}}} \tag{3.177}$$

and a domain $\partial\mathcal{B}_{\check{\boldsymbol{t}}}$, where the microscopic traction $\check{\boldsymbol{t}}_N(\boldsymbol{x}, t)$ is prescribed by a Neumann-type boundary condition. Obviously, the microscopic partition of the surface imposes the constraint $\partial\mathcal{B}_{\check{\boldsymbol{u}}} \cap \partial\mathcal{B}_{\check{\boldsymbol{t}}} = \emptyset$.

3.9.2. Constitutive Response of Generalized Continua. An adaption of the energy storage and dissipation functionals (3.28) to the scenario of small deformations reads

$$E(\bar{\boldsymbol{u}}, \check{\boldsymbol{u}}) := \int_{\mathcal{B}} \psi \, dV \quad \text{and} \quad D(\dot{\bar{\boldsymbol{u}}}, \dot{\check{\boldsymbol{u}}}; \bar{\boldsymbol{u}}, \check{\boldsymbol{u}}) := \int_{\mathcal{B}} \phi \, dV \tag{3.178}$$

in terms of the energy storage function ψ and the dissipation function ϕ. Regarding materials of grade one, they depend on the constitutive state

$$\mathfrak{c}_0 := \{\, \bar{\boldsymbol{u}}, \nabla\bar{\boldsymbol{u}}, \check{\boldsymbol{u}}, \nabla\check{\boldsymbol{u}} \,\} \tag{3.179}$$

containing the macro- and microscopic deformations and their gradients. Thus, the constitutive functions can be specified to

$$\psi = \psi(\mathfrak{c}_0) \quad \text{and} \quad \phi = \phi(\dot{\mathfrak{c}}_0; \mathfrak{c}_0) \,. \tag{3.180}$$

The constitutive functions (3.180) have to be invariant with respect to arbitrary superimposed macroscopic rigid body motions

$$\psi(\mathfrak{c}_0) = \psi(\mathfrak{c}_0^+) \quad \text{and} \quad \phi(\dot{\mathfrak{c}}_0; \mathfrak{c}_0) = \phi(\dot{\mathfrak{c}}_0^+; \mathfrak{c}_0^+) \,, \tag{3.181}$$

where $\mathfrak{c}_0^+ := \{\, \bar{\boldsymbol{u}}^+, \nabla\bar{\boldsymbol{u}}^+, \check{\boldsymbol{u}}^+, \nabla\check{\boldsymbol{u}}^+ \,\}$ denotes the transformed constitutive state. This modified constitutive state takes into account the transformed macroscopic contributions

$$\bar{\boldsymbol{u}}^+ := \bar{\boldsymbol{u}} + \bar{\boldsymbol{\omega}}\, \boldsymbol{x} + \bar{\boldsymbol{c}} \tag{3.182}$$

based on the time dependent, skew-symmetric, second-order tensor $\bar{\boldsymbol{\omega}}(t)$ with the properties $\bar{\boldsymbol{\omega}}^T = -\bar{\boldsymbol{\omega}}$ and $\|\bar{\boldsymbol{\omega}}\| < \epsilon$ describing an *infinitesimal rotation.* The vector $\bar{\boldsymbol{c}}(t)$ is a time dependent *translation* superimposed onto the displaced solid. In contrast, the microscopic variables are unaffected by a macroscopic superimposed rigid body motion

$$\check{\boldsymbol{u}}^+ := \check{\boldsymbol{u}} \,. \tag{3.183}$$

A direct consequence of (3.181) states that the free energy function ψ cannot depend on the macroscopic deformation $\bar{\boldsymbol{u}}$ and the skew part of its gradient skew$[\nabla\bar{\boldsymbol{u}}]$ and the dissipation function ϕ cannot depend on the macroscopic rate $\dot{\bar{\boldsymbol{u}}}$ and the skew part of its gradient skew$[\nabla\dot{\bar{\boldsymbol{u}}}]$, respectively. Thus, the *objective state* is introduced

$$\mathfrak{c} := \{\, \nabla_s\bar{\boldsymbol{u}}, \check{\boldsymbol{u}}, \nabla\check{\boldsymbol{u}} \,\}\,, \tag{3.184}$$

which finally allows for the introduction of the *reduced forms*

$$\psi = \psi(\mathfrak{c}) \quad \text{and} \quad \phi = \phi(\dot{\mathfrak{c}};\mathfrak{c}) \tag{3.185}$$

that a priori satisfy the principle of material frame invariance. In this formulation, the symmetric part of the macroscopic displacement gradient can be identified as the classical small strain displacement gradient

$$\boldsymbol{\varepsilon} := \nabla_s\bar{\boldsymbol{u}} = \tfrac{1}{2}\,[\boldsymbol{h} + \boldsymbol{h}^T] \quad \text{with} \quad \boldsymbol{h} := \nabla\bar{\boldsymbol{u}}\,. \tag{3.186}$$

3.9.3. Time-Discrete Incremental Variational Formulation. According to the large strain formulation, the governing coupled field equations in the geometric linear theory can be obtained by a time-discrete incremental variational formulation. The focus hereby lies on the canonical two-field setting and the viscous three field setting, the remaining representations follow accordingly.

3.9.3.1. Time-Discrete Field Variables. In a time-discrete setting, the field variables at the discrete solution times $0, t_1, \ldots, t_n, t_{n+1}, T$ are investigated. Within a typical time step $[t_n, t_{n+1}]$, the macro- and microscopic field variables evaluated at time t_{n+1} read

$$\bar{\boldsymbol{u}} := \bar{\boldsymbol{u}}(\boldsymbol{x}, t_{n+1}) \quad \text{and} \quad \check{\boldsymbol{u}} := \check{\boldsymbol{u}}(\boldsymbol{x}, t_{n+1})\,, \tag{3.187}$$

where all variables without subscript are meant to be evaluated at current time t_{n+1}. The global fields evaluated at the previous solution time t_n can be expressed by

$$\bar{\boldsymbol{u}}_n := \bar{\boldsymbol{u}}(\boldsymbol{x}, t_n) \quad \text{and} \quad \check{\boldsymbol{u}}_n := \check{\boldsymbol{u}}(\boldsymbol{x}, t_n)\,. \tag{3.188}$$

As a consequence, the rates of these global fields are constant quantities within the time increment under focus. They are defined by

$$\dot{\bar{\boldsymbol{u}}} := (\bar{\boldsymbol{u}} - \bar{\boldsymbol{u}}_n)/\tau \quad \text{and} \quad \dot{\check{\boldsymbol{u}}} := (\check{\boldsymbol{u}} - \check{\boldsymbol{u}}_n)/\tau\,. \tag{3.189}$$

The rate of the constitutive state (3.184) is approximated via

$$\dot{\mathfrak{c}} := (\mathfrak{c} - \mathfrak{c}_n)/\tau\,. \tag{3.190}$$

In the extended setting, the dual dissipative thermodynamic forces

$$\bar{\boldsymbol{\mathcal{F}}} := \bar{\boldsymbol{\mathcal{F}}}(\boldsymbol{x}, t_{n+1}) \quad \text{and} \quad \check{\boldsymbol{f}} := \check{\boldsymbol{f}}(\boldsymbol{x}, t_{n+1}) \quad \text{and} \quad \check{\boldsymbol{\mathcal{F}}} := \check{\boldsymbol{\mathcal{F}}}(\boldsymbol{x}, t_{n+1}) \tag{3.191}$$

have to be introduced which are summarized in the array

$$\mathfrak{f} := \{\, \bar{\boldsymbol{\mathcal{F}}}, \check{\boldsymbol{f}}, \check{\boldsymbol{\mathcal{F}}} \,\}\,. \tag{3.192}$$

This array of dissipative forces is dual to the rate of the constitutive state (3.184).

3.9.3.2. Incremental Energy, Dissipation, and Load Functionals. Associated with a typical discrete time interval, the incrementally stored energy in the solid reads

$$E^\tau(\bar{\boldsymbol{u}}, \check{\boldsymbol{u}}) := \int_{t_n}^{t_{n+1}} \dot{E}\, dt = \int_{\mathcal{B}} \{\, \psi(\mathfrak{c}) - \psi(\mathfrak{c}_n) \,\}\, dV \tag{3.193}$$

and bases on the energy functional defined in $(3.178)_1$. Recalling the constitutive relationship $(3.185)_1$, the incremental energy is considered as a functional of the macro- and microscopic displacements $\bar{\boldsymbol{u}}$ and $\check{\boldsymbol{u}}$ at time t_{n+1}, governed by the free energy function ψ. The incremental dissipation functional is obtained by the expression

$$D^\tau(\bar{\boldsymbol{u}}, \check{\boldsymbol{u}}) := \int_{t_n}^{t_{n+1}} D\, dt\,. \tag{3.194}$$

As discussed in Section 3.6, there exist different possibilities to model the constitutive dissipation function. Making use of definition $(3.185)_2$ and the approximated constitutive rates (3.190), a canonical setting of the incremental dissipation functional is introduced

$$D^\tau(\bar{\boldsymbol{u}}, \check{\boldsymbol{u}}) := \int_{\mathcal{B}} \{\, \tau\, \phi((\mathfrak{c} - \mathfrak{c}_n)/\tau; \mathfrak{c}_n) \,\}\, dV \tag{3.195}$$

depending on the primary field variables $\bar{\boldsymbol{u}}$ and $\check{\boldsymbol{u}}$ at current time t_{n+1}. Starting with the smooth dissipation function (3.70), the incremental dissipation functional

$$D^{*\tau}_\eta(\bar{\boldsymbol{u}}, \check{\boldsymbol{u}}, \mathfrak{f}) := \int_{\mathcal{B}} \{\, \mathfrak{f} \cdot (\mathfrak{c} - \mathfrak{c}_n) - \frac{\tau}{2\eta}\, \langle \varphi(\mathfrak{f}; \mathfrak{c}_n) \rangle_+^2 \,\}\, dV \tag{3.196}$$

is obtained, where $\eta > 0$ is the viscosity parameter. The incremental external work expended to the system within the discrete time interval by external actions on the multifield problem is given by the expression

$$W^\tau(\bar{\boldsymbol{u}}, \check{\boldsymbol{u}}) := \int_{t_n}^{t_{n+1}} \mathcal{P}_{ext}\, dt\,. \tag{3.197}$$

Here, $\mathcal{P}_{ext}$ is the total power of external loading consisting of macro- and microscopic contributions. Assuming constant rates within the time step under focus, see equation (3.189), the incremental work is considered as a functional of the macro- and microscopic displacement $\bar{\boldsymbol{u}}$ and $\check{\boldsymbol{u}}$, respectively. Thus, at current time t_{n+1} the external work is defined by the *algorithmic expression*

$$\begin{aligned} W^\tau(\bar{\boldsymbol{u}}, \check{\boldsymbol{u}}) := {} & \int_{\mathcal{B}} \bar{\boldsymbol{\gamma}} \cdot (\bar{\boldsymbol{u}} - \bar{\boldsymbol{u}}_n)\, dV + \int_{\partial\mathcal{B}_{\bar{\boldsymbol{t}}}} \bar{\boldsymbol{t}}_N \cdot (\bar{\boldsymbol{u}} - \bar{\boldsymbol{u}}_n)\, dA \\ & + \int_{\mathcal{B}} \check{\boldsymbol{\gamma}} \cdot (\check{\boldsymbol{u}} - \check{\boldsymbol{u}}_n)\, dV + \int_{\partial\mathcal{B}_{\check{\boldsymbol{t}}}} \check{\boldsymbol{t}}_N \cdot (\check{\boldsymbol{u}} - \check{\boldsymbol{u}}_n)\, dA\,, \end{aligned} \tag{3.198}$$

in terms of the *prescribed* macro- and microscopic body force fields $\bar{\boldsymbol{\gamma}}$ and $\check{\boldsymbol{\gamma}}$ and the macro- and microscopic surface tractions $\bar{\boldsymbol{t}}_N$ and $\check{\boldsymbol{t}}_N$ evaluated at the current time t_{n+1}.

3.9.3.3. Canonical Incremental Minimization Principle. The canonical incremental minimization principle for generalized solids undergoing macroscopically small deformations is governed by the incremental potential

$$\underbrace{\Pi^\tau(\bar{\boldsymbol{u}},\check{\boldsymbol{u}})}_{potential} := \underbrace{E^\tau(\bar{\boldsymbol{u}},\check{\boldsymbol{u}})}_{energy} + \underbrace{D^\tau(\bar{\boldsymbol{u}},\check{\boldsymbol{u}})}_{dissipation} - \underbrace{W^\tau(\bar{\boldsymbol{u}},\check{\boldsymbol{u}})}_{work} \tag{3.199}$$

and bases on the incremental energy storage (3.193), the incremental dissipation (3.195), and the incremental work (3.198). In view of a compact notation, the generalized constitutive state as a function of the generalized displacements

$$\boldsymbol{\mathfrak{c}}(\boldsymbol{\mathfrak{u}}) := \{\, \nabla_s\bar{\boldsymbol{u}}, \check{\boldsymbol{u}}, \nabla\check{\boldsymbol{u}} \,\} \quad \text{and} \quad \boldsymbol{\mathfrak{u}} := \{\, \bar{\boldsymbol{u}}, \check{\boldsymbol{u}} \,\} \tag{3.200}$$

is introduced. The generalized vector of macro- and microscopic body forces

$$\boldsymbol{\mathfrak{g}} := \{\, \bar{\gamma}_0, \check{\gamma}_0 \,\} \;\text{ in } \mathcal{B} \tag{3.201}$$

and the generalized surface traction vector

$$\boldsymbol{\mathfrak{t}}_N := \{\, \bar{\boldsymbol{t}}_N, \check{\boldsymbol{t}}_N \,\} \;\text{ on } \partial\mathcal{B}_{\boldsymbol{\mathfrak{t}}} := \{\, \partial\mathcal{B}_{\bar{\boldsymbol{t}}}, \partial\mathcal{B}_{\check{\boldsymbol{t}}} \,\}\,, \tag{3.202}$$

summarizing the macro- and microscopic surface tractions $\bar{\boldsymbol{t}}_N$ and $\check{\boldsymbol{t}}_N$ are defined. The incremental potential (3.199) can be reformulated in a compact format

$$\Pi^\tau(\boldsymbol{\mathfrak{u}}) = \int_{\mathcal{B}} \{\, \pi^\tau(\boldsymbol{\mathfrak{c}};\boldsymbol{\mathfrak{c}}_n) - \boldsymbol{\mathfrak{g}}\cdot(\boldsymbol{\mathfrak{u}}-\boldsymbol{\mathfrak{u}}_n) \,\}\, dV - \int_{\partial\mathcal{B}_{\boldsymbol{\mathfrak{t}}}} \boldsymbol{\mathfrak{t}}_N\cdot(\boldsymbol{\mathfrak{u}}-\boldsymbol{\mathfrak{u}}_n)\, dA\,. \tag{3.203}$$

In this expression, the *extended incremental internal work density*

$$\pi^\tau(\boldsymbol{\mathfrak{c}};\boldsymbol{\mathfrak{c}}_n) = \psi(\boldsymbol{\mathfrak{c}}) - \psi(\boldsymbol{\mathfrak{c}}_n) + \tau\,\phi((\boldsymbol{\mathfrak{c}}-\boldsymbol{\mathfrak{c}}_n)/\tau;\boldsymbol{\mathfrak{c}}_n) \tag{3.204}$$

is introduced, determined by the free energy function ψ and the dissipation function ϕ. In this sense, the finite step sized incremental minimum principle reads

$$\boxed{\{\, \bar{\boldsymbol{u}}, \check{\boldsymbol{u}} \,\} = \arg\{\, \inf_{\bar{\boldsymbol{u}}}\inf_{\check{\boldsymbol{u}}} \Pi^\tau(\bar{\boldsymbol{u}},\check{\boldsymbol{u}}) \,\}} \tag{3.205}$$

and determines the current macro- and microscopic displacements $\bar{\boldsymbol{u}}$ and $\check{\boldsymbol{u}}$ as the *minimum* of the incremental functional (3.203). The *non-smooth* necessary condition reads

$$0 \in \delta\Pi^\tau = \delta_{\bar{\boldsymbol{u}}}\Pi^\tau + \delta_{\check{\boldsymbol{u}}}\Pi^\tau\,, \tag{3.206}$$

where the single variations can be summarized by the explicit expressions

$$\begin{aligned} \delta_{\bar{\boldsymbol{u}}}\Pi^\tau_\eta := &\int_{\mathcal{B}} \{\, [\partial_{\nabla_s\bar{\boldsymbol{u}}}\psi + \partial_{\nabla_s\dot{\bar{\boldsymbol{u}}}}\phi] : \nabla_s\delta\bar{\boldsymbol{u}} - \bar{\boldsymbol{\gamma}}\cdot\delta\bar{\boldsymbol{u}} \,\}\, dV \\ &- \int_{\partial\mathcal{B}_{\bar{t}}} \bar{\boldsymbol{t}}_N\cdot\delta\bar{\boldsymbol{u}}\, dA \\ \delta_{\check{\boldsymbol{u}}}\Pi^\tau_\eta := &\int_{\mathcal{B}} \{\, [\partial_{\nabla\check{\boldsymbol{u}}}\psi + \partial_{\nabla_s\dot{\check{\boldsymbol{u}}}}\phi] : \nabla\delta\check{\boldsymbol{u}} + [\partial_{\check{\boldsymbol{u}}}\psi + \partial_{\dot{\check{\boldsymbol{u}}}}\phi - \check{\gamma}]\cdot\delta\check{\boldsymbol{u}} \,\}\, dV \\ &- \int_{\partial\mathcal{B}_{\check{t}}} \check{\boldsymbol{t}}_N\cdot\delta\check{\boldsymbol{u}}\, dA \end{aligned} \tag{3.207}$$

in terms of the admissible variations $\delta\bar{\boldsymbol{u}} \in \mathcal{W}^0_{\bar{\boldsymbol{u}}}$ and $\delta\check{\boldsymbol{u}} \in \mathcal{W}^0_{\check{\boldsymbol{u}}}$ of the current macro- and microscopic displacements. The Euler equations of the minimum principle (3.205) follow by application of Gauss' and localization theorem. They exhibit a structure formally similar to those obtained in the large strain setting as summarized in Table 3.1.

3.9.3.4. Rate-Dependent Principle with Threshold Function. The variational principle for the rate-dependent setting of the dissipation function is governed by the extended incremental potential

$$\underbrace{\Pi^{*\tau}_{\eta}(\bar{\boldsymbol{u}},\check{\boldsymbol{u}},\mathfrak{f})}_{potential} := \underbrace{E^{\tau}(\bar{\boldsymbol{u}},\check{\boldsymbol{u}})}_{energy} + \underbrace{D^{*\tau}_{\eta}(\bar{\boldsymbol{u}},\check{\boldsymbol{u}},\mathfrak{f})}_{dissipation} - \underbrace{W^{\tau}(\bar{\boldsymbol{u}},\check{\boldsymbol{u}})}_{work} \,. \tag{3.208}$$

It consists of the incremental energy storage (3.193), the incremental dissipation (3.196), and the incremental external work (3.198). A compact notation of the incremental variational principle is founded on the generalized constitutive state and displacements

$$\mathfrak{c}^{*}(\mathfrak{u}^{*}) := \{\, \nabla_s\bar{\boldsymbol{u}}, \check{\boldsymbol{u}}, \nabla\check{\boldsymbol{u}}, \mathfrak{f} \,\} \quad \text{with} \quad \mathfrak{u}^{*} := \{\, \bar{\boldsymbol{u}}, \check{\boldsymbol{u}}, \mathfrak{f} \,\} \tag{3.209}$$

that in addition to (3.200) contain the dissipative thermodynamic forces $\mathfrak{f}$. Thus, the incremental potential (3.208) can be reformulated in the compact format

$$\Pi^{*\tau}_{\eta}(\mathfrak{u}^{*}) = \int_{\mathcal{B}} \{\, \pi^{*\tau}_{\eta}(\mathfrak{c}^{*};\mathfrak{c}^{*}_{n}) - \mathfrak{g}\cdot(\mathfrak{u}-\mathfrak{u}_{n}) \,\}\, dV - \int_{\partial\mathcal{B}_{\mathfrak{t}}} \mathfrak{t}_{N}\cdot(\mathfrak{u}-\mathfrak{u}_{n})\, dA \,, \tag{3.210}$$

where the definitions of the generalized volume and surface forces (3.201) and (3.202) have been employed. The local quantity

$$\pi^{*\tau}_{\eta}(\mathfrak{c}^{*};\mathfrak{c}^{*}_{n}) = \psi(\mathfrak{c}) - \psi(\mathfrak{c}_{n}) + \mathfrak{f}\cdot(\mathfrak{c}-\mathfrak{c}_{n}) - \frac{\tau}{2\eta}\,\langle\varphi(\mathfrak{f};\mathfrak{c}_{n})\rangle^{2}_{+} \tag{3.211}$$

is denoted the *extended incremental internal work density* and is determined by the constitutive free energy function ψ and the yield function φ. In this sense, the finite step sized incremental stationary principle reads

$$\boxed{\{\, \bar{\boldsymbol{u}}, \check{\boldsymbol{u}}, \mathfrak{f} \,\} = \arg\{\, \inf_{\bar{\boldsymbol{u}}}\, \inf_{\check{\boldsymbol{u}}}\, \sup_{\mathfrak{f}}\, \Pi^{*\tau}_{\eta}(\bar{\boldsymbol{u}},\check{\boldsymbol{u}},\mathfrak{f}) \,\}} \tag{3.212}$$

and determines the current macro- and microscopic displacements $\bar{\boldsymbol{u}}$ and $\check{\boldsymbol{u}}$ and the dissipative thermodynamic driving force $\mathfrak{f}$ as the *saddle point* of the incremental functional (3.210). Its variation characterizes the *smooth* necessary condition

$$0 = \delta\Pi^{*\tau}_{\eta} = \delta_{\bar{\boldsymbol{u}}}\Pi^{*\tau}_{\eta} + \delta_{\check{\boldsymbol{u}}}\Pi^{*\tau}_{\eta} + \delta_{\mathfrak{f}}\Pi^{*\tau}_{\eta} \,, \tag{3.213}$$

where the single variations are summarized by the explicit expressions

$$\begin{aligned}
\delta_{\bar{\boldsymbol{u}}}\Pi^{*\tau}_{\eta} :=& \int_{\mathcal{B}} \{\, [\partial_{\nabla_s\bar{\boldsymbol{u}}}\psi + \bar{\boldsymbol{\mathcal{F}}}] : \nabla_s\delta\bar{\boldsymbol{u}} - \bar{\gamma}\cdot\delta\bar{\boldsymbol{u}} \,\}\, dV \\
&- \int_{\partial\mathcal{B}_{\bar{\boldsymbol{t}}}} \bar{\boldsymbol{t}}_{N}\cdot\delta\bar{\boldsymbol{u}}\, dA \\
\delta_{\check{\boldsymbol{u}}}\Pi^{*\tau}_{\eta} :=& \int_{\mathcal{B}} \{\, [\partial_{\nabla\check{\boldsymbol{u}}}\psi + \check{\boldsymbol{\mathcal{F}}}] : \nabla\delta\check{\boldsymbol{u}} + [\partial_{\check{\boldsymbol{u}}}\psi + \check{\boldsymbol{f}} - \check{\gamma}]\cdot\delta\check{\boldsymbol{u}} \,\}\, dV \\
&- \int_{\partial\mathcal{B}_{\check{\boldsymbol{t}}}} \check{\boldsymbol{t}}_{N}\cdot\delta\check{\boldsymbol{u}}\, dA \\
\delta_{\mathfrak{f}}\Pi^{*\tau}_{\eta} :=& \int_{\mathcal{B}} \{\, [\mathfrak{c} - \mathfrak{c}_{n} - \frac{\tau}{\eta}\,\langle\varphi\rangle_{+}\partial_{\mathfrak{f}}\varphi]\cdot\delta\mathfrak{f} \,\}\, dV
\end{aligned} \tag{3.214}$$

in terms of the admissible variations $\delta\bar{\boldsymbol{u}} \in \mathcal{W}^{0}_{\bar{\boldsymbol{u}}}$, $\delta\check{\boldsymbol{u}} \in \mathcal{W}^{0}_{\check{\boldsymbol{u}}}$, and $\delta\mathfrak{f}$ of the current macro- and microscopic displacements, and the dissipative forces. The Euler equations of the stationary principle (3.212) follow by application of Gauss' and localization theorem and exhibit a structure conceptually similar to the large strain setting, see Table 3.4. Such a formulation is particularly convenient due to its smooth, viscous character.

3.9.4. FE-Discretization of Incremental Variational Formulation. The first step towards a finite element treatment of the coupled set of equations consists of a discretization of the continuous solution domain $\mathcal{B}$ into a discrete domain $\mathcal{B}^h$. The discrete domain

$$\mathcal{B}^h = \mathop{\mathsf{A}}_{e=1}^{n_{en}} \mathcal{B}^e \tag{3.215}$$

consists of the entity of all element sub domains $\mathcal{B}^e$. The symbol $\mathsf{A}_{e=1}^{n_{en}}$ is introduced for the assembly operation of all elements $e = 1, \ldots, n_{en}$. Within the concept of isoparametric finite elements, the geometry is approximated on element level $\mathcal{B}^e$ by the relation

$$\boldsymbol{x}^{he} = \sum_{i=1}^{n_{el}} N_i \, \boldsymbol{x}_i^e \tag{3.216}$$

expressed in terms of the shape functions $N_i(\boldsymbol{\xi})$ as a function of the local isoparametric coordinates $\boldsymbol{\xi}$, the given nodal coordinates $\boldsymbol{x}_i^e$ of the element e under focus, and the number of nodes per element n_{el}.

3.9.4.1. Canonical Incremental Minimization Principle. In the canonical representation, the discretization of the generalized deformation $(3.200)_2$ contains the macro- and microscopic deformation only. They are approximated via

$$\mathfrak{u}^h = \mathop{\mathsf{A}}_{e=1}^{n_{en}} \left[\sum_{i=1}^{n_{el}} \begin{bmatrix} [\bar{\boldsymbol{N}}]_i^e & \boldsymbol{0} \\ \boldsymbol{0} & [\check{\boldsymbol{N}}]_i^e \end{bmatrix} \begin{bmatrix} \bar{\boldsymbol{d}} \\ \check{\boldsymbol{d}} \end{bmatrix}_i^e \right] = \mathop{\mathsf{A}}_{e=1}^{n_{en}} \begin{bmatrix} [\bar{\boldsymbol{N}}]^e & \boldsymbol{0} \\ \boldsymbol{0} & [\check{\boldsymbol{N}}]^e \end{bmatrix} \begin{bmatrix} \bar{\boldsymbol{d}} \\ \check{\boldsymbol{d}} \end{bmatrix}^e =: \mathfrak{N}(\boldsymbol{x}) \, \mathfrak{d} \tag{3.217}$$

in terms of the macro- and microscopic approximation matrices $[\bar{\boldsymbol{N}}]_i^e$ and $[\check{\boldsymbol{N}}]_i^e$ in combination with the nodal macro- and microscopic displacements $\bar{\boldsymbol{d}}_i^e$ and $\check{\boldsymbol{d}}_i^e$. In view of a compact notation, the approximation matrices are summarized by the generalized matrix $\mathfrak{N}$ that already includes the assembly procedure. At node i of the finite element mesh, the generalized nodal displacements are

$$\mathfrak{d}_i = [\, \bar{\boldsymbol{d}}, \check{\boldsymbol{d}} \,]_i^T \, . \tag{3.218}$$

Based on the discrete primary fields (3.217), the discrete constitutive state is evaluated

$$\mathfrak{c}^h(\mathfrak{d}) = \mathop{\mathsf{A}}_{e=1}^{n_{en}} \left[\sum_{i=1}^{n_{el}} \begin{bmatrix} [\bar{\boldsymbol{B}}]_i^e \bar{\boldsymbol{d}}_i^e \\ [\check{\boldsymbol{B}}]_i^e \check{\boldsymbol{d}}_i^e \end{bmatrix} \right] = \mathop{\mathsf{A}}_{e=1}^{n_{en}} \begin{bmatrix} [\bar{\boldsymbol{B}}]^e \bar{\boldsymbol{d}}^e \\ [\check{\boldsymbol{B}}]^e \check{\boldsymbol{d}}^e \end{bmatrix} \tag{3.219}$$

as a function of the generalized nodal displacements and the macro- and microscopic matrices $[\bar{\boldsymbol{B}}]_i^e$ and $[\check{\boldsymbol{B}}]_i^e$ for the approximation of the constitutive state. All element matrices mentioned so far depend on the geometric and microstructural dimension, they are specified in the corresponding chapters. With the discrete primary variables (3.219) and the discrete constitutive state (3.217), the incremental potential (3.203) is discretized

$$\Pi^h(\mathfrak{d}) = \int_{\mathcal{B}^h} \{ \, \pi^h(\mathfrak{c}^h(\mathfrak{d}); \mathfrak{c}^h(\mathfrak{d}_n)) - \mathfrak{g} \cdot \mathfrak{N}(\mathfrak{d} - \mathfrak{d}_n) \, \} \, dV - \int_{\partial \mathcal{B}_{\mathfrak{t}}^h} \mathfrak{t}_N \cdot \mathfrak{N}(\mathfrak{d} - \mathfrak{d}_n) \, dA \, . \tag{3.220}$$

As a consequence, the discrete incremental *minimization principle*

$$\boxed{\{ \, \mathfrak{d} \, \} = \arg\{ \inf_{\mathfrak{d}} \Pi^h(\mathfrak{d}) \, \}} \tag{3.221}$$

is introduced that determines the generalized nodal displacements $\boldsymbol{\mathfrak{d}}$ of the discrete problem at time t_{n+1}. Based on the variation of the discrete constitutive state vector (3.219) with respect to the generalized nodal displacements

$$\delta_{\boldsymbol{\mathfrak{d}}} \boldsymbol{\mathfrak{c}}^h = \mathop{\mathsf{A}}_{e=1}^{n_{en}} \left[\sum_{i=1}^{n_{el}} \begin{bmatrix} [\bar{\boldsymbol{B}}]_i^e & \boldsymbol{0} \\ \boldsymbol{0} & [\check{\boldsymbol{B}}]_i^e \end{bmatrix} \begin{bmatrix} \delta \bar{\boldsymbol{d}} \\ \delta \check{\boldsymbol{d}} \end{bmatrix}_i^e \right] =: \boldsymbol{\mathfrak{B}}(\boldsymbol{x})\, \delta \boldsymbol{\mathfrak{d}} \,, \tag{3.222}$$

the discrete necessary condition to the minimum principle (3.221) can be specified

$$\boldsymbol{0} \in \Pi^h_{,\boldsymbol{\mathfrak{d}}} = \int_{\mathcal{B}^h} \{ \boldsymbol{\mathfrak{B}}^T [\boldsymbol{S}] - \boldsymbol{\mathfrak{N}}^T \boldsymbol{\mathfrak{g}} \} \, dV - \int_{\partial \mathcal{B}^h_{\boldsymbol{\mathfrak{t}}}} \boldsymbol{\mathfrak{N}}^T \boldsymbol{\mathfrak{t}}_N \, dA \quad \text{with} \quad \boldsymbol{S} := \partial_{\boldsymbol{\mathfrak{c}}^h} \pi^h \tag{3.223}$$

expressed in terms of the *generalized stresses* $\boldsymbol{S}$. This system of nonlinear equations is solved iteratively in a Newton solution scheme that bases on the algorithm

$$\boldsymbol{\mathfrak{d}} \Leftarrow \boldsymbol{\mathfrak{d}} - [\Pi^h_{,\boldsymbol{\mathfrak{d}}\boldsymbol{\mathfrak{d}}}]^{-1} \cdot \Pi^h_{,\boldsymbol{\mathfrak{d}}} \quad \text{until} \quad \| \Pi^h_{,\boldsymbol{\mathfrak{d}}} \| \leq \text{tol} \,. \tag{3.224}$$

This algorithm contains the *symmetric* monolithic tangent matrix

$$\Pi^h_{,\boldsymbol{\mathfrak{d}}\boldsymbol{\mathfrak{d}}} = \int_{\mathcal{B}^h} \{ \boldsymbol{\mathfrak{B}}^T [\mathbb{C}] \boldsymbol{\mathfrak{B}} \} \, dV \quad \text{with} \quad \mathbb{C} := \partial^2_{\boldsymbol{\mathfrak{c}}^h \boldsymbol{\mathfrak{c}}^h} \pi^h \,, \tag{3.225}$$

where the *generalized moduli* $\mathbb{C}$ have been introduced.

3.9.4.2. Extended Incremental Variational Principle. In addition to the generalized constitutive state (3.219), the extended incremental variational principle involves the thermodynamic forces as global variables. In a compact notation, the generalized deformation vector $(3.209)_2$ is approximated via

$$\boldsymbol{\mathfrak{u}}^{*h} = \mathop{\mathsf{A}}_{e=1}^{n_{en}} \left[\sum_{i=1}^{n_{el}} \begin{bmatrix} [\boldsymbol{\mathfrak{N}}]_i^e & \boldsymbol{0} \\ \boldsymbol{0} & [\boldsymbol{A}]_i^e \end{bmatrix} \begin{bmatrix} \boldsymbol{\mathfrak{d}} \\ \boldsymbol{f} \end{bmatrix}_i^e \right] = \mathop{\mathsf{A}}_{e=1}^{n_{en}} \begin{bmatrix} [\boldsymbol{\mathfrak{N}}]^e & \boldsymbol{0} \\ \boldsymbol{0} & [\boldsymbol{A}]^e \end{bmatrix} \begin{bmatrix} \boldsymbol{\mathfrak{d}} \\ \boldsymbol{f} \end{bmatrix}^e =: \boldsymbol{\mathfrak{N}}^*(\boldsymbol{x})\, \boldsymbol{\mathfrak{d}}^* \,. \tag{3.226}$$

In addition to the approximation matrix of the canonical setting $[\boldsymbol{\mathfrak{N}}]_i^e$ in combination with the generalized displacements $\boldsymbol{\mathfrak{d}}_i^e$, a further matrix $[\boldsymbol{A}]_i^e$ is introduced to approximate the dissipative thermodynamic forces. Regarding a compact notation, the global matrix $\boldsymbol{\mathfrak{N}}^*$ is introduced that contains all these matrices in an assembled format. At node i of the mesh, the extended nodal unknowns are

$$\boldsymbol{\mathfrak{d}}_i^* = [\, \boldsymbol{\mathfrak{d}}, \boldsymbol{f} \,]_i^T = [\, \bar{\boldsymbol{d}}, \check{\boldsymbol{d}}, \boldsymbol{f} \,]_i^T \,. \tag{3.227}$$

Based on the discrete primary fields (3.226), the constitutive state is approximated via

$$\boldsymbol{\mathfrak{c}}^{*h}(\boldsymbol{\mathfrak{d}}^*) = \mathop{\mathsf{A}}_{e=1}^{n_{en}} \left[\sum_{i=1}^{n_{el}} \begin{bmatrix} [\bar{\boldsymbol{B}}]_i^e \, \bar{\boldsymbol{d}}_i^e \\ [\check{\boldsymbol{B}}]_i^e \, \check{\boldsymbol{d}}_i^e \\ [\boldsymbol{A}]_i^e \, \boldsymbol{f}_i^e \end{bmatrix} \right] = \mathop{\mathsf{A}}_{e=1}^{n_{en}} \begin{bmatrix} [\bar{\boldsymbol{B}}]^e \, \bar{\boldsymbol{d}}^e \\ [\check{\boldsymbol{B}}]^e \, \check{\boldsymbol{d}}^e \\ [\boldsymbol{A}]^e \, \boldsymbol{f}^e \end{bmatrix} \tag{3.228}$$

as a function of the extended nodal displacements (3.227) and in terms of the matrices $[\bar{\boldsymbol{B}}]_i^e$ and $[\check{\boldsymbol{B}}]_i^e$ for the approximation of the macro- and microscopic state and the matrix $[\boldsymbol{A}]_i^e$ to approximate the thermodynamic forces. All element matrices depend on the geometric dimension and the nature of the material's microstructure, they are introduced in the respective chapters. Based on the discretization (3.226) and (3.228), the extended potential (3.210) can be expressed in its discrete counterpart

$$\Pi^{*h}_{\eta}(\boldsymbol{\mathfrak{d}}^*) = \int_{\mathcal{B}^h} \{\, \pi^{*h}_{\eta}(\boldsymbol{\mathfrak{c}}^{*h}(\boldsymbol{\mathfrak{d}}^*); \boldsymbol{\mathfrak{c}}^{*h}(\boldsymbol{\mathfrak{d}}^*_n)) - \boldsymbol{\mathfrak{g}} \cdot \boldsymbol{\mathfrak{N}}(\boldsymbol{\mathfrak{d}} - \boldsymbol{\mathfrak{d}}_n) \,\}\, dV - \int_{\partial\mathcal{B}^h_{\mathfrak{t}}} \boldsymbol{\mathfrak{t}}_N \cdot \boldsymbol{\mathfrak{N}}(\boldsymbol{\mathfrak{d}} - \boldsymbol{\mathfrak{d}}_n)\, dA \quad (3.229)$$

allowing for the introduction of the discrete incremental *stationary principle*

$$\boxed{\{\, \boldsymbol{\mathfrak{d}}^* \,\} = \arg\{ \operatorname*{stat}_{\boldsymbol{\mathfrak{d}}^*} \Pi^{*h}_{\eta}(\boldsymbol{\mathfrak{d}}^*) \,\}\,.} \quad (3.230)$$

It determines the generalized nodal displacements $\boldsymbol{\mathfrak{d}}$ and the nodal thermodynamic forces $\boldsymbol{f}$ of the discrete problem at time t_{n+1}. Based on the variation of the discrete constitutive state vector (3.228) with respect to the extended generalized nodal displacements

$$\delta_{\boldsymbol{\mathfrak{d}}^*} \boldsymbol{\mathfrak{c}}^{*h} = \mathop{\mathsf{A}}_{e=1}^{n_{en}} \left[\sum_{i=1}^{n_{el}} \begin{bmatrix} [\bar{\boldsymbol{B}}]^e_i & \boldsymbol{0} & \boldsymbol{0} \\ \boldsymbol{0} & [\check{\boldsymbol{B}}]^e_i & \boldsymbol{0} \\ \boldsymbol{0} & \boldsymbol{0} & [\boldsymbol{A}]^e_i \end{bmatrix} \begin{bmatrix} \delta\bar{\boldsymbol{d}} \\ \delta\check{\boldsymbol{d}} \\ \delta\boldsymbol{f} \end{bmatrix}_i \right]^e =: \boldsymbol{\mathfrak{B}}^*(\boldsymbol{x})\, \delta\boldsymbol{\mathfrak{d}}^*\,, \quad (3.231)$$

the discrete necessary condition to the stationary principle (3.230) can be specified

$$\boldsymbol{0} = \Pi^{*h}_{\eta,\boldsymbol{\mathfrak{d}}^*} = \int_{\mathcal{B}^h} \{\, \boldsymbol{\mathfrak{B}}^{*T}[\boldsymbol{S}^*] - \boldsymbol{\mathfrak{N}}^T \boldsymbol{\mathfrak{g}} \,\}\, dV - \int_{\partial\mathcal{B}^h_{\mathfrak{t}}} \boldsymbol{\mathfrak{N}}^T \boldsymbol{\mathfrak{t}}_N \, dA \quad \text{with} \quad \boldsymbol{S}^* := \partial_{\boldsymbol{\mathfrak{c}}^{*h}} \pi^{*h}_{\eta}\,, \quad (3.232)$$

expressed in terms of the *extended generalized stresses* $\boldsymbol{S}^*$. This system of nonlinear equations is solved iteratively in a Newton solution scheme based on the algorithm

$$\boldsymbol{\mathfrak{d}}^* \Leftarrow \boldsymbol{\mathfrak{d}}^* - [\Pi^{*h}_{\eta,\boldsymbol{\mathfrak{d}}^*\boldsymbol{\mathfrak{d}}^*}]^{-1} \cdot \Pi^{*h}_{\eta,\boldsymbol{\mathfrak{d}}^*} \quad \text{until} \quad \|\Pi^{*h}_{\eta,\boldsymbol{\mathfrak{d}}^*}\| \le \text{tol}\,. \quad (3.233)$$

This algorithm contains the *symmetric* monolithic tangent matrix

$$\Pi^{*h}_{\eta,\boldsymbol{\mathfrak{d}}^*\boldsymbol{\mathfrak{d}}^*} = \int_{\mathcal{B}^h} \{\, \boldsymbol{\mathfrak{B}}^{*T}[\mathbb{C}^*]\boldsymbol{\mathfrak{B}}^* \,\}\, dV \quad \text{with} \quad \mathbb{C}^* := \partial^2_{\boldsymbol{\mathfrak{c}}^{*h}\boldsymbol{\mathfrak{c}}^{*h}} \pi^{*h}_{\eta}\,, \quad (3.234)$$

where the *extended generalized moduli* $\mathbb{C}^*$ have been introduced.

4. Variational-Based Formulation of Gradient-Type Damage

The overall goal of this chapter is the application of the previously introduced generalized continuum mechanical framework for gradient-type standard dissipative solids to a model problem of *gradient-type damage mechanics*. The books by Kachanov [90], Lemaitre & Chaboche [99], Lemaitre [98], and Lemaitre & Desmorat [100] provide an overview over the broad topic of damage mechanics. Among other strain softening materials, damage mechanics exhibits the phenomenon of localization. A good introduction to that subject can be found in the works by Forest & Lorentz [46] and de Borst [33], where the effect of material instability and the effect of mesh sensitivity are explained. Damage models that overcome this severe drawback are based on a damage-gradient extension of the constitutive functions, see e.g. Peerlings [146] and Peerling, Geers, de Borst & Brekelmans [147] and the references therein. The model introduced in the sequel shows resemblances to the model on gradient-type damage mechanics as discussed by Frémond & Nedjar [52]. In this work, the power of internal forces is modified to take into account additional terms related to the rate of damage and its gradient. As a consequence, an additional balance equation is obtained that describes the global evolution of the damage field. Thus, it seems to be obvious to fit such types of damage formulations into the variational-based framework for gradient-type standard dissipative solids.

This chapter is structured as follows. In a first step, the phenomena of material instabilities and mesh sensitivity in strain softening materials are reiterated. Then, the fundamentals of classical continuum damage mechanics are briefly reviewed. The basic kinematics are discussed and an isotropic degradation of the stored bulk energy and a rate-independent formulation of the dissipation function are introduced. Alternative smooth representations of the rate-independent/non-smooth dissipation function are discussed yielding a *penalty-type model I* and a *viscous over-force model II*. For these constitutive functions, the application of the incremental variational framework delivers the algorithmic representation of the governing balance equations and provides the basis for a unified numerical implementation. The local characteristics of both models are investigated and for model II representative numerical examples are discussed that demonstrate the performance of the gradient-type framework with regard to the regularization of shear bands.

4.1. Material Instabilities and Mesh Sensitivity

Failure of engineering structures through material instabilities can be related to the phenomenon of localization which describes the concentration of high inelastic deformations in inhomogeneous small deformation patterns. This effect shows up in a large variety of materials, the book by Nádai [138] provides some general information for that issue. A detailed discussion of failure and post-failure analyses of inelastic geomaterials can be found in the books by Vardoulakis & Sulem [173] and Jumikis [88] among others. In this class of materials, non-reversible deformation processes occur during the loading history. Inelastic deformations in geomaterials have an inherently non-uniform character. Whenever a deformation occurs, due to relative motions between grains or due to micro-cracking, the deformation at a lower scale is discontinuous. Considering size scales capturing groups of grains or cracks, the plastic deformation often appears uniform in specimens which are themselves subjected to macroscopically uniform loading conditions. But even on this larger macroscopic scale, a critical configuration of the body may ex-

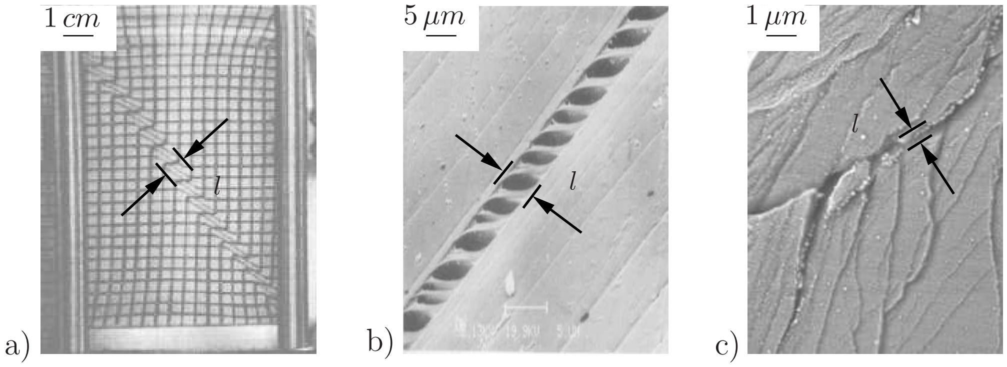

Figure 4.1: Localization phenomena in solids. a) Shear band formation in sand, taken from Alshibli, Batiste & Sture [1], b) detailed microscopy of shear band craze in polymers produced by tensile deformation, taken from Li [103], and c) electron micrograph showing shear bands in metallic glasses, taken from Lewandowski & Greer [101].

ist where the homogeneous deformation breaks down into bands of localized shearing. In the case of granular solids, shear localization induces intense inter granular slip leading to a strong dilatation of the material inside the localized zone. Experimental studies exhibiting the phenomenon of shear band formation are illustrated in Figure 4.1a) for the analysis of sand, taken from Alshibli, Batiste & Sture [1], in Figure 4.1b) for crazing effects in polymers, see Li [103], and in Figure 4.1c) for investigations on metallic glasses, taken from Lewandowski & Greer [101]. Mathematically speaking, localization is the result of strain concentrations in a critical zone as the result of a bifurcation of the local constitutive behavior of the material. The orientation of the localization zone thereby does not depend on the boundary conditions, it is an *intrinsic characteristic* of the material. Regarding numerical implementations of standard local material models, severe difficulties may arise with respect to mesh sensitivity. Localization then develops in a zone depending on the size of the triangulation. A mesh refinement results in a smaller width of the localization band, the associated energy dissipation decreases to physically unrealistic values. The necessary and sufficient condition for a unique solution has intensively been discussed by Hill [79, 80], and states the positive definiteness of the second order work. Thus, material instability occurs whenever the tangent tensor in the constitutive rate equation obtains a zero eigenvalue. In general, this effect shows up in the analysis of strain softening behavior of inelastic material response and can be identified by a negative slope in the resulting structural load-deflection curves. The loss of positive definiteness is equivalent to the loss of ellipticity of the governing partial differential equation. As a result, the post critical material response for strain-softening materials is not well posed, numerical results become meaningless. For a detailed discussion see e.g. Belytschko, Fish & Engelmann [12] and de Borst [32], among others. The implementation of classical damage mechanics as a standard continuum model exhibits the severe problem of mesh sensitivity in the post critical regime of the deformation process. The reason for this mesh sensitivity can directly be related to a local change in the character of the governing partial differential equations. The initial boundary value problem loses its well-posedness resulting in an infinite number of possible solutions. This means that an increase of the number of elements used in a simulation also increases the number of possible solutions. In a first step, the mechanical and mathematical reasons for this phenomenon are elucidated. Then, in a subsequent step a one-dimensional gradient-type technique is discussed to overcome this problem. This section closes with the explanation of mesh sensitivity for a simple material model with linear softening behavior.

4.1.1. Stability and Ellipticity. This section provides the reader a short summary of bifurcation and stability analysis and is by no means complete. For further investigations on this subject, the reader is referred to HILL [79, 80] and NEILSEN & SCHREYER [140]. Regarding small deformations, an important criterion for a limit point on the continuum level bases on the constitutive rate equation

$$\dot{\boldsymbol{\sigma}} : \dot{\boldsymbol{\varepsilon}} > 0\,. \tag{4.1}$$

This scalar product becomes negative when the slope of the overall load-deflection curve becomes negative. This is the so-called phenomenon of strain-softening and occurs in inelastic constitutive models, e.g. in damage mechanics and plasticity. Note that the overall load-deflection curve is the homogenized response of the specimen undergoing local stress concentrations that cause high inhomogeneous deformations. This information is lost when the global load-deflection curve is looked at only. Focusing on the constitutive rate expression (4.1), the relation between the stress rate $\dot{\boldsymbol{\sigma}}$ and the strain rate $\dot{\boldsymbol{\varepsilon}}$ reads

$$\dot{\boldsymbol{\sigma}} = \mathbb{D} : \dot{\boldsymbol{\varepsilon}}\,, \tag{4.2}$$

with the continuous material tangential stiffness $\mathbb{D}$. Thus, equation (4.1) is reformulated

$$\dot{\boldsymbol{\varepsilon}} : \mathbb{D} : \dot{\boldsymbol{\varepsilon}} > 0 \tag{4.3}$$

and allows to determine a limit point of material instability. Such a point is characterized by the loss of positive definiteness of the material tangential stiffness tensor

$$\det[\mathbb{D}] = 0\,. \tag{4.4}$$

Following HILL [79], structural instability occurs when the entire structure $\mathcal{B}$ violates the constitutive rate equation (4.1) in an integral format

$$\int_{\mathcal{B}} \dot{\boldsymbol{\sigma}} : \dot{\boldsymbol{\varepsilon}}\, dV > 0 \tag{4.5}$$

for kinematically admissible rates $\dot{\boldsymbol{\varepsilon}}$. This argument is violated if a local instability (4.1) occurs, finally yielding a structural instability. The facts considered so far do not explain the phenomenon of mesh sensitivity. The reason for this observation can be found in the loss of positive definiteness of the material tangent tensor $\mathbb{D}$ which causes the character of the governing equations to change, they lose their elliptic character. Mathematically speaking, ellipticity stands for the fact that discontinuous solutions are not possible. In order to obtain a criterion for localized bifurcation, a short review on the theory of *singular surfaces* with jumps in the rate expression is given. For further reading on this subject, see e.g. THOMAS [170] and HILL [80]. As depicted in Figure 4.2, a continuum $\mathcal{B}$ contains a surface $\Gamma \subset \mathcal{B}$ characterized by a normal $\boldsymbol{n}$ at the position $\boldsymbol{x} \in \Gamma$. The surface describes the place of possible localized bifurcations, where the deformation becomes discontinuous. In the context of *displacement-compatible singular surfaces*, the displacement field $\boldsymbol{u}$ is considered to be continuous across the singular surface

$$[\![\boldsymbol{u}]\!] = \boldsymbol{u}^{+} - \boldsymbol{u}^{-} = \boldsymbol{0} \quad \text{at} \quad \boldsymbol{x} \in \Gamma\,, \tag{4.6}$$

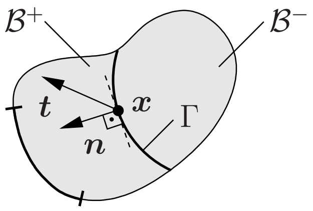

Figure 4.2: Singular surface Γ with normal $\boldsymbol{n} = \boldsymbol{n}^+ = \boldsymbol{n}^-$ at position $\boldsymbol{x} \in \Gamma$ in a homogeneous body $\mathcal{B} = \mathcal{B}^+ \cup \mathcal{B}^-$ and traction vector $\boldsymbol{t} = \boldsymbol{t}^+ = \boldsymbol{t}^-$ at the discontinuity Γ.

whereas the evolving localization is characterized by a jump in the velocity field $\dot{\boldsymbol{u}}$ and in the gradient of the velocity field $\nabla \dot{\boldsymbol{u}}$

$$[\![\dot{\boldsymbol{u}}]\!] = \dot{\boldsymbol{u}}^+ - \dot{\boldsymbol{u}}^- \neq \boldsymbol{0} \quad \text{and} \quad [\![\nabla \dot{\boldsymbol{u}}]\!] = \nabla \dot{\boldsymbol{u}}^+ - \nabla \dot{\boldsymbol{u}}^- \neq \boldsymbol{0} \quad \text{at} \quad \boldsymbol{x} \in \Gamma \, . \tag{4.7}$$

A particular compatibility condition for the strain rate can be introduced

$$[\![\nabla_s \dot{\boldsymbol{u}}]\!] = \frac{\gamma}{2}[\boldsymbol{m} \otimes \boldsymbol{n} + \boldsymbol{n} \otimes \boldsymbol{m}] \, , \tag{4.8}$$

where $\boldsymbol{m}$ defines the shape of the discontinuity. For $\boldsymbol{m} \cdot \boldsymbol{n} = 0$ the localization pattern corresponds to the simple shear mode, for $\boldsymbol{m} \cdot \boldsymbol{n} = 1$ localization occurs as a pure extension perpendicular to the discontinuity surface. Now, assume that localization has just begun to evolve. The stresses and strains are continuously distributed over the body, whereas their rates are discontinuously distributed, separated by the discontinuity surface Γ whose normal direction $\boldsymbol{n}$ has to be determined. Singularity points are identified by the postulate of continuity of the traction vector $\boldsymbol{t}$ across the discontinuity surface Γ, i.e.

$$[\![\boldsymbol{t}]\!] = \boldsymbol{t}^+ - \boldsymbol{t}^- = \boldsymbol{n} \cdot [\![\boldsymbol{\sigma}]\!] = \boldsymbol{0} \quad \text{at} \quad \boldsymbol{x} \in \Gamma \, . \tag{4.9}$$

A combination of the rate equation (4.2) and the compatibility condition (4.8) gives

$$[\![\dot{\boldsymbol{t}}]\!] = \boldsymbol{n} \cdot [\![\dot{\boldsymbol{\sigma}}]\!] = \gamma[\boldsymbol{n} \cdot \mathbb{D} \cdot \boldsymbol{n}] \cdot \boldsymbol{m} =: \gamma \boldsymbol{A} \cdot \boldsymbol{m} = \boldsymbol{0} \quad \text{at} \quad \boldsymbol{x} \in \Gamma \, , \tag{4.10}$$

where the minor symmetry of the tangential stiffness tensor $\mathbb{D}$ has been exploited. Furthermore, the second order tensor $\boldsymbol{A} = \boldsymbol{n} \cdot \mathbb{D} \cdot \boldsymbol{n}$ is introduced, often denoted as *acoustic tensor* or *localization tensor*. This tensor is a function of the orientation $\boldsymbol{n}$ of the singular surface Γ at position $\boldsymbol{x}$ with given tangential moduli $\mathbb{D}$. A nontrivial solution of (4.10) only exists when the determinant of the localization tensor changes its sign, i.e. for

$$\det[\boldsymbol{A}] = 0 \tag{4.11}$$

and identifies the first point in the deformation history where localization starts. If equation (4.11) is met, discontinuous solutions can emerge and a loss of ellipticity of the governing differential equations occurs. Note that ellipticity is a necessary condition for the well-posedness of the boundary value problem. The loss of ellipticity yields an infinite number of possible solutions, in particular those with discontinuities. When numerical solution procedures are applied to solve such systems, they tend to capture the discontinuity as accurately as possible and resolve the localization zone with the smallest volume that is available, of course limited by the local element size. To resolve the evolving discontinuity surface in an adequate manner, special approximation techniques have been discussed in literature, see e.g. MIEHE & SCHRÖDER [128].

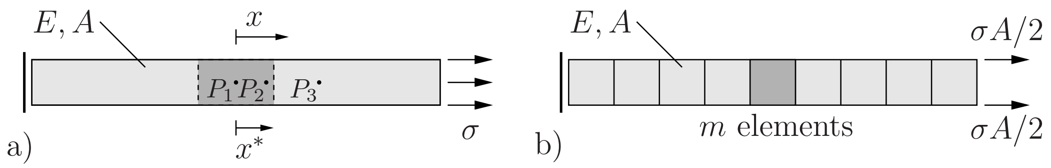

Figure 4.3: Localization and mesh sensitivity in one-dimensional bar. a) Continuous setting with localization starting at the weakest point P_1 and b) discretization with m elements.

4.1.2. Localization and Mesh Sensitivity in One Dimension. To clarify the effect of strain softening and localization, consider a bar with uniform cross-sectional area A subjected to an uni-axial tensile stress σ, see Figure 4.3. The specimen is fixed at the left side and the stress σ is applied at the opposite side of the bar. Suppose that the specimen deforms homogeneously up to a critical maximum tensile strength y_0 where the weakest point P_1 in the specimen starts to fail. A subsequent failure does not occur throughout the entire length of the bar, instead a local failure process zone develops uniformly across the specimen parametrized by the coordinate x^*. The constitutive response of the specimen is assumed to behave linear elastically first, followed by a simple linear softening law. The kinematic is additively decomposed into an elastic stress producing term ε^e and an inelastic term ε^p

$$\varepsilon = \varepsilon^e + \varepsilon^p \,. \tag{4.12}$$

Focusing on monotonic loading processes, the kinematic relation in the elastic regime of the deformation takes the form

$$\varepsilon^e = \varepsilon \quad \text{and} \quad \varepsilon^p = 0 \quad \text{for} \quad 0 \leq \varepsilon < \varepsilon_0 \,. \tag{4.13}$$

In the softening regime the elastic strain is scaled by a softening parameter $h \in \mathcal{R}_+$ via

$$\varepsilon^e = -h\varepsilon \quad \text{and} \quad \varepsilon^p = (1+h)\,\varepsilon \quad \text{for} \quad \varepsilon_0 \leq \varepsilon < \varepsilon_u \,. \tag{4.14}$$

Thus, the *local constitutive behavior* can be summarized by the relation

$$\sigma = \left\{ \begin{array}{ll} E\varepsilon & \text{if } 0 \leq \varepsilon < \varepsilon_0 \\ y_0 - hE(\varepsilon - \varepsilon_0) & \text{if } \varepsilon_0 \leq \varepsilon < \varepsilon_u \\ 0 & \text{if } \varepsilon \geq \varepsilon_u \,, \end{array} \right. \tag{4.15}$$

in terms of Young's modulus E, the ultimate tensile strength y_0 with its corresponding critical yield strain ε_0, and the ultimate stain ε_u prior complete loss of integrity. A visualization of the constitutive response is illustrated in Figure 4.4a). An alternative possibility to describe the constitutive response bases on the introduction of a yield function

$$\varphi = \left\{ \begin{array}{ll} y_0(1 - \varepsilon^p/\varepsilon^p_u) & \text{if } 0 \leq \varepsilon^p < \varepsilon^p_u \\ 0 & \text{if } \varepsilon^p \geq \varepsilon^p_u \,, \end{array} \right. \tag{4.16}$$

expressed in terms of the ultimate plastic strain

$$\varepsilon^p_u = \frac{1+h}{h}\frac{y_0}{E} =: n\,\frac{y_0}{E} \,, \tag{4.17}$$

for an illustration see Figure 4.4b). The discussion of an analytical solution of this problem can be found in Schreyer [156], where an additional gradient-term is introduced in the

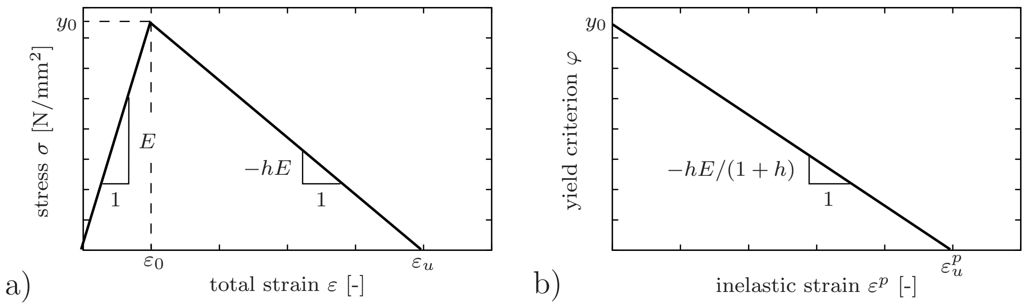

Figure 4.4: Local linear softening. a) Relationship between stress σ and axial strain ε with ultimate tensile strength y_0 and b) alternative description based on a yield criterion.

following way. In the softening equation (4.16), the local plastic strain ε^p is replaced by its *nonlocal counterpart*

$$\varphi = \begin{cases} y_0(1 - \varepsilon^p_{non}/\varepsilon^p_u) & \text{if } 0 \leq \varepsilon^p < \varepsilon^p_u \\ 0 & \text{if } \varepsilon^p \geq \varepsilon^p_u \,, \end{cases} \tag{4.18}$$

containing a first order gradient-type expansion of the local plastic strain.

$$\varepsilon^p_{non} = \varepsilon^p + l^2 \left(\frac{d\varepsilon^p}{dx} \right)^2 , \tag{4.19}$$

where the length scale parameter l enters the formulation. In a monotonic loading process, the material behaves linear elastically up to the peak stress. At this point, localization starts at the weakest position P_1 inside the specimen in combination with a local softening behavior. In the remaining parts of the bar, the material unloads elastically. The softening regime is characterized by $\sigma = \varphi$ which means that the differential equation (4.19) has to be solved for the plastic strain ε^p

$$\varepsilon^p + l^2 \left(\frac{d\varepsilon^p}{dx} \right)^2 = (1 - \sigma/y_0)\, \varepsilon^p_u \,. \tag{4.20}$$

In the one-dimensional setting, this equation corresponds to an ordinary differential equation that can be solved in combination with the appropriate boundary conditions. The trivial *local solution* is characterized by

$$\varepsilon^p = (1 - \sigma/y_0)\, \varepsilon^p_u \tag{4.21}$$

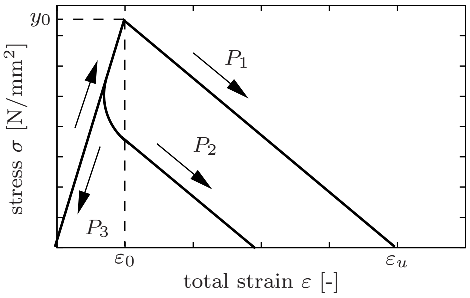

Figure 4.5: Local linear softening at the material point P_i of a one-dimensional bar.

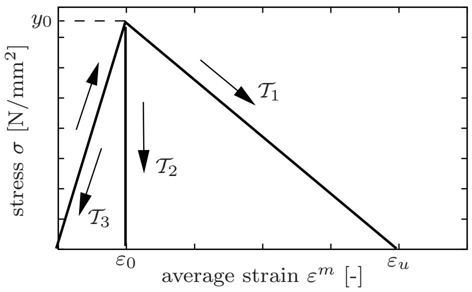

Figure 4.6: Average stress-strain response (4.25) for local analysis of a bar in tension. Load-deflection curves for triangulations $\mathcal{T}_1$ with $m = 1$, $\mathcal{T}_2$ with $m = n$ and $\mathcal{T}_3$ with $m \to \infty$.

and is associated with the homogeneous deformation in the softening regime. The *nonlocal solution* provides an evolving softening zone characterized by

$$\varepsilon^p = (1 - \sigma/y_0)\,\varepsilon_u^p - x^2/4l^2\,. \tag{4.22}$$

For positive plastic strains ε^p, the solution of (4.22) is only valid inside the domain

$$0 \le x \le x^* \quad \text{with} \quad x^* = 2l\sqrt{(1 - \sigma/y_0)\,\varepsilon_u^p}\,. \tag{4.23}$$

For a local theory with $l = 0$, the zone size vanishes $x^* = 0$ for all stress values. In a nonlocal or gradient-type theory, the size of the localization zone at the beginning of softening $\sigma = y_0$ is zero $x^* = 0$, at the end of the softening process $\sigma = 0$, the size of the localization zone reaches its maximum value

$$x_{max}^* = 2l\sqrt{\varepsilon_u^p}\,. \tag{4.24}$$

The key characteristic of a nonlocal approach is that softening is enforced over the domain $0 \le x \le x_{max}^*$ with a finite size, localization in a zone of zero width becomes impossible. As illustrated in Figure 4.5, softening is initiated at P_1 and strain-softening is followed continuously. An adjacent point P_2 inside the domain $0 \le x^* \le x_{max}^*$ initially unloads elastically until the present gradient reduces locally the yield limit as far as the stress point is on the yield surface. Then, strain softening of the stress-strain curve is followed. At a point P_3 outside or on the boundary of the softening zone $0 \le x^* \le x_{max}^*$, the stress goes back to zero, total elastic unloading is present. In a next step, a discretized counterpart of the bar is investigated with the local theory $l = 0$. As depicted in Figure 4.3b), one element in the center of the specimen has a reduced tensile strength causing localization to start inside this particular element. Consider again a monotonic loading process. The stress state in all elements grow homogeneously up to the point where the maximum tensile strength in the weakest element is reached. Localization then starts inside this element, whereas the neighboring elements unload elastically. Beyond the peak load, the average strain state in the bar is given by

$$\varepsilon^m = \frac{\sigma}{E} + \frac{n}{m}\frac{y_0 - \sigma}{E} \quad \text{with} \quad n := \frac{1 + h}{h}\,, \tag{4.25}$$

where m denotes the number of elements employed to discretize the bar. The results are plotted for different ratios n/m in Figure 4.6. Here, one can clearly observe that the computed post-peak curves do not converge to a unique curve. The reason is found in the fact that the governing equations predict the failure mechanism to be a line crack with zero width. The numerical solution scheme tries to resolve this line crack as accurately as possible. This results in a localization within one single element irrespective of the element's width. The impact on the averaged stress-strain curve is obvious. An infinite number of elements $m \to \infty$ forces the stress-strain curve in the post-critical regime to go back on the original loading path. For a more detailed discussion of this subject, the reader is referred to the works by DE BORST [32, 33], DE BORST & MÜHLHAUS [34], BAŽANT & OH [10], BAŽANT & LIN [9], and SCHREYER & CHEN [157].

4.2. Fundamentals of Continuum Damage Mechanics

The scope of this section is to give the reader some necessary information about the micro mechanics of continuum damage mechanics. The phenomenon of damage describes a physical evolution inside the material that causes materials to break. The mechanics of damaging processes bases on the introduction of mechanical variables that describe the deterioration of the material on a continuum level. On the micro-scale level, the accumulation of micro stresses near defects and the breaking of bonds damages the material. At the meso-scale level, this results into the evolution of surface discontinuities, micro-cracks, or volume discontinuities in the form of cavities. On these levels, the damage process can be characterized by damage variables in a continuous manner. This postulates that the medium is discontinuous at the micro- and meso-level, but is considered to be continuous at a larger continuum level. In the pioneering work by KACHANOV [89], a *scalar damage variable* is introduced to capture these mechanisms. Tensorial damage variables are used to describe anisotropic damage processes that are based on the observation that micro-cracking often occurs perpendicular to the largest positive principal stress. For an introductory treatise of these phenomena, the reader is referred to the books by KACHANOV [90], LEMAITRE & CHABOCHE [99], LEMAITRE [98] and LEMAITRE & DESMORAT [100], and the references therein. In an engineering language, the damage variable is an averaged quantity obtained by a homogenization procedure of variables living on the micro- or meso-scale. For this homogenization, the *representative volume element* must be small enough to capture effects that are responsible for the evolution of damage, i.e. the creation of micro-cracks or discontinuities, breaking of atomic bonds, and the plastic enlargement of micro cavities. To this end, consider a damaging material that possesses a representative volume element living at the material position $\boldsymbol{X} \in \mathcal{B}$. On the meso-scale, this representative volume element describes in an averaged sense the effect of failure due to micro defects over its volume. For anisotropic damage processes, the microscopic deformation map (3.4) can be specified to

$$\breve{\varphi}(\boldsymbol{X}, t) : \begin{cases} \mathcal{B} \times \mathcal{T} \to \mathcal{M} \\ (\boldsymbol{X}, t) \mapsto \mathbb{M}(\boldsymbol{X}, t) = \breve{\varphi}(\boldsymbol{X}, t)\,, \end{cases} \tag{4.26}$$

where the abstract microstructural configuration $\mathcal{M} \subset \mathcal{R}^{3\times3\times3\times3}$ shelters the fourth-order anisotropic structural tensors $\mathbb{M}$. Aiming at the construction of a continuum mechanical framework for damage mechanics, there exist two possible alternative approaches. A good overview over these approaches can be found in SIMO & JU [163, 164]. The first possibility bases on the *concept of effective stress*, where LEMAITRE [97] introduced the *hypothesis of strain equivalence*: the strain associated with a damaged state under the applied stress is equivalent to the strain associated with its undamaged state under the effective stress.

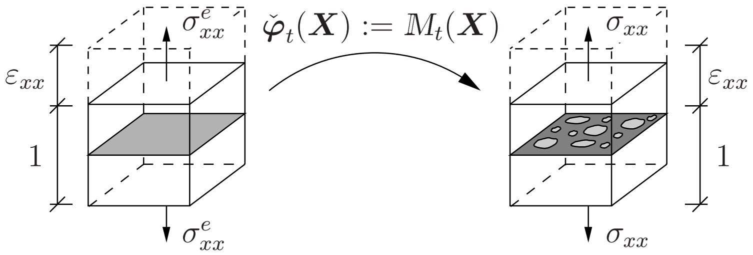
σ^e_{xx}
$\check{\boldsymbol{\varphi}}_t(\boldsymbol{X}) := \mathbb{M}_t(\boldsymbol{X})$
σ_{xx}
ε_{xx}
1
ε_{xx}
1
σ^e_{xx}
σ_{xx}

Figure 4.7: Hypothesis of strain equivalence. The strain associated with a damaged state ε_{xx} of the representative volume element under the applied stress σ_{xx} is equivalent to the strain ε_{xx} associated with its undamaged state under the effective stress σ^e_{xx}.

For a visualization, see Figure 4.7. This hypotheses yields the effective stress

$$\boldsymbol{\sigma}^e = \mathbb{M}^{-1} : \boldsymbol{\sigma} \,. \tag{4.27}$$

As illustrated in Figure 4.8, the second possibility bases on the *concept of effective strain*, where the *hypothesis of stress equivalence* is postulated: the stress associated with a damaged state under the applied strain is equivalent to the stress associated with its undamaged state under the effective strain. This yields the effective strain

$$\boldsymbol{\varepsilon}^e = \mathbb{M} : \boldsymbol{\varepsilon} \,. \tag{4.28}$$

For the isotropic case, the mechanical behavior of micro-cracks, or micro voids does not depend on their orientation inside the material and is characterized by a *scalar variable* d. Thus, the tensorial object $\mathbb{M}$ simply reduces to $\mathbb{M}_{iso} = (1-d)\,\mathbb{I}^{sym}$ where $\mathbb{I}^{sym}$ is the symmetric fourth order identity tensor and $d \in [0,1]$ the scalar-valued damage variable. As a result, the abstract microscopic manifold simply reduces to the one-dimensional space $\mathcal{M} \subset \mathcal{R}$. In order to get a clear understanding of isotropic damage processes, consider a representative volume element as shown in Figure 4.9. The representative volume element is cut at height h into two parts. The total cross section of the volume element A exhibits cracks and micro cavities with a total effective area $A_{d(h)}$. The amount of damage is then determined by

$$d(\boldsymbol{X}, \boldsymbol{N}, h) = \frac{A_{d(h)}}{A} \,. \tag{4.29}$$

A homogenized quantity of d that is used in the continuum mechanical formulation is obtained at the height h which is most damaged

$$d(\boldsymbol{X}, \boldsymbol{N}) = \max_h [\, d(\boldsymbol{X}, \boldsymbol{N}, h)\,] \,. \tag{4.30}$$

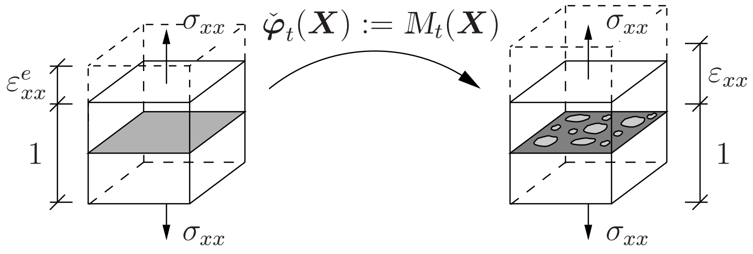
σ_{xx}
$\check{\boldsymbol{\varphi}}_t(\boldsymbol{X}) := \mathbb{M}_t(\boldsymbol{X})$
σ_{xx}
ε^e_{xx}
1
ε_{xx}
1
σ_{xx}
σ_{xx}

Figure 4.8: Hypothesis of stress equivalence. The stress associated with a damaged state σ_{xx} under the applied strain ε_{xx} is equivalent to the stress σ_{xx} associated with its undamaged state under the effective strain ε^e_{xx}.

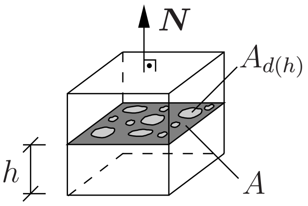

Figure 4.9: Motivation of damage variable d. $A_{d(h)}$ is the effective area of all microdefects that lie inside the total area A of the representative volume element's cut surface.

Starting with this definition, it is obvious that the value of the scalar-valued damage variable d lies in a bounded domain $d \in [0, 1]$. The value $d(\boldsymbol{X}, \boldsymbol{N}) = 1$ describes the fully broken and $d(\boldsymbol{X}, \boldsymbol{N}) = 0$ the undamaged state of the material. Thus, d can be looked at as an *effective surface density* of micro defects.

4.3. Isotropic Strain-Gradient Damage Mechanics at Small Strains

This section is concerned with the application of the proposed gradient-type framework for standard dissipative solids to a model problem of damage mechanics at small deformations. In a first step, the basic kinematics and state variables are introduced. Hereby, the focus lies on an isotropic damage process that is characterized by a scalar-valued damage variable d. A subsequent step is concerned with the introduction of the constitutive equations, namely the free energy function showing an additional damage-gradient term combined with an energetic length scale parameter and the dissipation function. For the latter one, a canonical two-field and an extended three-field representation is investigated. Having the constitutive equations at hand, the full boundary value problem is described and the governing equations derived from the argument of virtual power. As an alternative, two incremental variational statements are set up that build a perfect basis for the numerical implementation.

4.3.1. Basic Kinematics and State Variables. Focusing on a continuum mechanical description of isotropic damage mechanics, besides the macroscopic displacement field $\boldsymbol{u}$, a scalar quantity α is introduced that describes in a homogenized sense a gradual deterioration process of the microstructure via micro-crack and micro-void nucleation

$$\bar{\boldsymbol{u}} := \{\, \boldsymbol{u} \,\} \quad \text{and} \quad \check{\boldsymbol{u}} := \{\, \alpha \,\}\,. \tag{4.31}$$

The macroscopic strain $\boldsymbol{\varepsilon} = \nabla_s \boldsymbol{u}$ can additively be decomposed into elastic and inelastic parts yielding the definition of the stress producing elastic strain

$$\boldsymbol{\varepsilon}^e = \boldsymbol{\varepsilon} - \boldsymbol{\varepsilon}^d \quad \text{with} \quad \boldsymbol{\varepsilon}^d = d(\alpha)\, \boldsymbol{\varepsilon}\,. \tag{4.32}$$

In this expression, the inelastic part of the strain $\boldsymbol{\varepsilon}^d$ is assumed to be proportional to the total macroscopic strain $\boldsymbol{\varepsilon}$. Hereby, the proportionality factor $d(\alpha)$ corresponds to a function that relates the present microstructural deterioration α to a continuous damage variable d. This mapping function $d : \mathcal{R}_+ \to \mathcal{R}_+$ is a monotonic increasing, smooth function with the property $d \in [0, 1]$ for $\alpha \in [0, \infty)$. It is characterized by

$$d(\alpha) = 1 - (1 + \alpha)^{-\nu}\,, \tag{4.33}$$

where $d(\alpha) = 0$ describes the undamaged state and $d(\alpha) = 1$ the fully damaged state of the material. An increasing value for the parameter ν amplifies damage evolution, a

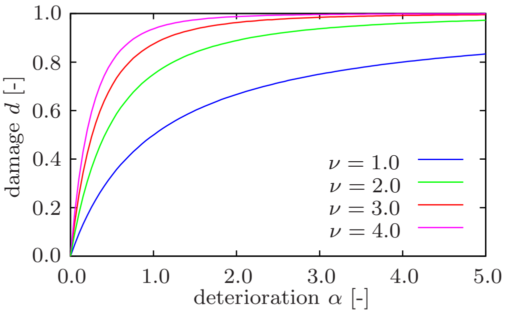

Figure 4.10: Mapping function for damage process. Increasing ν enforces damage evolution.

decreasing value for ν diminishes damage evolution, see Figure 4.10. As discussed earlier in Section 4.2, the elastic stress producing strain for isotropic damage processes $(4.32)_1$ can alternatively be obtained by the hypothesis of stress equivalence

$$\boldsymbol{\varepsilon}^e = \mathbb{M}_{iso} : \boldsymbol{\varepsilon} = (1 - d(\alpha))\, \boldsymbol{\varepsilon} \quad \text{with} \quad \mathbb{M}_{iso} = (1 - d(\alpha))\, \mathbb{I}^{sym}\,, \tag{4.34}$$

expressed in terms of the fourth-order identity tensor $\mathbb{I}^{sym}$. The effective strain $(4.34)_1$ is used as a state variable for the description of energy storage mechanisms related to elastic macroscopic distortions. Additional energy storage mechanisms are introduced that are related to homogeneously and inhomogeneously distributed distortions surrounding microscopic defects characterized by the field variable α and its gradient $\nabla\alpha$. Thus, the constitutive state can be specified to

$$\mathfrak{c} := \{\, \boldsymbol{\varepsilon}, \alpha, \nabla\alpha \,\}\,, \tag{4.35}$$

which builds the kinematic basis for the construction of the constitutive equations.

4.3.2. Isotropic Degradation of Stored Bulk Energy. In what follows, the constitutive equations for a model problem of isotropic gradient-type damage are introduced. According to $(3.28)_1$, the free energy stored in the solid $\mathcal{B}$ is defined by

$$E(\boldsymbol{u}, \alpha) = \int_{\mathcal{B}} \psi(\mathfrak{c})\, dV\,, \tag{4.36}$$

where the free energy function consists of contributions arising from elastic macroscopic distortions characterized by the effective strain $\boldsymbol{\varepsilon}^e$ and from microscopic inhomogeneously distributed distortions characterized by $\nabla\alpha$. A decoupled representation reads

$$\boxed{\psi(\mathfrak{c}) = \underbrace{\bar{\psi}_{loc}(\boldsymbol{\varepsilon}^e(\boldsymbol{\varepsilon}, \alpha))}_{\text{elast. macro-dist.}} + \underbrace{\check{\psi}_{non}(\nabla\alpha)}_{\text{inh. micro-dist.}}\ .} \tag{4.37}$$

For the particular model under focus, the energetic contributions take the specific form

$$\boxed{\begin{aligned} \bar{\psi}_{loc}(\boldsymbol{\varepsilon}^e(\boldsymbol{\varepsilon}, \alpha)) &= \tfrac{1}{2}\, \|\boldsymbol{\varepsilon}^e(\boldsymbol{\varepsilon}, \alpha)\|^2_{\mathbb{C}} = \tfrac{1}{2}\, (1 - d(\alpha))^2\, \|\boldsymbol{\varepsilon}\|^2_{\mathbb{C}} \\ \check{\psi}_{non}(\nabla\alpha) &= \tfrac{1}{2}\, \mu l^2\, \|\nabla\alpha\|^2\,, \end{aligned}} \tag{4.38}$$

where the elastic moduli $\mathbb{C} := \lambda \boldsymbol{1} \otimes \boldsymbol{1} + 2\mu \mathbb{I}^{sym}$ contain the Lamé constants λ and μ, and l is the length scale parameter. According to (3.39), the rate of energy storage

$$\mathcal{E}(\dot{\boldsymbol{\varepsilon}}, \dot{\alpha}; \boldsymbol{\varepsilon}, \alpha) := \frac{d}{dt} \int_{\mathcal{B}} \psi(\mathfrak{c}) \, dV = \int_{\mathcal{B}} \{ \, (\partial_{\boldsymbol{\varepsilon}} \psi) : \dot{\boldsymbol{\varepsilon}} + (\delta_\alpha \psi) \dot{\alpha} \, \} \, dV \tag{4.39}$$

is governed by the total stresses and the elastic driving force

$$\boldsymbol{\sigma} := \partial_{\boldsymbol{\varepsilon}} \psi = (1-d(\alpha))^2 \, \mathbb{C} : \boldsymbol{\varepsilon} \quad \text{and} \quad \beta^e := \delta_\alpha \psi = -(1-d(\alpha)) d'(\alpha) \, \|\boldsymbol{\varepsilon}\|^2_{\mathbb{C}} - \mu l^2 \, \Delta\alpha \, . \tag{4.40}$$

For monotonically increasing functions $d(\alpha)$ the elastic driving force β^e is strictly negative.

4.3.3. Dissipation Functions for Damage Evolution. In damage mechanics, reversible processes are not considered, effects of self-healing are excluded. The irreversibility constraint is satisfied by *locally* ensuring a positive evolution of the damage field

$$\dot{\alpha} \geq 0 \, . \tag{4.41}$$

For rate-independent processes, the dissipative material response is characterized by

$$D(\dot{d}; d) = \int_{\mathcal{B}} \phi(\dot{\mathfrak{c}}; \mathfrak{c}) \, dV = \int_{\mathcal{B}} \partial_{\dot{\mathfrak{c}}} \phi(\dot{\mathfrak{c}}; \mathfrak{c}) \cdot \dot{\mathfrak{c}} \, dV = \mathcal{D}(\dot{d}; d) \, , \tag{4.42}$$

where for positively homogeneous dissipation functions ϕ the dissipation potential functional D is identical to the dissipation $\mathcal{D}$. The dissipation function

$$\boxed{\phi(\dot{\mathfrak{c}}; \mathfrak{c}) = \underbrace{\check{\phi}_{loc}(\dot{\alpha}; \alpha)}_{\text{hom. micro-diss.}}} \tag{4.43}$$

is assumed to be influenced by homogeneously distributed damage only.

4.3.3.1. Model I: Canonical Two Field Setting. A dissipation function that a priori fulfills the growth condition (4.41) bases on the *non-smooth* representation

$$\boxed{\check{\phi}_{loc}(\dot{\alpha}; \alpha) = \psi_c \, \dot{\alpha} + I_+(\dot{\alpha}) \, ,} \tag{4.44}$$

where the parameter ψ_c is a constitutive threshold value and $I_+(x)$ is the non-smooth indicator function for the set $\mathcal{R}_+$ of positive real numbers. The latter is defined by

$$I_+(x) = \left\{ \begin{array}{cl} 0 & \text{if } x > 0 \\ +\infty & \text{otherwise} \, , \end{array} \right. \tag{4.45}$$

ensuring a positive damage evolution. For a visualization see Figure 4.11a). As depicted in Figure 4.11b), the indicator function can be approximated by the penalty-type expression

$$I^\epsilon_+(x) = \frac{\epsilon}{2} \langle x \rangle^2_- \, , \tag{4.46}$$

based on the ramp function $\langle x \rangle_- := (|x| - x)/2$ of the set $\mathcal{R}_-$ of negative real numbers. For an illustration see Figure 4.11d). The constant ϵ is a regularization parameter that enforces for $\epsilon \to \infty$ the exact satisfaction of the constraint condition (4.41). Making use of the approximation (4.46), a *smooth* representation of the dissipation function (4.44) is introduced

$$\boxed{\check{\phi}^\epsilon_{loc}(\dot{\alpha}; \alpha) = \psi_c \, \dot{\alpha} + \frac{\epsilon}{2} \langle \dot{\alpha} \rangle^2_- \, ,} \tag{4.47}$$

which is used as a first attempt to model the dissipation in damage mechanics.

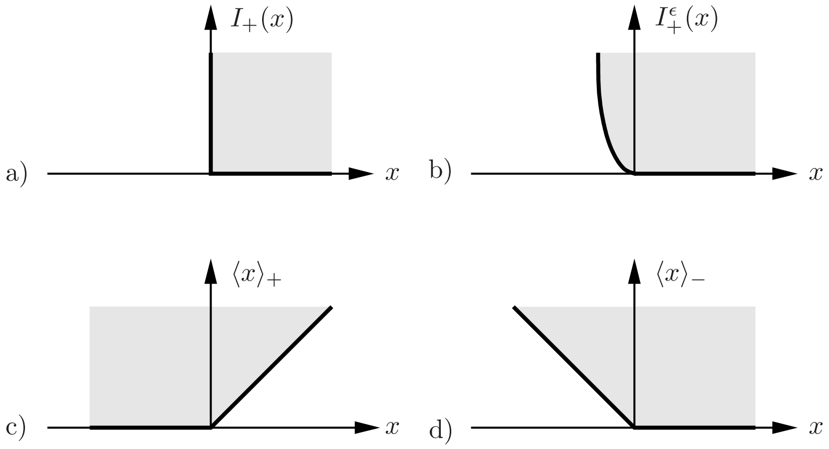

Figure 4.11: Convex functions. a) Indicator function of $\mathcal{R}_+$ and b) regularized indicator function $I_+(x) = \frac{\epsilon}{2}\langle x\rangle_-^2$ of the $\mathcal{R}_+$. c) Ramp function $\langle x\rangle_+ := (|x| + x)/2$ of $\mathcal{R}_+$ and d) ramp function $\langle x\rangle_- := (|x| - x)/2$ of $\mathcal{R}_-$.

4.3.3.2. Model II: Extended Three Field Setting. An alternative formulation of the dissipation function that also fulfills the damage growth condition (4.41) is constructed by taking into account the thermodynamic driving force dual to the damage field

$$\check{\boldsymbol{f}} := \{\, \beta \,\} \,. \tag{4.48}$$

An elastic domain $\mathbb{E}$ in the space of dissipative forces is bounded by the threshold function

$$\varphi(\beta) = \beta - \psi_c \leq 0 \tag{4.49}$$

and characterizes for $\varphi(\beta) < 0$ an elastic domain without damage accumulation. An appropriate dissipation function is obtained by the constrained optimization problem

$$\phi(\dot{\mathfrak{c}}; \mathfrak{c}) = \sup_{\beta \in \mathbb{E}} [\, \beta\, \dot{\alpha} \,] \quad \text{with} \quad \mathbb{E} := \{\, \beta \,|\, \varphi(\beta) \leq 0 \,\} \,, \tag{4.50}$$

also known as *principle of maximum dissipation.* The fully rate-independent constrained optimization problem $(4.50)_1$ is solved by a Lagrange-type solution strategy

$$\boxed{\check{\phi}_{loc}(\dot{\alpha}; \alpha) = \sup_{\beta,\, \lambda \geq 0} [\, \beta\, \dot{\alpha} - \lambda\, \varphi(\beta) \,]} \tag{4.51}$$

with the Lagrange multiplier λ. The necessary condition of this constraint optimization problem identifies the Lagrange multiplier $\lambda = \dot{\alpha}$ and the evolution of the damage field

$$\dot{\alpha} \geq 0 \quad \text{and} \quad \beta \leq \psi_c \quad \text{and} \quad \dot{\alpha}\,(\beta - \psi_c) = 0 \,. \tag{4.52}$$

These so-called Karush-Kuhn-Tucker loading/unloading conditions explicitly include the irreversibility condition (4.41). A *viscous regularization* of (4.51) bases on the over-force formulation

$$\boxed{\check{\phi}^{\eta}_{loc}(\dot{\alpha}; \alpha) = \sup_{\beta} [\, \beta\, \dot{\alpha} - \frac{1}{2\eta} \langle \beta - \psi_c \rangle_+^2 \,] \,.} \tag{4.53}$$

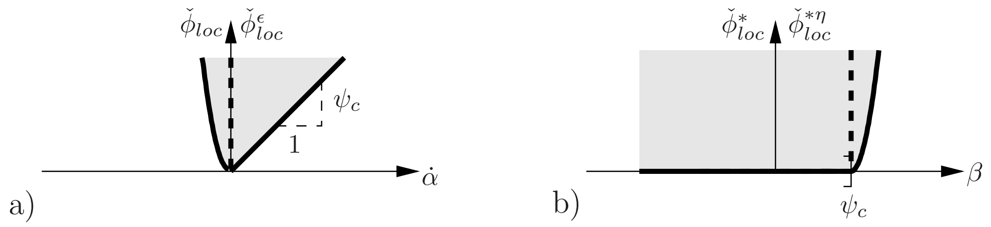

Figure 4.12: Dissipation functions for damage mechanics. a) Canonical penalty-type representation $\check{\phi}^{\epsilon}_{loc}$ and b) viscous over-force representation $\check{\phi}^{*\eta}_{loc} = \frac{1}{2\eta}\langle \beta - \psi_c \rangle_+^2$. The corresponding dual non-smooth counterparts $\check{\phi}_{loc}$ and $\check{\phi}^{*}_{loc}$ are given in dotted lines.

In this setting, the ramp function $\langle x \rangle_+ := (|x|+x)/2$ of the set $\mathcal{R}_+$ of positive real numbers has been employed, for an illustration see Figure 4.11c). The necessary condition of the smooth unconstrained optimization problem (4.53) defines the damage evolution

$$\dot{\alpha} = \frac{1}{\eta} \langle \beta - \psi_c \rangle_+ \tag{4.54}$$

and obviously satisfies the irreversibility constraint (4.41). The viscosity η characterizes a viscous over-force response which governs the damage evolution. For $\eta \to \infty$, the model degenerates to the rate-independent model (4.51) and the Lagrange-multiplier

$$\lambda := \frac{1}{\eta} \langle \beta - \psi_c \rangle_+ \tag{4.55}$$

is identified. Due to the limit character of the smooth over-force setting (4.53), this formulation is highly attractive for a numerical implementation and is considered as a second approach to model the dissipation in damage mechanics. A graphical interpretation of the four different dissipation functions is given in Figure 4.12. In the sense of convex analysis, the non-smooth dissipation functions (4.44) and (4.51) are identical, where the latter one bases on the dual dissipation function $\check{\phi}^{*}_{loc}(\beta) = \lambda\, \varphi(\beta)$. They are displayed in Figure 4.12 with dotted lines, their regularized counterparts are shown in solid lines.

4.3.4. Governing Balance Equations of Coupled Problem. The focus now lies on the derivation of the governing balance equations that determine the *displacement field* $\boldsymbol{u}$, the damage field α, and in the extended setting the *driving force* β. In view of the displacement field, the surface of the solid is decomposed into a part $\partial\mathcal{B}_{\boldsymbol{u}}$ where the displacements are prescribed by the Dirichlet boundary conditions

$$\boldsymbol{u} = \boldsymbol{u}_D \text{ on } \partial\mathcal{B}_{\boldsymbol{u}}\,, \tag{4.56}$$

and a Neumann part $\partial\mathcal{B}_{\boldsymbol{t}}$ with prescribed tractions $\boldsymbol{t}_N$. Obviously, the common set $\partial\mathcal{B}_{\boldsymbol{u}} \cap \partial\mathcal{B}_{\boldsymbol{t}} = \emptyset$ of these boundaries is empty. The power of external mechanical load reads

$$\mathcal{P}_{ext}(\dot{\boldsymbol{u}}) = \int_{\mathcal{B}} \boldsymbol{\gamma} \cdot \dot{\boldsymbol{u}}\, dV + \int_{\partial\mathcal{B}_{\boldsymbol{t}}} \boldsymbol{t}_N \cdot \dot{\boldsymbol{u}}\, dA\,, \tag{4.57}$$

in terms of a given body force field $\boldsymbol{\gamma}$ per unit volume. For the damage field no Dirichlet-type boundary conditions are set, the natural Neumann-type conditions $\nabla\alpha \cdot \boldsymbol{n} = 0$ on the full surface $\partial\mathcal{B}$ are chosen. The damage field α is considered to be driven by the displacement field $\boldsymbol{u}$ of the solid. Thus, no prescribed external loading associated with the damage field is considered. Having the external load functional (4.57), the rate of the energy storage functional (4.39), and the dissipation functional (4.42) at hand, the balance equations are obtained from the standard argument of virtual power

$$\boxed{\mathcal{E}(\dot{\boldsymbol{u}}, \dot{\alpha}) + \mathcal{D}(\dot{\alpha}) - \mathcal{P}_{ext}(\dot{\boldsymbol{u}}) = 0\,.} \tag{4.58}$$

This principle has to be valid for all admissible rates $\dot{\boldsymbol{u}}$ of the displacement field satisfying the homogeneous form of the Dirichlet boundary condition

$$\dot{\boldsymbol{u}} \in \mathcal{W}_{\boldsymbol{u}} := \{\, \dot{\boldsymbol{u}} \,|\, \dot{\boldsymbol{u}} = \boldsymbol{0} \text{ on } \partial\mathcal{B}_{\boldsymbol{u}} \,\}\,. \tag{4.59}$$

The description of the boundary value problem is now completed and the governing balance equations can be determined for the different representations of the dissipation function.

4.3.4.1. Model I: Rate-Independent Setting with Approximated Indicator. For the rate-independent dissipation function with approximated indicator function (4.47), the application of the principle of virtual power (4.58) yields the coupled balance equations

$$\begin{aligned} \boldsymbol{0} &= \operatorname{div}[\,(1-d(\alpha))^2\, \mathbb{C} : \boldsymbol{\varepsilon}\,] + \boldsymbol{\gamma} \\ 0 &= \mu l^2\, \Delta\alpha + [\,(1-d(\alpha))\, d'(\alpha)\, \|\boldsymbol{\varepsilon}\|^2_{\mathbb{C}} - \psi_c - \epsilon\langle\dot{\alpha}\rangle_-\,]\,, \end{aligned} \tag{4.60}$$

where the regularization term can be interpreted as an artificial viscous hardening term that penalizes the energy release in the non-physical range $\dot{\alpha} < 0$.

4.3.4.2. Model II: Rate-Dependent Setting with Threshold Function. For the rate-dependent over-force formulation of the dissipation function (4.53), the balance of internal and external power (4.58) gives the governing balance equations

$$\begin{aligned} \boldsymbol{0} &= \operatorname{div}[\,(1-d(\alpha))^2\, \mathbb{C} : \boldsymbol{\varepsilon}\,] + \boldsymbol{\gamma} \\ 0 &= \mu l^2\, \Delta\alpha + [\,(1-d(\alpha))\, d'(\alpha)\, \|\boldsymbol{\varepsilon}\|^2_{\mathbb{C}} - \beta\,] \\ 0 &= \dot{\alpha} - \frac{1}{\eta}\langle\beta - \psi_c\rangle_+\,, \end{aligned} \tag{4.61}$$

where for vanishing viscosity $\eta \to 0$ the rate-independent limit is obtained.

4.3.5. Incremental Variational Principles for Gradient-Type Damage. Following the general concept as discussed in Section 3.9, a time-discrete incremental variational principle is applied to the model problem of gradient-type damage mechanics, where the solutions of the global fields at discrete solution times $0, t_1, t_2, \ldots, t_n, t_{n+1}, \ldots, T$ are considered. The construction of such a principle depends on the incremental energy storage, dissipation, and load expended to the system within a typical time step $[t_n, t_{n+1}]$. Model I and II have in common the incrementally stored energy

$$E^\tau(\boldsymbol{u}, d) := \int_{t_n}^{t_{n+1}} \dot{E}\, dt = E(t_{n+1}) - E(t_n) = \int_{\mathcal{B}} \{\, \psi(\mathfrak{c}) - \psi(\mathfrak{c}_n) \,\}\, dV\,, \tag{4.62}$$

governed by the free energy function ψ, and the incremental external work

$$W^\tau(\boldsymbol{u}) := \int_{t_n}^{t_{n+1}} \mathcal{P}_{ext}\, dt = \int_{\mathcal{B}} \{\, \boldsymbol{\gamma} \cdot (\boldsymbol{u} - \boldsymbol{u}_n) \,\}\, dV + \int_{\partial\mathcal{B}} \{\, \boldsymbol{t}_N \cdot (\boldsymbol{u} - \boldsymbol{u}_n) \,\}\, dA\,, \tag{4.63}$$

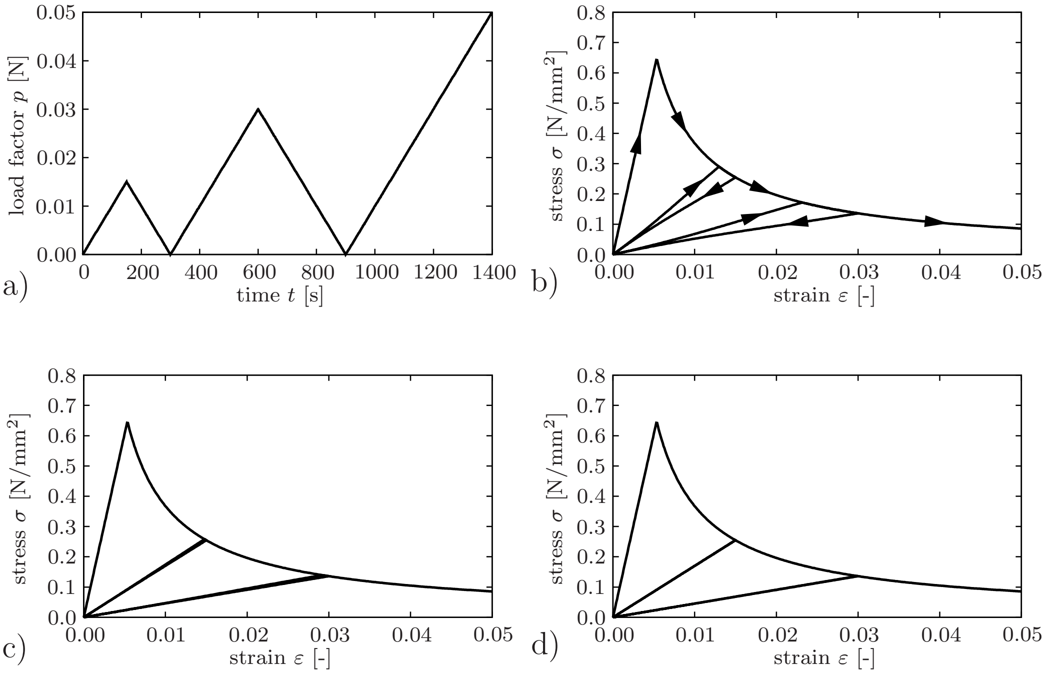

Figure 4.13: Model I: Rate-independent two-field setting with approximated indicator function. a) Cyclic loading and stress-strain curves for b) $\epsilon = 0.1$, c) $\epsilon = 1.0$, and d) $\epsilon = 10.0$. For small parameters ϵ, the model shows non-physical hysteresis in unloading-reloading.

where no external loading associated with the damage field is considered. The construction of the incremental dissipation bases on

$$D^\tau := \int_{t_n}^{t_{n+1}} D\, dt \tag{4.64}$$

and is discussed separately for the dissipation functions (4.47) and (4.53).

4.3.5.1. Model I: Rate-Independent Two-Field Representation. The first possibility to model the effective incremental potential bases on the rate-independent dissipation function with approximated indicator function (4.47). In this setting, the incremental dissipation is approximated in the discrete time interval by the algorithmic quantity

$$D^\tau_\epsilon(\alpha) := \int_{\mathcal{B}} \{\, \psi_c\,(\alpha - \alpha_n) + \frac{\epsilon}{2\tau}\langle d - d_n\rangle_-^2 \,\}\, dV\,. \tag{4.65}$$

With the constitutive state (4.35), the *incremental internal work density* is specified to

$$\pi^\tau(\mathfrak{c};\mathfrak{c}_n) = \tfrac{1}{2}\,(1-d(\alpha))^2\,\|\boldsymbol{\varepsilon}\|^2_{\mathbb{C}} + \tfrac{1}{2}\,\mu l^2\,\|\nabla\alpha\|^2 - \psi(\mathfrak{c}_n) + \psi_c\,(\alpha-\alpha_n) + \frac{\epsilon}{2\tau}\langle\alpha-\alpha_n\rangle_-^2\,. \tag{4.66}$$

The incremental minimum principle (3.205) yields the algorithmic coupled Euler equations

$$\begin{aligned} \boldsymbol{0} &= \mathrm{div}[\,(1-d(\alpha))^2\,\mathbb{C} : \boldsymbol{\varepsilon}\,] + \boldsymbol{\gamma} \\ 0 &= \mu l^2\,\Delta\alpha + [\,(1-d(\alpha))\,d'(\alpha)\,|\boldsymbol{\varepsilon}|^2_{\mathbb{C}} - \psi_c - \frac{\epsilon}{\tau}\langle\alpha-\alpha_n\rangle_-\,]\,, \end{aligned} \tag{4.67}$$

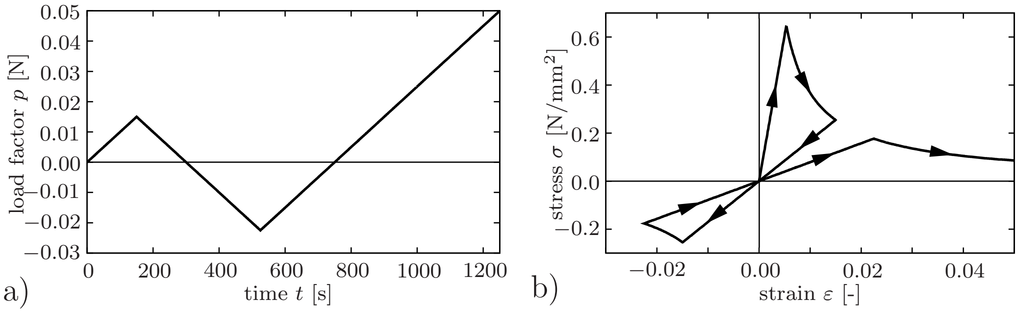

Figure 4.14: Model I/II: Rate-independent two-field setting with approximated indicator function and rate-dependent three-field setting with threshold function. a) Cyclic loading in positive and negative range and b) stress-strain curve for $\epsilon = 10.0$ and $\eta = 1.0 \times 10^{-10}$.

where the smooth penalty-type micro-balance $(4.67)_2$ describes the damage field α driven by the degraded strain energy $\partial_\alpha \psi = (1 - d(\alpha))\, d'(\alpha)\, \|\boldsymbol{\varepsilon}\|^2_{\mathbb{C}}$. The results of a one-dimensional local driver test of the rate-independent two-field representation are illustrated in Figure 4.13, where a cyclic load in the *tensile* range has been considered. Clearly, for an increasing penalty-parameter ϵ, the rate-independent limit that is characterized by the non-smooth dissipation function (4.44) is obtained. For small penalty parameters ϵ, the model shows a non-physical hysteresis in unloading-reloading. The results of a local driver test for cyclic loading in the positive and negative range are depicted in Figure 4.14, where the penalty-parameter ϵ has been chosen high enough to approximate the rate-independent limit. Clearly, the material behaves isotropically with damage evolution in tension and compression. More realistic material models, e.g. failure of concrete, exhibit damage evolution preferable in tension. In such a scenario, the damage-energy coupling $(4.38)_1$ has to be modified in such a way that the resulting energetic driving force, characterized by the degraded strain energy, only contains tensile contributions. This extended formulation is discussed later in Chapter 5 on phase-field modeling of fracture.

4.3.5.2. Model II: Rate-Dependent Three-Field Representation. The second possibility to model the incremental potential bases on the *rate-dependent* setting of the dissipation function (4.53). The extended constitutive state vector

$$\mathfrak{c}^* := \{\, \boldsymbol{\varepsilon}, \alpha, \nabla\alpha, \beta \,\} \tag{4.68}$$

allows for the compact representation of the *extended incremental internal work density*

$$\pi^{\tau *}_{\eta}(\mathfrak{c}^*; \mathfrak{c}^*_n) = \tfrac{1}{2}\,(1-d(\alpha))^2\, \|\boldsymbol{\varepsilon}\|^2_{\mathbb{C}} + \tfrac{1}{2}\,\mu l^2\, \|\nabla\alpha\|^2 - \psi(\mathfrak{c}_n) + \beta\,(\alpha-\alpha_n) - \frac{\tau}{2\eta}\langle \beta - \psi_c \rangle^2_+ \,. \tag{4.69}$$

The incremental variational principle (3.212) yields the algorithmic Euler equations

$$\begin{aligned} \boldsymbol{0} &= \operatorname{div}[\,(1-d(\alpha))^2\, \mathbb{C} : \boldsymbol{\varepsilon}\,] + \boldsymbol{\gamma} \\ 0 &= \mu l^2\, \Delta\alpha + [\,(1-d(\alpha))\, d'(\alpha)\, \|\boldsymbol{\varepsilon}\|^2_{\mathbb{C}} - \beta\,] \\ 0 &= \alpha - \alpha_n - \frac{\tau}{\eta}\langle \beta - \psi_c \rangle_+ \,. \end{aligned} \tag{4.70}$$

Here, the variational derivative of the free energy $-\delta_\alpha \psi = (1-d(\alpha))\, d'(\alpha)\, \|\boldsymbol{\varepsilon}\|^2_{\mathbb{C}} + \mu l^2\, \Delta\alpha$ in $(4.70)_2$ allows for the elimination of the dissipative force $\beta = -\delta_\alpha \psi$ in equation $(4.70)_3$.

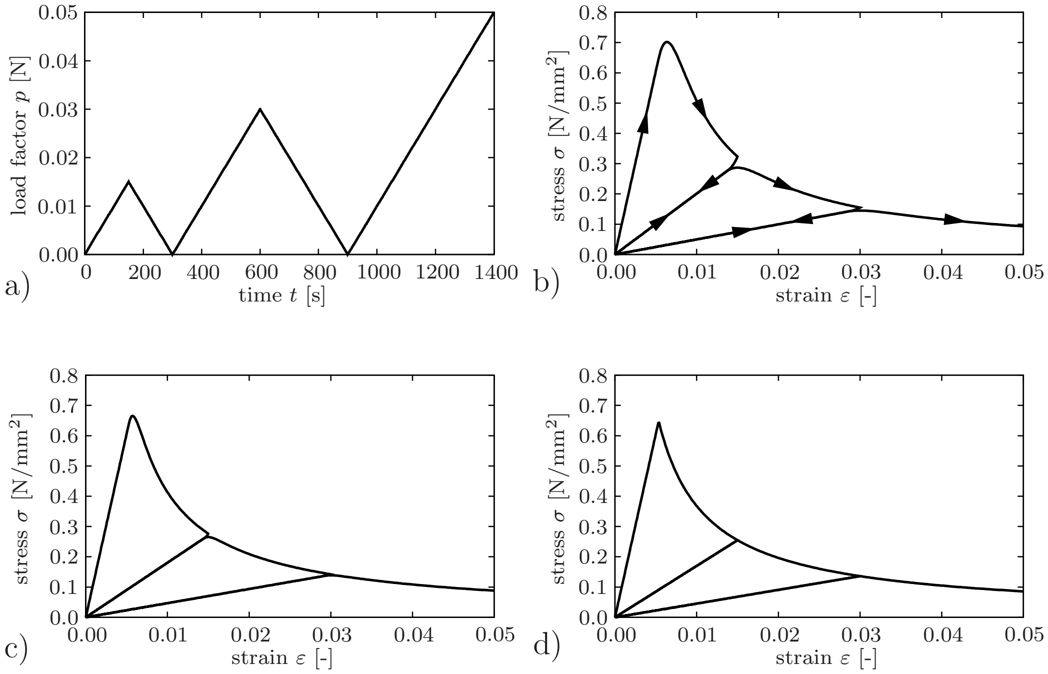

Figure 4.15: Model II: Rate-dependent three-field setting with threshold function. a) Cyclic loading and stress-strain curves for b) $\eta = 3.0{\times}10^{-3}$, c) $\eta = 2.0{\times}10^{-3}$ and d) $\eta = 1.0{\times}10^{-5}$.

Thus, the damage evolution can be reformulated

$$\alpha = \alpha_n + \frac{\tau}{\eta}\langle -\delta_\alpha \psi - \psi_c \rangle_+ \tag{4.71}$$

and shows via the variational derivative $\delta_\alpha \psi$ an implicit dependency of the yield resistance on the Laplacian term $\mu l^2\, \Delta\alpha$. In order to get an insight into the material's characteristics, a local one-dimensional driver test for the rate-dependent three-field setting is performed. Considering a cyclic loading process in the tensile range only, the model exhibits a classical over-force response, see the results in Figure 4.15. In contrast to model I, the underlying viscous-over force model does not exhibit a violation of the thermodynamics for regularization parameters far away from the limit case. Nevertheless the models I and II show the same limit behavior for $\epsilon \to \infty$ and $\eta \to 0$, respectively. For a viscosity close to the limit case $\eta \to 0$, the results of a local driver test in the tensile and compressive range are depicted in Figure 4.14 and show a coincidence with the rate-independent limit case for $\epsilon \to \infty$. The smooth character of the governing equations and the thermodynamic consistency even for viscosities far away from zero make this time-regularized setting with threshold function highly attractive for numerical implementations.

4.3.6. FE-Discretization of Incremental Variational Principle. The extended multi-field finite element solution algorithm outlined in Section 3.9.4 is now applied to *model II* of gradient-type damage mechanics. The according smooth Euler equations are summarized in equation (4.70). Restricting to two-dimensional problems, the global unknowns and the extended generalized constitutive state read

$$\mathfrak{u}^* := \{\, u_1, u_2, \alpha, \beta \,\} \quad \text{with} \quad \mathfrak{c}^*(\mathfrak{u}^*) := \{\, u_{1,1}, u_{2,2}, u_{1,2} + u_{2,1}, \alpha, \alpha_{,1}, \alpha_{,2}, \beta \,\}\,. \tag{4.72}$$

According to (3.226), the extended generalized displacements are approximated via

$$\mathfrak{u}^{*h} = \mathfrak{N}^*(\boldsymbol{x})\,\mathfrak{d}^* \quad \text{with} \quad [\mathfrak{N}^*]_i^e = \begin{bmatrix} N & 0 & 0 & 0 \\ 0 & N & 0 & 0 \\ 0 & 0 & N & 0 \\ 0 & 0 & 0 & M \end{bmatrix}_i \quad \text{and} \quad \mathfrak{d}_i^* = [\,d_1, d_2, a, b\,]_i^T\,, \tag{4.73}$$

where identical interpolations for the macro- and microscopic partition and the driving force are chosen, i.e. $N_i = M_i$. At node i of the finite element discretization, the generalized displacement vector $\mathfrak{d}^*$ contains the nodal displacements d_1 and d_2 in 1- and 2-direction, the nodal damage variable a, and the nodal thermodynamic driving force b dual to the damage field. In analogy to (3.231), the variation of the discrete extended constitutive state with respect to the extended nodal degrees of freedom reads

$$\delta_{\mathfrak{d}^*}\mathfrak{c}^{*h} = \mathfrak{B}^*(\boldsymbol{x})\,\delta\mathfrak{d}^* \quad \text{with} \quad [\mathfrak{B}^*]_i^e = \begin{bmatrix} N_{,1} & 0 & N_{,2} & 0 & 0 & 0 & 0 \\ 0 & N_{,2} & N_{,1} & 0 & 0 & 0 & 0 \\ 0 & 0 & 0 & N & N_{,1} & N_{,2} & 0 \\ 0 & 0 & 0 & 0 & 0 & 0 & M \end{bmatrix}_i^T . \tag{4.74}$$

For the particular model problem of gradient-type damage mechanics, the compact representations of the generalized stresses and the symmetric moduli are specified to

$$\boldsymbol{S}^* := \begin{bmatrix} \partial_{\boldsymbol{\varepsilon}}\pi_\eta^{*h} \\ \partial_\alpha\pi_\eta^{*h} \\ \partial_{\nabla\alpha}\pi_\eta^{*h} \\ \partial_\beta\pi_\eta^{*h} \end{bmatrix} \quad \text{and} \quad \mathbb{C}^* := \begin{bmatrix} \partial^2_{\boldsymbol{\varepsilon\varepsilon}}\pi_\eta^{*h} & \boldsymbol{0} & \boldsymbol{0} & \boldsymbol{0} \\ \boldsymbol{0} & \partial^2_{\alpha\alpha}\pi_\eta^{*h} & \boldsymbol{0} & 1 \\ \boldsymbol{0} & \boldsymbol{0} & \partial^2_{\nabla\alpha\nabla\alpha}\pi_\eta^{*h} & \boldsymbol{0} \\ \boldsymbol{0} & 1 & \boldsymbol{0} & \partial^2_{\beta\beta}\pi_\eta^{*h} \end{bmatrix} . \tag{4.75}$$

In the case of *elastic response* for $\varphi(\beta) < 0$, the components of the generalized stresses $(4.75)_1$ for isotropic gradient-type damage mechanics read

$$\begin{aligned} \partial_{\boldsymbol{\varepsilon}}\pi_\eta^{*h} &= (1 - d(\alpha))^2\, \mathbb{C} : \boldsymbol{\varepsilon} \\ \partial_\alpha\pi_\eta^{*h} &= -(1 - d(\alpha))\, d'(\alpha)\, \|\boldsymbol{\varepsilon}\|^2_{\mathbb{C}} + \beta \\ \partial_{\nabla\alpha}\pi_\eta^{*h} &= \mu l^2\, \nabla\alpha \\ \partial_\beta\pi_\eta^{*h} &= \alpha - \alpha_n \end{aligned} \tag{4.76}$$

and the according components of the generalized moduli $(4.75)_2$ are given by

$$\begin{aligned} \partial^2_{\boldsymbol{\varepsilon\varepsilon}}\pi_\eta^{*h} &= (1 - d(\alpha))^2\, \mathbb{C} \\ \partial^2_{\alpha\alpha}\pi_\eta^{*h} &= (d'^2(\alpha) - (1 - d(\alpha))\, d''(\alpha))\, \|\boldsymbol{\varepsilon}\|^2_{\mathbb{C}} \\ \partial^2_{\nabla\alpha\nabla\alpha}\pi_\eta^{*h} &= \mu l^2\, \boldsymbol{1} \\ \partial^2_{\beta\beta}\pi_\eta^{*h} &= 0\,. \end{aligned} \tag{4.77}$$

For *inelastic loading* $\varphi(\beta) \geq 0$, the ramp function becomes active and the generalized stresses and moduli have to be updated by an additional viscosity term

$$\partial_\beta\pi_\eta^{*h} \Leftarrow \partial_\beta\pi_\eta^{*h} - \frac{\tau}{\eta}(\beta - \psi_c) \quad \text{and} \quad \partial^2_{\beta\beta}\pi_\eta^{*h} \Leftarrow \partial^2_{\beta\beta}\pi_\eta^{*h} - \frac{\tau}{\eta}\,, \tag{4.78}$$

being characteristic for the viscous over-force response of model II.

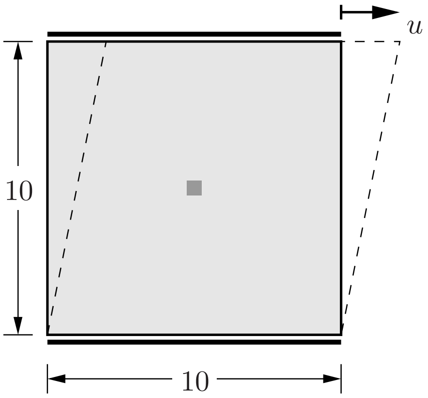

Figure 4.16: Shear-test of squared specimen. Geometry and boundary conditions. To trigger localization, the threshold energy ψ_c in the centered element is reduced by 5%.

4.3.7. Numerical Examples. Regularization of Shear Bands. The first section with numerical examples demonstrates the main characteristics of the proposed model for gradient-type damage mechanics by means of two representative numerical examples. The first elementary example under consideration is a *squared specimen subjected to shear loading*, where a horizontal shear-band is expected. The second example is concerned with a *rectangular specimen subjected to tensile loading*, where cross-shearing is expected.

4.3.7.1. Shear-Test of Squared Specimen. In a first numerical test damage localization in a squared specimen subjected to pure shear loading is investigated. The geometric setup and the according boundary conditions are depicted in Figure 4.16. The boundary value problem is discretized using 9×9, 19×19, and 29×29 three-field quadrilateral displacement elements discussed in the previous section. In order to trigger damage localization in the middle line of elements, the constitutive threshold energy ψ_c in the centered element is reduced by 5%. The bulk modulus is chosen to $\lambda = 121.15$ kN/mm^2, the shear modulus to $\mu = 80.77$ kN/mm^2, and the threshold energy to $\psi_c = 8.08 \times 10^{-3}$ kN/mm^2. In order to obtain a solution very close to the rate-independent limit, the viscosity is chosen to $\eta = 1{\times}10^{-6}$ kN s/mm^2. The parameter to control the damage function (4.33) is chosen to $\nu = 1.2$. Regarding the local computations, the global solution strategy bases on an updated normal plane method, in combination with a full Newton iteration. The application of a continuation method, in this scenario an arc-length method, is necessary to obtain

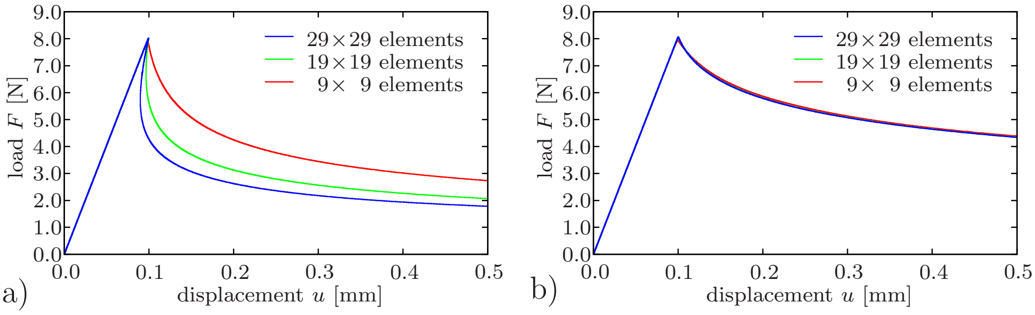

Figure 4.17: Shear-test of squared specimen. Load-deflection curves for a) mesh-dependent, local analysis with $l = 0.000$ mm and b) mesh-objective, nonlocal analysis with $l = 0.012$ mm, for computations with 9×9, 19×19 and 29×29 elements.

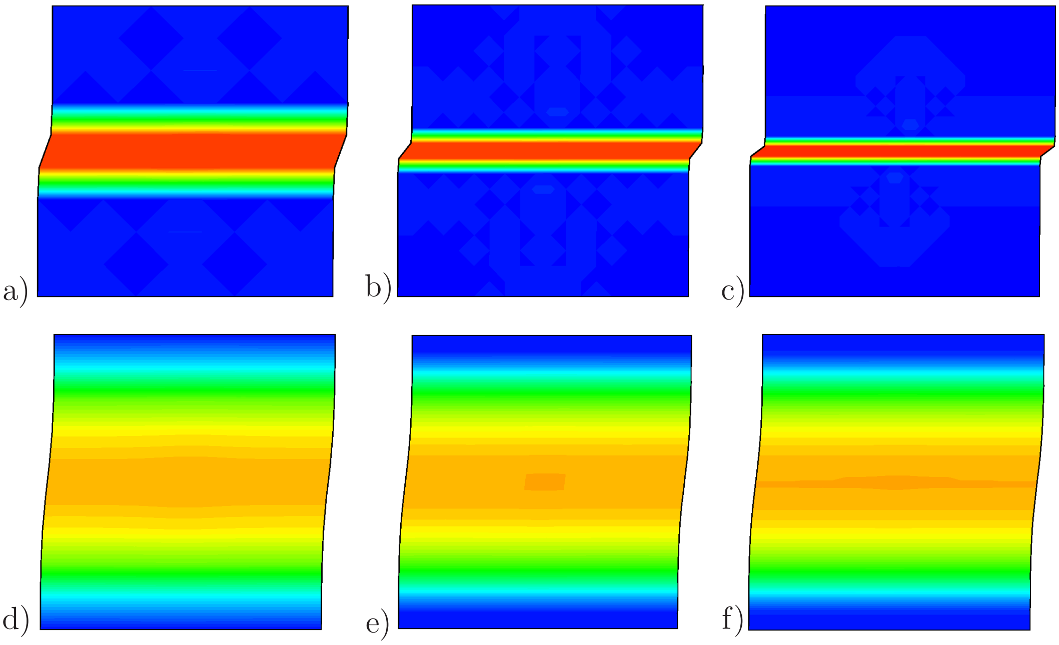

Figure 4.18: Shear-test of squared specimen. Damage distribution d at a final deformation of $u = 0.5$ mm for a)–c) local analysis $l = 0.000$ mm, and d)–f) nonlocal analysis $l = 0.012$ mm. Results are plotted for the three discretizations 9×9, 19×19, and 29×29 elements.

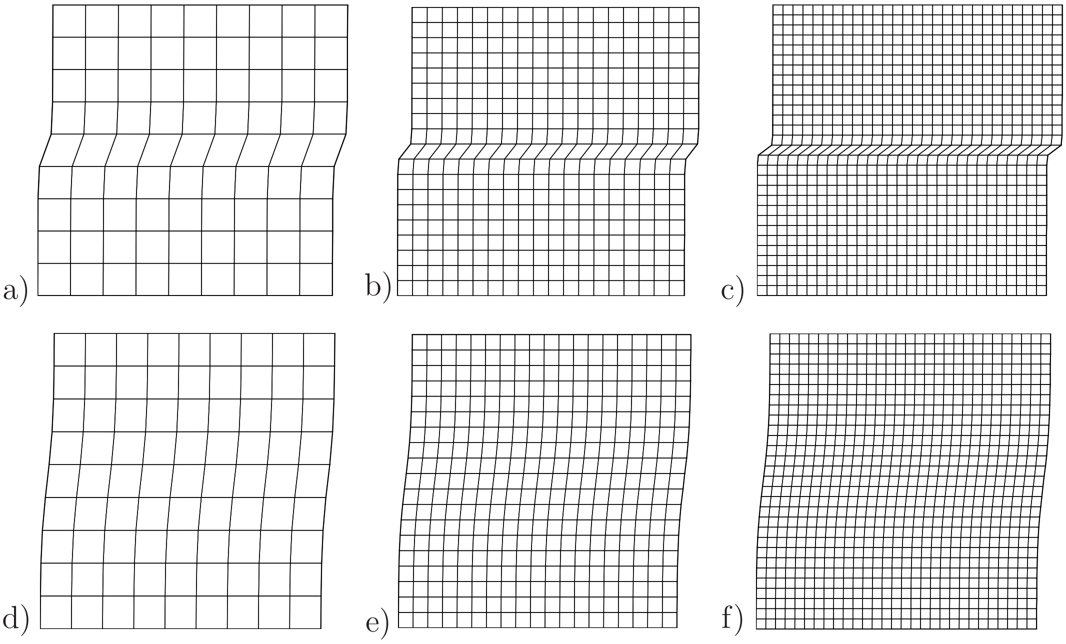

Figure 4.19: Shear-test of squared specimen. Deformed meshes at a final deformation of $u = 0.5$ mm for a)–c) local analysis $l = 0.000$ mm, and d)–f) nonlocal analysis $l = 0.012$ mm. Results are plotted for the three discretizations 9×9, 19×19, and 29×29 elements.

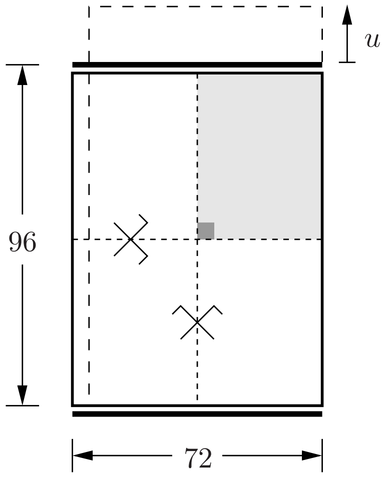

Figure 4.20: Cross shearing of specimen in tension. Geometry and boundary conditions. Due to the symmetry of the boundary value problem, only one quarter is discretized. To trigger localization, the threshold energy ψ_c in the lower left element is reduced by 5%.

results that lie beyond snap-through or snap-back points in the post-critical regime of the deformation process. A classical load- or deformation-driven solution strategy fails at these critical points, where the load-displacement curve shows a horizontal or vertical tangent, respectively. Unlike the local simulations, the nonlocal computations allow for a standard displacement driven solution scheme with constant displacement increments throughout the entire simulation. The particular structural response of the underlying boundary value problem is depicted in Figure 4.17. For local simulations with $l = 0.000$ mm and different discretizations, the load deflection curves document a severe mesh-dependency, see Figure 4.17a). In contrast, as depicted in Figure 4.17b), nonlocal simulations with $l = 0.012$ mm yield mesh-objective results. The according contour plots of the damage field d for a local analysis are depicted in Figure 4.18a)–c) and the corresponding contour plots of a nonlocal analysis are plotted in Figure 4.18d)–f). Clearly, in the case of local solutions for an increasing number of elements, the width of the localization zone tends to zero, i.e. localization occurs in one row of elements. In contrast, the nonlocal solutions exhibit shear bands with finite widths that spread over several elements. This effect is documented in Figure 4.19a)–c) for the deformed meshes of the local solutions, and in Figure 4.19d)–f) for the deformed meshes of the nonlocal ones. Hereby, the latter show the typical s-shaped deformed configuration.

4.3.7.2. Cross Shearing of Specimen in Tension. The second numerical test is concerned with a specimen subjected to tensile loading resulting into cross shearing. The geometric setup and the loading of the boundary value problem are depicted in Figure 4.20. Due to the underlying symmetry, only one quarter of the specimen is discretized using 9×20, 18×40, and 36×80 alternative $Q1E5$-enhanced strain elements. In contrast to the previous example, the shear band will not be aligned to the element edges. Thus, the employment of an enhanced strain formulation becomes necessary in order to resolve the more complex shear band pattern. For a detailed discussion of a Hu-Washizu-type enhanced strain formulation that is embedded into the multi-field context, the reader is referred to Appendix B. To trigger damage localization in the center of the specimen, the constitutive threshold energy ψ_c in the lower left element of the discretization is reduced

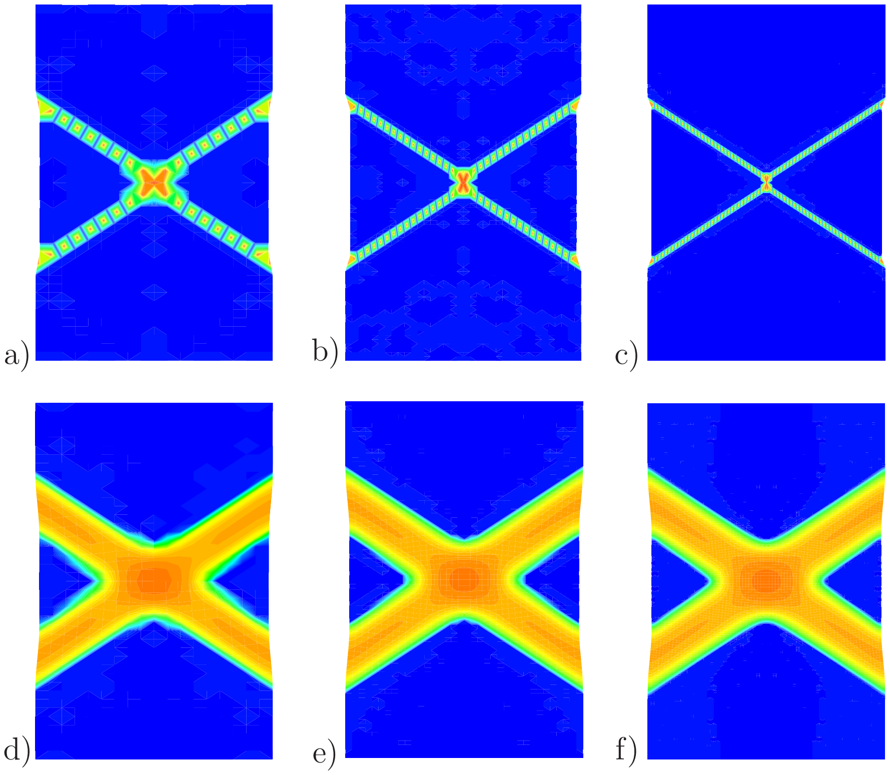

Figure 4.21: Cross shearing of specimen in tension. Damage distribution d at a final deformation of $u = 4.0$ mm for a)–c) local analysis $l = 0.000$ mm, and d)–f) nonlocal analysis $l = 0.003$ mm. Results are plotted for the discretizations 9×20, 18×40, and 36×80 elements.

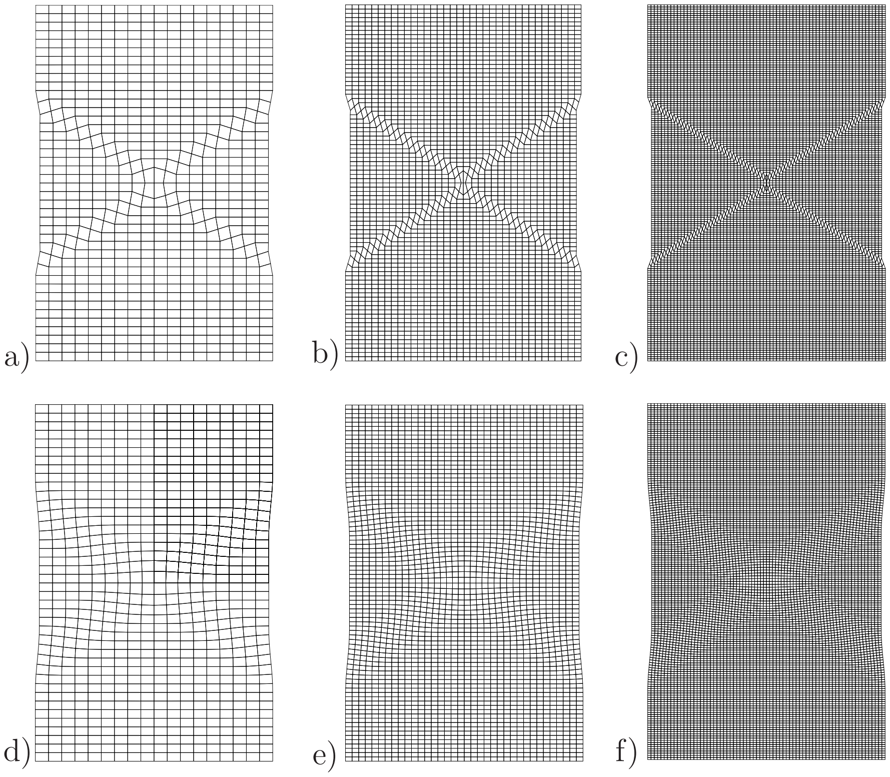

Figure 4.22: Cross shearing of specimen in tension. Deformed meshes at a final deformation of $u = 4.0$ mm for a)–c) local analysis $l = 0.000$ mm, and d)–f) nonlocal analysis $l = 0.003$ mm. Results are plotted for the discretizations 9×20, 18×40, and 36×80 elements.

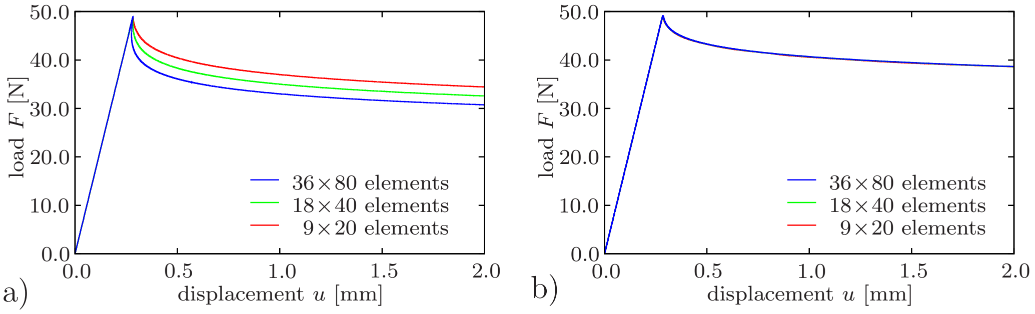

Figure 4.23: Cross shearing of specimen in tension. Load-deflection curves for a) mesh-dependent, local analysis with $l = 0.000$ mm and b) mesh-objective, nonlocal analysis with $l = 0.003$ mm for computations with 9×20, 18×40, and 36×80 elements.

by 5%. Again, the bulk modulus is chosen to $\lambda = 121.15$ kN/mm^2, the shear modulus to $\mu = 80.77$ kN/mm^2, and the threshold energy to $\psi_c = 8.08\times10^{-3}$ kN/mm^2. To obtain a solution very close to the rate-independent limit, the viscosity is chosen to $\eta = 1\times10^{-6}$ kN s/mm^2. The parameter to influence the damage function (4.33) is chosen to $\nu = 0.6$. The overall solution strategy is an updated normal plane method in combination with a full Newton-type iteration. Again, especially for the local simulations with dense meshes, an arc-length method becomes necessary to obtain results beyond the peak load. In contrast, the nonlocal simulations are performed in a standard displacement driven context, where the displacement increments are kept constant throughout the simulations. At the final stage of the deformation process, the corresponding contour plots of the damage field d are given in Figure 4.21. The resulting contour plots for a local analysis can be found in Figure 4.21a)–c), those obtained for a nonlocal solution in Figure 4.21d)–f). The deformed meshes for the three different discretizations at the final stage of the deformation are displayed in Figure 4.22. Clearly, the local computations exhibit a localization in one row of elements, whereas the nonlocal computations yield the typical double s-shaped deformations. For local computations with $l = 0.000$ mm, the mesh-dependent structural response is plotted in Figure 4.23a), the mesh-objective results of computations which involve a length scale of $l = 0.003$ mm are displayed in Figure 4.23b). Obviously, the local simulations yield unphysical, mesh-dependent results and exhibit damage localization in regions with vanishing width. In contrast, the nonlocal simulations, which are performed in combination with a length scale parameter $l = 0.003$ mm, yield mesh-objective results and localization zones with a finite width, independent of the discretization.

5. Variational-Based Phase Field Modeling of Fracture

The variational-based approach to phase field modeling of fracture offers new perspectives towards the theoretical and computational modeling of complex crack topologies. Classical numerical approaches towards the modeling of the sharp crack discontinuity, such as cohesive zone formulations, interface element formulations, or element and nodal enrichment strategies suffer when modeling three-dimensional problems with crack branching, see for example Miehe, Gürses & Birkle [123], Miehe & Gürses [122], and Gürses & Miehe [61] for a sharp modeling of crack surfaces. In contrast, the phase field approach towards fracture avoids the modeling of discontinuities and can be implemented into the multi-field finite element solution scheme as outlined at the end of Chapter 3 in a straight forward manner. The model discussed in Hakim & Karma [74] bases on a Ginzburg-Landau evolution equation for the fracture phase field and is fully viscous in nature. No differentiation is made between energy storage and dissipation. The rate-independent approach towards brittle fracture Bourdin, Francfort & Marigo [16] models the irreversible character of the fracturing processes on a time-discrete level by setting hard Dirichlet-type boundary conditions on the fracture phase field. Furthermore both models allow for an energy release in both tension and compression yielding an unrealistic material behavior. Only boundary value problems with tensile stresses in the full solid domain can be considered. In general, these approaches are not thermodynamically consistent and can only be applied to monotonous loading cases.

In the subsequent treatment of this chapter, according to the recent publication by Miehe, Welschinger & Hofacker [130], a thermodynamically consistent model of phase field fracture is constructed that overcomes the aforementioned difficulties. See also the proceeding contribution by Hofacker, Welschinger & Miehe [82]. Of particular interest is a descriptive and comprehensive representation of the basic ingredients and its embedding into the very general theory of gradient-type standard dissipative solids as outlined in Chapter 3. From the viewpoint of material modeling, the phase field approach to fracture is conceptually in line with the previously discussed formulation of damage mechanics. Thus, the underlying model of fracture can be looked at as a specific gradient-type damage model with a particular definition of the energy function in terms of a gradient-type regularized surface energy. In analogy to the gradient-type damage model, an emphasis is placed on a differentiation between energetic and dissipative mechanisms. The irreversibility of the fracturing/damaging process is hereby taken into account by the design of appropriate non-smooth, rate-independent dissipation functions. Alternative smooth representations of the dissipation functions are introduced yielding model I in a penalty-type two-field setting and model II in a viscous over-force three-field setting. Model I is very close to that of Bourdin, Francfort & Marigo [16] but differentiates between energy storage and dissipative mechanisms and takes into account the irreversibility in a different way. Model II can be considered as a time-regularization of model I, where the evolution equation of the fracture phase field exhibits a characteristic Ginzburg-Landau structure. Both models describe for a vanishing length scale parameter and vanishing viscosity Griffith's quasi-static crack propagation in solids.

This chapter is organized as follows. First, a short review on Griffith's energetic approach to fracture is presented which mainly bases on the introduction of an additional energetic term associated with the creation of new crack surfaces. A subsequent step is concerned with the design of a phase field approximation of sharp crack topologies that circumvents

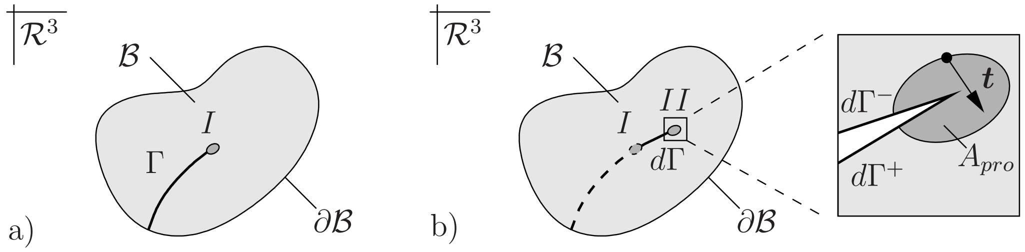

Figure 5.1: Crack propagation. a) Continuum with fracture process zone A_{pro} in its configuration I at time t. b) Continuum with cracked configuration II at time $t + dt$.

the numerical treatment of sharp crack discontinuities. This approximation is based on a *regularized crack surface functional* that Γ-converges for a vanishing length scale parameter towards the sharp crack topology. Hereby, the crack functional is considered as the crack surface itself that is only allowed to *stay constant* or *grow* in time. Dissipation functions that satisfy this postulate are then related to the evolution of the diffusive crack topology. As a consequence, the dissipation function depends on the rate of the fracture phase field and its gradient, characterizing a gradient-type dissipative material. A next step is concerned with the description of the energy storage mechanism. An *isotropic* and *anisotropic* degradation of the free energy is introduced, where the isotropic formulation yields unrealistic crack propagation in tension and compression and the anisotropic one a physically motivated crack propagation in tension only. With the constitutive functions at hand, the coupled balance equations for model I and model II are obtained from the argument of virtual power, their algorithmic representations from the application of the previously discussed incremental variational principle. The chapter closes with a representative set of numerical examples.

5.1. A Review on Griffith's Energetic Approach to Fracture

The scope of this section is to give the reader an introduction to Griffith's energetic approach to fracture introduced in the seminal work by GRIFFITH [58]. A comprehensive overview over fracture mechanics in the more general case provides the book by GROSS & SEELIG [59]. Crack propagation is accompanied by irreversible processes of breaking bonds on the micro-scale of the material. Energies related to this fracture process are taken into account by the introduction of additional energetic terms in the balance of energy (2.91). This fracture-related term describes e.g. a surface energy, an energy that is related to microscopic plastic deformations, possible chemical, or electro-magnetical energies. Without specifying these energies in detail, they are summarized in what follows by the quantity $\mathcal{T}$. As a consequence, the balance of energy (2.91) can be generalized to

$$\frac{d}{dt}\mathcal{E}_{tot} = \frac{d}{dt}[\mathcal{K} + \mathcal{U} + \mathcal{T}] = \mathcal{P}_{ext} + \mathcal{Q}_{ext}\,, \tag{5.1}$$

where $\mathcal{K}$ is the kinetic energy, $\mathcal{U}$ the internal energy, $\mathcal{P}_{ext}$, and $\mathcal{Q}_{ext}$ the mechanical and thermal external power. This balance principle has to be satisfied at the onset and the continuation of the fracturing process. For irreversible crack propagation the evolution of the fracture-related energetic term has to be positive

$$\dot{\mathcal{T}} \geq 0\,. \tag{5.2}$$

As depicted in Figure 5.1, fracture happens in a process zone A_{pro} with a volume that is small compared to the volume of the entire volume of the body $\mathcal{B}$. This motivates the split of the energy balance (5.1) into a part that is valid for the process zone

$$\dot{\mathcal{T}} =: -\mathcal{P}_{pro} \tag{5.3}$$

and a part that is valid in the remaining body

$$\frac{d}{dt}[\mathcal{K} + \mathcal{U}] = \mathcal{P}_{ext} + \mathcal{Q}_{ext} + \mathcal{P}_{pro}\,. \tag{5.4}$$

The minus sign in $-\mathcal{P}_{pro}$ describes the transport of energy into the process zone. Restricting to mechanical fracture energies, this term can be defined as

$$\mathcal{P}_{pro} := \int_{A_{pro}} \boldsymbol{t} \cdot \dot{\boldsymbol{u}}\, dA\,. \tag{5.5}$$

Crack propagation is accompanied by a continuous creation of new surface inside the bulk material. Thus, consider the states I and II of the fracture process evaluated at times t and $t + dt$ as depicted in Figure 5.1. Obviously, within this infinitesimal time dt, the material gets separated along the crack surface $d\Gamma$. Material points on that surface unload from the fully stressed state $\boldsymbol{t} \neq \boldsymbol{0}$ to the stress free state $\boldsymbol{t} = \boldsymbol{0}$. The work, i.e. the energy transport into the process zone, is summarized by

$$d\mathcal{W}_{pro} = \mathcal{P}_{pro}\, dt = \int_{d\Gamma^{\pm}} \int_{I}^{II} \boldsymbol{t} \cdot d\boldsymbol{u}\, dA\,. \tag{5.6}$$

Here $d\Gamma^{\pm}$ indicates that the work done by the forces on both sides of the newly created crack surface has to be considered. At the same time when $d\Gamma$ is created, the fracture energy changes by $d\mathcal{T}$ proportional to $d\Gamma$. Imagine the fully cracked state II as *fracture surface energy* distributed along the surface $d\Gamma^{\pm}$. Then, the relation holds

$$d\mathcal{T} = \dot{\mathcal{T}}\, dt = 2\gamma d\Gamma\,, \tag{5.7}$$

where in many cases the *specific fracture surface energy* γ is considered as material constant. Note in this context the different physical meaning of $\dot{\mathcal{T}}$ and $\mathcal{P}_{pro}$. When moving the process zone A_{pro} during crack propagation by $d\Gamma$, the energy $d\mathcal{T}$ is transformed to another type of energy, e.g. heat or surface energy, via the creation of new surfaces inside the material. In contrast $\mathcal{P}_{pro}$ describes the action of the surrounding continuum on the process zone A_{pro}. Focus now on the special case of an elastic solid with quasi-static crack propagation. In this setting, the process zone is identified as a small zone surrounding the crack tip where inelastic processes occur. The fracture energy $\mathcal{T}$ contains energies related to the separation process and the inelastic deformation processes inside the process zone A_{pro}. In quasi-static deformation processes, the kinetic energy term is not present $\mathcal{K} = 0$, restriction to mechanical loading furthermore yields $\mathcal{Q}_{ext} = 0$. In elastic materials, the internal energy $\mathcal{U}$ can be replaced by the *strain energy* Π_{int}, the external mechanical loads $\mathcal{P}_{ext}$ are assumed to possess a potential Π_{ext}. With these simplifications at hand, the energy balance can be rewritten

$$d\Pi_{int} + d\Pi_{ext} + d\mathcal{T} = 0 \quad \text{or} \quad \frac{d\Pi}{d\Gamma} + \frac{d\mathcal{T}}{d\Gamma} = 0\,. \tag{5.8}$$

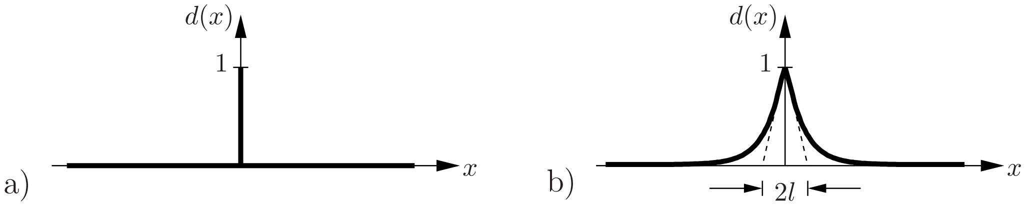

Figure 5.2: Sharp and diffusive crack modeling. a) Sharp crack at axial position $x = 0$ and b) diffusive crack at position $x = 0$ modeled with the length scale l.

As a result, the change of the sum of the total potential $\Pi = \Pi_{int} + \Pi_{ext}$ and the fracture energy $\mathcal{T}$ at crack propagation is zero. In this context, IRWIN [85] introduced the energy release rate $g = -d\Pi/d\Gamma$ and the critical energy release rate $g_c = 2\gamma$ allowing for a reformulation of the energy balance $(5.8)_2$ in the sense

$$\boxed{g = g_c \, .} \tag{5.9}$$

At crack initiation and for the subsequent crack propagation, the energy release rate g has to be equal to the critical energy g_c.

5.2. Phase Field Approximation of Crack Topology

In view of a numerical treatment, the most challenging part in fracture mechanics is the modeling of the crack itself, i.e. an evolving discontinuity in the solid domain. As initially mentioned, there exist several approaches to handle this problem, but they all come along with a strong numerical effort. Focusing on the crack as a purely geometric object first, the crack is not considered as a sharp discontinuity, it is approximated by a smooth phase field. It turns out that the governing equation for this phase field can be solved by a standard finite element method, which later plays an important role when defining the energy or the dissipation which is related to this regularized surface.

5.2.1. Motivation. One-Dimensional Cracked Bar. In order to motivate the smooth approximation of crack topologies, consider an infinitely expanded bar with cross-section A, occupying the domain $\mathcal{B} = \Gamma \times L$ with $L = [-\infty, +\infty]$ and the axial position $L \in x$. Assume at position $x = 0$ a crack of the bar, where Γ is the fully broken crack surface. This *sharp crack topology* is captured by an auxiliary field variable $d(x) \in [0, 1]$ with

$$d(x) := \begin{cases} 1 & \text{for } x = 0 \\ 0 & \text{otherwise} \, , \end{cases} \tag{5.10}$$

characterizing for $d = 0$ the unbroken state and for $d = 1$ the fully broken state of the material, see Figure 5.2a) for an illustration. In the following, the auxiliary variable $d(x)$ is denoted the *crack phase field*. Clearly, this interpretation is directly related to the continuum theory of damage, where the scalar valued parameter d describes in a homogenized macroscopic sense the development of micro cracks and micro voids, see also the definition (4.30). Based on these ideas, the non-smooth fracture phase field (5.10) is approximated via the exponential function

$$d(x) = e^{-|x|/l} \, . \tag{5.11}$$

It diffusively spreads the crack over the axial domain L of the bar and thus represents a *regularized* or *diffusive crack topology*, see Figure 5.2b). The degree of regularization is governed by the length scale parameter l and gives for $l \to 0$ the non-smooth crack topology (5.10). The exponential function (5.11) possesses the property

$$d(0) = 1 \quad \text{and} \quad d(\pm\infty) = 0 \tag{5.12}$$

and represents the solution of the homogeneous differential equation

$$d(x) - l^2 d''(x) = 0 \;\text{ in }\; \mathcal{B}\,, \tag{5.13}$$

subjected to the Dirichlet-type boundary conditions (5.12). Note that this differential equation is the Euler equation of the variational principle

$$\{\, d \,\} = \arg\{ \inf_{d \in \mathcal{W}_d} \Pi(d) \,\} \quad \text{with} \quad \mathcal{W}_d := \{\, d \,|\, d(0) = 1, d(\pm\infty) = 0 \,\}\,, \tag{5.14}$$

expressed in terms of the functional

$$\Pi(d) = \frac{1}{2} \int_{\mathcal{B}} \{\, d^2 + l^2 d'^2 \,\}\, dV\,. \tag{5.15}$$

This functional can easily be obtained by integrating a Galerkin-type weak form of the differential equation (5.13). The exponential function (5.15) together with $dV = \Gamma\, dx$ yields

$$\Pi(d = e^{-|x|/l}) = l\Gamma\,, \tag{5.16}$$

relating the functional Π to the crack surface Γ. As a consequence, the functional

$$\boxed{\Gamma_l(d) := \frac{1}{l}\Pi(d) = \frac{1}{2l} \int_{\mathcal{B}} \{\, d^2 + l^2 d'^2 \,\}\, dV} \tag{5.17}$$

is introduced as an alternative to the functional (5.15). Obviously, the minimization of this functional also gives the regularized crack topology (5.11) illustrated in Figure 5.2b). As a consequence of the scaling by the factor l, the functional can be considered as the *crack surface* itself. In the underlying one-dimensional problem, the evaluation of $\Gamma_l(d)$ at the solution point $x = 0$ gives for arbitrary length scale parameters l the crack surface Γ. Thus, the crack surface functional Γ_l is considered as a main component of the subsequent modeling of diffusive fracture. A convergence study of the crack surface functional towards the sharp crack surface in the sense of Γ-convergence is discussed in BRAIDES [18]. The Γ-limit of the crack surface functional (5.17) for $l \to 0$ yields the crack surface itself

$$\Gamma_l(d) \to \Gamma \quad \text{with} \quad \Gamma := \int_{\Gamma} dA\,. \tag{5.18}$$

Thus, the functional (5.17) provides the basis for an elliptic regularization of the free discontinuity problem of brittle fracture. BOURDIN, FRANCFORT & MARIGO [16] already used this type of functional to approximate the regularized surface energy in Griffith-type fracture. However, in the representation (5.17), the functional has been introduced in the purely geometric context with regard to the definition of a dissipation potential.

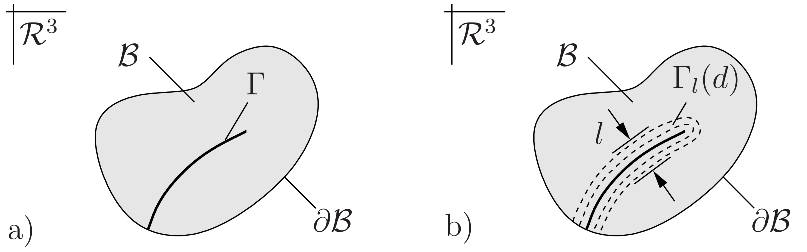

Figure 5.3: Sharp and diffusive crack topology. a) Sharp crack surface Γ embedded into the solid and b) regularized crack surface $\Gamma_l(d)$ as a functional of the crack phase field d.

5.2.2. Variational Problem of Regularized Crack Topology. The approximation of crack topologies outlined above can easily be extended to the multi-dimensional case. Let $\mathcal{B} \subset \mathcal{R}^3$ be the reference configuration of a material body and $\partial\mathcal{B} \subset \mathcal{R}^2$ its surface, see Figure 5.3. To study cracks evolving inside the solid within the time range $\mathcal{T} \subset \mathcal{R}_+$, the time-dependent crack phase field

$$d(\boldsymbol{x}, t) : \begin{cases} \mathcal{B} \times \mathcal{T} \rightarrow [0, 1] \\ (\boldsymbol{x}, t) \quad \mapsto d(\boldsymbol{x}, t) \end{cases} \tag{5.19}$$

is defined on the solid domain $\mathcal{B}$. A multi-dimensional extension of the regularized crack surface functional (5.17) reads

$$\Gamma_l(d) = \int_{\mathcal{B}} \gamma(d, \nabla d)\, dV\,, \tag{5.20}$$

where the *crack surface density function* per unit volume of the solid

$$\boxed{\gamma(d, \nabla d) = \frac{1}{2l} d^2 + \frac{l}{2} |\nabla d|^2} \tag{5.21}$$

has been introduced. This function depends on the crack phase field d and its spatial gradient ∇d and plays a critical role in the subsequent modeling of crack propagation. As illustrated in Figure 5.3a), consider a *sharp crack surface topology* $\Gamma(t) \subset \mathcal{R}^2$ embedded into the solid $\mathcal{B}$ at time t. In analogy to the one-dimensional variational principle (5.14), the regularized crack phase field $d(\boldsymbol{x}, t)$ in $\mathcal{B}$ is obtained from the minimization principle with the Dirichlet-type boundary conditions

$$\{\, d \,\} = \arg\{ \inf_{d \in \mathcal{W}_d} \Pi(d) \,\} \quad \text{with} \quad \mathcal{W}_d := \{\, d \,|\, d = 1 \;\text{ on } \Gamma \,\}\,. \tag{5.22}$$

For an illustration see Figure 5.3b). The Euler equations of this variational principle are

$$d - l^2 \Delta d = 0 \text{ in } \mathcal{B} \quad \text{with} \quad \nabla d \cdot \boldsymbol{n} = 0 \text{ on } \partial\mathcal{B}\,, \tag{5.23}$$

where Δd is the Laplacian of the fracture phase field and $\boldsymbol{n}$ the outward normal on $\partial\mathcal{B}$.

5.2.3. FE-Discretization of Variational Problem. The general numerical treatment is now applied to solve for the scalar valued crack phase field only. Restricting to two-dimensional problems, the discrete counterpart to the constitutive state

$$\mathfrak{u} := \{\, d \,\} \quad \text{and} \quad \mathfrak{c}(\mathfrak{u}) := \{\, d, d_{,1}, d_{,2} \,\} \tag{5.24}$$

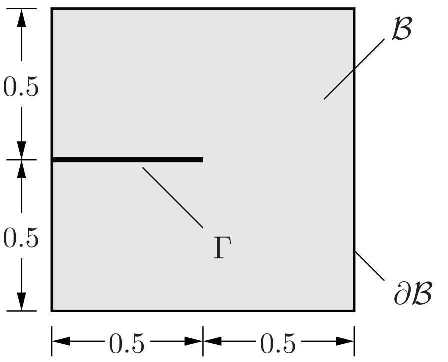

Figure 5.4: Approximation of crack topology. Squared domain with sharp crack $\Gamma = 0.5$.

has to be considered. In a global finite element solution procedure, the nodal fracture phase field is obtained in one solution step via

$$\boldsymbol{\mathfrak{d}} = -[\Gamma^h_{l,\boldsymbol{\mathfrak{d}}\boldsymbol{\mathfrak{d}}}]^{-1} \cdot \Gamma^h_{l,\boldsymbol{\mathfrak{d}}} \,, \tag{5.25}$$

based on the linear residual and the tangent matrix

$$\Gamma^h_{l,\boldsymbol{\mathfrak{d}}} := \int_{\mathcal{B}^h} \{ \check{\boldsymbol{B}}^T [\partial_{\boldsymbol{\mathfrak{c}}^h}\gamma] \} \, dV \quad \text{and} \quad \Gamma^h_{l,\boldsymbol{\mathfrak{d}}\boldsymbol{\mathfrak{d}}} := \int_{\mathcal{B}^h} \{ \check{\boldsymbol{B}}^T [\partial_{\boldsymbol{\mathfrak{c}}^h\boldsymbol{\mathfrak{c}}^h}\gamma] \check{\boldsymbol{B}} \} \, dV \,. \tag{5.26}$$

The approximation matrix for the constitutive state reads

$$[\check{\boldsymbol{B}}]^e_i = \begin{bmatrix} N & N_{,1} & N_{,2} \end{bmatrix}^T_i \,. \tag{5.27}$$

At node i of the finite element mesh, the generalized displacement vector is defined by

$$\boldsymbol{\mathfrak{d}}_i = [\, d \,]_i \,, \tag{5.28}$$

containing the nodal value of the fracture phase field d only.

5.2.4. Numerical Example. Approximation of Crack Topology. The following numerical example demonstrates the regularization of a crack topology for an elementary model problem. As depicted in Figure 5.4, consider a two-dimensional continuum with a *sharp crack surface* Γ from the left side to the center of the specimen. On the exterior boundary $\partial\mathcal{B}$, the natural Neumann-type boundary condition $(5.23)_2$ is prescribed on the crack surface Γ, the Dirichlet-type boundary condition $d = 1$ is set for the crack phase field. Consider the finite element computation of the crack phase field d in the domain $\mathcal{B}$ according to the linear solution procedure (5.25), in combination with given values of the length scale parameter l. The finite element mesh needs a certain minimum element size h in order to resolve this length scale. This is demonstrated in Figure 5.5 for finite element meshes with a constant element size h consisting of four node quadrilateral elements. This elementary study shows that an element size

$$h > l/2 \tag{5.29}$$

is needed in order to resolve the *regularized crack surface* $\Gamma_l(d)$ such that we have $\Gamma_l(d) \approx \Gamma$ in the finite element approximation. Clearly, this resolution is only needed in subdomains close to the crack surface. Hence, an h-adaptive finite element solution procedure with

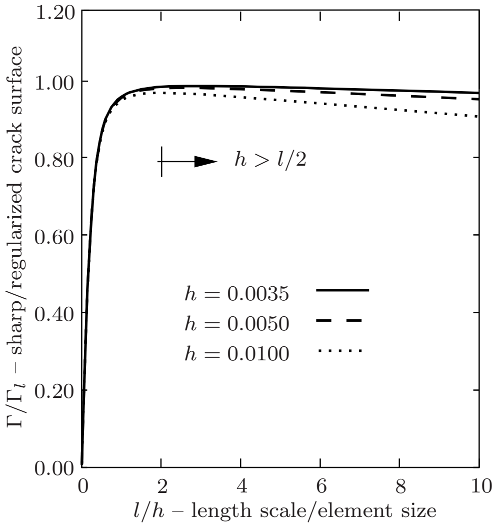

Figure 5.5: Minimum size of finite elements. A reasonable accuracy of the crack topology approximation $\Gamma_l \approx \Gamma$ needs for quadrilateral element meshes an element size $h > l/2$.

a minimum element size close to (5.29) is appropriate. Figure 5.6 shows finite element simulations for different length scales $l = \{\, 0.20, 0.10, 0.007 \,\}$ based on a very fine mesh with constant mesh size $h = 0.0035$ consisting of 90000 four node quadrilaterals. The large length scale $l = 0.20$ yields the approximated regularized crack surface $\Gamma_l = 0.5944$ depicted in Figure 5.6a). The smallest length scale $l = 0.007$ gives $\Gamma_l = 0.5090 \approx \Gamma = 0.5$ as shown in Figure 5.6c).

5.3. A Framework for Diffusive Fracture at Small Strains

5.3.1. Basic Kinematics and State Variables. Aiming at a continuum mechanical description of diffusive fracture at small deformations, besides the macroscopic displacement field $\boldsymbol{u}$ the scalar valued crack phase field d is introduced

$$\bar{\boldsymbol{u}} := \{\, \boldsymbol{u} \,\} \quad \text{and} \quad \check{\boldsymbol{u}} := \{\, d \,\}\,. \tag{5.30}$$

In accordance with the basic kinematics of damage mechanics (4.31), the fracture phase field can also be interpreted as a scalar quantity that describes in a homogenized sense the gradual deterioration process of the microstructure via micro-crack and micro-void

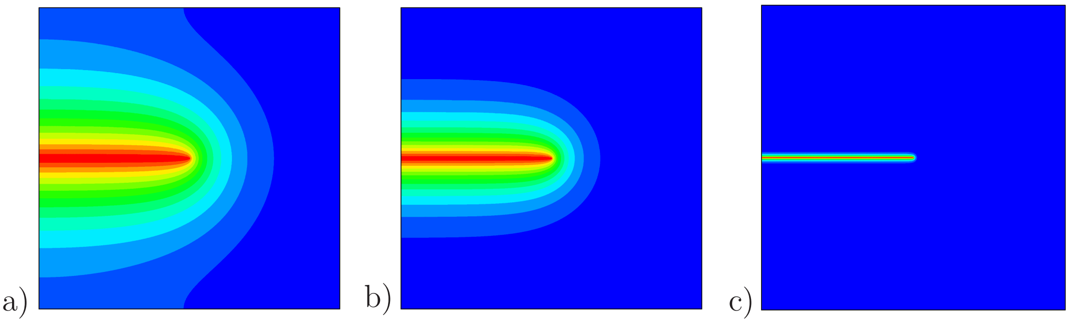

Figure 5.6: Regularized crack surfaces $\Gamma_l(d)$ governed by the crack phase field d for different length scales. a) $l = 0.20$ with $\Gamma_l = 0.5944$, b) $l = 0.10$ with $\Gamma_l = 0.5507$, and c) $l = 0.007$ with $\Gamma_l = 0.5090$ obtained with a mesh of size $h = 0.0035$.

nucleation. Recalling the regularized crack surface functional (5.20) that bases on the crack surface density function, the constitutive state

$$\mathfrak{c} := \{\, \boldsymbol{\varepsilon}, d, \nabla d \,\} \tag{5.31}$$

contains not only the strain tensor $\boldsymbol{\varepsilon} := \nabla_s \boldsymbol{u}$, but also the fracture phase field and its gradient. This set of state variables builds the basis for the further development.

5.3.2. Dissipation Functions for Crack Evolution. The above outlined definition of the regularized crack surface is exploited to model the time dependent crack evolution, which is governed by some energetic driving forces. Hereby, the crack is considered to be *fully dissipative* in nature. One basic feature is the irreversibility of the cracking process. As a consequence, the regularized crack surface is only allowed to grow or to stay constant in time

$$\dot{\Gamma}_l(\dot{d}; d) := \frac{d}{dt}\Gamma_l(d(\boldsymbol{x}, t)) \geq 0\,. \tag{5.32}$$

Making use of the regularized crack surface functional (5.20), this postulate is reformulated

$$\dot{\Gamma}_l(\dot{d}; d) = \int_{\mathcal{B}} \dot{\gamma}\, dV = \int_{\mathcal{B}} (\delta_d \gamma)\, \dot{d}\, dV \geq 0\,, \tag{5.33}$$

expressed in terms of the variational derivative of the crack surface density function

$$\delta_d \gamma := \partial_d \gamma - \operatorname{div}[\partial_{\nabla d}\gamma] = \frac{1}{l}[d - l^2 \Delta d]\,. \tag{5.34}$$

The irreversibility constraint of the crack evolution can be satisfied by *locally* ensuring a positive variational derivative of the crack surface function and a positive evolution of the fracture phase field

$$\delta_d \gamma \geq 0 \quad \text{and} \quad \dot{d} \geq 0\,. \tag{5.35}$$

The former condition is satisfied by a constitutive assumption relating the functional derivative to a positive energetic driving force. The latter condition guarantees the non-reversible character of the fracture phase field. According to the general consideration in Section 3.5.5, a dissipation functional is constructed

$$D(\dot{d}; d) = \int_{\mathcal{B}} \phi(\dot{\mathfrak{c}}; \mathfrak{c})\, dV = \int_{\mathcal{B}} \partial_{\dot{\mathfrak{c}}}\phi(\dot{\mathfrak{c}}; \mathfrak{c}) \cdot \dot{\mathfrak{c}}\, dV = \mathcal{D}(\dot{d}; d)\,, \tag{5.36}$$

which describes a rate-independent process, where the dissipation potential functional D is identical to the dissipation $\mathcal{D}$. Hereby, the dissipation function ϕ bases on the possible additive decomposition

$$\boxed{\phi(\dot{\mathfrak{c}}; \mathfrak{c}) = \underbrace{\check{\phi}_{loc}(\dot{d}; d)}_{\text{hom. micro-diss.}} + \underbrace{\check{\phi}_{non}(\nabla\dot{d}; \nabla d)}_{\text{inh. micro-diss.}}} \tag{5.37}$$

allowing for a separate discussion of the contributions that arise from homogeneously and inhomogeneously distributed rates of the fracture phase field.

5.3.2.1. Model I: Canonical Two-Field Setting. The first canonical approach to model the dissipative mechanism that a priori fulfills the growth condition $(5.35)_2$ bases on the *rate-independent* or *non-smooth* constitutive dissipation function per unit volume

$$\phi(\dot{\mathfrak{c}};\mathfrak{c}) = g_c\dot{\gamma}(\dot{d},\nabla\dot{d};d,d) + I_+(\dot{d})\,. \tag{5.38}$$

The material constant g_c is a constitutive threshold related to the critical Griffith-type fracture energy. Here, the first term indicates the local energy release due to the crack evolution and $I_+(x)$ is the non-smooth indicator function for the set $\mathcal{R}_+$ of positive real numbers. The latter has been introduced in the context of damage mechanics, it reads

$$I_+(x) = \left\{\begin{array}{cl} 0 & \text{if } x > 0 \\ +\infty & \text{otherwise}\end{array}\right. \tag{5.39}$$

and ensures a positive evolution of the fracture phase field. For a visualization see Figure 4.11a). An approximation of the non-smooth indicator function is given by

$$I_+^{\epsilon}(x) = \frac{\epsilon}{2}\langle x\rangle_-^2\,, \tag{5.40}$$

based on the ramp function $\langle x\rangle_- := (|x|-x)/2$ of the set $\mathcal{R}_-$ of negative real numbers, see Figure 4.11d). Obviously, the regularization parameter ϵ exactly ensures for $\epsilon\to\infty$ the growth condition $(5.35)_2$. All representations of the dissipation function discussed in the sequel have in common the nonlocal term

$$\boxed{\check{\phi}_{non}(\nabla\dot{d};\nabla d) = (g_c l\nabla d)\cdot\nabla\dot{d}\,,} \tag{5.41}$$

they only differ in the formulation of the local term. The first possibility bases on the purely rate-independent dissipation function

$$\boxed{\check{\phi}_{loc}(\dot{d};d) := \psi_c(d)\,\dot{d} + I_+(\dot{d}) \quad \text{with} \quad \psi_c(d) = \frac{g_c}{l}d} \tag{5.42}$$

that can alternatively be given as a penalty-type regularized dissipation function

$$\boxed{\check{\phi}_{loc}^{\epsilon}(\dot{d};d) := \psi_c(d)\,\dot{d} + \frac{\epsilon}{2}\langle\dot{d}\rangle_-^2\,.} \tag{5.43}$$

The latter one is used as a first model approach towards regularized fracture.

5.3.2.2. Model II: Extended Three-Field Setting. An alternative formulation of the dissipation function that a priori satisfies the growth condition $(5.35)_2$ of the fracture phase field is constructed by introducing the dissipative thermodynamic driving force dual to the rate of the fracture phase field

$$\check{\boldsymbol{f}} := \{\,\beta\,\}\,. \tag{5.44}$$

For rate-independent processes this force field is constrained by the threshold function

$$\varphi(\beta;d) = \beta - \psi_c(d) \le 0\,, \tag{5.45}$$

characterizing for $\varphi(\beta; d) < 0$ an elastic domain without diffusive crack accumulation. Note that in contrast to the threshold function used in damage mechanics (4.49), this threshold function also depends on the current fracture phase field d. An appropriate dissipation function is obtained by the constrained optimization problem

$$\check{\phi}_{loc}(\dot{d}; d) = \sup_{\beta \in \mathbb{E}} [\, \beta \, \dot{d} \,] \quad \text{with} \quad \mathbb{E} := \{\, \beta \,|\, \varphi(\beta; d) \leq 0 \,\} \, . \tag{5.46}$$

This fully rate-independent constrained optimization problem is solved by means of a Lagrange-multiplier method

$$\boxed{\check{\phi}_{loc}(\dot{d}; d) = \sup_{\beta, \, \lambda \geq 0} [\, \beta \, \dot{d} - \lambda \, \varphi(\beta; d) \,] \, ,} \tag{5.47}$$

which bases on the introduction of the Lagrange multiplier λ. The necessary condition of this local constrained optimization problem identifies the Lagrange parameter $\lambda = \dot{d}$ with the evolution of the fracture phase field and results into

$$\dot{d} \geq 0 \quad \text{and} \quad \beta \leq \psi_c(d) \quad \text{and} \quad \dot{d} \, (\beta - \psi_c(d)) = 0 \, . \tag{5.48}$$

These conditions determine the local evolution $\dot{d}$ of the phase field in terms of the local driving force β and the phase field d itself. Furthermore, $(5.48)_1$ includes explicitly the irreversibility condition. A *viscous regularization* of the above rate-independent formulation is founded on the following unconstrained optimization problem

$$\boxed{\check{\phi}^{\eta}_{loc}(\dot{d}; d) = \sup_{\beta} [\, \beta \, \dot{d} - \frac{1}{2\eta} \langle \, \beta - \psi_c(d) \, \rangle_+^2 \,] \, ,} \tag{5.49}$$

where $\langle x \rangle_+ := (|x| + x)/2$ is the ramp function of the set of positive real numbers $\mathcal{R}_+$, see Figure 4.11c). The necessary condition of this unconstrained optimization problem reads

$$\dot{d} = \frac{1}{\eta} \langle \, \beta - \psi_c(d) \, \rangle_+ \tag{5.50}$$

and satisfies the irreversibility constraint $(5.35)_2$. The viscosity η characterizes a viscous over-force response governing the evolution of the fracture phase field. For $\eta \to \infty$, the rate-independent model (5.47) is recovered. The Lagrange-multiplier λ is identified

$$\lambda := \frac{1}{\eta} \langle \, \beta - \psi_c(d) \, \rangle_+ \, . \tag{5.51}$$

Due to the limit character of the smooth over-force setting (5.49), this formulation is highly attractive for a numerical implementation and is considered as a second approach to model diffusive fracture. A graphical interpretation of the four different dissipation functions is given in Figure 5.7. In the sense of convex analysis, the local non-smooth dissipation functions (5.42) and (5.47) are identical, where in the latter one the dual dissipation function $\check{\phi}^*_{loc}(\beta; d) = \lambda \, \varphi(\beta; d)$ can be identified. In Figure 5.7, these dual functions are displayed in dotted lines, their regularized counterparts are shown in solid lines.

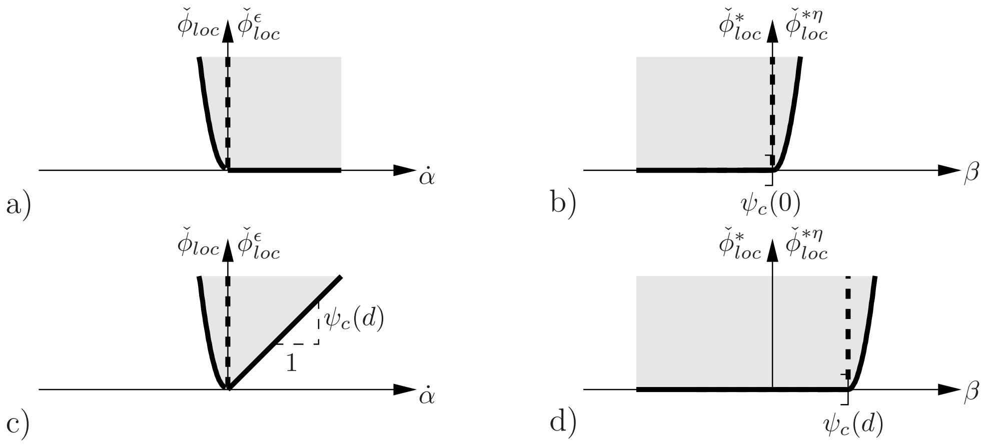

Figure 5.7: Dissipation functions for regularized fracture. Canonical penalty-type representation $\check{\phi}^{\epsilon}_{loc}$ evaluated for a) $d = 0$ and c) $d \in [0,1]$. Viscous over-force representation $\check{\phi}^{*\eta}_{loc} = \frac{1}{2\eta}\langle \beta - \psi_c(d)\rangle^2_+$ evaluated for b) $d = 0$ and d) $d \in [0,1]$. The corresponding self-dual non-smooth counterparts $\check{\phi}_{loc}$ and $\check{\phi}^{*}_{loc}$ are depicted in dotted lines.

5.3.3. Degradation of Energy in Fracturing Solids. In what follows, the focus is put on the constitutive modeling of the material's bulk response. Due to the fracturing process, a degradation of energy occurs that can be modeled in two different ways. Either in a simple, isotropic way where fracture occurs in tension and compression, or in a more realistic, anisotropic way where fracture occurs in tension only. According to the general definition $(3.28)_1$, the free energy stored in the solid $\mathcal{B}$ is given by

$$E(\boldsymbol{u}, d) = \int_{\mathcal{B}} \psi(\mathfrak{c})\, dV\,, \tag{5.52}$$

where the free energy function consists of a contribution that arises from elastic distortions

$$\boxed{\psi(\mathfrak{c}) = \underbrace{\bar{\psi}_{loc}(\boldsymbol{\varepsilon}, d)}_{\text{elast. macro-dist.}} \quad .} \tag{5.53}$$

As indicated before, this contribution has to be specified for isotropic and anisotropic material behavior in the sequel.

5.3.3.1. Isotropic Degradation of Stored Bulk Energy. In the scenario of an *isotropic* degradation process of the stored energy, only the local macroscopic term in the decoupled representation (5.52) has to be specified

$$\boxed{\bar{\psi}_{loc}(\boldsymbol{\varepsilon}, d) = (g(d) + k)\, \psi_0(\boldsymbol{\varepsilon})\,,} \tag{5.54}$$

where $\boldsymbol{\varepsilon} = \nabla_s \boldsymbol{u}$ is the small strain tensor. In this multiplicative ansatz, the ground state energy ψ_0 is the standard free energy function of an uncracked elastic solid, i.e.

$$\psi_0(\boldsymbol{\varepsilon}) = \tfrac{1}{2}\, \lambda\ \mathrm{tr}^{\,2}[\boldsymbol{\varepsilon}] + \mu\ \mathrm{tr}[\boldsymbol{\varepsilon}^2]\,, \tag{5.55}$$

in terms of the bulk modulus λ and the shear modulus μ. In (5.54), $g(d)$ is a monotonically decreasing function characterizing the degradation of stored energy due to the evolution of cracks. It possesses the properties

$$g(0) = 1 \quad \text{and} \quad g(1) = 0 \quad \text{and} \quad g'(1) = 0\,. \tag{5.56}$$

The first two conditions include the limit cases for the unbroken and fully broken state. The last condition ensures that the elastic driving force $\beta^e := \partial_d \psi$ converges to a final value when the fracture phase field converges to the fully broken state $d = 1$. A function that possesses these properties is defined by

$$g(d) = (1 - d)^2 \tag{5.57}$$

and is used for the subsequent treatment. In (5.54), the remaining parameter $k \approx 0$ avoids the complete degradation of the stored energy by leaving an artificial elastic rest energy density $k\psi_0(\boldsymbol{\varepsilon})$ at a fully broken state $d = 1$ of the material. Later, in the numerical analysis it is chosen as small as possible to keep the algebraic conditioning number of the discrete problem well posed. According to (3.39), the rate of the energy storage

$$\mathcal{E}(\dot{\boldsymbol{\varepsilon}}, \dot{d}; \boldsymbol{\varepsilon}, d) := \frac{d}{dt} \int_{\mathcal{B}} \psi(\mathfrak{c})\, dV = \int_{\mathcal{B}} \{\, (\partial_{\boldsymbol{\varepsilon}} \psi) : \dot{\boldsymbol{\varepsilon}} + (\delta_d \psi) \dot{d} \,\}\, dV \tag{5.58}$$

is governed by the total stresses and the elastic driving force

$$\boldsymbol{\sigma} := \partial_{\boldsymbol{\varepsilon}} \psi = [\, (1 - d)^2 + k \,]\, \boldsymbol{\sigma}_0(\boldsymbol{\varepsilon}) \quad \text{and} \quad \beta^e := \delta_d \psi = -2(1 - d)\psi_0(\boldsymbol{\varepsilon}) \tag{5.59}$$

in terms of the stress tensor of a fictitious undamaged solid

$$\boldsymbol{\sigma}_0 := \lambda\ \mathrm{tr}[\boldsymbol{\varepsilon}] \boldsymbol{1} + 2\mu\, \boldsymbol{\varepsilon}\,. \tag{5.60}$$

Note that the elastic driving force β^e is strictly negative and converges to a final value if the fracture phase field converges to the fully broken state $d = 1$.

5.3.3.2. Anisotropic Degradation of Stored Bulk Energy. In the scenario of an *anisotropic* degradation process of the stored energy, only the local macroscopic term in the decoupled representation (5.52) has to be specified

$$\boxed{\bar{\psi}_{loc}(\boldsymbol{\varepsilon}, d) = (g(d) + k)\, \psi_0^+(\boldsymbol{\varepsilon}) + \psi_0^-(\boldsymbol{\varepsilon})\,.} \tag{5.61}$$

It bases on the additive decomposition of the stored energy in the undamaged solid

$$\psi_0(\boldsymbol{\varepsilon}) = \psi_0^+(\boldsymbol{\varepsilon}) + \psi_0^-(\boldsymbol{\varepsilon}) \tag{5.62}$$

into a positive part ψ_0^+ related to tension and a negative part ψ_0^- related to compression. Note that in (5.61) the degradation function $g(d)$ acts on the tension part of the stored energy only. Thus, the model is able to predict crack closing for different loading paths in the case when the strains enter the fully compressive range. The definition of the positive and negative parts of the stored energy bases on the spectral representation of the strains

$$\boldsymbol{\varepsilon} = \sum_{a=1}^{3} \varepsilon_a\, \boldsymbol{n}_a \otimes \boldsymbol{n}_a\,, \tag{5.63}$$

where $\{\varepsilon_a\}_{a=1,2,3}$ are the principal strains and $\{\boldsymbol{n}_a\}_{a=1,2,3}$ the principal strain directions. The energy storage function of an isotropic undamaged solid

$$\psi_0(\boldsymbol{\varepsilon}) = \tfrac{1}{2}\, \lambda\, (\varepsilon_1 + \varepsilon_2 + \varepsilon_3)^2 + \mu\, (\varepsilon_1^2 + \varepsilon_2^2 + \varepsilon_3^2) \tag{5.64}$$

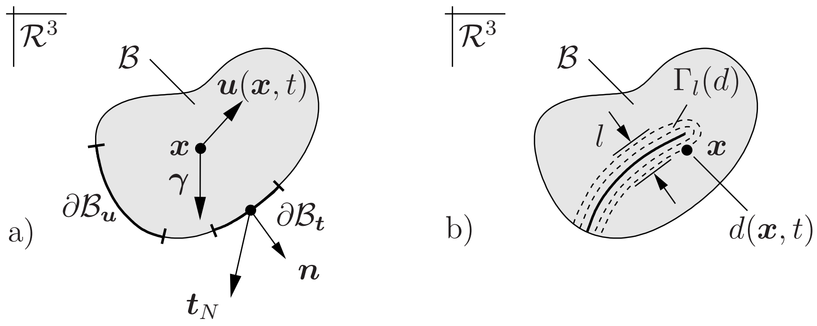

Figure 5.8: Two-field problem of phase field fracture. The displacement field $\boldsymbol{u}$ and the fracture phase field d are defined on the solid domain $\mathcal{B}$, the gradients of the latter account for the length scale l. $\boldsymbol{\gamma}$ is a prescribed body force field. a) The displacement field is constrained by Dirichlet and Neumann boundary conditions $\boldsymbol{u} = \boldsymbol{u}_D$ on $\partial\mathcal{B}_{\boldsymbol{u}}$ and $\boldsymbol{\sigma}\cdot\boldsymbol{n} = \boldsymbol{t}_N$ on $\partial\mathcal{B}_{\boldsymbol{t}}$ with $\partial\mathcal{B}_{\boldsymbol{u}} \cap \partial\mathcal{B}_{\boldsymbol{t}} = \emptyset$. b) The fracture phase field is constrained by the possible Dirichlet-type boundary condition $d = 1$ on Γ and the Neumann-type boundary condition $\nabla d \cdot \boldsymbol{n} = 0$ on the full surface $\partial\mathcal{B}$.

can be expressed in terms of the principal strains. Based on this form of the energy storage function, the positive and negative parts of the energy storage function are defined by

$$\psi_0^{\pm}(\boldsymbol{\varepsilon}) := \tfrac{1}{2}\,\lambda\,\langle\varepsilon_1+\varepsilon_2+\varepsilon_3\rangle_{\pm}^2 + \mu\,(\langle\varepsilon_1\rangle_{\pm}^2 + \langle\varepsilon_2\rangle_{\pm}^2 + \langle\varepsilon_3\rangle_{\pm}^2) \tag{5.65}$$

in terms of the ramp function $\langle x\rangle_+$ of the set of positive real numbers $\mathcal{R}_+$ depicted in Figure 4.11c) and the ramp function $\langle x\rangle_-$ of the set of negative real numbers $\mathcal{R}_-$ depicted in Figure 4.11d). Here, the positive/negative parts of the energy storage function describe contributions due to positive/negative volumetric deformations and due to positive/negative principal strains. For this anisotropic energy storage function, the evolution of the energy storage (5.58) contains the total stresses and the elastic driving force

$$\boldsymbol{\sigma} := \partial_{\boldsymbol{\varepsilon}}\psi = [\,(1-d)^2 + k\,]\,\boldsymbol{\sigma}_0^+(\boldsymbol{\varepsilon}) + \boldsymbol{\sigma}_0^-(\boldsymbol{\varepsilon}) \quad \text{and} \quad \beta^e := \delta_d\psi = -2(1-d)\psi_0^+(\boldsymbol{\varepsilon}) \tag{5.66}$$

in terms of the positive and negative parts of the stress tensor

$$\boldsymbol{\sigma}_0^{\pm} := \sum_{a=1}^{3}[\,\lambda\,\langle\varepsilon_1+\varepsilon_2+\varepsilon_3\rangle_{\pm} + 2\mu\,\langle\varepsilon_a\rangle_{\pm}\,]\,\boldsymbol{n}_a\otimes\boldsymbol{n}_a \tag{5.67}$$

in a fictitious undamaged solid. In this expression, the result $\partial_{\boldsymbol{\varepsilon}}\varepsilon_a = \boldsymbol{n}_a\otimes\boldsymbol{n}_a$ has been employed. Note that in the anisotropic setting the elastic driving force β^e is related to the positive part of the energy storage function only. The stress degradation only affects the positive part of the stress tensor.

5.3.4. Governing Balance Equations of Coupled Problem. In this section, the governing balance equations for the isotropic and anisotropic model in combination with two different representations of the dissipation function are derived. These equations determine the *displacement field* $\boldsymbol{u}$ of the solid and the *fracture phase field* d. The extended multi-field formulation additionally incorporates the local *driving force field* β dual to d. Regarding the displacement field, the boundary of the body is decomposed into a part $\partial\mathcal{B}_{\boldsymbol{u}}$ where the displacements are prescribed by the Dirichlet condition

$$\boldsymbol{u} = \boldsymbol{u}_D \text{ on } \partial\mathcal{B}_{\boldsymbol{u}} \tag{5.68}$$

and a part $\partial\mathcal{B}_{\boldsymbol{t}}$ where the tractions $\boldsymbol{t}_N$ are prescribed by Neumann boundary conditions, see Figure 5.8. Clearly, the common set of these boundaries is zero, i.e. $\partial\mathcal{B}_{\boldsymbol{u}} \cap \partial\mathcal{B}_{\boldsymbol{t}} = \emptyset$. The external mechanical loading is defined by the external power functional

$$\mathcal{P}_{ext}(\dot{\boldsymbol{u}}) = \int_{\mathcal{B}} \boldsymbol{\gamma} \cdot \dot{\boldsymbol{u}}\, dV + \int_{\partial\mathcal{B}_t} \boldsymbol{t}_N \cdot \dot{\boldsymbol{u}}\, dA \tag{5.69}$$

with a given body force field $\boldsymbol{\gamma}$ per unit volume. For the fracture phase field, the Dirichlet-type boundary condition is considered

$$d = 1 \text{ on } \Gamma\,, \tag{5.70}$$

where $\Gamma \subset \mathcal{B}$ is a possible a priori given sharp crack surface. The fracture phase field d is looked at to be driven by the displacement field $\boldsymbol{u}$ of the solid. Thus, no prescribed external loading associated with the fracture phase field is considered. Having the external load functional (5.69), the rate of the energy storage functional (5.58), and the dissipation functional (5.36) at hand, the balance equations are obtained from the standard argument of virtual power

$$\boxed{\mathcal{E}(\dot{\boldsymbol{u}}, \dot{d}) + \mathcal{D}(\dot{d}) - \mathcal{P}_{ext}(\dot{\boldsymbol{u}}) = 0\,.} \tag{5.71}$$

This principle has to be valid for admissible rates $\dot{\boldsymbol{u}}$ and $\dot{d}$ of the displacement and the fracture phase field satisfying the homogeneous form of the Dirichlet boundary conditions

$$\dot{\boldsymbol{u}} \in \mathcal{W}_{\boldsymbol{u}} := \{\, \dot{\boldsymbol{u}} \,|\, \dot{\boldsymbol{u}} = \boldsymbol{0} \text{ on } \partial\mathcal{B}_{\boldsymbol{u}} \,\} \quad \text{and} \quad \dot{d} \in \mathcal{W}_d := \{\, \dot{d} \,|\, \dot{d} = 0 \text{ on } \Gamma \,\}\,. \tag{5.72}$$

The full boundary value problem is now completely described. It only remains to specify the coupled balance equations for the different dissipation functions.

5.3.4.1. Model I: Rate-Independent Setting with Approximated Indicator. For the rate-independent model of diffusive fracture with a regularized dissipation function (5.43), the balance of internal and external power (5.71) yields

$$\begin{aligned} \boldsymbol{0} &= \operatorname{div}[\,((1-d)^2 + k)\,\partial_{\boldsymbol{\varepsilon}}\psi_0(\boldsymbol{\varepsilon})\,] + \boldsymbol{\gamma} \\ 0 &= \frac{g_c}{l}[\,d - l^2\Delta d\,] - [\,2(1-d)\,\psi_0(\boldsymbol{\varepsilon}) + \epsilon\langle\dot{d}\rangle_-\,] \end{aligned} \tag{5.73}$$

for the *isotropic* representation of the free energy function and

$$\begin{aligned} \boldsymbol{0} &= \operatorname{div}[\,((1-d)^2 + k)\,\partial_{\boldsymbol{\varepsilon}}\psi_0^+(\boldsymbol{\varepsilon}) + \partial_{\boldsymbol{\varepsilon}}\psi_0^-(\boldsymbol{\varepsilon})\,] + \boldsymbol{\gamma} \\ 0 &= \frac{g_c}{l}[\,d - l^2\Delta d\,] - [\,2(1-d)\,\psi_0^+(\boldsymbol{\varepsilon}) + \epsilon\langle\dot{d}\rangle_-\,] \end{aligned} \tag{5.74}$$

for the *anisotropic* formulation of the energy storage function.

5.3.4.2. Model II: Rate-Dependent Setting with Threshold Function. For the rate-dependent over-force formulation of the dissipation function (5.49), the balance of internal and external power (5.71) yields

$$\begin{aligned} \boldsymbol{0} &= \operatorname{div}[\,((1-d)^2 + k)\,\partial_{\boldsymbol{\varepsilon}}\psi_0(\boldsymbol{\varepsilon})\,] + \boldsymbol{\gamma} \\ 0 &= g_c l\Delta d + 2(1-d)\,\psi_0(\boldsymbol{\varepsilon}) - \beta \\ 0 &= \dot{d} - \frac{1}{\eta}\langle\beta - \psi_c(d)\rangle_+ \end{aligned} \tag{5.75}$$

for the *isotropic* ground state energy and

$$\begin{aligned} \boldsymbol{0} &= \operatorname{div}[\,((1-d)^2+k)\,\partial_{\boldsymbol{\varepsilon}}\psi_0^+(\boldsymbol{\varepsilon}) + \partial_{\boldsymbol{\varepsilon}}\psi_0^-(\boldsymbol{\varepsilon})\,] + \boldsymbol{\gamma} \\ 0 &= g_c l \Delta d + 2(1-d)\,\psi_0^+(\boldsymbol{\varepsilon}) - \beta \\ 0 &= \dot{d} - \frac{1}{\eta}\langle \beta - \psi_c(d)\rangle_+ \end{aligned} \tag{5.76}$$

for the *anisotropic case*. Due to the presence of the local driving force field β, this setting is a three field formulation. In the case of loading, $(5.76)_3$ may be recast into

$$g_c\delta_d\gamma + \eta\dot{d} = 2(1-d)\,\psi_0^+ \geq 0 \quad \text{for} \quad \dot{d} > 0\,, \tag{5.77}$$

which proves the positive evolution of the fracture phase field (5.35). Note that equation $(5.76)_3$ can be interpreted as a Ginzburg-Landau-type evolution equation for the fracture phase field if the driving force β is eliminated by $(5.76)_2$. See e.g. GURTIN [62] for a general discussion and HAKIM & KARMA [74] for an application to fracture mechanics. When defining the *specific work function* for the present model

$$w(\boldsymbol{\varepsilon}, d, \nabla d) = \psi(\boldsymbol{\varepsilon}, d) + g_c\gamma(d, \nabla d) \tag{5.78}$$

based on the energy density function (5.53) and the crack surface density function (5.21), equation $(5.76)_3$ can be recast into the Ginzburg-Landau-type evolution equation

$$\eta\dot{d} = \langle -\delta_d w(\boldsymbol{\varepsilon}, d, \nabla d)\rangle_+\,, \tag{5.79}$$

expressed in terms of the variational derivative of the specific work function and the kinetic coefficient that controls the rate of energy dissipation in the process zone η. In contrast to the model of HAKIM & KARMA [74], the formulation under focus contains explicitly the regularized crack surface and differentiates between energy storage and dissipation. However, the proposed three-field formulation (5.76) bases on a more transparent thermodynamic derivation of (5.79) that also includes the dissipation of the kinematic term with viscosity η.

5.3.5. Incremental Variational Principles for Phase Field Fracture. The general incremental variational framework discussed in Section 3.9 is now applied to the model problem of phase field fracture. In this setting, the state variables at the discrete solution times $0, t_1, t_2, \ldots, t_n, t_{n+1}, \ldots, T$ are obtained by the application of an incremental variational principle. The setup of such a principle critically depends on the incremental dissipation, energy storage, and load expended to the system within the characteristic time interval $[t_n, t_{n+1}]$. Based on either the dissipation function with local penalty-type character (5.43) or with viscous over-force character (5.49), two representations of the incremental dissipation are obtained via

$$D^\tau := \int_{t_n}^{t_{n+1}} D\,dt \tag{5.80}$$

and are discussed separately. Both models have in common the incrementally stored energy

$$E^\tau(\boldsymbol{u}, d) := \int_{t_n}^{t_{n+1}} \dot{E}\,dt = E(t_{n+1}) - E(t_n) = \int_{\mathcal{B}} \{\,\psi(\mathfrak{c}) - \psi(\mathfrak{c}_n)\,\}\,dV\,, \tag{5.81}$$

specified as a function of the current displacements $\boldsymbol{u}$ and the fracture phase field d governed by the free energy function ψ. The incremental work

$$W^{\tau}(\boldsymbol{u}) := \int_{t_n}^{t_{n+1}} \mathcal{P}_{ext}\, dt = \int_{\mathcal{B}} \boldsymbol{\gamma} \cdot (\boldsymbol{u} - \boldsymbol{u}_n)\, dV + \int_{\partial\mathcal{B}_t} \boldsymbol{t}_N \cdot (\boldsymbol{u} - \boldsymbol{u}_n)\, dA \tag{5.82}$$

is a function of the current displacements $\boldsymbol{u}$ for prescribed volume loads $\boldsymbol{\gamma}$ and surface loads $\boldsymbol{t}_N$. This functional has been obtained by a time integration of the functional (5.69), where obviously no external loading related to the fracture phase field is considered.

5.3.5.1. Model I: Rate-Independent Setting with Approximated Indicator. As denoted before, the first possibility to model the incremental potential bases on the canonical *penalty-type* setting of the dissipation function with the local contribution (5.43). In this scenario, the incremental dissipation associated with the discrete time interval is considered to be the algorithm

$$D^{\tau}_{\epsilon}(d) := g_c[\Gamma_l(d) - \Gamma_l(d_n)] + \frac{\epsilon}{2\tau} \int_{\mathcal{B}} \langle d - d_n \rangle_-^2\, dV \tag{5.83}$$

as a function of the current fracture phase field d governed by the crack surface functional (5.20). Together with the extended constitutive state vector (5.31), the incremental internal work density can now be expressed in the compact explicit representation

$$\pi^{\tau}(\mathfrak{c}; \mathfrak{c}_n) = \psi(\mathfrak{c}) - \psi(\mathfrak{c}_n) + \frac{g_c}{2l}[d^2 + l^2 \|\nabla d\|^2] - g_c \gamma_n + \frac{\epsilon}{2\tau} \langle d - d_n \rangle_-^2\,, \tag{5.84}$$

where either the isotropic or anisotropic representation of the free energy function (5.54) and (5.61) is chosen. Evaluation of the incremental minimum principle (3.205) gives with Gauss' and localization theorem the algorithmic Euler equations for the *isotropic case*

$$\begin{aligned} \boldsymbol{0} &= \operatorname{div}[\,((1-d)^2 + k)\, \partial_{\boldsymbol{\varepsilon}} \psi_0(\boldsymbol{\varepsilon})\,] + \boldsymbol{\gamma} \\ 0 &= \frac{g_c}{l}[\, d - l^2 \Delta d\,] - [\, 2(1-d)\, \psi_0(\boldsymbol{\varepsilon}) + \frac{\epsilon}{\tau} \langle d - d_n \rangle_-\,] \end{aligned} \tag{5.85}$$

and the algorithmic coupled Euler equations for the *anisotropic case*

$$\begin{aligned} \boldsymbol{0} &= \operatorname{div}[\,((1-d)^2 + k)\, \partial_{\boldsymbol{\varepsilon}} \psi_0^+(\boldsymbol{\varepsilon}) + \partial_{\boldsymbol{\varepsilon}} \psi_0^-(\boldsymbol{\varepsilon})\,] + \boldsymbol{\gamma} \\ 0 &= \frac{g_c}{l}[\, d - l^2 \Delta d\,] - [\, 2(1-d)\, \psi_0^+(\boldsymbol{\varepsilon}) + \frac{\epsilon}{\tau} \langle d - d_n \rangle_-\,]\,. \end{aligned} \tag{5.86}$$

Observe that the regularization term can be interpreted as artificial viscous hardening that penalizes the energy release in the non-physical range $\dot{d} < 0$. The parameter ϵ is an artificial parameter with no direct physical meaning. In the numerical analysis it has to be chosen according to the conditioning number of the global FE system. The material characteristic of model I for cyclic loading in the tensile range for different regularization parameters ϵ is illustrated in Figure 5.9. Clearly, for a small penalty parameter $\epsilon = 0.01$, the model exhibits non-physical hysteresis. For a discussion of the material response of model I for cyclic loading in tension and compression for the isotropic and anisotropic formulation, see Figure 5.10.

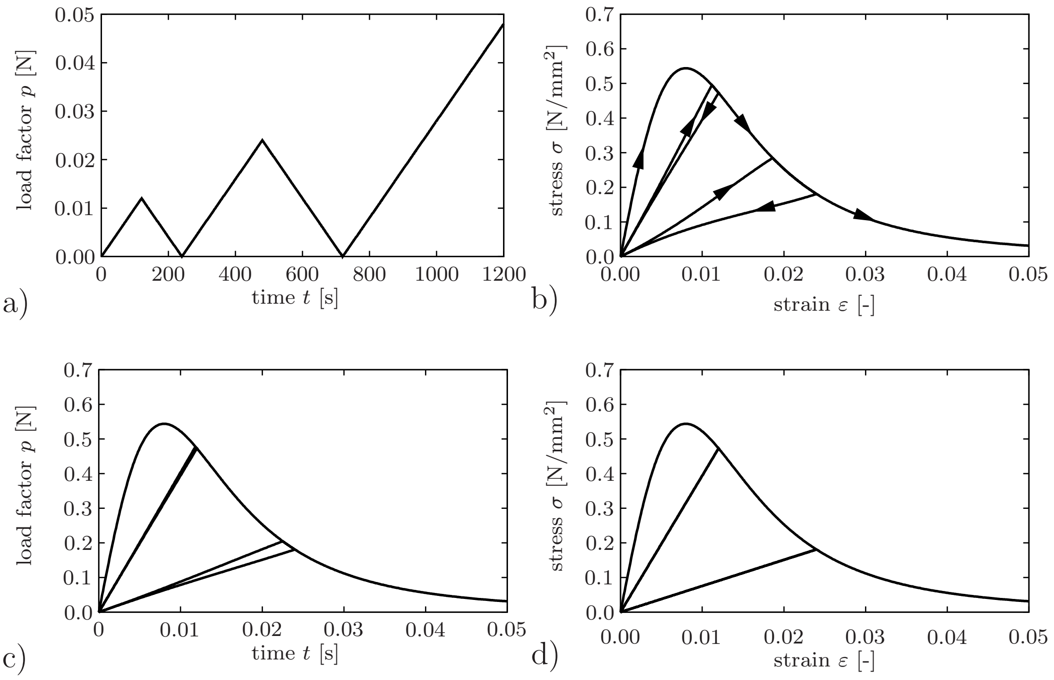

Figure 5.9: Model I: Rate-independent formulation with approximated indicator function. a) Cyclic loading and stress-strain curves for b) $\epsilon = 0.01$, c) $\epsilon = 0.05$, and d) $\epsilon = 2.0$. For small penalty parameters ϵ, the model shows a non-physical hysteresis in unloading/reloading.

5.3.5.2. Model II: Rate-Dependent Setting with Threshold Function. The second possibility to model the incremental potential bases on the extended *viscous over-force* setting of the dissipation function with the local contribution (5.49). Here, the incremental dissipation associated with the discrete time interval is considered as the algorithmic expression

$$D^{\tau}_{\eta}(d,\beta) := \int_{\mathcal{B}} \{\, \beta(d-d_n) - \frac{\tau}{2\eta}\,\langle\, \beta - \psi_c(d_n)\,\rangle^2_+ + \frac{g_c l}{2}[\|\nabla d\|^2 - \|\nabla d_n\|^2]\,\}\; dV \tag{5.87}$$

as a function of the current fracture phase field d and in addition the dissipative force field β. Thus, consider in addition to $\mathfrak{c} := \{\, \boldsymbol{\varepsilon}, d, \nabla d\,\}$ the extended constitutive state

$$\mathfrak{c}^* := \{\, \boldsymbol{\varepsilon}, d, \nabla d, \beta\,\} \tag{5.88}$$

allowing to express the incremental internal work density in the compact explicit form

$$\pi^{*\tau}_{\eta}(\mathfrak{c}^*;\mathfrak{c}^*_n) = \psi(\mathfrak{c}) - \psi(\mathfrak{c}_n) + \beta(d-d_n) - \frac{\tau}{2\eta}\,\langle\, \beta - \psi_c(d_n)\,\rangle^2_+ + \frac{g_c l}{2}[\|\nabla d\|^2 - \|\nabla d_n\|^2]\,, \tag{5.89}$$

where either the isotropic or anisotropic representation of the free energy function (5.54) and (5.61) is chosen. Evaluation of the incremental variational principle (3.212) gives with Gauss' and localization theorem the coupled Euler equations for the *isotropic case*

$$\begin{aligned} \boldsymbol{0} &= \operatorname{div}[\,((1-d)^2 + k)\,\partial_{\boldsymbol{\varepsilon}}\psi_0(\boldsymbol{\varepsilon})\,] + \boldsymbol{\gamma} \\ 0 &= g_c l \Delta d + 2(1-d)\,\psi_0(\boldsymbol{\varepsilon}) - \beta \\ 0 &= d - d_n - \frac{\tau}{\eta}\langle \beta - \psi_c(d_n)\rangle_+ \end{aligned} \tag{5.90}$$

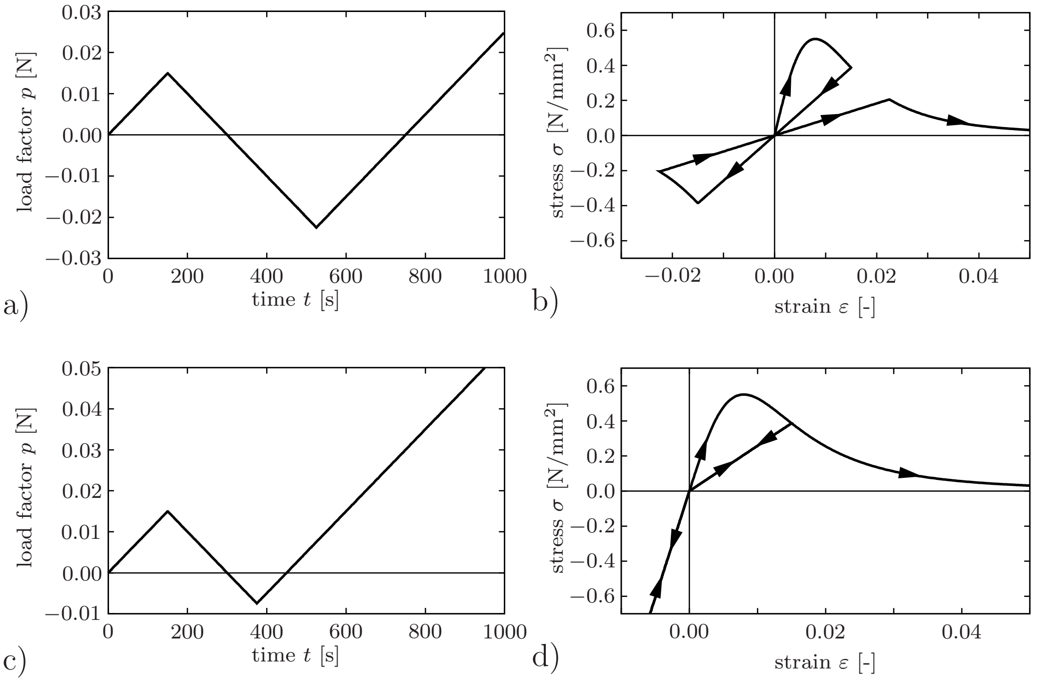

Figure 5.10: Model I/II: Rate-independent formulation with approximated indicator function and rate-dependent formulation with threshold function. Model Ia/IIa: *Isotropic* damage evolution in compression and tension with a) cyclic loading in positive and negative range and b) stress-strain curve for $\epsilon = 2.0$ and $\eta = 1\times10^{-6}$. Model Ib/IIb: *Anisotropic* damage evolution in tension only with c) cyclic loading in positive and negative range and d) stress-strain curve for $\epsilon = 2.0$ and $\eta = 1\times10^{-6}$.

in a time-discrete setting and the coupled Euler equations for the *anisotropic case*

$$\begin{aligned} \boldsymbol{0} &= \operatorname{div}[\,((1-d)^2+k)\,\partial_{\boldsymbol{\varepsilon}}\psi_0^+(\boldsymbol{\varepsilon}) + \partial_{\boldsymbol{\varepsilon}}\psi_0^-(\boldsymbol{\varepsilon})\,] + \boldsymbol{\gamma} \\ 0 &= g_c l \Delta d + 2(1-d)\,\psi_0^+(\boldsymbol{\varepsilon}) - \beta \\ 0 &= d - d_n - \frac{\tau}{\eta}\langle \beta - \psi_c(d_n)\rangle_+ \,. \end{aligned} \tag{5.91}$$

Recall that for $\eta \to 0$ the rate-independent case is obtained. The material characteristic of model II for cyclic loading in the tensile range for different viscosities η is illustrated in Figure 5.11. For a large viscosity $\eta = 1.25\times10^{-4}$, the model shows the typical effect of viscous over-stresses. For a discussion of the material response of model II for cyclic loading in tension and compression for the isotropic and anisotropic formulation, see Figure 5.10.

5.3.6. FE-Discretization of Incremental Variational Principle. The numerical solution procedure of the coupled multi-field problem for both the two- and three-field setting has been discussed in full length in Section 3.9.4. It only remains to specify the approximation matrices, the nodal unknowns, and the generalized stresses and moduli.

5.3.6.1. Model I: Canonical Two-Field Setting. The multi-field finite element treatment is now applied to *model I*. When restricting to two-dimensional problems only, the global unknowns and the constitutive state in the continuous setting read

$$\mathfrak{u} := \{\, u_1, u_2, d \,\} \quad \text{with} \quad \mathfrak{c}(\mathfrak{u}) := \{\, u_{1,1}, u_{2,2}, u_{1,2} + u_{2,1}, d, d_{,1}, d_{,2} \,\} \,. \tag{5.92}$$

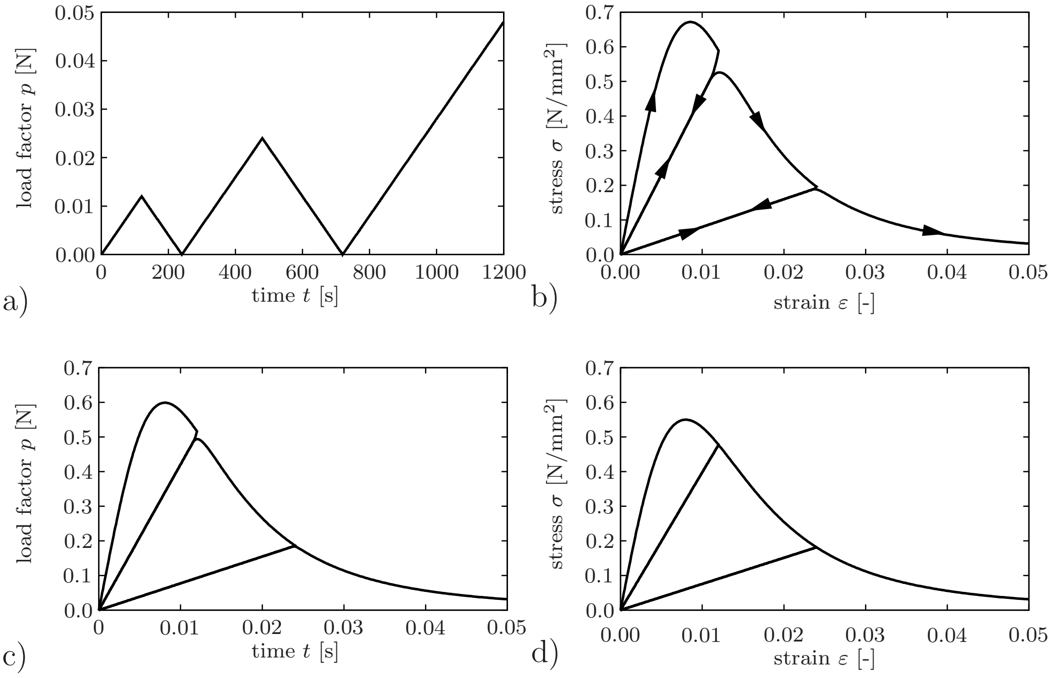

Figure 5.11: Model II: Rate-dependent formulation with threshold function. a) Cyclic loading and stress-strain curves for b) $\eta = 1.25{\times}10^{-4}$, c) $\eta = 5.0{\times}10^{-5}$, and d) $\eta = 1{\times}10^{-6}$. For large viscosity η, the model shows the typical effect of viscous over-stresses.

The generalized displacement is approximated according to (3.217) and reads

$$\mathfrak{u}^h = \mathfrak{N}(\boldsymbol{x})\,\mathfrak{d} \quad \text{with} \quad [\mathfrak{N}]_i^e = \begin{bmatrix} N & 0 & 0 \\ 0 & N & 0 \\ 0 & 0 & N \end{bmatrix}_i \quad \text{and} \quad \mathfrak{d}_i = [\,d_1, d_2, a\,]_i^T \,, \tag{5.93}$$

where identical interpolations N_i for the macro- and microscopic partition are chosen. At node i of the finite element discretization, the generalized displacement vector $\mathfrak{d}_i$ contains the nodal displacements d_1 and d_2 in 1- and 2-direction and the nodal damage variable a. In full analogy to (3.222), the variation of the discrete constitutive state with respect to the generalized nodal unknowns exhibits the discrete structure

$$\delta_{\mathfrak{d}}\mathfrak{c}^h = \mathfrak{B}(\boldsymbol{x})\,\delta\mathfrak{d} \quad \text{with} \quad [\mathfrak{B}]_i^e = \begin{bmatrix} N_{,1} & 0 & N_{,2} & 0 & 0 & 0 \\ 0 & N_{,2} & N_{,1} & 0 & 0 & 0 \\ 0 & 0 & 0 & N & N_{,1} & N_{,2} \end{bmatrix}_i^T . \tag{5.94}$$

For the model problem of phase field fracture, the compact representations of the generalized stresses and symmetric generalized moduli are specified to

$$\boldsymbol{S} := \begin{bmatrix} \partial_{\boldsymbol{\varepsilon}}\pi_\epsilon^h \\ \partial_d \pi_\epsilon^h \\ \partial_{\nabla d}\pi_\epsilon^h \end{bmatrix} \quad \text{and} \quad \mathbb{C} := \begin{bmatrix} \partial^2_{\boldsymbol{\varepsilon}\boldsymbol{\varepsilon}}\pi_\epsilon^h & \boldsymbol{0} & \boldsymbol{0} \\ \boldsymbol{0} & \partial^2_{dd}\pi_\epsilon^h & \boldsymbol{0} \\ \boldsymbol{0} & \boldsymbol{0} & \partial^2_{\nabla d \nabla d}\pi_\epsilon^h \end{bmatrix} . \tag{5.95}$$

For the case of an *inactive ramp function* for $d \leq d_n$, the components of the generalized stresses $(5.95)_1$ for the isotropic and anisotropic case can be summarized by

$$
\begin{array}{lllll}
\partial_{\boldsymbol{\varepsilon}} \pi_\epsilon^h &= ((1-d)^2 + k)\, \boldsymbol{\sigma}_0(\boldsymbol{\varepsilon}) & & \partial_{\boldsymbol{\varepsilon}} \pi_\epsilon^h &= ((1-d)^2 + k)\, \boldsymbol{\sigma}_0^+(\boldsymbol{\varepsilon}) + \boldsymbol{\sigma}_0^-(\boldsymbol{\varepsilon}) \\
\partial_d \pi_\epsilon^h &= \psi_c(d) - 2(1-d)\, \psi_0(\boldsymbol{\varepsilon}) & \text{or} & \partial_d \pi_\epsilon^h &= \psi_c(d) - 2(1-d)\, \psi_0^+(\boldsymbol{\varepsilon}) \\
\partial_{\nabla d} \pi_\epsilon^h &= g_c l\, \nabla d & & \partial_{\nabla d} \pi_\epsilon^h &= g_c l\, \nabla d
\end{array}
\tag{5.96}
$$

and the according components of the generalized moduli $(5.95)_2$ by

$$
\begin{array}{lllll}
\partial^2_{\boldsymbol{\varepsilon}\boldsymbol{\varepsilon}} \pi_\epsilon^h &= ((1-d)^2 + k)\, \mathbb{C}_0 & & \partial^2_{\boldsymbol{\varepsilon}\boldsymbol{\varepsilon}} \pi_\epsilon^h &= ((1-d)^2 + k)\, \mathbb{C}_0^+ + \mathbb{C}_0^- \\
\partial^2_{dd} \pi_\epsilon^h &= \dfrac{g_c}{l} + 2\psi_0(\boldsymbol{\varepsilon}) & \text{or} & \partial^2_{dd} \pi_\epsilon^h &= \dfrac{g_c}{l} + 2\psi_0^+(\boldsymbol{\varepsilon}) \\
\partial^2_{\nabla d \nabla d} \pi_\epsilon^h &= g_c l\, \boldsymbol{1} & & \partial^2_{\nabla d \nabla d} \pi_\epsilon^h &= g_c l\, \boldsymbol{1}\,.
\end{array}
\tag{5.97}
$$

In the case of *an active ramp function* for $d > d_n$, the generalized stresses and moduli have to be updated by an additional penalty term related to the ramp function

$$
\partial_d \pi_\epsilon^h \Leftarrow \partial_d \pi_\epsilon^h + \frac{\epsilon}{\tau}(d - d_n) \quad \text{and} \quad \partial^2_{dd} \pi_\epsilon^h \Leftarrow \partial^2_{dd} \pi_\epsilon^h + \frac{\epsilon}{\tau}
\tag{5.98}
$$

for both, the isotropic and anisotropic model. In (5.96), the elasticity moduli

$$
\mathbb{C}_0 = \partial_{\boldsymbol{\varepsilon}} \boldsymbol{\sigma}_0 \quad \text{or} \quad \mathbb{C}_0^+ = \partial_{\boldsymbol{\varepsilon}} \boldsymbol{\sigma}_0^+ \quad \text{and} \quad \mathbb{C}_0^- = \partial_{\boldsymbol{\varepsilon}} \boldsymbol{\sigma}_0^-
\tag{5.99}
$$

have been introduced as the derivatives of the stresses (5.60) and (5.67) with respect to the strains. For an algorithmic treatment of the anisotropic moduli $(5.99)_{2,3}$ as derivatives of the stresses (5.67) formulated in terms of the principal strains and principal strain directions with respect to the total strain, see Miehe [115].

5.3.6.2. Model II: Rate-Dependent Three-Field Setting. The extended multi-field finite element treatment is now applied to *model II*. Restricting to two-dimensional problems only, the global unknowns and the extended constitutive state read

$$
\boldsymbol{\mathfrak{u}}^* := \{\, u_1, u_2, d, \beta \,\} \quad \text{with} \quad \boldsymbol{\mathfrak{c}}^*(\boldsymbol{\mathfrak{u}}^*) := \{\, u_{1,1}, u_{2,2}, u_{1,2} + u_{2,1}, d, d_{,1}, d_{,2}, \beta \,\}\,.
\tag{5.100}
$$

In line with (3.226), the extended generalized displacements are approximated via

$$
\boldsymbol{\mathfrak{u}}^{*h} = \boldsymbol{\mathfrak{N}}^*(\boldsymbol{x})\, \boldsymbol{\mathfrak{d}}^* \quad \text{with} \quad [\boldsymbol{\mathfrak{N}}^*]_i^e = \begin{bmatrix} N & 0 & 0 & 0 \\ 0 & N & 0 & 0 \\ 0 & 0 & N & 0 \\ 0 & 0 & 0 & M \end{bmatrix}_i \quad \text{and} \quad \boldsymbol{\mathfrak{d}}_i^* = [\, d_1, d_2, a, b \,]_i^T\,,
\tag{5.101}
$$

where identical interpolations for the macro- and microscopic partition and the driving force are chosen, i.e. $N_i = M_i$. At node i of the finite element discretization, the extended generalized displacement vector $\boldsymbol{\mathfrak{d}}^*$ contains the nodal displacements d_1 and d_2 in 1- and 2-direction, the nodal damage variable a, and the nodal thermodynamic force b. In agreement with (3.231), the variation of the discrete extended constitutive state with respect to the extended nodal unknowns reads

$$
\delta_{\boldsymbol{\mathfrak{d}}^*} \boldsymbol{\mathfrak{c}}^{*h} = \boldsymbol{\mathfrak{B}}^*(\boldsymbol{x})\, \delta \boldsymbol{\mathfrak{d}}^* \quad \text{with} \quad [\boldsymbol{\mathfrak{B}}^*]_i^e = \begin{bmatrix} N_{,1} & 0 & N_{,2} & 0 & 0 & 0 & 0 \\ 0 & N_{,2} & N_{,1} & 0 & 0 & 0 & 0 \\ 0 & 0 & 0 & N & N_{,1} & N_{,2} & 0 \\ 0 & 0 & 0 & 0 & 0 & 0 & M \end{bmatrix}_i^T\,.
\tag{5.102}
$$

For the model problem of phase field fracture, the compact representations of the generalized stresses and symmetric generalized moduli are specified to

$$\boldsymbol{S}^* := \begin{bmatrix} \partial_{\boldsymbol{\varepsilon}}\pi^{*h}_{\eta} \\ \partial_{\alpha}\pi^{*h}_{\eta} \\ \partial_{\nabla\alpha}\pi^{*h}_{\eta} \\ \partial_{\beta}\pi^{*h}_{\eta} \end{bmatrix} \quad \text{and} \quad \mathbb{C}^* := \begin{bmatrix} \partial^2_{\boldsymbol{\varepsilon}\boldsymbol{\varepsilon}}\pi^{*h}_{\eta} & \boldsymbol{0} & \boldsymbol{0} & \boldsymbol{0} \\ \boldsymbol{0} & \partial^2_{\alpha\alpha}\pi^{*h}_{\eta} & \boldsymbol{0} & 1 \\ \boldsymbol{0} & \boldsymbol{0} & \partial^2_{\nabla\alpha\nabla\alpha}\pi^{*h}_{\eta} & \boldsymbol{0} \\ \boldsymbol{0} & 1 & \boldsymbol{0} & \partial^2_{\beta\beta}\pi^{*h}_{\eta} \end{bmatrix} . \tag{5.103}$$

For the case of *elastic loading* for $\varphi(\beta; d_n) < 0$, the components of the generalized stresses $(5.95)_1$ for the isotropic and anisotropic case can be summarized by

$$\begin{aligned} \partial_{\boldsymbol{\varepsilon}}\pi^{*h}_{\eta} &= ((1-d)^2 + k)\, \boldsymbol{\sigma}_0(\boldsymbol{\varepsilon}) \\ \partial_{d}\pi^{*h}_{\eta} &= \beta - 2(1-d)\, \psi_0(\boldsymbol{\varepsilon}) \\ \partial_{\nabla d}\pi^{*h}_{\eta} &= g_c l\, \nabla d \\ \partial_{\beta}\pi^{*h}_{\eta} &= d - d_n \end{aligned} \quad \text{or} \quad \begin{aligned} \partial_{\boldsymbol{\varepsilon}}\pi^{*h}_{\eta} &= ((1-d)^2 + k)\, \boldsymbol{\sigma}_0^+(\boldsymbol{\varepsilon}) + \boldsymbol{\sigma}_0^-(\boldsymbol{\varepsilon}) \\ \partial_{d}\pi^{*h}_{\eta} &= \beta - 2(1-d)\, \psi_0^+(\boldsymbol{\varepsilon}) \\ \partial_{\nabla d}\pi^{*h}_{\eta} &= g_c l\, \nabla d \\ \partial_{\beta}\pi^{*h}_{\eta} &= d - d_n \,, \end{aligned} \tag{5.104}$$

and the according components of the generalized moduli $(5.95)_2$ by

$$\begin{aligned} \partial^2_{\boldsymbol{\varepsilon}\boldsymbol{\varepsilon}}\pi^{*h}_{\eta} &= ((1-d)^2 + k)\, \mathbb{C}_0 \\ \partial^2_{dd}\pi^{*h}_{\eta} &= 2\psi_0(\boldsymbol{\varepsilon}) \\ \partial^2_{\nabla d\nabla d}\pi^{*h}_{\eta} &= g_c l\, \boldsymbol{1} \\ \partial^2_{\beta\beta}\pi^{*h}_{\eta} &= 0 \end{aligned} \quad \text{or} \quad \begin{aligned} \partial^2_{\boldsymbol{\varepsilon}\boldsymbol{\varepsilon}}\pi^{*h}_{\eta} &= ((1-d)^2 + k)\, \mathbb{C}_0^+ + \mathbb{C}_0^- \\ \partial^2_{dd}\pi^{*h}_{\eta} &= 2\psi_0^+(\boldsymbol{\varepsilon}) \\ \partial^2_{\nabla d\nabla d}\pi^{*h}_{\eta} &= g_c l\, \boldsymbol{1} \\ \partial^2_{\beta\beta}\pi^{*h}_{\eta} &= 0\,. \end{aligned} \tag{5.105}$$

In the case of *inelastic loading* for $\varphi(\beta; d_n) \geq 0$, the generalized stresses and moduli have to be updated by an additional penalty-type viscosity term related to the ramp function

$$\partial_{\beta}\pi^{*h}_{\eta} \Leftarrow \partial_{\beta}\pi^{*h}_{\eta} - \frac{\tau}{\eta}(\beta - \psi_c(d_n)) \quad \text{and} \quad \partial^2_{\beta\beta}\pi^{*h}_{\eta} \Leftarrow \partial^2_{\beta\beta}\pi^{*h}_{\eta} - \frac{\tau}{\eta} \tag{5.106}$$

for both, the isotropic and anisotropic model. For a definition of the moduli $\mathbb{C}_0$, $\mathbb{C}_0^+$, and $\mathbb{C}_0^-$, see equation (5.99).

5.3.7. Numerical Examples. Crack Propagation in Solids. In this section, the performance of the proposed model of phase field fracture is demonstrated by means of some representative numerical examples. In particular, the focus is put on a detailed discussion of the material's characteristics for model I and model II. The influence of the length scale parameter l, the penalty parameter ϵ, and the viscosity η is analyzed. The first numerical example is concerned with a *single edge notched tension test*, where a horizontal crack propagation is expected. The second numerical test focuses on a *pure shear test of a notched specimen*. Here, the difference between the isotropic and anisotropic formulation is elucidated. Another numerical study is concerned with the classical benchmark of a *symmetric three point bending test*. For this test, meaningful results are only obtained with the anisotropic formulation. The section closes with an *asymmetric notched three point bending test* that nicely demonstrates the evolution of a curved crack pattern.

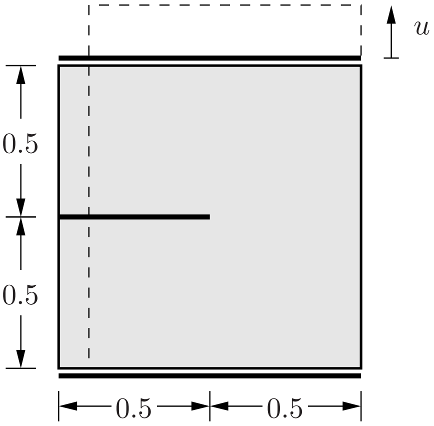

Figure 5.12: Single edge notched tension test. Geometry and boundary conditions.

5.3.7.1. Single Edge Notched Tension Test. At first, a squared plate is investigated that possesses a horizontal notch placed at middle height from the left outer surface to the center of the specimen. The geometric setup is depicted in Figure 5.12. In order to capture the crack pattern properly, the mesh is refined in areas where the crack is expected to propagate, i.e. in the center strip of the specimen. For a discretization with 20000 elements an effective element size of $h \approx 1.0 \times 10^{-3}$ mm, for a discretization with 30000 elements an effective element size of $h \approx 0.6 \times 10^{-3}$ mm in the critical zone is obtained. The elastic constants are chosen as $\lambda = 121.15$ kN/mm^2 and $\mu = 80.77$ kN/mm^2, the critical energy release rate as $g_c = 2.7 \times 10^{-3}$ kN/mm. The computation is performed in a monotonic displacement-driven context with constant displacement increments $\Delta u = 1.0 \times 10^{-5}$ mm. In order to point out the effects that arise due to the length scale parameter l and the viscosity η, different simulations with the anisotropic model in its rate-independent penalty-type setting (5.86) and in its rate-dependent over-force representation (5.91) are performed. Obviously, the underlying boundary value problem is subjected to tensile loading, a difference between isotropic and anisotropic material response is not visible. For fixed length scale parameters $l_1 = 0.0375$ mm and $l_2 = 0.0075$ mm the influence of the viscosity in model II is analyzed. The resulting load-deflection curves are depicted in Figure 5.13. Here, for vanishing viscosity $\eta \to 0$ the structural response approaches

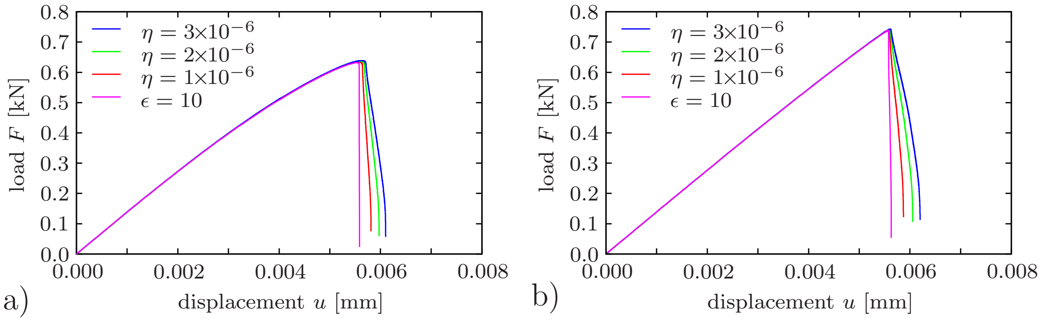

Figure 5.13: Single edge notched tension test. Load-deflection curves for simulations with length scale parameters a) $l_1 = 0.0375$ mm and b) $l_2 = 0.0075$ mm obtained for different viscosities η with rate-dependent model (5.91). Results are compared to the rate-independent limit case given by the two-field formulation (5.86) for $\epsilon = 10.0$ kN s/mm^2.

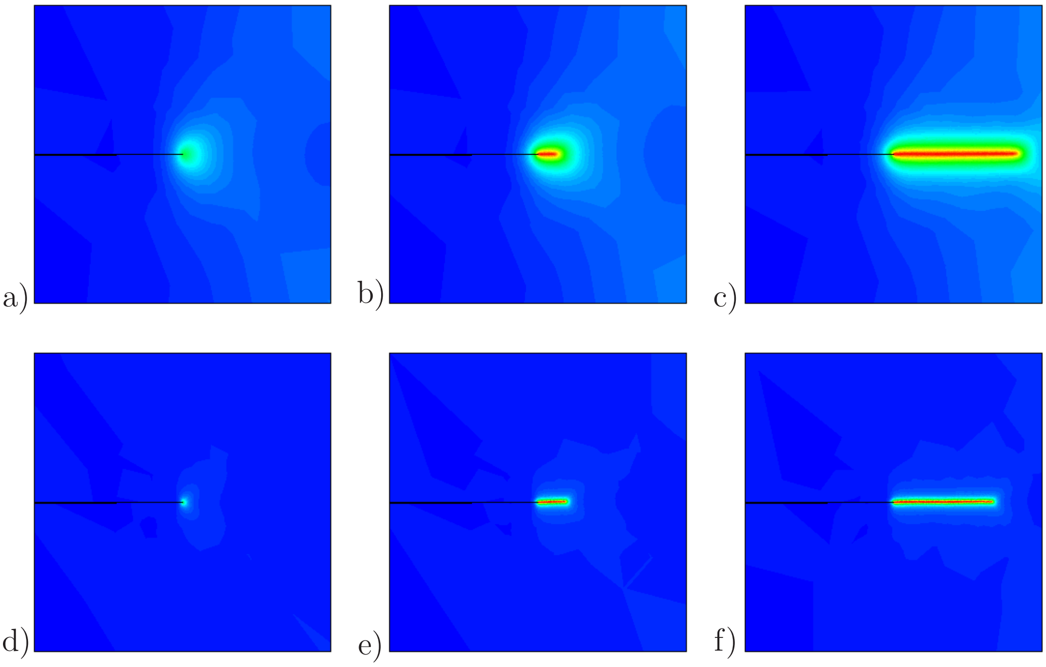

Figure 5.14: Single edge notched tension test. Crack pattern of the three-field formulation (5.91) at a displacement of a) $u = 5.5{\times}10^{-3}$ mm, b) $u = 5.9{\times}10^{-3}$ mm, and c) $u = 6.3{\times}10^{-3}$ mm for a length scale of $l_1 = 0.0375$ mm. Diffusive crack topology at the deformation stages d) $u = 5.5\times10^{-3}$ mm, e) $u = 5.9\times10^{-3}$ mm, and f) $u = 6.3\times10^{-3}$ mm for a length scale of $l_2 = 0.0075$ mm.

the rate-independent limit, characterized by the two-field model (5.86). Comparison of the incremental internal work densities (5.84) and (5.89) yields the relation between the regularization parameters ϵ and η used in the subsequent simulations

$$\eta \approx \frac{\tau^2}{\epsilon} \quad \Leftrightarrow \quad \epsilon \approx \frac{\tau^2}{\eta} \ . \tag{5.107}$$

The resulting crack patterns at different stages of the deformation are illustrated in Figure 5.14. As expected, the sharpest crack pattern is obtained for the smallest length scale parameter $l_2 = 0.0075$ mm. The last study of this boundary value problem analyzes the influence of the discretization on the overall global response. For a discretization with 20000 elements, an approximate effective element size in the critical zone of $h \approx 1.0{\times}10^{-3}$

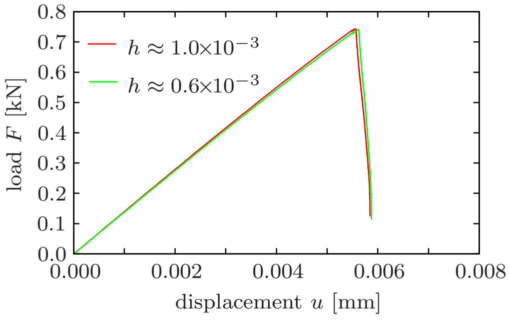

Figure 5.15: Single edge notched tension test. Objective load-deflection curves for simulations with 20000 and 30000 elements with identical viscosity $\eta = 4\times10^{-6}$ kN s/mm^2.

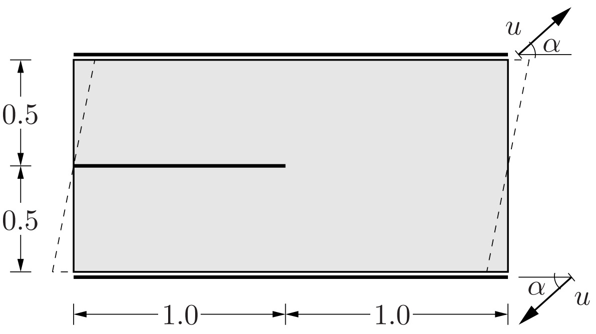

Figure 5.16: Pure shear test of notched specimen. Geometry and boundary conditions.

mm is obtained. In order to verify mesh-objectivity, the same simulation as discussed in Figure 5.13b) is repeated with a finer discretization of 30000 elements. With the fine discretization, an effective element size of $h \approx 0.6{\times}10^{-3}$ mm in the critical zone is obtained. As depicted in Figure 5.15, the global structural responses of both computations coincide. As a consequence, the finite element simulations provide mesh-independent results.

5.3.7.2. Pure Shear Test of Notched Specimen. The phase field formulation of fracture is now applied to a shear test of a rectangular notched specimen. In literature, this test has been numerically studied by Bourdin, Francfort & Marigo [16]. The boundary value problem depicted in Figure 5.16 is discretized using 30000 triangular elements. A pure shear deformation u is applied, where the displacement load direction has the angle $\alpha = 0°$ towards the horizontal plane. In the aforementioned reference, this system has been analyzed for different displacement angles α, where for $0° \leq \alpha \leq 7°$ unphysical crack branching has been observed. Throughout the analysis, the Lamé constants are chosen to $\lambda = 121.15$ kN/mm^2 and $\mu = 80.77$ kN/mm^2, the critical energy release rate to $g_c = 2.7 \times 10^{-3}$ kN/mm, the length scale parameter to $l = 0.01$ mm, and the viscosity to $\eta = 2.5{\times}10^{-5}$ kN s/mm^2. The specimen is subjected to a displacement-driven deformation by prescribed incremental displacements of $\Delta u = 1.0{\times}10^{-4}$ mm in the first 100 iterations. The subsequent deformation demands an adjustment of the displacement increments to $\Delta u = 1.0 \times 10^{-6}$ mm up to the final deformation. In Figure 5.17, the crack evolution at different stages of the deformation is displayed for the viscous *isotropic* and *anisotropic* models (5.90) and (5.91), respectively. The isotropic formulation of phase field fracture reproduces the aforementioned unphysical crack branching, the according diffusive crack topology that exhibits a crack propagation in regions with compression and tension is depicted in Figure 5.17a)–d). This phenomenon is related to the fact that in $(5.90)_2$ the crack propagation is driven by the entire energetic state ψ_0. This drawback motivates the improvement of the isotropic model to an anisotropic one, where the energetic crack driving force only contains contributions that are related to a tensile stress state. Thus, the improved anisotropic model (5.91) contains in $(5.91)_2$ only the positive part of the energy ψ_0^+ as crack driving force. The evolving crack topology for the anisotropic formulation can be found in Figure 5.17e)–h). Clearly, the unphysical effect of crack branching has vanished. Crack propagation takes only place in regions with a tensile stress state. Thus, the improved anisotropic model (5.91) represents the physically realistic approach.

5.3.7.3. Symmetric Three Point Bending Test. This benchmark represents a three point bending test of a simply-supported notched beam. The geometric setup and the loading conditions are illustrated in Figure 5.18. The discretization is refined in subdomains

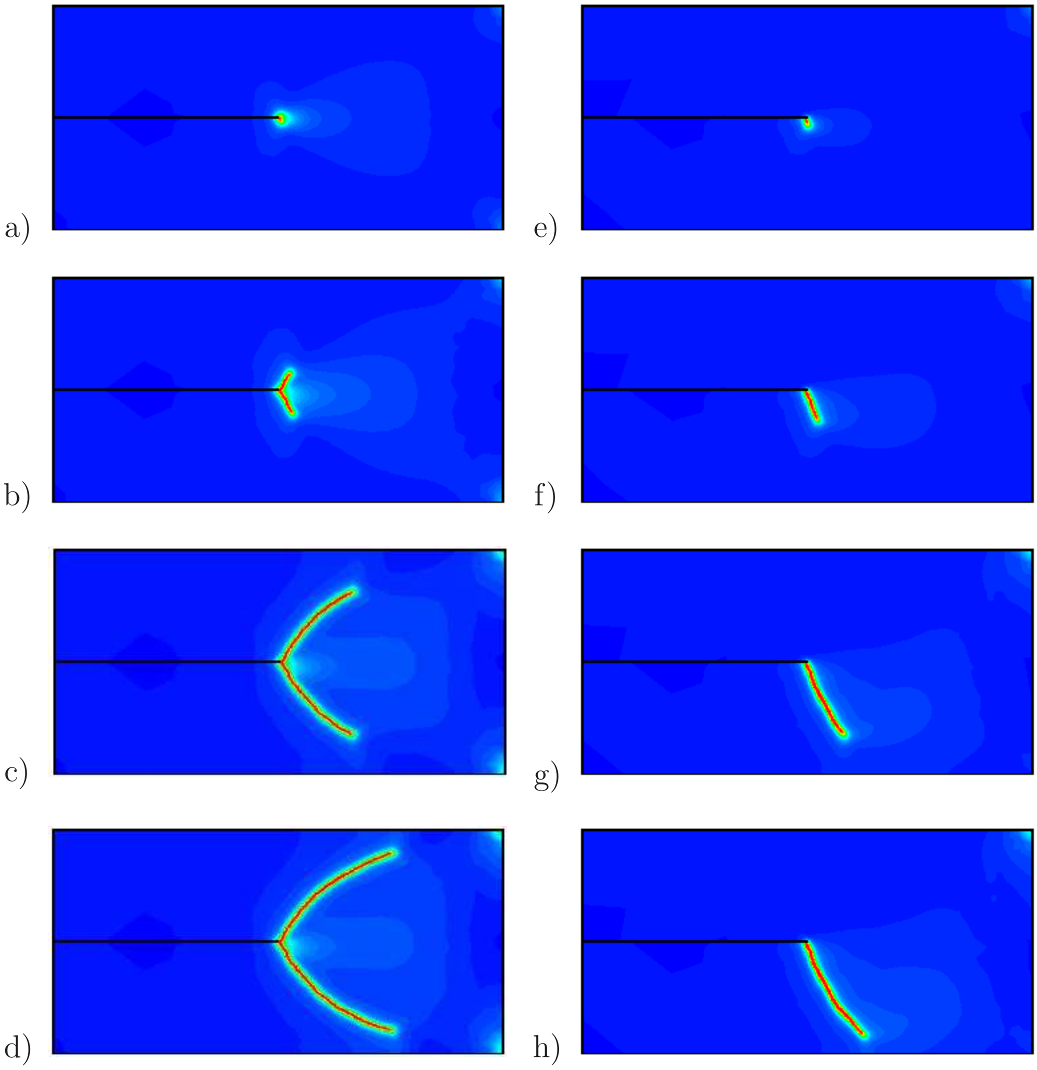

Figure 5.17: Pure shear test of notched specimen. a)–d) Crack patterns of viscous, *isotropic* model (5.90) and e)–h) viscous, *anisotropic* model (5.91) at the deformation states $u = 9.0\times10^{-3}$ mm, $u = 11.0\times10^{-3}$ mm, $u = 15.0\times10^{-3}$ mm, and $u = 17.0\times10^{-3}$ mm.

where the crack is expected to propagate, yielding a discretization with 20000 elements and an effective element size of $h \approx 0.8\times10^{-3}$ mm. The elastic parameters are chosen to $\lambda = 12.00$ kN/mm^2 and $\mu = 8.0$ kN/mm^2, the critical energy release rate to $g_c = 5.0\times10^{-4}$

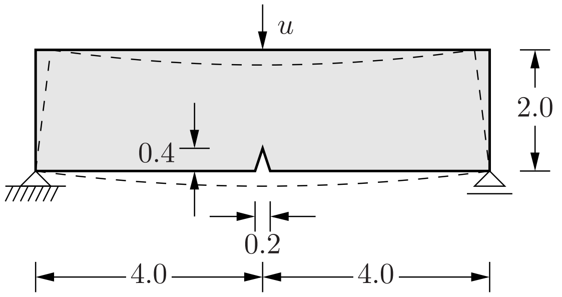

Figure 5.18: Symmetric three point bending test. Geometry and boundary conditions.

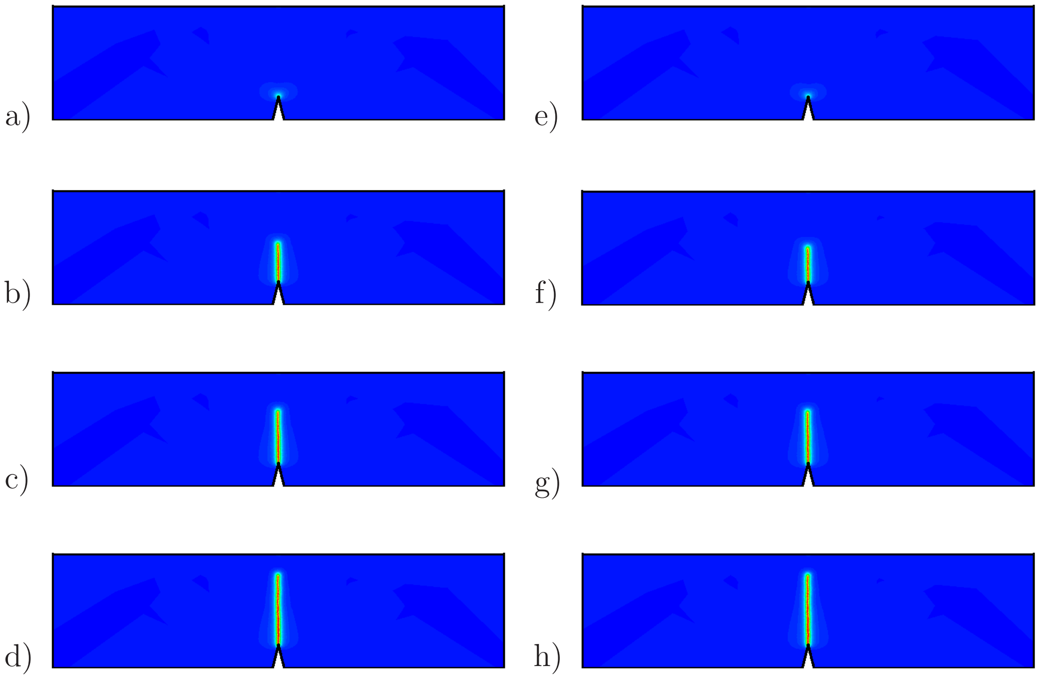

Figure 5.19: Symmetric three point bending test. Results of the two-field model (5.86) are depicted on the left hand side at the deformation state a) $u = 4.0{\times}10^{-2}$ mm, b) $u = 4.2{\times}10^{-2}$ mm, c) $u = 5.0 \times 10^{-2}$ mm, and d) $u = 7.1 \times 10^{-2}$ mm. Results of the viscous three-field formulation (5.91) are shown on the right hand side at the deformation state e) $u = 4.0{\times}10^{-2}$ mm, f) $u = 4.2 \times 10^{-2}$ mm, g) $u = 5.0 \times 10^{-2}$ mm, and h) $u = 7.1 \times 10^{-2}$ mm.

kN/mm. The computation is performed in a monotonic displacement-driven context with constant displacement increments $\Delta u = 1.0 \times 10^{-3}$ mm in the first 40 iteration steps. A continuing simulation then demands an adjustment of the displacement increment to $\Delta u = 1.0{\times}10^{-5}$ mm. The resulting contour plots of the two-field formulation (5.86) with $\epsilon = 10$ kN s/mm^2 and the extended three-field formulation (5.91) with $\eta = 1.0 \times 10^{-6}$ kN s/mm^2, in combination with a length scale parameter $l = 0.03$ mm, are shown in Figure 5.19. Blue and red colors correspond to the undamaged and the fully-cracked material, respectively. Note that for this boundary value problem the isotropic models fail, the effects discussed above cannot be obtained. Figure 5.20 compares the global response of the

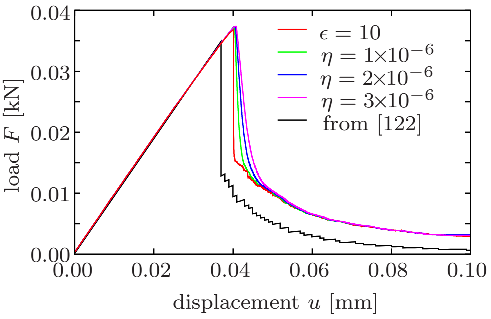

Figure 5.20: Symmetric three point bending test. Load-deflection curves of the two-field formulation (5.86) and the extended three-field formulation (5.91) with a length scale parameter $l = 0.03$ mm obtained for different viscosities η. Both formulations are compared to the material force based fracture algorithm, see Miehe & Gürses [122].

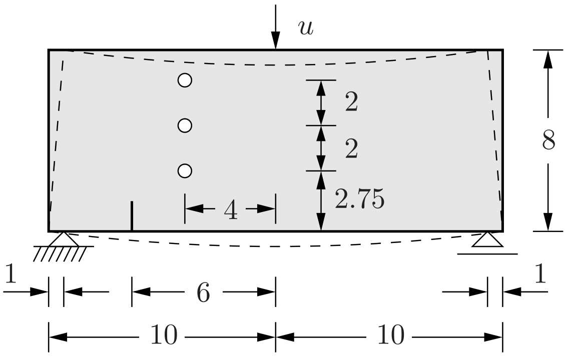

Figure 5.21: Asymmetric notched three point bending test. Geometry, loading, and boundary conditions from Bittencourt, Wawrzynek, Ingraffea & Sousa [15]. The three holes have a diameter of 0.5.

system with results obtained from a fracture model that is based on configurational-force-driven crack propagation, initially introduced by Miehe & Gürses [122] for a simulation with 10360 elements. For a length scale parameter $l = 0.03$ mm, Figure 5.20 compares the solutions obtained by the rate-independent two-field formulation (5.86), involving the parameter ϵ and the extended viscous three-field formulation (5.91), involving the viscosity η. Clearly, the load deflection curves of the three-field formulation depend on the viscosity parameter η. Observe that for a small viscosity $\eta = 1.0 \times 10^{-6}$ kN s/mm^2 the results of the three-field formulation almost coincide with those of the two-field formulation, η plays the role of a numerical stabilization parameter with almost no visible physical effect. In the post-critical range, the results of the phase field model differ from those of the sharp crack model. This effect can be related to the remaining artificial rest energy $k\psi_0^+$ which is present in the diffusive modeling of fracture.

5.3.7.4. Asymmetric Notched Three Point Bending Test. Aim of this benchmark problem is the investigation of curved crack patterns in an asymmetric notched beam with circular holes. This asymmetric three point bending test has been analyzed experimentally and numerically in Bittencourt, Wawrzynek, Ingraffea & Sousa [15]. As depicted in Figure 5.21, the boundary value problem consists of an asymmetrically notched beam with three circular holes. For the analysis, the elastic constants are chosen to $\lambda = 12.0$ kN/mm^2 and $\mu = 8.0$ kN/mm^2, the critical energy release rate to $g_c = 1.0{\times}10^{-3}$ kN/mm, and the viscosity to $\eta = 2.5{\times}10^{-5}$ kN s/mm^2. In a first study, the influence of the mesh density in combination with the respective minimum length scale parameter l on the crack pattern is investigated. Hereby, according to the relation (5.107), the length scale parameter l is always chosen to be approximately twice the element size h. Figure 5.22 shows the resulting crack trajectories for computations with different discretizations and length scale parameters. For a coarse mesh with a large length scale parameter crack initiation at the first hole can be observed. This crack path does not agree with the experimental observation. With increasing mesh density in combination with decreasing length scale parameter, the crack initiation at the first hole disappears. The crack pattern converges to the accurate experimentally observed path. This demonstrates the dramatic influence of the length scale parameter l on the results. Observe furthermore that an extremely fine mesh is needed to resolve the crack pattern properly, an h-adaptive solution procedure is desirable to obtain an efficient algorithm. Figure 5.23 compares the

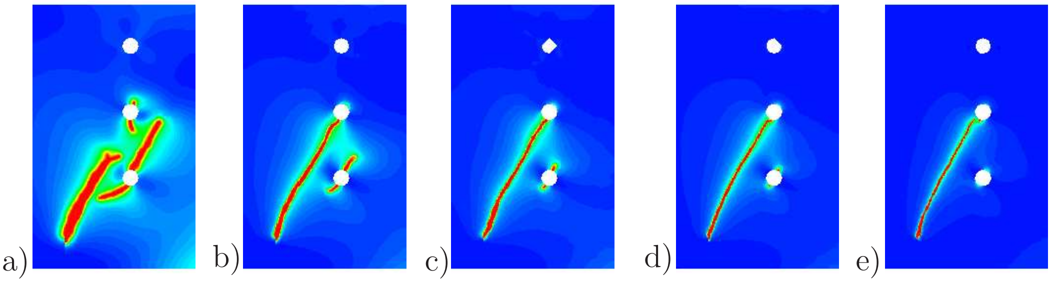

Figure 5.22: Asymmetric notched three point bending test. Crack topology of the viscous three-field formulation (5.91) for different discretizations and corresponding minimum length scale parameters. a) 20000 elements with $l = 0.15$ mm b) 25000 elements with $l = 0.05$ mm, c) 35000 elements with $l = 0.035$ mm, d) 58000 elements with $l = 0.025$ mm, and e) 79000 elements with $l = 0.01$ mm.

simulations with reasonable length scale parameters with the experimental crack trajectories obtained by Bittencourt, Wawrzynek, Ingraffea & Sousa [15]. The contour plots displayed in Figure 5.23a)-c) are based on the three-field viscous model (5.91), Figure 5.23d) shows the result of the configurational force based model discussed in Miehe & Guerses [122], and Figure 5.23e) exhibits the experimental result documented by Bittencourt, Wawrzynek, Ingraffea & Sousa [15]. The first two pictures illustrate the contour plots of the crack topology obtained by simulations with 58000 elements in combination with the viscosities $\eta = 2.5 \times 10^{-5}$ kN s/mm^2 and $\eta = 0.1 \times 10^{-5}$ kN s/mm^2. In the first picture, a slight crack initiation at the first hole can be observed. This can be prevented by repeating the computation with the same viscosity $\eta = 2.5{\times}10^{-5}$ kN s/mm^2, but with a higher mesh density in combination with a smaller length scale parameter. The results are depicted in Figure 5.23c). This behavior again shows the strong influence of both, the mesh density in combination with the minimum length scale parameter as well as the viscosity on the resulting crack pattern. Nevertheless, a comparison of the results in Figure 5.23b)-e) documents that both models capture the curved crack pattern very well. The configurational force based model with an adaptive reorientation of the segments at the crack tip yields appropriate crack trajectories for quite rough meshes. Figure 5.24 shows the evolution of the contour plots of the mesh with 79000 elements. Again, blue and red colors correspond to the undamaged and the fully damaged/cracked material, re-

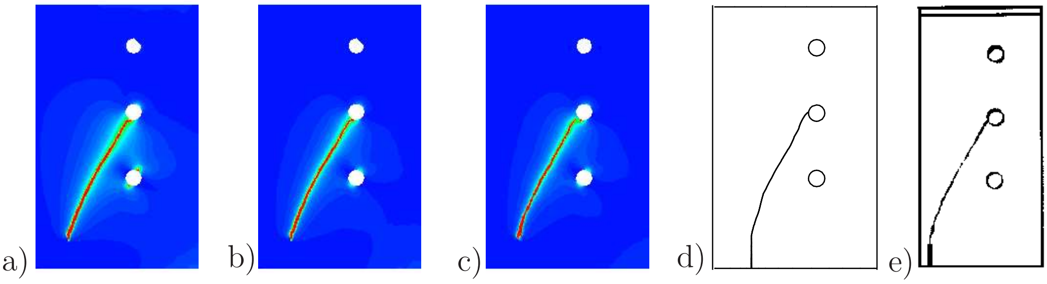

Figure 5.23: Asymmetric notched three point bending test. Crack topology of the viscous three-field formulation (5.91) for a) 58000 elements with $\eta = 2.5{\times}10^{-5}$ kN s/mm^2, b) 58000 elements with $\eta = 1.0{\times}10^{-6}$ kN s/mm^2, and c) 79000 elements with $\eta = 2.5{\times}10^{-5}$kN s/mm^2. d) Crack trajectories numerically obtained by Miehe & Gürses [122] and e) experimentally obtained crack patterns by Bittencourt, Wawrzynek, Ingraffea & Sousa [15].

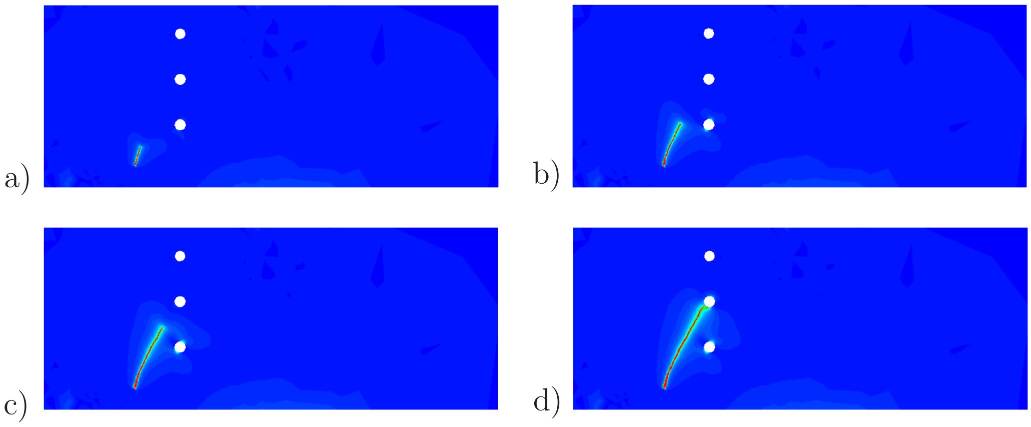

Figure 5.24: Asymmetric notched three point bending test. a)-d) Evolving crack topology for a mesh with 79000 elements with length scale parameter $l = 0.01$ mm.

spectively. However, the modeling of *discrete fracture* in the sense of the aforementioned publications is of limited applicability, because it cannot be applied to the modeling of crack initiation in solids free of defects and does not allow for the prediction of crack branching. These problems can be overcome by phase field modeling of fracture.

6. Material-Force-Based *h*-Adaptive Phase-Field-Type Fracture

As it turned out in the previous chapter, it is evident that for phase field modeling of fracture an h-adaptive finite element scheme has to be considered to reduce the computational costs. As intensively discussed in (5.29), for a given length scale parameter l the fractured zone has to be resolved at least by two elements of the size h. When performing computations with a static number of elements, this restraint results into finite element systems with many unknowns. Clearly, it makes sense to adapt the mesh locally with ongoing crack propagation. In order to control the mesh adaption during the computation, global and local mesh refinement indicators have to be set up. In what follows indicators are introduced that solely depend on discrete configurational forces. Hereby, the concept of configurational mechanics describes the effect of forces acting on singularities, inhomogeneities, and defects. The probably most prominent application of configuration mechanics can be found in the description of material configurational forces acting on crack tip singularities in the sense of Eshelby [39, 40] and Rice [152], see also Maugin [111], Gurtin [63, 64], Kienzler & Herrmann [92], Gurtin & Podio-Guidugli [72, 73], and Steinmann & Maugin [167] for a broader context. An exploitation of these configurational forces to model brittle crack propagation processes is discussed in Miehe & Gürses [122]. Even in the absence of true material inhomogeneities, in phase field modeling of fracture the evolving smooth crack topology is considered as a possible source of inhomogeneity that contributes to the resulting configurational forces. Parts of the material forces that are related to the diffusive surface created during crack propagation are considered as true material forces acting on an inhomogeneity. Thus, in a continuous setting the forces inside the bulk of a homogeneous fracturing solid have to vanish, whereas forces on the diffusive surface remain. When regarding the discrete solutions obtained by a finite element method, i.e. the satisfaction of the equilibrium in physical space, spurious discrete configurational forces even in the bulk domain remain. These spurious forces in the bulk domain can be related to an insufficient discretization which violates the equilibrium in material space. As a consequence, these spurious bulk forces are considered as a *measure* for the quality of the current finite element discretization and are exploited as global and local refinement indicators for an h-adaptive solution algorithm. Such h-adaptive schemes have been intensively discussed in the work by Zimmermann [184] for local elastic and inelastic material response. Follow up work in this spirit with application to gradient-type standard solids can be found in Baydoun [8], see also the proceeding contribution by Welschinger & Miehe[176].

To this end, the configurational setting of phase field fracture is introduced, the constitutive functions modified to take into account structural changes, and finally the governing balance equations in physical and material space are derived. Without changing the discretization, the evolution of discrete configurational forces in phase field fracture is discussed, where the aforementioned split of the material forces into a bulk and a diffusive surface part can be observed. This chapter closes with the setup of the h-adaptive algorithm and the discussion of a representative set of numerical examples.

6.1. Configurational Setting of Phase Field Fracture

The focus of this section is put on the formulation of phase field fracture when structural changes of the material are considered. Starting with the kinematic description of structural changes, their influence on the constitutive equations is investigated. The fo-

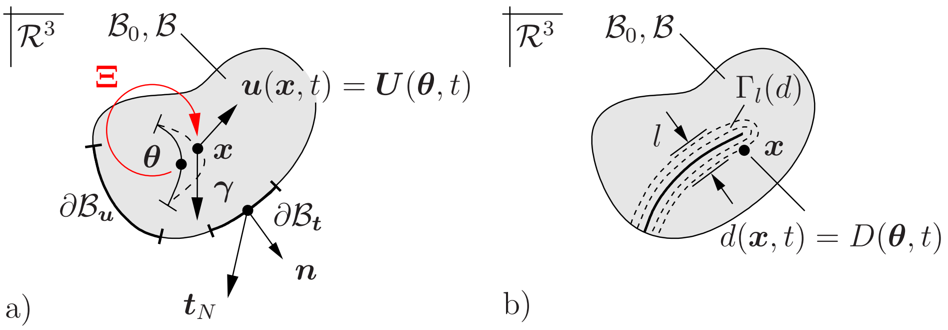
$\mathcal{R}^3$
$\mathcal{B}_0, \mathcal{B}$
Ξ
$\boldsymbol{u}(\boldsymbol{x},t) = \boldsymbol{U}(\boldsymbol{\theta},t)$
$\boldsymbol{\theta}$
$\boldsymbol{x}$
γ
$\partial\mathcal{B}_{\boldsymbol{u}}$
$\partial\mathcal{B}_{\boldsymbol{t}}$
$\boldsymbol{n}$
$\boldsymbol{t}_N$
a)
$\mathcal{R}^3$
$\mathcal{B}_0, \mathcal{B}$
$\Gamma_l(d)$
l
$\boldsymbol{x}$
$d(\boldsymbol{x},t) = D(\boldsymbol{\theta},t)$
b)

Figure 6.1: Configurational mechanics for the two-field problem of phase field fracture. Structural changes $\boldsymbol{x} = \Xi(\boldsymbol{\theta},t) \in \mathcal{B}$ are observed from time-invariant positions $\boldsymbol{\theta} \in \mathcal{B}_0$ allowing for a reparametrization of a) the displacement field $\boldsymbol{u}(\boldsymbol{x},t) = \boldsymbol{u}(\Xi(\boldsymbol{\theta},t),t) = \boldsymbol{U}(\boldsymbol{\theta},t)$ and b) the fracture phase field $d(\boldsymbol{x},t) = d(\Xi(\boldsymbol{\theta},t),t) = D(\boldsymbol{\theta},t)$.

cus hereby lies on model II that has intensively been discussed in the previous chapter. Finally, the governing dual balance equations in physical and material space are obtained from the standard argument of virtual power.

6.1.1. Basic Kinematics with Structural Changes. The first step towards configurational mechanics bases on the assumption that the reference coordinate is not fixed in time, the interior of the entire reference configuration is allowed to change. When analyzing small deformations only, these time-dependent structural changes read

$$\boldsymbol{x}(\boldsymbol{\theta},t) = \boldsymbol{X}(\boldsymbol{\theta},t) = \Xi(\boldsymbol{\theta},t) \tag{6.1}$$

and are observed from a time-invariant coordinate $\boldsymbol{\theta} \in \mathcal{B}_0$ that belongs to a time-invariant configuration $\mathcal{B}_0$. For an illustration see Figure 6.1. As a consequence, the global fields can either be expressed in terms of the convecting, time-variant coordinates $\boldsymbol{x} \in \mathcal{B}$ or in terms of the time-invariant coordinates $\boldsymbol{\theta} \in \mathcal{B}_0$. In the canonical two-field setting, the global fields are re-parametrized via

$$\boldsymbol{U}(\boldsymbol{\theta},t) = \boldsymbol{u}(\Xi(\boldsymbol{\theta},t),t) = \boldsymbol{u}(\boldsymbol{x},t) \quad \text{and} \quad D(\boldsymbol{\theta},t) = d(\Xi(\boldsymbol{\theta},t),t) = d(\boldsymbol{x},t)\,, \tag{6.2}$$

where $\boldsymbol{u}$ is the displacement field constrained by the Dirichlet and Neumann boundary conditions $\boldsymbol{u} = \boldsymbol{u}_D$ on $\partial\mathcal{B}_{\boldsymbol{u}}$ and $\boldsymbol{\sigma}\cdot\boldsymbol{n} = \boldsymbol{t}_N$ on $\partial\mathcal{B}_{\boldsymbol{t}}$ with $\partial\mathcal{B}_{\boldsymbol{u}} \cap \partial\mathcal{B}_{\boldsymbol{t}} = \emptyset$. The fracture phase field d is constrained by possible Dirichlet-type boundary conditions $d = 1$ on Γ and the natural Neumann-type condition $\nabla d \cdot \boldsymbol{n} = 0$ on the full surface $\mathcal{B}$. The spatial gradients

$$\frac{\partial \boldsymbol{U}}{\partial \boldsymbol{\theta}} = \frac{\partial \boldsymbol{u}}{\partial \Xi}\frac{\partial \Xi}{\partial \boldsymbol{\theta}} \quad \text{and} \quad \frac{\partial D}{\partial \boldsymbol{\theta}} = \frac{\partial d}{\partial \Xi}\frac{\partial \Xi}{\partial \boldsymbol{\theta}} \tag{6.3}$$

are simply obtained by considering the chain rule operation.

6.1.2. Time Derivatives of Kinematic Objects. As will be seen in the sequel, the reparametrization (6.1) dramatically influences the time derivatives of the basic kinematic objects. Due to the parametrization in the time-invariant coordinates $\boldsymbol{\theta}$, the total and partial time derivative of the reference coordinate commute, i.e.

$$\dot{\boldsymbol{x}} = \frac{\partial \boldsymbol{x}}{\partial t} \quad \text{and} \quad \dot{\Xi} = \frac{\partial \Xi}{\partial t}\,. \tag{6.4}$$

If the displacement and fracture phase field are defined on the time-independent configuration $\mathcal{B}_0$ with coordinates $\boldsymbol{\theta}$, their total and partial time derivatives commute. When the global fields are expressed in terms of the time-dependent, convecting coordinates $\boldsymbol{x} \in \mathcal{B}$, their rates have to be computed via

$$\dot{\boldsymbol{U}} = \frac{\partial \boldsymbol{U}}{\partial t} = \frac{\partial \boldsymbol{u}}{\partial \boldsymbol{x}} \frac{\partial \Xi}{\partial t} + \frac{\partial \boldsymbol{u}}{\partial t} \quad \text{and} \quad \dot{D} = \frac{\partial D}{\partial t} = \frac{\partial d}{\partial \boldsymbol{x}} \frac{\partial \Xi}{\partial t} + \frac{\partial d}{\partial t} \,. \tag{6.5}$$

Identification of the gradients $\nabla \boldsymbol{u} = \partial \boldsymbol{u} / \partial \boldsymbol{x}$ and $\nabla d = \partial d / \partial \boldsymbol{x}$ yields the representation

$$\partial_t \boldsymbol{u} = \dot{\boldsymbol{U}} - \nabla \boldsymbol{u} \, \dot{\Xi} \quad \text{and} \quad \partial_t d = \dot{D} - \nabla d \, \dot{\Xi} \,. \tag{6.6}$$

Notice hereby the classical split into a local and convective part. The total time derivatives of the gradients (6.3) follow by application of the chain rule

$$\frac{\partial}{\partial t} \frac{\partial \boldsymbol{U}}{\partial \boldsymbol{\theta}} = \frac{d}{dt} \left[\frac{\partial \boldsymbol{u}}{\partial \Xi} \frac{\partial \Xi}{\partial \boldsymbol{\theta}} \right] + \frac{\partial \boldsymbol{u}}{\partial \Xi} \frac{\partial}{\partial t} \frac{\partial \Xi}{\partial \boldsymbol{\theta}} \quad \text{and} \quad \frac{\partial}{\partial t} \frac{\partial D}{\partial \boldsymbol{\theta}} = \frac{d}{dt} \left[\frac{\partial d}{\partial \Xi} \frac{\partial \Xi}{\partial \boldsymbol{\theta}} \right] + \frac{\partial d}{\partial \Xi} \frac{\partial}{\partial t} \frac{\partial \Xi}{\partial \boldsymbol{\theta}} \,. \tag{6.7}$$

When in this expression the total time derivative is not performed explicitly, a simple reformulation yields the representation

$$\nabla \dot{\boldsymbol{u}} = \nabla \dot{\boldsymbol{U}} - \nabla \boldsymbol{u} \, \nabla \dot{\Xi} \quad \text{and} \quad \nabla \dot{d} = \nabla \dot{D} - \nabla d \, \nabla \dot{\Xi} \,. \tag{6.8}$$

The total time derivative of a volume element dV in the time-dependent reference configuration $\mathcal{B}$ is characterized by the relation

$$\dot{dV} = (\boldsymbol{1} : \nabla \dot{\boldsymbol{x}}) \, dV \,, \tag{6.9}$$

whereas the temporal change of a volume element dV_0 living in the time-invariant configuration $\mathcal{B}_0$ vanishes.

6.1.3. Dissipation Function for Crack Evolution. Point of departure to set up a dissipation function that takes into account structural changes is the temporal change of the diffusive crack topology (5.32). Together with the re-parametrization $(6.2)_2$ it reads

$$\dot{\Gamma}_l(\dot{d}, \dot{\boldsymbol{x}}; d, \boldsymbol{x}) = \frac{d}{dt} \Gamma_l(d(\Xi(\boldsymbol{\theta}, t), t)) \geq 0 \,. \tag{6.10}$$

Insertion of the regularized crack functional (5.20) and the temporal change of the volume element (6.9) allows for the reformulation

$$\dot{\Gamma}_l(\dot{d}, \dot{\boldsymbol{x}}; d, \boldsymbol{x}) = \int_{\mathcal{B}} \dot{\gamma} \, dV + \int_{\mathcal{B}} \gamma \, \dot{dV} = \int_{\mathcal{B}} \{ \, \partial_d \gamma \dot{d} + \partial_{\nabla d} \gamma \cdot \nabla \dot{d} + \gamma \boldsymbol{1} : \nabla \dot{\boldsymbol{x}} \, \} \, dV \geq 0 \,. \tag{6.11}$$

Replacement of the rate $(6.8)_2$ yields the re-parametrization of the crack topology evolution

$$\dot{\Gamma}_l(\dot{D}, \dot{\Xi}; D, \Xi) = \int_{\mathcal{B}} \{ \, \partial_d \gamma \dot{D} + \partial_{\nabla d} \gamma \cdot \nabla \dot{D} - (\nabla d \otimes \partial_{\nabla d} \gamma - \gamma \boldsymbol{1}) : \nabla \dot{\Xi} \, \} \, dV \geq 0 \,. \tag{6.12}$$

Note that for a time-independent configurational setting $\boldsymbol{x} = const$, which is the case in the subsequent staggered solution scheme, the irreversibility of the cracking process is guaranteed by a positive variational derivative of the crack surface density and a positive evolution of the fracture phase field

$$\delta_d\gamma := \partial_d\gamma - \operatorname{div}[\partial_{\nabla d}\gamma] \geq 0 \quad \text{and} \quad \dot{D} \geq 0\,. \tag{6.13}$$

According to (5.36), a dissipation functional for rate-independent processes is constructed

$$D(\dot{D}, \dot{\Xi}; D) = \int_{\mathcal{B}} \{\, \phi(\dot{\mathfrak{c}}; \mathfrak{c}) - (\nabla d \otimes \partial_{\nabla d}\gamma - \gamma \boldsymbol{1}) : \nabla\dot{\Xi} \,\}\, dV = \mathcal{D}(\dot{D}, \dot{\Xi}; D)\,, \tag{6.14}$$

where the dissipation function is positively homogeneous of degree one with the property $\phi(\dot{\mathfrak{c}}; \mathfrak{c}) = \partial_{\dot{\mathfrak{c}}}\phi(\dot{\mathfrak{c}}; \mathfrak{c}) \cdot \dot{\mathfrak{c}}$ and the dissipation potential functional D is identical to the dissipation $\mathcal{D}$. Here, $\mathfrak{c}$ denotes the generalized constitutive state as defined in (5.31). The dissipation function is additively decomposed via

$$\boxed{\phi(\dot{\mathfrak{c}}; \mathfrak{c}) = \underbrace{\check{\phi}_{loc}(\dot{D}; D)}_{\text{hom. micro-diss.}} + \underbrace{\check{\phi}_{non}(\nabla\dot{D}; \nabla D)}_{\text{inh. micro-diss.}}} \tag{6.15}$$

allowing for a separate discussion of homogeneous and inhomogeneous contributions. Instead of discussing the canonical two-field setting and the extended three-field setting, see Section 5.3.2.1 and Section 5.3.2.2, the focus is put on the latter one including its viscous regularized counterpart. To this end, the nonlocal term in (6.15) is specified to

$$\boxed{\check{\phi}_{non}(\nabla\dot{D}; \nabla D) = (g_c l \nabla D) \cdot \nabla\dot{D}\,.} \tag{6.16}$$

In the extended setting of the dissipation function, the thermodynamic force β dual to the fracture phase field D is introduced. This dissipative driving force is bounded by the threshold function

$$\varphi(\beta; D) = \beta - \psi_c(D) \leq 0 \quad \text{with} \quad \psi_c(D) = \frac{g_c}{l} D \tag{6.17}$$

and characterizes the local part of the dissipation function (6.15) as the constrained optimization problem

$$\boxed{\check{\phi}_{loc}(\dot{D}; D) = \sup_{\beta,\, \lambda \geq 0} [\, \beta\, \dot{D} - \lambda\, \varphi(\beta; D)\,]\,.} \tag{6.18}$$

It is solved by means of a Lagrange multiplier method involving the parameter λ. According to (5.48), the necessary condition yields the evolution equations

$$\dot{D} \geq 0 \quad \text{and} \quad \beta \leq \psi_c(D) \quad \text{and} \quad \dot{D}\,(\beta - \psi_c(D)) = 0\,. \tag{6.19}$$

The viscous regularization of (6.18) is given by the unconstrained optimization problem

$$\boxed{\check{\phi}^{\eta}_{loc}(\dot{D}; D) = \sup_{\beta} [\, \beta\, \dot{D} - \frac{1}{2\eta} \langle\, \beta - \psi_c(D)\, \rangle_+^2\,]\,,} \tag{6.20}$$

where the corresponding necessary condition determines the evolution of the phase field

$$\dot{D} = \frac{1}{\eta} \langle\, \beta - \psi_c(D)\, \rangle_+ \tag{6.21}$$

which satisfies the desired irreversibility property $(6.13)_2$. For $\eta \to 0$, the model degenerates to the rate-independent model considered above.

6.1.4. Anisotropic Degradation of Stored Bulk Energy. As it turned out in the previous chapter, the anisotropic formulation of the degrading bulk energy yields physically more reasonable results, where crack propagation in compression is excluded. The free energy stored in the entire solid $\mathcal{B}$ reads

$$E(\boldsymbol{u}, d, \boldsymbol{x}) = \int_{\mathcal{B}} \psi(\mathfrak{c}, \boldsymbol{x})\, dV\,, \tag{6.22}$$

where the dependency of the free energy function ψ on the position $\boldsymbol{x}$ indicates a possible inhomogeneous body. According to (5.53), the free energy function consists of a single contribution related to elastic distortions

$$\boxed{\psi(\mathfrak{c}, \boldsymbol{x}) = \underbrace{\bar{\psi}_{loc}(\nabla_s \boldsymbol{u}, d, \boldsymbol{x})}_{\text{elast. macro-dist.}}} \tag{6.23}$$

that has to be specified for anisotropic bulk response. In agreement with (5.61) it reads

$$\boxed{\bar{\psi}_{loc}(\nabla_s \boldsymbol{u}, d, \boldsymbol{x}) = (g(d) + k)\, \psi_0^+(\nabla_s \boldsymbol{u}, \boldsymbol{x}) + \psi_0^-(\nabla_s \boldsymbol{u}, \boldsymbol{x})\,.} \tag{6.24}$$

For a definition of the ground state energy $\psi_0^{\pm}$ and the degradation function $g(d)$, see Section 5.3.3.2. The evolution of the stored energy is expressed by

$$\begin{aligned} \mathcal{E}(\dot{\boldsymbol{u}}, \dot{d}, \dot{\boldsymbol{x}}; \boldsymbol{u}, d, \boldsymbol{x}) &= \frac{d}{dt} \int_{\mathcal{B}} \psi\, dV = \int_{\mathcal{B}} \dot{\psi}\, dV + \int_{\mathcal{B}} \psi\, d\dot{V} \\ &= \int_{\mathcal{B}} \{\, \partial_{\nabla_s \boldsymbol{u}} \psi : \nabla_s \dot{\boldsymbol{u}} + \partial_d \psi\, \dot{d} + \partial_{\boldsymbol{x}} \psi \cdot \dot{\boldsymbol{x}} + \psi \boldsymbol{1} : \nabla \dot{\boldsymbol{x}} \,\}\, dV\,. \end{aligned} \tag{6.25}$$

Exploitation of the kinematic relations introduced in Section 6.1.2 leads the representation

$$\begin{aligned} \mathcal{E}(\dot{\boldsymbol{U}}, \dot{D}, \dot{\Xi}; \boldsymbol{U}, D, \Xi) = &\int_{\mathcal{B}} \{\, \partial_{\nabla_s \boldsymbol{u}} \psi : \nabla_s \dot{\boldsymbol{U}} + \partial_d \psi \dot{D} \,\}\, dV \\ - &\int_{\mathcal{B}} \{\, (\nabla^T \boldsymbol{u} \cdot \partial_{\nabla_s \boldsymbol{u}} \psi - \psi \boldsymbol{1}) : \nabla \dot{\Xi} - \partial_{\boldsymbol{x}} \psi \cdot \dot{\Xi} \,\}\, dV\,, \end{aligned} \tag{6.26}$$

where possible structural changes are taken into account.

6.1.5. Governing Balance Equations in Physical and Material Space. The scope of this section is to derive the governing balance equations for phase field fracture for both in physical and material space. These equations govern the *displacement field* $\boldsymbol{U}$, the *fracture phase field* D, the *driving force field* β, and the *structural configuration* Ξ. In view of the displacement field, the boundary of the solid is decomposed into a part $\partial\mathcal{B}_{\boldsymbol{u}}$ with prescribed Dirichlet boundary condition

$$\boldsymbol{U} = \boldsymbol{U}_D \text{ on } \partial\mathcal{B}_{\boldsymbol{u}} \tag{6.27}$$

and a part $\partial\mathcal{B}_{\boldsymbol{t}}$ with prescribed Neumann tractions $\boldsymbol{t}_N$. The common set of these boundaries is zero, i.e. $\partial\mathcal{B}_{\boldsymbol{u}} \cap \partial\mathcal{B}_{\boldsymbol{t}} = \emptyset$. The power of external mechanical load is defined by

$$\mathcal{P}_{ext}(\partial_t \boldsymbol{u}) = \int_{\mathcal{B}} \boldsymbol{\gamma} \cdot \partial_t \boldsymbol{u}\, dV + \int_{\partial\mathcal{B}} \boldsymbol{t}_N \cdot \partial_t \boldsymbol{u}\, dA \tag{6.28}$$

with the prescribed volume body force $\boldsymbol{\gamma}$ and the partial rate $\partial_t \boldsymbol{u}$ that also takes into account the convective contributions, see equation $(6.6)_1$. In the sense of (6.12) and (6.26), a re-parametrization of the external power is obtained

$$\begin{aligned} \mathcal{P}_{ext}(\dot{\boldsymbol{U}}, \dot{\boldsymbol{\Xi}}) = & \int_{\mathcal{B}} \boldsymbol{\gamma} \cdot \dot{\boldsymbol{U}} \, dV + \int_{\partial \mathcal{B}_{\boldsymbol{t}}} \boldsymbol{t}_N \cdot \dot{\boldsymbol{U}} \, dA \\ & - \int_{\mathcal{B}} (\nabla^T \boldsymbol{u} \cdot \boldsymbol{\gamma}) \cdot \dot{\boldsymbol{\Xi}} \, dV - \int_{\partial \mathcal{B}_{\boldsymbol{t}}} (\nabla^T \boldsymbol{u} \cdot \boldsymbol{t}_N) \cdot \dot{\boldsymbol{\Xi}} \, dA \, . \end{aligned} \tag{6.29}$$

Regarding the fracture phase field, the Dirichlet-type boundary condition

$$D = 1 \text{ on } \Gamma \tag{6.30}$$

is considered, where $\Gamma \subset \mathcal{B}$ is a possible a priori given sharp crack surface. Furthermore, for the fracture phase field the natural Neumann-type boundary condition $\nabla D \cdot \boldsymbol{n} = 0$ on the entire boundary $\partial \mathcal{B}$ is postulated. The fracture phase field is assumed to be driven by the displacement field of the solid. Thus, no external power associated with the fracture phase field is considered. Having the dissipation functional (6.14) with local dissipation function (6.20), the rate of the energy storage functional (6.25), and the power of external loading (6.29) at hand, it remains to evaluate the argument of virtual power

$$\boxed{\mathcal{E}(\dot{\boldsymbol{U}}, \dot{D}, \dot{\boldsymbol{\Xi}}) + \mathcal{D}(\dot{D}, \dot{\boldsymbol{\Xi}}) - \mathcal{P}_{ext}(\dot{\boldsymbol{U}}, \dot{\boldsymbol{\Xi}}) = 0} \tag{6.31}$$

valid for the admissible rates $\dot{\boldsymbol{U}}$ and $\dot{D}$ of the displacement and the fracture phase field satisfying the homogeneous form of the Dirichlet boundary conditions in physical space

$$\dot{\boldsymbol{U}} \in \mathcal{W}_{\boldsymbol{u}} := \{ \dot{\boldsymbol{U}} \,|\, \dot{\boldsymbol{U}} = \boldsymbol{0} \text{ on } \partial \mathcal{B}_{\boldsymbol{u}} \} \quad \text{and} \quad \dot{D} \in \mathcal{W}_d := \{ \dot{D} \,|\, \dot{D} = 0 \text{ on } \Gamma \} \tag{6.32}$$

and the rate $\dot{\boldsymbol{\Xi}}$ of the structural configuration satisfying the homogeneous form of the Dirichlet boundary condition in material space

$$\dot{\boldsymbol{\Xi}} \in \mathcal{W}_{\boldsymbol{x}} := \{ \dot{\boldsymbol{\Xi}} \,|\, \dot{\boldsymbol{\Xi}} = \boldsymbol{0} \text{ on } \partial \mathcal{B} \} \, . \tag{6.33}$$

This condition states that the material positions $\boldsymbol{x}$ on the entire material surface $\partial \mathcal{B}$ are constant, i.e. the shape of the solid is not allowed to change. The global balance equilibrates the external and internal virtual power for the quasi-static setting. Insertion of the previously discussed functionals, application of Gauss' theorem, taking into account the admissible rates (6.32) and (6.33), and the natural Neumann-type constraint $\nabla d \cdot \boldsymbol{n} = 0$ on $\partial \mathcal{B}$ gives the explicit representation

$$\begin{aligned} 0 = & \int_{\mathcal{B}} \{ (- \operatorname{div}[\partial_{\nabla_s \boldsymbol{u}} \psi] - \boldsymbol{\gamma}) \cdot \dot{\boldsymbol{U}} \} \, dV + \int_{\partial \mathcal{B}_{\boldsymbol{t}}} (\partial_{\nabla_s \boldsymbol{u}} \psi \cdot \boldsymbol{n} - \boldsymbol{t}_N) \cdot \dot{\boldsymbol{U}} \, dA \\ & + \int_{\mathcal{B}} \{ (- \operatorname{div}[g_c l \nabla d] + [\partial_d \psi + \beta]) \, \dot{D} \} \, dV \\ & + \int_{\mathcal{B}} \{ (- \operatorname{div}[(\psi \boldsymbol{1} - \nabla^T \boldsymbol{u} \cdot \partial_{\nabla_s \boldsymbol{u}} \psi) + (g_c \gamma \boldsymbol{1} - g_c \nabla d \otimes \partial_{\nabla d} \gamma)]) \cdot \dot{\boldsymbol{\Xi}} \} \, dV \\ & + \int_{\mathcal{B}} \{ (\partial_{\boldsymbol{x}} \psi + \nabla^T \boldsymbol{u} \cdot \boldsymbol{\gamma}) \cdot \dot{\boldsymbol{\Xi}} \} \, dV \, . \end{aligned} \tag{6.34}$$

Application of the localization theorem finally yields the coupled balance equations for the three-field setting of phase field fracture in *physical space*

$$\begin{aligned}\boldsymbol{0} &= \operatorname{div}[\,((1-d)^2+k)\,\partial_{\nabla_s \boldsymbol{u}}\psi_0^+(\nabla_s \boldsymbol{u}) + \partial_{\nabla_s \boldsymbol{u}}\psi_0^-(\nabla_s \boldsymbol{u})\,] + \boldsymbol{\gamma}\\ 0 &= g_c l \Delta d + 2(1-d)\,\psi_0^+(\boldsymbol{\varepsilon}) - \beta\\ 0 &= \dot{d} - \frac{1}{\eta}\langle \beta - \psi_c(d)\rangle_+\end{aligned} \tag{6.35}$$

in combination with the Neumann-type boundary conditions for the displacement field and the fracture phase field

$$\partial_{\nabla_s \boldsymbol{u}}\psi \cdot \boldsymbol{n} = \boldsymbol{t}_N \text{ on } \partial\mathcal{B}_{\boldsymbol{t}} \quad \text{and} \quad \nabla d \cdot \boldsymbol{n} = 0 \text{ on } \partial\mathcal{B}\,. \tag{6.36}$$

The balance $(6.35)_1$ specifies the macroscopic equilibrium condition and $(6.35)_{2,3}$ may be considered as the microscopic evolution subproblem of the fracture phase field. In *configurational space*, the balance equation can be deduced

$$\operatorname{div}[(\psi \boldsymbol{1} - \nabla^T \boldsymbol{u} \cdot \partial_{\nabla_s \boldsymbol{u}}\psi) + (g_c\gamma \boldsymbol{1} - g_c \nabla d \otimes \partial_{\nabla d}\gamma)] + [-\partial_{\boldsymbol{x}}\psi - \nabla^T \boldsymbol{u} \cdot \boldsymbol{\gamma}] = \boldsymbol{0}\,. \tag{6.37}$$

In this expression, the generalized Eshelby tensor is identified and consists of two parts

$$\boldsymbol{\Sigma}^{\mathcal{B}} := \psi \boldsymbol{1} - \nabla^T \boldsymbol{u} \cdot \partial_{\nabla_s \boldsymbol{u}}\psi \quad \text{and} \quad \boldsymbol{\Sigma}^{\Gamma} := g_c\gamma \boldsymbol{1} - g_c \nabla d \otimes \partial_{\nabla d}\gamma\,, \tag{6.38}$$

the elastic bulk part $\boldsymbol{\Sigma}^{\mathcal{B}}$ and the surface part $\boldsymbol{\Sigma}^{\Gamma}$, see also KUHN & MÜLLER [95]. Furthermore, the generalized configurational volume force vector can be extracted

$$\boldsymbol{\Gamma} := -\partial_{\boldsymbol{x}}\psi - \nabla^T \boldsymbol{u} \cdot \boldsymbol{\gamma}\,. \tag{6.39}$$

Note that the aforementioned additive split of the generalized Eshelby tensor (6.38) into a bulk and a surface term later plays an important role when setting up global and local mesh refinement indicators for an h-adaptive finite element solution scheme.

6.2. Algorithmic Incremental Variational Principle

The subsequent treatment focuses on a staggered solution scheme of the balance equations in physical and material space. In this scenario, the structural configuration is frozen in time, the balance equations in physical space are solved in a standard procedure, and the balance equation in material space is simply evaluated. Having this understanding in mind, an algorithmic incremental variational statement can be set up.

6.2.1. Time-Discrete Field Variables in an Incremental Sense. The coupled balance equations for phase field fracture in physical and material space can alternatively be obtained from an incremental variational principle. To this end consider the time-discrete solutions of the field variables at discrete times $0, t_1, t_2, \ldots, t_n, t_{n+1}, \ldots, T$ within the process interval $[0, T]$. Within a typical time step $[t_n, t_{n+1}]$, the time step length reads

$$\tau_{n+1} := t_{n+1} - t_n > 0\,. \tag{6.40}$$

In what follows, all field variables at time t_n are assumed to be known. The global fields at time t_{n+1} are derived based on a variational principle valid for the current time interval.

Regarding a compact notation, the subscript $n+1$ is dropped, all variables without subscript are meant to be evaluated at the time t_{n+1}. In particular one can write

$$\boldsymbol{x} := \boldsymbol{x}(\boldsymbol{\theta}, t_{n+1}) = \Xi(\boldsymbol{\theta}, t_{n+1}) \quad \text{and} \quad \boldsymbol{x}_n := \boldsymbol{x}(\boldsymbol{\theta}, t_n) = \Xi(\boldsymbol{\theta}, t_n) \tag{6.41}$$

for the structural configuration. In the exact same manner

$$\boldsymbol{u} := \boldsymbol{u}(\boldsymbol{x}(\boldsymbol{\theta}, t_{n+1}), t_{n+1}) = \boldsymbol{U}(\boldsymbol{\theta}, t_{n+1}) \quad \text{and} \quad \boldsymbol{u}_n := \boldsymbol{u}(\boldsymbol{x}(\boldsymbol{\theta}, t_n), t_n) = \boldsymbol{U}(\boldsymbol{\theta}, t_n) \tag{6.42}$$

for the displacement field and finally

$$d := d(\boldsymbol{x}(\boldsymbol{\theta}, t_{n+1}), t_{n+1}) = D(\boldsymbol{\theta}, t_{n+1}) \quad \text{and} \quad d_n := d(\boldsymbol{x}(\boldsymbol{\theta}, t_n), t_n) = D(\boldsymbol{\theta}, t_n) \tag{6.43}$$

for the fracture phase field at the solution times t_{n+1} and t_n. As a consequence, the rates of the global fields are *constant quantities* within the time increment under focus, i.e.

$$\dot{\boldsymbol{u}} := (\boldsymbol{u} - \boldsymbol{u}_n)/\tau \quad \text{and} \quad \dot{d} := (d - d_n)/\tau\,. \tag{6.44}$$

In the extended three-field setting under focus, the dissipative driving force

$$\beta := \beta(\boldsymbol{x}(\boldsymbol{\theta}, t_{n+1}), t_{n+1}) = B(\boldsymbol{\theta}, t_{n+1}) \tag{6.45}$$

evaluated at time t_{n+1} has additionally to be provided.

6.2.2. Incremental Energy, Dissipation, and Work Functionals. The setup of incremental variational statements critically depends on the definition of internal and external incremental work done to the system within a typical time step. In what follows, ideas from Section 5.3.5 are extended to take into account the effects of structural changes. Within the discrete time interval $[t_n, t_{n+1}]$, the incremental energy is defined by

$$E^\tau := \int_{t_n}^{t_{n+1}} \dot{E}\, dt = E(t_{n+1}) - E(t_n) \tag{6.46}$$

expressed in terms of the energy functional (6.22). The incremental energy is considered as a functional depending on the current field variables

$$\begin{aligned} E^\tau(\boldsymbol{u}, d, \boldsymbol{x}) &:= \int_{\mathcal{B}} \psi(\mathfrak{c}, \boldsymbol{x})\, dV - \int_{\mathcal{B}_n} \psi(\mathfrak{c}_n, \boldsymbol{x}_n)\, dV_n \\ &= \int_{\mathcal{B}_n} \{ \frac{J}{J_n} \psi(\mathfrak{c}, \boldsymbol{x}) - \psi(\mathfrak{c}_n, \boldsymbol{x}_n) \}\, dV_n\,. \end{aligned} \tag{6.47}$$

Here, the relationship between the volume element dV_0 of the time-invariant configuration $\mathcal{B}_0$ and the current and previous volume elements are given by $dV = \det[\boldsymbol{J}]\, dV_0 =: J\, dV_0$ and $dV_n = \det[\boldsymbol{J}_n]\, dV_0 =: J_n\, dV_0$, where the fundamental mappings $\boldsymbol{J} := \nabla_{\boldsymbol{\theta}} \Xi$ and $\boldsymbol{J}_n := \nabla_{\boldsymbol{\theta}} \Xi_n$ are introduced. The incremental dissipation in the solid is defined by

$$D^\tau := \int_{t_n}^{t_{n+1}} D\, dt\,. \tag{6.48}$$

For the three-field model characterized by the rate-dependent dissipation function (6.20), the following algorithmic expression is constructed for the incremental dissipation

$$\begin{aligned} D^\tau_\eta(d, \beta, \boldsymbol{x}) := &\int_{\mathcal{B}_n} \{\beta(d - d_n) - \frac{\tau}{2\eta} \langle \beta - \psi_c(d_n) \rangle_+^2 + \frac{g_c l}{2} [\|\nabla d\|^2 - \|\nabla d_n\|^2]\}\, dV_n \\ + &\int_{\mathcal{B}_n} \{ g_c [\frac{J}{J_n} \gamma_n - \gamma_n] \}\, dV_n\,. \end{aligned} \tag{6.49}$$

The incremental work of the external actions of the multi-field problem associated with the discrete time interval can be given by

$$W^\tau := \int_{t_n}^{t_{n+1}} \mathcal{P}_{ext}\, dt\,. \tag{6.50}$$

Finally, the algorithmic representation of the incremental external work

$$\begin{aligned} W^\tau(\boldsymbol{u},\boldsymbol{x}) &:= \int_{\mathcal{B}_n} \boldsymbol{\gamma}\cdot\boldsymbol{u}\, dV + \int_{\partial\mathcal{B}_t} \boldsymbol{t}_N\cdot\boldsymbol{u}\, dA - \int_{\mathcal{B}_n} \boldsymbol{\gamma}\cdot\boldsymbol{u}_n\, dV_n - \int_{\partial\mathcal{B}_{tn}} \boldsymbol{t}_N\cdot\boldsymbol{u}_n\, dA_n \\ &= \int_{\mathcal{B}_n} \{\, \boldsymbol{\gamma}\cdot[\frac{J}{J_n}\boldsymbol{u}-\boldsymbol{u}_n]\,\}\, dV_n + \int_{\partial\mathcal{B}_{tn}} \{\, \boldsymbol{t}_N\cdot[\frac{J}{J_n}\boldsymbol{u}-\boldsymbol{u}_n]\,\}\, dA_n \end{aligned} \tag{6.51}$$

is introduced. Note that due to the essential boundary condition $\boldsymbol{x} = const$ on $\partial\mathcal{B}$ no structural changes on the entire surface are permitted.

6.2.3. Incremental Variational Principle in Physical and Material Space. An extended incremental variational principle of phase field fracture is now constructed that takes into account possible structural changes of the material. This principle bases on the incremental potential

$$\underbrace{\Pi^{*\tau}_\eta(\boldsymbol{u},d,\beta,\boldsymbol{x})}_{potential} := \underbrace{E^\tau(\boldsymbol{u},d,\boldsymbol{x})}_{energy} + \underbrace{D^{*\tau}_\eta(d,\beta,\boldsymbol{x})}_{dissipation} - \underbrace{W^\tau(\boldsymbol{u},\boldsymbol{x})}_{work} \tag{6.52}$$

and contains the incremental energy storage (6.47), the incremental dissipation (6.49), and the incremental external work (6.51). Regarding a compact notation of the four-field setting, the generalized constitutive state and displacement vector

$$\mathfrak{c}^*(\mathfrak{u}^*) := \{\, \nabla_s\boldsymbol{u}, d, \nabla d, \beta \,\} \quad \text{with} \quad \mathfrak{u}^* := \{\, \boldsymbol{u}, d, \beta \,\} \tag{6.53}$$

are introduced. The former contains the strains, the fracture phase field, its gradient, and the dissipative driving force. With this compact notation at hand, the incremental potential (6.52) may be reformulated

$$\begin{aligned} \Pi^{*\tau}_\eta(\mathfrak{u}^*,\boldsymbol{x}) := &\int_{\mathcal{B}_n} \{\, \pi^{*\tau}_\eta(\mathfrak{c}^*,\boldsymbol{x};\mathfrak{c}^*_n,\boldsymbol{x}_n) - \boldsymbol{\gamma}\cdot[\frac{J}{J_n}\boldsymbol{u}-\boldsymbol{u}_n]\,\}\, dV_n \\ &- \int_{\partial\mathcal{B}_{tn}} \boldsymbol{t}_N\cdot[\frac{J}{J_n}\boldsymbol{u}-\boldsymbol{u}_n]\, dA_n\,. \end{aligned} \tag{6.54}$$

The local quantity $\pi^{*\tau}_\eta$ is denoted *incremental internal work density for solids undergoing structural changes* and is defined by the expression

$$\begin{aligned} \pi^{*\tau}_\eta(\mathfrak{c}^*,\boldsymbol{x};\mathfrak{c}^*_n,\boldsymbol{x}_n) = &\frac{J}{J_n}\psi(\mathfrak{c},\boldsymbol{x}) - \psi(\mathfrak{c}_n,\boldsymbol{x}_n) \\ &+ \beta(d-d_n) - \frac{\tau}{2\eta}\langle\beta-\psi_c(d_n)\rangle^2_+ + \frac{g_c l}{2}[\,\|\nabla d\|^2 - \|\nabla d_n\|^2\,] \\ &+ g_c[\frac{J}{J_n}\gamma_n - \gamma_n]\,. \end{aligned} \tag{6.55}$$

The stationary principle in a finite step sized incremental setting reads

$$\{\, \boldsymbol{u}, d, \beta, \boldsymbol{x} \,\} = \arg\{ \inf_{\boldsymbol{u}} \inf_{d} \sup_{\beta} \inf_{\boldsymbol{x}} \Pi^{*\tau}_\eta(\boldsymbol{u},d,\beta,\boldsymbol{x}) \,\} \tag{6.56}$$

and determines the displacement field $\boldsymbol{u}$, the fracture phase field d, the dissipative driving force β, and the structural configuration $\boldsymbol{x}$ at current time t_{n+1} as the *saddle point* of the incremental potential (6.54). The necessary condition reads

$$0 = \delta\Pi^{*\tau}_{\eta} = \delta_{\mathbf{u}^*}\Pi^{*\tau}_{\eta} + \delta_{\boldsymbol{x}}\Pi^{*\tau}_{\eta} = \underbrace{\delta_{\boldsymbol{u}}\Pi^{*\tau}_{\eta} + \delta_{d}\Pi^{*\tau}_{\eta} + \delta_{\beta}\Pi^{*\tau}_{\eta}}_{\text{phys. space}} + \underbrace{\delta_{\boldsymbol{x}}\Pi^{*\tau}_{\eta}}_{\text{mat. space}} \tag{6.57}$$

and can be split into a part related to the equilibrium in physical space and a part related to the equilibrium in material space. The former one can be given in the compact form

$$\delta_{\mathbf{u}^*}\Pi^{*\tau}_{\eta} = \int_{\mathcal{B}_n} \{\, \partial_{\boldsymbol{\mathfrak{c}}^*}\pi^{*\tau}_{\eta} \cdot \delta_{\mathbf{u}^*}\boldsymbol{\mathfrak{c}}^* - \frac{J}{J_n}\boldsymbol{\gamma}\cdot\delta\boldsymbol{u} \,\}\, dV_n - \int_{\partial\mathcal{B}_{tn}} \frac{J}{J_n}\boldsymbol{t}_N \cdot \delta\boldsymbol{u}\, dA_n \,, \tag{6.58}$$

where $\delta_{\mathbf{u}^*}\boldsymbol{\mathfrak{c}}^*$ contains the admissible variations $\delta\mathbf{u}^* := \{\, \delta\boldsymbol{u}, \delta d, \delta\beta \,\}^T$ with $\delta\boldsymbol{u} \in \mathcal{W}_{\boldsymbol{u}}$ and $\delta d \in \mathcal{W}_d$. Performing the variation explicitly and application of Gauss' theorem yields

$$\begin{aligned}
\delta_{\mathbf{u}^*}\Pi^{*\tau}_{\eta} = & \int_{\mathcal{B}_n} \{\, -\frac{J}{J_n}(\mathrm{div}[\partial_{\nabla_s\boldsymbol{u}}\psi] + \boldsymbol{\gamma}) \cdot \delta\boldsymbol{u} \,\}\, dV_n \\
& + \int_{\mathcal{B}_n} \{\, (\frac{J}{J_n}\partial_d\psi + \beta - g_c l \Delta d]\, \delta d \,\}\, dV_n \\
& + \int_{\mathcal{B}_n} \{\, (d - d_n - \frac{\tau}{\eta}\langle \beta - \psi_c(d_n)\rangle_+)\, \delta\beta \,\}\, dV_n \\
& + \int_{\partial\mathcal{B}_{tn}} \{\, \frac{J}{J_n}(\partial_{\nabla_s\boldsymbol{u}}\psi \cdot \boldsymbol{n} - \boldsymbol{t}_N) \cdot \delta\boldsymbol{u} \,\}\, dA_n \,.
\end{aligned} \tag{6.59}$$

The equation $(6.59)_1$ describes the macroscopic equilibrium and the equations $(6.59)_{2,3}$ characterize the evolution subproblem of the fracture phase field. Application of localization theorem finally yields the *algorithmic* representation of the governing field equations

$$\begin{aligned}
\boldsymbol{0} &= \frac{J}{J_n}\,\mathrm{div}[\,((1-d)^2 + k)\,\partial_{\nabla_s\boldsymbol{u}}\psi_0^+(\nabla_s\boldsymbol{u}) + \partial_{\nabla_s\boldsymbol{u}}\psi_0^-(\nabla_s\boldsymbol{u})\,] + \frac{J}{J_n}\boldsymbol{\gamma} \\
0 &= g_c l \Delta d + \frac{J}{J_n} 2(1-d)\,\psi_0^+(\boldsymbol{\varepsilon}) - \beta \\
0 &= d - d_n - \frac{\tau}{\eta}\langle \beta - \psi_c(d_n)\rangle_+
\end{aligned} \tag{6.60}$$

in *physical space* together with the Neumann boundary conditions (6.36). According to (6.57), the equilibrium condition in material space is determined by

$$\delta_{\boldsymbol{x}}\Pi^{*\tau}_{\eta} = \int_{\mathcal{B}_n} \{\, \delta_{\boldsymbol{x}}\pi^{*\tau}_{\eta} - \frac{J}{J_n}\boldsymbol{\gamma}\cdot\nabla\boldsymbol{u}\cdot\delta\boldsymbol{x} - \frac{J}{J_n}(\boldsymbol{\gamma}\cdot\boldsymbol{u})\boldsymbol{1} : \nabla\delta\boldsymbol{x} \,\}\, dV_n \,. \tag{6.61}$$

Performing the variation explicitly and application of Gauss' theorem yields

$$
\begin{aligned}
\delta_{\boldsymbol{x}}\Pi^{*\tau}_{\eta} = & \int_{\mathcal{B}_n} \{\, [-\frac{J}{J_n}(\operatorname{div}[\partial_{\nabla_s \boldsymbol{u}}\psi] + \boldsymbol{\gamma}) \cdot \nabla \boldsymbol{u}] \cdot \delta \boldsymbol{x} \,\}\, dV_n \\
& + \int_{\mathcal{B}_n} \{\, [(\frac{J}{J_n}\partial_d \psi + \beta - g_c l \Delta d)\nabla d] \cdot \delta \boldsymbol{x} \,\}\, dV_n \\
& + \int_{\mathcal{B}_n} \{\, [(d - d_n - \frac{\tau}{\eta}\langle \beta - \psi_c(d)\rangle_+)\nabla \beta] \cdot \delta \boldsymbol{x} \,\}\, dV_n \\
& + \int_{\mathcal{B}_n} \{\, \frac{J}{J_n}[\partial_{\boldsymbol{x}}\psi + \nabla^T \boldsymbol{u} \cdot \boldsymbol{\gamma}] \cdot \delta \boldsymbol{x} \,\}\, dV_n \\
& + \int_{\mathcal{B}_n} \{\, [\frac{J}{J_n}\psi \boldsymbol{1} - \frac{J}{J_n}\nabla^T \boldsymbol{u} \cdot \partial_{\nabla_s \boldsymbol{u}}\psi] : \nabla \delta \boldsymbol{x} \,\}\, dV_n \\
& + \int_{\mathcal{B}_n} \{\, [\frac{J}{J_n} g_c \gamma_n \boldsymbol{1} - g_c l \nabla d \otimes \nabla d] : \nabla \delta \boldsymbol{x} \,\}\, dV_n \,.
\end{aligned}
\tag{6.62}
$$

In this expression, the equations $(6.62)_{1,2,3}$ are identified as the equilibrium in physical space as presented in (6.59). The remaining balance in *material space* takes the form

$$
\boldsymbol{0} = \operatorname{div}[\frac{J}{J_n}(\psi \boldsymbol{1} - \nabla^T \boldsymbol{u} \cdot \partial_{\nabla_s \boldsymbol{u}}\psi) + (\frac{J}{J_n} g_c \gamma_n \boldsymbol{1} - g_c l \nabla d \otimes \nabla d)] - \frac{J}{J_n}[\partial_{\boldsymbol{x}}\psi + \nabla^T \boldsymbol{u} \cdot \boldsymbol{\gamma}] \,. \tag{6.63}
$$

In this algorithmic setting, the Eshelby tensor for phase field fracture takes the structure

$$
\boldsymbol{\Sigma}^{\mathcal{B}} := \frac{J}{J_n}\psi \boldsymbol{1} - \frac{J}{J_n}\nabla^T \boldsymbol{u} \cdot \partial_{\nabla_s \boldsymbol{u}}\psi \quad \text{and} \quad \boldsymbol{\Sigma}^{\Gamma} := \frac{J}{J_n} g_c \gamma_n \boldsymbol{1} - g_c l \nabla d \otimes \nabla d \,, \tag{6.64}
$$

where again the additive split into a bulk $\boldsymbol{\Sigma}^{\mathcal{B}}$ and surface part $\boldsymbol{\Sigma}^{\Gamma}$ is considered. Furthermore, the configurational volume force vector is identified

$$
\boldsymbol{\Gamma} := -\frac{J}{J_n}[\partial_{\boldsymbol{x}}\psi - \nabla^T \boldsymbol{u} \cdot \boldsymbol{\gamma}] \,. \tag{6.65}
$$

Note that for the specific choice of the incremental potential (6.55), the algorithmic representation of the governing balance equations in physical (6.60) and material space (6.63) contain the term J/J_n that is related to the fact that the domain of integration changes from time t_n to t_{n+1}. Hereby, only interior points of the solid are affected, structural changes on the boundary of the solid are not permitted, see the boundary restraint (6.33).

6.3. Finite Element Formulation of Incremental Variational Principle

In this section, the focus is put on the discretization of the previously discussed incremental variational statement. First of all, the interpolation matrices for the primary fields in physical and material space are introduced. In a second step, a staggered solution scheme for the physical and material space is investigated which finally allows for the computation of discrete configurational forces.

6.3.1. Discrete Variational Principle in Physical and Material Space. The extended multi-field finite element method has to be generalized to take into account possible structural changes. Restricting to two-dimensional problems, the physical subproblem consists of the global fields and the related generalized constitutive state

$$
\boldsymbol{\mathfrak{u}}^* := \{\, u_1, u_2, d, \beta \,\} \quad \text{and} \quad \boldsymbol{\mathfrak{c}}^*(\boldsymbol{\mathfrak{u}}^*) := \{\, u_{1,1}, u_{2,2}, u_{1,2} + u_{2,1}, d, d_{,1}, d_{,2}, \beta \,\} \,. \tag{6.66}
$$

In complete analogy to Section 3.9, the generalized deformation vector $(6.66)_1$ and the variation of the generalized constitutive state vector $(6.66)_2$ are approximated via

$$\boldsymbol{\mathfrak{u}}^{*h} = \boldsymbol{\mathfrak{N}}^*(\boldsymbol{\theta})\,\boldsymbol{\mathfrak{d}}^* \quad \text{and} \quad \delta_{\boldsymbol{\mathfrak{d}}^*}\boldsymbol{\mathfrak{c}}^{*h} = \boldsymbol{\mathfrak{B}}^*(\boldsymbol{\theta})\,\delta\boldsymbol{\mathfrak{d}}^*\,. \tag{6.67}$$

The generalized displacement vector $\boldsymbol{\mathfrak{d}}^*$ and the generalized matrices $[\boldsymbol{\mathfrak{N}}^*]^e_i$ and $[\boldsymbol{\mathfrak{B}}^*]^e_i$ have been defined at the end of the previous chapter, see equations (5.100), (5.101), and (5.102). The problem in material space consists of the structural configuration and its gradient

$$\boldsymbol{x} := \{\, x_1, x_2 \,\} \quad \text{and} \quad \nabla\boldsymbol{x} := \{\, x_{1,1}, x_{2,2}, x_{1,2}, x_{2,1} \,\}\,, \tag{6.68}$$

the discrete representations of the corresponding variations are defined by

$$\boldsymbol{x}^h(\boldsymbol{\theta}) = \boldsymbol{N}(\boldsymbol{\theta})\,\boldsymbol{D} \quad \text{with} \quad \nabla\boldsymbol{x}^h(\boldsymbol{\theta}) = \boldsymbol{B}(\boldsymbol{\theta})\,\boldsymbol{D}\,. \tag{6.69}$$

These expressions contain the discrete nodal values of the structural configuration

$$\boldsymbol{D}_i = [\, D_1, D_2 \,]^T_i \tag{6.70}$$

in 1- and 2-direction and the approximation matrices for the primary field and its gradient

$$[\boldsymbol{N}]^e_i = \begin{bmatrix} N & 0 \\ 0 & N \end{bmatrix}_i \quad \text{and} \quad [\boldsymbol{B}]^e_i = \begin{bmatrix} N_{,1} & 0 & N_{,2} & 0 \\ 0 & N_{,2} & 0 & N_{,1} \end{bmatrix}^T_i\,. \tag{6.71}$$

Based on these discretizations of physical and configurational objects, the discrete version of the necessary condition (6.57) can be introduced

$$0 = \delta\Pi^{*h}_\eta = \delta_{\boldsymbol{\mathfrak{u}}^{*h}}\Pi^{*h}_\eta + \delta_{\boldsymbol{x}^h}\Pi^{*h}_\eta = \Pi^{*h}_{\eta,\boldsymbol{\mathfrak{d}}^*}\cdot\delta\boldsymbol{\mathfrak{d}}^* + \Pi^{*h}_{\eta,\boldsymbol{D}}\cdot\delta\boldsymbol{D}\,. \tag{6.72}$$

For arbitrary variations in physical $\delta\boldsymbol{\mathfrak{d}}^*$ and material space $\delta\boldsymbol{D}$, the discrete residuals

$$\begin{aligned} \boldsymbol{0} = \Pi^{*h}_{\eta,\boldsymbol{\mathfrak{d}}^*} &= \int_{\mathcal{B}^h_n} \{\, \boldsymbol{\mathfrak{B}}^{*T}[\boldsymbol{S}^*(\boldsymbol{\mathfrak{d}}^*, \boldsymbol{D})] - \boldsymbol{\mathfrak{N}}^T\boldsymbol{\mathfrak{g}} \,\}\, dV_n - \int_{\partial\mathcal{B}^h_{n\mathfrak{t}}} \boldsymbol{\mathfrak{N}}^T\boldsymbol{\mathfrak{t}}_N\, dA_n \\ \boldsymbol{0} = \Pi^{*h}_{\eta,\boldsymbol{x}} &= \int_{\mathcal{B}^h_n} \{\, \boldsymbol{B}^T[\boldsymbol{\Sigma}^{\mathcal{B}}(\boldsymbol{\mathfrak{d}}^*, \boldsymbol{D}) + \boldsymbol{\Sigma}^{\Gamma}(\boldsymbol{\mathfrak{d}}^*, \boldsymbol{D})] - \boldsymbol{N}^T\boldsymbol{\Gamma}(\boldsymbol{\mathfrak{d}}^*, \boldsymbol{D}) \,\}\, dV_n \end{aligned} \tag{6.73}$$

have to vanish. The generalized stresses are $\boldsymbol{S}^*(\boldsymbol{\mathfrak{d}}^*, \boldsymbol{D}) := \partial_{\boldsymbol{\mathfrak{c}}^*}\pi^{*\tau}_\eta(\boldsymbol{\mathfrak{d}}^*, \boldsymbol{D})$, the components of the Eshelby tensor $\boldsymbol{\Sigma}^{\mathcal{B}}(\boldsymbol{\mathfrak{d}}^*, \boldsymbol{D})$ and $\boldsymbol{\Sigma}^{\Gamma}(\boldsymbol{\mathfrak{d}}^*, \boldsymbol{D})$, and the configurational volume force $\boldsymbol{\Gamma}$ are defined in equation (6.64) and (6.65). Note hereby the dependency on the current physical and configurational nodal unknowns $\boldsymbol{\mathfrak{d}}^*$ and $\boldsymbol{D}$.

6.3.2. Staggered Computation of Discrete Configurational Nodal Forces. The computation of discrete configurational nodal forces does not imply the solution of the fully coupled problem (6.73). When freezing the reference coordinate in time

$$\boldsymbol{x} = \Xi(\boldsymbol{\theta}, t)|_{t=const} = \boldsymbol{\theta}\,, \tag{6.74}$$

the volume map of the current and previous structural configuration simply take the unit value. Thus, the domain of integration is constant during the deformation process

$$\det[\boldsymbol{J}] = \det[\boldsymbol{J}_n] = 1 \quad \text{and} \quad dV = dV_n = dV_0\,. \tag{6.75}$$

Box 1: Computation of Discrete Configurational Nodal Forces.

1. *Finite Element Interpolations for Physical Space.* Approximate generalized displacement vector and variation of constitutive state in *physical space*

$$\boldsymbol{\mathfrak{u}}^{*h} := \boldsymbol{\mathfrak{N}}^*(\boldsymbol{x})\,\boldsymbol{\mathfrak{d}}^* \quad \text{and} \quad \delta_{\boldsymbol{\mathfrak{d}}^*}\boldsymbol{\mathfrak{c}}^{*h} := \boldsymbol{\mathfrak{B}}^*(\boldsymbol{x})\,\delta\boldsymbol{\mathfrak{d}}^*\,.$$

2. *Solve equilibrium in physical space.* Solve algebraic coupled system

$$\boldsymbol{0} = \Pi^{*h}_{\eta,\boldsymbol{\mathfrak{d}}^*} = \int_{\mathcal{B}^h} \{\, \boldsymbol{\mathfrak{B}}^{*T}[\boldsymbol{S}^*] - \boldsymbol{\mathfrak{N}}^T \boldsymbol{\mathfrak{g}} \,\}\, dV - \int_{\partial\mathcal{B}^h_{\mathfrak{t}}} \boldsymbol{\mathfrak{N}}^T \boldsymbol{\mathfrak{t}}_N \, dA$$

for generalized displacement vector $\boldsymbol{\mathfrak{d}}^*$, based on the generalized stress vector, the generalized body forces, and surface tractions

$$\boldsymbol{S}^* := \partial_{\boldsymbol{\mathfrak{c}}^{*h}} \pi^{*h}_{\eta} \quad \text{and} \quad \boldsymbol{\mathfrak{g}} := [\,\boldsymbol{\gamma}, 0\,]^T \quad \text{and} \quad \boldsymbol{\mathfrak{t}}_N := [\,\boldsymbol{t}_N, 0\,]^T\,.$$

3. *Finite Element Interpolations for Material Space.* Approximate the structural configuration and its gradient in *configurational space*

$$\boldsymbol{x}^h := \boldsymbol{N}(\boldsymbol{x})\,\boldsymbol{D} \quad \text{and} \quad \nabla\boldsymbol{x}^h := \boldsymbol{B}(\boldsymbol{x})\,\boldsymbol{D}\,.$$

4. *Evaluate Configurational Nodal Forces.* With known generalized displacements $\boldsymbol{\mathfrak{d}}^*$ evaluate the discrete nodal material forces within a postprocessing step via

$$\boldsymbol{R}^h := \Pi^{*h}_{\eta,\boldsymbol{D}} = \int_{\mathcal{B}^h} \{\, \boldsymbol{B}^T[\boldsymbol{\Sigma}^{\mathcal{B}} + \boldsymbol{\Sigma}^{\Gamma}] - \boldsymbol{N}^T \boldsymbol{\Gamma} \,\}\, dV$$

in terms of the Eshelby stress tensor for phase field fracture

$$\boldsymbol{\Sigma}^{\mathcal{B}} := \psi \boldsymbol{1} - \nabla^T \boldsymbol{u} \cdot \partial_{\nabla_s \boldsymbol{u}} \psi \quad \text{and} \quad \boldsymbol{\Sigma}^{\Gamma} := g_c \gamma_n \boldsymbol{1} - g_c l \nabla d \otimes \nabla d$$

and the configurational volume force vector

$$\boldsymbol{\Gamma} := -\partial_{\boldsymbol{x}} \psi - \nabla^T \boldsymbol{u} \cdot \boldsymbol{\gamma}\,.$$

As a crucial consequence, the governing equations in physical space (6.60) take the identical representation as initially discussed in the previous chapter, see equation (5.91). With frozen configuration, the computation of discrete configurational nodal forces simply reduces to an evaluation procedure. In the first step of the staggered solution algorithm, the equilibrium in physical space

$$\boldsymbol{0} = \Pi^{*h}_{\eta,\boldsymbol{\mathfrak{d}}^*} = \int_{\mathcal{B}^h} \{\, \boldsymbol{\mathfrak{B}}^{*T}[\boldsymbol{S}^*(\boldsymbol{\mathfrak{d}}^*)] - \boldsymbol{\mathfrak{N}}^T \boldsymbol{\mathfrak{g}} \,\}\, dV - \int_{\partial\mathcal{B}^h_{\mathfrak{t}}} \boldsymbol{\mathfrak{N}}^T \boldsymbol{\mathfrak{t}}_N \, dA \tag{6.76}$$

has to be solved. This nonlinear algebraic system of equations is solved for the generalized nodal displacements $\boldsymbol{\mathfrak{d}}^*$. For a detailed discussion of the numerical solution scheme with the according generalized stresses and moduli see Section 5.3.6.2. Having the solution in

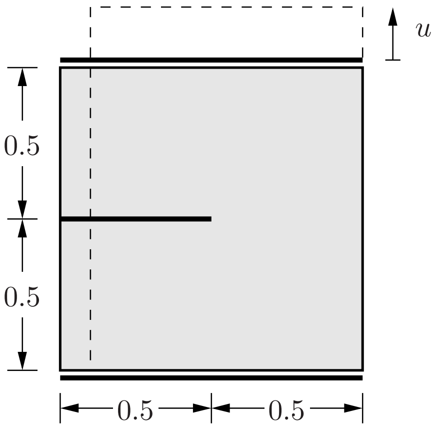

Figure 6.2: Single edge notched tension test. Geometry and boundary conditions.

physical space at hand, the material forces are evaluated in a post-processing step via

$$\boldsymbol{0} \neq \Pi^{*h}_{\eta,\boldsymbol{D}} = \int_{\mathcal{B}^h} \{ \boldsymbol{B}^T[\boldsymbol{\Sigma}^{\mathcal{B}}(\boldsymbol{\mathfrak{d}}^*) + \boldsymbol{\Sigma}^{\Gamma}(\boldsymbol{\mathfrak{d}}^*)] - \boldsymbol{N}^T\boldsymbol{\Gamma}(\boldsymbol{\mathfrak{d}}^*) \} \, dV \, . \tag{6.77}$$

Together with the frozen reference coordinates, the consequence (6.75) allows for the representation of the generalized Eshelby stress tensor

$$\boldsymbol{\Sigma}^{\mathcal{B}} := \psi \boldsymbol{1} - \nabla^T \boldsymbol{u} \cdot \partial_{\nabla_s \boldsymbol{u}} \psi \quad \text{and} \quad \boldsymbol{\Sigma}^{\Gamma} := g_c \gamma_n \boldsymbol{1} - g_c l \nabla d \otimes \nabla d \, , \tag{6.78}$$

where again the additive split into a bulk $\boldsymbol{\Sigma}^{\mathcal{B}}$ and surface part $\boldsymbol{\Sigma}^{\Gamma}$ is considered. Furthermore, the configurational volume force vector is identified

$$\boldsymbol{\Gamma} := -\partial_{\boldsymbol{x}} \psi - \nabla^T \boldsymbol{u} \cdot \boldsymbol{\gamma} \, . \tag{6.79}$$

The staggered computation of discrete configurational forces is summarized in Box 1.

6.3.3. Numerical Example. Evolving Discrete Material Forces. In the following treatment a numerical example is investigated in order to demonstrate the evolution of material forces in phase field modeling of fracture mechanics. Taking into account the additive decomposition of Eshelby's stress tensor, the discrete configurational forces read

$$\boldsymbol{R}^{\mathcal{B},h} := \int_{\mathcal{B}^h} \{ \boldsymbol{B}^T[\boldsymbol{\Sigma}^{\mathcal{B}}] - \boldsymbol{N}^T \boldsymbol{\Gamma} \} \, dV \quad \text{and} \quad \boldsymbol{R}^{\Gamma,h} := \int_{\mathcal{B}^h} \{ \boldsymbol{B}^T[\boldsymbol{\Sigma}^{\Gamma}] \} \, dV \, , \tag{6.80}$$

where the relation $\boldsymbol{R}^h := \boldsymbol{R}^{\mathcal{B},h} + \boldsymbol{R}^{\Gamma,h}$ holds. Regarding a homogeneous body without any body force loading one obtains $\boldsymbol{\Gamma} = \boldsymbol{0}$. The characteristics of the evolving configurational forces are discussed for a boundary value problem representing a squared plate with horizontal notch which is placed at middle height and is running from the left outer surface to the center of the specimen. The geometric setup is depicted in Figure 6.2. For the analysis the bulk modulus is chosen to be $\lambda = 12.00$ kN/mm^2, the shear modulus $\mu = 8.00$ kN/mm^2, and the critical energy release rate $g_c = 5.0 \times 10^{-4}$ kN/mm. The simulation is performed in a monotonic incremental displacement driven context with constant displacement increments of $\Delta u = 1.0 \times 10^{-6}$ mm. The contour plot of the fracture phase field, the evolution of configurational forces related to the bulk terms $\boldsymbol{R}^{\mathcal{B},h}$ and the configurational forces acting on the newly created diffusive crack surface $\boldsymbol{R}^{\Gamma,h}$ at different

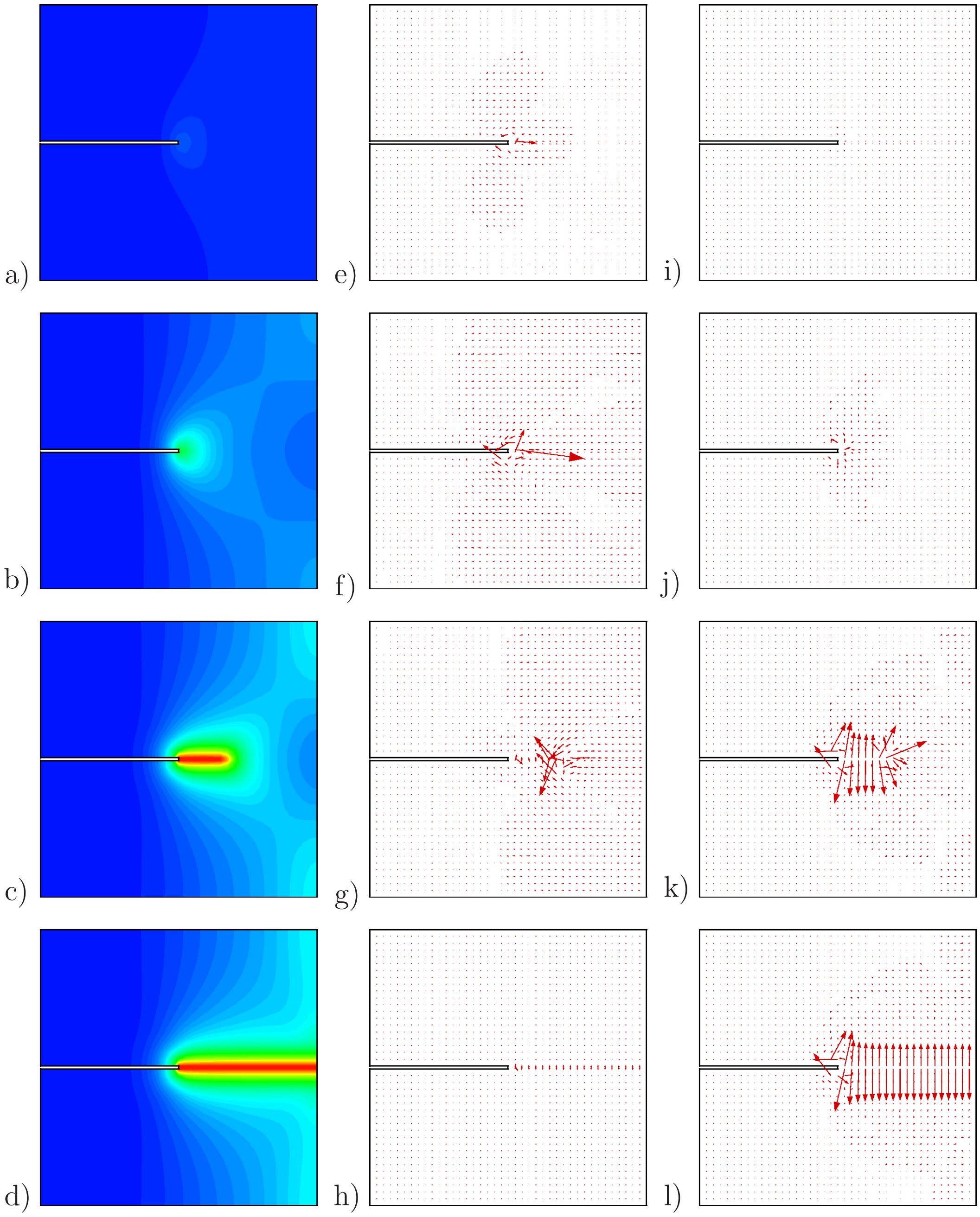

Figure 6.3: Single edge notched tension test. a)–d) Evolution of diffusive crack topology, e)–h) internal material forces $\boldsymbol{R}^{\mathcal{B},h}$, and i)–l) material forces on the crack surface $\boldsymbol{R}^{\Gamma,h}$.

stages of the deformation are illustrated in Figure 6.3, where only interior parts of the configurational forces are displayed. One important characteristic lies in the different behavior of the two contributions. The bulk part $\boldsymbol{R}^{\mathcal{B},h}$ moves along the diffusive crack tip, whereas the surface part $\boldsymbol{R}^{\Gamma,h}$ acts on the diffusive crack surface. This difference will be exploited in a configurational-force-driven h-adaptive refinement procedure.

6.4. Material-Force-Based h-Adaptive Algorithm for Phase Field Fracture

6.4.1. Configurational-Force-Based Indicators for Mesh-Refinement. The spatial discretization violates the equivalence between the material and spatial balance equations which is given in the continuous setting. Due to an insufficient discretization numerically caused spurious nodal forces occur. To this end, consider the residual $\boldsymbol{R}_I^h$ in the configurational space as a quantity defined at the nodal points I. As discussed in the previous numerical example, the total material forces are split into a part resulting from bulk contributions $\boldsymbol{R}_I^{\mathcal{B},h}$ and a part related to the growing diffusive crack surface $\boldsymbol{R}_I^{\Gamma,h}$. Possible inhomogeneities and body force loads are not treated in the sequel. For an *optimal mesh* with optimal nodal positions in the reference configuration, vanishing bulk material forces are postulated

$$\boldsymbol{R}_I^{\mathcal{B},h} = \boldsymbol{0} \quad \text{for} \quad I \in int\ \mathcal{T}_t^h \tag{6.81}$$

at interior nodes of the current triangulation $\mathcal{T}_t^h$. Configurational forces acting on the approximated crack surface are physically motivated and preserve the shape of the solid

$$\boldsymbol{R}_I^{\Gamma,h} \neq \boldsymbol{0} \quad \text{for} \quad I \in int\ \mathcal{T}_t^h\,, \tag{6.82}$$

they do not vanish at interior nodes of the current triangulation $\mathcal{T}_t^h$. Regarding a *non-optimal mesh*, the bulk material forces do not vanish at interior nodal points

$$\boldsymbol{R}_I^{\mathcal{B},h} \neq \boldsymbol{0} \quad \text{for} \quad I \in int\ \mathcal{T}_t^h\,, \tag{6.83}$$

which plays a crucial role as the key measure for the setup of *global* and *local mesh refinement indicators*. In the proposed h-adaptive strategy, these forces are treated as an energetic misfit of the non-optimal mesh. Based on this idea, a *global refinement indicator*

$$r^{\mathcal{B},h}(\boldsymbol{R}^{\mathcal{B},h}) := \frac{R^{\mathcal{B},h}}{N_{int}} \leq r^{tol} \quad \text{with} \quad R^{\mathcal{B},h} := \sum_{I \in int\ \mathcal{T}_t^h} |\boldsymbol{R}_I^{\mathcal{B},h}| \tag{6.84}$$

is introduced, expressed in terms of the current total number of internal nodal points N_{int}. This means that an averaged sum of all nodal bulk material force norms $r^{\mathcal{B},h}(\boldsymbol{R}^{\mathcal{B},h})$ is introduced that depends on the current state of the system. This global indicator has to be less or equal than an absolute given permissible tolerance r^{tol}. If condition $(6.84)_1$ is violated, a mesh refinement procedure of the finite element triangulation is performed, based on the nodal ratio

$$\xi_I := \frac{|\boldsymbol{R}_I^{\mathcal{B},h}|}{r^{tol}} \quad \text{for} \quad I \in int\ \mathcal{T}_t^h\,. \tag{6.85}$$

For $\xi_I > 1$ the current norm of the nodal residual exceeds the permissible norm and as a consequence a local mesh refinement is enforced. A possible mesh coarsening for $\xi_I < 1$ is not considered for phase field modeling of brittle fracture. Regarding the derivation of a statement for the change of the mesh size at node I, the *asymptotic convergence rate criterion* is exploited where the following proportionality is assumed

$$|\boldsymbol{R}_I^{\mathcal{B},h}| \approx (k_I^h)^p \tag{6.86}$$

between the current norm of the residual at node I and the current element size k_I^h powered by the polynomial order p of the element approximation functions. In order to improve the mesh quality in problems with singularities, the exponent p can be interpreted as singularity parameter which lies in the range $p \in [0.5, 1.0]$, see Zienkiewicz, Taylor & Zhu [183]. Focusing on two meshes h and $h+1$, the following relation holds

$$|\boldsymbol{R}_I^{\mathcal{B},h}| = c\,(k_I^h)^p \quad \text{and} \quad |\boldsymbol{R}_I^{\mathcal{B},h+1}| = c\,(k_I^{h+1})^p\,, \tag{6.87}$$

where a simple reformulation yields the estimate

$$\frac{|\boldsymbol{R}_I^{\mathcal{B},h+1}|}{|\boldsymbol{R}_I^{\mathcal{B},h}|} = \left(\frac{k_I^{h+1}}{k_I^h}\right)^p \tag{6.88}$$

for the ratio of the material forces for two mesh sizes k_I^h and k_I^{h+1}, evaluated at an interior nodal point I. An alternative representation of equation (6.88) follows from the replacement of $|\boldsymbol{R}_I^{\mathcal{B},h+1}|$ by the given permissible norm r^{tol}

$$k_I^{h+1} = \left(\frac{|\boldsymbol{R}_I^{\mathcal{B},h}|}{r^{tol}}\right)^{-1/p} k_I^h \tag{6.89}$$

and determines the local mesh refinement exclusively defined in terms of the bulk material force vector $\boldsymbol{R}^{\mathcal{B},h}$ of the finite element triangulation.

6.4.2. Staggered Solution Algorithm for Physical and Material Balances. In analogy to Section 6.3.2, the fully coupled problem in physical and material space is not treated monolithically. The reference coordinates are frozen in time, the coupled problem in physical space is solved for the generalized displacements, and the material forces are evaluated in a post-processing step. The proposed h-adaptive algorithm combines this staggered scheme with the previously discussed material-force-based indicators for mesh refinement and builds the basis for an efficient h-adaptive frame for regularized brittle fracture. Within one typical time step of the simulation, the staggered solution algorithm for the physical and material balances in the sense of an h-adaptive procedure can be summarized as follows. In an *initializing step*, the time is set $t \Leftarrow t_n + \tau$ and the external loads $\boldsymbol{\mathfrak{g}}(t)$ and $\mathbf{t}_N(t)$ are applied. In this context, all variables without subscript are meant to be evaluated at time $t = t_{n+1}$. The discretization counter that counts the number of refinement steps within the time interval $[t_n, t]$ is set to zero $h = 0$ and the discretization $\mathfrak{D}_t^h$ is initialized according to

$$\mathfrak{D}_t^h := \mathfrak{D}_n^{h_n} = \{\, \mathcal{T}_n^{h_n}, \boldsymbol{\mathfrak{N}}^*(\boldsymbol{x}^{h_n}), \boldsymbol{\mathfrak{B}}^*(\boldsymbol{x}^{h_n}), \boldsymbol{N}(\boldsymbol{x}^{h_n}), \boldsymbol{B}(\boldsymbol{x}^{h_n}) \,\} \tag{6.90}$$

consisting of the triangulation $\mathcal{T}_n^{h_n}$ which was valid for the previous time interval, in combination with the according number of refinement steps h_n, the generalized interpolation matrices in physical space $\boldsymbol{\mathfrak{N}}^*(\boldsymbol{x}^{h_n})$ and $\boldsymbol{\mathfrak{B}}^*(\boldsymbol{x}^{h_n})$, the interpolation matrices in configurational space $\boldsymbol{N}(\boldsymbol{x}^{h_n})$ and $\boldsymbol{B}(\boldsymbol{x}^{h_n})$, and the nodal positions $\boldsymbol{x}^{h_n}$. Note that regarding an h-adaptive procedure, these quantities are dynamically growing fields. In the subsequent step, the *equilibrium in physical space* is solved, based on the compact representation (6.76) of the fully coupled problem

$$\boldsymbol{0} = \Pi^{*h}_{\eta,\boldsymbol{\mathfrak{d}}^*} = \int_{\mathcal{T}_t^h} \{\, \boldsymbol{\mathfrak{B}}^{*T}(\boldsymbol{x}^h)[\boldsymbol{S}^*] - \boldsymbol{\mathfrak{N}}^T(\boldsymbol{x}^h)\boldsymbol{\mathfrak{g}} \,\}\, dV - \int_{\partial\mathcal{T}_t^h} \boldsymbol{\mathfrak{N}}^T(\boldsymbol{x}^h)\mathbf{t}_N \, dA\,. \tag{6.91}$$

A Newton solution method of the nonlinear system provides the generalized increments $\Delta\boldsymbol{\mathfrak{d}}_t^{*,h}$ and the *trial solution* is updated via

$$\boldsymbol{\mathfrak{d}}_t^{*,h} = \boldsymbol{\mathfrak{d}}_n^{*,h} + \Delta\boldsymbol{\mathfrak{d}}_t^{*,h}\,. \tag{6.92}$$

The next step is concerned with an *evaluation* of the equilibrium in configurational space. Based on the frozen discretization $\mathfrak{D}_t^h$ and the trial solution $\mathfrak{d}_t^{*,h}$, the discrete material bulk forces are evaluated

$$\boldsymbol{R}^{\mathcal{B},h} := \int_{int\,\mathcal{T}_t^h} \{\, \boldsymbol{B}^T(\boldsymbol{x}^h)[\boldsymbol{\Sigma}^{\mathcal{B}}] - \boldsymbol{N}^T(\boldsymbol{x}^h)\boldsymbol{\Gamma} \,\}\, dV \tag{6.93}$$

at internal nodal points of the discretization. Based on these discrete bulk material forces $\boldsymbol{R}^{\mathcal{B},h}$ a norm-type *global refinement criterion* is computed

$$r^{\mathcal{B},h}(\boldsymbol{R}^{\mathcal{B},h}; \mathfrak{D}_t^h) \leq r^{tol} \tag{6.94}$$

and has to be smaller than a given tolerance r^{tol}, for a more detailed interpretation see equation (6.84). If the global criterion is not violated then exit and increase the time counter. Otherwise a *mesh density function* based on the material bulk forces is set up

$$\chi_t^h = Dens(\boldsymbol{R}^{\mathcal{B},h}; \mathfrak{D}_t^h) \tag{6.95}$$

controlling the local mesh adaption. A closer look at the density function is taken in the subsequent section. Based on this mesh density function a new mesh is generated

$$\mathfrak{D}_t^{h+1} = Mesh(\chi_t^h; \mathfrak{D}_t^h) \tag{6.96}$$

which is locally adapted to the local nodal norm of the bulk material forces $\boldsymbol{R}^{\mathcal{B},h}$. In a last step the *mapping of state variables* $\boldsymbol{d}_n^{h_n}$ of the previous time step onto the new discretization $\mathfrak{D}_t^{h+1}$ is performed

$$\mathfrak{d}_n^{*,h+1} = Map(\mathfrak{d}_n^{*,h_n}; \mathfrak{D}_t^{h+1}, \mathfrak{D}_n^{h_n})\,. \tag{6.97}$$

The trial solution $\mathfrak{d}_t^{*,h}$ is discarded, the mesh adaption counter increased $h \Leftarrow h+1$, and the computation of the same time step is repeated with the adapted discretization $\mathfrak{D}_t^{h+1}$ until the global criterion is satisfied. The solution procedure is summarized in Box 2.

6.4.3. Mesh Generation and Mapping of State Variables. Whenever the current triangulation $\mathcal{T}_t^h$ is identified to be inappropriate for the current load step, the mesh has to be adapted according to some local refinement rules. As already pointed out in the previous section, the local meshing procedure is driven by a so-called mesh density function $\chi_t^h = Dens(\boldsymbol{R}^{\mathcal{B},h}; \mathfrak{D}_t^h)$. The function $\chi_t^h(\boldsymbol{x}^h)$ lives at every nodal point $\boldsymbol{x}^h$ of the current triangulation and is defined in the range $\chi_t^h \in [0,1]$. It is proportional to the local mesh size. Based on the standard shape functions $N_I(\boldsymbol{x}^h)$, the density function reads

$$\chi^h(\boldsymbol{x}) = \sum_{I\,\in\, int\ \mathcal{T}_t^h} N_I(\boldsymbol{x}) k_I^{h+1} \quad \text{with} \quad k_I^{h+1} = k_I^h \left(\frac{|\boldsymbol{R}_I^{\mathcal{B},h}|}{r^{tol}} \right)^{-1/p} \tag{6.98}$$

and is exclusively determined by the nodal material bulk forces $\boldsymbol{R}_I^{\mathcal{B},h}$ at the interior nodes I. A subsequent mesh generation algorithm that bases on an initial Delaunay-triangulation in combination with a successive point insertion algorithm has been discussed in full length by Koch [93]. Here, new nodes are inserted into the triangulation $\mathcal{T}_t^{h+1}$ until the local meshing criterion (6.98) is satisfied everywhere in the solution domain. All elements in the new discretization have an equivalent radius of circumcenter which is less or equal

Box 2: Staggered Solution Algorithm for Physical and Material Balances.

1. *Initialization.* Update time $t \Leftarrow t_n + \tau$, loads $\mathfrak{g}(t)$, and tractions $\mathfrak{t}_N(t)$. Set refinement counter $h = 0$, start with discretization $\mathfrak{D}_n^{h_n}$, and counter h_n of time t_n
$$\mathfrak{D}_t^h := \mathfrak{D}_n^{h_n} = \{\, \mathcal{T}_n^{h_n}, \boldsymbol{\mathfrak{N}}^*(\boldsymbol{x}^{h_n}), \boldsymbol{\mathfrak{B}}^*(\boldsymbol{x}^{h_n}), \boldsymbol{N}(\boldsymbol{x}^{h_n}), \boldsymbol{B}(\boldsymbol{x}^{h_n}) \,\} \,.$$
2. *Solve Equilibrium in Physical Space.* At frozen discretization $\mathfrak{D}_t^h$ solve algebraic coupled system of diffusive fracture in physical space
$$\boldsymbol{0} = \Pi^{*h}_{\eta,\mathfrak{d}^*} = \int_{\mathcal{T}_t^h} \{\, \boldsymbol{\mathfrak{B}}^{*T}(\boldsymbol{x}^h)[\boldsymbol{S}^*] - \boldsymbol{\mathfrak{N}}^T(\boldsymbol{x}^h)\mathfrak{g} \,\}\, dV - \int_{\partial\mathcal{T}_t^h} \boldsymbol{\mathfrak{N}}^T(\boldsymbol{x}^h)\mathfrak{t}_N \, dA$$
for the generalized increments $\Delta\mathfrak{d}_t^{*,h}$ and update the solution $\mathfrak{d}_t^{*,h} = \mathfrak{d}_n^{*,h} + \Delta\mathfrak{d}_t^{*,h}$.
3. *Evaluate Equilibrium in Configurational Space.* For the discretization $\mathfrak{D}_t^h$ with generalized displacements $\mathfrak{d}_t^{*,h}$ evaluate the discrete material bulk forces
$$\boldsymbol{R}^{\mathcal{B},h} := \int_{int\,\mathcal{T}_t^h} \{\, \boldsymbol{B}^T(\boldsymbol{x}^h)[\boldsymbol{\Sigma}^{\mathcal{B}}] - \boldsymbol{N}^T(\boldsymbol{x}^h)\boldsymbol{\Gamma} \,\}\, dV$$
and compute norm-type global refinement indicator
$$\text{If } [r^{\mathcal{B},h}(\boldsymbol{R}^{\mathcal{B},h}; \mathfrak{D}_t^h) \le r^{tol}] \text{ exit and go to step 1.}$$
4. *Compute Mesh Density Function.* Based on the discretization $\mathfrak{D}_t^h$ determine the mesh density function for local mesh adaption
$$\chi_t^h = Dens(\boldsymbol{R}^{\mathcal{B},h}; \mathfrak{D}_t^h) \,.$$
5. *Refine Discretization.* Generate triangulation based on mesh density function χ_t^h
$$\mathfrak{D}_t^{h+1} = Mesh(\chi_t^h; \mathfrak{D}_t^h) \,.$$
6. *Map State Variables.* Map generalized displacements $\mathfrak{d}_n^{h_n}$ on current discretization
$$\mathfrak{d}_n^{*,h+1} = Map(\mathfrak{d}_n^{*,h_n}; \mathfrak{D}_t^{h+1}, \mathfrak{D}_n^{h_n}) \,.$$
Discard trial solution $\mathfrak{d}_t^{*,h}$, set discretization counter $h \Leftarrow h + 1$, and go to step 2.

than its unrefined correspondent, weighted by the distribution function $(6.98)_1$. Once the mesh is generated, the generalized solution vector of the previous time step $\mathfrak{d}_n^{*,h_n}$ has to be mapped onto the current discretization. To this end, consider a newly created nodal point I of the discretization $\mathcal{T}_t^{h+1}$ where the solution vector $[\mathfrak{d}_n^{*,h_n}]_I$ has to be transferred to. In a first step the element e of the discretization $\mathfrak{D}_n^{h_n}$ containing this point has to be located. Following Koch [93], a quadtree-algorithm is employed that guarantees an effective element search. When the element e is located, the element coordinates of point I are determined and the solution vector $[\mathfrak{d}_n^{*,h_n}]_I$ is computed by an interpolation procedure on element level e with the aid of the element's shape functions.

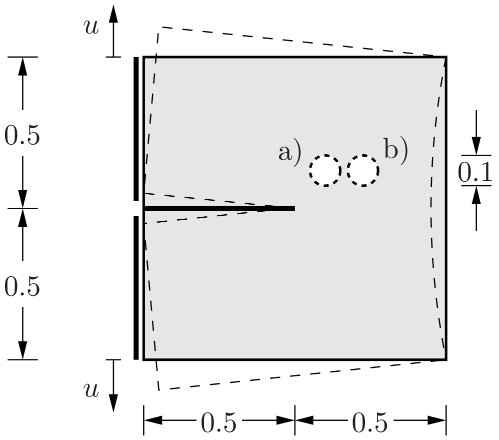

Figure 6.4: Tension test of specimen with circular hole. Geometry and boundary conditions for a) geometry I and b) geometry II.

6.4.4. Numerical Examples. h-Adaptive Phase Field Fracture. Two numerical examples are discussed that demonstrate the performance of the proposed h-adaptive solution scheme. The first example is concerned with a *tension test of a notched specimen with circular hole*. In this test two geometries are investigated, where depending on the hole's position two different crack patterns are obtained. The second numerical test focuses on the benchmark of an *L-shaped specimen subjected to tensile loading*.

6.4.4.1. Tension Test of Notched Specimen with Circular Hole. The first numerical study deals with crack propagation in a two-dimensional compact tension specimen which is loaded by a dead displacement u at the left edge in upper and lower direction. The boundary value problem was conceptually discussed by Müller & Maugin [136] in the context of discrete configurational-based crack propagation. For a detailed visualization of the problem see Figure 6.4. In order to examine a curved crack pattern, a circular hole with radius $r = 0.05$ and a vertical distance to the lower edge of 0.63 is introduced at two positions in the specimen. For geometry I the center of the circular hole is placed at an horizontal distance to the left edge of 0.60 and of 0.74 for geometry II, respectively. For the analysis the bulk modulus is chosen to $\lambda = 12.00$ kN/mm^2, the shear modulus to $\mu = 8.00$ kN/mm^2, and the critical energy release rate to $g_c = 5.0 \times 10^{-4}$ kN/mm. The simulation is performed in a displacement driven context with constant displace-

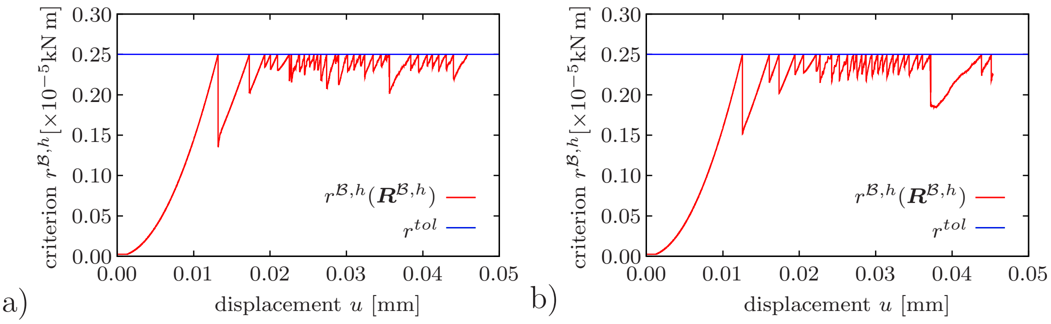

Figure 6.5: Tension test of specimen with circular hole. Evolution of global refinement criterion $r^{\mathcal{B},h}(\boldsymbol{R}^{\mathcal{B},h})$ and permissible norm r^{tol} for a) geometry I and b) geometry II.

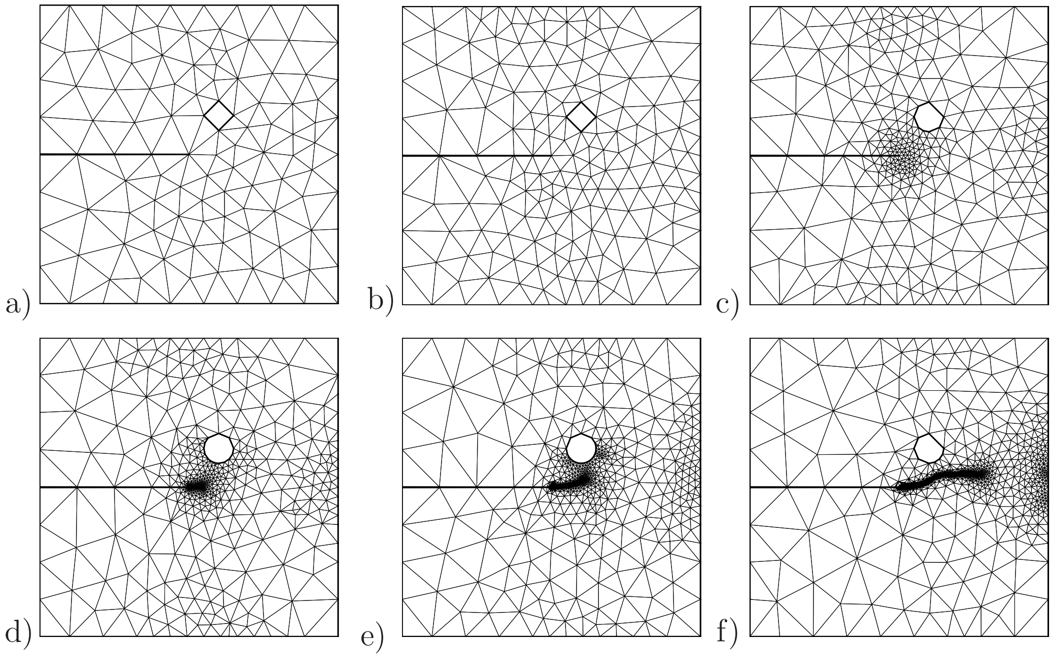

Figure 6.6: Tension test of specimen with circular hole. Discretizations at different stages of the deformation with 103 to 11228 elements for geometry I.

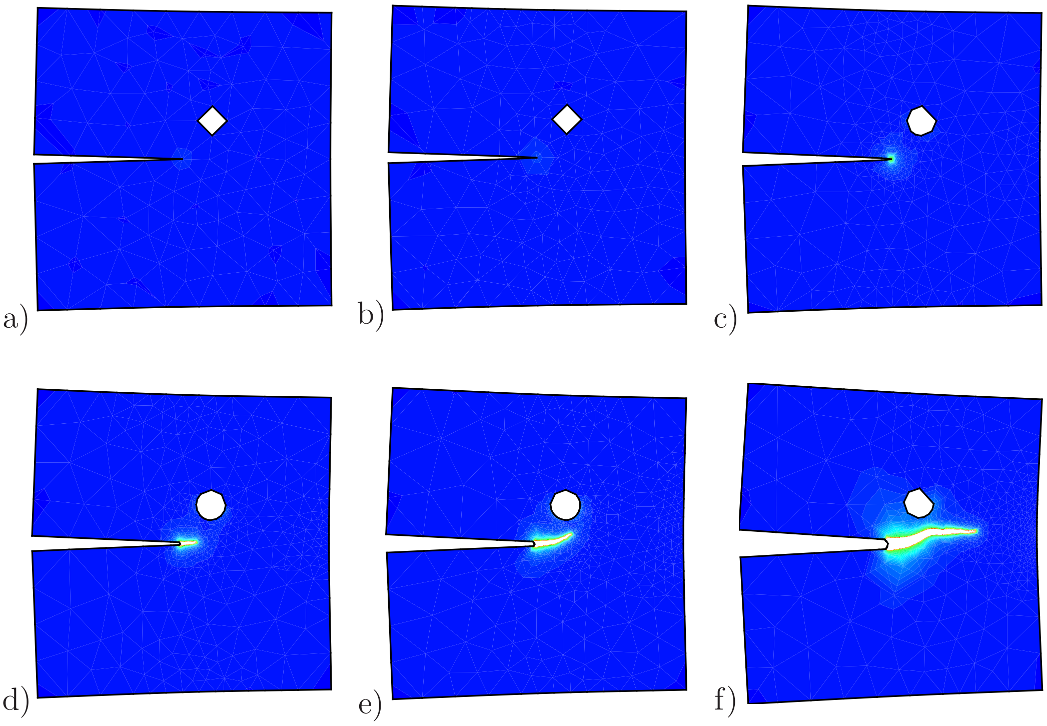

Figure 6.7: Tension test of specimen with circular hole. Evolution of diffusive crack topology at different stages of the deformation for geometry I.

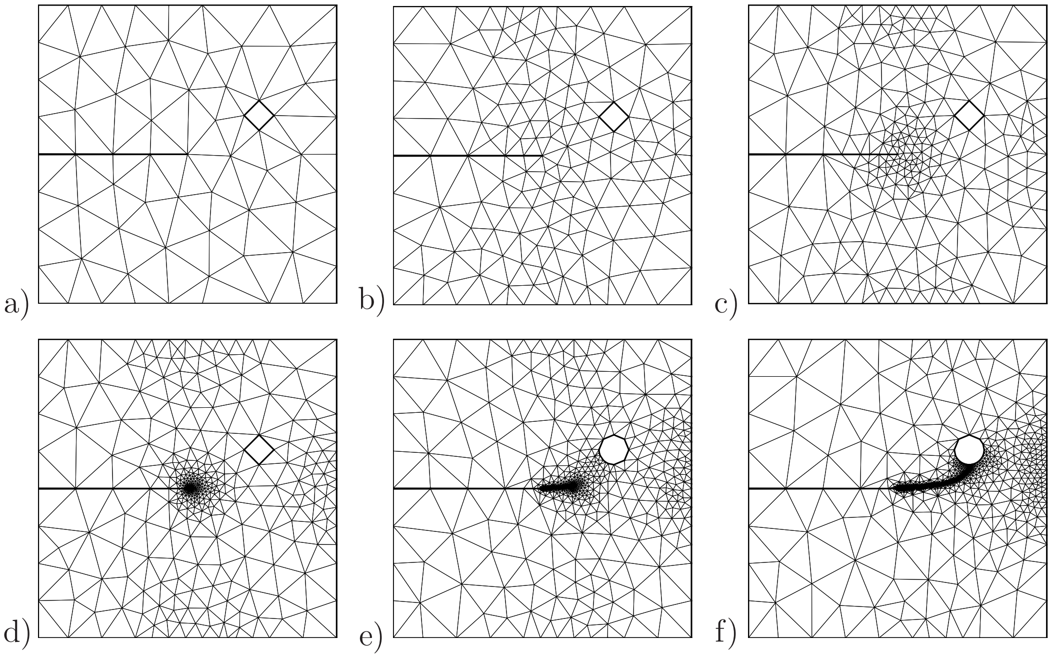

Figure 6.8: Tension test of specimen with circular hole. Discretizations at different stages of the deformation with 107 to 10698 elements for geometry II.

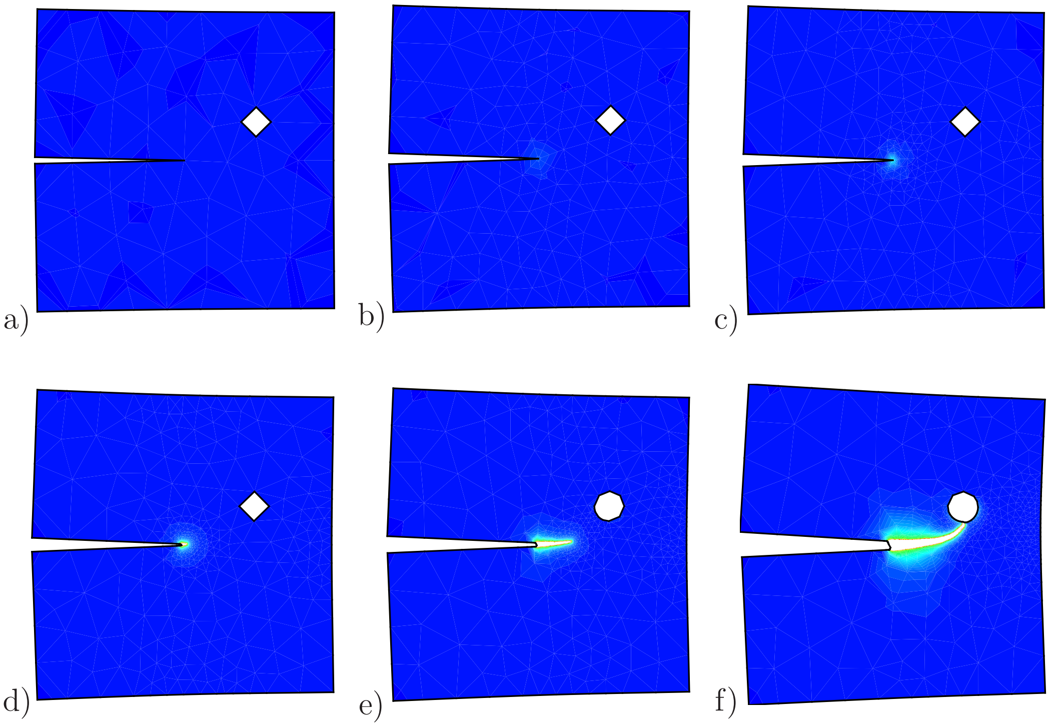

Figure 6.9: Tension test of specimen with circular hole. Evolution of diffusive crack topology at different stages of the deformation for geometry II.

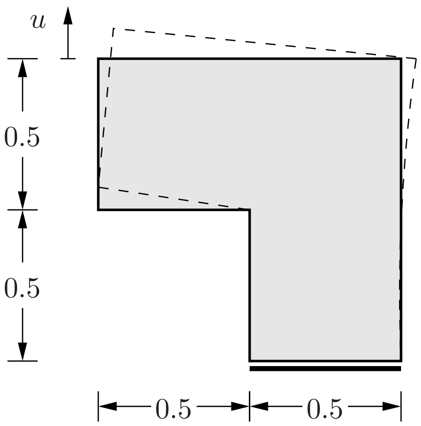

Figure 6.10: Tension test of L-shaped specimen. Geometry and boundary conditions.

ment increments of $\Delta u = 5.0 \times 10^{-5}$ mm. For both geometries Figure 6.5 illustrates the evolution of the global refinement criterion $r^{\mathcal{B},h}$ during the computation. Every time the current global criterion reaches the permissible value r^{tol} a mesh refinement is enforced. Starting with an initial triangulation with 103 elements ongoing h-adaptive computation ends with a final discretization of 11228 elements. For geometry I, the evolution of the discretization at different stages of the deformation is displayed in Figure 6.6. Comparing the mesh adaption with the diffusive crack pattern displayed in Figure 6.7, one can observe that the configurational-force-based h-adaptive procedure yields a local mesh refinement which resolves the diffusive crack zone very properly. As observed in the aforementioned publication for geometry I, the crack tip does not change its direction rapidly enough to reach the hole and passes the hole. In contrast, for geometry II the crack is attracted by the hole. This is documented in Figure 6.8, where the evolution of the mesh during the computation is illustrated. In this example the total number of elements ranges from 107 to 10698 elements. In Figure 6.9 the according evolution of the crack phase field at the same deformation steps is displayed. Again, the material force based h-adaptive scheme yields an adequate discretization in critical regions with diffusive crack propagation and allows for the employment of very fine length scale parameters.

6.4.4.2. Tension Test of L-Shaped Specimen. The next numerical test is concerned with a benchmark problem of fracture mechanics which is very often discussed in literature. For a recent discussion of this boundary value problem in the context of energy-based crack propagation with the help of the extended finite element method see e.g. MESCHKE & DUMSTORFF [113]. The geometry and the loading conditions are illustrated in Figure 6.10. For the analysis the bulk modulus is chosen to $\lambda = 12.00$ kN/mm^2, the shear modulus to $\mu = 8.00$ kN/mm^2, and the critical energy release rate to $g_c = 5.0 \times 10^{-4}$ kN/mm. The simulation is performed in a displacement driven context with constant displacement increments of $\Delta u = 1.0 \times 10^{-5}$ mm. In order to control the h-adaptive algorithm a permissible norm $r^{tol} = 2.6 \times 10^{-5}$kN m of the interior material bulk forces is chosen. The adaption of the discretization during the computation is given in Figure 6.11. The proposed h-adaptive solution strategy enforces a mesh refinement in areas where the crack evolves, allowing for the usage of a very small length scale parameter. This makes the algorithm extremely efficient and renders the phase-field-modeling of diffusive fracture to an attractive alternative. The evolution of the fracture phase field in the L-shaped specimen is shown in Figure 6.12, where the resulting curved crack pattern is in a very

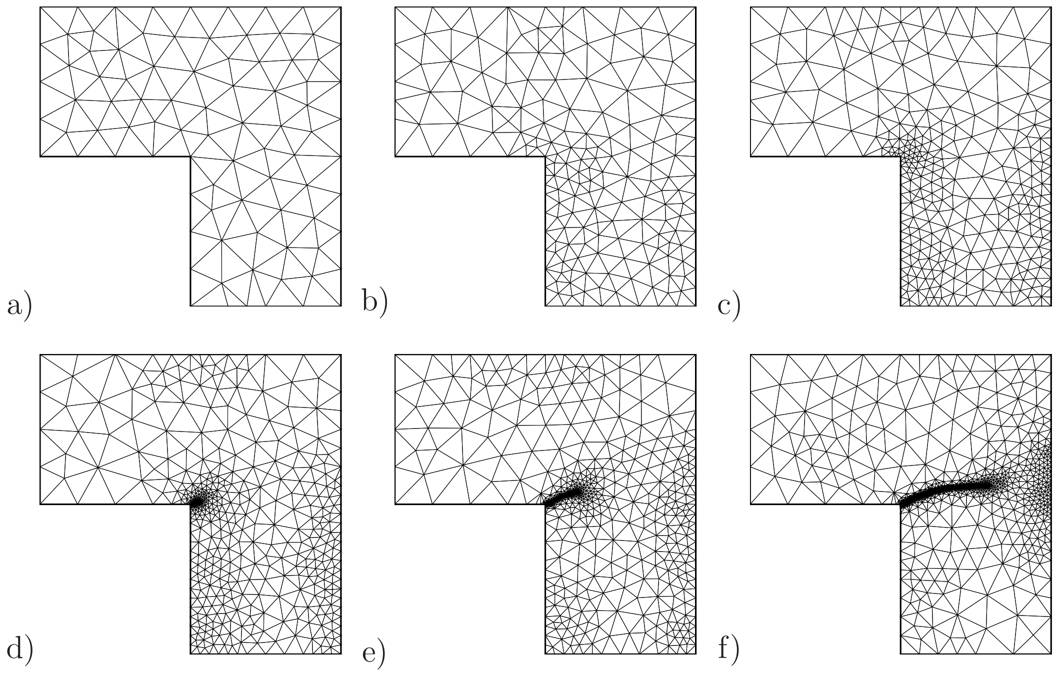

Figure 6.11: Tension test of L-shaped specimen. Adaption of the discretization at different stages of the deformation with triangulations ranging from 141 to 11956 elements.

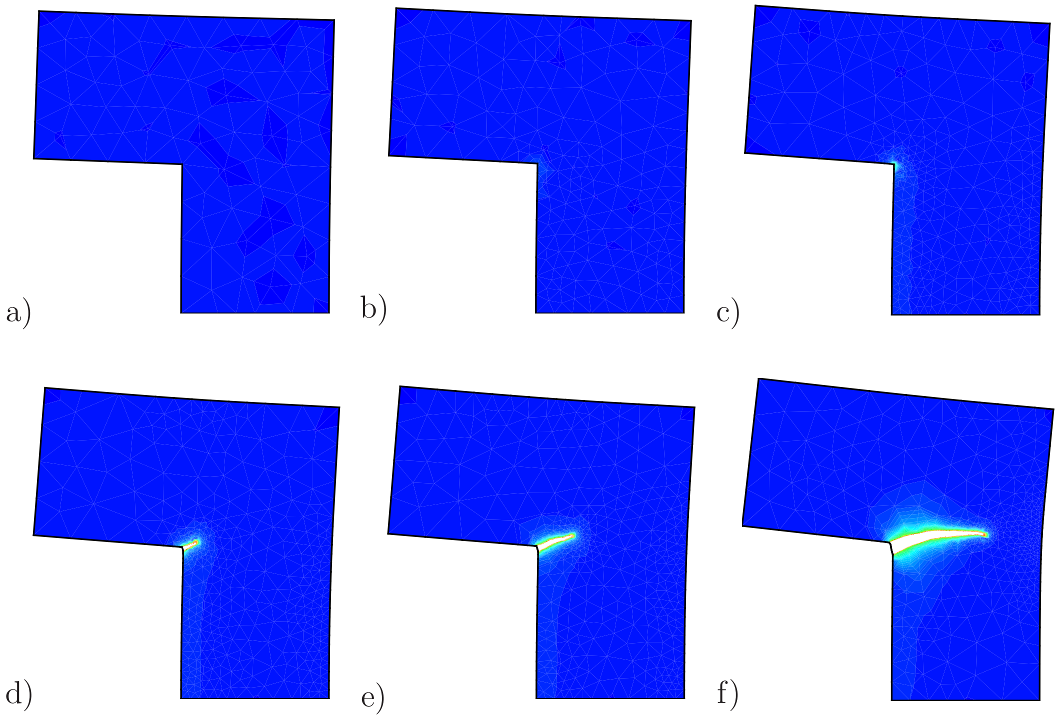

Figure 6.12: Tension test of L-shaped specimen. Evolution of diffusive crack topology at different stages of the deformation.

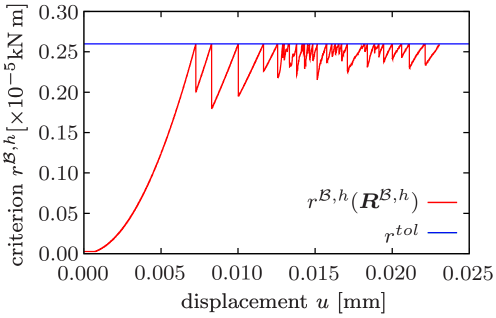

Figure 6.13: Tension test of L-shaped specimen. Evolution of global refinement criterion $r^{\mathcal{B},h}(\boldsymbol{R}^{\mathcal{B},h})$ and permissible norm r^{tol}.

good agreement to the aforementioned publication. The evolution of the global criterion is displayed in Figure 6.13. Obviously, ongoing deformation causes growing configurational forces in the bulk material that are caused by an insufficient triangulation. The mesh density function at three stages of the deformation is displayed in Figure 6.14. In Figure 6.14a) the initial triangulation is obtained for a unit distribution function $\chi_t^h = 1$ in the domain $\mathcal{B}^h$, a local mesh adaption is obtained for $0 \leq \chi_t^h \leq 1$, see Figure 6.14b) and c), and a maximum refinement is obtained for $\chi_t^h = 0$.

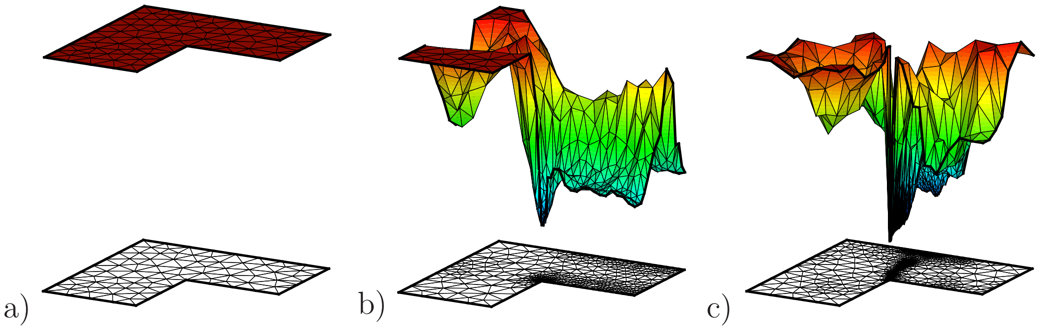

Figure 6.14: Tension test of L-shaped specimen. Mesh density functions $\chi_t^h(\boldsymbol{R}^{\mathcal{B},h})$ to control local mesh adaption at different stages of the deformation. a) Uniform initial discretization for $\chi_t^h = 1$ in the domain $\mathcal{B}^h$, b) discretization at the onset of crack propagation, and c) at the end of the process. Maximum mesh refinement for $\chi_t^h = 0$ and no refinement for $\chi_t^h = 1$.

7. Variational-Based Gradient-Type von Mises Plasticity

The main focus of this chapter lays on the development of phenomenological plasticity at small and large deformations with gradient-type hardening that is embedded into the variational-based framework of gradient-type standard dissipative solids. Formulations conceptually similar can be found in the works by Gurtin [67], Gudmundson [60], and Anand, Gurtin, Lele & Gething [3], where additional microstructural fields with according microscopic balance equations are considered. Hereby, the microscopic balance equations characterize the evolution of the order-parameter fields.

A first part of this chapter is devoted to the introduction of the basic kinematics and the state variables. In addition to the global displacement and hardening fields, the local field of plastic strains is introduced. Subsequently, the constitutive equations in the context of small deformations are introduced. An emphasis is thereby put on a rate-independent formulation of the dissipation function yielding model I and its viscous regularized counterpart yielding model II. Both representations are based on the classical yield function of phenomenological plasticity. For the smooth model II, a fast update algorithm for the local plastic strains is discussed. The application of the incremental variational framework for gradient-type solids with local history then provides the governing balance equations and delivers a unified finite element treatment of the coupled system. The numerical analysis of some elementary boundary value problems confirms mesh-independent results. The developed model of gradient-type plasticity is extended to the case of large deformations by an additive approach to finite plasticity in the logarithmic strain space in the spirit of Miehe [116, 117] and Miehe, Apel & Lambrecht [121]. To this end, a brief review of additive finite plasticity in the logarithmic strain space is given and a modular structure is introduced that consists in its core of the initially introduced small strain material model for gradient-type plasticity. This logarithmic core is framed by purely geometric pre- and post-processing steps. This kinematic approach is embedded into the proposed variational framework for gradient-type standard dissipative solids. The application of this general framework then allows for an extremely compact notation and the unified numerical treatment of the resulting symmetric problem. Several numerical tests are discussed at the end of this chapter. They are mainly concerned with the regularization of shear bands and the prediction of the well-known Hall-Petch effect.

7.1. Gradient-Type von Mises Plasticity at Small Strains

This section is dedicated to the embedding of the classical phenomenological von Mises plasticity into the variational framework for gradient-extended dissipative continua. In a first step, the basic kinematics and the state variables are introduced that govern the material response. The necessary incremental potential is specified and the resulting governing equations are discussed. Hereby, besides the global strong equations, an effective local update algorithm is proposed to solve for the local plastic strains. A suitable numerical solution scheme is set up and finally some elementary numerical tests are discussed.

7.1.1. Basic Kinematics and State Variables. Aiming at a continuum mechanical description of von Mises plasticity with isotropic gradient-type hardening at small strains, besides the macroscopic displacement field $\boldsymbol{u}$, a scalar-valued microscopic quantity α is introduced, describing on a phenomenological level an isotropic hardening process of the microstructure due to the accumulation of dislocations. In addition, the macroscopic plastic strain $\boldsymbol{\varepsilon}^p$ is introduced as local history

$$\bar{\boldsymbol{u}} := \{\, \boldsymbol{u} \,\} \quad \text{and} \quad \check{\boldsymbol{u}} := \{\, \alpha \,\} \quad \text{and} \quad \boldsymbol{\mathcal{I}} := \{\, \boldsymbol{\varepsilon}^p \,\}\,. \tag{7.1}$$

The macroscopic strain $\boldsymbol{\varepsilon} = \nabla_s \boldsymbol{u}$ can be additively decomposed into an elastic and inelastic part, allowing for the introduction of the stress producing *elastic strain*

$$\boldsymbol{\varepsilon}^e = \boldsymbol{\varepsilon} - \boldsymbol{\varepsilon}^p\,. \tag{7.2}$$

It is used as state variable for the description of an energy storage mechanism that is related to elastic macro-distortions of the material. Additional energy storage mechanisms are related to *homogeneously* distributed microscopic hardening effects, captured by the hardening variable α, and to *inhomogeneously* distributed microscopic hardening effects, specified by the micro-gradient $\nabla\alpha$. Thus, the constitutive state can be summarized by

$$\mathfrak{c} := \{\, \boldsymbol{\varepsilon}, \alpha, \nabla\alpha, \boldsymbol{\varepsilon}^p \,\} \tag{7.3}$$

and builds the kinematic framework for the formulation of the constitutive equations.

7.1.2. Energy Storage Mechanism. In the sequel, the constitutive equations for a model problem of phenomenological gradient-type von Mises plasticity are introduced. According to $(3.178)_1$, the energy stored in the entire solid reads

$$E(\boldsymbol{u}, \alpha, \boldsymbol{\varepsilon}^p) = \int_{\mathcal{B}} \psi(\mathfrak{c})\, dV\,. \tag{7.4}$$

The free energy function ψ exhibits contributions arising from macroscopic elastic distortions, characterized by the stress producing strain $\boldsymbol{\varepsilon}^e$, and from homogeneously and inhomogeneously distributed dislocations, characterized on the phenomenological level by the scalar hardening field α and its gradient $\nabla\alpha$. A decoupled representation of the free energy function is assumed to be governed by the form

$$\boxed{\psi(\mathfrak{c}) = \underbrace{\bar{\psi}_{loc}(\boldsymbol{\varepsilon}^e(\boldsymbol{\varepsilon}, \boldsymbol{\varepsilon}^p))}_{\text{elast. macro-dist.}} + \underbrace{\check{\psi}_{loc}(\alpha)}_{\text{hom. micro-hard.}} + \underbrace{\check{\psi}_{non}(\nabla\alpha)}_{\text{inh. micro-hard.}}\,.} \tag{7.5}$$

For the specific model under focus, the energetic contributions take the particular form

$$\boxed{\begin{array}{lcl} \bar{\psi}_{loc}(\boldsymbol{\varepsilon}^e(\boldsymbol{\varepsilon}, \boldsymbol{\varepsilon}^p)) & = & \frac{1}{2}\kappa\ \mathrm{tr}^2[\boldsymbol{\varepsilon}] + \mu\, \|\,\mathrm{dev}[\boldsymbol{\varepsilon}^e(\boldsymbol{\varepsilon}, \boldsymbol{\varepsilon}^p)]\|^2 \\ \check{\psi}_{loc}(\alpha) & = & \frac{1}{2}\, h\alpha^2 \\ \check{\psi}_{non}(\nabla\alpha) & = & \frac{1}{2}\,\mu l^2\, \|\nabla\alpha\|^2\,, \end{array}} \tag{7.6}$$

where the bulk modulus κ, the shear modulus μ, the isotropic hardening modulus h, and the internal length scale parameter l have been introduced. With these definitions at hand, the rate of energy storage

$$\mathcal{E}(\dot{\boldsymbol{\varepsilon}}, \dot{\alpha}, \dot{\boldsymbol{\varepsilon}^p}; \boldsymbol{\varepsilon}, \alpha, \boldsymbol{\varepsilon}^p) := \frac{d}{dt}\int_{\mathcal{B}} \psi(\mathfrak{c})\, dV = \int_{\mathcal{B}} \{\, \partial_{\boldsymbol{\varepsilon}}\psi : \dot{\boldsymbol{\varepsilon}} + \delta_\alpha\psi\, \dot{\alpha} + \partial_{\boldsymbol{\varepsilon}^p}\psi : \dot{\boldsymbol{\varepsilon}^p} \,\}\, dV \tag{7.7}$$

contains the total stresses

$$\boldsymbol{\sigma} := \partial_{\boldsymbol{\varepsilon}}\psi = \kappa\ \mathrm{tr}[\boldsymbol{\varepsilon}]\boldsymbol{1} + 2\mu\ \mathrm{dev}[\boldsymbol{\varepsilon} - \boldsymbol{\varepsilon}^p] \tag{7.8}$$

and the elastic driving forces for the hardening field and the plastic strain field

$$\beta^e := \delta_\alpha\psi = h\alpha - \mu l^2\, \Delta\alpha \quad \text{and} \quad \boldsymbol{B}^e := \partial_{\boldsymbol{\varepsilon}^p}\psi = -2\mu\ \mathrm{dev}[\boldsymbol{\varepsilon} - \boldsymbol{\varepsilon}^p]\,. \tag{7.9}$$

Note hereby that the Laplacian term $\mu l^2\, \Delta\alpha$ renders the elastic driving force β^e *nonlocal.*

7.1.3. Threshold-Type Dissipation Functions. Having the free energy function ψ at hand it remains to specify the dissipation function ϕ. For rate-independent processes, the dissipative material response is characterized by

$$D(\dot\alpha, \dot{\boldsymbol{\varepsilon}}^p; \alpha, \boldsymbol{\varepsilon}^p) = \int_{\mathcal{B}} \phi(\dot{\mathfrak{c}}; \mathfrak{c})\, dV = \int_{\mathcal{B}} \partial_{\dot{\mathfrak{c}}}\phi(\dot{\mathfrak{c}}; \mathfrak{c}) \cdot \dot{\mathfrak{c}}\, dV = \mathcal{D}(\dot\alpha, \dot{\boldsymbol{\varepsilon}}^p; \alpha, \boldsymbol{\varepsilon}^p)\,, \tag{7.10}$$

where for positively homogeneous dissipation functions ϕ the dissipation potential functional D is identical to the dissipation $\mathcal{D}$. The dissipation function

$$\boxed{\phi(\dot{\mathfrak{c}}; \mathfrak{c}) = \underbrace{\breve{\phi}_{loc}(\dot\alpha, \dot{\boldsymbol{\varepsilon}}^p; \alpha, \boldsymbol{\varepsilon}^p)}_{\text{hom. micro-diss.}}} \tag{7.11}$$

is assumed to be influenced by homogeneously distributed hardening and plastic strains only. According to the considerations in Section 3.7.7, the thermodynamic dissipative driving forces dual to the global hardening field α and the local plastic strain $\boldsymbol{\varepsilon}^p$ are introduced

$$\breve{\boldsymbol{f}} := \{\,\beta\,\} \quad \text{and} \quad \boldsymbol{\mathcal{F}} := \{\,\boldsymbol{B}\,\}\,. \tag{7.12}$$

An elastic domain $\mathbb{E}$ in the space of dissipative forces is bounded by the threshold function

$$\varphi(\boldsymbol{B}, \beta) = \|\,\mathrm{dev}[\boldsymbol{B}]\| - \sqrt{2/3}\,(y_0 - \beta)\,, \tag{7.13}$$

characterizing for $\varphi(\boldsymbol{B}, \beta) < 0$ an elastic domain, without an evolution of hardening α and plastic strains $\boldsymbol{\varepsilon}^p$. The constrained optimization problem defines the dissipation function

$$\breve{\phi}_{loc}(\dot{\mathfrak{c}}; \mathfrak{c}) = \sup_{(\boldsymbol{B},\beta)\,\in\,\mathbb{E}} [\,\boldsymbol{B} : \dot{\boldsymbol{\varepsilon}}^p + \beta\,\dot\alpha\,] \quad \text{with} \quad \mathbb{E} := \{\,(\boldsymbol{B},\beta)\,|\,\varphi(\boldsymbol{B},\beta) \le 0\,\}\,, \tag{7.14}$$

also known as *principle of maximum dissipation.* The *fully rate-independent* constrained minimization problem $(7.14)_1$ is solved by a Lagrange solution method

$$\boxed{\breve{\phi}_{loc}(\dot{\mathfrak{c}}; \mathfrak{c}) = \sup_{\boldsymbol{B},\beta,\lambda\ge 0} [\,\boldsymbol{B} : \dot{\boldsymbol{\varepsilon}}^p + \beta\dot\alpha - \lambda\,\varphi(\boldsymbol{B},\beta)\,]} \tag{7.15}$$

involving the Lagrange multiplier λ. The necessary condition of this local constrained optimization problem yields the evolution of the hardening and the plastic strain

$$\dot\alpha = \lambda\,\sqrt{2/3} \quad \text{and} \quad \dot{\boldsymbol{\varepsilon}}^p = \lambda\,\boldsymbol{n} \quad \text{with} \quad \boldsymbol{n} := \partial_{\boldsymbol{B}}\varphi(\boldsymbol{B},\beta) = \frac{\mathrm{dev}[\boldsymbol{B}]}{\|\,\mathrm{dev}[\boldsymbol{B}]\|}\,, \tag{7.16}$$

where the direction of plastic evolution $\boldsymbol{n}$ is identified. The non-smooth evolutions (7.16) are supplemented by the loading/unloading conditions

$$\lambda \ge 0 \quad \text{and} \quad \varphi(\boldsymbol{B},\beta) \le 0 \quad \text{and} \quad \lambda\,\varphi(\boldsymbol{B},\beta) = 0\,, \tag{7.17}$$

also known as *Karush-Kuhn-Tucker conditions.* A *viscous regularization* of the rate-independent dissipation function (7.15) bases on the over-force formulation

$$\boxed{\breve{\phi}^{\eta}_{loc}(\dot{\mathfrak{c}}; \mathfrak{c}) = \sup_{\boldsymbol{B},\beta}[\,\boldsymbol{B} : \dot{\boldsymbol{\varepsilon}}^p + \beta\,\dot\alpha - \frac{1}{2\eta}\langle\,\varphi(\boldsymbol{B},\beta)\,\rangle^2_+\,]\,.} \tag{7.18}$$

In this setting the ramp function $\langle x\rangle_+ := (|x|+x)/2$ of the set $\mathcal{R}_+$ of positive real numbers has been employed, for an illustration see Figure 4.11c). The necessary condition of the smooth unconstrained optimization problem (7.18) gives the evolution equations

$$\dot{\alpha} = \frac{1}{\eta}\langle\, \varphi(\boldsymbol{B},\beta)\,\rangle_+ \sqrt{2/3} \quad \text{and} \quad \dot{\boldsymbol{\varepsilon}}^p = \frac{1}{\eta}\langle\, \varphi(\boldsymbol{B},\beta)\,\rangle_+ \boldsymbol{n}\,, \tag{7.19}$$

expressed in terms of the direction of plastic evolution $\boldsymbol{n}$. The viscosity stands for a viscous over-force response which governs the evolution of the hardening field and the plastic strain, respectively. For $\eta \to 0$, the model degenerates to the rate-independent setting (7.15). In the viscous setting, the Lagrange-multiplier λ is identified by

$$\lambda := \frac{1}{\eta}\langle\, \varphi(\boldsymbol{B},\beta)\,\rangle_+ \geq 0\,, \tag{7.20}$$

being characteristic for rate-dependent loading. Due to the limit character of the smooth viscous over-force formulation and the well-posed setting of the power-type formulation (7.18), this formulation is of particular interest for numerical implementations.

7.1.4. Governing Balance Equations of Coupled Problem. In this section the governing balance equations are derived that determine the displacement field $\boldsymbol{u}$, the hardening field α with its thermodynamic driving force β as global fields, and the plastic strain $\boldsymbol{\varepsilon}^p$ with its driving force $\boldsymbol{B}$ as local fields. Regarding the displacement field, the surface of the solid is decomposed into a part $\partial\mathcal{B}_{\boldsymbol{u}}$, where the displacements are prescribed by Dirichlet boundary conditions

$$\boldsymbol{u} = \boldsymbol{u}_D \ \text{ on } \ \partial\mathcal{B}_{\boldsymbol{u}}\,, \tag{7.21}$$

and a Neumann part $\partial\mathcal{B}_{\boldsymbol{t}}$ with prescribed tractions $\boldsymbol{t}_N$. Clearly, the common set $\partial\mathcal{B}_{\boldsymbol{u}} \cap \partial\mathcal{B}_{\boldsymbol{t}} = \emptyset$ of these boundaries is empty. The power of external mechanical load reads

$$\mathcal{P}_{ext}(\dot{\boldsymbol{u}}) = \int_{\mathcal{B}} \boldsymbol{\gamma} \cdot \dot{\boldsymbol{u}}\, dV + \int_{\partial\mathcal{B}_{\boldsymbol{t}}} \boldsymbol{t}_N \cdot \dot{\boldsymbol{u}}\, dA \tag{7.22}$$

expressed in terms of a prescribed body force field $\boldsymbol{\gamma}$ per unit volume. For the hardening field no Dirichlet-type boundary conditions are set, the natural Neumann-type conditions $\nabla\alpha \cdot \boldsymbol{n} = 0$ on the full surface $\partial\mathcal{B}$ are chosen. The hardening field α is considered to be driven by the macroscopic deformation $\boldsymbol{u}$ of the solid. As a consequence, no prescribed external loading associated with the hardening field is considered. The local plastic strains $\boldsymbol{\varepsilon}^p$ have no field character, thus no boundary conditions have to be specified. With the power of external load (7.22), the rate of energy storage (7.7), and the dissipation functional (7.10) at hand, it remains to evaluate the standard argument of virtual power

$$\boxed{\mathcal{E}(\dot{\boldsymbol{u}}, \dot{\alpha}, \dot{\boldsymbol{\varepsilon}}^p) + \mathcal{D}(\dot{\alpha}, \dot{\boldsymbol{\varepsilon}}^p) - \mathcal{P}_{ext}(\dot{\boldsymbol{u}}) = 0} \tag{7.23}$$

for admissible rates $\dot{\boldsymbol{u}}$ of the displacement field that satisfy the homogeneous form of the Dirichlet boundary conditions

$$\dot{\boldsymbol{u}} \in \mathcal{W}_{\boldsymbol{u}} := \{\, \dot{\boldsymbol{u}} \,|\, \dot{\boldsymbol{u}} = \boldsymbol{0} \text{ on } \partial\mathcal{B}_{\boldsymbol{u}}\}\,. \tag{7.24}$$

The boundary value problem is now fully described, the principle (7.23) is evaluated for the two dissipation functions (7.15) and (7.18) under focus.

7.1.4.1. Model I: Rate-Independent Setting with Threshold Function. For the rate-independent dissipation function with threshold function (7.15), the application of the principle of virtual power (7.24) yields the coupled balance equations

$$\begin{aligned} \boldsymbol{0} &= \operatorname{div}[\,\kappa\ \operatorname{tr}[\boldsymbol{\varepsilon}]\boldsymbol{1} + 2\mu\ \operatorname{dev}[\boldsymbol{\varepsilon} - \boldsymbol{\varepsilon}^p]\,] + \boldsymbol{\gamma} \\ 0 &= \mu l^2\,\Delta\alpha - [\,h\alpha + \beta\,] \\ 0 &= \dot{\alpha} - \lambda\sqrt{2/3} \\ \boldsymbol{0} &= 2\mu\ \operatorname{dev}[\boldsymbol{\varepsilon} - \boldsymbol{\varepsilon}^p] - \boldsymbol{B} \\ \boldsymbol{0} &= \dot{\boldsymbol{\varepsilon}}^p - \lambda\,\boldsymbol{n}\,, \end{aligned} \tag{7.25}$$

valid in combination with the time discrete loading/unloading conditions

$$\lambda \geq 0 \quad \text{and} \quad \varphi(\boldsymbol{B},\beta) \leq 0 \quad \text{and} \quad \lambda\,\varphi(\boldsymbol{B},\beta) = 0\,. \tag{7.26}$$

The direction of plastic evolution $\boldsymbol{n}$ has been defined in equation (7.16).

7.1.4.2. Model II: Rate-Dependent Setting with Threshold Function. Evaluation of the balance of internal and external power (7.23) for the rate-dependent over-force representation of the dissipation function (7.18) yields the coupled balance equations

$$\begin{aligned} \boldsymbol{0} &= \operatorname{div}[\,\kappa\ \operatorname{tr}[\boldsymbol{\varepsilon}]\boldsymbol{1} + 2\mu\ \operatorname{dev}[\boldsymbol{\varepsilon} - \boldsymbol{\varepsilon}^p]\,] + \boldsymbol{\gamma} \\ 0 &= \mu l^2\,\Delta\alpha - [\,h\alpha + \beta\,] \\ 0 &= \dot{\alpha} - \frac{1}{\eta}\langle\,\|\operatorname{dev}[\boldsymbol{B}]\| - \sqrt{2/3}\,(y_0 - \beta)\,\rangle_+ \sqrt{2/3} \\ \boldsymbol{0} &= 2\mu\ \operatorname{dev}[\boldsymbol{\varepsilon} - \boldsymbol{\varepsilon}^p] - \boldsymbol{B} \\ \boldsymbol{0} &= \dot{\boldsymbol{\varepsilon}}^p - \frac{1}{\eta}\langle\,\|\operatorname{dev}[\boldsymbol{B}]\| - \sqrt{2/3}\,(y_0 - \beta)\,\rangle_+\,\boldsymbol{n}\,, \end{aligned} \tag{7.27}$$

where for vanishing viscosity $\eta \to 0$ the rate-independent limit (7.25) is obtained.

7.1.5. Incremental Variational Principle for Gradient-Type Plasticity. The previously discussed incremental variational principle is now applied to the model problem of gradient-type von Mises plasticity. Thus, the state variables at the discrete solution times $0, t_1, t_2, \ldots, t_n, t_{n+1}, \ldots, T$ are considered. Hereby, the setup of the incremental potential depends on the energy storage, the dissipation, and the external load that is expended to the system within the typical time step $[t_n, t_{n+1}]$. Recalling the non-smooth and smooth representations of the dissipation function (7.15) and (7.18), the incremental dissipation possesses different forms, yielding two models that are discussed separately.

7.1.5.1. Model I: Rate-Independent Four-Field Setting. The first possibility to model the incremental potential bases on the *rate-independent* representation of the dissipation function (7.15) and demands the solution of a constrained optimization problem. Regarding a Lagrange-multiplier solution, the extended constitutive state vector and the local solution pair are summarized

$$\mathfrak{c}^*_\lambda := \{\,\boldsymbol{\varepsilon}, \alpha, \nabla\alpha, \beta, \lambda\,\} \quad \text{and} \quad \mathfrak{p} := \{\,\boldsymbol{\varepsilon}^p, \boldsymbol{B}\,\}\,, \tag{7.28}$$

allowing for the compact formulation of the *incremental internal work density*

$$\begin{aligned}\pi_\lambda^{*\tau}(\mathfrak{c}^*_\lambda, \mathfrak{p}; \mathfrak{c}^*_{\lambda n}, \mathfrak{p}_n) = {} & \tfrac{1}{2}\,\kappa\ \mathrm{tr}^2[\boldsymbol{\varepsilon}] + \mu\,\|\,\mathrm{dev}[\boldsymbol{\varepsilon}^e(\boldsymbol{\varepsilon}, \boldsymbol{\varepsilon}^p)]\|^2 \\ & + \tfrac{1}{2}\,h\alpha^2 + \tfrac{1}{2}\,\mu l^2\,\|\nabla\alpha\|^2 - \psi(\mathfrak{c}_n) \\ & + \beta\,(\alpha - \alpha_n) + \boldsymbol{B} : (\boldsymbol{\varepsilon}^p - \boldsymbol{\varepsilon}^p_n) \\ & - \tau\lambda\,(\|\,\mathrm{dev}[\boldsymbol{B}]\| - \sqrt{2/3}\,(y_0 - \beta))\,.\end{aligned} \tag{7.29}$$

Application of the Lagrange multiplier type representation of the incremental variational principle (3.133) for small deformations gives the algorithmic Euler equations

$$\begin{aligned}\boldsymbol{0} &= \mathrm{div}[\,\kappa\ \mathrm{tr}[\boldsymbol{\varepsilon}]\,\boldsymbol{1} + 2\mu\ \mathrm{dev}[\boldsymbol{\varepsilon} - \boldsymbol{\varepsilon}^p]\,] + \boldsymbol{\gamma} \\ 0 &= \mu l^2\,\Delta\alpha - [\,h\alpha + \beta\,] \\ 0 &= \alpha - \alpha_n - \tau\lambda\,\sqrt{2/3} \\ \boldsymbol{0} &= 2\mu\ \mathrm{dev}[\boldsymbol{\varepsilon} - \boldsymbol{\varepsilon}^p] - \boldsymbol{B} \\ \boldsymbol{0} &= \boldsymbol{\varepsilon}^p - \boldsymbol{\varepsilon}^p_n - \tau\lambda\,\boldsymbol{n}\,,\end{aligned} \tag{7.30}$$

coming in combination with the time discrete loading/unloading conditions

$$\tau\lambda \geq 0 \quad \text{and} \quad \tau\,\varphi(\boldsymbol{B}, \beta) \leq 0 \quad \text{and} \quad \tau\lambda\,\varphi(\boldsymbol{B}, \beta) = 0\,. \tag{7.31}$$

Reformulation of equation $(7.30)_5$ together with the property $\|\boldsymbol{n}\| = 1$ yields the relation $\tau\lambda = \|\boldsymbol{\varepsilon}^p - \boldsymbol{\varepsilon}^p_n\|$ and identifies in $(7.30)_3$ the hardening variable α as the equivalent plastic strain. Thus, the evolution of the hardening field can be reformulated

$$\alpha = \alpha_n + \sqrt{2/3}\,\|\boldsymbol{\varepsilon}^p - \boldsymbol{\varepsilon}^p_n\|\,. \tag{7.32}$$

Solving $(7.30)_2$ for the thermodynamic force β and insertion into the yield function (7.13) gives the alternative representation of the yield function

$$\chi := \|\,\mathrm{dev}[\boldsymbol{B}]\| - \sqrt{2/3}\,(y_0 + h\alpha - \mu l^2\,\Delta\alpha)\,. \tag{7.33}$$

Accordingly, the loading/unloading conditions (7.31) are reformulated to

$$\alpha \geq \alpha_n \quad \text{and} \quad \chi \leq 0 \quad \text{and} \quad (\alpha - \alpha_n)\,\chi = 0 \tag{7.34}$$

and a model of strain-gradient plasticity in the sense of Aifantis is obtained, where the yield resistance is modified by the Laplacian term $\mu l^2\,\Delta\alpha$.

7.1.5.2. Model II: Rate-Dependent Three-Field Setting. The second possibility to approach the incremental potential bases on the *rate-dependent* formulation of the dissipation function (7.18). For the solution of the smooth problem, the constitutive state

$$\mathfrak{c}^* := \{\,\boldsymbol{\varepsilon}, \alpha, \nabla\alpha, \beta\,\} \quad \text{and} \quad \mathfrak{p} := \{\,\boldsymbol{\varepsilon}^p, \boldsymbol{B}\,\} \tag{7.35}$$

is introduced, allowing for the compaction of the *incremental internal work density*

$$\begin{aligned}\pi_\eta^{*\tau}(\mathfrak{c}^*, \mathfrak{c}^*_n; \mathfrak{p}, \mathfrak{p}_n) = {} & \tfrac{1}{2}\,\kappa\ \mathrm{tr}^2[\boldsymbol{\varepsilon}] + \mu\,\|\,\mathrm{dev}[\boldsymbol{\varepsilon}^e(\boldsymbol{\varepsilon}, \boldsymbol{\varepsilon}^p)]\|^2 \\ & + \tfrac{1}{2}\,h\alpha^2 + \tfrac{1}{2}\,\mu l^2\,\|\nabla\alpha\|^2 - \psi(\mathfrak{c}_n) \\ & + \beta\,(\alpha - \alpha_n) + \boldsymbol{B} : (\boldsymbol{\varepsilon}^p - \boldsymbol{\varepsilon}^p_n) \\ & - \frac{\tau}{2\eta}\langle\,\|\,\mathrm{dev}[\boldsymbol{B}]\| - \sqrt{2/3}\,(y_0 - \beta)\,\rangle_+^2\,.\end{aligned} \tag{7.36}$$

Application of the small strain version of the incremental variational principle (3.133) provides the algorithmic Euler equations

$$\begin{aligned}
\boldsymbol{0} &= \operatorname{div}[\,\kappa \operatorname{tr}[\boldsymbol{\varepsilon}]\boldsymbol{1} + 2\mu \operatorname{dev}[\boldsymbol{\varepsilon} - \boldsymbol{\varepsilon}^p]\,] + \boldsymbol{\gamma} \\
0 &= \mu l^2\, \Delta\alpha - [\, h\alpha + \beta\,] \\
0 &= \alpha - \alpha_n - \frac{\tau}{\eta}\langle\, \|\operatorname{dev}[\boldsymbol{B}]\| - \sqrt{2/3}\,(y_0 - \beta)\,\rangle_+ \sqrt{2/3} \\
\boldsymbol{0} &= 2\mu \operatorname{dev}[\boldsymbol{\varepsilon} - \boldsymbol{\varepsilon}^p] - \boldsymbol{B} \\
\boldsymbol{0} &= \boldsymbol{\varepsilon}^p - \boldsymbol{\varepsilon}^p_n - \frac{\tau}{\eta}\langle\, \|\operatorname{dev}[\boldsymbol{B}]\| - \sqrt{2/3}\,(y_0 - \beta)\,\rangle_+ \boldsymbol{n}\,.
\end{aligned} \tag{7.37}$$

Combination of $(7.30)_{2,3}$ allows to reformulate the evolution of the equivalent plastic strain

$$\alpha = \alpha_n + \frac{\tau}{\eta}\langle\, \|\operatorname{dev}[\boldsymbol{B}]\| - \sqrt{2/3}\,(y_0 + h\alpha - \mu l^2 \Delta\alpha)\,\rangle_+ \sqrt{2/3}\,, \tag{7.38}$$

and shows again the dependency of the yield resistance on the Laplacian term $\mu l^2 \Delta\alpha$. The smooth character of the governing equations makes this time-regularized setting with threshold function highly attractive for a numerical implementation.

7.1.6. Fast Update Algorithm for Local Plastic Strains. Aiming at a first step towards a numerical implementation, the focus is put on the previously discussed rate-dependent three-field setting of *model II*. Based on the state variables

$$\mathfrak{c}^*(\mathfrak{u}^*) := \{\,\boldsymbol{\varepsilon}, \alpha, \nabla\alpha, \beta\,\} \quad \text{with} \quad \mathfrak{u}^* := \{\,\boldsymbol{u}, \alpha, \beta\,\} \quad \text{and} \quad \mathfrak{p} := \{\,\boldsymbol{\varepsilon}^p, \boldsymbol{B}\,\}\,, \tag{7.39}$$

the local evolution subproblem $(7.37)_{4,5}$ can be rewritten as residual

$$\pi^{*\tau}_{\eta,\mathfrak{p}}(\mathfrak{u}^*, \mathfrak{p}) := \left[\begin{array}{l} 2\mu \operatorname{dev}[\boldsymbol{\varepsilon} - \boldsymbol{\varepsilon}^p] - \boldsymbol{B} \\[1ex] \boldsymbol{\varepsilon}^p - \boldsymbol{\varepsilon}^p_n - \dfrac{\tau}{\eta}\langle\, \|\operatorname{dev}[\boldsymbol{B}]\| - \sqrt{2/3}\,(y_0 - \beta)\,\rangle_+ \boldsymbol{n} \end{array}\right] = \boldsymbol{0}\,, \tag{7.40}$$

see also the discrete expression (3.165). From equation $(7.40)_1$, the thermodynamic dissipative driving force can be identified as

$$\boldsymbol{B} = 2\mu \operatorname{dev}[\boldsymbol{\varepsilon} - \boldsymbol{\varepsilon}^p]\,. \tag{7.41}$$

Equation $(7.40)_2$ determines the local update rule of the plastic strain

$$\boldsymbol{\varepsilon}^p = \boldsymbol{\varepsilon}^p_n + \frac{\tau}{\eta}\langle\, \|\operatorname{dev}[\boldsymbol{B}]\| - \sqrt{2/3}\,(y_0 - \beta)\,\rangle_+ \boldsymbol{n} \tag{7.42}$$

expressed in terms of the direction of plastic evolution $\boldsymbol{n}$. Making use of the decomposition of the plastic strain into its volumetric and isochoric part $\boldsymbol{\varepsilon}^p = \frac{1}{3}\operatorname{tr}[\boldsymbol{\varepsilon}^p]\boldsymbol{1} + \operatorname{dev}[\boldsymbol{\varepsilon}^p]$ and further demand plastic incompressibility $\operatorname{tr}[\boldsymbol{\varepsilon}^p] = 0$, the update (7.42) can be recast into

$$\operatorname{dev}[\boldsymbol{\varepsilon}^p] = \operatorname{dev}[\boldsymbol{\varepsilon}^p_n] + \Delta\gamma^p\, \boldsymbol{n} \quad \text{with} \quad \Delta\gamma^p := \frac{\tau}{\eta}\langle\, \|\operatorname{dev}[\boldsymbol{B}]\| - \sqrt{2/3}\,(y_0 - \beta)\,\rangle_+\,, \tag{7.43}$$

where the scalar valued plastic increment $\Delta\gamma^p$ is introduced. Insertion of the deviatoric plastic strain $(7.43)_1$ into equation (7.41) yields the deviatoric driving force

$$\operatorname{dev}[\boldsymbol{B}] = \operatorname{dev}[\boldsymbol{B}^{tr}] - 2\mu\, \Delta\gamma^p\, \boldsymbol{n} \quad \text{with} \quad \operatorname{dev}[\boldsymbol{B}^{tr}] := 2\mu \operatorname{dev}[\boldsymbol{\varepsilon} - \boldsymbol{\varepsilon}^p_n]\,, \tag{7.44}$$

where the deviatoric thermodynamic trial force $\operatorname{dev}[\boldsymbol{B}^{tr}]$ has been introduced. A simple reformulation of $(7.44)_1$ gives the alternative representation

$$\|\operatorname{dev}[\boldsymbol{B}]\|\,\boldsymbol{n} = \|\operatorname{dev}[\boldsymbol{B}^{tr}]\|\,\boldsymbol{n}^{tr} - 2\mu\,\Delta\gamma^p\,\boldsymbol{n} \quad \text{with} \quad \boldsymbol{n}^{tr} := \frac{\operatorname{dev}[\boldsymbol{B}^{tr}]}{\|\operatorname{dev}[\boldsymbol{B}^{tr}]\|}\,. \tag{7.45}$$

By comparing coefficients, one can easily obtain the following conclusions

$$\|\operatorname{dev}[\boldsymbol{B}]\| = \|\operatorname{dev}[\boldsymbol{B}^{tr}]\| - 2\mu\,\Delta\gamma^p \quad \text{and} \quad \boldsymbol{n} = \boldsymbol{n}^{tr}\,. \tag{7.46}$$

This means that the update equation for the tensorial plastic strains is solely determined by the computation of a *scalar plastic increment* $\Delta\gamma^p$, the direction of plastic evolution $\boldsymbol{n}$ is computed based on known values. Insertion of $(7.46)_1$ into the definition of the plastic increment $(7.43)_2$ yields the governing equation

$$\Delta\gamma^p = \frac{\tau}{\eta}\langle\,\|\operatorname{dev}[\boldsymbol{B}^{tr}]\| - 2\mu\,\Delta\gamma^p - \sqrt{2/3}\,(y_0 - \beta)\,\rangle_+ \tag{7.47}$$

which is a linear equation that has to be solved for the plastic increment $\Delta\gamma^p$. Assuming plastic loading first, a trial value of the plastic increment can be introduced

$$\Delta\gamma^{p,tr} = \frac{\tau}{2\mu\tau + \eta}\langle\,\|\operatorname{dev}[\boldsymbol{B}^{tr}]\| - \sqrt{2/3}\,(y_0 - \beta)\,\rangle_+\,. \tag{7.48}$$

This trial state has to be checked backwards in order to approve or discard the plastic loading case. Thus, the actual plastic increment is determined by the *closed form solution*

$$\Delta\gamma^p = \begin{cases} \Delta\gamma^{p,tr} & \text{if } \varphi(\boldsymbol{B},\beta) \geq 0 \\ 0 & \text{otherwise}\,. \end{cases} \tag{7.49}$$

An iterative solution in the sense of (3.170) is not required. With known plastic increment $\Delta\gamma^p$ and flow direction $\boldsymbol{n} = \boldsymbol{n}^{tr}$, the total plastic strain $\boldsymbol{\varepsilon}^p$ can easily be updated according to $(7.43)_1$, where the plastic incompressibility $\operatorname{tr}[\boldsymbol{\varepsilon}^p] = 0$ is a priori preserved by the deviatoric structure. The thermodynamic driving force $\boldsymbol{B}$ is determined according to (7.41). Note that the update algorithm for the local solution pair $\boldsymbol{\mathfrak{p}} := \{\,\boldsymbol{\varepsilon}^p, \boldsymbol{B}\,\}$ implicitly depends on the global fields, becoming of particular importance when computing the algorithmic sensitivities within a finite element formulation. For a more detailed discussion of this update algorithm see also the thesis by WIDMER [178].

7.1.7. FE-Discretization of Incremental Variational Principle. The general numerical multi-field treatment as intensively discuss in Section 3.9.4.2 is specified for *model II* whose strong form is summarized in equation (7.37). Focusing on two-dimensional boundary value problems, the generalized displacements and the constitutive state read

$$\boldsymbol{\mathfrak{u}}^* := \{\,u_1, u_2, \alpha, \beta\,\} \quad \text{with} \quad \boldsymbol{\mathfrak{c}}^*(\boldsymbol{\mathfrak{u}}^*) := \{\,u_{1,1}, u_{2,2}, u_{1,2} + u_{2,1}, \alpha, \alpha_{,1}, \alpha_{,2}, \beta\,\}\,. \tag{7.50}$$

Following (3.226), the extended generalized displacements are approximated by

$$\boldsymbol{\mathfrak{u}}^{*h} =: \boldsymbol{\mathfrak{N}}^*(\boldsymbol{x})\,\boldsymbol{\mathfrak{d}}^* \quad \text{with} \quad [\boldsymbol{\mathfrak{N}}^*]_i^e = \begin{bmatrix} N & 0 & 0 & 0 \\ 0 & N & 0 & 0 \\ 0 & 0 & N & 0 \\ 0 & 0 & 0 & M \end{bmatrix}_i \quad \text{and} \quad \boldsymbol{\mathfrak{d}}_i^* = [\,d_1, d_2, a, b\,]_i^T\,. \tag{7.51}$$

To keep things simple, the same shape functions N_i and M_i are chosen. At node i of the finite element discretization, the generalized displacement vector $\boldsymbol{\mathfrak{d}}^*$ contains the nodal 1- and 2-displacements d_1 and d_2, the nodal hardening variable a, and the nodal thermodynamic driving force b. According to (3.231), the variation of the discrete extended constitutive state with respect to the extended nodal unknowns reads

$$\delta_{\boldsymbol{\mathfrak{d}}^*} \boldsymbol{\mathfrak{c}}^{*h} =: \boldsymbol{\mathfrak{B}}^*(\boldsymbol{x})\, \delta \boldsymbol{\mathfrak{d}}^* \quad \text{with} \quad [\boldsymbol{\mathfrak{B}}^*]_i^e = \begin{bmatrix} N_{,1} & 0 & N_{,2} & 0 & 0 & 0 & 0 \\ 0 & N_{,2} & N_{,1} & 0 & 0 & 0 & 0 \\ 0 & 0 & 0 & N & N_{,1} & N_{,2} & 0 \\ 0 & 0 & 0 & 0 & 0 & 0 & M \end{bmatrix}_i^T . \tag{7.52}$$

For the model problem of gradient-type von Mises plasticity, the generalized stresses and the symmetric generalized moduli take the specific form

$$\boldsymbol{S}^* := \begin{bmatrix} \partial_{\boldsymbol{\varepsilon}} \pi_\eta^{*\tau} \\ \partial_\alpha \pi_\eta^{*\tau} \\ \partial_{\nabla\alpha} \pi_\eta^{*\tau} \\ \partial_\beta \pi_\eta^{*\tau} \end{bmatrix} \quad \text{and} \quad \mathbb{C}^* := \begin{bmatrix} \partial^2_{\boldsymbol{\varepsilon}\boldsymbol{\varepsilon}} \pi_\eta^{*\tau} & \boldsymbol{0} & \boldsymbol{0} & \partial^2_{\boldsymbol{\varepsilon}\beta} \pi_\eta^{*\tau} \\ \boldsymbol{0} & \partial^2_{\alpha\alpha} \pi_\eta^{*\tau} & \boldsymbol{0} & 1 \\ \boldsymbol{0} & \boldsymbol{0} & \partial^2_{\nabla\alpha\nabla\alpha} \pi_\eta^{*\tau} & \boldsymbol{0} \\ \partial^2_{\beta\boldsymbol{\varepsilon}} \pi_\eta^{*\tau} & 1 & \boldsymbol{0} & \partial^2_{\beta\beta} \pi_\eta^{*\tau} \end{bmatrix} . \tag{7.53}$$

In the case of *elastic response* for $\varphi(\boldsymbol{B}, \beta) < 0$, the single unspecified components of the generalized stresses $(7.53)_1$ are summarized by

$$\begin{aligned} \partial_{\boldsymbol{\varepsilon}} \pi_\eta^{*\tau} &= \kappa \operatorname{tr}[\boldsymbol{\varepsilon}]\boldsymbol{1} + 2\mu \operatorname{dev}[\boldsymbol{\varepsilon} - \boldsymbol{\varepsilon}^p] \\ \partial_\alpha \pi_\eta^{*\tau} &= h\alpha + \beta \\ \partial_{\nabla\alpha} \pi_\eta^{*\tau} &= \mu l^2 \, \nabla\alpha \\ \partial_\beta \pi_\eta^{*\tau} &= \alpha - \alpha_n \, , \end{aligned} \tag{7.54}$$

the according components of the generalized moduli $(7.53)_2$ are given by

$$\begin{aligned} \partial^2_{\boldsymbol{\varepsilon}\boldsymbol{\varepsilon}} \pi_\eta^{*\tau} &= \kappa \, \boldsymbol{1} \otimes \boldsymbol{1} + 2\mu \, \mathbb{P}^{sym} \\ \partial^2_{\alpha\alpha} \pi_\eta^{*\tau} &= h \\ \partial^2_{\nabla\alpha\nabla\alpha} \pi_\eta^{*\tau} &= \mu l^2 \, \boldsymbol{1} \\ \partial^2_{\beta\beta} \pi_\eta^{*\tau} &= 0 \\ \partial^2_{\boldsymbol{\varepsilon}\beta} \pi_\eta^{*\tau} &= \boldsymbol{0} \, . \end{aligned} \tag{7.55}$$

In the case of *inelastic loading* for $\varphi(\boldsymbol{B}, \beta) \geq 0$, the ramp function becomes active and the generalized stresses (7.54) have to be updated according to

$$\partial_\beta \pi_\eta^{*\tau} \Leftarrow \partial_\beta \pi_\eta^{*\tau} - \frac{\tau}{\eta} \big(\, \| \operatorname{dev}[\boldsymbol{B}] \| - \sqrt{2/3}\, (y_0 - \beta) \, \big) \sqrt{2/3} \, . \tag{7.56}$$

The generalized moduli (7.55) have to be updated by additional softening terms that arise from the local update algorithm and the penalty-type ramp function, i.e.

$$\begin{aligned} \partial^2_{\boldsymbol{\varepsilon}\boldsymbol{\varepsilon}} \pi_\eta^{*\tau} &\Leftarrow \partial^2_{\boldsymbol{\varepsilon}\boldsymbol{\varepsilon}} \pi_\eta^{*\tau} - \frac{4\mu^2\tau}{2\mu\tau + \eta} \boldsymbol{n}^{tr} \otimes \boldsymbol{n}^{tr} - \frac{4\mu^2 \Delta\gamma^p}{\| \operatorname{dev}[\boldsymbol{B}^{tr}] \|} [\mathbb{P}^{sym} - \boldsymbol{n}^{tr} \otimes \boldsymbol{n}^{tr}] \\ \partial^2_{\beta\beta} \pi_\eta^{*\tau} &\Leftarrow \partial^2_{\beta\beta} \pi_\eta^{*\tau} - \frac{2\tau}{3\eta} + \frac{4\mu\tau^2}{6\mu\tau\eta + \eta^2} \\ \partial^2_{\boldsymbol{\varepsilon}\beta} \pi_\eta^{*\tau} &\Leftarrow \partial^2_{\boldsymbol{\varepsilon}\beta} \pi_\eta^{*\tau} - \frac{2\sqrt{2}\mu\tau}{2\sqrt{3}\mu\tau + \sqrt{3}\eta} \boldsymbol{n}^{tr} \, , \end{aligned} \tag{7.57}$$

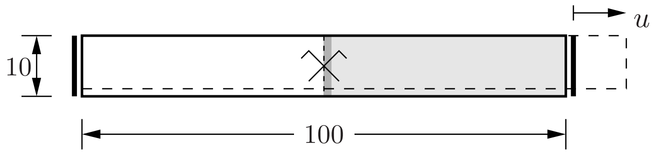

Figure 7.1: Bar under axial loading. Geometry and boundary conditions. Due to the symmetry of the boundary value problem only one half is discretized. To trigger localization, the yield limit y_0 in the left element is reduced by 3%.

where the fourth order symmetric deviatoric projection tensor $\mathbb{P}^{sym} = \mathbb{I}^{sym} - \frac{1}{3}\boldsymbol{1} \otimes \boldsymbol{1}$ and the direction of plastic loading $\boldsymbol{n}^{tr}$ have been employed.

7.1.8. Numerical Examples. Regularization of Shear Bands. In this section, the performance of the proposed model for von Mises plasticity with gradient-type hardening at small deformations is demonstrated by means of some representative numerical examples. The first elementary example is concerned with a *bar subjected to axial loading*. Note that this problem has been introduced in Section 4.1.2 to motivate the phenomena of localization and mesh sensitivity, even though for a more simple material model with local linear strain softening behavior. The second numerical test is concerned with *cross shearing in a perforated plate under tensile loading*. For both examples, the regularizing effect of the additional gradient term on the shear band width is investigated.

7.1.8.1. Bar under Axial Loading. The first numerical test under focus is concerned with a bar that is subjected to axial tensile loading. The geometric setup and the corresponding boundary conditions are depicted in Figure 7.1. Due to the symmetry of the boundary value problem, only one half of the bar is discretized using 20, 40, and 80 elements. The analysis is carried out using the bulk modulus $\kappa = 164.21$ kN/mm^2, the shear modulus $\mu = 80.19$ kN/mm^2, the hardening (softening) parameter $h = -0.129$ kN/mm^2, the initial yield stress $y_0 = 0.45$ kN/mm^2, and the viscosity $\eta = 1 \times 10^{-5}$ kN s/mm^2. In order to trigger localization in the centered strip of the bar, the yield stress y_0 in the first element is reduced by 3%. The computations are performed in a monotonic displacement driven context with constant displacement increments of $\Delta u = 1 \times 10^{-3}$ mm. The structural responses for this elementary boundary value problem obtained for computations with two different length scales are depicted in Figure 7.2a) and Figure 7.2b), respectively. Clearly, for a length scale $l = 0$ mm the results are completely mesh dependent, whereas

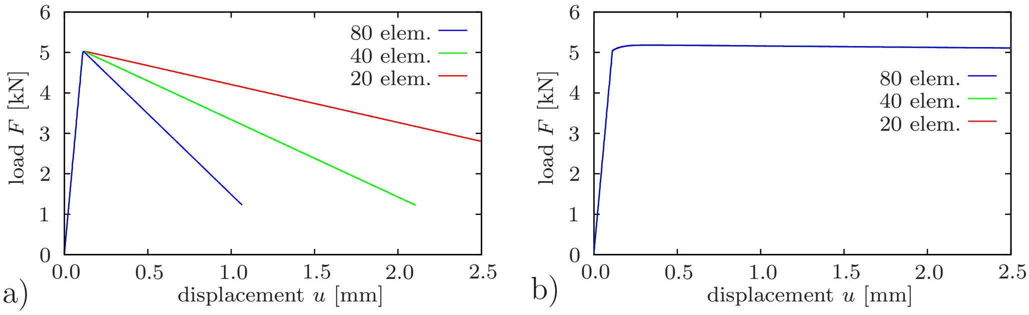

Figure 7.2: Bar under axial loading. a) Mesh dependent load-deflection curves for computations with a length scale $l = 0$ mm and b) objective structural response for $l = 3$ mm.

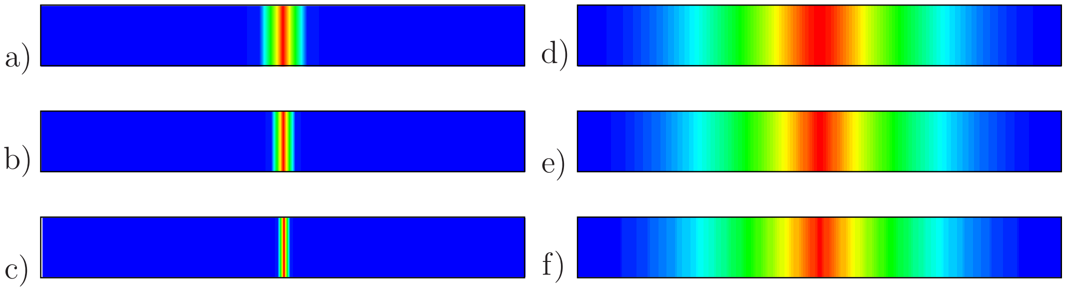

Figure 7.3: Bar under axial loading. Equivalent plastic strains α for discretizations with 20, 40, and 80 elements for a)–c) a local analysis with $l = 0$ mm and d)–f) a nonlocal analysis with $l = 3$ mm evaluated at a deformation stage of $u = 0.55$ mm.

for a length scale $l = 3$ mm the responses are mesh objective. The corresponding contour plots of the equivalent plastic strains α, at a deformation stage of $u = 0.55$ mm are depicted in Figure 7.3, again for the local and nonlocal analysis. Obviously, in the local analysis localization occurs in one single element, whereas for $l = 3$ mm the equivalent plastic strains spread over a region with a size proportional to the length scale parameter l.

7.1.8.2. Perforated Plate under Tensile Loading. The second example under focus describes a squared specimen with centered circular hole. The geometric setup and the boundary conditions are illustrated in Figure 7.4. Due to the symmetry of the boundary value problem, only one quarter is discretized using 622, 2393, and 9556 elements in a structured mesh. For the analysis, the bulk modulus is chosen to $\kappa = 164.21$ kN/mm^2, the shear modulus to $\mu = 80.19$ kN/mm^2, the hardening (softening) parameter to $h = -0.129$ kN/mm^2, the initial yield stress to $y_0 = 0.45$ kN/mm^2, and the viscosity to $\eta = 1 \times 10^{-5}$ kN s/mm^2. The deformation is applied in a deformation driven context with constant displacement increments of $\Delta u = 1 \times 10^{-5}$ mm. The corresponding contour plots of the equivalent plastic strain α for three exemplary discretizations with 622, 2393, and 9556 elements, evaluated at a deformation stage of $u = 0.025$ mm are displayed in Figure 7.5. Obviously, for the local analysis with $l = 0.000$ mm, see Figure 7.5a)–c), the equivalent plastic strain localizes in a zone with vanishing width for decreasing element size. In a local analysis, the finite element method tries to resolve the evolving discontinuity as

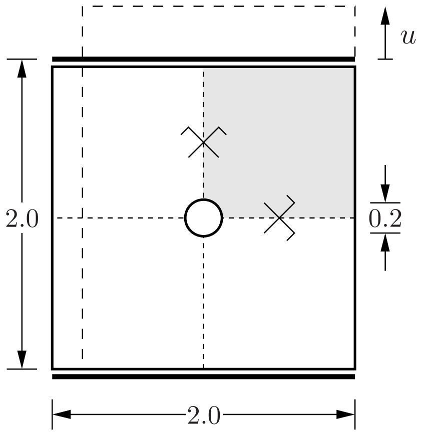

Figure 7.4: Perforated plate under tensile loading. Geometry and boundary conditions. Due to the symmetry of the boundary value problem, only one quarter is discretized.

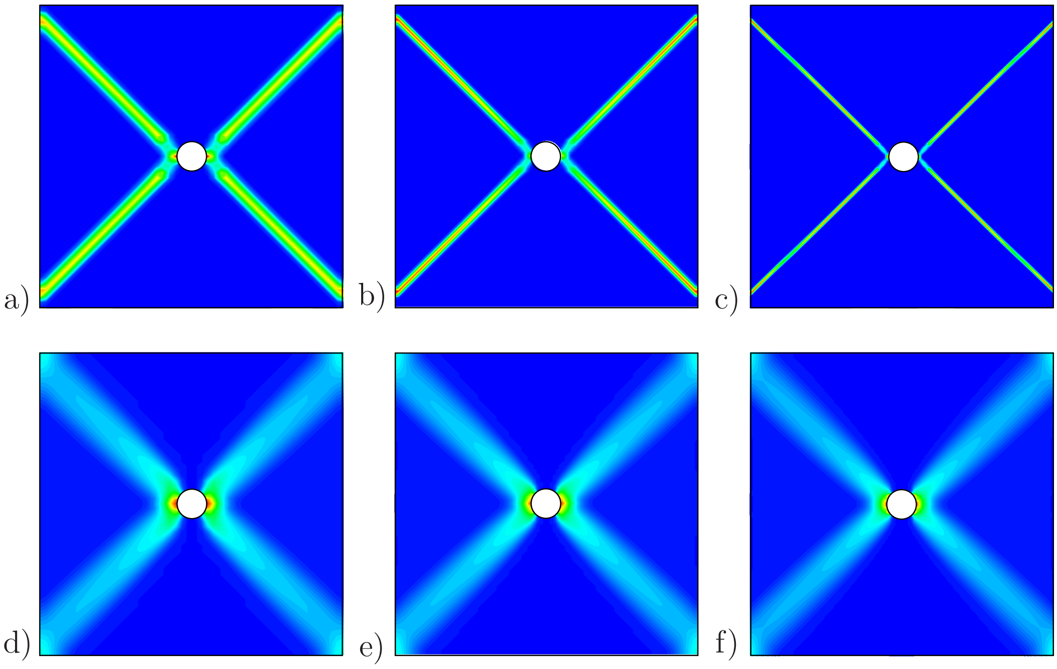

Figure 7.5: Perforated plate under tensile loading. Equivalent plastic strain α for a)–c) an analysis with $l = 0.000$ mm and d)–f) an analysis with $l = 0.004$ mm obtained for discretizations with 622, 2393, and 9556 elements at a deformation stage of $u = 0.025$ mm.

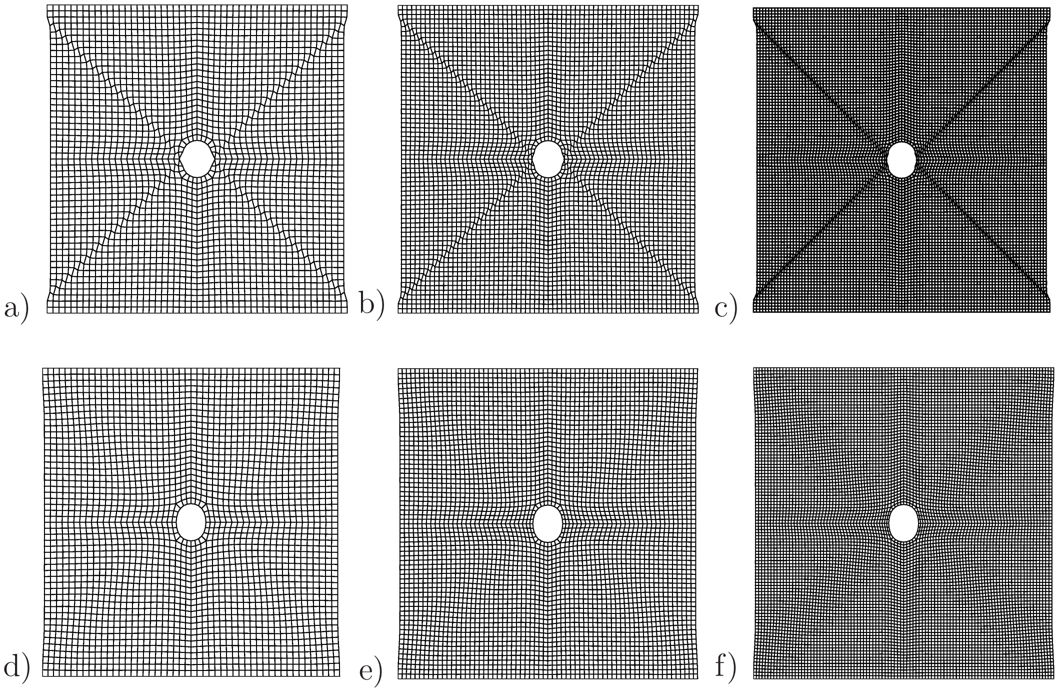

Figure 7.6: Perforated plate under tensile loading. Deformed meshes for a)–c) an analysis with $l = 0.000$ mm and d)–f) an analysis with $l = 0.004$ mm obtained for discretizations with 622, 2393, and 9556 elements at a deformation stage of $u = 0.025$ mm.

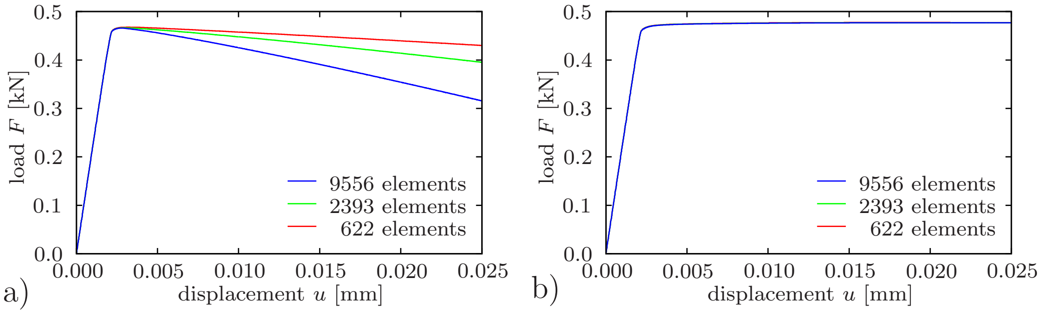

Figure 7.7: Perforated plate under tensile loading. a) Mesh dependent load-deflection curves for a length scale $l = 0.000$ mm and b) objective structural response for $l = 0.004$ mm.

accurately as possible which yields the concentration of the localized zone within one row of elements. In contrast, the nonlocal analysis with a length scale parameter $l = 0.004$ mm, see Figure 7.5d)–f), yields a localized zone which spreads over several elements, independent of the discretization that has been employed. The deformed meshes at the same stage of the analysis are illustrated in Figure 7.6a)–c) for the local solution and in Figure 7.6d)–f) for the nonlocal computations. The structural response of the boundary value problem under focus is illustrated in Figure 7.7. Clearly, the local analysis for $l = 0.000$ mm yields mesh dependent results in the post-critical regime, whereas an analysis with $l = 0.004$ mm yields mesh objective results.

7.2. Additive Finite Plasticity in the Logarithmic Strain Space

In literature, the construction of a kinematic approach to finite inelasticity is still controversially discussed. A wide-spreading access to this broad field of research is given by the overview works by Naghdi [139] and Xiao, Bruhns & Meyers [180]. Roughly speaking, the different kinematic approaches may be subdivided into two classes: i) Following Kröner [94] and Lee [96], a multiplicative decomposition of the deformation gradient $\boldsymbol{F} = \boldsymbol{F}^e \boldsymbol{F}^p$ is introduced, often denoted as *Kröner-Lee decomposition*. This approach is widely used to model micro-mechanically-based crystalline or phenomenological plasticity theories. ii) Starting with Green & Naghdi [57], the key kinematic measure to describe inelastic large deformations bases on the introduction of a Lagrangian plastic deformation measure $\boldsymbol{E}^p$. This so-called *Green-Naghdi theory* has been further developed by Miehe [116, 117]. In these works a strong emphasis is put on the geometric interpretation of the kinematic ingredients and the notion of an *evolving plastic metric* $\boldsymbol{G}^p$ is introduced. Inspired by the Lagrangian plastic metric, an additive kinematic frame is introduced by Miehe, Apel & Lambrecht [121] which is defined in the logarithmic strain space. In the aforementioned reference, a comparison of the additive approach in the logarithmic strain space with the multiplicative approach is performed. Numerical tests confirm a very good agreement.

7.2.1. Strain Measures based on Current Metric and Plastic Metric. In agreement with the multiplicative Kröner-Lee decomposition of the total deformation gradient $\boldsymbol{F} = \boldsymbol{F}^e \boldsymbol{F}^p$ into an elastic and plastic part, an objective strain measure is introduced

$$\widetilde{\boldsymbol{\varepsilon}}^e_m := \boldsymbol{f}_m(\widetilde{\boldsymbol{C}}) \quad \text{with} \quad \widetilde{\boldsymbol{C}} := \boldsymbol{F}^{p-T} \boldsymbol{C} \boldsymbol{F}^{p-1} \tag{7.58}$$

based on the *elastic right Cauchy-Green tensor* $\widetilde{\boldsymbol{C}}$ as a function of the right Cauchy-Green tensor $\boldsymbol{C} := \boldsymbol{F}^T \boldsymbol{g} \boldsymbol{F}$. The elastic strain measure (7.58) can be identified as a mapping

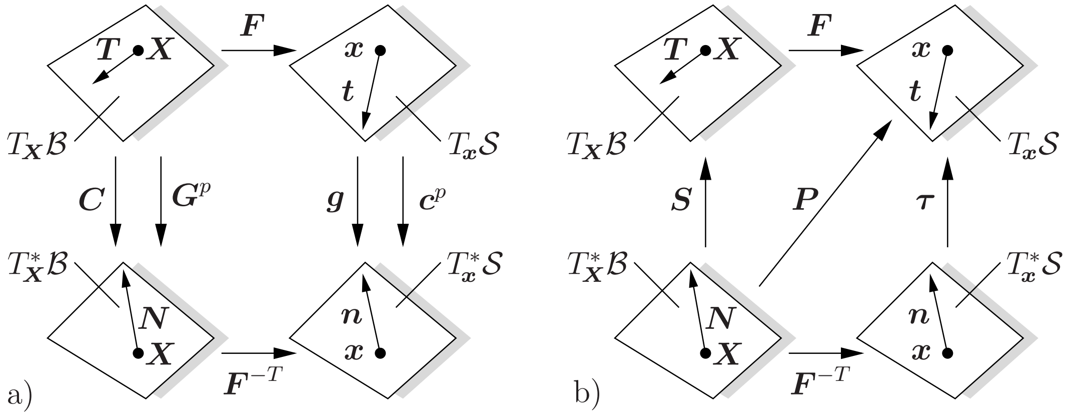
$\boldsymbol{T}$
$\boldsymbol{X}$
$\boldsymbol{F}$
$\boldsymbol{x}$
$\boldsymbol{t}$
$T_{\boldsymbol{X}}\mathcal{B}$
$T_{\boldsymbol{x}}\mathcal{S}$
$\boldsymbol{C}$
$\boldsymbol{G}^p$
$\boldsymbol{g}$
$\boldsymbol{c}^p$
$T^*_{\boldsymbol{X}}\mathcal{B}$
$T^*_{\boldsymbol{x}}\mathcal{S}$
$\boldsymbol{N}$
$\boldsymbol{X}$
$\boldsymbol{n}$
$\boldsymbol{x}$
$\boldsymbol{F}^{-T}$
a)
$\boldsymbol{T}$
$\boldsymbol{X}$
$\boldsymbol{F}$
$\boldsymbol{x}$
$\boldsymbol{t}$
$T_{\boldsymbol{X}}\mathcal{B}$
$T_{\boldsymbol{x}}\mathcal{S}$
$\boldsymbol{S}$
$\boldsymbol{P}$
$\boldsymbol{\tau}$
$T^*_{\boldsymbol{X}}\mathcal{B}$
$T^*_{\boldsymbol{x}}\mathcal{S}$
$\boldsymbol{N}$
$\boldsymbol{X}$
$\boldsymbol{n}$
$\boldsymbol{x}$
$\boldsymbol{F}^{-T}$
b)

Figure 7.8: Mapping properties of metric and stress tensors. a) The *right Cauchy-Green* tensor $\boldsymbol{C} = \boldsymbol{F}^T\boldsymbol{g}\boldsymbol{F}$ as current metric $\boldsymbol{g}$ in the Lagrangian configuration and the *convected plastic metric* $\boldsymbol{c}^p = \boldsymbol{F}^{-T}\boldsymbol{G}^p\boldsymbol{F}^{-T}$ as reference plastic metric $\boldsymbol{G}^p$ in the Eulerian configuration. b) Two-point first Piola-Kirchhoff stress $\boldsymbol{P}$, Eulerian Kirchhoff stress $\boldsymbol{\tau}$, and Lagrangian second Piola-Kirchhoff stress $\boldsymbol{S}$.

between the tangent and co-tangent spaces of an *intermediate configuration* that is characteristic for the multiplicative Kröner-Lee approach to finite inelasticity and enters the constitutive free energy function to model the energy storage mechanism. In this multiplicative setting, the plastic part of the deformation gradient $\boldsymbol{F}^p$ is considered as an internal variable that characterizes the plastic flow in crystalline materials. The isotropic tensor function $\boldsymbol{f}_m$ describes the *Seth-Hill family of generalized strain measures* with

$$\boldsymbol{f}_m(\boldsymbol{A}) = \begin{cases} \frac{1}{m}(\boldsymbol{A}^{m/2} - \boldsymbol{1}) & \text{for} \quad m \neq 0 \\ \frac{1}{2}\ln[\boldsymbol{A}] & \text{for} \quad m = 0 \end{cases} \tag{7.59}$$

for all symmetric tensors $\boldsymbol{A}$, see SETH [158] and HILL [81]. In MIEHE [116, 117] it is intensively discussed that for isotropic and anisotropic materials with preferred structural directors which deform with the material, the plastic map enters the energy storage function only through the plastic metric $\boldsymbol{G}^p := \boldsymbol{F}^{pT}\widetilde{\boldsymbol{G}}\boldsymbol{F}^p$ in terms of the standard metric $\widetilde{\boldsymbol{G}}$ associated with the intermediate configuration. Using the plastic metric $\boldsymbol{G}^p$ a priori as an internal variable, the intermediate configuration becomes insignificant and can be dropped, see Figure 7.8a). The plastic metric $\boldsymbol{G}^p$ is a symmetric, positive definite tensor field which restricts the models a priori to six-dimensional flow rules and develops within the elastic-plastic deformation process starting from the initial condition

$$\boldsymbol{G}^p(t_0) := \boldsymbol{G}\,, \tag{7.60}$$

where $\boldsymbol{G}$ is the time invariant Lagrangian metric. A *Lagrangian elastic strain measure* is introduced that bases on the particular dependency on the right Cauchy-Green tensor and the Lagrangian plastic metric in the additive format

$$\boldsymbol{\varepsilon}^e_m := \boldsymbol{f}_m(\boldsymbol{C}) - \boldsymbol{f}_m(\boldsymbol{G}^p)\,. \tag{7.61}$$

For the Green-Lagrangian strains with $m = 2$ the invariants of (7.58) coincide with those of (7.61) when the latter are computed with respect to the plastic metric, i.e. $\mathrm{tr}[(\widetilde{\boldsymbol{\varepsilon}}^e_2)^\alpha] = \mathrm{tr}[(\boldsymbol{\varepsilon}^e_2\boldsymbol{G}^{p-1})^\alpha]$ for $\alpha = 1, 2, 3$. This makes clear for an isotropic integrity basis that the use of the Lagrangian elastic strain measure (7.61) is in general consistent with the ansatz (7.58) only if the energy storage function depends on $\boldsymbol{\varepsilon}^e_m$ and $\boldsymbol{G}^p$. However, choosing $m = 0$ in (7.58) and (7.61) yields $\widetilde{\boldsymbol{\varepsilon}}^e_0 = \boldsymbol{\varepsilon}^e_0$ for the special case of coaxial total and plastic deformations where $\boldsymbol{C}$ and $\boldsymbol{G}^p$ commute and the plastic map is identified by $\boldsymbol{F}^p = \boldsymbol{G}^{p1/2}$. In this sense, the logarithmic strain measure

$$\boldsymbol{\varepsilon}^e := \tfrac{1}{2}\ln[\boldsymbol{C}] - \boldsymbol{\varepsilon}^p \tag{7.62}$$

brings the additive ansatz (7.61) at least close to the multiplicative ansatz (7.58). Here, the logarithmic plastic strain $\boldsymbol{\varepsilon}^p := \frac{1}{2}\ln[\boldsymbol{G}^p]$ may be considered as the internal variable that enters the formulation.

7.2.2. Geometric Pre-Processing of the Logarithmic Strain Space. A key point in the setting up of a framework for finite plasticity is the definition of an elastic strain measure $\boldsymbol{\varepsilon}^e$. This variable enters the constitutive function that describes the macroscopic energy storage. This strain measure is assumed to be a function of the above introduced Lagrangian current and plastic metric tensors, i.e.

$$\boldsymbol{\varepsilon}^e(\boldsymbol{C}, \boldsymbol{G}^p) := \tfrac{1}{2}\ln[\boldsymbol{C}] - \boldsymbol{\varepsilon}^p\,. \tag{7.63}$$

As sketched briefly above, there exist several conceptual possibilities for the definition of the elastic strain measure. In the remaining part of this chapter, the focus is put on the elementary additive form

$$\boldsymbol{\varepsilon}^e := \boldsymbol{\varepsilon} - \boldsymbol{\varepsilon}^p\,, \tag{7.64}$$

according to (7.62) in terms of the logarithmic Lagrangian total and plastic strains

$$\boxed{\boldsymbol{\varepsilon} := \tfrac{1}{2}\ln[\boldsymbol{C}] \quad \text{and} \quad \boldsymbol{\varepsilon}^p := \tfrac{1}{2}\ln[\boldsymbol{G}^p]\,,} \tag{7.65}$$

respectively. The logarithmic tensor function maps the multiplicative characteristics of large strain elasto-plasticity to the additive structure of the geometrically linear theory. In particular, observe the relationship for the plastic Jacobian

$$J^p := \sqrt{\det[\boldsymbol{G}^p]} = \exp[\operatorname{tr}[\boldsymbol{\varepsilon}^p]] \tag{7.66}$$

that governs the change of volume due to the plastic part of the deformation. In the context of metal plasticity, the plastic incompressibility is one main characteristic, which is in the underlying context described by

$$\det[\boldsymbol{G}^p] = 1 \quad \Leftrightarrow \quad \operatorname{tr}[\boldsymbol{\varepsilon}^p] = 0\,. \tag{7.67}$$

The *multiplicative* constraint on the determinant of the plastic metric $\boldsymbol{G}^p$ in context with an isochoric plastic flow is described by the *additive* constraint on the trace of the logarithmic plastic strain $\boldsymbol{\varepsilon}^p$. Due to the one-to-one relationship $(7.65)_2$ between $\boldsymbol{G}^p$ and $\boldsymbol{\varepsilon}^p$, the logarithmic plastic strain measure $\boldsymbol{\varepsilon}^p$ is chosen as an internal variable alternative to $\boldsymbol{G}^p$. In what follows $\boldsymbol{\varepsilon}^p$ is considered as a variable that lives exclusively in a constitutive box associated with the logarithmic strain space defined below. Of key importance for the subsequent treatment is the sensitivity of the strain measure $(7.65)_1$ with respect to a change of the deformation

$$\dot{\boldsymbol{\varepsilon}} := \mathbb{P}_L : \dot{\boldsymbol{C}} \quad \text{with} \quad \mathbb{P}_L := \partial_{\boldsymbol{C}}\boldsymbol{\varepsilon} \tag{7.68}$$

and the sensitivity of the projection tensor $\mathbb{P}_L$ with respect to a change of the deformation

$$\dot{\mathbb{P}}_L := \mathbb{L}_L : \dot{\boldsymbol{C}} \quad \text{with} \quad \mathbb{L}_L := \partial^2_{\boldsymbol{CC}} \boldsymbol{\varepsilon} \,. \tag{7.69}$$

Insertion of the inverse form of $(7.68)_1$ into the stress power with respect to the unit volume of the reference configuration of the material (2.74) yields the identification

$$\mathcal{P} = \boldsymbol{S} : \tfrac{1}{2}\dot{\boldsymbol{C}} = \boldsymbol{S} : (\, \tfrac{1}{2}\, \mathbb{P}_L^{-1} : \dot{\boldsymbol{\varepsilon}}) =: \boldsymbol{\sigma} : \dot{\boldsymbol{\varepsilon}} \quad \text{with} \quad \boldsymbol{\sigma} := \tfrac{1}{2}\, \boldsymbol{S} : \mathbb{P}_L^{-1} \,. \tag{7.70}$$

It identifies the Lagrangian stress tensor $\boldsymbol{\sigma}$ as a work-conjugate quantity to the logarithmic strain measure $\boldsymbol{\varepsilon}$. The symmetric Lagrangian tensors $\boldsymbol{\sigma}$ and $\boldsymbol{\varepsilon}$ provide a convenient pair of dual variables of the local material element associated with the logarithmic strain space.

7.2.3. Constitutive Model in the Logarithmic Strain Space. Now assume a constitutive model of plasticity that is exclusively restricted to the logarithmic strain space. This model is considered as a constitutive box, its input is given by the logarithmic strain measure $\boldsymbol{\varepsilon}$ and a set of internal variables $\boldsymbol{\mathcal{I}} := \{\, \boldsymbol{\varepsilon}^p, \dots \}$ consisting of the logarithmic plastic strain tensor $\boldsymbol{\varepsilon}^p$ and some additional hardening variables. The output of the box is the current stress $\boldsymbol{\sigma}$ dual to the logarithmic strain and the corresponding elastic-plastic tangent moduli $\mathbb{E}^{ep}$

$$\boxed{\{\, \boldsymbol{\varepsilon}, \boldsymbol{\mathcal{I}} \,\} \quad \Rightarrow \quad MODEL \quad \Rightarrow \quad \{\, \boldsymbol{\sigma}, \mathbb{E}^{ep} \,\} \,.} \tag{7.71}$$

In the continuous setting, the tangent moduli exist for rate-independent theories of plasticity and govern the rate of the stress with respect to the rate of the logarithmic strain

$$\dot{\boldsymbol{\sigma}} = \mathbb{E}^{ep} : \dot{\boldsymbol{\varepsilon}} \,. \tag{7.72}$$

The attractive feature of the constitutive model is that it preserves the structure of plasticity models of the geometrically linear theory. Thus, the model may adopt standard constitutive structures of the small strain theory.

7.2.4. Geometric Post-Processing of Lagrangian Objects. Once the stresses and tangent moduli in the logarithmic strain space have been obtained from the constitutive box (7.71) they are mapped to the initial Lagrangian space by a straightforward application of the transformation rules for Lagrangian objects introduced in Section 7.2.2. According to (7.68) and (7.69), the stresses and moduli are mapped onto the Lagrangian second Piola-Kirchhoff stress tensor and corresponding moduli via

$$\boxed{\boldsymbol{S} = 2\, \boldsymbol{\sigma} : \mathbb{P}_L \quad \text{and} \quad \mathbb{C}_L^{ep} = 4\, \mathbb{P}_L^T : \mathbb{E}^{ep} : \mathbb{P}_L + 4\, \boldsymbol{\sigma} : \mathbb{L}_L \,.} \tag{7.73}$$

In this expression, the fourth-order Lagrangian elastic-plastic tangent moduli $\mathbb{C}_L^{ep}$ govern the sensitivity of the symmetric second Piola-Kirchhoff stresses

$$\dot{\boldsymbol{S}} = \mathbb{C}_L^{ep} : \tfrac{1}{2}\dot{\boldsymbol{C}} \tag{7.74}$$

with respect to the Lagrangian rate $\tfrac{1}{2}\dot{\boldsymbol{C}}$ of deformation. The transformation tensors $\mathbb{P}_L$ and $\mathbb{L}_L$ in (7.73) play a crucial role for the underlying treatment, closed-form algorithmic approaches to these kind of tensors have been outlined in Miehe & Lambrecht [125] in a more general context for the class of Seth-Hill strain measures.

7.3. Gradient-Type von Mises Plasticity at Large Deformations

The underlying model problem addresses a phenomenological model of gradient plasticity at large strains that extends in an elementary format the established von Mises theory. One main ingredient of the proposed model is the kinematic framework for additive finite elasto-plasticity, recently published by Miehe, Apel & Lambrecht [121]. This framework exploits ideas of the so-called *additive metric plasticity* which exhibits a structure very similar to the geometrically linear plasticity theory. The large strain implementation is based on a modular kinematic setting, consisting in its core of a constitutive model which is formulated in the *logarithmic strain space*. In this setting, the elastic part $\boldsymbol{E}^e$ of the Lagrangian Hencky strain $\boldsymbol{E} := \ln[\boldsymbol{C}]/2$ is defined as $\boldsymbol{E}^e := \boldsymbol{E} - \ln[\boldsymbol{G}^p]/2 = \boldsymbol{E} - \boldsymbol{E}^p$ with the right Cauchy-Green tensor $\boldsymbol{C}$. Following Miehe [116, 117], the reference plastic metric $\boldsymbol{G}^p$ is directly considered as internal variable. The constitutive core in the logarithmic strain space is then framed by purely geometric pre- and post-processing steps. In the following treatment, a focus is put on the kinematic embedding of the previously discussed model of gradient-type plasticity at small deformations into the theory of generalized continua at large deformations. Details of the numerical implementation are elucidated and finally a representative set of numerical examples is presented.

7.3.1. Basic Kinematics and State Variables. The central kinematics for the description of a model problem of von Mises plasticity with gradient-type hardening within the context of generalized continua is summarized by the set of independent state variables

$$\bar{\boldsymbol{\varphi}} := \{\boldsymbol{u}\} \quad \text{and} \quad \check{\boldsymbol{\varphi}} := \{\alpha\} \quad \text{and} \quad \boldsymbol{\mathcal{I}} := \{\boldsymbol{G}^P\}\,. \tag{7.75}$$

Here, the macro-motion is described by the displacement field $\boldsymbol{u} := \boldsymbol{x} - \boldsymbol{X}$ as a function of the nonlinear deformation map $\boldsymbol{\varphi} = \boldsymbol{x}$, the micro-motion is identified as the global hardening field α, and the plastic metric $\boldsymbol{G}^p$, characterizing the inelastic deformation process, is treated as local history field. For an intense discussion of formulations of finite inelasticity that base on the notion of a plastic metric, the reader is referred to Miehe [116]. Aiming at a Lagrangian approach to the modeling of the inelastic material response, a symmetric and positive definite tensor is introduced as the pull-back of the constant Eulerian standard metric $\boldsymbol{g}$ to the Lagrangian manifold

$$\boldsymbol{C} = \boldsymbol{F}^T \boldsymbol{g} \boldsymbol{F}\,, \tag{7.76}$$

often denoted as right Cauchy-Green tensor. In the purely Lagrangian setting, the constitutive state for the model problem under focus can be summarized by

$$\mathfrak{c}_L := \{\, \boldsymbol{\varepsilon}(\boldsymbol{C}), \alpha, \nabla_{\boldsymbol{X}} \alpha, \boldsymbol{\varepsilon}^p(\boldsymbol{G}^p)\,\}\,, \tag{7.77}$$

and builds the kinematic framework for setting up the objective constitutive equations.

7.3.2. Incremental Variational Principle. This section is concerned with a straightforward extension of the *rate-dependent* variational formulation of model II discussed in Section 7.1.5.2 to the large strain setting. Here, the extended constitutive state reads

$$\mathfrak{c}_L^* := \{\, \boldsymbol{\varepsilon}(\boldsymbol{C}), \alpha, \nabla_{\boldsymbol{X}} \alpha, \beta\,\} \quad \text{and} \quad \mathfrak{p} := \{\, \boldsymbol{\varepsilon}^p(\boldsymbol{G}^p), \boldsymbol{B}\,\}\,, \tag{7.78}$$

where the thermodynamic dissipative driving forces dual to the global Lagrangian hardening field α and the dissipative driving force dual to the local logarithmic Lagrangian plastic strain $\boldsymbol{\varepsilon}^p$ are introduced

$$\check{\boldsymbol{f}} := \{\, \beta\,\} \quad \text{and} \quad \boldsymbol{\mathcal{F}} := \{\, \boldsymbol{B}\,\}\,. \tag{7.79}$$

For the sake of simplicity, throughout Chapter 3 only the macroscopic two-point formulation has been introduced. However, a modification of the large strain incremental variational principle (3.133) to the macroscopic Lagrangian setting can easily be obtained, a summary is given in Appendix A. It bases on the *incremental internal work density*

$$\begin{aligned}\pi^{*\tau}(\mathfrak{c}^*_L, \mathfrak{p}; \mathfrak{c}^*_{Ln}, \mathfrak{p}_n) = {} & \tfrac{1}{2}\,\kappa\, \operatorname{tr}^2[\boldsymbol{\varepsilon}] + \mu \,\|\operatorname{dev}[\boldsymbol{\varepsilon}^e(\boldsymbol{\varepsilon}, \boldsymbol{\varepsilon}^p)]\|^2 \\ & + \tfrac{1}{2}\, h\alpha^2 + \tfrac{1}{2}\,\mu L^2 \,\|\nabla_{\boldsymbol{X}}\alpha\|^2 - \psi(\mathfrak{c}_{Ln}) \\ & + \beta\,(\alpha - \alpha_n) + \boldsymbol{B} : (\boldsymbol{\varepsilon}^p - \boldsymbol{\varepsilon}^p_n) \\ & - \frac{\tau}{2\eta}\langle\, \|\operatorname{dev}[\boldsymbol{B}]\| - \sqrt{2/3}\,(y_0 - \beta)\,\rangle^2_+ \,.\end{aligned} \tag{7.80}$$

Roughly speaking, this representation contains the small strain internal work density, where the input $\boldsymbol{\varepsilon}(\boldsymbol{C})$ and $\boldsymbol{\varepsilon}^p(\boldsymbol{G}^p)$ has been converted to the logarithmic strain space. Furthermore, a Lagrangian nonlocality with the length scale parameter L is introduced that describes a constant amount of material points inside the nonlocal domain of influence independent of the deformation. Application of the incremental variational principle (A.8) for the macroscopic Lagrangian problem and taking into account the local dependency on $\mathfrak{p}$ in the sense of (3.133) provides the algorithmic Euler equations

$$\begin{aligned}\boldsymbol{0} &= \operatorname{DIV}[\, 2\boldsymbol{gF}(\kappa\, \operatorname{tr}[\boldsymbol{\varepsilon}]\boldsymbol{1} + 2\mu\, \operatorname{dev}[\boldsymbol{\varepsilon} - \boldsymbol{\varepsilon}^p]) : \mathbb{P}_L \,] \\ 0 &= \mu L^2\, \Delta_{\boldsymbol{X}}\alpha - [\, h\alpha + \beta\,] \\ 0 &= \alpha - \alpha_n - \frac{\tau}{\eta}\langle\, \|\operatorname{dev}[\boldsymbol{B}]\| - \sqrt{2/3}\,(y_0 - \beta)\,\rangle_+ \sqrt{2/3} \\ \boldsymbol{0} &= 2\mu\, \operatorname{dev}[\boldsymbol{\varepsilon} - \boldsymbol{\varepsilon}^p] - \boldsymbol{B} \\ \boldsymbol{0} &= \boldsymbol{\varepsilon}^p - \boldsymbol{\varepsilon}^p_n - \frac{\tau}{\eta}\langle\, \|\operatorname{dev}[\boldsymbol{B}]\| - \sqrt{2/3}\,(y_0 - \beta)\,\rangle_+ \boldsymbol{n}\,.\end{aligned} \tag{7.81}$$

Note that in this representation the latter two equations describe the evolution subproblem of the local history variables that exist exclusively in the *logarithmic strain space*. In contrast, the stresses $\boldsymbol{\sigma} = \kappa\, \operatorname{tr}[\boldsymbol{\varepsilon}]\boldsymbol{1} + 2\mu\, \operatorname{dev}[\boldsymbol{\varepsilon} - \boldsymbol{\varepsilon}^p]$ that are dual to the logarithmic total strain $\boldsymbol{\varepsilon}$ are brought to the initial Lagrangian setting via the projection tensor $\mathbb{P}_L$. For a definition of this projection tensor as a result of a chain-rule operation, see equation $(7.68)_2$. Combination of $(7.81)_{2,3}$ yields the evolution of the equivalent plastic strain

$$\alpha = \alpha_n + \frac{\tau}{\eta}\langle\, \|\operatorname{dev}[\boldsymbol{B}]\| - \sqrt{2/3}\,(y_0 + h\alpha - \mu L^2 \Delta_{\boldsymbol{X}}\alpha)\,\rangle_+ \sqrt{2/3} \tag{7.82}$$

and shows again the dependency of the yield resistance on the Laplacian term $\mu L^2 \Delta_{\boldsymbol{X}}\alpha$. The smooth character of the governing equations makes this time-regularized setting with threshold function highly attractive for a numerical implementation.

7.3.3. Finite Element Discretization of Incremental Variational Principle. The general finite element treatment of the variational principle for gradient-type solids in a macroscopic Lagrangian setting has been discussed in full length in Appendix A.2. It is now specified for the model problem of gradient-type plasticity. Restricting to two-dimensional problems, the generalized displacements and constitutive state are given by

$$\mathfrak{u}^* := \{\, u_1, u_2, \alpha, \beta \,\} \quad \text{with} \quad \mathfrak{c}^*_L(\mathfrak{u}^*) := \{\, C_{11}, C_{22}, C_{12}, \alpha, \alpha_{,1}, \alpha_{,2}, \beta \,\}\,. \tag{7.83}$$

According to (A.12), the generalized primary variables are approximated via

$$\boldsymbol{\mathfrak{u}}^{*h} =: \boldsymbol{\mathfrak{N}}^*(\boldsymbol{X})\,\boldsymbol{\mathfrak{d}}^* \quad \text{with} \quad [\boldsymbol{\mathfrak{N}}^*]_i^e = \begin{bmatrix} N & 0 & 0 & 0 \\ 0 & N & 0 & 0 \\ 0 & 0 & N & 0 \\ 0 & 0 & 0 & M \end{bmatrix}_i \quad \text{and} \quad \boldsymbol{\mathfrak{d}}_i^* := [\,d_1, d_2, a, b\,]_i^T \,. \tag{7.84}$$

For simplicity, identical interpolations are chosen for the macro- and microscopic problem $N_i = M_i$. In this scenario, the generalized nodal unknowns $\boldsymbol{\mathfrak{d}}^*$ consist of the nodal displacements in 1- and 2-direction d_1 and d_2, the nodal hardening variable a, and the nodal thermodynamic force b dual to the hardening field. In agreement with (A.16), the variation of the discrete extended constitutive state with respect to the generalized nodal unknowns needed for the coupled residual (A.17) is defined by

$$\delta_{\boldsymbol{\mathfrak{d}}^*}\boldsymbol{\mathfrak{c}}_L^{*h} =: \boldsymbol{\mathfrak{B}}_M^*(\boldsymbol{X})\,\delta\boldsymbol{\mathfrak{d}}^* \tag{7.85}$$

in terms of the approximation matrix

$$[\boldsymbol{\mathfrak{B}}_M^*]_i^e = \begin{bmatrix} 2F_{11}^{he}N_{,1} & 2F_{12}^{he}N_{,2} & 2(F_{11}^{he}N_{,2}+F_{12}^{he}N_{,1}) & 0 & 0 & 0 & 0 \\ 2F_{21}^{he}N_{,1} & 2F_{22}^{he}N_{,2} & 2(F_{21}^{he}N_{,2}+F_{22}^{he}N_{,1}) & 0 & 0 & 0 & 0 \\ 0 & 0 & 0 & N & N_{,1} & N_{,2} & 0 \\ 0 & 0 & 0 & 0 & 0 & 0 & M \end{bmatrix}_i^T \,. \tag{7.86}$$

The symmetric monolithic tangent matrix of the global finite element solution algorithm (A.19) contains a geometric contribution characterized by the geometric element matrix and the macroscopic stresses in matrix notation. They are specified to

$$[\boldsymbol{\mathfrak{B}}_G^*]_i^e = \begin{bmatrix} N_{,1} & 0 & N_{,2} & 0 \\ 0 & N_{,2} & 0 & N_{,1} \\ 0 & 0 & 0 & 0 \\ 0 & 0 & 0 & 0 \end{bmatrix}_i^T \quad \text{and} \quad \bar{\mathbb{S}}_L^* = 2\begin{bmatrix} \partial_{C_{11}}\pi_\eta^{*\tau} & 0 & \partial_{C_{12}}\pi_\eta^{*\tau} & 0 \\ 0 & \partial_{C_{22}}\pi_\eta^{*\tau} & 0 & \partial_{C_{12}}\pi_\eta^{*\tau} \\ \partial_{C_{12}}\pi_\eta^{*\tau} & 0 & \partial_{C_{22}}\pi_\eta^{*\tau} & 0 \\ 0 & \partial_{C_{12}}\pi_\eta^{*\tau} & 0 & \partial_{C_{11}}\pi_\eta^{*\tau} \end{bmatrix} \,. \tag{7.87}$$

Observe that in $(7.87)_1$ only the macroscopic slots are affected by the additional contribution. The hardening and the driving force field are not influenced. For the underlying model problem of gradient-type J_2-plasticity the components of the generalized stresses and the non-zero components of the generalized moduli

$$\boldsymbol{S}_L^* := \begin{bmatrix} \partial_{\boldsymbol{C}}\pi_\eta^{*\tau} \\ \partial_\alpha\pi_\eta^{*\tau} \\ \partial_{\nabla\alpha}\pi_\eta^{*\tau} \\ \partial_\beta\pi_\eta^{*\tau} \end{bmatrix} \quad \text{and} \quad \mathbb{C}_L^* := \begin{bmatrix} \partial^2_{\boldsymbol{C}\boldsymbol{C}}\pi_\eta^{*\tau} & \boldsymbol{0} & \boldsymbol{0} & \partial^2_{\boldsymbol{C}\beta}\pi_\eta^{*\tau} \\ \boldsymbol{0} & \partial^2_{\alpha\alpha}\pi_\eta^{*\tau} & \boldsymbol{0} & 1 \\ \boldsymbol{0} & \boldsymbol{0} & \partial^2_{\nabla\alpha\nabla\alpha}\pi_\eta^{*\tau} & \boldsymbol{0} \\ \partial^2_{\beta\boldsymbol{C}}\pi_\eta^{*\tau} & 1 & \boldsymbol{0} & \partial^2_{\beta\beta}\pi_\eta^{*\tau} \end{bmatrix} \tag{7.88}$$

have to be specified. Taking into account the formulation of the macroscopic subproblem in the logarithmic strain space, the macroscopic components of the stresses and moduli

$$\partial_{\boldsymbol{C}}\pi_\eta^{*\tau} = \partial_{\boldsymbol{\varepsilon}}\pi_\eta^{*\tau} : \mathbb{P}_L \quad \text{and} \quad \partial^2_{\boldsymbol{C}\boldsymbol{C}}\pi_\eta^{*\tau} = \mathbb{P}_L^T : \partial^2_{\boldsymbol{\varepsilon}\boldsymbol{\varepsilon}}\pi_\eta^{*\tau} : \mathbb{P}_L + \partial_{\boldsymbol{\varepsilon}}\pi_\eta^{*\tau} : \mathbb{L}_L \tag{7.89}$$

and the coupling off-diagonal terms in the generalized moduli

$$\partial^2_{\beta\boldsymbol{C}}\pi_\eta^{*\tau} = \partial^2_{\beta\boldsymbol{\varepsilon}}\pi_\eta^{*\tau} : \mathbb{P}_L \quad \text{with} \quad \partial^2_{\boldsymbol{C}\beta}\pi_\eta^{*\tau} = [\partial^2_{\beta\boldsymbol{C}}\pi_\eta^{*\tau}]^T \tag{7.90}$$

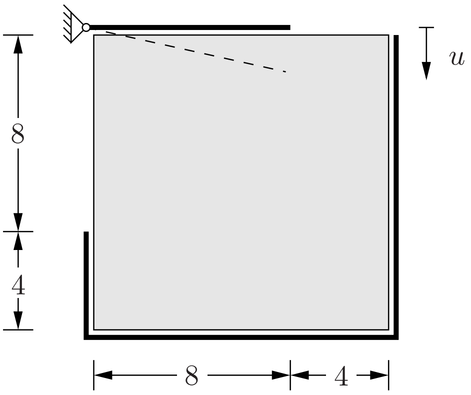

Figure 7.9: Rotation of Rigid Plate. Geometry and boundary conditions. The rigid plate is rotated around its hinged support at the upper left corner.

have to be treated according to the transformation rules $(7.68)_2$ and $(7.69)_2$. The single components of the stresses and moduli are identical to those of the small strain setting, for a definition see equations (7.53)–(7.55). In order to describe more complex localization phenomena, the proposed multi-field finite element formulation has to be enhanced by an incompatible mode formulation. A detailed discussion of an enhanced assumed strain formulation with multi-field character in a macroscopic Lagrangian setting can be found in Appendix B.2, see also Widmer [178].

7.3.4. Numerical Examples. Regularization of Shear Bands. This section demonstrates the performance of the proposed variational framework for gradient-type standard dissipative solids by means of several numerical tests. Different simulations are investigated that document the gradient-type regularization of shear bands. The first test is concerned with the *rotation of a rigid plate* in an elasto-plastic matrix yielding a curved shear band. A second test discusses Prandtl's indentation test, where a more complicated shear band pattern occurs. Both tests approve the mesh-objectivity of the gradient-extended model that incorporates an intrinsic length scale.

7.3.4.1. Rotation of Rigid Plate. The first numerical test is concerned with a squared elasto-plastic specimen as illustrated in Figure 7.9. The horizontal and vertical displacements along the right edge, the lower edge, and the lower third of the left edge are con-

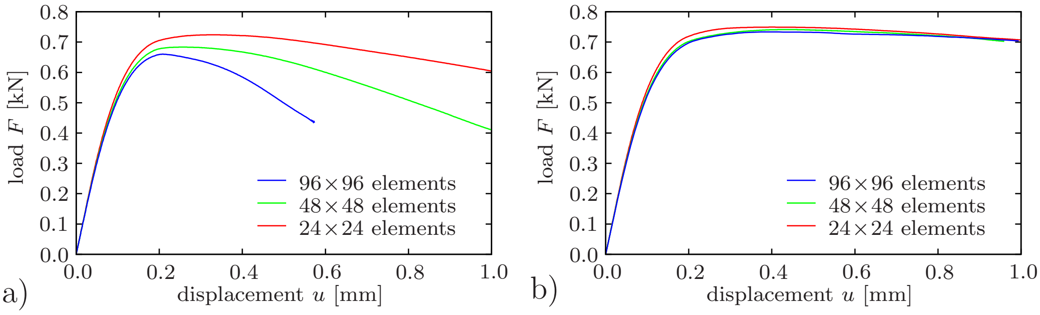

Figure 7.10: Rotation of Rigid Plate. Load-deflection curves for a) mesh-dependent, local analysis with $L = 0.00$ mm and b) mesh-objective, nonlocal analysis with $L = 0.04$ mm for computations with 24×24, 48×48, and 96×96 bulk elements.

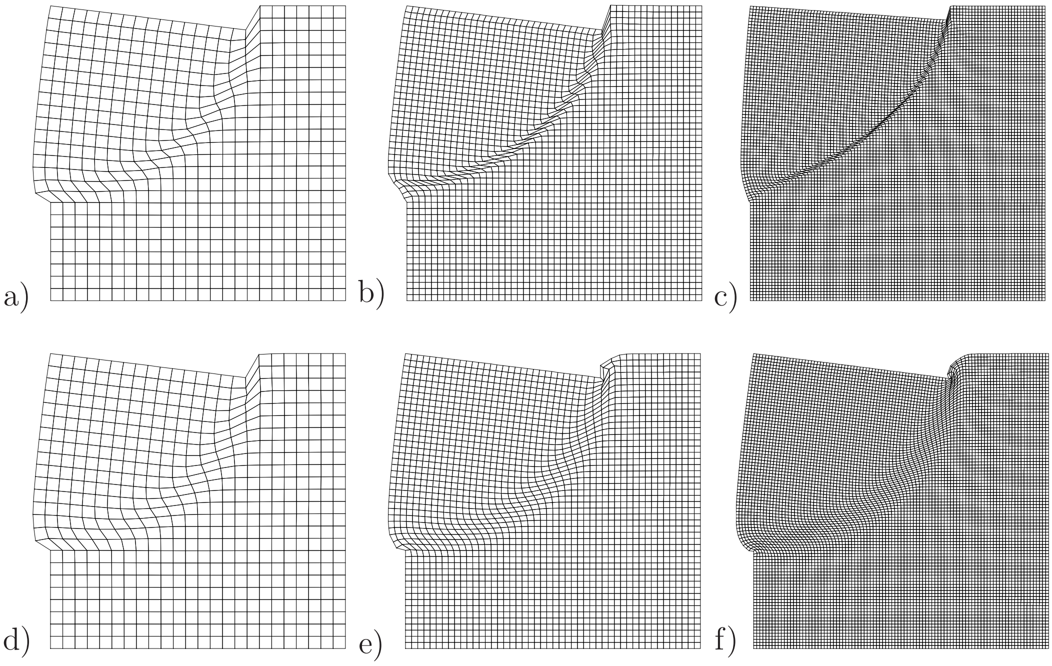

Figure 7.11: Rotation of Rigid Plate. Deformed meshes at a)–c) the corresponding final deformations of the local analysis $L = 0.00$ mm and d)–f) the deformation $u = 1.0$ mm of the nonlocal analysis $L = 0.04$ mm obtained for computations with 24×24, 48×48, and 96×96 elements.

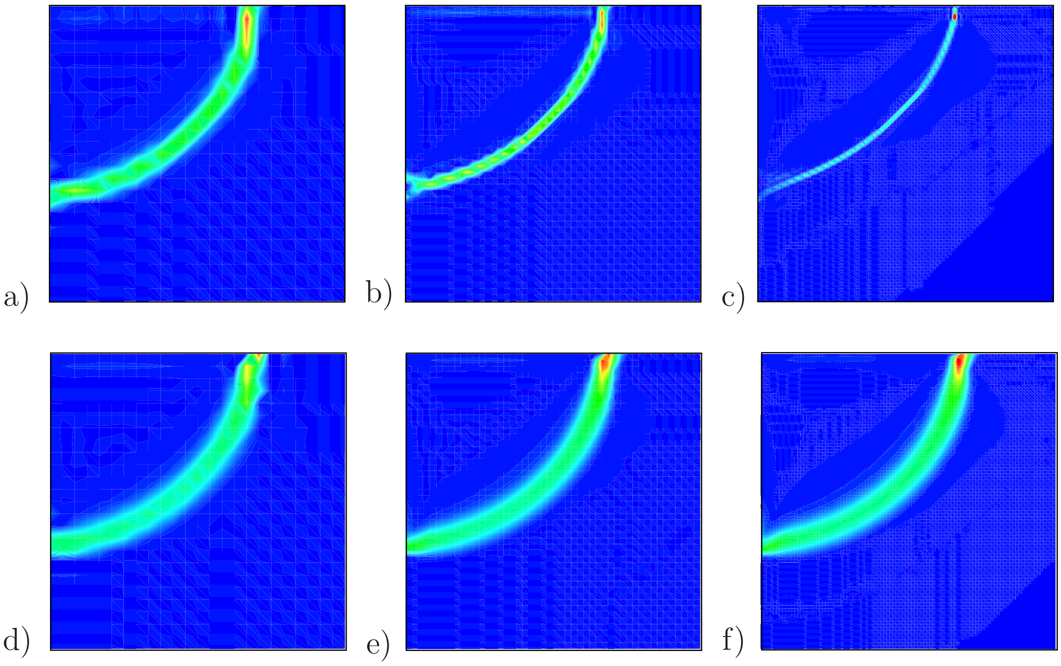

Figure 7.12: Rotation of Rigid Plate. Equivalent plastic strain α for a)–c) a local analysis with $L = 0.00$ mm and d)–f) a nonlocal analysis with $L = 0.04$ mm obtained for computations with 24×24, 48×48, and 96×96 elements.

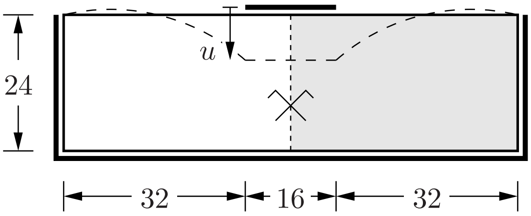

Figure 7.13: Prandtl's indentation test. Geometry and boundary conditions. Due to the symmetry of the boundary value problem, only one half of the geometry is discretized.

strained. The rigid plate is hinged at the upper left support and indents the solid material in a rotational movement. The boundary value problem is discretized using 24×24, 48×48, and 96×96 multi-field $Q1E4$-elements, for a detailed discussion of an enhanced strain formulation at large deformations see Appendix B.2. For the numerical simulation, the bulk modulus of the material is chosen to $\kappa = 16.67$ kN/mm^2, the shear modulus to $\mu = 3.57$ kN/mm^2, the isotropic hardening (or softening) modulus to $h = -0.10$ kN/mm^2, and the yield limit to $y_0 = 0.10$ kN/mm^2. The viscosity is chosen to $\eta = 1{\times}10^{-5}$ kN s/mm^2 which guarantees a solution very close to the rate-independent limit. The structural response for the local analysis with $L = 0.00$ mm is given in Figure 7.10a), which documents the obvious mesh dependence of the simulation. Figure 7.10b) shows the mesh-objective load deflection curves for the nonlocal simulations with $L = 0.04$ mm. The deformed meshes, and the corresponding contour plots of the hardening field α for the local and nonlocal computations are illustrated in Figure 7.11 and Figure 7.12, respectively.

7.3.4.2. Prandtl's Indentation Test. A further numerical test is concerned with an indentation problem of a rigid indenter into an elasto-plastic medium. Initially, this problem has been discussed analytically by Prandtl [151], using the so-called *theory of gliding lines*. The geometric setup and the according boundary conditions are illustrated in Figure 7.13. Here the displacements along the vertical edges are restrained in horizontal and free in vertical direction. The lower edge is restrained in vertical and horizontal direction. Due to the symmetry of the boundary value problem, only one half of the geometry is discretized, using 60×36, 80×48, and 100×60 multi-field $Q1E4$-elements. For a detailed discussion of an enhanced strain formulation at large deformations, the reader is referred to Appendix B.2. The computation is performed in a displacement driven context, for both the local and the nonlocal analysis. Throughout the computation, the bulk modulus of the material is chosen to $\kappa = 160.00$ kN/mm^2, the shear modulus to $\mu = 80.00$ kN/mm^2, the isotropic hardening (or softening) modulus to $h = -0.16$ kN/mm^2, and the yield limit to $y_0 = 0.50$ kN/mm^2. Aiming at solutions that are very close to the rate-independent limit, the viscosity is chosen to $\eta = 1 \times 10^{-5}$ kN s/mm^2. The resulting deformed meshes for the local and nonlocal computations obtained for the different discretizations are illustrated in Figure 7.14a)–c) and Figure 7.14d)–f), respectively. The distribution of the equivalent plastic strain is given in Figure 7.15a)–c) and Figure 7.15d)–f) for the local and nonlocal analysis. The according structural responses of the computations can be found in Figure 7.16. Clearly, the local simulations with $L = 0.00$ mm yield mesh-dependent results, see Figure 7.16a), and the nonlocal computations with $L = 0.06$ mm yield mesh-objective results, see Figure 7.16b).

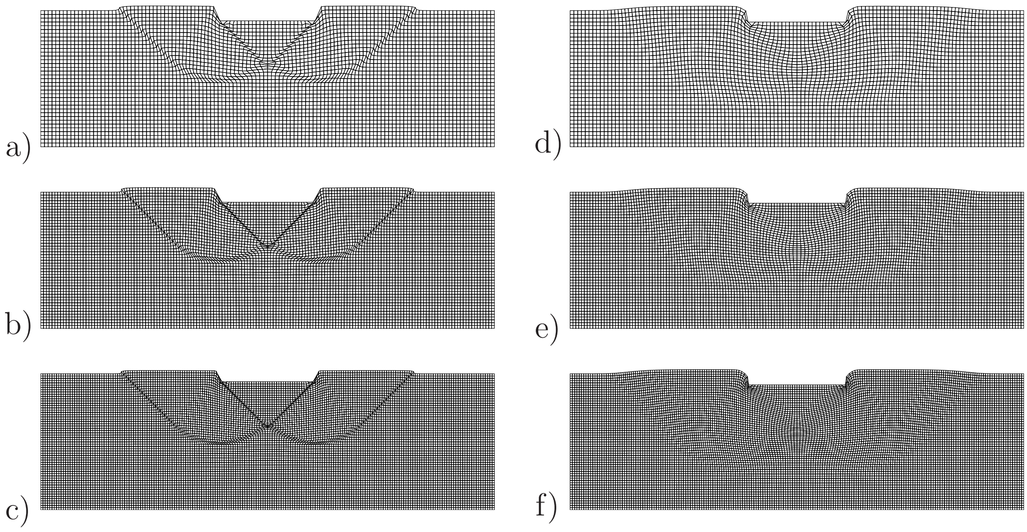

Figure 7.14: Prandtl's indentation test. Deformed meshes at a)–c) the corresponding final deformations of the local analysis $L = 0.00$ mm and d)–f) the deformation $u = 1.8$ mm of the nonlocal analysis $L = 0.06$ mm obtained for 60×36, 80×48, and 100×60 elements.

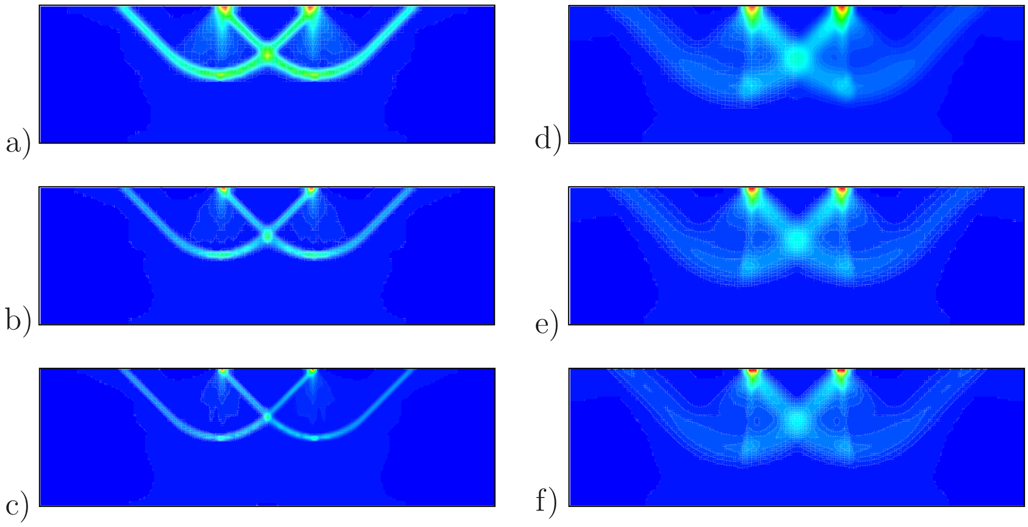

Figure 7.15: Prandtl's indentation test. Equivalent plastic strain α at a)–c) the corresponding final deformations of the local analysis $L = 0.00$ mm and d)–f) the deformation $u = 1.8$ mm of the nonlocal analysis $L = 0.06$ mm obtained for 60×36, 80×48, and 100×60 elements.

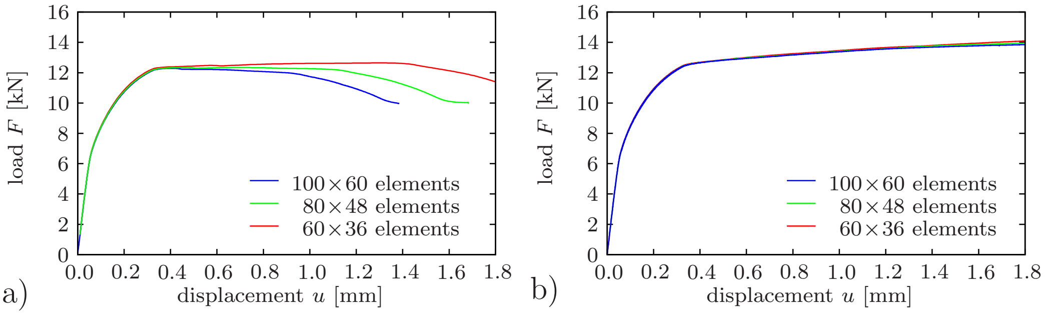

Figure 7.16: Prandtl's indentation test. Load-deflection curves for a) mesh-dependent, local analysis with $L = 0.00$ mm and b) mesh-objective, nonlocal analysis with $L = 0.06$ mm for computations with 60 × 36, 80 × 48, and 100 × 60 elements.

7.3.5. Numerical Examples. Hall-Petch Effect. The application of the proposed model for gradient-type J_2-plasticity is not restricted to the regularization of shear bands only, it can also be employed to model the so-called Hall-Petch effect. In Hall [75] and Petch [150] the authors observed that the yield strength of a polycrystalline metallic specimen scales linearly with the inverse square root of the grain size. This grain size can be considered as an intrinsic length scale parameter that takes into account the increasing yield strength with decreasing specimen size. In the underlying model of gradient-type J_2-plasticity, the micro-mechanics of plastic deformations is not investigated, a relation between the length scale parameter L and the grain size is not provided. However, instead of modifying the specimen's dimension, an increasing length scale parameter L yields a stiffer response. This behavior is documented in the following numerical test that is concerned with a *shear-test of a composite material*.

7.3.5.1. Shear-Test of Composite Material. In the subsequent numerical test, shearing of a two-dimensional specimen made up of a composite material with elastic reinforcements in an elasto-plastic matrix is analyzed. In literature, this boundary value problem has been investigated to compare dislocation-based plasticity models and continuum crystal plasticity models. The former contain a characteristic length scale, i.e. the Burgers vector, the latter ones have no intrinsic length scale parameter and thus are unable to reproduce the size effects that are documented e.g. in Cleveringa, van der Giessen &

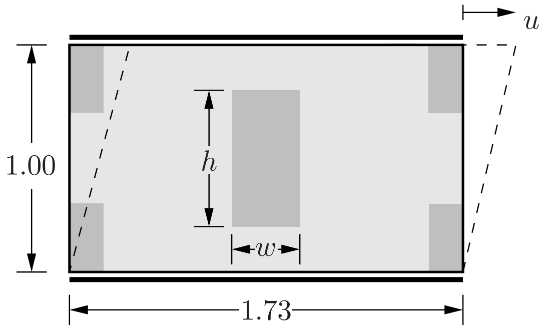

Figure 7.17: Shear-test of composite material. Geometry and boundary conditions of unit cell with double-periodic array of elastic particles with width w and height h taken from Cleveringa, van der Giessen & Needleman [28].

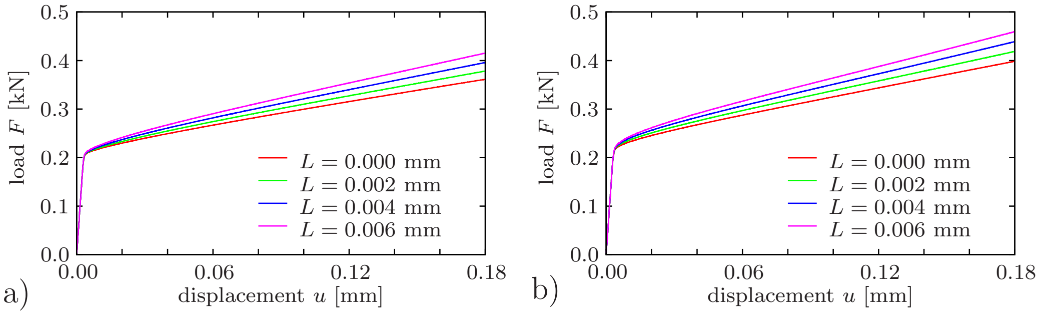

Figure 7.18: Shear-test of composite material. Load-deflection curves a) for geometry (i) and b) for geometry (ii) obtained for computation involving length scale parameters ranging from $L = 0.000$ mm to $L = 0.006$ mm.

Needleman [28]. The same boundary value problem has been adopted by Becker [11] to predict the size effect with the aid of a gradient-extended theory for crystal plasticity that incorporates an intrinsic material length scale. The main observation that has been made by the aforementioned authors is the so-called Hall-Petch effect: the smaller the specimen's dimensions, the stiffer the structural response. Instead of varying the size of the specimen with constant intrinsic length scale, i.e. the Burgers vector, the dimensions of the specimen are kept constant and the length scale parameter L is varied. The

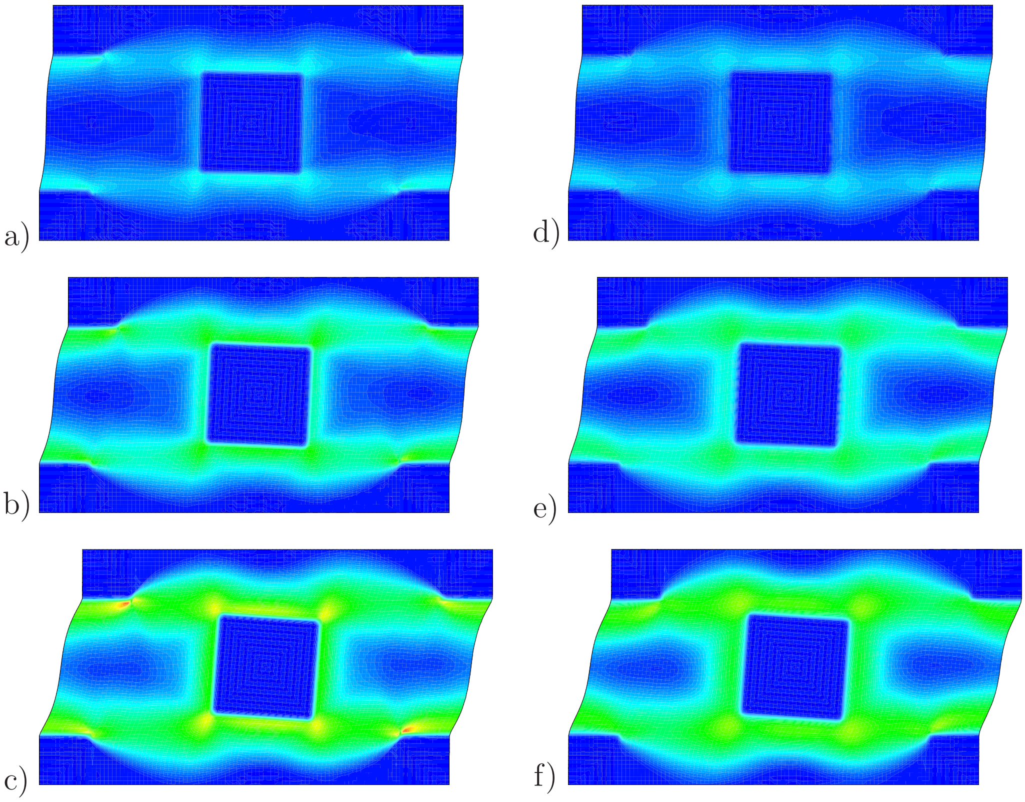

Figure 7.19: Shear-test of composite material. Distribution of equivalent plastic strain α in geometry (i) for a)–c) a length scale parameter $L = 0.002$ mm, and d)–f) a length scale parameter $L = 0.006$ mm, plotted at the deformation stages $u = 0.06$ mm, $u = 0.12$ mm, and $u = 0.18$ mm.

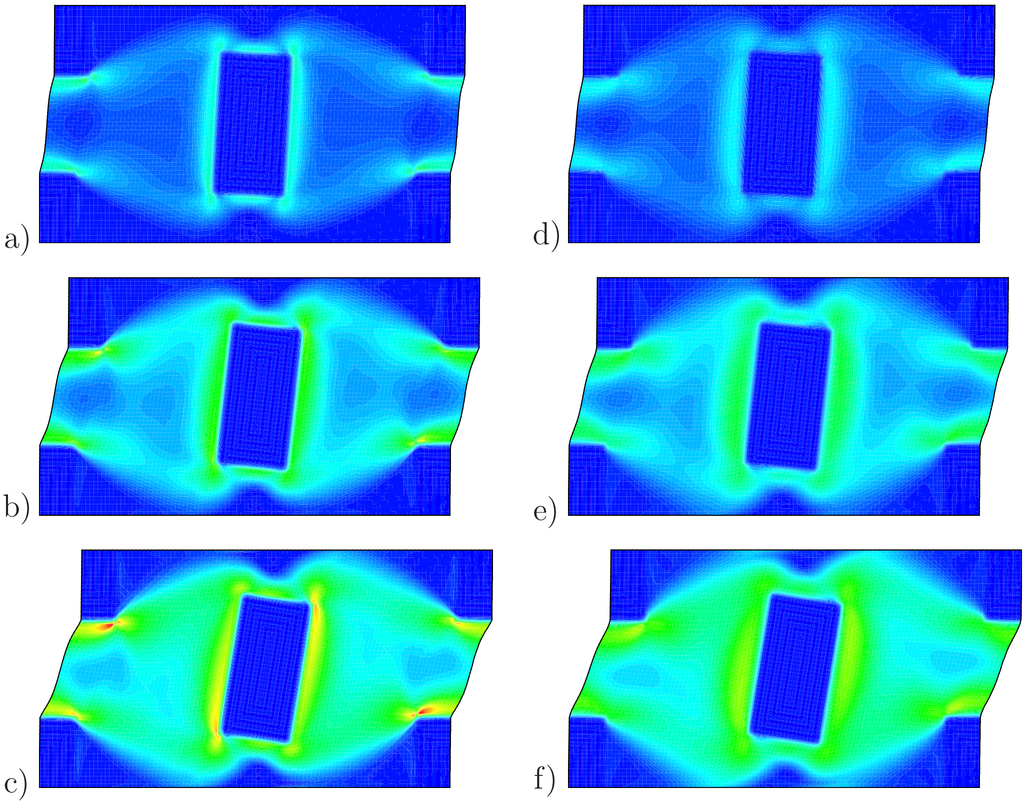

Figure 7.20: Shear-test of composite material. Distribution of equivalent plastic strain α in geometry (ii) for a)–c) a length scale parameter $L = 0.002$ mm and d)–f) a length scale parameter $L = 0.006$ mm plotted at the deformation stages $u = 0.06$ mm, $u = 0.12$ mm, and $u = 0.18$ mm.

geometric setup and the boundary conditions are depicted in Figure 7.17. According to Cleveringa, van der Giessen & Needleman [28], two geometries of the elastic inclusion are investigated: (i) square particles $h = w = 0.416$, and (ii) rectangular particles $h = 2w = 0.588$, both exhibiting an area fraction of $f = 0.200$. The periodicity of the unit cell is taken into account by setting proper boundary and linking conditions: at the lower edge the horizontal and vertical displacements are constrained, at the upper edge the horizontal displacement is prescribed and the vertical displacement is constrained, the horizontal and vertical displacements of the left and the right edge are linked. For the microscopic degrees of freedom, the natural boundary conditions are chosen, the upper and lower, as well as the left and the right edge are microscopically linked. The bulk modulus of the elasto-plastic matrix is chosen to $\kappa = 74.51$ kN/mm^2, the shear modulus to $\mu = 28.57$ kN/mm^2, the isotropic hardening modulus to $h = 0.70$ kN/mm^2, and the yield limit to $y_0 = 0.208$ kN/mm^2. In order to obtain a solution which is very close to the rate-independent limit, the viscosity is chosen to $\eta = 1 \times 10^{-5}$ kN s/mm^2. The bulk modulus of the elastic particles is chosen to $\kappa = 215.66$ kN/mm^2 and the shear modulus to $\mu = 182.48$ kN/mm^2. This set of material parameters is representative for an aluminum matrix with silicon-carbide particles. The boundary value problem is discretized with 60×104 $Q1E4$-elements. For a detailed discussion of the multi-field enhanced strain formulation at large strains see Appendix B.2. The computation is performed in a displacement-driven context using an automated time-stepping procedure. The structural responses for the two geometries (i) and (ii) are given in Figure 7.18a) and Figure 7.18b). Clearly, for an increasing length scale parameter L the response becomes stiffer. For geometry (i), where the inclusions do not overlap, the overall behavior is softer, whereas for geometry (ii) the inclusions overlap and cause a stiffer material response. This characteristic can considerably be observed in the corresponding contour plots of the hardening field α. Figure 7.19 displays the evolution of the hardening field α in geometry (i) for a)–c) the length scale $L = 0.002$ mm and d)–f) the length scale $L = 0.006$ mm. Obviously, for the larger length scale L the hardening field α spreads over a larger neighborhood, causing the stiffer response. A similar characteristic is shown in Figure 7.20 for geometry (ii). Here, the stiffer structural response is caused by hardening accumulation in a region surrounding the inclusions, whose size is proportional to the length scale parameter L. Clearly, the larger the length scale parameter L, the stiffer the response.

8. Conclusion

This thesis is concerned with a *unifying theoretical* and *numerical development* of a *variational-based framework for gradient-type standard dissipative solids.* Throughout the present work three applications of the developed framework have been discussed: *(i) a gradient-type formulation of damage mechanics*, *(ii) phase field modeling of fracture*, and *(iii) a phenomenological model for plasticity with gradient-type hardening.*

The theoretical foundation of the *framework for continua with substructure* has been laid and a precise geometric interpretation of the basic kinematic ingredients has been given. An intense focus is put on the strict duality of macro- and microscopic motions allowing for a *compact representation* of the main ingredients of gradient-type standard dissipative solids, namely the free energy function and the dissipation function. The latter constitutive function is chosen to describe rate-independent processes resulting into a non-smooth dissipation function that is positively homogeneous of degree one. Several alternative representations of this dissipation function are elucidated yielding a penalty-type two-field formulation, a conjugate dissipation function that is based on a Lagrange-multiplier solution in a four-field setting, and the viscous regularization of the conjugate dissipation function in a three-field setting. For all these representations *incremental variational principles* are introduced that characterize the algorithmic balance equations of the fully coupled *symmetric systems.* A *unifying finite element treatment* for these symmetric systems is suggested, where details of the necessary matrix notation are highlighted.

A first application of the proposed general framework for gradient-type standard dissipative solids has been discussed in the context of *gradient-type damage mechanics.* Starting with a canonical version of the rate-independent dissipation function alternative dual representations are derived based on a Legendre transformation. Hereby, the relationship between the dual dissipation function and a classical threshold-type formulation is highlighted. The unified numerical treatment is specified for two-dimensional problems allowing for the discussion of several numerical tests. Problems like *mesh-dependent simulations* arising with standard local damage formulations are overcome by the damage-gradient enhancement of the constitutive functions that incorporates an *intrinsic length scale parameter.* The analysis of some elementary boundary value problems documents the performance of the proposed method with regard to shear band formation and approves the *mesh-independence* of the results.

A further application of the proposed frame for gradient-type standard dissipative solids also covers *phase field modeling of fracture.* The formulation of such models of fracture are closely linked to the previously discussed models of gradient-type damage mechanics. Starting with a purely geometric, approximate description of crack topologies, a dissipation function for rate-independent processes is introduced. This dissipation function contains not only the rate of the fracture phase field, but also its gradient. As a consequence, the model of phase field fracture can be considered as a *specific gradient-type damage formulation* with a particular dissipation function. In analogy to the model of gradient-type damage mechanics, alternative representations of the dissipation function are discussed. Regarding the energy storage mechanism, an *anisotropic degradation of the stored bulk energy* based on a spectral representation of the strains has been introduced, which restricts the crack evolution in tensile regions of the solid domain. The application of the incremental variational frame and specification of the finite element matrices yield the governing symmetric FE-system. Several numerical benchmark tests document the performance of the proposed model. The suggested model of phase field modeling of fracture offers the possibility for *further research*. Follow up work with an emphasis on an effective staggered numerical scheme can be found in MIEHE, HOFACKER & WELSCHINGER [124]. The modular structure of phase field fracture makes this theory highly attractive for the description of more complex fracturing processes in coupled problems of continuum mechanics. An extension of the phase field modeling of fracture towards electromechanical fracture processes can be found in the recent work by MIEHE, WELSCHINGER & HOFACKER [129].

Another part of this thesis is concerned with an *improvement of the numerical efficiency* of phase field modeling of fracture. To this end, an *h-adaptive finite element solution procedure* has been introduced that is exclusively driven by *discrete configurational forces*. In a first step, the configurational setting of phase field fracture has been investigated. The governing balance equation in configurational space are derived, where an algorithmic counterpart of the balance in configurational space can alternatively be obtained by the design of an incremental variational principle. In order to obtain the discrete configurational forces, a numerical staggered solution scheme is introduced which allows for the discussion of the evolution of discrete configurational forces in phase field modeling of fracture. Hereby, the discrete configurational forces consist of two contributions. A bulk part that originates from bulk terms and a surface part that originates from the evolving diffusive crack surface inside the solid domain. The forces acting on the diffusive surface are considered as physically motivated forces, whereas the material bulk forces are related to an insufficient discretization. Thus, the material bulk forces have been employed to define global and local mesh refinement indicators needed in an h-adaptive solution strategy. A representative set of numerical examples is discussed that demonstrates the performance of the proposed solution algorithm.

A last application of the framework for gradient-type standard dissipative solids is found in the description of *size effects* in a *model of phenomenological plasticity with gradient-type hardening*. In a first step, a version of this model has been developed for the case of geometrically small deformations. The exploitation of the incremental variational procedure for gradient-type solids with local internal variables yields the governing algorithmic balance equations. The unified finite element treatment is specified for two-dimensional problems which finally allows for the analysis of two elementary examples regarding the *regularization of shear bands*. In a second step, this small strain model is embedded into the *logarithmic core* of a large deformation formulation. *Mesh-independent* numerical simulations on the one hand side are performed to demonstrate the regularization of shear band formation in more complex boundary value problems and on the other hand side to predict the so-called *Hall-Petch effect*.

A. Gradient-Type Continua in Macroscopic Lagrangian Setting

In this chapter, the focus is laid on the variational formulation of generalized continua in the macroscopic Lagrangian setting that a priori fulfills the invariance property. Regarding a straightforward numerical implementation, the rate-dependent principle with threshold function is investigated. As defined in $(3.37)_1$, the generalized constitutive state for models in the macroscopic Lagrangian setting is defined by

$$\mathfrak{c}_L(\mathfrak{u}) := \{ \bar{\boldsymbol{C}}, \breve{\boldsymbol{\varphi}}, \breve{\boldsymbol{F}} \} \quad \text{with} \quad \mathfrak{u} := \{ \bar{\boldsymbol{\varphi}}, \breve{\boldsymbol{\varphi}} \} \tag{A.1}$$

in terms of the generalized displacement vector $\mathfrak{u}$. Aiming at a rate-dependent variational principle with threshold function, the extended generalized constitutive state is introduced

$$\mathfrak{c}^*_L(\mathfrak{u}^*_L) := \{ \bar{\boldsymbol{C}}, \breve{\boldsymbol{\varphi}}, \breve{\boldsymbol{F}}, \mathfrak{f}_L \} \quad \text{with} \quad \mathfrak{u}^*_L := \{ \bar{\boldsymbol{\varphi}}, \breve{\boldsymbol{\varphi}}, \mathfrak{f}_L \} \tag{A.2}$$

based on the extended generalized displacement vector $\mathfrak{u}^*_L$ that additionally contains the *thermodynamic dissipative force array*

$$\mathfrak{f}_L := \{ \bar{\boldsymbol{\mathcal{F}}}_L, \breve{\boldsymbol{f}}, \breve{\boldsymbol{\mathcal{F}}} \} \,. \tag{A.3}$$

Here, the thermodynamic force $\bar{\boldsymbol{\mathcal{F}}}_L$ is dual to the macroscopic right Cauchy-Green tensor $\bar{\boldsymbol{C}}$, the force $\breve{\boldsymbol{f}}$ dual to the microscopic deformation $\breve{\boldsymbol{\varphi}}$, and the force $\breve{\boldsymbol{\mathcal{F}}}$ dual to the microscopic deformation gradient $\breve{\boldsymbol{F}}$. In contrast to Chapter 3, solely the over-force representation of the viscous dissipation function

$$\phi(\dot{\mathfrak{c}}_L; \mathfrak{c}_L) = \sup_{\mathfrak{f}_L} [\, \mathfrak{f}_L \cdot \dot{\mathfrak{c}}_L - \frac{1}{2\eta} \langle \varphi(\mathfrak{f}_L; \mathfrak{c}_L) \rangle^2_+ \,] \tag{A.4}$$

is discussed. Formulations that base on this smooth representation of the dissipation function are highly attractive for a numerical treatment.

A.1. Time-Discrete Rate-Dependent Variational Principle

In what follows, an incremental variational principle for gradient-type standard dissipative solids is set up that bases on the extended dissipation function (A.4). In the macroscopic Lagrangian setting, the variational principle is governed by the incremental potential

$$\underbrace{\Pi^{*\tau}_\eta(\bar{\boldsymbol{\varphi}}, \breve{\boldsymbol{\varphi}}, \mathfrak{f}_L)}_{potential} := \underbrace{E^\tau(\bar{\boldsymbol{\varphi}}, \breve{\boldsymbol{\varphi}})}_{energy} + \underbrace{D^{*\tau}_\eta(\bar{\boldsymbol{\varphi}}, \breve{\boldsymbol{\varphi}}, \mathfrak{f}_L)}_{dissipation} - \underbrace{W^\tau(\bar{\boldsymbol{\varphi}}, \breve{\boldsymbol{\varphi}})}_{work} \,. \tag{A.5}$$

Based on the generalized deformation vectors $(A.1)_2$ and $(A.2)_2$, the generalized constitutive state vector $(A.2)_1$, the generalized volume force vector (3.94), and the generalized surface traction vector (3.95), the incremental potential (A.5) may be reformulated

$$\Pi^{*\tau}_\eta(\mathfrak{u}^*_L) = \int_{\mathcal{B}} \{\, \pi^{*\tau}_\eta(\mathfrak{c}^*_L; \mathfrak{c}^*_{Ln}) - \mathfrak{g} \cdot (\mathfrak{u} - \mathfrak{u}_n) \,\} \, dV - \int_{\partial\mathcal{B}_{\mathfrak{t}}} \mathfrak{t}_N \cdot (\mathfrak{u} - \mathfrak{u}_n) \, dA \tag{A.6}$$

expressed in terms of the *extended incremental internal work density*

$$\pi^{*\tau}_\eta(\mathfrak{c}^*_L; \mathfrak{c}^*_{Ln}) = \psi(\mathfrak{c}_L) - \psi(\mathfrak{c}_{Ln}) + \mathfrak{f}_L \cdot (\mathfrak{c}_L - \mathfrak{c}_{Ln}) - \frac{\tau}{2\eta} \langle \varphi(\mathfrak{f}_L; \mathfrak{c}_{Ln}) \rangle^2_+ \,, \tag{A.7}$$

Table A.1: Rate-dependent balances of gradient-type solids.

Macroscopic equilibrium condition

$$\boldsymbol{0} = \mathrm{DIV}[\, 2\bar{\boldsymbol{g}}\bar{\boldsymbol{F}}(\partial_{\bar{\boldsymbol{C}}}\psi + \bar{\boldsymbol{\mathcal{F}}}_L)\,] + \bar{\boldsymbol{\gamma}}_0 \quad \text{in} \;\; \mathcal{B}$$

$$\bar{\boldsymbol{g}}\bar{\boldsymbol{T}}_N = \bar{\boldsymbol{g}}\bar{\boldsymbol{F}}(2\partial_{\bar{\boldsymbol{C}}}\psi + 2\bar{\boldsymbol{\mathcal{F}}}_L) \cdot \boldsymbol{N} \quad \text{on} \;\; \partial\mathcal{B}_{\bar{t}}$$

Microscopic evolution equation

$$\boldsymbol{0} = \mathrm{DIV}[\, \partial_{\check{\boldsymbol{F}}}\psi + \check{\boldsymbol{\mathcal{F}}}\,] - [\, \partial_{\check{\boldsymbol{\varphi}}}\psi + \check{\boldsymbol{f}}\,] + \check{\boldsymbol{\gamma}}_0 \quad \text{in} \;\; \mathcal{B}$$

$$\check{\boldsymbol{g}}\check{\boldsymbol{T}}_N = (\partial_{\check{\boldsymbol{F}}}\psi + \check{\boldsymbol{\mathcal{F}}}) \cdot \boldsymbol{N} \quad \text{on} \;\; \partial\mathcal{B}_{\check{t}}$$

Inverse smooth definition of dissipative driving forces with $\lambda := \frac{1}{\eta}\,\langle \varphi(\mathfrak{f}_L; \mathfrak{c}_L)\rangle_+$

$$\dot{\bar{\boldsymbol{C}}} = \lambda\,\partial_{\bar{\boldsymbol{\mathcal{F}}}_L}\varphi \quad \text{and} \quad \dot{\check{\boldsymbol{\varphi}}} = \lambda\,\partial_{\check{\boldsymbol{f}}}\varphi \quad \text{and} \quad \dot{\check{\boldsymbol{F}}} = \lambda\,\partial_{\check{\boldsymbol{\mathcal{F}}}}\varphi \quad \text{in } \mathcal{B}$$

---

and is determined by the constitutive free energy function ψ and the yield function φ, respectively. In this manner, the finite step sized incremental stationary principle reads

$$\boxed{\{\, \bar{\boldsymbol{\varphi}}, \check{\boldsymbol{\varphi}}, \mathfrak{f}_L \,\} = \arg\{ \inf_{\bar{\boldsymbol{\varphi}}} \inf_{\check{\boldsymbol{\varphi}}} \sup_{\mathfrak{f}_L} \Pi^{*\tau}_{\eta}(\bar{\boldsymbol{\varphi}}, \check{\boldsymbol{\varphi}}, \mathfrak{f}_L) \,\}\,.} \tag{A.8}$$

It uniquely determines the current macro- and microscopic deformation $\bar{\boldsymbol{\varphi}}$ and $\check{\boldsymbol{\varphi}}$ and the dissipative thermodynamic driving force $\mathfrak{f}_L$ as the *saddle point* of the incremental functional (A.7). The variation of this incremental potential yields the *smooth* necessary condition

$$\delta\Pi^{*\tau}_{\eta} = \delta_{\bar{\boldsymbol{\varphi}}}\Pi^{*\tau}_{\eta} + \delta_{\check{\boldsymbol{\varphi}}}\Pi^{*\tau}_{\eta} + \delta_{\mathfrak{f}_L}\Pi^{*\tau}_{\eta} = 0\,. \tag{A.9}$$

The single components can be summarized by the explicit expressions

$$\begin{aligned}
\delta_{\bar{\boldsymbol{\varphi}}}\Pi^{*\tau}_{\eta} :=& \int_{\mathcal{B}} \{\, [\partial_{\bar{\boldsymbol{C}}}\psi + \bar{\boldsymbol{\mathcal{F}}}_L] : (2\bar{\boldsymbol{F}}^T\bar{\boldsymbol{g}}\nabla_{\boldsymbol{X}}\delta\bar{\boldsymbol{\varphi}}) - \bar{\boldsymbol{\gamma}}_0 \cdot \delta\bar{\boldsymbol{\varphi}} \,\}\, dV \\
&- \int_{\partial\mathcal{B}_{\bar{t}}} \bar{\boldsymbol{g}}\bar{\boldsymbol{T}}_N \cdot \delta\bar{\boldsymbol{\varphi}}\, dA \\
\delta_{\check{\boldsymbol{\varphi}}}\Pi^{*\tau}_{\eta} :=& \int_{\mathcal{B}} \{\, [\partial_{\check{\boldsymbol{F}}}\psi + \check{\boldsymbol{\mathcal{F}}}] : \nabla_{\boldsymbol{X}}\delta\check{\boldsymbol{\varphi}} + [\partial_{\check{\boldsymbol{\varphi}}}\psi + \check{\boldsymbol{f}} - \check{\boldsymbol{\gamma}}_0] \cdot \delta\check{\boldsymbol{\varphi}} \,\}\, dV \\
&- \int_{\partial\mathcal{B}_{\check{t}}} \check{\boldsymbol{g}}\check{\boldsymbol{T}}_N \cdot \delta\check{\boldsymbol{\varphi}}\, dA \\
\delta_{\mathfrak{f}_L}\Pi^{*\tau}_{\eta} :=& \int_{\mathcal{B}} \{\, [\mathfrak{c}_L - \mathfrak{c}_{Ln} - \frac{\tau}{\eta}\,\langle\varphi\rangle_+ \partial_{\mathfrak{f}_L}\varphi] \cdot \delta\mathfrak{f}_L \,\}\, dV
\end{aligned} \tag{A.10}$$

in terms of the admissible variations $\delta\bar{\boldsymbol{\varphi}} \in \mathcal{W}^0_{\bar{\boldsymbol{\varphi}}}$, $\delta\check{\boldsymbol{\varphi}} \in \mathcal{W}^0_{\check{\boldsymbol{\varphi}}}$, and $\delta\mathfrak{f}_L$ of the current macro- and microscopic deformation and the dissipative forces. Note that the variation of the macroscopic right Cauchy-Green tensor $\delta\bar{\boldsymbol{C}} = 2\,\mathrm{sym}[\bar{\boldsymbol{F}}^T\bar{\boldsymbol{g}}\nabla_{\boldsymbol{X}}\delta\bar{\boldsymbol{\varphi}}]$ enters the macroscopic balance $(\mathrm{A.10})_1$, where due to the symmetry property of the stresses $\partial_{\bar{\boldsymbol{C}}}\psi$ and the forces $\bar{\boldsymbol{\mathcal{F}}}_L$ it is sufficient to consider the non-symmetric part only. The Euler equations of the stationary principle (A.8) evaluated at current time t_{n+1} are summarized in Table A.1.

Such a formulation is particularly convenient due to the smooth nature of the viscous dissipation function.

A.2. Finite Element Discretization of Variational Principle

Focusing on a discrete representation of the extended incremental variational principle (A.8), the discrete counterpart to the extended generalized deformation vector in a macroscopic Lagrangian formulation has to be introduced

$$\boldsymbol{\mathfrak{u}}^{*h}_{L} = \mathop{\mathsf{A}}\limits_{e=1}^{n_{en}} \left[\sum_{i=1}^{n_{el}} \begin{bmatrix} [\boldsymbol{\mathfrak{N}}]^e_i & \boldsymbol{0} \\ \boldsymbol{0} & [\boldsymbol{A}]^e_i \end{bmatrix} \begin{bmatrix} \boldsymbol{\mathfrak{d}} \\ \boldsymbol{f}_{L} \end{bmatrix}_i \right]^e = \mathop{\mathsf{A}}\limits_{e=1}^{n_{en}} \begin{bmatrix} [\boldsymbol{\mathfrak{N}}]^e & \boldsymbol{0} \\ \boldsymbol{0} & [\boldsymbol{A}]^e \end{bmatrix} \begin{bmatrix} \boldsymbol{\mathfrak{d}} \\ \boldsymbol{f}_{L} \end{bmatrix}^e =: \boldsymbol{\mathfrak{N}}^*(\boldsymbol{X})\, \boldsymbol{\mathfrak{d}}^*_{L} \,. \tag{A.11}$$

This expression contains the element matrix $[\boldsymbol{\mathfrak{N}}]^e_i$ defined in equation (3.141) and an additional approximation matrix $[\boldsymbol{A}]^e_i$ for the thermodynamic forces. Regarding a compact notation, both are summarized by the global matrix $\boldsymbol{\mathfrak{N}}^*$, where the nodal unknowns are

$$\boldsymbol{\mathfrak{d}}^*_{L\,i} = [\, \boldsymbol{\mathfrak{d}}, \boldsymbol{f}_{L} \,]^T_i = [\, \bar{\boldsymbol{d}}, \check{\boldsymbol{d}}, \boldsymbol{f}_{L} \,]^T_i \,, \tag{A.12}$$

namely the nodal displacements $\bar{\boldsymbol{d}}$, the nodal microscopic deformation $\check{\boldsymbol{d}}$, and the thermodynamic forces $\boldsymbol{f}_{L}$. According to the representation (3.143), the constitutive state in the macroscopic Lagrangian setting is given by the expression

$$\boldsymbol{\mathfrak{c}}^{*h}_{L}(\boldsymbol{\mathfrak{d}}^*_{L}) = \mathop{\mathsf{A}}\limits_{e=1}^{n_{en}} \begin{bmatrix} \bar{\boldsymbol{C}}^{he}(\bar{\boldsymbol{d}}^e) \\ [\check{\boldsymbol{B}}]^e \check{\boldsymbol{d}}^e \\ [\boldsymbol{A}]^e \boldsymbol{f}^e \end{bmatrix} \quad \text{with} \quad \bar{\boldsymbol{C}}^{he}(\bar{\boldsymbol{d}}^e) = \bar{\boldsymbol{F}}^{he^T}(\bar{\boldsymbol{d}}^e) \bar{\boldsymbol{g}} \bar{\boldsymbol{F}}^{he}(\bar{\boldsymbol{d}}^e) \,. \tag{A.13}$$

The macroscopic right Cauchy-Green tensor $\bar{\boldsymbol{C}}^{he}(\bar{\boldsymbol{d}}^e)$ is evaluated on element level as a *nonlinear* function of the discrete macroscopic deformation gradient $\bar{\boldsymbol{F}}^{he}(\bar{\boldsymbol{d}}^e)$, see also equation (3.153) for more details. With the discretizations (A.11) and (A.13) at hand, the extended potential (A.6) is reformulated

$$\Pi^{*h}_{\eta}(\boldsymbol{\mathfrak{d}}^*_{L}) = \int_{\mathcal{B}^h} \{\, \pi^{*h}_{\eta}(\boldsymbol{\mathfrak{c}}^{*h}_{L}; \boldsymbol{\mathfrak{c}}^{*h}_{Ln}) - \boldsymbol{\mathfrak{g}} \cdot \boldsymbol{\mathfrak{N}}(\boldsymbol{\mathfrak{d}} - \boldsymbol{\mathfrak{d}}_n) \,\}\, dV - \int_{\partial\mathcal{B}^h_{\mathfrak{t}}} \boldsymbol{\mathfrak{t}}_N \cdot \boldsymbol{\mathfrak{N}}(\boldsymbol{\mathfrak{d}} - \boldsymbol{\mathfrak{d}}_n)\, dA \tag{A.14}$$

allowing finally for the discrete representation of the incremental *stationary principle*

$$\boxed{\{\, \boldsymbol{\mathfrak{d}}^*_{L} \,\} = \arg\{ \operatorname*{stat}_{\boldsymbol{\mathfrak{d}}^*_{L}} \Pi^{*h}_{\eta}(\boldsymbol{\mathfrak{d}}^*_{L}) \,\} \,.} \tag{A.15}$$

It identifies the generalized nodal displacements $\boldsymbol{\mathfrak{d}}$ and the nodal thermodynamic forces $\boldsymbol{f}_{L}$ of the discrete problem at time t_{n+1}. Starting with the variation of the discrete constitutive state (A.13) with respect to the nodal generalized displacements

$$\delta_{\boldsymbol{\mathfrak{d}}^*_{L}} \boldsymbol{\mathfrak{c}}^{*h}_{L} = \mathop{\mathsf{A}}\limits_{e=1}^{n_{en}} \left[\sum_{i=1}^{n_{el}} \begin{bmatrix} [2\bar{\boldsymbol{B}}_{M}(\bar{\boldsymbol{d}}^e)]^e_i & \boldsymbol{0} & \boldsymbol{0} \\ \boldsymbol{0} & [\check{\boldsymbol{B}}]^e_i & \boldsymbol{0} \\ \boldsymbol{0} & \boldsymbol{0} & [\boldsymbol{A}]^e_i \end{bmatrix} \begin{bmatrix} \delta\bar{\boldsymbol{d}} \\ \delta\check{\boldsymbol{d}} \\ \delta\boldsymbol{f} \end{bmatrix}_i \right]^e =: \boldsymbol{\mathfrak{B}}^*_{M}(\boldsymbol{X})\, \delta\boldsymbol{\mathfrak{d}}^*_{L} \,, \tag{A.16}$$

the necessary condition of the discrete variational principle (A.15) reads

$$\boldsymbol{0} = \Pi^{*h}_{\eta,\boldsymbol{\mathfrak{d}}^*_{L}} = \int_{\mathcal{B}^h} \{\, \boldsymbol{\mathfrak{B}}^{*\,T}_{M} [\boldsymbol{S}^*_{L}] - \boldsymbol{\mathfrak{N}}^T \boldsymbol{\mathfrak{g}} \,\}\, dV - \int_{\partial\mathcal{B}^h_{\mathfrak{t}}} \boldsymbol{\mathfrak{N}}^T \boldsymbol{\mathfrak{t}}_N \, dA \quad \text{with} \quad \boldsymbol{S}^*_{L} := \partial_{\boldsymbol{\mathfrak{c}}^{*h}_{L}} \pi^{*\tau}_{\eta} \,. \tag{A.17}$$

This coupled system of nonlinear equations is solved iteratively in a Newton solution scheme that bases on the update algorithm

$$\boldsymbol{\mathfrak{d}}^*_L \Leftarrow \boldsymbol{\mathfrak{d}}^*_L - [\Pi^{*h}_{\eta,\boldsymbol{\mathfrak{d}}^*_L\boldsymbol{\mathfrak{d}}^*_L}]^{-1} \cdot \Pi^{*h}_{\eta,\boldsymbol{\mathfrak{d}}^*_L} \quad \text{until} \quad \|\Pi^{*h}_{\eta,\boldsymbol{\mathfrak{d}}^*_L}\| \leq \text{tol}\,. \tag{A.18}$$

This expression contains the symmetric monolithic tangent matrix

$$\Pi^{*h}_{\eta,\boldsymbol{\mathfrak{d}}^*_L\boldsymbol{\mathfrak{d}}^*_L} = \int_{\mathcal{B}^h} \{\, \boldsymbol{\mathfrak{B}}^{*\,T}_M [\mathbb{C}^*_L] \boldsymbol{\mathfrak{B}}^*_M + \boldsymbol{\mathfrak{B}}^{*T}_G [\bar{\mathbb{S}}^{*h}_L] \boldsymbol{\mathfrak{B}}^*_G \,\}\, dV \quad \text{with} \quad \mathbb{C}^*_L := \partial^2_{\boldsymbol{\mathfrak{c}}^{*h}_L \boldsymbol{\mathfrak{c}}^{*h}_L} \pi^{*h}_\eta \tag{A.19}$$

that contains material and geometric contributions. The geometric term arises, because the approximation matrix $\bar{\boldsymbol{B}}_M(\bar{\boldsymbol{d}}^e)$ in (A.16) is a function of the actual macroscopic deformation $\bar{\boldsymbol{d}}^e$. Thus, its increment has to be taken into account via

$$\boldsymbol{\mathfrak{B}}^*_G := \mathop{\mathsf{A}}_{e=1}^{n_{en}} \left[\sum_{i=1}^{n_{el}} \left[[\bar{\boldsymbol{B}}]^e_i \;\; \boldsymbol{0} \right] \right] = \mathop{\mathsf{A}}_{e=1}^{n_{en}} \left[[\bar{\boldsymbol{B}}]^e \;\; \boldsymbol{0} \right] \quad \text{and} \quad \bar{\mathbb{S}}^*_L = 2\partial_{\bar{\boldsymbol{C}}^h} \pi^{*h}_\eta \tag{A.20}$$

based on the macroscopic stresses $\bar{\mathbb{S}}^*_L$ that are restored in matrix format. The matrices $\boldsymbol{\mathfrak{B}}^*_M$ and $\boldsymbol{\mathfrak{B}}^*_G$ depend on the geometric dimension and the nature of the material's microstructure.

B. Enhanced Multi-Field Finite Element Formulations

The numerical simulation of strain softening effects in damage mechanics at small strains discussed in Section 4 or in phenomenological plasticity at small and large deformations presented in Section 7 necessitates the development of an enhanced strain formulation that is embedded into the multi-field framework for generalized continua. Standard displacement formulations fail in situations with highly distorted elements in shear bands and exhibit the severe effect of locking. In general, the enhanced strain formulation can be traced back to the method of incompatible modes as introduced by WILSON, TAYLOR, DOHERTY & GHABOUSSI [179] and TAYLOR, BERESFORD & WILSON [169]. A variational-based approach to an enhanced strain formulation at small strains that bases on a Hu-Washizu principle can be found in SIMO & RIFAI [165]. For a more general treatise of the Hu-Washizu variational principle, see WASHIZU [174]. An extension of the Simo-Rifai element to the large strain setting is discussed in SIMO & ARMERO [160] and SIMO, ARMERO & TAYLOR [161] which is conceptually in line with MIEHE [114].

B.1. Enhanced Strain Formulation for Geometrically Linear Problems

This section aims at the construction of an enhanced strain formulation that is embedded into the multi-field framework for continua with microstructure. Following the work by SIMO & RIFAI [165] and SIMO & HUGHES [162], the central idea of an enhanced strain formulation bases on a re-parametrization of the actual macroscopic strain field in the form

$$\bar{\boldsymbol{\varepsilon}}(\bar{\boldsymbol{u}}, \bar{\boldsymbol{\varepsilon}}^E) = \nabla_s \bar{\boldsymbol{u}} + \bar{\boldsymbol{\varepsilon}}^E \,, \tag{B.1}$$

where $\nabla_s \bar{\boldsymbol{u}}$ is the symmetric part of the gradient of the displacement field and $\bar{\boldsymbol{\varepsilon}}^E$ the *enhanced* part of the actual strain field. The actual macroscopic strain (B.1) then enters the generalized constitutive state for the description of continua with microstructure.

B.1.1. Time-Discrete Incremental Variational Formulation. According to the kinematic enhancement (B.1), the generalized constitutive state (3.200) is rewritten

$$\mathfrak{c}(\mathfrak{u}, \bar{\boldsymbol{\varepsilon}}^E) := \{\, \bar{\boldsymbol{\varepsilon}}(\bar{\boldsymbol{u}}, \bar{\boldsymbol{\varepsilon}}^E), \check{\boldsymbol{u}}, \nabla \check{\boldsymbol{u}} \,\} \quad \text{with} \quad \mathfrak{u} := \{\, \bar{\boldsymbol{u}}, \check{\boldsymbol{u}} \,\} \,. \tag{B.2}$$

Restricting to a formulation of the incremental dissipation in its rate-dependent setting with threshold-function (3.196), the extended constitutive state (3.209) has to be adjusted

$$\mathfrak{c}^*(\mathfrak{u}^*, \bar{\boldsymbol{\varepsilon}}^E) := \{\, \bar{\boldsymbol{\varepsilon}}(\bar{\boldsymbol{u}}, \bar{\boldsymbol{\varepsilon}}^E), \check{\boldsymbol{u}}, \nabla \check{\boldsymbol{u}}, \mathfrak{f} \,\} \quad \text{with} \quad \mathfrak{u}^* := \{\, \bar{\boldsymbol{u}}, \check{\boldsymbol{u}}, \mathfrak{f} \,\} \,, \tag{B.3}$$

containing in addition the thermodynamic driving forces $\mathfrak{f}$. This extended constitutive state then enters the incremental potential

$$\Pi^{*\tau}_{\eta}(\mathfrak{u}^*, \bar{\boldsymbol{\varepsilon}}^E, \bar{\boldsymbol{\sigma}}) = \int_{\mathcal{B}} \{\, \pi^{\tau *}_{\eta}(\mathfrak{c}^*; \mathfrak{c}^*_n) - \mathfrak{g} \cdot (\mathfrak{u} - \mathfrak{u}_n) \,\}\, dV - \int_{\partial \mathcal{B}_{\mathfrak{t}}} \mathbf{t}_N \cdot (\mathfrak{u} - \mathfrak{u}_n) \, dA \tag{B.4}$$

founded on the *extended incremental internal work density* that is macroscopically extended in the sense of a Hu-Washitsu principle

$$\pi^{*\tau}_{\eta}(\mathfrak{c}^*; \mathfrak{c}^*_n) = \psi(\mathfrak{c}) - \bar{\boldsymbol{\sigma}} : \bar{\boldsymbol{\varepsilon}}^E - \psi(\mathfrak{c}_n) + \bar{\boldsymbol{\sigma}}_n : \bar{\boldsymbol{\varepsilon}}^E_n + \mathfrak{f} \cdot (\mathfrak{c} - \mathfrak{c}_n) - \frac{\tau}{2\eta} \, \langle \varphi(\mathfrak{f}; \mathfrak{c}_n) \rangle^2_+ \,. \tag{B.5}$$

It is governed by the free energy function ψ as a function of the enhanced constitutive state (B.2)$_1$, the yield function φ, and the *actual stress tensor* $\bar{\boldsymbol{\sigma}}$. The stationary principle

$$\boxed{\{\, \bar{\boldsymbol{u}}, \check{\boldsymbol{u}}, \mathfrak{f}, \bar{\boldsymbol{\varepsilon}}^E, \bar{\boldsymbol{\sigma}} \,\} = \arg\{ \inf_{\bar{\boldsymbol{u}}} \inf_{\check{\boldsymbol{u}}} \sup_{\mathfrak{f}} \inf_{\bar{\boldsymbol{\varepsilon}}^E} \sup_{\bar{\boldsymbol{\sigma}}} \Pi_\eta^{*\tau}(\bar{\boldsymbol{u}}, \check{\boldsymbol{u}}, \mathfrak{f}, \bar{\boldsymbol{\varepsilon}}^E, \bar{\boldsymbol{\sigma}}) \,\}} \tag{B.6}$$

determines the macro- and microscopic displacement $\bar{\boldsymbol{u}}$ and $\check{\boldsymbol{u}}$, the dissipative thermodynamic driving force $\mathfrak{f}$, the enhanced part of the strains $\bar{\boldsymbol{\varepsilon}}^E$, and the actual stresses $\bar{\boldsymbol{\sigma}}$ as the *saddle point* of the incremental functional (B.3). The necessary condition reads

$$\delta\Pi_\eta^{*\tau} = \delta_{\mathfrak{u}^*}\Pi_\eta^{*\tau} + \delta_{\bar{\boldsymbol{\varepsilon}}^E}\Pi_\eta^{*\tau} + \delta_{\bar{\boldsymbol{\sigma}}}\Pi_\eta^{*\tau} = 0\,. \tag{B.7}$$

The generalized displacements $\mathfrak{u}^*$ allow for the compact formulation

$$\begin{aligned} \delta_{\mathfrak{u}^*}\Pi_\eta^{*\tau} &:= \int_{\mathcal{B}} \{\, [\partial_{\mathfrak{c}^*}\pi_\eta^{*\tau}] \cdot \delta_{\mathfrak{u}^*}\mathfrak{c}^* - \mathfrak{g} \cdot \delta\mathfrak{u} \,\}\, dV - \int_{\partial\mathcal{B}_{\mathfrak{t}}} \mathfrak{t}_N \cdot \delta\mathfrak{u}\, dA \\ \delta_{\bar{\boldsymbol{\varepsilon}}^E}\Pi_\eta^{*\tau} &:= \int_{\mathcal{B}} \{\, [\partial_{\bar{\boldsymbol{\varepsilon}}}\pi_\eta^{*\tau} - \bar{\boldsymbol{\sigma}}] : \delta\bar{\boldsymbol{\varepsilon}}^E \,\}\, dV \\ \delta_{\bar{\boldsymbol{\sigma}}}\Pi_\eta^{*\tau} &:= \int_{\mathcal{B}} \{\, [\partial_{\bar{\boldsymbol{\sigma}}}\pi_\eta^{*\tau}] : \delta\bar{\boldsymbol{\sigma}} \,\}\, dV\,. \end{aligned} \tag{B.8}$$

Here, the variation of the constitutive state (B.3) with respect to the generalized deformation vector $\mathfrak{u}^*$ is given by the expression

$$\delta_{\mathfrak{u}^*}\mathfrak{c}^* := \{\, \nabla_s\delta\bar{\boldsymbol{u}}, \delta\check{\boldsymbol{u}}, \nabla\delta\check{\boldsymbol{u}}, \delta\mathfrak{f} \,\}\,. \tag{B.9}$$

Equation (B.8)$_1$ represents in a compact format the Euler equations of the stationary principle (B.6). The strong form of the balance equations evaluated at current time t_{n+1} is summarized in Table 3.4. The local form of the enhanced subproblem (B.8)$_{2,3}$ reads

$$\bar{\boldsymbol{\sigma}} = \partial_{\bar{\boldsymbol{\varepsilon}}}\psi(\mathfrak{c}) + \bar{\boldsymbol{\mathcal{F}}} \quad \text{and} \quad \bar{\boldsymbol{\varepsilon}}^E = \boldsymbol{0}\,. \tag{B.10}$$

The first expression describes the *actual stresses* $\bar{\boldsymbol{\sigma}}$, the second one enforces vanishing enhanced strains $\bar{\boldsymbol{\varepsilon}}^E = \boldsymbol{0}$ in the domain $\mathcal{B}$. This is obvious in the continuous setting, but is not satisfied within a finite element approximation, i.e. $\bar{\boldsymbol{\varepsilon}}^{Eh} \neq \boldsymbol{0}$ in $\mathcal{B}^h$.

B.1.2. Algorithmic Finite Element Discretization of the Weak Form. Prior to the discretization of the weak form (B.6), the L_2-orthogonality between the discrete stresses $\bar{\boldsymbol{\sigma}}^h$ and the enhanced part of the strains $\bar{\boldsymbol{\varepsilon}}^{Eh}$ is exploited

$$\delta_{\bar{\boldsymbol{\sigma}}^h}\Pi_\eta^{*h} = -\int_{\mathcal{B}^h} \{\, \bar{\boldsymbol{\varepsilon}}^{Eh} : \delta\bar{\boldsymbol{\sigma}}^h \,\}\, dV = -\int_{\mathcal{B}^h} \{\, \bar{\boldsymbol{\sigma}}^h : \delta\bar{\boldsymbol{\varepsilon}}^{Eh} \,\}\, dV = 0\,, \tag{B.11}$$

where the explicit term $[\partial_{\bar{\boldsymbol{\sigma}}}\pi_\eta^{*\tau}] : \delta\bar{\boldsymbol{\sigma}} = -\boldsymbol{\varepsilon}^E : \delta\bar{\boldsymbol{\sigma}}$ has been used. In the discrete setting this equation is identically satisfied if the last term in equation (B.8)$_2$ vanishes. Thus, the L_2-orthogonality between the stresses and the enhanced strains eliminates the stress field from the finite element equations. The reduced set of *discrete* equations is obtained

$$\begin{aligned} \delta_{\mathfrak{u}^{*h}}\Pi_\eta^{*h} &:= \int_{\mathcal{B}^h} \{\, [\partial_{\mathfrak{c}^{*h}}\pi_\eta^{*h}] \cdot \delta_{\mathfrak{u}^{*h}}\mathfrak{c}^{*h} - \mathfrak{g} \cdot \delta\mathfrak{u}^h \,\}\, dV - \int_{\partial\mathcal{B}^h_{\mathfrak{t}}} \mathfrak{t}_N \cdot \delta\mathfrak{u}^h\, dA \\ \delta_{\bar{\boldsymbol{\varepsilon}}^{Eh}}\Pi_\eta^{*h} &:= \int_{\mathcal{B}^h} \{\, [\partial_{\bar{\boldsymbol{\varepsilon}}^h}\pi_\eta^{*h}] : \delta\bar{\boldsymbol{\varepsilon}}^{Eh} \,\}\, dV\,. \end{aligned} \tag{B.12}$$

This reduced weak form is a priori chosen as starting point for a numerical treatment. To this end, in $(\text{B.12})_1$ the discrete variation of the generalized deformation vector

$$\delta\boldsymbol{\mathfrak{u}}^{*h} = \mathop{\mathsf{A}}\limits_{e=1}^{n_{en}} \left[\sum_{i=1}^{n_{el}} \begin{bmatrix} [\boldsymbol{\mathfrak{N}}]_i^e & \boldsymbol{0} \\ \boldsymbol{0} & [\boldsymbol{A}]_i^e \end{bmatrix} \begin{bmatrix} \delta\boldsymbol{\mathfrak{d}} \\ \delta\boldsymbol{f} \end{bmatrix}_i^e \right] = \mathop{\mathsf{A}}\limits_{e=1}^{n_{en}} \begin{bmatrix} [\boldsymbol{\mathfrak{N}}]^e & \boldsymbol{0} \\ \boldsymbol{0} & [\boldsymbol{A}]^e \end{bmatrix} \begin{bmatrix} \delta\boldsymbol{\mathfrak{d}} \\ \delta\boldsymbol{f} \end{bmatrix}^e =: \boldsymbol{\mathfrak{N}}^*(\boldsymbol{x})\,\delta\boldsymbol{\mathfrak{d}}^* \tag{B.13}$$

and the discrete variation of the enhanced constitutive state vector with respect to the generalized deformation

$$\delta_{\boldsymbol{\mathfrak{u}}^{*h}}\boldsymbol{\mathfrak{c}}^{*h} = \mathop{\mathsf{A}}\limits_{e=1}^{n_{en}} \left[\sum_{i=1}^{n_{el}} \begin{bmatrix} [\bar{\boldsymbol{B}}]_i^e & \boldsymbol{0} & \boldsymbol{0} \\ \boldsymbol{0} & [\check{\boldsymbol{B}}]_i^e & \boldsymbol{0} \\ \boldsymbol{0} & \boldsymbol{0} & [\boldsymbol{A}]_i^e \end{bmatrix} \begin{bmatrix} \delta\bar{\boldsymbol{d}} \\ \delta\check{\boldsymbol{d}} \\ \delta\boldsymbol{f} \end{bmatrix}_i^e \right] =: \boldsymbol{\mathfrak{B}}^*(\boldsymbol{x})\,\delta\boldsymbol{\mathfrak{d}}^* \tag{B.14}$$

have to be considered, see also equations (3.226) and (3.231). These expressions contain the approximation matrices for the coupled problem $[\boldsymbol{\mathfrak{N}}]_i^e$, $[\bar{\boldsymbol{B}}]_i^e$, $[\check{\boldsymbol{B}}]_i^e$, and $[\boldsymbol{A}]_i^e$ initially presented in Section 3.9.4 in combination with the variations of the nodal unknowns $\delta\boldsymbol{\mathfrak{d}}^*$. In $(\text{B.12})_2$, the variation of the enhanced strains is approximated on *element level* by

$$\delta\bar{\boldsymbol{\varepsilon}}^{Eh} = \mathop{\mathsf{A}}\limits_{e=1}^{n_{en}} [\bar{\boldsymbol{G}}]^e\,\delta\bar{\boldsymbol{a}}^e = \bar{\boldsymbol{G}}(\boldsymbol{x})\,\delta\bar{\boldsymbol{a}} \tag{B.15}$$

based on the variation of the nodal incompatible modes $\delta\bar{\boldsymbol{a}}$ in combination with the element approximation matrix $[\bar{\boldsymbol{G}}]^e$. Making use of these discretizations, the reduced weak form (B.12) can be recast into its discrete counterpart

$$\begin{aligned} \Pi^{*h}_{\eta,\,\boldsymbol{\mathfrak{d}}^*} &:= \int_{\mathcal{B}^h} \{\, \boldsymbol{\mathfrak{B}}^{*T} [\partial_{\boldsymbol{\mathfrak{c}}^{*h}} \pi_\eta^{*h}] - \boldsymbol{\mathfrak{N}}^T \boldsymbol{\mathfrak{g}} \,\}\, dV - \int_{\partial\mathcal{B}^h_{\boldsymbol{\mathfrak{t}}}} \boldsymbol{\mathfrak{N}}^T \boldsymbol{\mathfrak{t}}_N \, dA \\ \Pi^{*h}_{\eta,\,\bar{\boldsymbol{a}}} &:= \int_{\mathcal{B}^h} \{\, \bar{\boldsymbol{G}}^T [\partial_{\bar{\boldsymbol{\varepsilon}}^h} \pi_\eta^{*h}] \,\}\, dV\,. \end{aligned} \tag{B.16}$$

This system of nonlinear equations can alternatively be rewritten as residual in the sense

$$\boldsymbol{r}(\boldsymbol{\mathfrak{d}}^*, \bar{\boldsymbol{a}}) := \begin{bmatrix} \Pi^{*h}_{\eta,\,\boldsymbol{\mathfrak{d}}^*} \\ \Pi^{*h}_{\eta,\,\bar{\boldsymbol{a}}} \end{bmatrix} = \boldsymbol{0}\,. \tag{B.17}$$

It is solved by a Newton iteration scheme that is based on the Taylor series expansion of the residual with truncation after the linear terms

$$\operatorname{Lin}\boldsymbol{r}(\boldsymbol{\mathfrak{d}}^*, \bar{\boldsymbol{a}}) := \boldsymbol{r}(\boldsymbol{\mathfrak{d}}^*, \bar{\boldsymbol{a}}) + \mathbb{K}(\boldsymbol{\mathfrak{d}}^*, \bar{\boldsymbol{a}}) \cdot \begin{bmatrix} \Delta\boldsymbol{\mathfrak{d}}^* \\ \Delta\bar{\boldsymbol{a}} \end{bmatrix} \quad \text{with} \quad \mathbb{K}(\boldsymbol{\mathfrak{d}}^*, \bar{\boldsymbol{a}}) := \begin{bmatrix} \Pi^{h*}_{\eta,\boldsymbol{\mathfrak{d}}^*\boldsymbol{\mathfrak{d}}^*} & \Pi^{h*}_{\eta,\boldsymbol{\mathfrak{d}}^*\bar{\boldsymbol{a}}} \\ \Pi^{*h}_{\eta,\bar{\boldsymbol{a}}\boldsymbol{\mathfrak{d}}^*} & \Pi^{*h}_{\eta,\bar{\boldsymbol{a}}\bar{\boldsymbol{a}}} \end{bmatrix}, \tag{B.18}$$

where the symmetric tangent matrix is introduced containing the second derivatives

$$\begin{aligned} \Pi^{h*}_{\eta,\boldsymbol{\mathfrak{d}}^*\boldsymbol{\mathfrak{d}}^*} &:= \int_{\mathcal{B}^h} \{\, \boldsymbol{\mathfrak{B}}^{*T} [\partial^2_{\boldsymbol{\mathfrak{c}}^{*h}\boldsymbol{\mathfrak{c}}^{*h}} \pi_\eta^{*h}] \boldsymbol{\mathfrak{B}}^* \,\}\, dV \\ \Pi^{h*}_{\eta,\boldsymbol{\mathfrak{d}}^*\bar{\boldsymbol{a}}} &:= \int_{\mathcal{B}^h} \{\, \boldsymbol{\mathfrak{B}}^{*T} [\partial^2_{\boldsymbol{\mathfrak{c}}^{*h}\bar{\boldsymbol{\varepsilon}}^h} \pi_\eta^{*h}] \bar{\boldsymbol{G}} \,\}\, dV \\ \Pi^{*h}_{\eta,\bar{\boldsymbol{a}}\boldsymbol{\mathfrak{d}}^*} &:= \int_{\mathcal{B}^h} \{\, \bar{\boldsymbol{G}}^T [\partial^2_{\bar{\boldsymbol{\varepsilon}}^h\boldsymbol{\mathfrak{c}}^{*h}} \pi_\eta^{*h}] \boldsymbol{\mathfrak{B}}^* \,\}\, dV \\ \Pi^{*h}_{\eta,\bar{\boldsymbol{a}}\bar{\boldsymbol{a}}} &:= \int_{\mathcal{B}^h} \{\, \bar{\boldsymbol{G}}^T [\partial^2_{\bar{\boldsymbol{\varepsilon}}^h\bar{\boldsymbol{\varepsilon}}^h} \pi_\eta^{*h}] \bar{\boldsymbol{G}} \,\}\, dV\,. \end{aligned} \tag{B.19}$$

Here, in full analogy to the discrete variations (B.14) and (B.15), the discrete increments have been expressed by the approximations

$$\Delta_{\mathfrak{u}^{*h}} \mathfrak{c}^{*h} = \mathfrak{B}^{*}(\boldsymbol{x})\, \Delta\mathfrak{d}^{*} \quad \text{and} \quad \Delta\bar{\boldsymbol{\varepsilon}}^{Eh} = \bar{\boldsymbol{G}}(\boldsymbol{x})\, \Delta\bar{\boldsymbol{a}}\,. \tag{B.20}$$

In order to eliminate the incompatible modes $\bar{\boldsymbol{a}}$ from the global finite element equations, a static condensation is performed, yielding the condensed residual

$$\boldsymbol{r}_{|\bar{\boldsymbol{a}}}(\mathfrak{d}^{*}) := \Pi^{*h}_{\eta,\mathfrak{d}^{*}} - \Pi^{*h}_{\eta,\mathfrak{d}^{*}\bar{\boldsymbol{a}}} \cdot [\Pi^{*h}_{\eta,\bar{\boldsymbol{a}}\bar{\boldsymbol{a}}}]^{-1} \cdot \Pi^{*h}_{\eta,\bar{\boldsymbol{a}}} = \boldsymbol{0}\,. \tag{B.21}$$

The condensed version of the linearization (B.18) can then be expressed by

$$\operatorname{Lin} \boldsymbol{r}_{|\bar{\boldsymbol{a}}}(\mathfrak{d}^{*}, \Delta\mathfrak{d}^{*}) := \boldsymbol{r}_{|\bar{\boldsymbol{a}}}(\mathfrak{d}^{*}) + \mathbb{K}_{|\bar{\boldsymbol{a}}}(\mathfrak{d}^{*}) \cdot \Delta\mathfrak{d}^{*}\,, \tag{B.22}$$

and bases on the modified stiffness matrix

$$\mathbb{K}_{|\bar{\boldsymbol{a}}}(\mathfrak{d}^{*}) := \Pi^{*h}_{\eta,\mathfrak{d}^{*}\mathfrak{d}^{*}} - \Pi^{*h}_{\eta,\mathfrak{d}^{*}\bar{\boldsymbol{a}}} \cdot [\Pi^{*h}_{\eta,\bar{\boldsymbol{a}}\bar{\boldsymbol{a}}}]^{-1} \cdot \Pi^{*h}_{\eta,\bar{\boldsymbol{a}}\mathfrak{d}^{*}}\,. \tag{B.23}$$

The solution of the reduced residual is performed in a classical Newton iteration scheme, where the according update directive is given by the expression

$$\mathfrak{d}^{*} \Leftarrow \mathfrak{d}^{*} - \mathbb{K}^{-1}_{|\bar{\boldsymbol{a}}}(\mathfrak{d}^{*}) \cdot \boldsymbol{r}_{|\bar{\boldsymbol{a}}}(\mathfrak{d}^{*}) \quad \text{until} \quad \|\boldsymbol{r}_{|\bar{\boldsymbol{a}}}(\mathfrak{d}^{*})\| \leq \text{tol}\,. \tag{B.24}$$

Note that regarding a finite element implementation, *no inter-element continuity* of the enhanced strains $\bar{\boldsymbol{\varepsilon}}^{Eh}$ has to be enforced. Thus, the static condensation can be performed locally on *element level* $\mathcal{B}^e$. For two-dimensional problems, the enhanced incompatible modes are approximated directly on element level via the element matrix

$$[\bar{\boldsymbol{G}}]^e := \frac{\det[\boldsymbol{J}^0]}{\det[\boldsymbol{J}]}\, [\boldsymbol{F}_0]^e\, [\boldsymbol{E}]^e \tag{B.25}$$

based on the element matrices $[\boldsymbol{F}_0]^e$ and $[\boldsymbol{E}]^e$ describing a transformation law to connect the parameter space with the physical space and a matrix containing the shape functions for the enhanced strains. According to Simo & Rifai [165], they can be specified to

$$[\boldsymbol{F}_0]^e = \begin{bmatrix} J^0_{11}J^0_{11} & J^0_{21}J^0_{21} & J^0_{11}J^0_{21} \\ J^0_{12}J^0_{12} & J^0_{22}J^0_{22} & J^0_{12}J^0_{22} \\ 2J^0_{11}J^0_{12} & 2J^0_{21}J^0_{22} & J^0_{11}J^0_{22}+J^0_{12}J^0_{21} \end{bmatrix} \quad \text{and} \quad [\boldsymbol{E}]^e = \begin{bmatrix} \xi_1 & 0 & 0 & 0 & \xi_1\xi_2 \\ 0 & \xi_2 & 0 & 0 & -\xi_1\xi_2 \\ 0 & 0 & \xi_1 & \xi_2 & \xi_1^2\xi_2^2 \end{bmatrix}, \tag{B.26}$$

where the components J^0_{ij} are the entries of the Jacobian $\boldsymbol{J}$, evaluated at the local element coordinates $\boldsymbol{\xi} = \boldsymbol{0}$. The overall solution algorithm is summarized in Box 3.

B.2. Enhanced Strain Formulation for Geometrically Nonlinear Problems

This section shortly outlines the multi-field implementation of an enhanced assumed strain method in the macroscopic Lagrangian setting. Following Simo & Armero [160] and Simo, Armero & Taylor [161], the current macroscopic displacement gradient

$$\bar{\boldsymbol{H}} = \nabla_{\boldsymbol{X}} \bar{\boldsymbol{u}} + \nabla_{\boldsymbol{X}} \bar{\boldsymbol{u}}^{E} \tag{B.27}$$

is re-parametrized by a *compatible* and an *enhanced* displacement gradient $\nabla_{\boldsymbol{X}} \bar{\boldsymbol{u}}$ and $\nabla_{\boldsymbol{X}} \bar{\boldsymbol{u}}^{E}$. Thus, the actual macroscopic deformation gradient $\bar{\boldsymbol{F}} = \boldsymbol{1} + \bar{\boldsymbol{H}}$ can be rewritten

$$\bar{\boldsymbol{F}}(\bar{\boldsymbol{\varphi}}, \bar{\boldsymbol{u}}^{E}) = \nabla_{\boldsymbol{X}} \bar{\boldsymbol{\varphi}} + \nabla_{\boldsymbol{X}} \bar{\boldsymbol{u}}^{E} \quad \text{with} \quad \nabla_{\boldsymbol{X}} \bar{\boldsymbol{\varphi}} = \boldsymbol{1} + \nabla_{\boldsymbol{X}} \bar{\boldsymbol{u}} \tag{B.28}$$

as a function of the compatible deformation map $\bar{\boldsymbol{\varphi}}$ and the *enhanced displacement field* $\bar{\boldsymbol{u}}^{E}$. In a macroscopic Lagrangian formulation, the macroscopic right Cauchy-Green tensor

$$\bar{\boldsymbol{C}}(\bar{\boldsymbol{\varphi}}, \bar{\boldsymbol{u}}^{E}) = \bar{\boldsymbol{F}}^{T} \bar{\boldsymbol{g}} \bar{\boldsymbol{F}} \tag{B.29}$$

contains the re-parametrization (B.28) and enters the generalized constitutive state.

Box 3: Solution procedure of enhanced strain formulation.

1. *Compute enhanced residual* $\Pi^{*h^e}_{\eta\, n,\bar{\boldsymbol{a}}}$ on element level by equation (B.16)$_2$ or (B.46)$_2$, evaluated at time t_n, and *update* incompatible modes $\bar{\boldsymbol{a}}^e$ according to

$$\bar{\boldsymbol{a}}^e = \bar{\boldsymbol{a}}^e_n - [\Pi^{*h^e}_{\eta\, n,\bar{\boldsymbol{a}}\bar{\boldsymbol{a}}}]^{-1} \cdot [\Pi^{*h^e}_{\eta\, n,\bar{\boldsymbol{a}}\boldsymbol{\mathfrak{d}}^*} \cdot \boldsymbol{\mathfrak{d}}^{*e}_{\;n} - \Pi^{*h^e}_{\eta\, n,\bar{\boldsymbol{a}}}] \, .$$

2. *Compute modified residual* by static condensation on element level

$$\boldsymbol{r}^e_{n|\bar{\boldsymbol{a}}}(\boldsymbol{\mathfrak{d}}^{*e}_n) := \Pi^{*h^e}_{\eta\, n,\boldsymbol{\mathfrak{d}}^*} - \Pi^{*h^e}_{\eta\, n,\boldsymbol{\mathfrak{d}}^*\bar{\boldsymbol{a}}} \cdot [\Pi^{*h^e}_{\eta\, n,\bar{\boldsymbol{a}}\bar{\boldsymbol{a}}}]^{-1} \cdot \Pi^{*h^e}_{\eta\, n,\bar{\boldsymbol{a}}} \, .$$

3. *Compute modified tangent* by static condensation on element level

$$\mathbb{K}^e_{n|\bar{\boldsymbol{a}}}(\boldsymbol{\mathfrak{d}}^{*e}_n) := \Pi^{*h^e}_{\eta\, n,\boldsymbol{\mathfrak{d}}^*\boldsymbol{\mathfrak{d}}^*} - \Pi^{*h^e}_{\eta\, n,\boldsymbol{\mathfrak{d}}^*\bar{\boldsymbol{a}}} \cdot [\Pi^{*h^e}_{\eta\, n,\bar{\boldsymbol{a}}\bar{\boldsymbol{a}}}]^{-1} \cdot \Pi^{*h^e}_{\eta\, n,\bar{\boldsymbol{a}}\boldsymbol{\mathfrak{d}}^*} \, .$$

4. *Assemble global residual and tangent arrays*

$$\boldsymbol{r}_{n|\bar{\boldsymbol{a}}}(\boldsymbol{\mathfrak{d}}^*{}_n) = \mathop{\mathsf{A}}_{e=1}^{n_{en}} \boldsymbol{r}^e_{n|\bar{\boldsymbol{a}}}(\boldsymbol{\mathfrak{d}}^{*e}_n) \quad \text{and} \quad \mathbb{K}_{n|\bar{\boldsymbol{a}}}(\boldsymbol{\mathfrak{d}}^*{}_n) = \mathop{\mathsf{A}}_{e=1}^{n_{en}} \mathbb{K}^e_{n|\bar{\boldsymbol{a}}}(\boldsymbol{\mathfrak{d}}^{*e}_n) \, .$$

5. *Solve for increments* and *update solution* in Newton scheme

$$\boldsymbol{\mathfrak{d}}^* \Leftarrow \boldsymbol{\mathfrak{d}}^*_n - \mathbb{K}^{-1}_{n|\bar{\boldsymbol{a}}}(\boldsymbol{\mathfrak{d}}^*_n) \cdot \boldsymbol{r}_{n|\bar{\boldsymbol{a}}}(\boldsymbol{\mathfrak{d}}^*_n) \quad \text{until} \quad \|\boldsymbol{r}_{n|\bar{\boldsymbol{a}}}(\boldsymbol{\mathfrak{d}}^*_n)\| \leq \text{tol} \, .$$

B.2.1. Time-Discrete Incremental Variational Principle. The re-parametrization of the macroscopic right Cauchy-Green tensor (B.29) is employed to modify the generalized constitutive state (A.1) in a macroscopic Lagrangian setup

$$\boldsymbol{\mathfrak{c}}_L(\boldsymbol{\mathfrak{u}}, \bar{\boldsymbol{u}}^E) := \{\, \bar{\boldsymbol{C}}(\bar{\boldsymbol{\varphi}}, \bar{\boldsymbol{u}}^E), \check{\boldsymbol{\varphi}}, \check{\boldsymbol{F}} \,\} \quad \text{with} \quad \boldsymbol{\mathfrak{u}} := \{\, \bar{\boldsymbol{\varphi}}, \check{\boldsymbol{\varphi}} \,\} \, . \tag{B.30}$$

In order to formulate the rate-dependent variational principle with threshold function, the extended constitutive state (A.2) in the re-parametrized version is employed

$$\boldsymbol{\mathfrak{c}}^*_L(\boldsymbol{\mathfrak{u}}^*_L, \bar{\boldsymbol{u}}^E) := \{\, \bar{\boldsymbol{C}}(\bar{\boldsymbol{\varphi}}, \bar{\boldsymbol{u}}^E), \check{\boldsymbol{\varphi}}, \check{\boldsymbol{F}}, \boldsymbol{\mathfrak{f}}_L \,\} \quad \text{with} \quad \boldsymbol{\mathfrak{u}}^*_L := \{\, \bar{\boldsymbol{\varphi}}, \check{\boldsymbol{\varphi}}, \boldsymbol{\mathfrak{f}}_L \,\} \tag{B.31}$$

in terms of the thermodynamic driving forces (A.3). It enters the incremental potential

$$\Pi^{*\tau}_\eta(\boldsymbol{\mathfrak{u}}^*_L, \bar{\boldsymbol{u}}^E, \bar{\boldsymbol{P}}) = \int_{\mathcal{B}} \{\, \pi^{*\tau}_\eta(\boldsymbol{\mathfrak{c}}^*_L; \boldsymbol{\mathfrak{c}}^*_{Ln}) - \boldsymbol{\mathfrak{g}} \cdot (\boldsymbol{\mathfrak{u}} - \boldsymbol{\mathfrak{u}}_n) \,\} \, dV - \int_{\partial\mathcal{B}_{\mathfrak{t}}} \boldsymbol{\mathfrak{t}}_N \cdot (\boldsymbol{\mathfrak{u}} - \boldsymbol{\mathfrak{u}}_n) \, dA \, . \tag{B.32}$$

In contrast to (A.7), this incremental potential bases on an extension of the Hu-Washitsu principle to the underlying multi-field problem. Its main ingredient is the *extended incremental internal work density*

$$\begin{aligned} \pi^{*\tau}_\eta(\boldsymbol{\mathfrak{c}}^*_L; \boldsymbol{\mathfrak{c}}^*_{Ln}) = {} & \psi(\boldsymbol{\mathfrak{c}}_L) - \bar{\boldsymbol{g}}\bar{\boldsymbol{P}} : \nabla_{\boldsymbol{X}} \bar{\boldsymbol{u}}^E - \psi(\boldsymbol{\mathfrak{c}}_{Ln}) + \bar{\boldsymbol{g}}\bar{\boldsymbol{P}}_n : \nabla_{\boldsymbol{X}} \bar{\boldsymbol{u}}^E_n \\ & + \boldsymbol{\mathfrak{f}}_L \cdot (\boldsymbol{\mathfrak{c}}_L - \boldsymbol{\mathfrak{c}}_{Ln}) - \frac{\tau}{2\eta} \langle \varphi(\boldsymbol{\mathfrak{f}}_L; \boldsymbol{\mathfrak{c}}_{Ln}) \rangle^2_+ \end{aligned} \tag{B.33}$$

governed by the free energy function ψ as a function of the enhanced constitutive state $(\mathrm{B}.30)_1$, the yield function φ, and the *actual stress* $\bar{\boldsymbol{P}}$. The variational principle

$$\boxed{\{\,\bar{\boldsymbol{\varphi}}, \check{\boldsymbol{\varphi}}, \mathfrak{f}_L, \bar{\boldsymbol{u}}^E, \bar{\boldsymbol{P}}\,\} = \arg\{\,\inf_{\bar{\boldsymbol{\varphi}}} \inf_{\check{\boldsymbol{\varphi}}} \sup_{\mathfrak{f}_L} \inf_{\bar{\boldsymbol{u}}^E} \sup_{\bar{\boldsymbol{P}}} \Pi^{*\tau}_\eta(\bar{\boldsymbol{\varphi}}, \check{\boldsymbol{\varphi}}, \mathfrak{f}_L, \bar{\boldsymbol{u}}^E, \bar{\boldsymbol{P}})\,\}} \tag{B.34}$$

determines the macro- and microscopic deformation map $\bar{\boldsymbol{\varphi}}$ and $\check{\boldsymbol{\varphi}}$, the dissipative thermodynamic driving force $\mathfrak{f}_L$, the enhanced displacements $\bar{\boldsymbol{u}}^E$, and the actual stresses $\bar{\boldsymbol{P}}$ as the *saddle point* of the incremental functional (B.32). The necessary condition reads

$$\delta\Pi^{*\tau}_\eta = \delta_{\mathfrak{u}^*_L}\Pi^{*\tau}_\eta + \delta_{\bar{\boldsymbol{u}}^E}\Pi^{*\tau}_\eta + \delta_{\bar{\boldsymbol{P}}}\Pi^{*\tau}_\eta = 0\,, \tag{B.35}$$

where the generalized unknowns $\mathfrak{u}^*_L$ allow for the compact representation

$$\begin{aligned} \delta_{\mathfrak{u}^*_L}\Pi^{*\tau}_\eta &:= \int_{\mathcal{B}} \{\,[\partial_{\mathfrak{c}^*_L}\pi^{*\tau}_\eta]\cdot\delta_{\mathfrak{u}^*_L}\mathfrak{c}^*_L - \mathfrak{g}\cdot\delta\mathfrak{u}\,\}\,dV - \int_{\partial\mathcal{B}_{\mathfrak{t}}} \mathfrak{t}_N\cdot\delta\mathfrak{u}\,dA \\ \delta_{\bar{\boldsymbol{u}}^E}\Pi^{*\tau}_\eta &:= \int_{\mathcal{B}} \{\,[\partial_{\bar{\boldsymbol{C}}}\pi^{*\tau}_\eta] : \delta_{\bar{\boldsymbol{u}}^E}\bar{\boldsymbol{C}} - \bar{\boldsymbol{g}}\bar{\boldsymbol{P}} : \nabla_{\boldsymbol{X}}\delta\bar{\boldsymbol{u}}^E\,\}\,dV \\ \delta_{\bar{\boldsymbol{P}}}\Pi^{*\tau}_\eta &:= \int_{\mathcal{B}} \{\,[\partial_{\bar{\boldsymbol{P}}}\pi^{*\tau}_\eta] : \delta\bar{\boldsymbol{P}}\,\}\,dV\,. \end{aligned} \tag{B.36}$$

Here, the variation of the enhanced constitutive state (B.31) with respect to the generalized deformation vector $\mathfrak{u}^*_L$ can be summarized by

$$\delta_{\mathfrak{u}^*_L}\mathfrak{c}^*_L := \{\,2\,\mathrm{sym}[\bar{\boldsymbol{F}}^T\bar{\boldsymbol{g}}\nabla_{\boldsymbol{X}}\delta\bar{\boldsymbol{\varphi}}], \delta\check{\boldsymbol{\varphi}}, \nabla_{\boldsymbol{X}}\delta\check{\boldsymbol{\varphi}}, \delta\mathfrak{f}_L\,\}\,. \tag{B.37}$$

Similarly, the variation of the right Cauchy-Green tensor with respect to the enhanced displacement field $\bar{\boldsymbol{u}}^E$ can be specified

$$\delta_{\bar{\boldsymbol{u}}^E}\bar{\boldsymbol{C}} := 2\,\mathrm{sym}[\bar{\boldsymbol{F}}^T\bar{\boldsymbol{g}}\nabla_{\boldsymbol{X}}\delta\bar{\boldsymbol{u}}^E]\,. \tag{B.38}$$

Note that due to the specific re-parametrization (B.29) only the macroscopic entries are affected. Equation $(\mathrm{B}.36)_1$ represents in a compact format the Euler equations of the stationary principle (A.10) whose strong form is summarized in Table A.1. The local form of the enhanced modes subproblem $(\mathrm{B}.36)_{2,3}$ is given by

$$\bar{\boldsymbol{P}} = 2\bar{\boldsymbol{F}}(\partial_{\bar{\boldsymbol{C}}}\psi(\mathfrak{c}_L) + \bar{\boldsymbol{\mathcal{F}}}_L) \quad \text{and} \quad \nabla_{\boldsymbol{X}}\bar{\boldsymbol{u}}^E = \boldsymbol{0}\,. \tag{B.39}$$

The first equation describes the *actual stress* $\bar{\boldsymbol{P}}$, the second one enforces vanishing enhanced strains $\nabla_{\boldsymbol{X}}\bar{\boldsymbol{u}}^E = \boldsymbol{0}$ in the solution domain $\mathcal{B}$. This is obvious in the continuous setting, but is violated by a finite element approximation, i.e. $\nabla_{\boldsymbol{X}}\bar{\boldsymbol{u}}^{Eh} \neq \boldsymbol{0}$ in $\mathcal{B}^h$.

B.2.2. Finite-Element Discretization of Weak Form. Before discretizing the weak form, the L_2-orthogonality of the discrete actual stresses $\bar{\boldsymbol{P}}^h$ and the discrete enhanced displacement gradient $\nabla_{\boldsymbol{X}}\bar{\boldsymbol{u}}^{Eh}$ is exploited. Thus, consider the discretized version of $(\mathrm{B}.35)_3$

$$\delta_{\bar{\boldsymbol{P}}^h}\Pi^{*h}_\eta = -\int_{\mathcal{B}^h}\{\,\bar{\boldsymbol{g}}\nabla_{\boldsymbol{X}}\bar{\boldsymbol{u}}^{Eh} : \delta\bar{\boldsymbol{P}}^h\,\}\,dV = -\int_{\mathcal{B}^h}\{\,\bar{\boldsymbol{g}}\bar{\boldsymbol{P}}^h : \nabla_{\boldsymbol{X}}\delta\bar{\boldsymbol{u}}^{Eh}\,\}\,dV = 0\,, \tag{B.40}$$

where the explicit expression $[\partial_{\bar{\boldsymbol{P}}}\pi^{*\tau}_\eta] : \delta\bar{\boldsymbol{P}} = -\bar{\boldsymbol{g}}\nabla_{\boldsymbol{X}}\bar{\boldsymbol{u}}^E : \delta\bar{\boldsymbol{P}}$ has been employed. As a consequence, equation (B.40) is identical satisfied in the discrete setting, if the last term in (B.36)$_2$ vanishes. Thus, the L_2-orthogonality effectively eliminates the stress field from the finite element equations, the reduced set of *discrete* equations is obtained

$$\begin{aligned} \delta_{\mathfrak{u}_L^{*h}} \Pi_\eta^{*h} &= \int_{\mathcal{B}^h} \{ [\partial_{\mathfrak{c}_L^{*h}} \pi_\eta^{*h}] \cdot \delta_{\mathfrak{u}_L^*} \mathfrak{c}_L^{*h} - \mathfrak{g} \cdot \delta \mathfrak{u}^h \} \, dV - \int_{\partial \mathcal{B}_{\mathfrak{t}}} \mathfrak{t}_N \cdot \delta \mathfrak{u}^h \, dA \\ \delta_{\bar{\boldsymbol{u}}^{Eh}} \Pi_\eta^{*h} &= \int_{\mathcal{B}^h} \{ [\partial_{\bar{\boldsymbol{C}}^h} \pi_\eta^{*h}] : \delta_{\bar{\boldsymbol{u}}^E} \bar{\boldsymbol{C}}^h \} \, dV \, . \end{aligned} \tag{B.41}$$

Instead of discretizing the entire variational principle as discussed in Section A.2 for the general FE-treatment, the discretization starts with the reduced weak form (B.41). According to (A.11), the discrete generalized displacements are approximated via

$$\mathfrak{u}_L^{*h} = \mathop{\mathsf{A}}_{e=1}^{n_{en}} \left[\sum_{i=1}^{n_{el}} \begin{bmatrix} [\mathfrak{N}]_i^e & \boldsymbol{0} \\ \boldsymbol{0} & [\boldsymbol{A}]_i^e \end{bmatrix} \begin{bmatrix} \mathfrak{d} \\ \boldsymbol{f}_L \end{bmatrix}_i \right]^e = \mathop{\mathsf{A}}_{e=1}^{n_{en}} \begin{bmatrix} [\mathfrak{N}]^e & \boldsymbol{0} \\ \boldsymbol{0} & [\boldsymbol{A}]^e \end{bmatrix} \begin{bmatrix} \mathfrak{d} \\ \boldsymbol{f}_L \end{bmatrix}^e =: \mathfrak{N}^*(\boldsymbol{X}) \, \mathfrak{d}_L^* \, . \tag{B.42}$$

In addition to the discrete generalized displacements $\mathfrak{u}_L^{*h}$, the discrete version of the enhanced displacement field is defined by the approximation

$$\bar{\boldsymbol{u}}^{Eh} = \mathop{\mathsf{A}}_{e=1}^{n_{en}} \left[\sum_{i=1}^{n_{fi}} G_i \, \bar{\boldsymbol{a}}_i^e \right] \tag{B.43}$$

that bases on the incompatible shape functions G_i and the incompatible modes $\bar{\boldsymbol{a}}_i$. Note that the summation is not performed over the number of nodes per element n_{el}, it is performed over the number of fictitious internal nodes n_{fi}. In line with (A.16), the discrete variation of the generalized constitutive state is given by

$$\delta_{\mathfrak{u}_L^*} \mathfrak{c}_L^{*h} = \mathop{\mathsf{A}}_{e=1}^{n_{en}} \left[\sum_{i=1}^{n_{el}} \begin{bmatrix} [2\bar{\boldsymbol{B}}_M(\bar{\boldsymbol{d}}^e, \bar{\boldsymbol{a}}^e)]_i^e & \boldsymbol{0} & \boldsymbol{0} \\ \boldsymbol{0} & [\check{\boldsymbol{B}}]_i^e & \boldsymbol{0} \\ \boldsymbol{0} & \boldsymbol{0} & [\boldsymbol{A}]_i^e \end{bmatrix} \begin{bmatrix} \delta \bar{\boldsymbol{d}} \\ \delta \check{\boldsymbol{d}} \\ \delta \boldsymbol{f}_L \end{bmatrix}_i \right]^e =: \mathfrak{B}_M^*(\boldsymbol{X}) \, \delta \mathfrak{d}_L^* \, . \tag{B.44}$$

The discrete variation of the generalized constitutive state with respect to the nodal incompatible modes takes the form

$$\delta_{\bar{\boldsymbol{a}}} \mathfrak{c}_L^{*h} = \mathop{\mathsf{A}}_{e=1}^{n_{en}} \left[\sum_{i=1}^{n_{fi}} [2\bar{\boldsymbol{G}}_M(\bar{\boldsymbol{d}}^e, \bar{\boldsymbol{a}}^e)]_i^e \delta \bar{\boldsymbol{a}}_i^e \right] =: \bar{\boldsymbol{G}}_M(\boldsymbol{X}) \, \delta \bar{\boldsymbol{a}} \, . \tag{B.45}$$

Based on these discretizations, the weak form (B.41) can be recast into

$$\begin{aligned} \Pi_{\eta\,,\,\mathfrak{d}_L^*}^{*h} &:= \int_{\mathcal{B}^h} \{ \mathfrak{B}_M^{*\,T} [\partial_{\mathfrak{c}_L^{*h}} \pi_\eta^{*h}] - \mathfrak{N}^T \mathfrak{g} \} \, dV - \int_{\partial \mathcal{B}_{\mathfrak{t}}^h} \mathfrak{N}^T \mathfrak{t}_N \, dA \\ \Pi_{\eta\,,\,\bar{\boldsymbol{a}}}^{*h} &:= \int_{\mathcal{B}^h} \{ \bar{\boldsymbol{G}}_M^T [\partial_{\bar{\boldsymbol{C}}^h} \pi_\eta^{*h}] \} \, dV \, . \end{aligned} \tag{B.46}$$

This system of nonlinear algebraic equations can alternatively be reformulated as residual

$$\boldsymbol{r}(\mathfrak{d}_L^*, \bar{\boldsymbol{a}}) := \begin{bmatrix} \Pi_{\eta\,,\,\mathfrak{d}_L^*}^{*h} \\ \Pi_{\eta\,,\,\bar{\boldsymbol{a}}}^{*h} \end{bmatrix} = \boldsymbol{0} \, . \tag{B.47}$$

The first step towards a Newton iterative solution scheme bases on a Taylor series expansion of the residual with truncation after the linear terms

$$\operatorname{Lin} \boldsymbol{r}(\boldsymbol{\mathfrak{d}}^*_L,\bar{\boldsymbol{a}}) = \boldsymbol{r}(\boldsymbol{\mathfrak{d}}^*_L,\bar{\boldsymbol{a}}) + \mathbb{K}(\boldsymbol{\mathfrak{d}}^*_L,\bar{\boldsymbol{a}}) \cdot \begin{bmatrix} \Delta \boldsymbol{\mathfrak{d}}^*_L \\ \Delta \bar{\boldsymbol{a}} \end{bmatrix} \quad \text{with} \quad \mathbb{K}(\boldsymbol{\mathfrak{d}}^*_L,\bar{\boldsymbol{a}}) := \begin{bmatrix} \Pi^{*h}_{\eta,\,\boldsymbol{\mathfrak{d}}^*_L\boldsymbol{\mathfrak{d}}^*_L} & \Pi^{*h}_{\eta,\,\boldsymbol{\mathfrak{d}}^*_L\bar{\boldsymbol{a}}} \\ \Pi^{*h}_{\eta,\,\bar{\boldsymbol{a}}\boldsymbol{\mathfrak{d}}^*_L} & \Pi^{*h}_{\eta,\,\bar{\boldsymbol{a}}\bar{\boldsymbol{a}}} \end{bmatrix} \tag{B.48}$$

consisting of the symmetric tangent matrix of the finite element system

$$\begin{aligned}
\Pi^{*h}_{\eta,\,\boldsymbol{\mathfrak{d}}^*_L\boldsymbol{\mathfrak{d}}^*_L} &:= \int_{\mathcal{B}^h} \{\, \boldsymbol{\mathfrak{B}}^{*\,T}_M [\partial^2_{\boldsymbol{\mathfrak{c}}^{*h}_L \boldsymbol{\mathfrak{c}}^{*h}_L} \pi^{*h}_\eta] \boldsymbol{\mathfrak{B}}^*_M + \boldsymbol{\mathfrak{B}}^{*T}_G [\bar{\mathbb{S}}^*_L] \boldsymbol{\mathfrak{B}}^*_G \,\}\, dV \\
\Pi^{*h}_{\eta,\,\boldsymbol{\mathfrak{d}}^*_L\bar{\boldsymbol{a}}} &:= \int_{\mathcal{B}^h} \{\, \boldsymbol{\mathfrak{B}}^{*\,T}_M [\partial^2_{\boldsymbol{\mathfrak{c}}^{*h}_L \bar{\boldsymbol{C}}^h} \pi^{*h}_\eta] \bar{\boldsymbol{G}}_M + \boldsymbol{\mathfrak{B}}^{*T}_G [\bar{\mathbb{S}}^*_L] \bar{\boldsymbol{G}}_G \,\}\, dV \\
\Pi^{*h}_{\eta,\,\bar{\boldsymbol{a}}\boldsymbol{\mathfrak{d}}^*_L} &:= \int_{\mathcal{B}^h} \{\, \bar{\boldsymbol{G}}^T_M [\partial^2_{\bar{\boldsymbol{C}}^h \boldsymbol{\mathfrak{c}}^{*h}_L} \pi^{*h}_\eta] \boldsymbol{\mathfrak{B}}^*_M + \bar{\boldsymbol{G}}^T_G [\bar{\mathbb{S}}^*_L] \boldsymbol{\mathfrak{B}}^*_G \,\}\, dV \\
\Pi^{*h}_{\eta,\,\bar{\boldsymbol{a}}\bar{\boldsymbol{a}}} &:= \int_{\mathcal{B}^h} \{\, \bar{\boldsymbol{G}}^T_M [\partial^2_{\bar{\boldsymbol{C}}^h \bar{\boldsymbol{C}}^h} \pi^{*h}_\eta] \bar{\boldsymbol{G}}_M + \bar{\boldsymbol{G}}^T_G [\bar{\mathbb{S}}^*_L] \bar{\boldsymbol{G}}_G \,\}\, dV\,.
\end{aligned} \tag{B.49}$$

In analogy to the tangent matrix (A.19) material and geometric terms occur. The geometric term is related to the approximation matrices $[\bar{\boldsymbol{\mathfrak{B}}}_M(\bar{\boldsymbol{d}}^e, \bar{\boldsymbol{a}}^e)]^e_i$ and $[\bar{\boldsymbol{G}}_M(\bar{\boldsymbol{d}}^e, \bar{\boldsymbol{a}}^e)]^e_i$ that are (linear) functions of the actual macroscopic deformation $\bar{\boldsymbol{d}}^e$ and the incompatible modes $\bar{\boldsymbol{a}}^e$. For a definition of the geometric approximation tensors $\boldsymbol{\mathfrak{B}}^*_G$ and the macroscopic stresses in matrix notation $\bar{\mathbb{S}}^*_L$ see equation (A.20). In addition to (A.19), the enhanced increment has to be taken into account via

$$\bar{\boldsymbol{G}}^*_G := \mathop{\mathsf{A}}_{e=1}^{n_{en}} \left[\sum_{i=1}^{n_{fi}} [\bar{\boldsymbol{G}}]^e_i \right] = \mathop{\mathsf{A}}_{e=1}^{n_{en}} [\bar{\boldsymbol{G}}]^e\,. \tag{B.50}$$

In analogy to the small strain setting, the nodal incompatible modes $\bar{\boldsymbol{a}}$ are eliminated by a static condensation procedure. Regarding a finite element implementation, *no inter-element continuity* of the enhanced displacement field $\bar{\boldsymbol{u}}^{Eh}$ has to be enforced. Thus, the static condensation is performed locally on *element level* $\mathcal{B}^e$. For setting $\boldsymbol{\mathfrak{d}}^* := \boldsymbol{\mathfrak{d}}^*_L$ in equations (B.21)-(B.24) and in Box 3, this solution procedure is recovered. For two-dimensional problems, the matrices for the approximation of the enhanced gradients (B.45) and the geometric tangent contributions (B.50) can be specified

$$[\bar{\boldsymbol{G}}_M]^e_i = \begin{bmatrix} \bar{F}^{he}_{11} G_{,1} & \bar{F}^{he}_{12} G_{,2} & (\bar{F}^{he}_{11} G_{,2} + \bar{F}^{he}_{12} G_{,1}) \\ \bar{F}^{he}_{21} G_{,1} & \bar{F}^{he}_{22} G_{,2} & (\bar{F}^{he}_{21} G_{,2} + \bar{F}^{he}_{22} G_{,1}) \end{bmatrix}^T_i \quad \text{and} \quad [\bar{\boldsymbol{G}}_G]^e_i = \begin{bmatrix} G_{,1} & 0 & G_{,2} & 0 \\ 0 & G_{,2} & 0 & G_{,1} \end{bmatrix}^T_i . \tag{B.51}$$

In line with Miehe [114], the enhanced shape functions and the incompatible modes are

$$G_i = \tfrac{1}{2}\,(\xi_i^2 - 1) \quad \text{and} \quad \bar{\boldsymbol{a}}_i = [\bar{a}_1, \bar{a}_2]^T_i \quad \text{for} \quad i = 1, \dots, n_{fi} \tag{B.52}$$

for the number of fictitious internal nodes per element $n_{fi} = 2$. Thus, in total there are 4 element parameters for the approximation of the incompatible modes on element level. In (B.52), the derivatives of the shape functions G_i with respect to the Lagrangian coordinates are obtained by the relation

$$\nabla_{\boldsymbol{X}} G_i = \frac{\det[\boldsymbol{J}_0]}{\det[\boldsymbol{J}]} \nabla_{\boldsymbol{\xi}} G_i \boldsymbol{J}_0^{-1} \quad \text{with} \quad \boldsymbol{J} := \nabla_{\boldsymbol{\xi}} \boldsymbol{x}^h = \sum_{i=1}^{n_{el}} \nabla_{\boldsymbol{\xi}} N_i \boldsymbol{x}_i\,, \tag{B.53}$$

in terms of the Jacobian $\boldsymbol{J}_0$ evaluated at the local element coordinates $\boldsymbol{\xi} = \boldsymbol{0}$, the standard isoparametric shape functions N_i, and the local coordinates $\boldsymbol{x}_i$ of the element.

References

[1] Alshibli, K. A.; Batiste, S. N.; Sture, S. [2003]: *Strain localization in sand: plane strain versus triaxial compression.* Journal of Geotechnical and Geoenvironmental Engineering, 6: 483–494.

[2] Ambrosio, L.; Tortorelli, V. M. [1990]: *Approximation of functionals depending on jumps by elliptic functionals via* Γ*-convergence.* Communications on Pure and Applied Mathematics, 153: 999–1036.

[3] Anand, L.; Gurtin, M. E.; Lele, S. P.; Gething, C. [2005]: *A one-dimensional theory of strain-gradient plasticity: formulation, analysis, numerical results.* Journal of the Mechanics and Physics of Solids, 53: 1789–1826.

[4] Arzt, E. [1998]: *Size effects in materials due to microstructural and dimensional constraints: a comparative review.* Acta Materialia, 46: 5611–5626.

[5] Ashby, M. F. [1970]: *The deformation of plastically non-homogeneous materials.* The Philosophical Magazine A, 21: 399–424.

[6] Barenblatt, G. I. [1962]: *The mathematical theory of equilibrium cracks in brittle fracture.* Advances in Applied Mechanics, 7: 55–129.

[7] Başar, Y.; Weichert, D. [2000]: *Nonlinear Continuum Mechanics of Solids.* Springer.

[8] Baydoun, M. [2009]: *Configurational-force-based h-adaptive methods in gradient-type standard solids with application to regularized fracture.* Technical Report 09-I-02, Institut für Mechanik (Bauwesen), Lehrstuhl I, Universität Stuttgart.

[9] Bažant, Z. P.; Lin, F. B. [1988]: *Non-local yield limit degradation.* International Journal for Numerical Methods in Engineering, 26: 1805–1823.

[10] Bažant, Z. P.; Oh, O. H. [1983]: *Crack band theory for fracture of concrete.* Materials and Structures, 16: 155–177.

[11] Becker, M. [2006]: *Incompatibility and instability based size effects in crystals and composites at finite elastoplastic strains.* Ph.D. Thesis, Institut für Mechanik (Bauwesen), Lehrstuhl I, Universität Stuttgart.

[12] Belytschko, T.; Fish, J.; Engelmann, E. [1988]: *A finite element with embedded localization zones.* Computer Methods in Applied Mechanics and Engineering, 70: 59–89.

[13] Biot, M. A. [1954]: *Theory of stress-strain relations in anisotropic viscoelasticity and relaxation phenomena.* Journal of Applied Physics, 25: 1385–1391.

[14] Biot, M. A. [1965]: *Mechanics of Incremental Deformations.* John Wiley & Sons, New York.

[15] Bittencourt, T. N.; Wawrzynek, P. A.; Ingraffea, A. R.; Sousa, J. L. [1996]: *Quasi-automatic simulation of crack propagation for 2D LEFM problems.* Engineering Fracture Mechanics, 55: 321–334.

[16] Bourdin, B.; Francfort, G. A.; Marigo, J.-J. [2000]: *Numerical experiments in revisited brittle fracture.* Journal of the Mechanics and Physics of Solids, 48: 797–826.

[17] Bourdin, B.; Francfort, G.; Marigo, J.-J. [2008]: *The Variational Approach to Fracture.* Springer.

[18] Braides, A. [1998]: *Approximation of Free-Discontinuity Problems.* Springer.

[19] Braides, A. [2002]: Γ-*Convergence for Beginners.* Oxford University Press.

[20] Capriz, G. [1989]: *Continua with Microstructure.* Springer.

[21] Capriz, G. [2000]: *Continua with substructure. Part I.* Physical Mesomechanics, 3: 5–13.

[22] Capriz, G. [2000]: *Continua with substructure. Part II.* Physical Mesomechanics, 3: 35–46.

[23] Capriz, G.; Podio-Guidugli, P. [1983]: *Structured continua from a Lagrangian point of view.* Annali di Matematica Pura ed Applicata, 135: 1–25.

[24] Capriz, G.; Podio-Guidugli, P.; Williams, W. [1982]: *On balance equations of materials with affine structure.* Meccanica, 17: 80–84.

[25] Capriz, G.; Virga, E. G. [1990]: *Interactions in generalized continua with microstructure.* Archive for Rational Mechanics and Analysis, 109: 323–342.

[26] Carstensen, C.; Hackl, K.; Mielke, A. [2002]: *Non-convex potentials and microstructures in finite-strain plasticity.* Proceedings of the Royal Society London A, 458: 299–317.

[27] Chadwick, P. [1999]: *Continuum Mechanics. Concise Theory and Problems.* Dover Publications, New York.

[28] Cleveringa, H. H. M.; Van der Giessen, E.; Needleman, A. [1997]: *Comparison of discrete dislocation and continuum plasticity predictions for a composite material.* Acta Materialia, 45: 3163–3179.

[29] Coleman, B. D.; Gurtin, M. E. [1967]: *Thermodynamics with internal state variables.* The Journal of Chemical Physics, 47: 597–613.

[30] Cosserat, E.; Cosserat, F. [1909]: *Sur la Théorie des Corps Deformables.* Dunod, Paris.

[31] Dal Maso, G.; Toader, R. [2002]: *A model for the quasi-static growth of brittle fractures: existence and approximation results.* Archive for Rational Mechanics and Analysis, 162: 101–135.

[32] de Borst, R. [1987]: *Computation of post-bifurcation and post-failure behavior of strain-softening solids.* Computers & Structures, 25: 211–224.

[33] de Borst, R. [2004]: *Damage, material instabilities, and failure.* In Stein, E.; de Borst, R.; Hughes, T. J. R. (Editors): *Encyclopedia of Computational Mechanics*, Vol. 2, pp. 335–373. John Wiley & Sons.

[34] de Borst, R.; Mühlhaus, H. B. [1992]: *Gradient-dependent plasticity: formulation and algorithmic aspects.* International Journal for Numerical Methods in Engineering, 35: 521–539.

[35] Eastgate, L. O.; Sethna, J. P.; Rauscher, M.; Cretegny, T.; Chen, C.-S.; Myers, C. R. [2002]: *Fracture in mode I using a conserved phase-field model.* Physical Review E, 65: 1–10.

[36] Ericksen, J. L.; Truesdell, C. A. [1958]: *Exact theory of stress and strain in rods and shells.* Archive for Rational Mechanics and Analysis, 1: 295–323.

[37] Eringen, A. C. [1976]: *Continuum Physics, Volume IV – Polar and Nonlocal Field Theories.* Academic Press, New York.

[38] Eringen, A. C. [1999]: *Microcontinuum Field Theories I: Foundations and Solids.* Springer.

[39] Eshelby, J. D. [1951]: *The force on an elastic singularity.* Philosophical Transactions of the Royal Society of London A, 244: 87–112.

[40] Eshelby, J. D. [1970]: *Energy relations and the energy-momentum tensor in continuum mechanics.* In Kanninen, M. F.; Adler, W. F.; Rosenfield, A. R.; Jaffee, R. I. (Editors): *Inelastic Behavior of Solids*, pp. 77–115. McGraw-Hill, New York.

[41] Evers, L. P.; Brekelmans, W. A. M.; Geers, M. G. D. [2004]: *Non-local crystal plasticity model with intrinsic SSD and GND effects.* Journal of the Mechanics and Physics of Solids, 52: 2379–2401.

[42] Fleck, N. A.; Hutchinson, J. W. [1997]: *Strain gradient plasticity.* Advances in Applied Mechanics, 33: 295–362.

[43] Fleck, N. A.; Muller, G. M.; Ashby, M. F.; Hutchinson, J. W. [1994]: *Strain gradient plasticity: theory and experiment.* Acta Materialia, 42: 475–487.

[44] Forest, S. [2007]: *Generalized continuum modelling of crystal plasticity.* In *Generalized Continua and Dislocation Theory: Theoretical Concepts, Computational Methods and Experimental Verification.* CISM, International Centre for Mechanical Sciences.

[45] Forest, S. [2009]: *Micromorphic approach for gradient elasticity, viscoplasticity, and damage.* Journal of Engineering Mechanics, 135: 117–131.

[46] Forest, S.; Lorentz, E. [2004]: *Localization phenomena and regularization methods.* In Besson, J. (Editor): *Local Approach to Fracture*, Chapter 11, pp. 311–373. École des Mines de Paris/Les Presses.

[47] Forest, S.; Sievert, R. [2003]: *Elastoviscoplastic constitutive frameworks for generalized continua.* Acta Mechanica, 160: 71–117.

[48] Forest, S.; Sievert, R. [2006]: *Nonlinear microstrain theories.* International Journal of Solids and Structures, 43: 7224–7245.

[49] Francfort, G.; Mielke, A. [2006]: *Existence results for a class of rate-independent material models with nonconvex elastic energies.* Journal für die reine und angewandte Mathematik, 595: 55–91.

[50] Francfort, G. A.; Marigo, J.-J. [1998]: *Revisiting brittle fracture as an energy minimization problem.* Journal of the Mechanics and Physics of Solids, 46: 1319–1342.

[51] Frémond, H. [2001]: *Non-Smooth Thermomechanics.* Springer, 1st Edition.

[52] Frémond, M.; Nedjar, B. [1996]: *Damage, gradient of damage, and principle of virtual power.* International Journal of Solids and Structures, 33: 1083–1103.

[53] Fried, E.; Gurtin, M. E. [1993]: *Continuum theory of thermally induced phase transitions based on an order parameter.* Physica D, 68: 326–343.

[54] Geers, M. G. D.; Ubachs, R. L. J. M.; Engelen, R. A. B. [2003]: *Strongly nonlocal gradient-enhanced finite strain elastoplasticity.* International Journal for Numerical Methods in Engineering, 56: 2039–2068.

[55] Germain, P. [1973]: *La méthode des puissances virtuelles en mécanique des milieux continus.* Journal de Mécanique, 12: 235–274.

[56] Glocker, C. [1995]: *Dynamik von Starrkörpersystemen mit Reibung und Stößen.* Ph.D. Thesis, Fakultät für Maschinenwesen, Technische Universität München.

[57] Green, A. E.; Naghdi, P. M. [1965]: *A general theory of an elastic-plastic continuum.* Archive of Rational Mechanics and Analysis, 18: 251–281.

[58] Griffith, A. A. [1921]: *The phenomena of rupture and flow in solids.* Philosophical Transactions of the Royal Society of London. Series A, 221: 163–198.

[59] Gross, D.; Seelig, T. [2007]: *Bruchmechanik.* Springer.

[60] Gudmundson, P. [2004]: *A unified treatment of strain gradient plasticity.* Journal of the Mechanics and Physics of Solids, 52: 1379–1406.

[61] Gürses, E.; Miehe, C. [2009]: *A computational framework of three dimensional configurational force driven brittle crack propagation.* Computer Methods in Applied Mechanics and Engineering, 198: 1413–1428.

[62] Gurtin, M. [1996]: *Generalized Ginzburg-Landau and Cahn-Hilliard equations based on a microforce balance.* Physica D, 92: 178–192.

[63] Gurtin, M. E. [1979]: *On the energy release rate in quasistatic elastic crack propagation.* Journal of Elasticity, 9: 187–195.

[64] Gurtin, M. E. [2000]: *Configurational Forces as Basic Concepts of Continuum Physics.* Springer.

[65] Gurtin, M. E. [2000]: *On the plasticity of single crystals: free energy, microforces, plastic-strain gradients.* Journal of the Mechanics and Physics of Solids, 48: 989–1036.

[66] Gurtin, M. E. [2002]: *A gradient theory of single-crystal viscoplasticity that accounts for geometrically necessary dislocations.* Journal of the Mechanics and Physics of Solids, 50: 5–32.

[67] Gurtin, M. E. [2003]: *On a framework for small-deformation viscoplasticity: free energy, microforces, strain gradients.* International Journal of Plasticity, 19: 47–90.

[68] Gurtin, M. E. [2006]: *The burgers vector and the flow of screw and edge dislocations in finite-deformation single-crystal plasticity.* Journal of the Mechanics and Physics of Solids, 54: 1882–1898.

[69] Gurtin, M. E. [2008]: *A finite-deformation, gradient theory of single-crystal plasticity with free energy dependent on densities of geometrically necessary dislocations.* International Journal of Plasticity, 24: 702–725.

[70] Gurtin, M. E.; Anand, L. [2009]: *Thermodynamics applied to gradient theories involving the accumulated plastic strain: the theories of Aifantis and Fleck and Hutchinson and their generalization.* Journal of the Mechanics and Physics of Solids, 57: 405–421.

[71] Gurtin, M. E.; Anand, L.; Lele, S. P. [2007]: *Gradient single-crystal plasticity with free energy dependent on dislocation densities.* Journal of the Mechanics and Physics of Solids, 55: 1853–1878.

[72] Gurtin, M. E.; Podio-Guidugli, P. [1996]: *Configurational forces and the basic laws for crack propagation.* Journal of the Mechanics and Physics of Solids, 44: 905–927.

[73] Gurtin, M. E.; Podio-Guidugli, P. [1998]: *Configurational forces and a constitutive theory for crack propagation that allows for kinking and curving.* Journal of the Mechanics and Physics of Solids, 46: 1343–1378.

[74] Hakim, V.; Karma, A. [2009]: *Laws of crack motion and phase-field models of fracture.* Journal of the Mechanics and Physics of Solids, 57: 342–368.

[75] Hall, E. O. [1951]: *The deformation and aging of mild steel. Part III: discussion and results.* Proceedings of the Physical Society of London, 64: 747–753.

[76] Halphen, B.; Nguyen, Q. S. [1975]: *Sur les matériaux standards généralisés.* Journal de Mécanique, 14: 39–63.

[77] Haupt, P. [2000]: *Continuum Mechanics and Theory of Materials.* Springer.

[78] Heinrich, C.; Demoment, G. [2000]: *Minimization of strictly convex functions: an improved optimality test based on Fenchel duality.* Inverse Problems, 16: 795–810.

[79] Hill, R. [1958]: *A general theory of uniqueness and stability in elastic-plastic solids.* Journal of the Mechanics and Physics of Solids, 6: 236–249.

[80] Hill, R. [1962]: *Acceleration waves in solids.* Journal of the Mechanics and Physics of Solids, 10: 1–16.

[81] Hill, R. [1968]: *On constitutive inequalities for simple materials I.* Journal of the Mechanics and Physics of Solids, 16: 229–242.

[82] Hofacker, M.; Welschinger, F.; Miehe, C. [2010]: *A variational-based formulation of regularized brittle fracture.* In *Proceedings in Applied Mathematics and Mechanics*, Vol. 9, pp. 207–208.

[83] Holzapfel, G. A. [2000]: *Nonlinear Solid Mechanics: A Continuum Approach for Engineering.* John Wiley & Sons, New York.

[84] Iben, H. K. [1999]: *Tensorrechnung.* Teubner.

[85] Irwin, G. R. [1957]: *Analysis of stresses and strains near the end of a crack traversing a plate.* Journal of Applied Mechanics, 24: 361–364.

[86] Irwin, G. R. [1958]: *Fracture.* In Flügge, S. (Editor): *Encyclopedia of Physics*, Vol. 6, Elasticity and Plasticity, pp. 551–590. Springer.

[87] Itskov, M. [2007]: *Tensor Algebra and Tensor Analysis for Engineers.* Springer.

[88] Jumikis, A. R. [1964]: *Mechanics of Soils.* New Jersey Van Nostrand.

[89] Kachanov, L. M. [1958]: *Rupture time under creep conditions.* International Journal of Fracture, 97: 26–31.

[90] Kachanov, L. M. [1986]: *Introduction to Continuum Damage Mechanics.* Maritinus Nijhoff Publishers, 1st Edition.

[91] Karma, A.; Kessler, D. A.; Levine, H. [2008]: *Phase-field model of mode III dynamic fracture.* Physical Review Letters, 92: 245510.

[92] Kienzler, R.; Herrmann, G. (Editors) [2000]: *Mechanics in Material Space with Applications to Defect and Fracture Mechanics.* Springer.

[93] Koch, A. [2003]: *Adaptive Finite-Elemente-Berechnungen der nichtlinearen Festkörpermechanik bei kleinen und großen Verzerrungen.* Ph.D. Thesis, Institut für Mechanik (Bauwesen), Lehrstuhl I, Universität Stuttgart.

[94] Kröner, E. [1960]: *Allgemeine Kontinuumstheorie der Versetzungen und Eigenspannungen.* Archive for Rational Mechanics and Analysis, 4: 273–334.

[95] Kuhn, C.; Müller, R. [2010]: *A continuum phase field model for fracture.* Engineering Fracture Mechanics, 77: 3625–3634.

[96] Lee, E. [1969]: *Elastic-plastic deformations at finite strains.* Journal of Applied Mechanics, 36: 1–6.

[97] Lemaitre, J. [1972]: *Evaluation of dissipation and damage in metals submitted to dynamic loading.* In *Proceedings of the International Conference on Mechanical Behavior of Materials*, Vol. 1, pp. 540–549, Kyoto.

[98] Lemaitre, J. [1996]: *A Course on Damage Mechanics.* Springer.

[99] Lemaitre, J.; Chaboche, J.-L. [1990]: *Mechanics of Solid Materials.* Cambridge University Press.

[100] Lemaitre, J.; Desmorat, R. [2005]: *Engineering Damage Mechanics.* Springer.

[101] Lewandowski, J. J.; Greer, A. L. [2006]: *Temperature rise at shear bands in metallic glasses.* Nature Materials, 5: 15–18.

[102] Liebe, T.; Steinmann, P. [2001]: *Theory and numerics of a thermodynamically consistent framework for geometrically linear gradient plasticity.* International Journal for Numerical Methods in Engineering, 51: 1437–1467.

[103] Li, J. C. M. [1984]: *Behavior and properties of shear bands.* Polymer Engineering and Science, 24: 750–760.

[104] Malvern, L. E. [1969]: *Introduction to the Mechanics of a Continuous Medium.* Prentice-Hall, New Jersey.

[105] Mariano, P. M. [2000]: *Configurational forces in continua with microstructure.* Zeitschrift für angewandte Mathematik und Physik, 51: 752–791.

[106] Mariano, P. M. [2001]: *Multifield theories in mechanics of solids.* Advances in Applied Mechanics, 38: 1–93.

[107] Mariano, P. M.; Augusti, G. [1998]: *Multifield description of microcracked continua: a local model.* Mathematics and Mechanics of Solids, 3: 183–200.

[108] Marsden, J. E.; Hughes, T. J. R. [1983]: *Mathematical Foundations of Elasticity.* Dover Publications, New York.

[109] Martin, J. B. [1975]: *Plasticity. Fundamentals and General Results.* The MIT Press, Cambridge, Massachusetts.

[110] Maugin, G. A. [1992]: *The Thermomechanics of Plasticity and Fracture.* Cambridge University Press.

[111] Maugin, G. A. [1993]: *Material Inhomogeneities in Elasticity.* Chapman & Hall, London.

[112] Maugin, G. A.; Morro, A. [1989]: *Constitutive equations in viscoelasticity through the Legendre-Fenchel transformation.* Rheologica Acta, 28: 190–192.

[113] Meschke, G.; Dumstorff, P. [2007]: *Energy-based modeling of cohesive and cohesionless cracks via X-FEM.* Computer Methods in Applied Mechanics and Engineering, 196: 2338–2357.

[114] Miehe, C. [1994]: *Aspects of the formulation and finite element implementation of large strain isotropic elasticity.* International Journal for Numerical Methods in Engineering, 37: 1981–2004.

[115] Miehe, C. [1998]: *Comparison of two algorithms for the computation of fourth-order isotropic tensor functions.* Computers & Structures, 66: 37–43.

[116] Miehe, C. [1998]: *A constitutive frame of elastoplasticity at large strains based on the notion of a plastic metric.* International Journal of Solids and Structures, 35: 3859–3897.

[117] Miehe, C. [1998]: *A formulation of finite elastoplasticity based on dual co- and contra-variant eigenvector triads normalized with respect to a plastic metric.* Computer Methods in Applied Mechanics and Engineering, 159: 223–260.

[118] Miehe, C. [2002]: *Strain-driven homogenization of inelastic microstructures and composites based on an incremental variational formulation.* International Journal for Numerical Methods in Engineering, 55: 1285–1322.

[119] Miehe, C. [2007]: *Geometrische Methoden der Nichtlinearen Kontinuumsmechanik und Kontinuumsthermodynamik.* Lecture Notes, University of Stuttgart.

[120] Miehe, C. [2010]: *A multi-field incremental variational framework for gradient-type standard dissipative solids.* Journal of the Mechanics and Physics of Solids, doi: 10.1016/j.jmps.2010.11.001.

[121] Miehe, C.; Apel, N.; Lambrecht, M. [2002]: *Anisotropic additive plasticity in the logarithmic strain space: modular kinematic formulation and implementation based on incremental minimization principles for standard materials.* Computer Methods in Applied Mechanics and Engineering, 191: 5383–5425.

[122] Miehe, C.; Gürses, E. [2007]: *A robust algorithm for configurational-force-driven brittle crack propagation with* r*-adaptive mesh alignment.* International Journal for Numerical Methods in Engineering, 72: 127–155.

[123] Miehe, C.; Gürses, E.; Birkle, M. [2007]: *A computational framework of configurational-force-driven brittle fracture based on incremental energy minimization.* International Journal of Fracture, 145: 245–259.

[124] Miehe, C.; Hofacker, M.; Welschinger, F. [2010]: *A phase field model for rate-independent crack propagation: robust algorithmic implementation based on operator splits.* Computer Methods in Applied Mechanics and Engineering, 199: 2765–2778.

[125] Miehe, C.; Lambrecht, M. [2001]: *Algorithms for computation of stresses and elasticity moduli in terms of Seth-Hill's family of generalized strain tensors.* Communications in Numerical Methods in Engineering, 17: 337–353.

[126] Miehe, C.; Lambrecht, M.; Gürses, E. [2004]: *Analysis of material instabilities in inelastic solids by incremental energy minimization and relaxation methods: evolving deformation microstructures in finite plasticity.* Journal of the Mechanics and Physics of Solids, 52: 2725–2769.

[127] Miehe, C.; Schotte, J.; Lambrecht, M. [2002]: *Homogenization of inelastic solid materials at finite strains based on incremental minimization principles. Application to the texture analysis of polycrystals.* Journal of the Mechanics and Physics of Solids, 50: 2123–2167.

[128] Miehe, C.; Schröder, J. [1994]: *Post-critical discontinuous localization analysis of small-strain softening elastoplastic solids.* Archive of Applied Mechanics, 64: 267–285.

[129] Miehe, C.; Welschinger, F.; Hofacker, M. [2010]: *A phase field model of electromechanical fracture.* Journal of the Mechanics and Physics of Solids, 58: 1716–1740.

[130] Miehe, C.; Welschinger, F.; Hofacker, M. [2010]: *Thermodynamically consistent phase-field models of fracture: variational principles and multi-field FE implementations.* International Journal for Numerical Methods in Engineering, 83: 1273–1311.

[131] Mielke, A.; Müller, S. [2006]: *Lower semicontinuity and existence of minimizers in incremental finite-strain plasticity.* Zeitschrift für angewandte Mathematik und Mechanik, 86: 233–250.

[132] Mielke, A.; Roubíček, T. [2006]: *Rate-independent damage processes in nonlinear elasticity.* Mathematical Models and Methods in Applied Sciences, 16: 177–209.

[133] Mindlin, R. A. [1964]: *Micro-structure in linear elasticity.* Archive for Rational Mechanics and Analysis, 16: 51–78.

[134] Mindlin, R. A. [1965]: *On the equations of elastic materials with microstructure.* International Journal of Solids and Structures, 1: 73–78.

[135] Moreau, J. J. [1976]: *Application of convex analysis to the treatment of elastoplastic systems.* Lecture Notes in Mathematics, 503: 56–89.

[136] Müller, R.; Maugin, G. A. [2002]: *On material forces and finite element discretizations.* Computational Mechanics, 29: 52–60.

[137] Mumford, D.; Shah, J. [1989]: *Optimal approximations by piecewise smooth functions and associated variational problems.* Communications on Pure and Applied Mathematics, 42: 577–685.

[138] Nádai, A. [1950]: *Theory of Flow and Fracture of Solids, Vol. I.* McGraw-Hill, New York.

[139] Naghdi, P. M. [1990]: *A critical review of the state of finite plasticity.* Journal of Applied Mathematics and Physics (ZAMP), 41: 315–387.

[140] Neilsen, M. K.; Schreyer, H. L. [1993]: *Bifurcations in elastic-plastic materials.* International Journal of Solids and Structures, 30: 521–544.

[141] Nguyen, Q. S. [1973]: *Matériaux élasto-visco-plastiques et élasto-plastiques à potentiel généralisé.* Comptes Rendus Hebdomadaires des Seances de l'Académie des Sciences/A, 277: 915–918.

[142] Nguyen, Q. S.; Andrieux, S. [2005]: *The non-local generalized standard approach: a consistent gradient theory.* Comptes Rendus Mecanique, 333: 139–145.

[143] Nix, W. D.; Gao, H. [1998]: *Indentation size effects in crystalline materials: a law for strain gradient plasticity.* Journal of the Mechanics and Physics of Solids, 46: 411–425.

[144] Nye, J. F. [1953]: *Some geometrical relations in dislocated crystals.* Acta Metallurgica, 1: 153–162.

[145] Ortiz, M.; Repetto, E. A. [1999]: *Nonconvex energy minimization and dislocation structures in ductile single crystals.* Journal of the Mechanics and Physics of Solids, 47: 397–462.

[146] Peerlings, R. H. J. [1999]: *Enhanced damage modelling for fracture and fatigue.* Ph.D. Thesis, Technische Universiteit Eindhoven.

[147] Peerlings, R. H. J.; Geers, M. G. D.; de Borst, R.; Brekelmans, W. A. M. [2001]: *A critical comparison of nonlocal and gradient-enhanced softening continua.* International Journal of Solids and Structures, 38: 7723–7746.

[148] Perzyna, P. [1966]: *Fundamental problems in viscoplasticity.* Advances in Applied Mechanics, 9: 243–377.

[149] Perzyna, P. [1971]: *Thermodynamics of rheological materials with internal changes.* Journal de Mécanique, 10: 391–408.

[150] Petch, N. J. [1953]: *The cleavage strength of polycrystals.* Journal of the Iron and Steel Institute, 174: 25–28.

[151] Prandtl, L. T. [1923]: *Anwendungsbeispiele zu einem Henckyschen Satz über das plastische Gleichgewicht.* Zeitschrift für angewandte Mathematik und Mechanik, 3: 401–406.

[152] Rice, J. R. [1968]: *A path independent integral and the approximate analysis of strain concentration by notches and cracks.* Journal of Applied Mechanics, 35: 379–386.

[153] Rockafellar, R. T. [1987]: *Conjugate Duality and Optimization.* Society for Industrial Mathematics.

[154] Rockafellar, R. T. [1996]: *Convex Analysis.* Princeton Landmarks in Mathematics and Physics.

[155] Salençon, J. [2001]: *Handbook of Continuum Mechanics.* Springer.

[156] Schreyer, H. L. [1990]: *Analytical solutions for nonlinear strain-gradient softening and localization.* Journal of Applied Mechanics, 57: 522–528.

[157] Schreyer, H. L.; Chen, Z. [1986]: *One-dimensional softening with localization.* Journal of Applied Mechanics, 53: 791–797.

[158] Seth, B. R. [1964]: *Generalized strain measure with application to physical problems.* In Reiner, M., Abir D. (Editor): *Second-Order Effects in Elasticity, Plasticity and Fluid Dynamics*, pp. 162–172. Pergamon Press, Oxford.

[159] Šilhavý, M. [1997]: *The Mechanics and Thermodynamics of Continuous Media.* Springer.

[160] Simo, J. C.; Armero, F. [1992]: *Geometrically non-linear enhanced strain mixed methods and the method of incompatible modes.* International Journal for Numerical Methods in Engineering, 33: 1413–1449.

[161] Simo, J. C.; Armero, F.; Taylor, R. L. [1993]: *Improved versions of assumed enhanced strain tri-linear elements for 3D finite deformation problems.* Computer Methods in Applied Mechanics and Engineering, 110: 359–386.

[162] Simo, J. C.; Hughes, T. J. R. [1986]: *On the variational foundations of assumed strain methods.* Journal of Applied Mechanics, 53: 51–54.

[163] Simo, J. C.; Ju, J. W. [1987]: *Strain- and stress-based continuum damage models I. Formulation.* International Journal of Solids and Structures, 23: 821–840.

[164] Simo, J. C.; Ju, J. W. [1987]: *Strain- and stress-based continuum damage models II. Computational aspects.* International Journal of Solids and Structures, 23: 841–869.

[165] Simo, J. C.; Rifai, M. S. [1990]: *A class of mixed assumed strain methods and the method of incompatible modes.* International Journal for Numerical Methods in Engineering, 29: 1595–1638.

[166] Steinmann, P. [1999]: *Formulation and computation of geometrically non-linear gradient damage.* International Journal for Numerical Methods in Engineering, 46: 757–779.

[167] Steinmann, P.; Maugin, G. A. [2005]: *Mechanics of Material Forces.* Springer.

[168] Svendsen, B. [2002]: *Continuum thermodynamic models for crystal plasticity including the effects of geometrically-necessary dislocations.* Journal of the Mechanics and Physics of Solids, 50: 1297–1329.

[169] Taylor, R. L.; Beresford, P. J.; Wilson, E. L. [1976]: *A non-conforming element for stress analysis.* International Journal for Numerical Methods in Engineering, 10: 1211–1219.

[170] Thomas, T. Y. [1961]: *Mathematics in Science and Engineering: Plastic Flow and Fracture in Solids.* Elsevier B. V.

[171] Toupin, R. A. [1964]: *Theories of elasticity with couple stress.* Archive for Rational Mechanics and Analysis, 17: 85–112.

[172] Truesdell, C.; Noll, W. [1965]: *The non-linear field theories of mechanics.* In Flügge, S. (Editor): *Handbuch der Physik*, Vol. 3. Springer.

[173] Vardoulakis, I.; Sulem, J. [1995]: *Bifurcation Analysis in Geomechanics.* Blackie Academic & Professional.

[174] Washizu, K. [1982]: *Variational Methods in Elasticity and Plasticity.* Pergamon Press.

[175] Welschinger, F.; Miehe, C. [2009]: *Variational formulations and FE active set strategies for rate-independent nonlocal material response.* In *Proceedings in Applied Mathematics and Mechanics*, Vol. 8, pp. 10475–10476.

[176] Welschinger, F.; Miehe, C. [2010]: *Configurational-force-based adaptive methods in nonlocal gradient-type inelastic solids.* In *Proceedings in Applied Mathematics and Mechanics*, Vol. 9, pp. 345–346.

[177] WELSCHINGER, F.; ZIMMERMANN, D.; MIEHE, C. [2008]: *A variational formulation of nonlocal materials with microstructure based on dual macro- and micro-balances.* In *Proceedings in Applied Mathematics and Mechanics*, Vol. 7, pp. 4080015–4080016.

[178] WIDMER, A. [2010]: *Variational based formulation of gradient-type J_2-plasticity in the logarithmic strain space.* Technical Report 10-I-10, Institut für Mechanik (Bauwesen), Lehrstuhl I, Universität Stuttgart.

[179] WILSON, E. L.; TAYLOR, R. L.; DOHERTY, W. P.; GHABOUSSI, J. [1973]: *Incompatible displacement models.* In FENVES, S. J. (Editor): *Numerical and Computer Methods in Structural Mechanics*, pp. 43–57. Academic Press, New York.

[180] XIAO, H.; BRUHNS, O. T.; MEYERS, A. [2006]: *Elastoplasticity beyond small deformations.* Acta Mechanica, 182: 31–111.

[181] ZÄH, D. [2009]: *Geometric aspects of strain gradient theories in finite inelasticity and damage mechanics.* Technical Report 09-I-01, Institut für Mechanik (Bauwesen), Lehrstuhl I, Universität Stuttgart.

[182] ZIEGLER, H.; WEHRLI, C. [1987]: *The derivation of constitutive relations from the free energy and the dissipation function.* Advances in Applied Mechanics, 25: 183–238.

[183] ZIENKIEWICZ, O. C.; TAYLOR, R. L.; ZHU, J. Z. [2005]: *The Finite Element Method: Its Basis and Fundamentals.* Elsevier.

[184] ZIMMERMANN, D. [2008]: *Material forces in finite inelasticity and structural dynamics: topology optimization, mesh refinement and fracture.* Ph.D. Thesis, Institut für Mechanik (Bauwesen), Lehrstuhl I, Universität Stuttgart.

Curriculum Vitae

Personal Details

Name	Fabian Richard Welschinger
Date of Birth	March 26, 1980
Place of Birth	Radolfzell am Bodensee, Germany
Parents	Brigitte and Alois Welschinger
Siblings	Patrick and Markus Welschinger

School Education/Civilian Service

1986-1990	Elementary School: Radolfzell-Markelfingen
1990-1999	Secondary School: „Friedrich-Hecker-Gymnasium Radolfzell“
June 1999	General Qualification for University Entrance („Abitur“)
1999-2000	Basic Civilian Service: „Rettungsdienst Deutsches Rotes Kreuz Radolfzell“

University Education

2000-2005	Studies of Civil Engineering, Universität Stuttgart
2003-2004	Studies of Civil Engineering, University of Calgary, Canada
Fall 2005	Graduation as Diplom-Ingenieur

Professional Occupation

Since 2005	Research Associate and Assistant Lecturer, Institute of Applied Mechanics (Civil Engineering), Universität Stuttgart

In dieser Schriftenreihe bisher erschienene Berichte:

I-1(1996)	*Theoretische und algorithmische Konzepte zur phänomenologischen Beschreibung anisotropen Materialverhaltens*, J. Schröder, Dissertation, 1996.
I-2(1996)	*Zur Theorie und Numerik finiter elastoplastischer Deformationen von Schalentragwerken*, B. Seifert, Dissertation, 1996.
I-3(1996)	*Zur Modellierung des künstlichen Infrarot-Dichroismus in Polymerfolien bei großen Verformungen*, J. Buhler, Dissertation, 1996.
I-4(1998)	*Verfahren zur Ermittlung der Erdbebenlasten mit Berücksichtigung des stochastischen Charakters des Bebens*, S. Zhang, Dissertation, 1998.
I-5(1998)	*Zur Beschreibung finiter Deformationen von Polymeren: Experimente, Modellbildung, Parameteridentifikation und Finite-Elemente-Formulierung*, J. Keck, Dissertation, 1998.
I-6(1999)	*Berechnungsverfahren instationär erregter Systeme im Frequenzbereich*, A. Jaworek, Dissertation, 1999.
I-7(2000)	*Homogenisierungsmethoden der nichtlinearen Kontinuumsmechanik unter Beachtung von Stabilitätsproblemen*, J. Schröder, Habilitation, 2000.
I-8(2002)	*Theorie und Numerik von Materialinstabilitäten elastoplastischer Festkörper auf der Grundlage inkrementeller Variationsformulierungen*, M. Lambrecht, Dissertation, 2002.
I-9(2002)	*Mikromechanisch motivierte Modelle zur Beschreibung finiter Deformationen gummiartiger Polymere: physikalische Modellbildung und numerische Simulation*, F. Lulei, Dissertation, 2002.
I-10(2003)	*Adaptive Finite-Elemente-Berechnungen der nichlinearen Festkörpermechanik bei kleinen und großen Verzerrungen*, A. Koch, Dissertation, 2003.
I-11(2003)	*Theorie und Numerik der Parameteridentifikation von Materialmodellen der finiten Elastizität und Inelastizität auf der Grundlage optischer Feldmeßmethoden*, G. Scheday, Dissertation, 2003.
I-12(2004)	*Approaches to the Description of Anisotropic Material Behaviour at Finite Elastic and Plastic Deformations, Theory and Numerics*, N. Apel, Dissertation, 2004.
I-13(2004)	*Temperaturabhängige Beschreibung visko-elasto-plastischer Deformationen kurzglasfaserverstärkter Thermoplaste: Modellbildung, Numerik und Experimente*, S. Rieger, Dissertation, 2004.
I-14(2005)	*Zur Parameteridentifikation komplexer Materialmodelle auf der Basis realer und virtueller Testdaten*, A. Rieger, Dissertation, 2005.
I-15(2005)	*Viskoelastisches Verhalten von Elastomeren bei finiten Verzerrungen: Experimente, Modellierung und Simulationen*, H. Zecha, Dissertation, 2005.

I-16(2005) *Mehrskalenmodelle in der Festkörpermechanik und Kopplung von Mehrgittermethoden mit Homogenisierungsverfahren*, C.G. Bayreuther, Dissertation, 2005.

I-17(2005) *Static and Dynamic Homogenization Analyses of Discrete Granular and Atomistic Structures on Different Time and Length Scales*, J. Dettmar, Dissertation, 2005.

I-18(2006) *Incompatibility and Instability Based Size Effects in Crystals and Composites at Finite Elastoplastic Strains*, M. Becker, Dissertation, 2006.

I-19(2007) *Aspects of Energy Minimization in Solid Mechanics: Evolution of Inelastic Microstructures and Crack Propagation*, E. Gürses, Dissertation, 2007.

I-20(2007) *Micro-Macro Approaches to Rubbery and Glassy Polymers: Predictive Micromechanically-Based Models and Simulations*, S. Göktepe, Dissertation, 2007.

I-21(2008) *Material Forces in Finite Inelasticity and Structural Dynamics: Topology Optimization, Mesh Refinement and Fracture*, D. Zimmermann, Dissertation, 2008.

I-22(2010) *Thermoviscoplasticity of Glassy Polymers: Experimental Characterization, Parameter Identification and Model Validation*, J. Méndez Diez, Dissertation, 2010.

I-23(2010) *On the Formulation and Numerical Implementation of Dissipative Electro-Mechanics at Large Strains*, D. Rosato, Dissertation, 2010.

I-24(2011) *A Variational Framework for Gradient-Extended Dissipative Continua. Application to Damage Mechanics, Fracture, and Plasticity*, F. Welschinger, Dissertation, 2011.